On the hierarchy of electronic and magnetic energy scales in novel 3*d*, 4*d* and 5*d* transition metal oxides probed by X-ray techniques

Davide Pincini

A dissertation submitted in fulfillment of the requirements
for the degree of

Doctor of Philosophy

University College London
Department of Physics and Astronomy

United Kingdom
November 29, 2018

I, Davide Pincini, confirm that the work presented in this thesis is my own. Where information has been derived from other sources, I confirm that this has been indicated in the work.

Abstract

Transition metal oxides (TMOs) represent the natural playground for the investigation of the exotic phases produced by electronic correlations, which include high-temperature superconductivity, giant magnetoresistance and topological insulators. The peculiar electronic and magnetic properties of TMOs stem from the interplay between the electron-electron correlations, the crystal field and the spin-orbit coupling (SOC) of the transition metal (TM) d valence electrons. The balance of these energy scales significantly depends on the TM element considered: moving from the $3d$ to the $5d$ row of the periodic table, the electronic correlations decrease due to the larger size of the atomic orbitals, while SOC increases as a result of the increased atomic charge.

In this work, I present three separate case studies of $3d$, $4d$ and $5d$ TMOs which highlight the impact of the competing interactions just mentioned on the electronic and magnetic properties of the system. Concerning $3d$ TMOs, I investigate the magnetic ground state of a family of weak ferromagnets, where the weak SOC is responsible for the appearance of a net magnetisation in the main antiferromagnetic order. I then examine the intermediate case of the $4d$ oxide Ca_2RuO_4. Here, electronic correlations, SOC and octahedral distortions act on an equal footing to determine the TM ground state. In particular, I show how the crystal field tuning achieved by La substitution affects the electronic and magnetic properties. Finally, I address the spin-wave spectrum of the electron-doped perovskite iridate $(Sr_{1-x}La_x)_2IrO_4$, where the strong SOC of $5d$ electrons gives rise to a spin-orbit entangled Mott state with peculiar exchange interactions.

Most of the experimental findings are the results of measurements performed by means of several synchrotron radiation scattering and absorption techniques: the latter proved to be extremely powerful and versatile in the investigation of many aspects of the physics of the systems discussed.

Impact statement

The results presented in this thesis contribute to our fundamental understanding of materials with strongly correlated electrons and thus advance the field of solid-state physics. In particular, some of the measurements address magnetic properties of potential interest for information storage and processing (spintronics) and for the development of a complete theory of high-temperature superconductivity. The work here discussed has resulted in several publications in peer-reviewed journals of interest for the general physics and condensed matter physics community.

The measurements have also prompted and contributed to the technical development of X-ray techniques for the investigation of the properties of solids. These include new approaches based on interference methods to address the so-called *phase problem* in scattering experiments (i.e. the loss of the scattering phase in the measured intensity) and the extension of existing techniques to the "tender" region of the X-ray spectrum ($1 - 5$ keV) between the energy ranges of most "soft" (< 1 keV) and "hard" (> 5 keV) synchrotron X-ray facilities. The impact of these technical improvements go beyond the specific materials discussed in this thesis and will be beneficial for the whole solid-state physics community.

List of publications

1. **D. Pincini**, L.S.I Veiga, C.D. Dashwood, F. Forte, M. Cuoco, R.S. Perry, P. Bencok, A.T. Boothroyd, D.F. McMorrow. "*Tuning of the Ru^{4+} ground-state orbital population in the $4d^4$ Mott insulator Ca_2RuO_4 achieved by La doping*", arXiv:1810.11044 (2018). Submitted to Physical Review B.

2. **D. Pincini**, F. Fabrizi, G. Beutier, G. Nisbet, H. Elnaggar, V.E. Dmitrienko, M.I Katsnelson, Y.O. Kvashnin, A.I. Lichtenstein, V.V. Mazurenko, E.N. Ovchinnikova, O.V. Dimitrova and S.P. Collins. "*Role of the orbital moment in a series of isostructural weak ferromagnets*", Physical Review B **98**, 104424 (2018).

3. **D. Pincini**, S. Boseggia, R. Perry, M.J. Gutmann, S. Riccò, L.S.I. Veiga, C.D. Dashwood, S.P. Collins, G. Nisbet, A. Bombardi, D.G. Porter, F. Baumberger, A.T. Boothroyd and D.F. McMorrow. "*Persistence of antiferromagnetic order upon La substitution in the $4d^4$ Mott insulator Ca_2RuO_4*", Physical Review B **98**, 014429 (2018).

4. **D. Pincini**, J.G. Vale, C. Donnerer, A. de la Torre, E.C. Hunter, R. Perry, M. Moretti Sala, F. Baumberger and D.F. McMorrow. "*Anisotropic exchange and spin-wave damping in pure and electron-doped Sr_2IrO_4*", Physical Review B **96**, 075162 (2017).

5. G. Beutier, S.P. Collins, O.V. Dimitrova, V.E. Dmitrienko, M.I Katsnelson, Y.O. Kvashnin, A.I. Lichtenstein, V.V. Mazurenko, A.G.A. Nisbet, E.N. Ovchinnikova and **D. Pincini**. "*Band Filling Control of the Dzyaloshinskii-Moriya Interaction in Weakly Ferromagnetic Insulators*", Physical Review Letters **119**, 167201 (2017).

6. J.G. Vale, S. Calder, C. Donnerer, **D. Pincini**, Y.G. Shi, Y. Tsujimoto, K. Yamaura, M. Moretti Sala, J. van den Brink, A.D. Christianson and D.F. McMorrow. "*Evolution of the Magnetic Excitations in $NaOsO_3$ through its Metal-Insulator Transition*", Physical Review Letters **120**, 227203 (2018).

7. J. G. Vale, S. Calder, C. Donnerer, **D. Pincini**, Y. G. Shi, Y. Tsujimoto, K. Yamaura, M. Moretti Sala, J. van den Brink, A.D. Christianson and D.F. McMorrow. "*Crossover from itinerant to localized magnetic excitations through the metal-insulator transition in $NaOsO_3$*". Physical Review B **97**, 184429 (2018).

8. S. Calder, J. G. Vale, N. Bogdanov, C. Donnerer, **D. Pincini**, M. Moretti Sala, X. Liu, M.H. Upton, D. Casa, Y.G. Shi, Y. Tsujimoto, K. Yamaura, J.P. Hill, J. van den Brink, D.F. McMorrow and A.D. Christianson. "*Strongly gapped spin-wave excitation in the insulating phase of $NaOsO_3$*". Physical Review B **95**, 020413(R) (2017).

9. C. Donnerer, M. C. Rahn, M. Moretti Sala, J. G. Vale, **D. Pincini**, J. Strempfer, M. Krisch, D. Prabhakaran, A. T. Boothroyd, and D. F. McMorrow. "*All-in-all-Out Magnetic Order and Propagating Spin Waves in $Sm_2Ir_2O_7$*". Physical Review Letters **117**, 037201 (2016).

Acknowledgements

It has been quite a journey, made of many experiments around the world, countless days spent analysing data and writing proposals and papers, conferences and meetings and, above all, an incredible community of people which I had the privilege to be a part of. They all contributed, in different ways, to make the past four years an enriching and memorable experience, which I will always look back on with a mixture of joy and nostalgia. Some of them, however, deserve a special mention.

I would like to express my gratitude to my supervisors, Des and Steve, for several reasons: first, for giving me the amazing opportunity to join their group, take part in cutting-edge scientific research and travelling around the world for experiments and conferences and, second, for always having faith in my potential and providing me a stress-free working environment, with an unparalleled freedom to choose my methods and pursue my ideas. They have been incredible mentors from both a scientific and, most importantly, a personal level: I realize now how lucky I was to have them as my supervisors. I will always bring with me Steve's impressive scientific intuition and original (sometimes crazy) ideas and Des's ability of writing a story out of scientific data (as well as his constant insights into English language idioms, my favourite of which remains "by the close of play").

I would like to thank all the rest of the I16 team at Diamond which welcomed me in the past four years: Gareth, Federica, Ben, Alessandro, Dan, Isabel and Rob. Gareth deserves a special mention for being an extremely patient and supportive local contact and for his company during the many beamtimes and our friendly conversations (about robots and much more): I hope I managed to convince him that doing research in magnetism can sometimes be at least as exciting as his multiple scattering calculations. Many thanks also to the I10 team for the support provided during the numerous beamtimes and for making available their SQUID setup. In particular, thanks to Peter for the nice time on the beamline. Thanks also to Robin Perry for the effort he put into the sample preparation and characterisation, without which all my work would have not been possible, and Sara Riccò for her help provided during the sample growth and characterisation and insightful discussions.

I must mention my I15-1 office mates, Phil, Dean and Michael (now replaced

by Geoff) and the rest of the I15 team Simone and Dom for having accepted me in the I15 family despite my I16 origin. Thanks for our conversations about politics, sports and much more over lunch (my diet will never be the same after the adoption of the canteen “soup and salad” combo), the countless Nespresso coffees in our office, the wine tasting and pub sessions. I hope Dean will keep working on his Italian after I will have left. Remaining at Diamond, I would also like to thank Diego, Giulio, Stefania and Marco for the company, with a particular mention for Diego and Giulio for our lunches and table tennis games together and their constant need for always disruptive “coffee” (“tea”) breaks.

A special thanks to the many people I had the pleasure to share endless hours of beamtime and questionable meals at the various facilities’ canteens (or to simply have an interesting conversation) with, in particular, the other members of my group in London - Christian, James, Larissa, Cameron and Stefano - our collaborators in Oxford - Marein and Henrik - and Matteo, Marco and Andrea in Grenoble. A few special mentions. Firstly Marein, for the pleasant moments spent together drinking, eating and conversing about always interesting topics in Oxford. I will always be glad of Marein’s appreciation for my “decency” in keeping a tidy beamline log-book. Secondly Matteo and Andrea, who have been my life companions for the past ten years, from our studies in Milan all the way up to now. Thanks for our nice conversations about science and future choices, dinners in town (particularly memorable the cheese-based feasts at La Ferme à Dédé) and our skiing sessions in sometimes prohibitive weather conditions (and prohibitive slopes) during my frequent visits to Grenoble. Thirdly Marco who, as well as being one of the best local contacts anybody can wish for, made my beamtimes on ID20 always fruitful and pleasant. Thanks for the insightful conversations about science, the all-important experiment soundtracks and eccentric macro names and, above all, the advice and support provided for my future choices in the last period. Thanks also to Stefano for his support during my last few beamtimes and our nice chats. Of all the beamtimes I have done, I will always have a nice memory of my first time in the USA for an experiment at the APS with James and Matteo - and the following trip to Chicago with Matteo spent eating deep-dish pizza and hunting movie locations - as well as my trips to Japan and California.

The past four years would have not been the same without all the people I met during the HERCULES school in Grenoble, with whom I spent some of the most memorable moments of my life both during the school in Grenoble and Villigen (I was in the lucky group which did not go to Paris) and afterwards, during our weekends in Copenhagen and Rome. I feel like I am now part of a big group of friends spread all over the world, which I will always be able to count on. A special

mention goes to Pau, Steffen, Giacomo, Mikkel, Ursula, Monika, Casper, Kirill, Ashley, Øystein, Liya, Anastasya, Stephanie, Lourdes, Natalia and the Italian crew: Salvo, Stefano "il Checchia", Mattia, Tommaso, Ilaria, Andrea Troian, Valentina, Margherita, Veronica and Giorgia. I would also like to mention the people I met in Prague for the SCES2017 conference and San Francisco for ICM2018 for the stimulating exchange of ideas and pleasant moments spent together.

A sincere thanks to all the new friends I made during my wonderful time in Oxford, a city which I love and in which I have always felt at home. Thanks to Erik, Diego, Dimmy, Federico, Steve, Davide, Michele, Donato, Sara, Mirco, Marta, Marie, Valentina, Simone Sala and the French crew Arnaud, David, Camille, Elsa, Remie and Benoit for all the memorable experiences we have been through together, including the endless bus rides to and from Harwell Campus chatting and planning weekends together. A special mention goes to the Oxford old guard formed by Erik, Diego and Dimmy (with Federico providing a convincing replacement after Erik moved to Bristol) for all the fun we had together during trips, movies, lunches, dinners, brunches, picnics, drinks, unforgettable nights out and, in particular, for taking part in the dreadful "sequence" The Four Candles, Wig and Pen and Maxwell's (or Atik) way too often. I will never forget these moments.

I would also like to thank my family for their incredible support throughout my entire life and for the nice moments spent together in London and Oxford during my stay in England. I apologize for not being present enough in the past four years and I hope I have made you proud.

A heartfelt thanks to my girlfriend Myriam for all the beautiful memories we created together in the past four years and for her unconditional love and support. Thank you for putting up with me constantly being away for experiments and busy writing my thesis in the past few months. I am looking forward to the next step in my life, with you.

Finally, I would like to apologise to all the people I neglected during the past few months spent writing this thesis and trying to figure out what I really wanted to do with my life after the PhD. It was an incredibly busy and stressful, but in a way exciting at the same time, period of my life, during which I was lucky enough to have the opportunity to meet and speak to many people who provided me with great insights and advice. Thanks to all their help and support, I believe I am a more mature person now than I used to be just a few months ago. I will do my best to make the most of all I learned.

All this would, of course, not have been possible without the financial assistance of the Impact Studentship jointly awarded by Diamond Light Source and UCL.

Contents

1 Introduction **31**

1.1 Overview of the physics of strongly-correlated transition metal oxides 35

1.1.1 Hubbard model: Mott-Hubbard insulators 35

1.1.2 Exchange interactions in a Mott insulator 36

1.1.3 Single-atom physics for an isolated atom: Hund's coupling and SOC 38

1.1.4 Single-atom physics for an atom in a crystal: crystal field . . 40

1.2 Outline of the thesis and authors' contributions 43

2 Overview of experimental techniques **47**

2.1 Magnetic scattering with X-rays 49

2.1.1 Elastic scattering: magnetic diffraction 51

2.1.1.1 Non-resonant X-ray magnetic scattering 52

2.1.1.2 Resonant elastic X-ray scattering 56

2.1.1.3 The Materials and Magnetism beamline (I16) at the Diamond Light Source 60

2.1.2 Resonant inelastic X-ray scattering 64

2.1.2.1 ID20 beamline at the European Synchrotron Radiation Facility 67

2.2 Absorption measurements with X-rays 71

2.2.1 X-ray absorption spectroscopy 71

2.2.2 X-ray magnetic circular dichroism 73

2.2.3 I10: Beamline for Advanced Dichroism Experiments (BLADE) at the Diamond Light Source 77

3 The 3d case: systematic investigation of the ground-state magnetic properties of the weak ferromagnets (Mn,Co,Ni)CO_3 and $FeBO_3$ **79**

3.1 Introduction 80

3.2 Crystal and magnetic structure: the Dzyaloshinskii-Moriya interaction 82

3.2.1 Magnetic structure factors and rotating field measurements . 88
3.3 Bulk magnetisation measurements 91
3.4 Band filling control of the Dzyaloshinskii-Moriya interaction 95
3.4.1 Magnetic domain imaging 105
3.5 Orbital contribution to the magnetic moment across the series 110
3.6 Role of the orbital moment in $CoCO_3$ 118
3.6.1 Orbital moment contribution investigated by XMCD 118
3.6.2 Magnetocrystalline anisotropy 121
3.6.3 Forbidden charge scattering 126
3.6.3.1 Experimental data and empirical model 126
3.6.3.2 Microscopic model and role of the SOC 136
3.6.4 Magneto-striction 138
3.7 Conclusions 141

4 The 4d case: persistence of antiferromagnetic order and Ru^{4+} orbital population tuning upon La substitution in $Ca_{2-x}La_xRuO_4$ 143
4.1 Introduction 144
4.2 Overview of the magnetic and electronic properties of $Ca_{2-x}La_xRuO_4$ 146
4.2.1 Pure Ca_2RuO_4 146
4.2.2 Impact of chemical substitution on Ca_2RuO_4 153
4.3 Ru^{4+} single-ion Hamiltonian 156
4.4 Sample growth and characterisation 163
4.4.1 Bulk magnetisation measurements 164
4.4.2 Structural characterisation by neutron diffraction 166
4.5 Impact of La doping on the low-temperature magnetic structure studied by REXS 169
4.6 Evolution of the Ru^{4+} 4d orbital population upon La substitution: an O K-edge XANES study 183
4.7 Impact of La doping on the local electronic properties of the Ru^{4+} ion: a Ru L-edge XANES and XMCD study 193
4.8 Conclusions 200

5 The 5d case: anisotropic exchange and spin-wave damping in $(Sr_{1-x}La_x)_2IrO_4$ 203
5.1 Introduction 204
5.2 Overview of the magnetic and electronic properties of $(Sr_{1-x}La_x)_2IrO_4$ 205
5.2.1 Pure Sr_2IrO_4 205
5.2.2 $(Sr_{1-x}La_x)_2IrO_4$: impact of La doping 211

5.3 Sr_2IrO_4 magnetic Hamiltonian . . . 214
5.3.1 Ir^{4+} single-ion Hamiltonian . . . 215
5.3.2 Exchange interaction between $J_{\text{eff}} = 1/2$ magnetic moments 219
5.3.3 Single-magnon excitation spectrum . . . 223
5.3.3.1 Magnetic excitations in pure and electron-doped Sr_2IrO_4: previous reports . . . 228
5.4 Magnetic excitations in $(Sr_{1-x}La_x)_2IrO_4$ studied by means of RIXS at the Ir L_3 edge . . . 232
5.4.1 Doping evolution of long-range magnetic order . . . 233
5.4.2 Single-magnon excitation spectrum . . . 235
5.4.2.1 Energy gap and impact of the momentum resolution 240
5.4.2.2 Anisotropic magnon damping . . . 243
5.4.2.3 Energy dispersion: anisotropic exchange interactions . . . 245
5.5 Conclusions . . . 251

6 Conclusions and future perspectives **253**
6.1 The 3d case: the weak ferromagnets (Mn,Co,Ni)CO_3 and $FeBO_3$ . . . 253
6.2 The 4d case: $Ca_{2-x}La_xRuO_4$ . . . 255
6.3 The 5d case: $(Sr_{1-x}La_x)_2IrO_4$ . . . 257

Appendices **259**

A Weak ferromagnets: supporting data **259**

B $Ca_{2-x}La_xRuO_4$: additional measurements and data analysis details **265**
B.1 Anisotropic tensor of susceptibility (ATS) scattering . . . 265
B.2 Representational analysis of the space group Pbca with the propagation vector $\mathbf{k} = (0,0,0)$ . . . 268
B.3 Neutron structural refinement details . . . 270

C $(Sr_{1-x}La_x)_2IrO_4$: alternative Hamiltonian and details of the spectra **273**
C.1 Alternative magnetic Hamiltonian: XYh_4 model . . . 273
C.2 Charge excitations . . . 276

Bibliography **279**

List of Figures

1.1 Schematic representation of the interplay of electronic and structural degrees of freedom at the origin of complex correlated phases in transition metal oxides. 33

1.2 Evolution of the electronic correlations U and the spin-orbit coupling constant λ across the d block of the periodic table (top) and resulting phase digram proposed by Witczak-Krempa *et al.* [7] (bottom). 34

1.3 Schematic representation of the evolution of the band structure as a function of the electron-electron Coulomb repulsion to hopping matrix element ratio U/t in the Hubbard model of Eq. (1.1). 36

1.4 Schematic representation of the d energy levels of an isolated TM atom (blue sphere) and in the case of a TM atom in octahedral coordination with O atoms (green spheres). 40

2.1 The brilliance of X-ray sources as a function of time. 48

2.2 Schematic representation of the diffraction geometry of a magnetic scattering experiment in the common case of a vertical scattering plane and linearly polarised incident X-rays perpendicular to the latter (σ polarisation). 53

2.3 Schematic of the two-step REXS process. 56

2.4 Schematic view of the optics and experimental hutch of the Materials and Magnetism beamline (I16) of the DLS. 61

2.5 (a) Schematic of the RIXS two-step process. (b) Different elementary excitations probed by RIXS in condensed matter systems and their approximate energy scales in strongly correlated electron materials such as TMOs. 65

2.6 Schematic setup of the optics hutch and RIXS end station of the ID20 beamline of the ESRF at the Ir L_3 edge X-ray energy ($E \approx$ 11.2 keV). 67

2.7 (a) Drawing of the RIXS spectrometer at beamline ID20 of the ESRF. Adapted from Ref. [62]. (b) Rowland circle geometry which the ID20 spectrometer in (a) is based on. 69

2.8 XAS and XMCD spectra of iron. Figure adapted from Ref. [80]. . . 74

2.9 (a) Schematic view of the Beamline for Advanced Dichroism Experiments (BLADE) at the DLS. (b) Drawing of the high-field magnet in the absorption end station. 77

3.1 Trigonal crystal structure (space group $R\bar{3}c$, No. 167) of the weak ferromagnets ACO_3 (A = Mn,Co,Ni) and $FeBO_3$ in the hexagonal axes description. 83

3.2 (a) Local environment of the TM ion at $(0,0,0)$ (magnetic sublattice A) and its six nearest neighbours (magnetic sublattice B) in the $R\bar{3}c$ crystal structure. (b),(c) Possible spin arrangements for a fixed direction of an external magnetic field. **H**. 85

3.3 Schematic representation of the effect of the rotating magnetic field used to perform the scattering measurements discussed in Secs. 3.4 and 3.5 on the magnetic structure of the weak ferromagnets for the representative case of a specular geometry. 89

3.4 Magnetisation *vs* field measurements for the compounds of the series A(C,B)O_3 (A = Mn,Fe,Co,Ni) 92

3.5 Field cooled (FC) and zero-field cooled (ZFC) magnetisation *vs* temperature for different members of the carbonates series. 93

3.6 Normalized (009) intensity in the σ-π' polarisation channel as a function of the magnetic field direction η measured off-resonance (blue squares) and at the quadrupole resonance energy (red circles) for $0^\circ \leq \psi \leq 30^\circ$ in the different compounds of the series below their respective Néel transition temperature. 97

3.7 Imaginary part of the quadrupole resonance term $Q(E)$ discussed in the text for the different compounds of the series as a function of the incident X-ray energy. 101

3.8 Dependence of the (009) space-group forbidden reflection in the σ-π' polarisation channel on the magnetic field direction η for different energy values across the K pre-edge quadrupolar resonance in $CoCO_3$ ($E \approx 7.708$ keV). 102

3.9 (a) Imaginary part of the quadrupole resonance term $Q(E)$ discussed in the text for $CoCO_3$ as a function of the incident X-ray energy. The inset schematically represents the expected magnetic field dependence of the (009) reflection in the σ-π' channel for $\psi > 30^\circ$ at E_1 (red curve) and E_2 (green curve). (b) Temperature dependence of the (009) total scattered intensity measured at the two energies marked by the vertical dashed lines in (a). 105

3.10 $CoCO_3$ magnetic domain pattern as a function of temperature. . . . 106

3.11 $CoCO_3$ magnetic domain pattern at T = 8 K for different temperature cycles across the Néel transition and corresponding difference. . 109

3.12 Temperature dependence of the (009) magnetic reflection for different members of the carbonates series. 112

3.13 Dependence of representative magnetic reflections on the magnetic field direction for two different polarisation states of the diffracted X-ray beam in $CoCO_3$. 113

3.14 Orbital-to-spin angular momenta ratio for the different compounds of the series as a function of the momentum transfer. 116

3.15 Absorption spectra measured with the external magnetic field parallel (XAS^-) and antiparallel (XAS^+) to the helicity of the incident circularly polarised light and corresponding circular dichroism (XMCD). The data were collected at T = 3 K using a magnetic field $\mu_0 H = 0.4$ T applied in the **ab** plane of the crystal. 119

3.16 Absorption spectra measured with the external magnetic field parallel (XAS^-) and antiparallel (XAS^+) to the helicity of the incident circularly polarised light and corresponding circular dichroism (XMCD). The data were collected at T = 3 K by applying a magnetic field $\mu_0 H = 14$ T along the crystallographic **c** axis (normal incidence). 120

3.17 Direction of the weak net magnetisation **M** as a function of the external magnetic field **H** direction in the basal plane of the crystal for different values of the anisotropy parameter $h = \frac{\mu_0 HM}{K}$ discussed in the text. 121

3.18 Calculated dependence of the (009) magnetic reflection in the σ-π' polarisation channel on the external magnetic field direction for different values of the anisotropy parameter $h = \frac{\mu_0 HM}{K}$ discussed in the text. 123

3.19 Dependence of the $CoCO_3$ (009) reflection on the magnetic field direction in σ-π' at different temperatures across the Néel transition at $T_N = 16.7(5)$ K. 124
3.20 Fit detail of two representative data sets of Fig. 3.19 measured well below and close to the Néel transition. 125
3.21 Temperature dependence of the in-plane magnetocrystalline anisotropy constant K in $CoCO_3$. 126
3.22 (a),(b) Magnetic field direction dependence of the $(\bar{2}07)$ intensity as a function of the sample azimuth ψ for two different polarisation states of the diffracted X-ray beam. (c),(d) Global fit of the $(\bar{2}07)$ magnetic field direction dependence shown in (a),(b). 127
3.23 $(\bar{2}07)$ intensity magnetic field dependence in (left) σ-σ' and (right) σ-π' at (a),(b) $\psi = 65°$ and (c),(d) $\psi = 80°$. 128
3.24 (a),(b) Magnetic field direction dependence of the $(\bar{2}07)$ intensity as a function of the incident X-ray energy for two different polarisation states of the diffracted X-ray beam at $\psi = 65°$. (c),(d) Global fit of the $(\bar{2}07)$ magnetic field direction dependence shown in (a),(b). 129
3.25 $(\bar{2}07)$ multiple scattering energy and azimuth (ψ) dependence in the σ-σ' polarisation channel. 130
3.26 Magnetic field directiondependence of the forbidden charge scattering amplitude $C^{FS}_{\sigma\sigma'}$ normalized to its peak value. The drawing illustrates the empirical model for the Co electron cloud distortion discussed in the text. 131
3.27 (a) $(\bar{2}07)$ σ-σ' intensity dependence on the magnetic field direction for different temperatures below the Néel transition. (b) Magnetic and forbidden charge amplitudes as a function of temperature resulting from the fit shown in (a). 132
3.28 Multiple scattering (a) σ-σ' amplitude and (b) σ-π' intensity azimuthal dependence. 133
3.29 Dependence of the forbidden charge scattering amplitude in $CoCO_3$ on the canting angle of the Co^{2+} magnetic moments. 134
3.30 Peak amplitude of the forbidden charge scattering contribution of Fig. 3.26 for different space-group forbidden reflections in $CoCO_3$. . 135
3.31 Multiplet calculations of the Co L_3 absorption spectrum measured with the external magnetic field (a) antiparallel and (b) parallel to the helicity of the incident circularly polarised light and (c) corresponding XMCD for different values of the trigonal distortion parameter D_σ in eV. 137

3.32 Charge density of the Co^{2+} $3d$ valence electrons for an external field direction (a) 0°, (b) 60° and (c) 90° away from the crystallographic **a** axis as derived from the multiplet calculations discussed in the text. 137
3.33 Magnetic field dependence of the $(\bar{2}07)$ forbidden charge scattering amplitude (normalized to its peak value) calculated using the Co^{2+} atomic form factor derived from the multiplet calculations discussed in the text. 139
3.34 (a) Angular shift of the (119) Bragg peak as a function of the magnetic field direction at T = 5 K. (b) Relative deformation of the in-plane lattice parameters of the $R\bar{3}c$ hexagonal unit cell at T = 5 K as obtained from the fit of the (119) angular shift shown in (a). . . . 139
3.35 (a) (119) magnetic field direction dependence as a function of temperature. (b) Temperature dependence of the (119) intensity oscillations as extracted from the fits shown in (a). 141

4.1 Ca_2RuO_4 crystal structure (*Pbca* space group, No. 61) highlighting the RuO_6 octahedra tilt and rotation discussed in the text. (b) Magnetic ordering of neighbouring RuO_2 layers for the A- and B-centred magnetic modes [172] 147
4.2 Ca_2RuO_4 structural changes as a function of temperature reported in the literature. 148
4.3 Summary of the inelastic neutron scattering investigation on the magnetic excitations in Ca_2RuO_4 by Jain *et al.* [169]. 149
4.4 Summary of the combined angle-resolved photoemission spectroscopy (ARPES) and first-principle investigation on the band structure in the paramagnetic insulating phase of Ca_2RuO_4 by Sutter *et al.* [175]. 152
4.5 $Ca_{2-x}La_xRuO_4$ temperature-doping phase diagram. 154
4.6 Summary of the bulk measurements performed on single crystals of $Ca_{2-x}La_xRuO_4$ with varying La content x by Fukazawa and Maeno [179]. (a) Temperature dependence of the in-plane resistivity. (b) Magnetic susceptibility in the **ab** plane of the crystal as a function of temperature. 155
4.7 Schematic representation of the energy levels of a TM ion with four electrons in the d orbitals (d^4) in a cubic crystal field ($10Dq$) under the influence of strong (a) spin-orbit interaction λ or (b) tetragonal compressive field Δ. 157

4.8 Summary of the electronic structure calculations of the Ru^{4+} ion in Ca_2RuO_4 performed by different authors. (a) Electronic structure of the Ru^{4+} ion in Ca_2RuO_4 as a function of the relative strength δ of the tetragonal field (Δ) and SOC (λ) as calculated by Jain *et al.* [169]. (b) Ru^{4+} multiplet structure as a function of the SOC constant for $\Delta = 0.3$ eV calculated by Das *et al.* [178]. 158
4.9 Calculated orbital hole population dependence of the Ru^{4+} ground state on the tetragonal field ($\Delta < 0$ for tetragonal compression and $\Delta > 0$ for tetragonal elongation) and SOC (λ) relative strength [187] 161
4.10 Bulk magnetisation SQUID measurements for the undoped ($x = 0$) and doped ($x = 0.05, 0.10$) samples. 164
4.11 Magnetisation *vs* field at different temperatures below the Néel transition in the $x = 0.05$ compound. 165
4.12 Structural changes of $Ca_{2-x}La_xRuO_4$ as a function of doping at T = 10 K. 169
4.13 Ru L_3 and L_2 energy resonances of the $(0\,1\,3)$ magnetic diffraction peak at different temperatures across the Néel transition in the undoped sample. 172
4.14 Temperature dependence of the $(0\,1\,3)$ (dark blue circles) and $(0\,1\,4)$ magnetic diffraction peaks in the undoped and $x = 0.05$ (light blue squares), $x = 0.07$ (red triangles) samples, respectively. 173
4.15 Polarisation dependence of magnetic diffraction peaks in the (a) undoped, (b) $x = 0.05$ and (c) $x = 0.07$ samples at T = 7 − 8 K. 174
4.16 Azimuthal dependence of the $(0\,1\,3)$ magnetic diffraction peak in the undoped sample at T = 8 K. 175
4.17 Comparison between the $(0\,1\,3)$ (blue circles) and $(0\,1\,4)$ (red squares) Ru L_3 resonances in the (a) undoped, (b) $x = 0.05$ and (c) $x = 0.07$ sample. 177
4.18 Ru L_3 and L_2 energy resonances of the $(0\,1\,4)$ magnetic diffraction peak at different temperatures across the Néel transition in the (a) $x = 0.05$ and (b) $x = 0.07$ sample. 178
4.19 Intensity ratio of the Ru L_3 and L_2 energy resonances of magnetic diffraction peaks as a function of the La content. 179
4.20 Azimuthal dependence of the (a) $(0\,1\,4)$ and (b) $(1\,0\,3)$ magnetic diffraction peaks in the doped samples at T = 7 − 10 K. 180
4.21 Intensity maps of the $(0\,0\,4)$ Bragg peak and $(0\,1\,4)$ magnetic reflection (T = 8 K, $\psi = 0°$) in the $x = 0.05$ sample as a function of the incident X-ray beam position on the crystal (beam size 0.1×0.1 mm^2). 181

4.22 (a) $Ca_{2-x}La_xRuO_4$ temperature-doping phase diagram showing the paramagnetic metallic (P-M), paramagnetic insulating (P-I) and AFM insulating (AFM-I) phases. (b) Hole occupancy ratio $n_{xy}/n_{yz,zx}$ at different temperatures as a function of the La content extracted from the angular dependence of the apical and in-plane O $2p$ - Ru t_{2g} features of the XANES spectra. 184
4.23 O K-edge XANES spectra for the parent (blue circles) and $x = 0.07$ (red squares) compound collected at normal incidence and low temperature. 185
4.24 XANES spectra collected at different values of the angle θ_S between the incident X-ray beam and the sample surface normal (**c** axis) for samples with different La contents and at different temperature values within the insulating region of the phase diagram. 186
4.25 Angular dependence of the apical and in-plane O $2p$ - Ru t_{2g} features of the XANES spectra in the (a) parent, (b) $x = 0.05$ and (c) $x = 0.07$ compound at low temperature. 187
4.26 XANES spectra collected at different values of the angle θ_S between the incident X-ray beam and the sample surface normal in (a) the $x = 0.12$ sample at T = 10 K and the (b) $x = 0.05$, (c) $x = 0.07$ and (d) $x = 0.12$ sample at room temperature. 189
4.27 (a) Angular dependence of the apical and in-plane O $2p$ - Ru t_{2g} features of the XANES spectra in the metallic $x = 0.12$ sample at low temperature as extracted through the fit shown in Fig. 4.26(a). (b) Apical and in-plane angular dependence calculated using Eq. (4.6) with $n_{xy}/n_{yz,zx} = 1.5$. 191
4.28 Parent compound XAS spectra measured in TEY at T = 10 K. . . . 194
4.29 Normalized XAS (black circles) and corresponding XMCD (red squares) measured in TFY at T = 10 K for different levels x of La content. 197
4.30 (a) XANES L_3/L_2 BR as a function of the doping level for two different temperatures. (b) Ratio of the orbital (L) and spin (S) magnetic moments as extracted from the application of the sum rules to the XMCD data at T = 10 K of Fig. 4.29. 198

5.1 (a) Sr_2IrO_4 tetragonal crystal structure (space group $I4_1/acd$, $a = b = 5.48$ Å, $c = 25.8$ Å). (b) Magnetic ordering of the Ir^{4+} moments. (c) Detail of the moment arrangement of different IrO_2 planes inside the unit cell. 205

5.2 Overview of the static magnetic order in Sr_2IrO_4 investigated by REXS at the Ir L_3 absorption edge. (a) Resonant enhancement of the $(1\,0\,22)$ magnetic reflection and Ir L_3 XANES spectrum. Adapted from Ref. [215]. (b),(c) l dependence (with l out-of-plane Miller index) of magnetic Bragg peaks arising from the main AFM order of the Ir moments (b) and the moments canting (c) measured at T = 10 K. Adapted from Ref. [51]. The inset in (b) shows the temperature dependence of the $(1\,0\,24)$ scattered intensity. Adapted from Ref. [242]. 206

5.3 (a) Crystal and magnetic structure of a representative IrO_2 plane. (b) First BZ for the two choices of unit cell shown in (a). 208

5.4 Sr_2IrO_4 optical conductivity measurements from Ref. [254]. The diagram on the right shows the effect of the cubic crystal field ($10Dq$), SOC and electronic correlations (U) on the Ir $5d$ bands and highlights the origin of the α and β features seen in the optical conductivity. 209

5.5 Summary of the ARPES investigation in $(Sr_{1-x}La_x)_2IrO_4$ from Ref. [222]. (a) Constant energy cuts for $x = 0$ ($E = E_F - 200$ meV), 0.01 ($E = E_F - 10$ meV) and 0.05 ($E = E_F$). (b) Tight binding calculation of the Fermi surface performed considering $U = 0$ and $1 + 2x$ free carriers per Ir site. (c) Detail of the pseudogap values along the Fermi arcs in the $x = 0.05$ sample. 210

5.6 Bulk resistivity (a) and magnetisation (b) as a function of temperature for pure Sr_2IrO_4 and different levels x of La substitution. 212

5.7 Temperature-doping phase diagram proposed by Chen *et al.* [87]. . . 214

5.8 Electron energy level diagram of the Ir^{4+} ion showing the effect of the relevant term in the Hamiltonian in order of decreasing strength (going from left to right) for the representative case of tetragonal elongation. 215

5.9 (a) Ir^{4+} eigenvalues of Eq. (5.2) as a function of the tetragonal distortion Δ. (b) Relative contributions of the different t_{2g} orbitals to the ground state wave function $|0,\pm\rangle$. 216

5.10 Real-space representation of the $|J_{\text{eff}} = 1/2, +\rangle_{ab}$ charge density. . . 218

5.11 Ir-O-Ir 180°-bond geometry relevant for the case of Sr_2IrO_4 and Ir t_{2g} and O p orbitals which contribute to the superexchange interaction between the Ir^{4+} magnetic moment in the model discussed in the text. 221

5.12 Ir^{4+} magnetic moment canting angle ϕ (in units of the IrO_6 octahedra rotation α) as a function of the tetragonal distortion parameter $\theta = 1/2 \arctan[2\sqrt{2}\lambda/(\lambda - 2\Delta)]$. 222

5.13 Energy (a) and spectral weight (b) of the in-plane (dashed line) and out-of-plane (solid line) single-magnon modes in the model of Eq. (5.10) calculated for $J_{ex} = 60$ meV, $J'_{ex} = -20$ meV, $J''_{ex} = 15$ meV, $J_z = -1.8$ meV and $J_{xy} = 1.8$ meV 225

5.14 Energy (left) and spectral weight (right) of the 2DAH model linear spin-wave solutions for vanishing (a) and finite (b) values of the anisotropy parameter Δ_λ. 226

5.15 Sr_2IrO_4 single-magnon (a) energy and (b) spectral weight as a function of the in-plane momentum transfer reported by Kim *et al.* [236]. Figure adapted from Ref. [236]. 228

5.16 $(Sr_{1-x}La_x)_2IrO_4$ single-magnon energy dispersion reported by (a) Gretarsson *et al.* [248] and (b) Liu *et al.* [247]. 229

5.17 (a) RIXS spectra collected along high-symmetry directions of the first BZ in Sr_2IrO_4 by Kim *et al.* [237]. Adapted from Ref. [237] (b),(c) Single-magnon energy dispersion and spectral weight in-plane momentum dependence extracted by Vale *et al.* [242] fitting the RIXS spectra shown in (a). Adapted from Ref. [242]. 231

5.21 Proposed $(Sr_{1-x}La_x)_2IrO_4$ temperature-doping phase diagram based on the REXS measurements presented in this section. 235

5.22 RIXS spectra as a function of the in-plane momentum transfer $\mathbf{Q}_\perp$ along high-symmetry directions of the $(0\,0\,33)$ first BZ for (a) $x = 0$, (b) $x = 0.01$, (c) $x = 0.04$ and (d) $x = 0.1$. 236

5.23 Extended RIXS spectra collected at high-symmetry $\mathbf{Q}_\perp$ values of the $(0\,0\,33)$ first BZ as a function of the doping level. 237

5.24 Fit detail of representative RIXS spectra for (a) $x = 0$, (b) $x = 0.01$, (c) $x = 0.04$ and (d) $x = 0.1$. 238

5.25 Doping level dependence of the low-energy region of the RIXS spectra at (a) $(0,0)$ and (b) (π,π). 240

5.26 Impact of the RIXS spectrometer momentum resolution at (a) (π,π) and (b) $(0,0)$ in the case of gapless magnetic excitations ($\Delta_\lambda = 0$). . 241

5.27 Calculated values of the measured vs *real* spin-wave energy gap in the case of $\Delta Q_\perp = 0.18\,\text{Å}^{-1}$ (solid lines) and an ideal spectrometer with $\Delta Q_\perp = 0$ (dashed lines). 242

5.28 Doping level dependence of the low-energy region of the RIXS spectra at two different $\mathbf{Q}_\perp$ values along the (a) antinodal and (b) nodal direction . . . 244
5.29 Single-magnon Lorentzian lifetime broadening for (a) $x = 0$, (b) $x = 0.01$, (c) $x = 0.04$ and (d) $x = 0.1$. . . . 246
5.30 Q-resolution-corrected single-magnon energy dispersion for (a) $x = 0$, (b) $x = 0.01$, (c) $x = 0.04$ and (d) $x = 0.1$. . . . 247
5.31 Single-magnon spectral weight for different values x of La content. . 250

A.1 Dependence of representative $MnCO_3$ magnetic reflections on the magnetic field direction for two different polarisation states of the diffracted X-ray beam. . . . 261
A.2 Dependence of $FeBO_3$ magnetic reflections on the magnetic field direction for two different polarisation states of the diffracted X-ray beam. . . . 262
A.3 Dependence of $FeBO_3$ magnetic reflections on the magnetic field direction for two different polarisation states of the diffracted X-ray beam. . . . 262
A.4 Dependence of the $NiCO_3$ (009) magnetic reflection on the magnetic field direction for two different polarisation states of the diffracted X-ray beam. . . . 263

B.1 Ru L_3 and L_2 energy resonances of the (a) (003) ($\psi = 90°$) and (b) (013) ($\psi = 0°$) ATS scattering peaks at different temperatures across the Néel transition in the $x = 0.05$ sample. The inset in (a) shows the polarisation dependence of the (003) reflection measured at $E = 2.838$ keV. . . . 266
B.2 Azimuthal dependence of the (a) (003) and (b) (013) ATS scattering peaks at (a) $E = 2.967$ keV and (b) $E = 2.9704$ keV in the $x = 0.05$ sample. . . . 266
B.3 Temperature dependence of the (001), (003) and (013) ATS scattering peaks in the $x = 0.05$ sample. . . . 267

C.1 Energy (left) and spectral weight (right) of the XYh_4 model linear spin-wave solutions for (a) vanishing anisotropy and (b),(c) different values of the anisotropy parameters D and e. . . . 274
C.2 (a) Parent compound RIXS spectra as a function of the in-plane momentum transfer $\mathbf{Q}_\perp$ along the nodal direction of the (0033) first BZ. (b) Fit detail of the $(0,0)$ spectrum. . . . 277

List of Tables

3.1 The Moriya rules [91] which govern the DM vector **D** between two spins at points A and B with a mid-point at C. 88

3.2 Spontaneous magnetisation at low temperature and Néel transition temperature resulting from the VSM-SQUID measurements and reported in the literature. 94

3.3 Experimental and theoretical values of the canting angle. 95

3.4 Spin and orbital angular momenta in units of $\hbar$ for the different compounds of the series A(C,B)O_3 (A = Mn,Fe,Co,Ni) as derived from DFT calculations and measured by means of NXMS. 110

3.5 Hamiltonian parameters used to perform the multiplet calculations of the Co^{2+} ground-state wave function in $CoCO_3$ and corresponding spin and orbital angular momenta expectations values. 136

4.1 Summary of the results of the neutron structural refinement for the parent and La-doped samples at T = 10 K and room temperature. . . 167

4.2 Space-group forbidden magnetic reflections arising from the main AFM order of the two magnetic modes in Ca_2RuO_4 [172] and from the moment canting in the A-centred magnetic structure. 170

5.1 Nearest-neighbour (J_{ex}), next-nearest-neighbour (J'_{ex}) and third-nearest-neighbour (J''_{ex}) isotropic exchange integrals and anisotropy parameter Δ_λ for different values of the La content x as reported by different authors. 230

5.2 Measured and Q-resolution-corrected magnon energy gap values for the different doping concentrations. 239

5.3 Best-fit parameters of the 2DAH model as extracted from the Q-resolution-corrected single-magnon dispersion (Fig. 5.30) for the different doping concentrations. The values of the anisotropic exchange integrals of the model of Eq. (5.10) derived from a similar fit are also reported. 249

5.4 Comparison of the anisotropy parameter Δ_λ derived from the present investigation with previous values reported by other authors. 249

A.1 Space-group forbidden reflections measured for each compound of the series A(C,B)O_3 (A = Mn, Fe, Co, Ni) along with the relevant experimental parameters and the average $I(Q)/s(Q)$ ratio over all temperatures and sample azimuth values. 260

B.1 Basis vectors for the space group *Pbca* with $\mathbf{k} = (0,0,0)$. 270

B.2 R factors, goodness of fit and components of the thermal ellipsoid tensor (in units of Å^2) resulting from the neutron structural refinement at T = 10 K. 271

B.3 R factors, goodness of fit and components of the thermal ellipsoid tensor (in units of Å^2) resulting from the neutron structural refinement at T = 300 K. 272

Chapter 1

Introduction

Contents

1.1 Overview of the physics of strongly-correlated transition metal oxides 35

1.1.1 Hubbard model: Mott-Hubbard insulators 35

1.1.2 Exchange interactions in a Mott insulator 36

1.1.3 Single-atom physics for an isolated atom: Hund's coupling and SOC 38

1.1.4 Single-atom physics for an atom in a crystal: crystal field 40

1.2 Outline of the thesis and authors' contributions 43

Transition metal oxides (TMOs) host some of the most intriguing phenomena in condensed matter physics [1]. Prominent examples include high-temperature superconductivity in copper oxides [2], colossal magnetoresistance in manganese oxides [3], multiferroicity [4] and other charge- and spin-ordered states. These phases are extremely interesting in terms of the fundamental understanding of the underlying physics while offering, at the same time, great potential for future multifunctional materials with applications in various fields, such as information storage and processing [5, 6]. The exceptional properties of TMOs can largely be attributed to the strong correlations between electrons, which arise from the electron-electron Coulomb repulsion (U). The latter competes with other relevant energy scales (Hund's coupling, bandwidth, crystal field...) and produces a complex interplay between charge, spin, orbital and lattice degrees of freedom (Fig. 1.1). The resulting correlated phases pose one of the greatest challenges to our understanding of emergent phenomena in condensed matter systems.

Electronic correlations are expected to be the strongest for transition metals (TMs) in the 3d series of the periodic table (Fig. 1.2) due to the presence of well-localised atomic d orbitals. Moving to the heavier 4d and 5d TMs, the electronic correlations tend to decrease as a result of the increased radius of the d valence orbitals caused by the screening of the core electrons. However, the larger nuclear charge gives rise to a significantly enhanced spin-orbit coupling (SOC), which can produce a sizeable splitting of the electronic levels. The corresponding narrow energy bands can then be affected by the moderate electronic correlations [7, 8]. The competition between the electronic correlations and SOC is represented in Fig. 1.2, which shows a schematic phase diagram as a function of U and the SOC constant λ recently proposed by Witczak-Krempa *et al.* [7]. On the left-hand side of the diagram are the conventional 3d TMOs with negligible SOC (e.g. copper and manganese oxides). In this regime, one finds simple metals or band insulators for small U values and Mott insulators for large U: in the former case the electronic properties are governed by the interactions of the electrons with the periodic lattice, while in the latter they are dictated by the electron-electron Coulomb repulsion. At larger values of the SOC constant λ, a whole new series of exotic phases of matter may be expected [7]: for moderate electronic correlations, as is the case for 5d TMOs, these include, among others, topological insulators [9–12] and Weyl semi-metals [10, 11, 13]. Within the 5d series particular attention has been attracted by iridium (and to a lesser extent osmium) oxides, after the report of a novel spin-orbit coupled Mott insulating state [8].

Although Fig. 1.2 captures some general trends of the physics of TMOs, the situation is more complicated in most practical cases. This is due to the fact that other

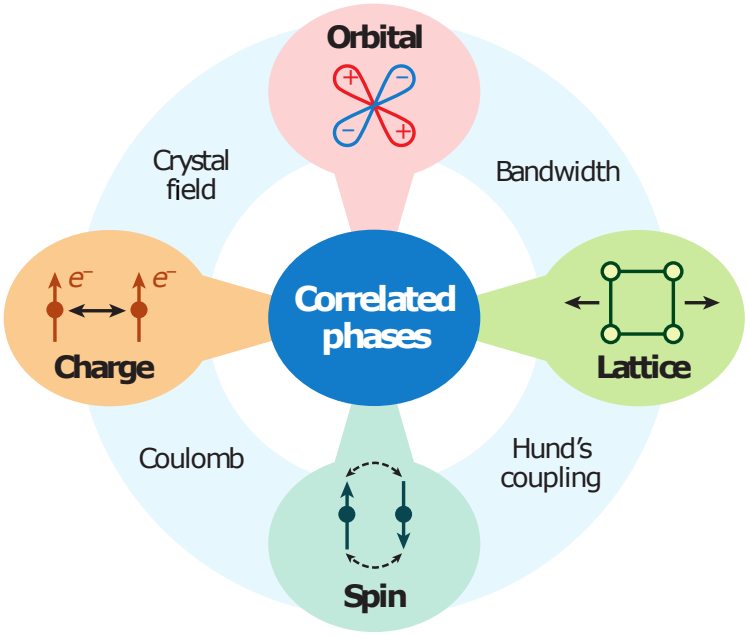

Figure 1.1: Schematic representation of the interplay of electronic and structural degrees of freedom at the origin of complex correlated phases in TMOs. Figure taken from Ref. [6].

energy scales, such as the already mentioned Hund's coupling and crystal field, can generally contribute to the electronic and magnetic properties of the system. The resulting ground state will then depend on the exact balance of all different contributions which is, in turn, subject to the details of the specific compound studied. The crystal field, for instance, is determined by the local crystalline environment surrounding the TM atom and ground states with significantly different properties can be present in compounds with different crystal symmetries. As a result, the physics of TMOs is extremely rich: each compound has to be considered separately and can exhibit novel and sometimes unexpected properties.

The present work focuses on three different case studies of oxides containing $3d$ (Mn, Fe, Co, Ni), $4d$ (Ru) and $5d$ (Ir) TM elements (see Fig. 1.2). In each compound, I will discuss how the competition between the different energy scales impacts the ground state and the corresponding low-energy physics. Particular emphasis will be devoted to the role of SOC in the electronic and magnetic properties of the system. As I will extensively show in the experimental chapters, the treatment can be significantly simplified using perturbation theory whenever one of the energy scales is predominant compared to the others (as in the case for SOC in iridium oxides). On the other hand, those cases where several interactions compete on an equal footing (as in ruthenium oxides) are much more challenging. A more detailed introduction to the scientific case behind the study of each compound will be provided in the corresponding experimental chapters. In this chapter, Sec. 1.1

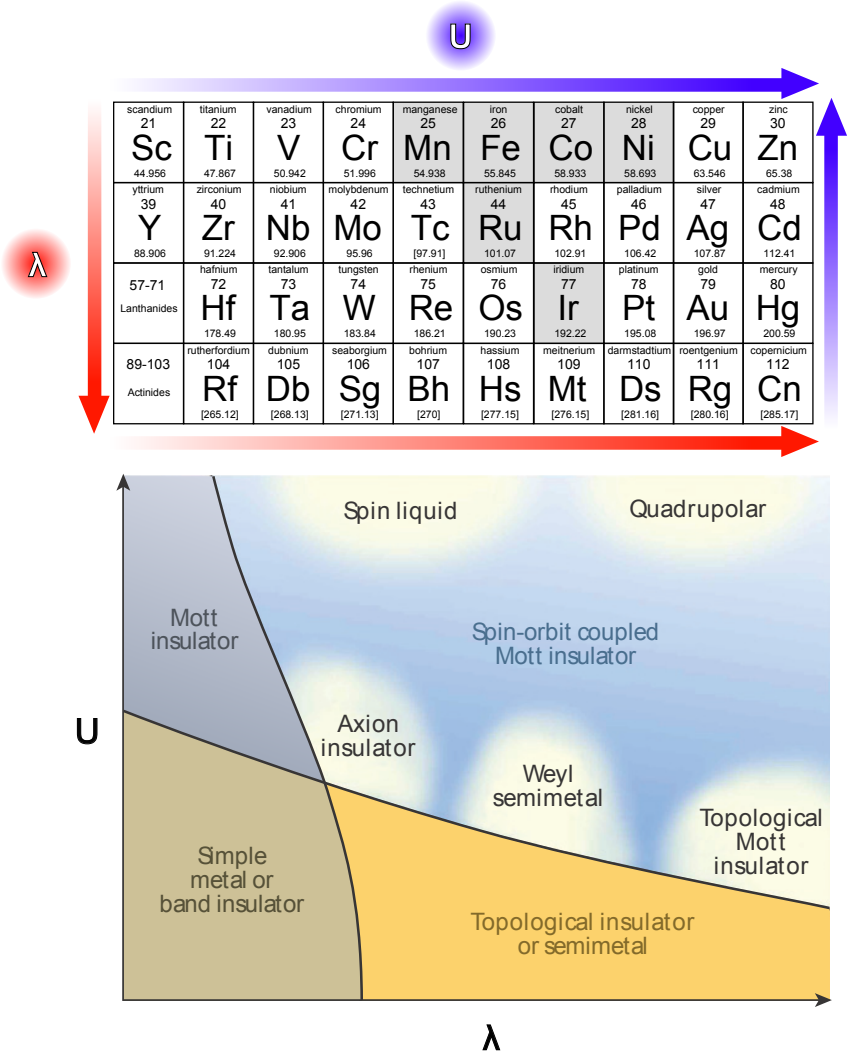

Figure 1.2: Evolution of the electronic correlations U (blue arrows) and the SOC constant λ (red arrows) across the d block of the periodic table (top) and resulting phase digram proposed by Witczak-Krempa *et al.* [7] (bottom). The TM elements entering the composition of the oxides discussed in the present work are highlighted through the shaded regions.

provides the reader with a brief overview of the main ingredients of the physics of TMOs which will be helpful to understand the experimental discussion (the reader is referred to Khomskii [1] for a more extensive treatment), while a more detailed outline of the thesis with the different authors' contributions is given in Sec. 1.2.

1.1 Overview of the physics of strongly-correlated transition metal oxides

1.1.1 Hubbard model: Mott-Hubbard insulators

The compounds discussed in this thesis are Mott insulators (also referred to as Mott-Hubbard insulators). In these materials the insulating state is not caused by the periodic potential of the crystal lattice, such as in ordinary band insulators, but is due to the electron-electron interaction U [14–16]. The Hamiltonian of the system is given by the Hubbard model [14, 15]:

$$\mathscr{H} = -t \sum_{\langle ij \rangle, \sigma} (c^{\dagger}_{i\sigma} c_{j\sigma} + h.c.) + U \sum_{i} n_{i\uparrow} n_{i\downarrow} \tag{1.1}$$

where $c^{\dagger}_{i\sigma}$ and $c_{i\sigma}$ are the creation and annihilation operators of electrons at site i with spin σ, t is the hopping matrix element, $n_{i\sigma} = c^{\dagger}_{i\sigma} c_{i\sigma}$ is the density of electrons with spin σ on site i and the summation $\langle ij \rangle$ runs over nearest neighbours. Here, I have considered for simplicity a one-dimensional chain of atoms with one electron level per site, so that one can put only two electrons with opposite spins at each site. The first term in Eq. (1.1) favours the hopping of each electron to neighbouring sites, with the consequent formation of a doubly occupied site (*doublon*) and a hole. The doublon and the hole can move across the crystal and thus contribute to the delocalisation of the electronic charge. This leads to the formation of an energy band of width $W = 2zt$, where z is the number of nearest neighbours. The formation of a doublon-hole pair causes a total energy gain equal to W, as resulting from a kinetic energy gain for both the electron and the hole equal to $W/2$. However, a doubly occupied site also costs the energy of Coulomb repulsion U: the latter is expressed by the second contribution in Eq. (1.1), which will then favour a situation where the electrons remain localised at the corresponding sites.

The band structure for a system of N sites with $n = 1$ electrons per site arising from Eq. (1.1) is schematically represented in Fig. 1.3. For small U the system is a metal with a half-filled energy band containing $2N$ states. At the critical value $U_{\text{crit}} \sim W$ a so-called Mott transition to an insulating state occurs, where a fully occupied lower Hubbard band (LHB) with N states is separated by an energy gap $E_g \sim U - W$ from an empty upper Hubbard band (UHB) with N states. In real materials, a metal-to-insulator transition (MIT) can be driven by a change in pres-

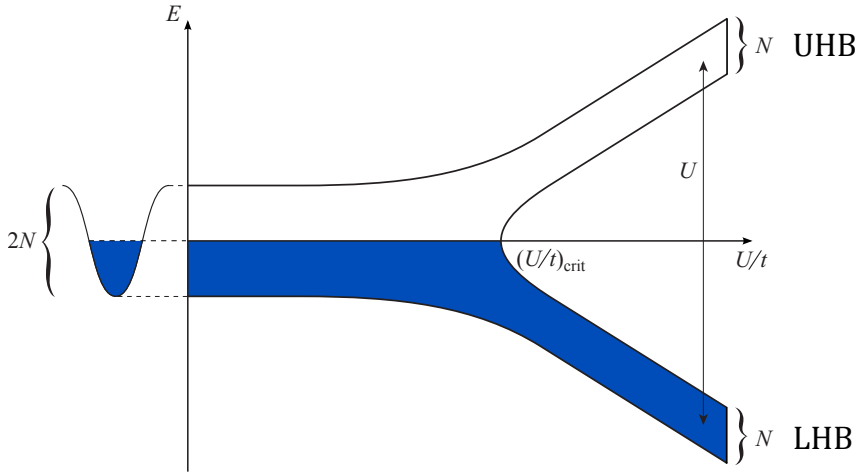

Figure 1.3: Schematic representation of the evolution of the band structure as a function of the electron-electron Coulomb repulsion to hopping matrix element ratio U/t in the Hubbard model of Eq. (1.1) for a system with N sites and one electron per site. $(U/t)_{\text{crit}}$ represents the critical value at which the Mott transition from a metallic state with a half-filled band to a Mott insulating state with a fully occupied LHB and an empty UHB occurs. Figure adapted from Ref. [1].

sure, temperature or composition and can be accompanied by a change in the crystal and/or magnetic structure (see Imada *et al.* [17] for more details). The role played by the electronic correlations and structural distortions in the transition varies from one compound to another, but is united by the essential ingredients outlined above. The situation can be made even more complex by the fact that more than one band can take part in the Mott transition, with the initial bands being degenerate or not depending, for instance, on the presence of a significant crystal field. In this case the electronic correlations can act differently on each sub-band and result in a rich phenomenology of possible ground states [18]. As mentioned in relation to Fig. 1.2, the Coulomb repulsion decreases significantly in going from $3d$ ($U \approx 3-6$ eV) to $5d$ ($U \approx 1.5-2$ eV) TMs.

1.1.2 Exchange interactions in a Mott insulator

In a Mott insulator the electronic correlations force the electrons to remain localised at each site. As a result, the magnetic properties can be described in terms of localised spins or, more generally, localised magnetic moments. In TMOs, magnetism arises from the unpaired electrons in the TM d orbitals. Given the electron localisation, the direct exchange interaction between the corresponding spins in neigh-

bouring sites is normally negligible[1]. The dominant exchange mechanism is the so-called *superexchange* [19], which can be derived by considering the hopping term in Eq. (1.1) as a small perturbation to the fully localised ground state with one electron per site generated by the Coulomb repulsion. The fundamental process at the origin of superexchange is a double hopping of an electron from a site i to a site j and back to site i and can be understood in terms of the simple model with one electron per site considered earlier. For parallel spins, this process is forbidden by the Pauli exclusion principle. For antiparallel alignment, on the other hand, it results in the energy gain $\Delta E = 2t^2/U$: the t^2 term in the numerator arises from the fact that two hopping events are involved, while the denominator corresponds to the energy of the intermediate state with a doubly occupied site (as prescribed by second-order perturbation theory). Therefore superexchange tends to favour an antiparallel alignment of neighbouring spins, thus leading to an antiferromagnetic (AFM) ground state. It is possible to show [20] that the magnetic state of the system can be described by the following effective Heisenberg Hamiltonian:

$$\mathscr{H}_{\text{eff}} = J \sum_{\langle ij \rangle} \mathbf{S}_i \cdot \mathbf{S}_j \,, \quad J = \frac{2t^2}{U} \tag{1.2}$$

where $\mathbf{S}_i$ and $\mathbf{S}_j$ are the spins at site i and j, respectively[2]. Although it has the form of the well-known Heisenberg exchange interaction, superexchange is caused by a decrease of the kinetic energy of the electrons due to the delocalisation produced by the hopping mechanism [1].

In real TMOs the magnetic exchange can be significantly more complicated and is not necessarily AFM. The resulting magnetic structure will depend on several factors, including the specific geometry of the material, the presence of different possible exchange routes and the specific orbital structure (occupancy and degeneracy) of the ions involved in the exchange. Moreover, in many oxides, including the ones investigated in the present work, the superexchange between two neighbouring TM cations is mediated by an intermediate oxygen anion: in this case hopping occurs via the oxygen $2p$ orbitals. There are many possible cases to consider, each one leading to a generally different strength and sign of the superexchange constant. These are generally formulated as a set of rules, known as Goodenough-Kanamori-

[1] The direct exchange constant is given by $J = \int \psi_1^*(\mathbf{r})\psi_2^*(\mathbf{r}')\frac{e^2}{|\mathbf{r}-\mathbf{r}'|}\psi_1(\mathbf{r}')\psi_2(\mathbf{r})$, where ψ_1 and ψ_2 are two distinct one-electron wave functions and $\mathbf{r}$ and $\mathbf{r}'$ are the electron coordinates. The strength of J directly depends on the degree of overlap of the two wave functions.

[2] The sum of Eq. (1.2) is carried out over the indices i and j independently, so that each pair of spins is counted twice. Certain authors define the sum so to count each interaction only once: in this case the correct definition of the exchange constant is $J = 4t^2/U$.

Anderson rules [19, 21–23] (see Khomskii [1] for more details). In general, AFM interactions are encountered much more often than ferromagnetic (FM) ones in oxides. In fact, all compounds considered in the present work exhibit an AFM ground state. It is worth noticing at this point that the magnetic interactions in real materials can be significantly more complex than the ones of Eq. (1.2) and additional anisotropic terms can in general be present. Detailed discussions of the Hamiltonians describing the materials investigated in the context of this thesis are provided in the respective chapters.

1.1.3 Single-atom physics for an isolated atom: Hund's coupling and SOC

The electronic and magnetic properties of TMOs can be often understood in terms of the single-atom[3] physics of the TM element, which is determined by the valence d shell. For d electrons ($l = 2$), there are $2l + 1 = 5$ different orbital states ($l_z = 2, 1, 0, -1, -2$). In an isolated atom, these levels are degenerate, as illustrated in Fig. 1.4. The ground state of a system of n electrons (each with spin $s = 1/2$ and orbital quantum number $l = 2$) is given by Hund's rules:

- electrons fill the different levels so to maximize their total spin S;
- among different possible configurations with maximum total spin S, or maximum multiplicity $(2S+1)$, the ground state is the one with maximum possible orbital angular momentum L, or maximum multiplicity $(2L+1)$;
- the total atomic spin $\mathbf{S} = \sum_i \mathbf{s}_i$ and orbital $\mathbf{L} = \sum_i \mathbf{l}_i$ angular momenta couple together to produce a total angular momentum $\mathbf{J} = \mathbf{S} + \mathbf{L}$ characterised by the possible values of the quantum number $J = L+S, L+S-1, \ldots |L-S|$. For a less than half-filled shell, the ground state is the one with $J = |L-S|$ (so-called *normal multiplet structure*), while for a more than half-filled shell it is the one with $J = L+S$ (so-called *inverted multiplet structure*).

The interaction leading to the first Hund's rule is often called the intra-atomic Hund's exchange and is usually written in the form [1]

$$\mathscr{H}_{\text{Hund}} \sim -J_H \sum_{\alpha \neq \beta} \left(\frac{1}{2} + 2\mathbf{s}_{i\alpha} \cdot \mathbf{s}_{i\beta} \right) + \text{const.} \tag{1.3}$$

[3] I will often use the term *ion* instead of atom when referring to the TMs and the oxygens in a crystal. This is due to the fact that the nature of the bonding is in the many cases of ionic character and the TM (oxigen) assumes a positive (negative) charge.

where J_H is called Hund's exchange constant and $\mathbf{s}_{i\alpha}$ is the spin of an electron at site i with orbital quantum number $\alpha = l_z$. Its origin is the standard Coulomb interaction, which is minimized for electrons with parallel spins (triplet state) due to the antisymmetric character of the spatial part of the wave function. Similar considerations apply to orbitals as well. One can show that Hund's coupling enters the relation between the direct Coulomb repulsion of electrons in different orbitals U_{mn} ($m \neq n$) and the Coulomb (Hubbard) repulsion on the same orbital U_{mm}, which is given by

$$U_{mn} = U_{mm} - 2J_H \tag{1.4}$$

Typical values of the Hund's exchange constant are $J_H \approx 0.8 - 0.9$ eV for $3d$, $J_H \approx 0.6 - 0.7$ eV for $4d$ and $J_H \approx 0.5$ eV for $5d$ TM elements.

The third Hund's rule arises from the relativistic spin-orbit interaction between the spin and orbital angular momenta of each electron:

$$\mathscr{H}_{\text{SOC}} = \sum_i \xi_i \mathbf{l}_i \cdot \mathbf{s}_i \tag{1.5}$$

where the sum runs over all electrons. For the case of strong Coulomb interactions, as described by the *Russell-Saunders* (or *LS*) coupling scheme, the spin and orbital angular momenta of each electron will first couple together following the first two Hund's rules to give rise to a total spin $\mathbf{S}$ and orbital $\mathbf{L}$ angular momenta for the whole atom. The weaker SOC will then act on $\mathbf{S}$ and $\mathbf{L}$ to result in a total angular momentum $\mathbf{J}$. The ground-state value of the corresponding quantum number J is then dictated by the third rule. For electrons belonging to the same shell ($\xi_i = \xi$), the SOC in the *LS* scheme can be written as

$$\mathscr{H}_{\text{SOC}} = \lambda \mathbf{L} \cdot \mathbf{S}, \quad \lambda = \pm \frac{\xi}{2S} \tag{1.6}$$

where the $+(-)$ sign is used for less(more) than half-filled shells. From the relativistic treatment one can show that $\xi > 0$, so that $\lambda > 0$ ($\lambda < 0$) for less(more) than half-filled shells. In general, *LS* coupling is valid whenever the SOC can be considered weak compared to the Hubbard repulsion. As already mentioned in the introduction of this chapter (see Fig. 1.2), SOC increases in going from $3d$ to the heavier $4d$ and $5d$ TMs. This is due to the fact that the SOC constant strongly increases with the atomic number Z according to $\xi \sim Z^4$ (hence $\lambda \sim Z^4$). Typical values are $\lambda \approx 20 - 70$ meV for $3d$ and $\lambda \approx 0.5$ eV for $5d$ TMs. *LS* coupling is applicable to $3d$ TM elements and generally represents a good description in the $4d$

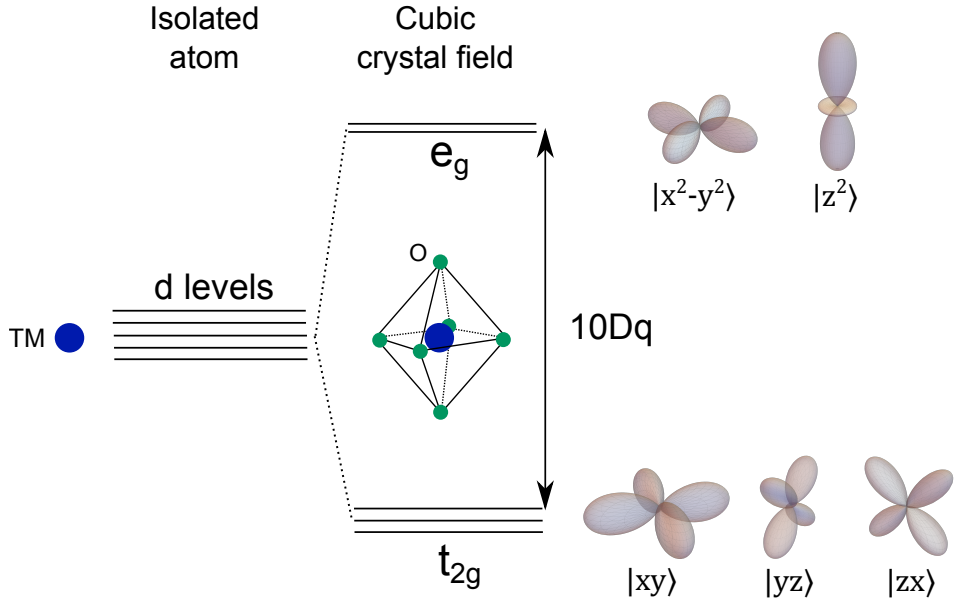

Figure 1.4: Schematic representation of the d energy levels of an isolated TM atom (blue sphere) and in the case of a TM atom in octahedral coordination with O atoms (green spheres). In the latter case, the cubic crystal field ($10Dq$) splits the d levels into a lower t_{2g} sextet ($|xy\rangle$, $|yz\rangle$, $|zx\rangle$) and an upper e_g quartet ($|x^2-y^2\rangle$, $|z^2\rangle = |3z^2-r^2\rangle$). A real space representation of the corresponding orbital wave functions is also given.

and $5d$ cases as well[4].

1.1.4 Single-atom physics for an atom in a crystal: crystal field

When a TM atom resides in a crystal, the degeneracy of the d orbitals is lifted due to the crystal field produced from the surrounding ligands. In TMOs these are typically O atoms. The type of splitting and the character of the corresponding levels depend on the symmetry of the local crystalline environment. A detailed study of the crystal field splitting requires group-theoretical method and can be found in many specialized textbooks (see, for instance, Ballhausen [24]). A very common situation encountered in TMOs involves a TM atom at the centre of a regular octahedron of O atoms. In this case, the crystal field sensed by the TM has cubic symmetry (O_h point group) and the d levels are split in two upper e_g and three

[4]For these heavy elements the situation may actually be intermediate between LS and the so-called jj coupling, applicable for example for $4f$ and $5f$ elements. In the latter, the spin and orbital angular momenta of each electron are coupled for each electronic site, $\mathbf{j}_i = \mathbf{l}_i + \mathbf{s}_i$. The total angular momentum is then given by $\mathbf{J} = \sum_i \mathbf{j}_i$.

lower t_{2g} orbitals[5] separated by an energy $\Delta_{\mathrm{CF}} = 10Dq$[6], as shown in Fig. 1.4. The latter have the following expression [1]:

$$e_g : \begin{cases} |z^2\rangle = |3z^2 - r^2\rangle = |2,0\rangle \\ |x^2 - y^2\rangle = \dfrac{1}{\sqrt{2}}\left(|2,2\rangle + |2,-2\rangle\right) \end{cases} \tag{1.7}$$

$$t_{2g} : \begin{cases} |xy\rangle = -\dfrac{i}{\sqrt{2}}\left(|2,2\rangle - |2,-2\rangle\right) \\ |yz\rangle = \dfrac{i}{\sqrt{2}}\left(|2,1\rangle + |2,-1\rangle\right) \\ |zx\rangle = -\dfrac{1}{\sqrt{2}}\left(|2,1\rangle - |2,-1\rangle\right) \end{cases} \tag{1.8}$$

where $|l, m_l\rangle$ are the one-electron spherical harmonics. In the absence of non-cubic crystal field terms and neglecting SOC, the t_{2g} orbitals $|xy\rangle$, $|yz\rangle$, $|zx\rangle$ form a triplet of degenerate states, which, for reasons of convenience, can be expressed according to the following linear combinations [1]:

$$\begin{aligned} |t_{2g}^0\rangle &= -\frac{i}{\sqrt{2}}(|2,2\rangle - |2,-2\rangle) = -|xy\rangle \\ |t_{2g}^1\rangle &= |1,1\rangle = -\frac{1}{\sqrt{2}}(|zx\rangle + i|yz\rangle) \\ |t_{2g}^{-1}\rangle &= |1,-1\rangle = \frac{1}{\sqrt{2}}(|zx\rangle - i|yz\rangle) \end{aligned} \tag{1.9}$$

Applying the orbital angular momentum operator $\hat{L}_z$ to the combinations of t_{2g} states of Eq. (1.9), one can easily show that $\langle t_{2g}^0|\hat{L}_z|t_{2g}^0\rangle = 0$, $\langle t_{2g}^{\pm1}|\hat{L}_z|t_{2g}^{\pm1}\rangle = \pm 1$, while the non-diagonal terms are all zero. The linear combinations $|t_{2g}^{0,\pm1}\rangle$ of t_{2g} states are thus eigenstates of the orbital angular momentum operator $\hat{L}_z$ with matrix elements analogous to the ones of a p ($l = 1$) electron: the t_{2g} orbitals can then be mapped onto a triplet of states with an effective orbital angular momentum $L_{\mathrm{eff}} = 1$ [1, 26]. In marked contrast to the case of e_g orbitals, where the orbital angular momentum is said to be *quenched* ($\langle e_g|\hat{L}_z|e_g\rangle = 0$), the latter is non-zero for t_{2g} states.

As I will show in more detail in the experimental chapters, this very well-known fact has important consequences on the role played by the SOC in the electronic and magnetic properties of the system. TM elements with valence e_g elec-

[5] This notation of crystal field levels comes from group theory.

[6] According to Khomskii [1], the notation $10Dq$ for the cubic crystal field splitting apparently originated from the paper by Schlapp and Penney [25], where D was a constant specifying the strength of the main component of the cubic crystal field $\sim D(x^2 + y^2 + z^2)$ and q was the ratio of certain matrix elements used in calculating the crystal field splitting.

trons, as is the case for the Cu^{2+} ($3d^9$) ion of the high-T_c superconducting cuprates, are in first approximation unaffected by the SOC (which is already weak for $3d$ oxides). On the other hand, SOC can act on the t_{2g} states and lead to a splitting of the corresponding energy levels. This is of particular importance for $4d$ and $5d$ TMs with partially occupied t_{2g} levels, where the sizeable SOC plays an important role in the single-ion physics (as I will show in Chapters 4 and 5). The SOC acting on the t_{2g} levels can be conveniently expressed in terms of the effective orbital moment $L_{\text{eff}} = 1$:

$$\mathscr{H}_{\text{SOC}}^{t_{2g}} = \hat{\lambda}\mathbf{L}_{\text{eff}} \cdot \mathbf{S}, \quad \hat{\lambda} \propto -\lambda \tag{1.10}$$

where $\mathbf{S}$ is the total spin angular momentum of the t_{2g} sub-shell. As can be seen from Eq. (1.10), one important difference [1, 26] with respect to the case of an isolated ion with $L = 1$, i.e. in the absence of an external crystal field, is that $\tilde{\lambda}$ is proportional in magnitude but opposite in sign to the SOC constant λ which would be applicable to the case of $L = 1$. From now on I will drop the tilde and simply use the symbol λ. As a result, the third Hund's rule (see Sec. 1.1.3) for the t_{2g} sub-shell changes to the opposite and the multiplet structure is inverted compared to the isolated case: the ground state is the one with $J_{\text{eff}} = L_{\text{eff}} + S$ for a less than half-filled t_{2g} sub-shell and $J_{\text{eff}} = |L_{\text{eff}} - S|$ for a more than half-filled one[7]. Apart from SOC, the degeneracy of the e_g and t_{2g} levels can be lifted also by non-cubic crystal field contributions. A very common term is the tetragonal crystal field (see Chapters 4 and 5), which is present whenever the TMO_6 octahedron is either compressed (elongated) along the TM-O apical direction. In this case, the $|xy\rangle$ and $|x^2 - y^2\rangle$ are lowered (raised) in energy compared to the $|yz\rangle$, $|zx\rangle$ and $|z^2\rangle$ ones, respectively. The t_{2g} levels can be also split by a trigonal distortion (see Chapter 3), i.e. a compression (elongation) of the octahedron along one of the $[1\,1\,1]$ diagonals, into a lower (upper) a_{1g} orbital singlet and an upper (lower) e_g^{π} orbital doublet.

Finally, it should be noted that when filling crystal-field-split energy levels a competition arises between the value of the crystal field splitting and the Hund's exchange constant J_H. This can be illustrated in the case of four electrons and a cubic crystal field. The first three will occupy the lower t_{2g} states with parallel spins following Hund's first rule. The fourth, however, can occupy either the e_g levels with spin parallel to the t_{2g} electrons (*high-spin* state) or one of the remaining t_{2g} ones with antiparallel spin (*low-spin* state). In the former case, there is an energy gain associated to the Hund's energy term of Eq. (1.3) at the expense of the extra energy contribution Δ_{CF}, while the opposite is true for the low-spin configuration.

[7] Although it is normally referred to as the total moment, for ions sensing the crystal field J_{eff} is not a good quantum number. However, the multiplicity of the resulting levels is correctly described by $2J_{\text{eff}} + 1$.

Which one of the two will occur in practice depends on the exact balance between the two energy scales. High-spin states are the typical situation for 3*d* TM elements, while low-spin ones are more common for 4*d* and 5*d* elements (see Chapters 4 and 5), where J_H is lower and the crystal field splitting is generally higher as a result of the larger radial extent of the *d* orbitals.

1.2 Outline of the thesis and authors' contributions

The thesis is organized as follows. Chapter 2 describes the main experimental techniques used to collected the data discussed in the following chapters. A brief description of the physical principles underlying each technique is provided, along with the relevant formalism and definitions of the cross sections used in the experimental discussion. Emphasis will be given to the kind of information on the physics of TMOs that can be extracted with each technique and advantages and disadvantages compared to other investigation methods. A concise description of the setup of the major laboratories where the measurements were performed is also provided.

Chapters 3, 4 and 5 deal with three separate investigations of 3*d*, 4*d* and 5*d* TMOs, respectively. Each chapter includes a detailed introduction to the scientific case and the motivations behind the study and a concluding remarks section summarizing the main results.

In particular, Chapter 3 presents the results of a joint resonant elastic X-ray scattering (REXS), non-resonant X-ray magnetic scattering (NXMS) and X-ray magnetic circular dichroism (XMCD) investigation on the magnetic ground state of the family of 3*d* isostructural weak ferromagnets $MnCO_3$, $FeBO_3$, $CoCO_3$ and $NiCO_3$. The X-ray data are complemented by bulk magnetisation measurements and supported by first-principle calculations of the electronic structure. The results of the measurements agree extremely well with the calculations. Some interesting trends are revealed across the series as a function of the electronic occupation of the 3*d* orbitals and several peculiar properties are found in $CoCO_3$ as a result of the large orbital angular momentum of Co^{2+}. The NXMS and XMCD X-ray measurements were performed at beamline I16 (local contacts S. Collins and G. Nisbet) and I10 (local contact P. Bencok) of the Diamond Light Source (DLS) in Didcot, UK mainly by myself with the help of S. Collins, G. Nisbet and F. Fabrizi, while the data were analysed mainly by myself with the help of S. Collins and F. Fabrizi. The bulk measurements were also performed, and corresponding data analysed, by myself. The first-principle calculations were performed by Y.O. Kvashnin, V.V.

Mazurenko, A.I. Lichtenstein, M.I. Katsnelson (density functional theory) and H. Elnaggar (multiplet). The $MnCO_3$, $CoCO_3$ and $FeBO_3$ samples were kindly provided by N.M. Kreines and Y. Shvyd'ko, respectively. The $NiCO_3$ crystals were grown by O.V. Dimitrova and characterised by myself by means of X-ray diffraction with a laboratory source. For the sake of completeness, I also include the REXS measurements performed on the same compounds by S. Collins, G. Beutier and G. Nisbet at beamline I16 of the DLS mainly before the start of my PhD research program, with preliminary measurements carried out at beamline BM28 (XMaS) of the European Synchrotron Radiation Facility (ESRF) in Grenoble, France. My contribution to the REXS investigation consisted in taking part in the $NiCO_3$ data collection and performing the preliminary sample characterisation. The REXS data were mainly analysed by G. Beutier and S. Collins.

Chapter 4 discusses the main findings of an investigation on the impact of La substitution on the ground-state magnetic structure and single-ion electronic properties of the 4*d* oxide Ca_2RuO_4, by means of REXS at the Ru *L* edges and X-ray absorption spectroscopy (XAS) at the O *K* edge, respectively. Additional preliminary results obtained by means of XAS and XMCD measurements at the Ru *L* edges using a novel setup are also presented. The X-ray data are complemented by bulk magnetisation and neutron diffraction measurements. The magnetic structure of the doped compounds, where one of two magnetic structures allowed by symmetry is found to be suppressed in favour of the second one, is established for the first time and compared to the one induced by Sr doping and external pressure. At the same time, my results suggest that La substitution alters the crystal field acting on the Ru ion and changes the local physics accordingly. The X-ray experiments were performed at beamline I16 (local contacts S. Collins, G. Nisbet and F. Fabrizi) and I10 (local contact P. Bencok) of the DLS and beamline ID12 (local contacts A. Rogalev and F. Wilhelm) of the ESRF by myself, S. Boseggia, L.S.I. Veiga and C. Dashwood, while the data were analysed by myself. The bulk measurements and corresponding data were also performed and analysed by myself. The neutron diffraction data were collected at the SXD instrument of the ISIS Neutron and Muon Facility in Didcot by R. Perry and M. Gutmann, who also analysed the data. The samples were grown and characterised by R. Perry and S. Riccò.

In Chapter 5, a resonant inelastic X-ray scattering (RIXS) investigation on the magnetic excitations of the 5*d* electron-doped oxide $(Sr_{1-x}La_x)_2IrO_4$ at the Ir L_3 edge is discussed. Thanks to a thorough analysis of the experimental data, previously overlooked features of the magnon spectrum are found which are interpreted in light of existing theories on the peculiar magnetism of 5*d* oxides. The RIXS measurements were performed at beamline ID20 (local contact M. Moretti) of the

ESRF by myself, M. Moretti, J.G. Vale, C. Donnerer and A. de la Torre with the help of S. Boseggia and M. Rossi. The data were analysed by myself with the help of J.G. Vale, who also contributed to the modelling of the magnon dispersion and the linear spin-wave solutions of the magnetic Hamiltonians. The samples were grown and characterised by R. Perry and A. de la Torre.

The thesis concludes with a summary of the key results of the three case studies. I discuss the relevance of my findings in the wider context of TMOs research and outline future perspectives for the application of synchrotron radiation to this field.

Chapter 2

Overview of experimental techniques and laboratory setups

Contents

2.1 Magnetic scattering with X-rays 49

2.1.1 Elastic scattering: magnetic diffraction 51

2.1.1.1 Non-resonant X-ray magnetic scattering . . . 52

2.1.1.2 Resonant elastic X-ray scattering 56

2.1.1.3 The Materials and Magnetism beamline (I16) at the Diamond Light Source 60

2.1.2 Resonant inelastic X-ray scattering 64

2.1.2.1 ID20 beamline at the European Synchrotron Radiation Facility 67

2.2 Absorption measurements with X-rays 71

2.2.1 X-ray absorption spectroscopy 71

2.2.2 X-ray magnetic circular dichroism 73

2.2.3 I10: Beamline for Advanced Dichroism Experiments (BLADE) at the Diamond Light Source 77

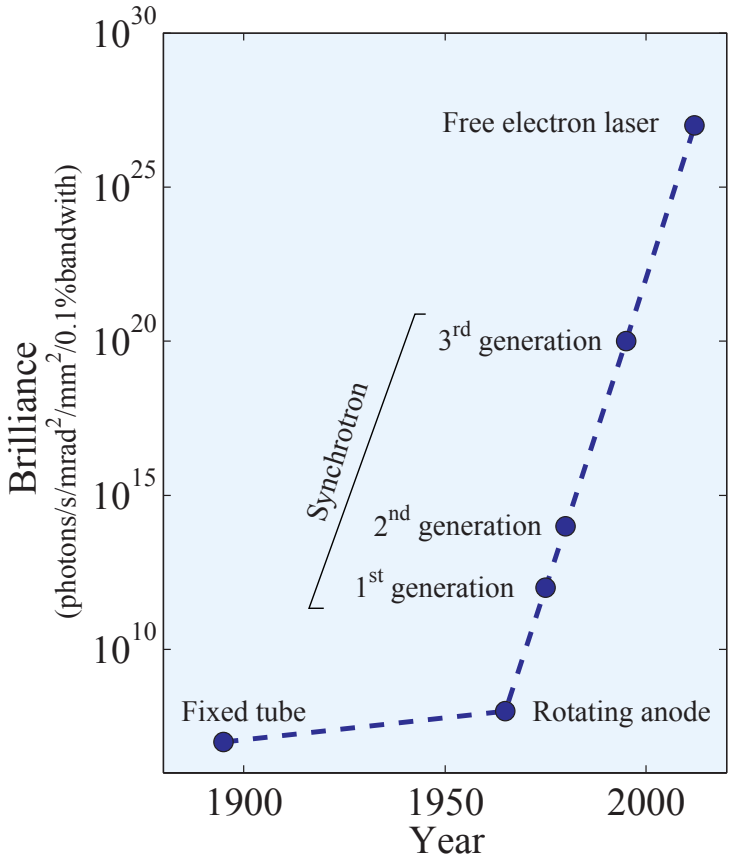

Figure 2.1: The brilliance of X-ray sources as a function of time. Figure adapted from Ref. [27].

The key results presented in this thesis were obtained in several synchrotron experiments performed at the DLS and the ESRF. The measurements covered a wide range of X-ray scattering and absorption techniques, which are outlined in Sec. 2.1 and Sec. 2.2, respectively.

Modern third-generation synchrotron facilities represent extremely powerful and versatile sources of X-ray radiation. Compared to conventional lab-based sources, they offer a brilliance 12 orders of magnitude higher (see Fig. 2.1), energy tunability and a high degree of polarisation and coherence. Consequently, X-ray techniques have become a common experimental tool in the condensed matter physics community, where they complement the possibilities offered by other probes, such as neutron scattering, in the investigation of the structural, magnetic and electronic properties of solids. In contrast to neutrons, X-rays can be tuned to elementary absorption edges, thus making absorption spectroscopy (Sec. 2.2) and other resonant spectroscopic techniques (see Secs. 2.1.1.2 and 2.1.2) possible. For the investigation of both structural and magnetic degrees of freedom, X-ray scattering is often an important alternative to the corresponding neutron technique. This

is the case especially where neutron scattering is complicated by the requirement of large sample masses and/or the presence of strongly absorbing isotopes in the sample. In certain cases, X-ray scattering can also allow the investigation of properties which are simply not accessible with neutrons (see, for instance, Sec. 2.1.1.1).

Most of the measurements presented in Chapters 3-5 rely on some of the specificities of the interaction between X-ray radiation and matter and would have been impossible (or significantly more difficult) using other probes. The only exceptions are the REXS-NXMS interference measurements on the weak ferromagnets (Sec. 3.4) and the REXS measurements on the magnetic structure of La-doped Ca_2RuO_4 (Sec. 4.5), where similar information could have been obtained by polarised and unpolarised neutron diffraction, respectively. In the former case, one of the motivations behind the study was to prove the possibility of using X-rays as an alternative approach, while both in the former and in the latter case the small sample size would have meant a significant lower data quality and higher counting time in the case of neutrons.

Below, I provide a brief overview of the key techniques and corresponding experimental setups used for the investigations presented in the following chapters. For more detailed information on synchrotron physics and instrumentation the reader is referred to Als-Nielsen and McMorrow [27] and Willmott [28].

2.1 Magnetic scattering with X-rays

The scattering of X-rays from matter is due to the coupling of the electronic charge and spin degrees of freedom[1] to the electromagnetic field of the incident beam. The corresponding cross section is extremely rich and a detailed treatment goes beyond the scope of the present work. In the following, I will present a brief overview of the main aspects which will be relevant for the discussion of the experimental data. For a complete derivation of the cross sections the reader is referred to Refs. [29–37] for elastic scattering (Sec. 2.1.1) and Refs. [31, 38, 39] for resonant inelastic scattering (Sec. 2.1.2).

The system of atomic electrons in the presence of an electromagnetic field is generally described [34, 36, 40] by the Hamiltonian $\mathscr{H} = \mathscr{H}_{\rm el} + \mathscr{H}_{\rm rad} + \mathscr{H}'$ consisting of an electronic ($\mathscr{H}_{\rm el}$), a radiation field ($\mathscr{H}_{\rm rad}$) and an interaction ($\mathscr{H}'$)

[1] One can show that the interaction with the atomic nuclei is a factor of about $\approx Z/(2 \times m_n/m)$ smaller than the interaction with the electrons, where Z is the nuclear charge, m_n is the nucleon mass and m is the electron mass. Given that $m_n/m \approx 1850$, the interaction with the nuclei can be neglected.

term. The scattering process arises from the interaction term, which consists of four different contributions:

$$\begin{aligned}\mathscr{H}' &= \mathscr{H}_1 + \mathscr{H}_2 + \mathscr{H}_3 + \mathscr{H}_4 = \\ &= \sum_i \frac{e^2}{2m}[A(\mathbf{r}_i,t)]^2 - \sum_i \frac{e^2\hbar}{2m^2c^2}\mathbf{s}_i \cdot \left[\frac{\partial \mathbf{A}(\mathbf{r}_i,t)}{\partial t} \times \mathbf{A}(\mathbf{r}_i,t)\right] - \\ &- \sum_i \frac{e}{m}[\mathbf{A}(\mathbf{r}_i,t)\cdot \mathbf{p}_i] - \sum_i \frac{e}{m}\mathbf{s}_i \cdot [\nabla \times \mathbf{A}(\mathbf{r}_i,t)] \end{aligned} \tag{2.1}$$

where $\mathbf{r}_i$, $\mathbf{s}_i$ and $\mathbf{p}_i$ are the position, spin and momentum of the i-th electron and $\mathbf{A}$ is the position- and time-dependent vector potential of the incident electromagnetic field[2]. $\mathscr{H}_1$ and $\mathscr{H}_3$ arise from the interaction of the electron charge with the electromagnetic field, $\mathscr{H}_4$ represents the interaction of the electron spin with the magnetic field of the incident wave and $\mathscr{H}_2$ stems from the spin-orbit interaction term. The interaction terms given in Eq. (2.1) can be treated as a perturbation to the sum of the electronic and radiation field terms and the scattering process can then be described in the framework of perturbation theory.

During the interaction process, a photon is scattered from the initial state $|\mathbf{k}_{\text{in}}, \boldsymbol{\varepsilon}_{\text{in}}\rangle$ to the final state $|\mathbf{k}_{\text{out}}, \boldsymbol{\varepsilon}_{\text{out}}\rangle$, where $\mathbf{k}$ is the photon wave vector (so that $\mathbf{p} = \hbar\mathbf{k}$ is the corresponding momentum) and $\boldsymbol{\varepsilon}$ is the photon polarisation vector. As a result, the electron system evolves from the initial state $|i\rangle$, which can be assumed to be the ground state $|g\rangle$, to the final state $|f\rangle$ with a transition probability given by Fermi's golden rule of time-dependent perturbation theory to second order:

$$w = \frac{2\pi}{\hbar}\left|\langle F|\mathscr{H}_1 + \mathscr{H}_2|G\rangle + \sum_n \frac{\langle F|\mathscr{H}_3 + \mathscr{H}_4|n\rangle\,\langle n|\mathscr{H}_3 + \mathscr{H}_4|G\rangle}{E_G - E_n}\right|^2 \delta(E_F - E_G) \tag{2.2}$$

where $|G\rangle = |g;\mathbf{k}_{\text{in}}, \boldsymbol{\varepsilon}_{\text{in}}\rangle$ is the initial state of the whole system (electrons plus radiation field) with energy $E_G = E_g + \hbar\omega_{\mathbf{k}_{\text{in}}}$, $|F\rangle = |f;\mathbf{k}_{\text{out}}, \boldsymbol{\varepsilon}_{\text{out}}\rangle$ is the final state with energy $E_F = E_f + \hbar\omega_{\mathbf{k}_{\text{out}}}$ and $|n\rangle$ is an intermediate state of energy E_n, where no photons are present. Here $E_{\text{in}} = \hbar\omega_{\mathbf{k}_{\text{in}}}$ ($E_{\text{out}} = \hbar\omega_{\mathbf{k}_{\text{out}}}$) is the energy of the incident (scattered) photon. It should be noted that the interaction Hamiltonian terms $\mathscr{H}_1$ and $\mathscr{H}_2$ are quadratic in the vector potential and enter Fermi's golden rule through the first-order perturbation term. On the other hand, $\mathscr{H}_3$ and $\mathscr{H}_4$ are linear in the vector potential and appear in Eq. (2.2) via second-order perturbation theory.

The quantity measured in a scattering experiment is the double differential cross section, defined as the number of photons scattered per unit time in the solid

[2]The corresponding electric field is given by $\mathbf{E}(\mathbf{r},t) = -\nabla V(\mathbf{r}) - \frac{\partial \mathbf{A}(\mathbf{r},t)}{\partial t}$, where $V(\mathbf{r})$ is the scalar potential.

angle $(\Omega, \Omega + d\Omega)$ with energy $(\hbar\omega_{\mathbf{k}_{\text{out}}}, \hbar\omega_{\mathbf{k}_{\text{out}}} + d\hbar\omega_{\mathbf{k}_{\text{out}}})$ normalised to $d\Omega$, $d\hbar\omega_{\mathbf{k}_{\text{out}}}$ and the incident photon flux (number of incident photons per unit area and unit time). The double differential cross section is obtained by multiplying the transition probability of Eq. (2.2) by the density of photon states $\rho(\omega_{\mathbf{k}_{\text{out}}}) = \dfrac{V\omega^2_{\mathbf{k}_{\text{out}}}}{(2\pi)^3\hbar c^3}$ and dividing by the incident flux $I_0 = c/V$ (being V the quantization volume):

$$\frac{d^2\sigma}{d\Omega\, d\hbar\omega_{\mathbf{k}_{\text{out}}}} = \frac{V^2\omega^2_{\mathbf{k}_{\text{out}}}}{\hbar c^4} w \tag{2.3}$$

2.1.1 Elastic scattering: magnetic diffraction

X-ray elastic scattering generated by the periodic spatial arrangement of magnetic moments in a magnetically-ordered material (magnetic diffraction) was first reported in the seminal paper by De Bergevin and Brunel [41], where a diffraction peak arising from the AFM order of NiO was observed using a laboratory X-ray source. X-ray magnetic scattering far from any absorption edge of the material under study stems from the interaction between the magnetic field of the X-ray electromagnetic wave and the magnetic moment of the electron. In contrast to the neutron case, in which the magnetic and nuclear interactions are of comparable strength, the X-ray magnetic cross section is several orders of magnitude weaker than standard Thomson scattering (Sec. 2.1.1.1). As a result, it was only with the advent of modern synchrotron sources (see, for instance, Gibbs *et al.* [42]) that X-ray magnetic scattering established itself as a valid alternative tool for the investigation of magnetic phenomena in condensed matter physics. A new boost to the field came with the observation of a large resonant enhancement of the magnetic diffraction intensity when the energy of the incident photons is tuned to an elementary absorption edge of the compound studied [32, 43, 44] (Sec. 2.1.1.2).

Elastic scattering is accounted for by the transition probability of Eq. (2.2) in the particular case where $E_{\text{in}} = E_{\text{out}}$ and the system of atomic electrons is left in its ground state by the scattering process, i.e. $|f\rangle = |g\rangle$. Following the formalism of Ref. [36], the total diffraction intensity can be written as:

$$I(\omega) \propto \left| \sum_j e^{i\mathbf{Q}\cdot\mathbf{r}_j} \left(f_j^{\text{Thom}} + f_j^{\text{spin}} + f_j'(\omega) + i f_j''(\omega) \right) \right|^2 \tag{2.4}$$

where the sum is over all atoms j, $\mathbf{Q} = \mathbf{k}_{\text{out}} - \mathbf{k}_{\text{in}}$ is the so-called scattering vec-

tor[3] and $E_{in} = E_{out} = E = \hbar\omega$ is the photon energy. The three atomic scattering amplitudes are given by [36]:

$$\begin{aligned} f_j^{\text{Thom}} &= \langle \psi_g^j | \mathscr{H}_1 | \psi_g^j \rangle \\ f_j^{\text{spin}} &= \langle \psi_g^j | \mathscr{H}_2 | \psi_g^j \rangle \\ f_j'(\omega) + i f_j''(\omega) &= \sum_n \frac{\langle \psi_g^j | \mathscr{H}_3^* + \mathscr{H}_4^* | \psi_n \rangle \langle \psi_n | \mathscr{H}_3 + \mathscr{H}_4 | \psi_g^j \rangle}{\hbar\omega - (E_n - E_g) + i\frac{\Gamma}{2}} \end{aligned} \tag{2.5}$$

where ψ_g^j is the core level wave function at site j (of energy E_g), ψ_n are all possible intermediate states that can be reached by the absorption/emission process (with a lifetime $\approx \hbar/\Gamma$) and the terms $\mathscr{H}_i$ are defined in Eq. (2.1). The first two amplitudes in Eq. (2.5) are energy-independent non-resonant terms. In particular, the first one describes the usual Thomson scattering, while the second one is a pure non-resonant magnetic amplitude. An additional non-resonant magnetic term is hidden in the third amplitude of Eq. (2.5). Once summed to f_j^{spin}, this contribution results in the total non-resonant magnetic scattering amplitude discussed in Sec. 2.1.1.1. It should be noted that, although the orbital moment of the electron does not explicitly appear in Eq. (2.1), an orbital contribution enters the magnetic cross section through the third amplitude of Eq. (2.5) [30, 31, 34].

Thomson scattering and non-resonant magnetic scattering are the only elastic contributions to the diffracted intensity far from any absorption edges of the scattering medium. In proximity of an absorption edge, the third amplitude in Eq. (2.5) includes a dispersive correction to the scattering amplitude via an energy-dependent denominator. This contribution is strongly enhanced for a resonant photon energy $\hbar\omega \approx E_n - E_g$ and is therefore the one responsible for resonant scattering. In the next section I will provide a brief description of the non-resonant amplitude, while the resonant case will be discussed in Sec. 2.1.1.2.

2.1.1.1 Non-resonant X-ray magnetic scattering

The total NXMS amplitude is given by [29–31, 33, 37]:

$$f_{\text{mag}} = -i\frac{\hbar\omega}{mc^2}\left(\frac{1}{2}\mathbf{L}(\mathbf{Q})\cdot\mathbf{A} + \mathbf{S}(\mathbf{Q})\cdot\mathbf{B}\right) \tag{2.6}$$

[3] The momentum transferred to the system of atomic electrons is $\hbar\mathbf{Q}$.

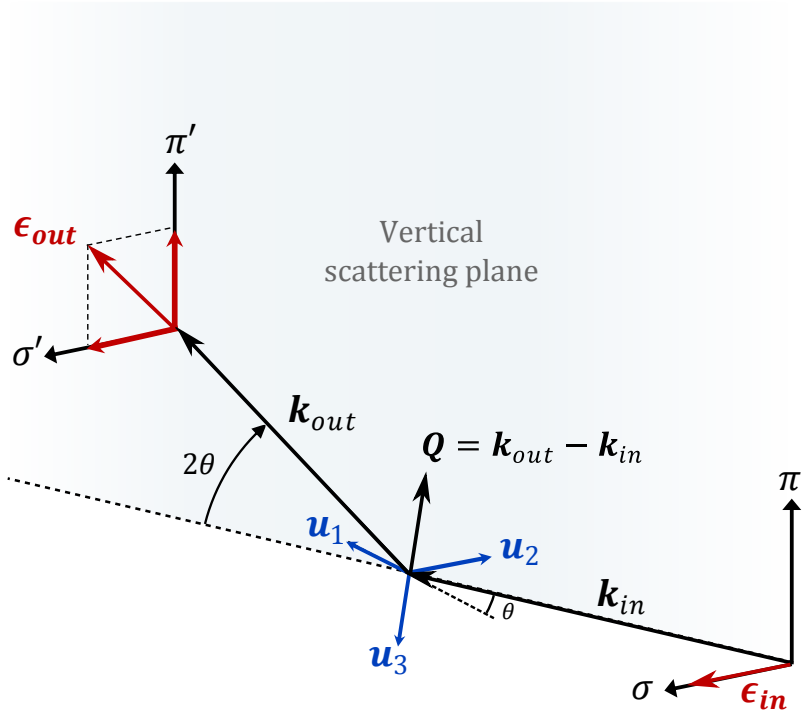

Figure 2.2: Schematic representation of the diffraction geometry of a magnetic scattering experiment in the common case of a vertical scattering plane and linearly polarised incident X-rays perpendicular to the latter (σ polarisation). (σ,π) and (σ',π') are the bases of two vectors used to express the polarisation vector (electric field direction) of the incident ($\boldsymbol{\varepsilon}_{\text{in}}$) and scattered ($\boldsymbol{\varepsilon}_{\text{out}}$) wave, respectively. The reference frame $\mathbf{u}_1\mathbf{u}_2\mathbf{u}_3$ introduced by Blume and Gibbs [30] to express the NXMS cross section (2.6) is also shown. The definitions of all the vectors are given in the text.

where $mc^2 = 511$ keV is the rest mass of the electron, $\mathbf{L}$ and $\mathbf{S}$ are the orbital and spin structure factors and the quantities $\mathbf{A}$ and $\mathbf{B}$ are vectors defined as follows[4] [37]:

$$\begin{aligned}\mathbf{A} &= -2(1-\hat{\mathbf{k}}_{\text{in}}\cdot\hat{\mathbf{k}}_{\text{out}})(\boldsymbol{\varepsilon}_{\text{out}}\times\boldsymbol{\varepsilon}_{\text{in}}) + (\hat{\mathbf{k}}_{\text{in}}-\hat{\mathbf{k}}_{\text{out}})\cdot(\boldsymbol{\varepsilon}_{\text{out}}\times\boldsymbol{\varepsilon}_{\text{in}})(\hat{\mathbf{k}}_{\text{in}}-\hat{\mathbf{k}}_{\text{out}}) \\ \mathbf{B} &= \boldsymbol{\varepsilon}_{\text{out}}\times\boldsymbol{\varepsilon}_{\text{in}} - (\hat{\mathbf{k}}_{\text{in}}\times\boldsymbol{\varepsilon}_{\text{in}})(\hat{\mathbf{k}}_{\text{in}}\cdot\boldsymbol{\varepsilon}_{\text{out}}) + (\hat{\mathbf{k}}_{\text{out}}\times\boldsymbol{\varepsilon}_{\text{out}})(\hat{\mathbf{k}}_{\text{out}}\cdot\boldsymbol{\varepsilon}_{\text{in}}) - \\ &\quad - (\hat{\mathbf{k}}_{\text{out}}\times\boldsymbol{\varepsilon}_{\text{out}})\times(\hat{\mathbf{k}}_{\text{in}}\times\boldsymbol{\varepsilon}_{\text{in}})\end{aligned} \tag{2.7}$$

where $\hat{\mathbf{k}}_{\text{in}} = \mathbf{k}_{\text{in}}/|\mathbf{k}_{\text{in}}|$, $\hat{\mathbf{k}}_{\text{out}} = \mathbf{k}_{\text{out}}/|\mathbf{k}_{\text{out}}|$. The orbital and spin structure factors represent the Fourier transform of the orbital and spin angular momenta density. Considering the case of a periodic arrangement of magnetic moments localised at the

[4] The expression of the quantity $\mathbf{A}$ given by Blume and Gibbs [30] was found [37, 45] to contain an error and therefore does not coincide with the expression here reported.

positions $\mathbf{r}_i$ of interest for the present work, the structure factors can be written as:

$$\begin{aligned}\mathbf{S} &= \sum_i \mathbf{s}_i f_s^i(\mathbf{Q}) e^{i\mathbf{Q}\cdot\mathbf{r}_i} \\ \mathbf{L} &= \sum_i \mathbf{l}_i f_l^i(\mathbf{Q}) e^{i\mathbf{Q}\cdot\mathbf{r}_i}\end{aligned} \tag{2.8}$$

where $\mathbf{s}_i$ and $\mathbf{l}_i$ are the spin and orbital angular momenta at site i and $f_s^i(\mathbf{Q})$ and $f_l^i(\mathbf{Q})$ are the spin and orbital form factors, respectively. The latter, in analogy with the form factor for Thomson scattering, represent the Fourier transform of the magnetic electron density at site i. In a crystal, the sums of Eq. (2.8) are extended to the magnetic atoms (or ions) of the magnetic unit cell describing the spatial periodicity of the magnetic structure.

The scattering geometry is conveniently described in terms of the $\mathbf{u}_1\mathbf{u}_2\mathbf{u}_3$ reference frame first introduced by Blume and Gibbs [30]. The latter is defined such that the unit vectors $\mathbf{u}_1 = (\hat{\mathbf{k}}_{\text{in}} + \hat{\mathbf{k}}_{\text{out}})/(2\cos\theta)$ and $\mathbf{u}_3 = (\hat{\mathbf{k}}_{\text{in}} - \hat{\mathbf{k}}_{\text{out}})/(2\sin\theta)$ lie in the scattering plane[5], while $\mathbf{u}_2 = (\hat{\mathbf{k}}_{\text{in}} \times \hat{\mathbf{k}}_{\text{out}})/(\sin 2\theta)$ is perpendicular to it (see Fig. 2.2). Here, 2θ is the scattering angle. The NXMS amplitude depends on the polarisation of the incident and scattered beam through the quantities of Eq. (2.7), which can be expressed in terms of the orthonormal vectors $\boldsymbol{\varepsilon}_\sigma = -\mathbf{u}_2$, $\boldsymbol{\varepsilon}_\pi = \sin\theta\mathbf{u}_1 - \cos\theta\mathbf{u}_3$ and $\boldsymbol{\varepsilon}'_\sigma = -\mathbf{u}_2$, $\boldsymbol{\varepsilon}'_\pi = -(\sin\theta\mathbf{u}_1 + \cos\theta\mathbf{u}_3)$, respectively. The latter are normally referred to simply as σ and π (or σ' and π' for the scattered beam) polarisations, which correspond to an electric field direction perpendicular (σ) or parallel (π) to the scattering plane. Expressing the quantities in Eq. (2.7) with respect to the (σ,π) and (σ',π') bases and the magnetic structure factors of Eq. (2.8) in the $\mathbf{u}_1\mathbf{u}_2\mathbf{u}_3$ reference frame, the magnetisation-dependent part of the amplitude of Eq. (2.6) is given by the following 2×2 matrix [30]:

$$\begin{aligned}M_{\text{mag}} &= \begin{bmatrix} M_{\sigma\sigma'} & M_{\pi\sigma'} \\ M_{\sigma\pi'} & M_{\pi\pi'} \end{bmatrix} = \\ &= \begin{bmatrix} \sin 2\theta\, S_2 & -2\sin^2\theta\,[\cos\theta\,(L_1+S_1) - \sin\theta\, S_3] \\ 2\sin^2\theta\,[\cos\theta\,(L_1+S_1) + \sin\theta\, S_3] & \sin 2\theta[2\sin^2\theta L_2 + S_2] \end{bmatrix}\end{aligned} \tag{2.9}$$

For X-ray radiation generated by a synchrotron source, the incident X-ray wave naturally exhibits linear polarisation in the plane of the electron storage ring. This corresponds to σ incident polarisation (i.e. perpendicular to the scattering plane) in the common case of a vertical scattering geometry, which is the one used for

[5] Defining the scattering vector as $\mathbf{Q} = \mathbf{k}_{\text{out}} - \mathbf{k}_{\text{in}}$, $\mathbf{u}_3$ is thus antiparallel to $\mathbf{Q}$.

the measurements presented in Chapter 3 (see Fig. 2.2). While Thomson scattering preserves the polarisation of the incident wave, resulting in σ'-polarised radiation, Eq. (2.9) implies that both σ'- and π'-polarised components will be generally present in the case of magnetic scattering. These are described by the amplitude terms $M_{\sigma\sigma'}$ and $M_{\sigma\pi'}$, respectively.

The magnetic form factors entering the definition of the structure factors in Eq. (2.8) generally depend on both the magnitude and the direction of $\mathbf{Q}$. However, an isotropic approximation is usually considered, which only takes into account the dependence on the magnitude Q of the scattering vector, such that $f_s(\mathbf{Q}) \equiv f_s(Q)$ and $f_l(\mathbf{Q}) \equiv f_l(Q)$. In this case, the magnetic form factors can be expressed as follows [46–48]:

$$\begin{aligned} f_s(Q) &= \langle j_0 \rangle \\ f_l(Q) &= \langle j_0 \rangle + \langle j_2 \rangle \end{aligned} \tag{2.10}$$

Here, $\langle j_0 \rangle$ and $\langle j_2 \rangle$ are radial integrals of the type $\langle j_k \rangle_{nl}(Q) = \int_0^\infty R_{nl}^2(r)\, j_k(Qr) r^2\, dr$ where $R_{nl}(r)$ is the radial part of the magnetic ion wave function and $j_k(Qr)$ is the spherical Bessel function of order k. The radial integrals (expressed as a function of the normalised momentum transfer $s = Q/4\pi = \sin\theta/\lambda$, being θ the Bragg angle of the magnetic reflection and λ the wavelength of the incident X-ray beam) can be approximated by the following relations [46]:

$$\begin{aligned} \langle j_0 \rangle (s) &= Ae^{-as^2} + Be^{-bs^2} + Ce^{-cs^2} + D \\ \langle j_2 \rangle (s) &= s^2(A'e^{-as^2} + B'e^{-bs^2} + C'e^{-cs^2} + D') \end{aligned} \tag{2.11}$$

where the values of the coefficients are tabulated for different oxidation states of each element in Ref. [46].

Because of the prefactor $\hbar\omega/mc^2 \approx 10^{-2}$ in the amplitude (2.6), the X-ray magnetic scattering intensity is four orders of magnitude weaker than in the case of conventional Bragg diffraction. In practice, the magnetic intensity is further suppressed by the fact that, while all the electrons contribute to charge scattering, magnetic scattering is only sensitive to the unpaired ones. Although this constitutes a significant limitation compared to neutrons, X-ray techniques present a number of advantages, such as (i) a generally better momentum resolution, which makes X-rays well suited for the study of incommensurate magnetic structures extending over large length scales (see, for instance, Gibbs *et al.* [42]), (ii) the possibility to measure extremely small single crystals (down to a few micrometers) as a result of the much stronger interaction with matter and the possibility to easily focus the

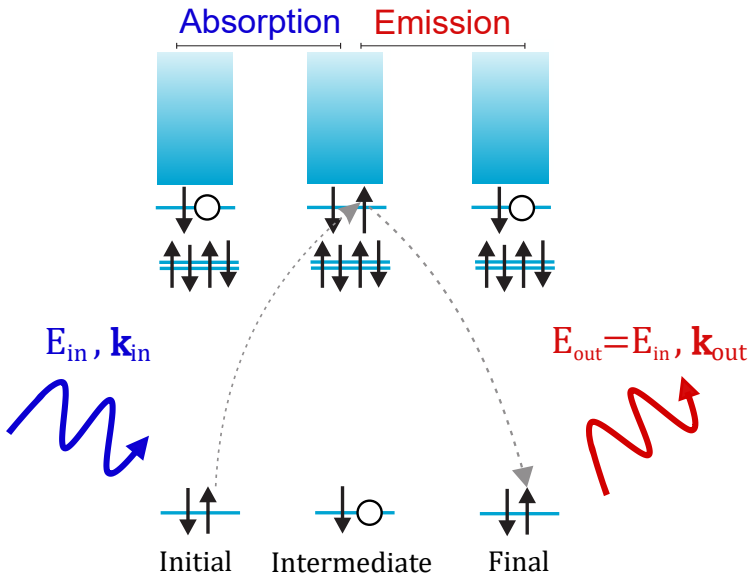

Figure 2.3: Schematic of the two-step REXS process. An X-ray photon with energy E_{in} and wave vector $\mathbf{k}_{\text{in}}$ is absorbed in a resonant transition from a core energy level to an empty valence state. The resonant atom subsequently returns to its ground state through emission of a photon with the same energy and generally different wave vector $\mathbf{k}_{\text{out}}$.

X-ray beam down to a few microns and (iii) the higher incident fluxes than for neutron sources. Most importantly, the polarisation dependence of the NXMS cross section (2.9) allows the separate determination of the spin and orbital contributions to the magnetic moment. This will be of crucial importance for the measurements presented in Chapter 3. Pioneering examples of this kind of investigation are found in the works of Gibbs *et al.* [42] and Fernandez *et al.* [49] on holmium and NiO, respectively.

2.1.1.2 Resonant elastic X-ray scattering

X-ray resonant scattering is a second order process, which can be schematically described in terms of the two-step mechanism illustrated in Fig. 2.3. In the first step, a photon with energy E_{in} and wave vector $\mathbf{k}_{\text{in}}$ is absorbed by the resonant atom and promotes a core electron to an empty valence level. The intermediate state [$|n\rangle$ in Eq. (2.5)] is unstable due to the presence of a hole in the core level. Therefore, in the second step the system decays back to its ground state by the emission of a photon with energy E_{out} and wave vector $\mathbf{k}_{\text{out}}$. In the present section, I consider the elastic process where $E_{\text{out}} = E_{\text{in}}$ and only a momentum transfer takes place: in this case the scattering mechanism is normally referred to as resonant elastic X-

ray scattering (REXS) [50] (or, alternatively, X-ray resonant exchange scattering). When the technique is used to investigate the magnetic ground state of the system under study, it is usually referred to as X-ray resonant magnetic scattering (XRMS). The inelastic case will be briefly outlined in Sec. 2.1.2.

In addition to the possibility to study small samples and the better momentum resolution with respect to neutron techniques already mentioned in relation to the non-resonant case, the resonant nature of the scattering process makes REXS element specific [50]. In a compound with more than one magnetic element for instance, this allows to disentangle the magnetic contribution of the different chemical species to the overall magnetic properties. Moreover, the resonant transition is sensitive to the oxidation state of the absorbing atom and involves a particular set of valence orbitals. Consequently, REXS also offers the unique possibility to investigate charge and orbital ordering phenomena [50]. In the present case of TM L edges, a strong dipole resonance is normally present when promoting the core $2p$ electrons to the valence $3d$, $4d$ and $5d$ levels responsible for the magnetic and electronic properties. The corresponding transition involves photon energies in the "soft" (< 1 keV), "tender" ($1-5$ keV) and "hard" (> 5 keV) X-ray windows, respectively. Finally, similar to the case of NXMS outlined in the previous section, the polarisation of the outgoing (incident) X-rays can be measured (manipulated) in a REXS experiment to provide further insight into the nature of the scattering process.

REXS arises from the third amplitude of Eq. (2.5). The latter involves matrix elements of the form $\langle\psi_n|\hat{O}_A|\psi_g\rangle$ and $\langle\psi_n|\hat{O}_B|\psi_g\rangle$ where, following from Eq. (2.1), $\hat{O}_A = \mathbf{A}(\mathbf{r},t)\cdot\mathbf{p}$ and $\hat{O}_B = \mathbf{s}_i\cdot[\nabla\times\mathbf{A}(\mathbf{r},t)]$. The vector potential $\mathbf{A}(\mathbf{r},t)$ can be expressed as a series of plane waves: $\mathbf{A}(\mathbf{r},t) = \sum_{\mathbf{k}}\left[a_{\mathbf{k}}\boldsymbol{\varepsilon}_{\mathbf{k}}e^{i(\mathbf{k}\cdot\mathbf{r}-\omega t)} + c.c.\right]$, where $a_{\mathbf{k}}$ and $\boldsymbol{\varepsilon}_{\mathbf{k}}$ are the amplitude and polarisation vector of the mode with wave vector $\mathbf{k}$, respectively (I shall drop the label $\mathbf{k}$ in the following). It is then possible to exploit the so-called *multipole expansion* of the vector potential, based on the following series expansion of its phase factor:

$$e^{i\mathbf{k}\cdot\mathbf{r}} = 1 + i\mathbf{k}\cdot\mathbf{r} - \frac{1}{2}(\mathbf{k}\cdot\mathbf{r})^2 + \ldots \tag{2.12}$$

Substitution of the first term of the expansion (2.12) in the operator $\hat{O}_A$ yields the *electric dipole* term (normally referred to as E1):

$$M_{ng,E1} = \langle\psi_n|\boldsymbol{\varepsilon}\cdot\mathbf{p}|\psi_g\rangle = i\frac{m}{\hbar}(E_n - E_g)\langle\psi_n|\boldsymbol{\varepsilon}\cdot\mathbf{r}|\psi_g\rangle \tag{2.13}$$

where I have used the fact that $\mathbf{p} = m\frac{d\mathbf{r}}{dt} = \frac{im}{\hbar}[\mathscr{H}_{\text{el}}, \mathbf{r}]$, $\mathscr{H}_{\text{el}}$ being the Hamiltonian operator acting on the ground-state and intermediate-state wave functions. The substitution of the second term of the expansion (2.12) in the operator $\hat{O}_A$ results in two different contributions. The first one corresponds to the *electric quadrupole* (E2) term:

$$M_{ng,E2} = -\frac{m}{2\hbar}(E_n - E_g)\,\langle\psi_n|(\boldsymbol{\varepsilon}\cdot\mathbf{r})(\mathbf{k}\cdot\mathbf{r})|\psi_g\rangle \tag{2.14}$$

The second one is magnetic in origin and can be grouped with the contribution obtained by substituting the first term of Eq. (2.12) in the operator $\hat{O}_B$. Together they result in the so-called *magnetic dipole* (M1) amplitude:

$$M_{ng,M1} = -\frac{1}{2}\,\langle\psi_n|(\mathbf{k}\times\boldsymbol{\varepsilon})\cdot(\mathbf{L}+2\mathbf{S})|\psi_g\rangle \tag{2.15}$$

where $\boldsymbol{\mu} = \mu_B(\mathbf{L}+2\mathbf{S})$ is the magnetic moment[6]. Including higher order terms in the multipole expansion results in an electric octupole term (E3), a magnetic quadrupole term (M2) and so on.

The electric dipole (E1) and electric quadrupole (E2) are normally the dominant terms of the REXS cross section. Although they arise from the coupling of the electrons of the resonant atom with the electric field of the incident X-rays [the magnetic moment of the resonant atom does not appear explicitly in Eqs. (2.13) and (2.14)], the corresponding scattering process is also sensitive to the magnetic degrees of freedom. This is due to the joint effect of the Pauli exclusion principle, allowing only transitions to unoccupied orbitals, and SOC [32, 34, 51]. This can be intuitively understood assuming a magnetic polarisation of the valence levels probed in the intermediate state (see Fig. 2.3), which corresponds to a prevalence of unoccupied states with the minority spin polarization. Keeping in mind that the spin is conserved in optical transitions[7], the exclusion principle allows only electrons with the same spin as the unoccupied states to be promoted from a core level to the valence band. Considering core levels with a finite SOC, as is the case for the p states at the L edges of TMs, the spin selection rule indirectly impacts the matrix elements of the resonant transition and produces a non-vanishing magnetic scattering amplitude [34, 51].

Electric dipole scattering usually dominates the REXS cross section for the optically allowed $2p \rightarrow nd$ ($n = 3,4,5$) transitions of the TMs L edges, as is the case for the measurement presented in Chapter 4. The intermediate state probes, in this case, the d valence levels responsible for the magnetic and electronic properties

[6] Different to Eq. (2.8), here $\mathbf{L}$ and $\mathbf{S}$ refer to the orbital and spin angular momenta, respectively.

[7] The spin selection rule strictly applies only when the electron spin is a good quantum number, i.e. in the case of negligible SOC.

of the system. Resonant scattering arising from the quadrupole term of the expansion will be discussed in more detail in the context of Chapter 3, where it plays a fundamental role in the interpretation of the results.

Hannon *et al.* [32] showed that the electric multipole terms in the REXS cross section can be conveniently expressed by expanding the matrix elements appearing in the third line of Eq. (2.5) in terms of vector spherical harmonics[8]. The REXS amplitude can then be explicitly written in terms of the polarisation states of the incident and scattered photons and the direction $\hat{\mathbf{z}}_j$ of the magnetic moment of the resonant atom. Following the formalism from Hill and McMorrow [33], the electric dipole amplitude reads:

$$f_{j,E1} = (\boldsymbol{\varepsilon}^*_{\text{out}} \cdot \boldsymbol{\varepsilon}_{\text{in}})F^{(0)} - i(\boldsymbol{\varepsilon}^*_{\text{out}} \times \boldsymbol{\varepsilon}_{\text{in}}) \cdot \hat{\mathbf{z}}_j F^{(1)} + (\boldsymbol{\varepsilon}^*_{\text{out}} \cdot \hat{\mathbf{z}}_j)(\boldsymbol{\varepsilon}_{\text{in}} \cdot \hat{\mathbf{z}}_j)F^{(2)} \tag{2.16}$$

where

$$\begin{aligned} F^{(0)} &= \frac{3}{4k}(F_{1,1} + F_{1,-1}) \\ F^{(1)} &= \frac{3}{4k}(F_{1,1} - F_{1,-1}) \\ F^{(2)} &= \frac{3}{4k}(2F_{1,0} - F_{1,1} - F_{1,-1}) \end{aligned} \tag{2.17}$$

Here, $F_{L,M}$ are factors which determine the strength of the resonance and depend on the atomic properties of the resonating element. The first term in Eq. (2.16) does not depend on the magnetic moment and displays an analogous polarisation dependence as Thomson scattering: the resulting scattering intensity thus contributes to the charge Bragg peak. The second term depends linearly on the direction of the magnetic moment and is responsible for first-harmonic satellites in antiferromagnets. The third contribution is quadratic in the moment direction and produces second-harmonic satellites in incommensurate magnetic structures.

The polarisation vectors appearing in Eq. (2.16) can be conveniently written in terms of the (σ, π) and (σ', π') bases already introduced in Sec. 2.1.1.1 to express the NXMS cross section. Considering the term linear in the moment direction, which is the only one relevant for discussion of the REXS results of Chapter 4, the

[8] This approach is strictly valid only for isotropic systems in which the symmetry is only broken by the magnetic moment, e.g. a free atom under the influence of a magnetic field. The application of the point-group symmetries of the local crystalline environment of the resonant atom in a crystal will in general modify the description.

REXS amplitude reads [33]:

$$f_{j,E1} = -iF^{(1)} \begin{bmatrix} 0 & \hat{z}_{j,1}\cos\theta + \hat{z}_{j,3}\sin\theta \\ \hat{z}_{j,3}\sin\theta - \hat{z}_{j,1}\cos\theta & -\hat{z}_{j,2}\sin 2\theta \end{bmatrix} \tag{2.18}$$

where $\hat{z}_{j,i}$ $(i = 1,2,3)$ are the components of the moment direction at site j with respect to the $\mathbf{u}_1\mathbf{u}_2\mathbf{u}_3$ frame defined in Fig. 2.2 and θ is the Bragg angle. Although a quantitative calculation of the REXS cross section requires the knowledge of the atomic factor $F^{(1)}$, many aspects of a REXS experiment can be accounted for by the 2×2 matrix of Eq. (2.18). The latter immediately implies that σ-σ' scattering is forbidden for dipole resonant scattering: considering the case of a vertical scattering geometry depicted in Fig. 2.2, the σ-polarised incident X-rays of a synchrotron source will result in purely π'-polarised scattering. Moreover, the different components of the magnetic moment direction can be calculated for a given experimental geometry (i.e. a given orientation of the sample crystal axes with respect to the scattering plane): Eq. (2.18) can then be used to calculate the scattered intensity variations upon an azimuthal rotation of the crystal. This in turn, allows the determination of the moment direction from a so-called azimuthal scan. This principle was applied in the interpretation of the data presented in Chapter 4.

I conclude the present discussion by noticing that the imaginary part of the forward (i.e. $\mathbf{Q} = 0$) resonant scattering amplitude of an atom at site j [see Eq. (2.4)] is proportional to the absorption cross-section $\sigma_j(\omega) = \sum_{n,g} \left|\langle\psi_n|\mathscr{H}_3 + \mathscr{H}_4|\psi_g^j\rangle\right|^2 \delta[\hbar\omega - (E_n - E_g)]$ at the same site [36]. REXS and absorption spectroscopy (see Sec. 2.2.1) are thus intimately related. The main difference is that, compared to other spectroscopic techniques, all atomic scattering processes coherently interfere as expressed by the exponential factor in Eq. (2.4).

2.1.1.3 The Materials and Magnetism beamline (I16) at the Diamond Light Source

The NXMS and REXS measurements discussed in the present work were carried out at the Materials and Magnetism beamline (I16) of the DLS. A schematic of the beamline setup is reported in Fig. 2.4. Below, I provide a brief overview of the main beamline features. For more details the reader is referred to Ref. [52].

The source of X-rays is a 2 m Diamond U27 (27 mm period) in-vacuum undulator insertion device, which can provide radiation with energy between 3.3 keV (below the uranium M-edges) to around $15-25$ keV depending on the optical con-

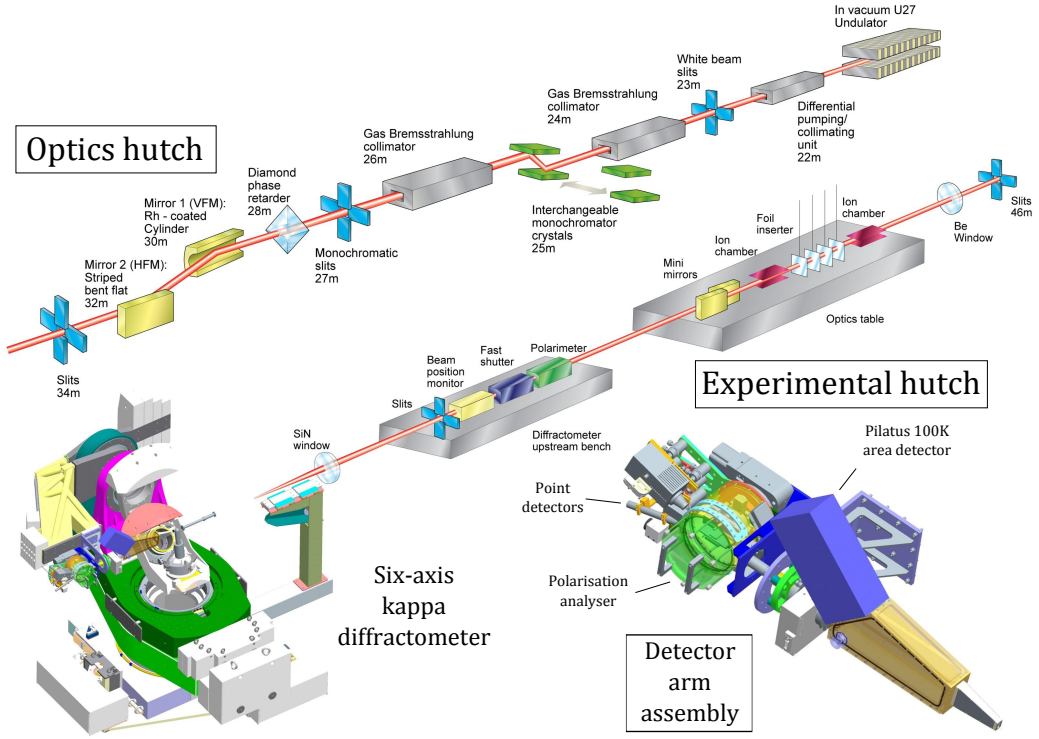

Figure 2.4: Schematic view of the optics and experimental hutch of the Materials and Magnetism beamline (I16) of the DLS, showing the 6-axis kappa diffractometer with the closed-cycle cryostat mounted on the goniometer rotational stages. A detail of the detector assembly is also reported, illustrating the polarisation analyser stage with the in-vacuum crystal and the five point detectors and the Pilatus 100K area detector mounted at a $\approx 9^\circ$ offset. Figure adapted from Ref. [52].

figuration. Energies in the tender X-ray window $2.7 - 3.3$ keV are also available but require a special setup where the monochromator is used in a non-standard four-bounce mode and extra-care must be taken in order to minimize air absorption. A liquid-nitrogen-cooled monochromator, placed downstream with respect to a gas bremsstrahlung collimator, is used to monochromatise the beam. A choice between a channel-cut Si(111) crystal and a Si(111) or Si(311) double crystal is available. However, given its stability and ease of use, the channel-cut crystal is used for most of the measurements, including the ones discussed in this work. The energy resolution is determined by the Darwin width of the particular reflection chosen, which is about $\Delta E/E = 1.33 \times 10^{-4}$ for Si (111) [53]. The monochromatic beam is focused by a pair of 1.2 m mirrors. The first one is a 96 mm radius sagittal cylinder, which focuses the beam vertically, while the second is a flat mirror with a circular mechanical bender (tangetial radius ≈ 5.8 km), which provides horizontal focusing. This results in a beam of Gaussian shape with a spot size at the sample around $20(\mathrm{V}) \times 200(\mathrm{H})\ \mu\mathrm{m}^2$. The coating of the first mirror can be selected between

Si and Rh depending on the energy of the incident beam in order to reject higher harmonics coming from the monochromator and the undulator. Kirkpatrick-Baez (KB) mirrors can be also used when additional focusing is needed, e.g. for spatially resolved magnetic domain mapping. The polarisation of the incident beam can be tuned by means of a quarter-wave phase retarder placed between the monochromator and the mirrors. After the mirrors, several components for beam conditioning and monitoring are present along the beam path. In particular, different sets of slits can be used to control the beam size while the intensity and precise position of the beam can be measured by two ionization chambers and a beam position monitor, respectively, installed in the experimental hutch. Motorized metallic foils can be inserted along the beam between the two ionization chambers in order to attenuate the incident intensity when necessary. The experimental hutch is further equipped with a polarimeter to measure the polarisation of the incoming beam and a fast shutter, which can be used to block the beam between two consecutive detector acquisitions[9].

The core of the beamline is a Newport 6-axis N-6050 Kappa diffractometer, which can be used to perform experiments in both vertical and horizontal scattering geometry. The former one was used for all the measurements presented in this work. Following the framework introduced by Lohmeier and Vlieg [54], which the reader is referred to for a rigorous definition of all the relevant rotational degrees of freedom and the corresponding rotation matrices, the goniometer geometry is conveniently described in terms of three sample angles (ω, χ, Φ), two detector angles (δ, γ) and one shared between the two (α). γ and α are not used in vertical scattering geometry, thus effectively resulting in a 4-axis configuration. In this case, the detector angle δ coincides with the scattering angle 2θ, ω is the rocking angle with rotation axis perpendicular to the scattering plane and the χ axis lies in the scattering plane along the incident beam direction. Another angle often mentioned in the magnetic scattering literature is the sample azimuth ψ, which describes a rotation around an axis parallel to the scattering vector $\mathbf{Q}$ (see Fig. 2.2). This is a so-called "virtual" rotation since it is realized by a combination of multiple goniometer rotations coupled together. The sample azimuth is particularly relevant in magnetic scattering as it permits to vary the projection of the magnetic moments in a magnetic system with respect to the scattering plane while keeping $\mathbf{Q}$ fixed to satisfy the Bragg condition. The kappa geometry provides greater flexibility compared to a standard eulerian diffractometer. In particular it allows the goniometer rotational stages to be varied without any particular constraints over a wider angu-

[9]This is particularly useful to prevent beam-induced damage of sensitive samples or minimize beam-heating effects.

lar range and leaves sufficient room for a variety of different sample environments to be installed. These include the closed-cycle Displex cryostat normally used to cool the samples below the magnetic transition temperature and equipment for the application of electric or magnetic fields. The downside of the extra flexibility is a generally larger sphere of confusion with respect to the eulerian case: the latter was estimated to $\approx 70\mu$m. For the investigation of Chapter 3, a pair of small rare-earth permanent magnets was mounted on the goniometer Φ rotational stage on either side of the sample holder. The magnet was fixed on the goniometer stages so that it rigidly followed the diffractometer sample rotations. However, the direction of the magnetic field could be independently rotated around the Φ axis by an additional motor.

The detector arm assembly (Fig. 2.4) supports a Pilatus 100K area detector mounted with an angular offset of about 9° off the main diffractometer detector arm. The Pilatus detector collects the total scattered intensity over a large solid angle and is particularly useful in those cases when a wide portion of the reciprocal space needs to be covered (e.g. for reciprocal space mapping measurements or during the crystal alignment). A polarisation analyser (PA) is also mounted along the main detector arm. This consists of an interchangeable single crystal which can be rocked by an angle θ_P with respect to the scattered beam direction and five different point detectors [namely, an avalanche photodiode (APD) detector, a Si drift detector, a scintillator, a PIN diode and a high-resolution imager] placed downstream with respect to the crystal. Each one of them can be rotated to form an angle $2\theta_P$ with the scattered beam direction and thus measure the diffracted signal from the crystal. Considering the polarisation dependence of Thomson scattering [55], it is possible to show that for $\theta_P = 45°$ the diffraction from the PA crystal filters the polarisation component perpendicular to the scattering plane. Therefore, by rotating the whole crystal-detector assembly around the scattered beam direction, it is possible to select either the σ'- or π'-polarised component of the diffracted signal. The crystal must then be chosen in order to provide an (hkl) reflection with $\theta_P \approx 45°$ for the X-ray energy at which the measurements are performed. While the latter is fixed by the absorption edge of the material in a resonant experiment (see Sec. 2.1.1.2), in the case of NXMS the X-ray energy can be chosen to match a suitable reflection of the PA crystal.

2.1.2 Resonant inelastic X-ray scattering

RIXS is a spectroscopic technique which represents the extension of the REXS process schematically represented in Fig. 2.3 to the inelastic case where the energy $E_{\text{in}} = \hbar\omega_{\mathbf{k}_{\text{in}}}$ of the incident photon is different from the energy $E_{\text{out}} = \hbar\omega_{\mathbf{k}_{\text{out}}}$ of the scattered one. In the case of RIXS, energy as well as momentum is transferred from the incident photon to the system of atomic electrons. The latter is thus left in an excited state by the scattering process so that an excitation is created with energy E_{exc} and momentum $\hbar\mathbf{Q}$ given by:

$$\begin{aligned} E_{\text{exc}} &= E_{\text{in}} - E_{\text{out}} \\ \hbar\mathbf{Q} &= \hbar\mathbf{k}_{\text{out}} - \hbar\mathbf{k}_{\text{in}} \end{aligned} \tag{2.19}$$

This is schematically shown in Fig. 2.5(a), where a valence electron is promoted to an empty level at higher energy in the final state. In a typical RIXS experiment, the energy of the incident X-rays is fixed to one of the sample absorption edges and inelastic spectra are collected for a fixed value of the scattering vector $\mathbf{Q}$, i.e. a fixed scattering geometry, by measuring the energy of the scattered photons. The energy loss[10] $E_{\text{in}} - E_{\text{out}}$ directly reflects the energy of the excitations of the system of atomic electrons. The incident photon can also transfer angular momentum, which results in a rotation of the incident wave polarisation.

Fig. 2.5(b) summarises the main elementary excitations and their approximate energy scales in the case of TMOs. RIXS offers the unique possibility to measure excitations over a wide energy range from phonons and magnons at the meV energy scale to electronic excitations at an energy of a few eV. Particularly relevant in the case of TMOs are the excitations of orbital (charge) and magnetic origin. An example of the former is represented by the so called *d*-*d* excitations, which involve the promotion of a valence *d* electron to another empty *d* levels split from the first one as a result of crystal field or SOC [similar to the case of Fig. 2.5(a)]. On the other hand, excitations of magnetic origin correspond to the generation of collective spin-wave modes (magnons) where the ordered moments of a magnetic material oscillate in phase in a wave-like fashion. In contrast to *d*-*d* excitations, which are usually well-localised, magnons generally show a dispersion as a function of the momentum transfer throughout the Brillouin zone (BZ).

Similar to REXS [see third line of Eq. (2.5)], RIXS originates from the terms of the electron-radiation interaction Hamiltonian linear in the vector potential [$\mathscr{H}_3$

[10] In general, the incident photon can also gain energy as a result of the interaction process. However, only energy loss processes are of interest for the present work.

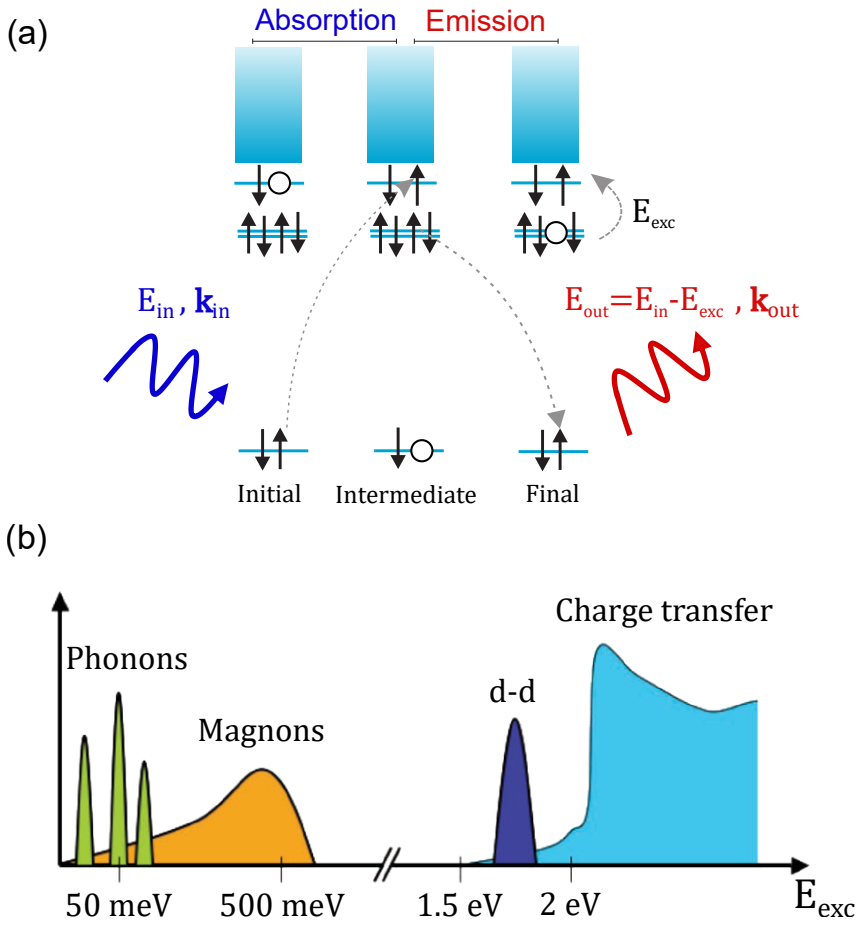

Figure 2.5: (a) Schematic of the RIXS two-step process. An X-ray photon with energy E_{in} and wave vector $\mathbf{k}_{\text{in}}$ is absorbed in a resonant transition from a core level to an empty valence state. The resonant atom subsequently returns to its ground state through emission of a photon with a different energy E_{out} and wave vector $\mathbf{k}_{\text{out}}$. The energy and momentum transferred to the system correspond to an elementary excitation with energy $E_{\text{exc}} = E_{\text{in}} - E_{\text{out}}$ and momentum $\hbar\mathbf{Q} = \hbar\mathbf{k}_{\text{out}} - \hbar\mathbf{k}_{\text{in}}$. (b) Different elementary excitations probed by RIXS in condensed matter systems and their approximate energy scales in strongly correlated electron materials such as TMOs. Figure adapted from Ref. [39].

and $\mathscr{H}_4$ in Eq. (2.1)]. The spin-dependent term $\mathscr{H}_4$ is generally weaker than the $\mathscr{H}_3$ term proportional to $\mathbf{A}\cdot\mathbf{p}$ and can be neglected [38, 39]. Following from Eqs. (2.2) and (2.3), the RIXS double differential cross section, proportional to the measured intensity, can be written as [39]:

$$\begin{aligned}\frac{d^2\sigma}{d\Omega\, d\hbar\omega_{\mathbf{k}_{\text{out}}}} &= \frac{V^2\omega_{\mathbf{k}_{\text{out}}}^2}{\hbar c^4} w = \\ &= \frac{\pi e^4}{2\varepsilon_0^2 m^4 c^4}\frac{\omega_{\mathbf{k}_{\text{out}}}}{\omega_{\mathbf{k}_{\text{in}}}}\sum_f \left|\sum_n\sum_{i,j}\frac{\langle f|e^{-i\mathbf{k}_{\text{out}}\cdot\mathbf{r}_i}\boldsymbol{\varepsilon}^*_{\text{out}}\cdot\mathbf{p}_i|n\rangle\langle n|e^{i\mathbf{k}_{\text{in}}\cdot\mathbf{r}_j}\boldsymbol{\varepsilon}_{\text{in}}\cdot\mathbf{p}_j|g\rangle}{E_g+\hbar\omega_{\mathbf{k}_{\text{in}}}-E_n+i\Gamma_n}\right|^2 \times \\ &\times\,\delta[E_f - E_g + \hbar(\omega_{\mathbf{k}_{\text{out}}} - \omega_{\mathbf{k}_{\text{in}}})] \end{aligned} \tag{2.20}$$

Eq. (2.20), which is normally referred to as Kramers-Heisenberg cross section, is very general and includes all possible transitions from an initial to a final state through an intermediate one. In many cases its expression can be be further simplified by including only the first term in the mutipole expansion of the vector potential (2.12). The delta function expresses the conservation of energy and imposes that the energy lost by the photon ($\hbar\omega_{\mathbf{k}_{\text{in}}} - \hbar\omega_{\mathbf{k}_{\text{out}}}$) is transferred to a sample excitation of energy $E_{\text{exc}} = E_f - E_g$. Similar to the case of REXS, an enhancement of the scattered intensity occurs when the energy of the incident photon is tuned to one of the absorption edges of the material under study, so that $\hbar\omega_{\mathbf{k}_{\text{in}}} = E_n - E_g$. Despite the resonant enhancement, the transition matrix elements of Eq. (2.20) are small: as a result, RIXS is a photon-hungry technique which requires the high photon flux of third-generation synchrotron sources.

One of the features which contributed to the success of RIXS as an experimental technique lies in its already mentioned ability to measure spin-wave excitations. A single magnon excitation corresponds to a single spin-flip transition ($\Delta S_z = 1$) between the initial and final state of the electron system and results in a rotation of the incident beam polarisation. Given the angular momentum $l = 1$ of the incident photon, the latter can transfer $\Delta m_l = 0, 1, 2$ to the solid: therefore, bimagnon excitations with $\Delta S_z = 2$ are also potentially allowed [39]. The detailed microscopic mechanism behind the sensitivity of RIXS to magnetic excitations has been only recently described [56] and experimentally demonstrated [57]. Considering the cross section of Eq. (2.20), these studies showed that spin-flip processes strongly depend on the polarisation of the electromagnetic radiation and the symmetry of the atomic wave functions. These are generally allowed when the RIXS transition involves an intermediate state with a large core-hole SOC (as is the case for the $2p$ orbitals in L-edge RIXS considered in Chapter 5)[11], due to the fact that, in this case, the spin is not a good quantum number in the intermediate state [39].

Although, at present, the technique of choice for the study of magnetic excitations in solids remains inelastic neutron scattering (INS), RIXS represents a valid alternative in cases where (i) the material under investigation contains elements with a large neutron absorption cross section, such as iridium (see Chapter 5) or (ii) the large sample volumes required by INS (in the order of 1 cm^3) are not available, as is the case for many TMOs of modern interest. Similar to the case of REXS, another advantage offered by RIXS with respect to INS is [39] the element and orbital selectivity, due to the possibility of tuning the incident energy to a particular absorption edge of a given chemical species of the sample under study. On the other hand, INS still offers a significantly better energy resolution due to the much lower energy

[11] The single spin-flip channel is forbidden, for instance, at the K edge of TMs [58].

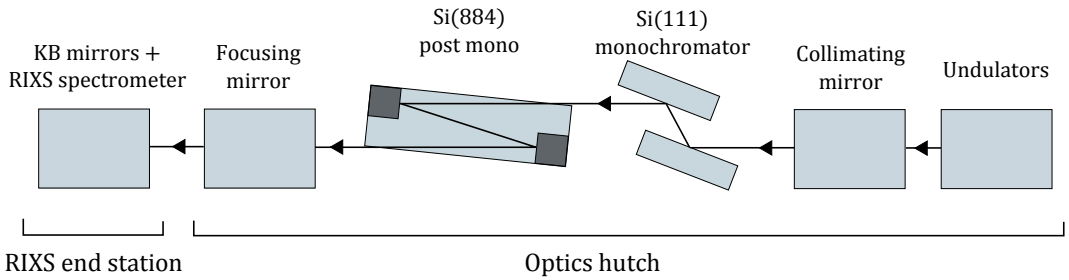

Figure 2.6: Schematic setup of the optics hutch and RIXS end station of the ID20 beamline of the ESRF at the Ir L_3 edge X-ray energy ($E \approx 11.2$ keV).

of neutrons (meV as compared to keV for X-rays) for wavelengths $\lambda \approx 1$ Å comparable to typical interatomic spacings. Modern RIXS spectrometers in the hard X-ray range provide energy resolution of $\Delta E \approx 25$ meV which, considering the case of the Ir L_3 edge of interest for the measurements of Chapter 5, corresponds to a tremendous resolving power of $E/\Delta E \approx 4.5 \times 10^5$. Although poorer than the energy resolution reached by state-of-the-art INS instruments, this value is sufficient to investigate the low-energy excitations of many TMOs. Moreover, contrary to RIXS, the relation between the INS cross section and the dynamic structure factor is well understood and allows the extraction of absolute cross section values from the measured intensity.

2.1.2.1 ID20 beamline at the European Synchrotron Radiation Facility

The RIXS measurements discussed in the present work were performed at the RIXS end station of the ID20 beamline of the ESRF [59, 60]. The layout of the beamline is schematically illustrated in Fig. 2.6. The photon source is a 6 m straight section equipped with four in-vacuum U26 undulators and three in-vacuum U32 undulators which produce a continuum spectrum from 4 to 20 keV. The first optical component is a water-cooled total-reflection collimating mirror, which collimates the beam in the vertical direction and provides harmonic rejection with cut-off energies of 12 and 23 keV thanks to SiC- and Rh-coated stripes, respectively. The X-rays are monochromatised by means of a liquid-nitrogen-cooled Si(111) double-crystal monochromator to achieve a bandwidth of about 1.5 eV (comparable to the typical energy resolution of a REXS beamline). In order to achieve the high energy resolution necessary to study low-energy excitations in solids a set of different post-monochromators are available, which are chosen depending on the resonant energy

used for the experiment. In the case of the Ir L_3 edge ($E \approx 11.2$ keV), a Si(884) channel-cut backscattering crystal is used (Bragg angle $\theta_B \approx 85.7^\circ$). The latter provides a bandwidth of about 15 meV. The monochromatic beam is then focused in two steps. In the first one, a total-reflection toroidal mirror focuses the beam down to a minimal spot size of $250(\mathrm{H}) \times 40(\mathrm{V})$ $\mu\mathrm{m}^2$. In the second one, KB mirrors [61] are used to achieve a spot size on the sample smaller than $20(\mathrm{H}) \times 10(\mathrm{V})$ $\mu\mathrm{m}^2$. All the optical elements of the beamline are kept in ultra-high vacuum (10^{-8} mbar) in order to minimize photon-flux losses.

The core of the RIXS end station is the spectrometer, which is shown in Fig. 2.7(a). This is mounted on a 4-axis Huber goniometer which allows to vary the momentum tranfer of the photons[12] both in horizontal and vertical scattering geometry. RIXS experiments are normally performed in horizontal scattering in proximity of 90° scattering angle in order to suppress the elastic Thomson scattering signal from the sample. Energy analysis at the Ir L_3 edge is achieved by means of five Si(844) crystal analysers which operate at the same Bragg angle θ_B as the back-scattering channel-cut post-monochromator to improve the energy resolution[13]. The analysers are installed inside a helium-filled chamber to reduce air scattering. They collect the scattered radiation from the sample and reflect it back towards the detector.

The ID20 spectrometer operates in the Rowland circle geometry [see Fig. 2.7(b)]: the sample, analysers and detector lie on the same circumference and the curvature radius of the analysers ($R = 2$ m) matches the circle diameter. This geometry allows to focus the scattered X-rays on the detector position and simultaneously guarantees that the radiation is reflected from the whole crystal analyser surface with the same Bragg angle. Although this geometry would require a single spherically-bent single crystal, bending a crystal introduces strain, which significantly deteriorates the spectrometer energy resolution. Therefore diced analysers are used in practice: the latter consist of a polygonal approximation to a spherical crystal made by cubic-shaped dices (edge size $c = 0.72$ mm) glued on a spherical substrate, where each dice is a strain-free crystal.

The Bragg angle seen by the scattered radiation from the sample depends on the position on the single dice surface due to the fact that the latter is flat. As a result, the single dice works in a dispersive manner and reflects the incoming photon over

[12] The available angular range, in particular for the χ circle, is significantly limited with respect to the case of a standard diffraction setup (such as the one outlined in Sec. 2.1.1.3) and a careful pre-alignment of the sample crystal axes is normally needed.

[13] For a certain Bragg reflection the energy resolution is given by $\frac{\Delta E}{E} = \frac{\omega_D}{\tan\theta_B}$, where ω_D is the Darwin width of the reflection [63, 64]. The resolution thus improves when approaching the backscattering condition $\theta_B = 90^\circ$.

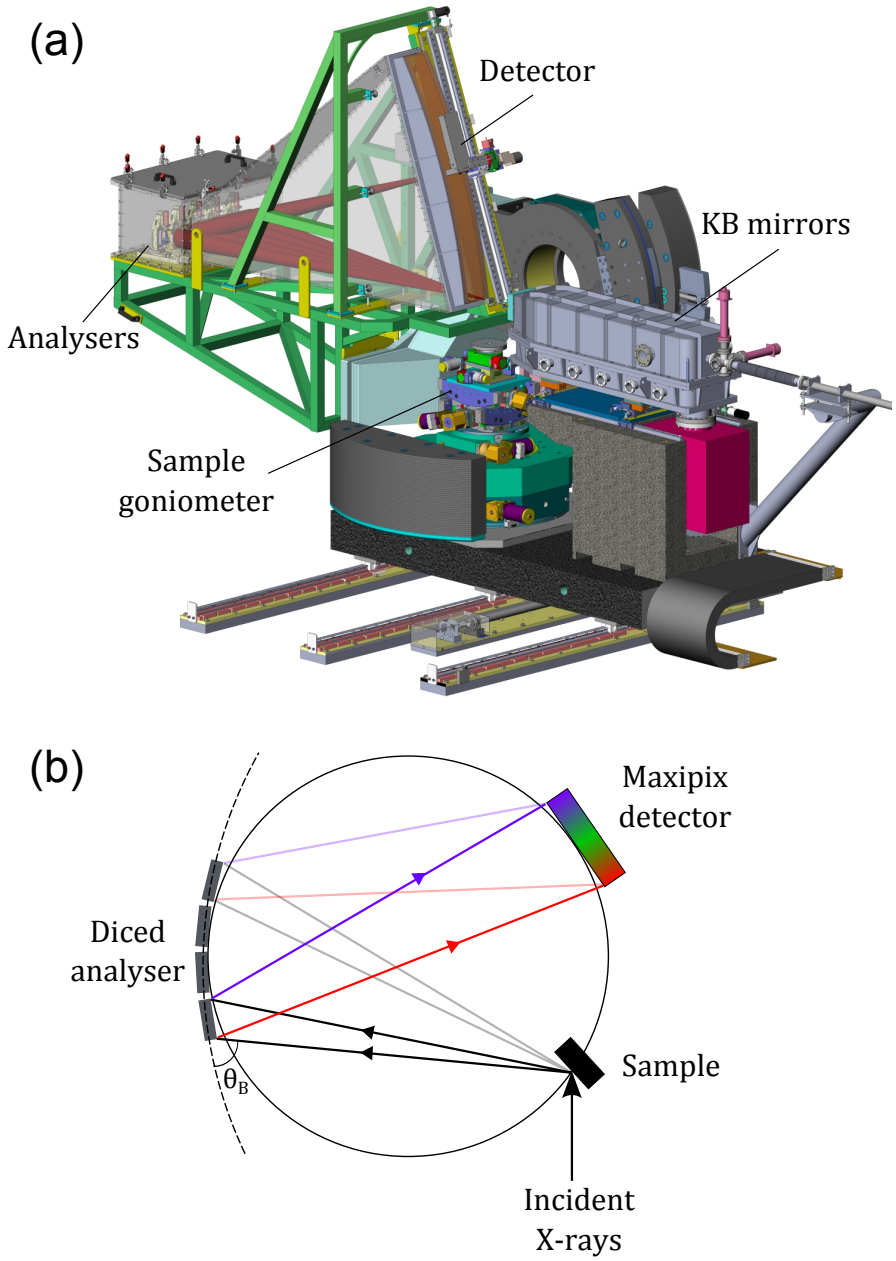

Figure 2.7: (a) Drawing of the RIXS spectrometer at beamline ID20 of the ESRF. Adapted from Ref. [62]. (b) Rowland circle geometry which the ID20 spectrometer in (a) is based on. The sample, diced analyser and 2D position-sensitive detector lie on the same circumference, with the radius of curvature of the detector being equal to the circumference diameter. Each dice of the analyser reflects different wavelengths of the incoming radiation (represented through different colours) depending on the corresponding angle of incidence (Bragg angle θ_B): the different energies within the reflected bandwidth impinge on the $2D$ detector in different positions and can therefore be distinguished.

a bandwidth given by [65, 66]:

$$\frac{\Delta E}{E} = \frac{c}{R}\frac{1}{\tan\theta_B} \tag{2.21}$$

If the entire bandwidth scattered by the analyser was collected simultaneously by a point detector, this would correspond to an energy resolution of around 300 meV at the Ir L_3 edge. In order to overcome this limitation, a 2D position-sensitive detector can be used to discriminate the different energies reflected by each dice at a slightly different angle [65, 66]: this is schematically represented in Fig. 2.7(b), where different wavelengths are represented by different colours. At ID20, a detector of the Maxipix family is used [67]. The detector consists of five chips, where the X-rays from the five analysers are detected separately. Each chip is made of a matrix of 256×256 square pixels of size $p = 55\ \mu$m. Since the Rowland condition is satisfied, the image of a single dice on the detector will be twice the size of a single dice $2c$, and the contribution of different dices almost perfectly superimpose at the detector surface. In this case, the following relation between the position on the detector surface along the dispersive direction (x) and the energy of the photons exists:

$$\frac{dE}{dx} = \frac{E}{2R}\frac{1}{\tan\theta_B} \tag{2.22}$$

The energy resolution is then limited by the detector pixel size:

$$\frac{\Delta E}{E} = \frac{p}{2R}\frac{1}{\tan\theta_B} \tag{2.23}$$

This corresponds to $\Delta E \approx 11$ meV at the Ir L_3 edge energy. Other effects also contribute to the energy resolution, namely the finite size of the source (i.e. the sample) and the so called Johann aberration [68], which becomes important when the analyser Bragg angle departs from 90°. These additional contributions (see Ref. [62] for the corresponding mathematical expressions) result in an overall resolution of about 25 meV.

Finally, the momentum resolution of the RIXS spectrometer is given by the angular coverage of the analysers and can be calculated by differentiating the expression of the photon momentum transfer $\hbar\mathbf{Q} = (4\pi\hbar)/\lambda \sin\theta_B$. This leads, for the case of interest of horizontal scattering geometry, to the following expression [62]:

$$\Delta Q = \frac{4\pi}{\lambda}\frac{\sin 2\theta_B}{\sqrt{2-2\cos 2\theta_B}}\Delta\theta_B \tag{2.24}$$

where $\Delta\theta_B = A/(R\sin\theta_B)$ is the solid angle of collection, which depends on the

analyser aperture A. The latter can be controlled by masking parts of the analyser. For $2\theta_B \approx 90°$, Eq. (2.24) gives $\Delta Q \approx 0.1$ Å^{-1} at the Ir L_3 edge. More details on the momentum resolution for different scattering geometries can be found in Ref. [59].

2.2 Absorption measurements with X-rays

2.2.1 X-ray absorption spectroscopy

XAS is a powerful tool for the study of the electronic structure and local coordination environment of crystalline and amorphous materials. Extensive literature can be found on the topic (see, for instance, Refs. [27, 69–72]). I will limit my discussion to an overview of the main information on the physics of TMOs that can be extracted through absorption spectra. In a XAS experiment the absorption coefficient $\mu(E)$ of the material under study is acquired as a function of the incident photon energy E in proximity of an absorption edge of one the chemical species present in the sample. The necessity of a tunable X-ray source naturally places XAS in the realm of synchrotron techniques. The region including a few tens of eV before and after the edge, which is the one of interest for the present work, is usually referred to as X-ray absorption near-edge spectroscopy (XANES). A few tens of eV after the edge the extended X-ray absorption fine structure (EXAFS) region starts and can be extended up to more than 1 keV. The spectrum in this regime provides information on the interatomic distances and the coordination numbers of the absorbing atom. On the other hand, the XANES signal mainly reflects the structure of the unoccupied atomic levels of the absorbing species and is therefore sensitive not only to interatomic distances, but also to the symmetry of the coordinated atoms, distribution of charges, and potential around the absorbing atom.

XANES originates from the resonant photoelectric absorption of the incident photon from one of the atomic core electrons. The latter is promoted to an empty state above the Fermi level and a hole is left on the core level. The hole is subsequently filled by either emission of a fluorescent photon (radiative decay) or Auger decay (non-radiative process). As already mentioned in Sec. 2.1.1.2, photoelectric absorption is related to the terms of the radiation-electron interaction Hamiltonian linear in the vector potential and is described by matrix element of the type $\langle f|\frac{e}{m}\mathbf{p}\cdot\mathbf{A}|i\rangle$ (neglecting the spin-dependent term). A typical XANES spectrum of a TM in a TMOs consists of three main features: (i) a pre-edge background due to the absorption associated to all other edges of the material under study at lower

energy, (ii) a step-like edge which corresponds to transitions from the core level (a $2p$ orbital for the L absorption edge) to a continuum of electronic excitations and (iii) a sharp peak in proximity of the edge, referred to as *white line*, due to dipole transitions from the core level to the bound nd ($n = 3,4,5$) valence states.

The intensity of the white line is proportional to the local density of unoccupied states in proximity of the Fermi energy (i.e. the population of holes) and is particularly pronounced in TMOs as a result of the presence of the well-localised d orbitals. The seminal works from van der Laan and Thole [73] and Thole and van der Laan [74, 75] showed that the intensity ratio of the white lines at the L_3 and L_2 edges (normally referred to as *branching ratio*) is directly related to the ground-state expectation value of the angular part of the d states spin-orbit operator in units of $\hbar^2$:

$$BR = \frac{2+r}{1-r} \tag{2.25}$$

where BR is the branching ratio, $r = \langle \mathbf{L} \cdot \mathbf{S} \rangle / \langle n_h \rangle$ and n_h is the number of holes in the d levels. The sensitivity of the XANES spectra to the SOC splitting stems from the fact that the resonant absorption of the incident photon obeys the dipole selection rule $\Delta J = 0, \pm 1$. The L_2 edge involves transitions from the core $p_{1/2}$ orbital to the $d_{3/2}$ unoccupied states only, whereas the L_3 edge involves transition from the $p_{3/2}$ orbital to both the $d_{3/2}$ and $d_{5/2}$ empty levels. In the limit of zero SOC of the d electrons, the white line intensity reflects the degeneracy of the initial states (2 and 4 for $p_{1/2}$ and $p_{3/2}$, respectively) and $BR \approx 2$.

In principle, the absorption coefficient of a material can be directly obtained through the Lambert-Beer law by measuring the transmitted X-ray flux across the sample. However, this approach would require extremely thin samples and is practically unfeasible for most solid-state systems, in particular in the soft X-ray regime. Therefore the absorption coefficient is normally measured indirectly: the two most widely used approaches are total-electron yield (TEY) and total-fluorescence yield (TFY) detection. In the former, the current of photoelectrons and Auger electrons emitted as a result of the de-excitation process is measured as a function of the incident X-ray energy. The TEY signal is proportional, at least in first approximation, to the absorption coefficient and thus represents a very convenient way of performing XANES measurements. The main drawbacks of this approach are: (i) the small electron mean free path, which makes the measurements surface sensitive (only the electrons generated in proximity of the surface are detected), (ii) TEY is generally more problematic for insulating samples, where the signal may be weak and charging effects may occur and (iii) the electrons emitted by the sample are sensitive to the application of external magnetic fields, which could have an impact on the

measured signal in XMCD experiments (see Sec. 2.2.2).

On the other hand, TFY detection is based on detecting the fluorescence generated by the radiative decay of the excited atoms resulting from the resonant absorption. Although it overcomes all the limitations of TEY detection, the fluorescence signal is proportional to the absorption coefficient only when the sample is "diluted"[14], i.e. when the contribution of the element of interest is much smaller than the total absorption coefficient, or very thin. When none of the two assumptions just mentioned holds, the TFY signal is affected by the so-called *self-absorption* effect. The latter is due to the fact that the fluorescent photon emitted by the absorbing atom can be re-absorbed by the other chemical species in the compound (as well as the other absorbing atoms) before exiting the material and being detected. In this case, the intensity of the fluorescence signal $I_{\text{fluo}}(E)$ at the incident photon energy E is related to the absorption coefficient of the chemical species of interest $\mu_X(E)$ by the following relation valid for a thick sample (sample thickness much larger than the X-ray penetration depth) [76–79]:

$$I_{\text{fluo}}(E) = C \frac{\mu_X(E)}{\mu_{\text{tot}}(E) + \mu_{\text{tot}}(E_{\text{fluo}}) \dfrac{\sin\phi}{\sin\theta\cos\tau}} \tag{2.26}$$

where C is a constant which includes all the energy independent factors, E_{fluo} is the energy of the fluorescence photons, $\mu_{\text{tot}} = \mu_X + \mu_{\text{back}}$ is the total absorption coefficient depending on μ_X and the background absorption μ_{back} due to all other atoms and other edges of the element of interest, ϕ (θ) is the angle formed by the incident (outgoing) X-rays with respect to the sample surface and τ is the detector solid angle. In order to extract $\mu_X(E)$ from measurements of $I_{\text{fluo}}(E)$ one has to solve Eq. (2.26) at every energy value E. This is practically done by either measuring two independent fluorescence spectra at two different geometries [76] or by measuring a single spectrum and taking tabulated values for μ_{back} [77–79].

2.2.2 X-ray magnetic circular dichroism

XMCD stems from the difference in absorption of right- and left-handed circularly polarised X-ray radiation in a material with a net macroscopic magnetisation[15] [81–

[14] The term is borrowed from the chemistry world, where absorption measurements are often performed on solutions rather then solid-state systems.

[15] XMCD is traditionally applied in ferromagnets, where a large net magnetisation results from the exchange interactions between magnetic moments. However, canted antiferromagnets and antiferromagnets in an applied magnetic field will also give rise to a (small) XMCD signal.

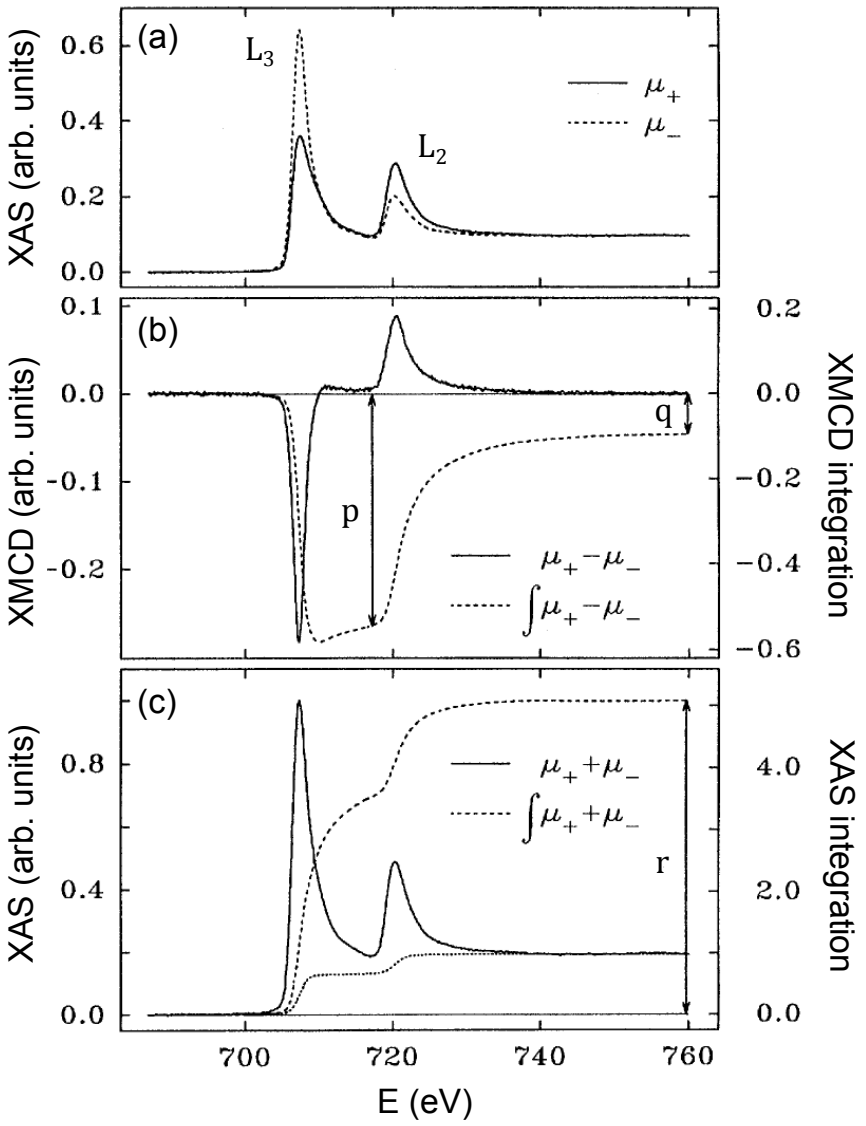

Figure 2.8: XAS and XMCD spectra of iron. Figure adapted from Ref. [80]. (a) L_3 and L_2 absorption spectra of iron measured for opposite directions of an applied external magnetic field. (b) XMCD spectrum (solid line) and corresponding integral (dashed line) derived from the absorption spectra shown in (a). p and q correspond to the integrated XMCD signal at the L_3 and L_2 post edge, respectively. (c) Sum of the absorption spectra shown in (a) (solid line) and corresponding integrated signal (dashed line) after subtraction of the absorption steps (dotted line). r represents the total integrated signal across the L_3 and L_2 edges.

84]. In a typical XMCD experiment, the magnetic sample is polarised through the application of a magnetic field and the absorption coefficient close to an absorption edge of the material under study is measured for different relative orientations of the sample magnetisation and the angular momentum of the incident photons. This is normally done by reversing the field direction and/or the helicity of the X-ray radiation. The difference, i.e. the XMCD signal, is sensitive to the component of the magnetisation along the photon angular momentum (i.e. the direction of propagation), which also coincides with the external field direction in a typical XMCD setup. In comparison with other techniques, such as bulk magnetisation measurements or neutron scattering, XMCD experiments offer several advantages, in particular: (i) the dichroic signal can be directly used to extract the spin and orbital magnetisation separately, (ii) by measuring the dichroism at absorption edges the technique is element specific and allows to disentangle the contribution to the magnetisation from different chemical species and (iii) the technique is extremely sensitive, so that magnetic moments as small as $0.001\,\mu_B$ per atom can be detected [27]. The sensitivity is greatly enhanced when the absorption process involves a final state which is strongly magnetically polarised, as is the case for the $2p_{3/2} \rightarrow nd$ and $2p_{1/2} \rightarrow nd$ transitions at the TMs L_3 and L_2 edges, respectively.

The origin of the XMCD signal can be understood in terms of the dipole selection rules of the electronic transition from a core state to a bound state at higher energy involved in the absorption process. The photon angular momentum projection along the propagation direction is equal to $\hbar$ and $-\hbar$ for right and left circularly-polarised radiation, respectively. The latter are defined such that the electric field of the X-ray wave rotates clockwise (anti-clockwise) for right-handed (left-handed) light as viewed along the wave vector $\mathbf{k}$. In a dipole-allowed electronic transition ($\Delta l = \pm 1$), the angular momentum of the incident photon is transferred to the absorbing electron so that

$$\Delta m_l = \begin{cases} +1\,, & \text{right-handed polarisation} \\ -1\,, & \text{left-handed polarisation} \end{cases} \tag{2.27}$$

When a magnetic field is applied to the sample, final states with different values of the m_l quantum number are split by the Zeeman interaction term and thus generally have a different electron occupation number. Therefore, given the selection rules of Eq. (2.27), the absorption of right and left circular polarisation, which is proportional to the number of empty final states available, will be different.

One of the reasons that contributed to the success of XMCD as a standard technique for the investigation of magnetic properties of matter was the introduction

of the so-called *sum rules* [85, 86], which directly relate integrals of the dichroic signal over the relevant absorption edges to the orbital (m_{orb}) [85] and spin (m_{spin}) [86] magnetic moment of the absorbing atom. Following Chen *et al.* [87], the sum rules of TM elements can be written as:

$$\begin{aligned} m_{\text{orb}}[\mu_B/\text{atom}] &= -\frac{4q}{3r}(10-n_d) \\ m_{\text{spin}}[\mu_B/\text{atom}] &\approx -\frac{6p-4q}{r}(10-n_d) \end{aligned} \tag{2.28}$$

where n_d is the number of electrons in the TM d orbitals and the integrals p,q,r are defined as follows:

$$\begin{aligned} p &= \int_{L_3} (\mu^+ - \mu^-)dE \\ q &= \int_{L_3+L_2} (\mu^+ - \mu^-)dE \\ r &= \int_{L_3+L_2} (\mu^+ + \mu^-)dE \end{aligned} \tag{2.29}$$

Here, $\mu^+(E)$ [$\mu^-(E)$] corresponds to the absorption spectrum measured for parallel (antiparallel) orientation of the sample magnetisation and photon angular momentum [so that $(\mu^+ - \mu^-)$ is the XMCD signal] and E is the energy of the incident photons. In the second line of Eq. (2.28), I have neglected the expectation value of the z component of the magnetic dipole operator, normally referred to as $\langle T_z \rangle$. This approximation is motivated by the fact that this extra contribution is much smaller than the spin moment in a wide majority of practical cases [88] (e.g. this introduces an error of only a few percent in 3d TMOs [27]). Representative XMCD spectra collected on an iron thin film by Chen *et al.* [87] are shown in Fig. 2.8, along with visual definitions of the integrals p,q,r. It should be noted that in the integral defining the quantity r, $\mu^\pm$ refer to the absorption spectra after subtraction of the pre-edge background and the L_3 and L_2 absorption steps (as evidenced by the fact that r is constant in the flat post-edge region). This means that the absolute values of m_{orb} and m_{spin} are generally sensitive to the functional form used to model the absorption step and the pre-edge background. On the other hand, the ratio

$$\frac{m_{\text{orb}}}{m_{\text{spin}}} \approx \frac{2q}{9p-6q} \tag{2.30}$$

does not directly depend on the XAS signal but only on their difference, and therefore it is generally more robust.

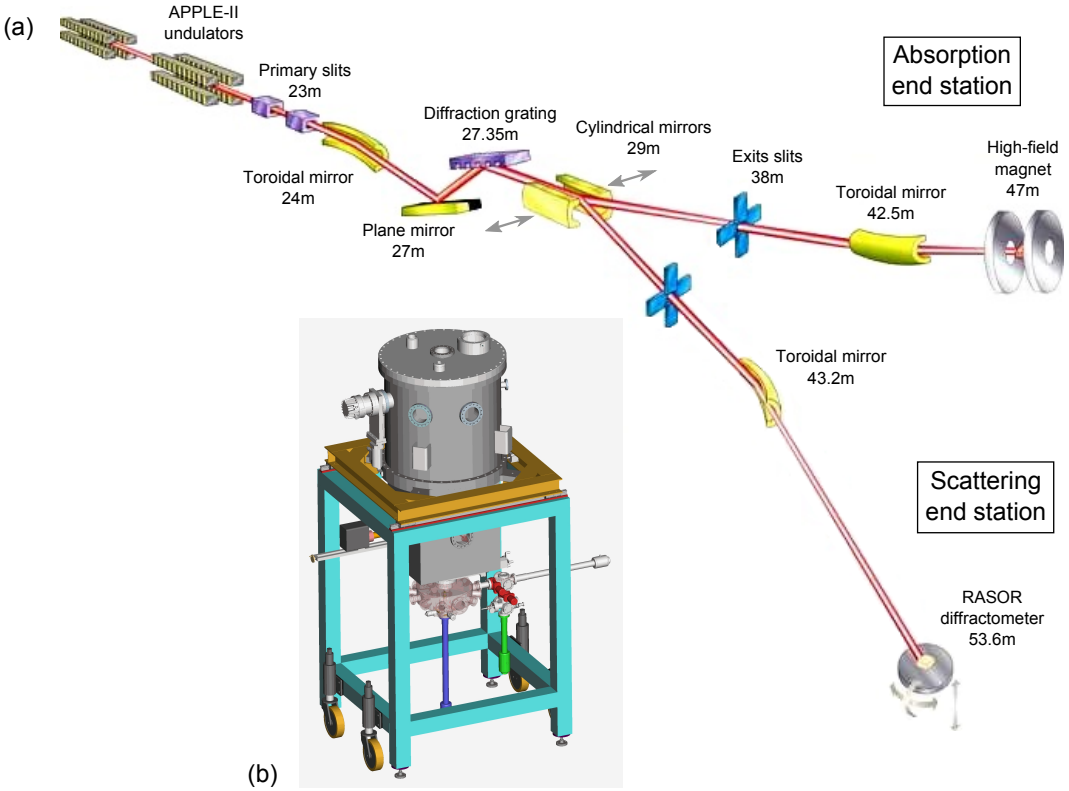

Figure 2.9: (a) Schematic view of the Beamline for Advanced Dichroism Experiments (BLADE) at the DLS. (b) Drawing of the high-field magnet in the absorption end station.

2.2.3 I10: Beamline for Advanced Dichroism Experiments (BLADE) at the Diamond Light Source

The Co *L*-edge (Chapter 3) and O *K*-edge (Chapter 4) XANES and XMCD measurements were performed at the absorption end station of the Beamline for Advanced Dichroism Experiments (BLADE) at the DLS[16]. The light source consists of two identical APPLE-II undulators [89] [see Fig. 2.9(a)]. Each undulator consists of four movable magnet arrays with 40 full-size periods of length 48 mm and a variable undulator gap. Any arbitrary polarisation state (linear in any direction, circular left, circular right) can be achieved by varying the relative alignment of neighbouring magnets (the so-called *row phase*), while the energy of the beam can be tuned in the soft X-ray window $400 - 1600$ eV by either simultaneously shifting the two upper magnets with respect to the lower ones (the so-called *jaw phase*) or by changing the undulator gap. Monochromatisation of the X-ray beam is achieved by a collimated plane-grating monochromator. This gives flexibility to operational modes of the beamline such as being able to operate in either high-resolution mode or high-

[16]The setup used for the Ru *L*-edge measurements will be briefly outlined in Chapter 4.

harmonic suppression mode. Other optical components include a toroidal and a plane mirror upstream with respect to the grating and a cylindrical and toroidal (one for each experimental hutch) mirror placed downstream of the grating. The grating line density is 400 lines mm^{-1} and gold coating were used for both the grating and the mirrors. The depolarisation effect from the beamline optics can be neglected at the working energy since the grazing angles for the mirrors and grating are less than 1.5° [89].

The core component of the absorption end station is the high-field superconducting magnet [Fig. 2.9(b)]. This allows to vary the magnetic field applied to the sample in the range ± 14 T at ≈ 0.5 T min^{-1}. The system is equipped with a ^{4}He cryostat which can reach any temperature between 3 and 420 K. The sample is placed in ultra-high vacuum and can be translated in both directions in a plane normal to the incident beam and rotated by $\pm 90^{\circ}$ about the vertical axis in order to vary the X-ray angle of incidence. The absorption can be measured in both TEY and TFY detection mode. TEY detection is achieved by grounding the electrically-isolated sample through a sensitive current amplifier, while the fluorescence is measured by means of a photodiode placed close to the sample surface.

Chapter 3

The 3d case: systematic investigation of the ground-state magnetic properties of the weak ferromagnets (Mn,Co,Ni)CO_3 and $FeBO_3$

Contents

3.1 Introduction 80

3.2 Crystal and magnetic structure: the Dzyaloshinskii-Moriya interaction 82

3.2.1 Magnetic structure factors and rotating field measurements 88

3.3 Bulk magnetisation measurements 91

3.4 Band filling control of the Dzyaloshinskii-Moriya interaction 95

3.4.1 Magnetic domain imaging 105

3.5 Orbital contribution to the magnetic moment across the series 110

3.6 Role of the orbital moment in $CoCO_3$ 118

3.6.1 Orbital moment contribution investigated by XMCD . . 118

3.6.2 Magnetocrystalline anisotropy 121

3.6.3 Forbidden charge scattering 126

3.6.3.1 Experimental data and empirical model 126

3.6.3.2 Microscopic model and role of the SOC . . . 136

3.6.4 Magneto-striction 138

3.7 Conclusions 141

3.1 Introduction

In the common paradigm of the physics of TMOs, SOC is generally regarded as negligible for 3*d* electrons, where its role is merely of a small perturbation to the ground-state Hamiltonian [1]. This contrasts with the case of heavier (4*d* and 5*d*) TM compounds (which will be discussed in the following chapters) where SOC competes with the crystal field and other relevant energy scales on an equal footing and gives rise to more exotic ground states [7]. Nonetheless, even for 3*d* TM compounds, SOC is expected to have a significant impact on the magnetic properties of the system whenever a finite orbital moment is present [1]. Considering the very common case of a TM in an octahedral environment of oxygen atoms, the cubic crystal fields splits the TM *d* levels into lower t_{2g} and upper e_g states. For fully occupied t_{2g} orbitals, the electronic ground state can be described in terms of the sole e_g orbitals, where the orbital moment is quenched [1]. A prominent example is represented by the Cu^{2+} ion in the superconducting cuprates, where most aspects of the physics of the system are accounted for, to first order, by a spin-only Hamiltonian [90]. This is generally not the case for partially filled t_{2g} levels, which can be mapped into states with an effective orbital moment $L_{\text{eff}} = 1$ (see Sec 1.1.4): SOC can then act on these states and have a sizeable impact on the electronic and magnetic properties.

One of the manifestations of the presence of SOC in 3*d* TMOs is the appearance of an anisotropic exchange term in the coupling between spins, known as Dzyaloshinskii-Moriya interaction (DMI) [91, 92]. In magnetically-ordered systems, the DMI favours a spin canting of otherwise (anti)parallel-aligned magnetic moments. The canting is at the origin of the so called *weak ferromagnetism*, the existence of a small spontaneous net magnetisation in certain classes of AFM materials. In the latter, the moments of the two magnetic sublattices are not exactly antiparallel as in a conventional antiferromagnet: this gives rise to a small FM moment in the direction orthogonal to the AFM axis. Weak ferromagnetism played a crucial role in the development of the theory of the antisymmetric exchange interaction: in fact, the first studies by Dzyaloshinskii and Moriya aimed at providing an explanation to the small spontaneous magnetisation observed in some AFM crystals, such as α-Fe_2O_3 and the carbonates $MnCO_3$ and $CoCO_3$ considered in the present investigation. Weak ferromagnets are very well-known compounds, which have been intensively studied since the early reports from Dzyaloshinskii and Moriya in the late 1950s [91, 93–117]. However, the underlying physics is in many respects analogous to the one behind several materials of modern interest: in particular, the DMI

is responsible for various non-collinear magnetic ground states, such as spin-spirals [118] and Skyrmions [119–121]. These exotic phases of matter are of great interest for both the fundamental understanding of the physics involved and their potential technological impact. Skyrmions, for instance, are topologically protected states, which makes them particularly promising for spintronics applications. The DMI is also an important ingredient in multiferroic compounds with spiral magnetic order, where it is thought to couple the spin with the lattice and results in the appearance of an electric polarisation [4, 122, 123]. The DMI also stabilizes chiral domain walls, which can be driven by an electric current rather than a magnetic field and can be used for the manipulation of spin-wave currents [124, 125]. The ability to model and predict magnetic properties of materials hosting a finite DMI is thus of great contemporary interest.

Weak ferromagnets are ideally placed in this respect, since, in contrast to the complex non-collinear phases just mentioned, they are well characterised materials with a rather simple magnetic structure. For these reasons, they represent an ideal model system where to check the reliability of modern first principles calculations to predict material properties. In this chapter, I present a detailed systematic investigation of the magnetic properties of the series of isostructural weak ferromagnets $MnCO_3$, $FeBO_3$, $CoCO_3$ and $NiCO_3$ by means of a combination of *ab-initio* calculations performed by our collaborators, REXS, NXMS and XMCD. The calculations predict a previously unreported change in the sign of the DMI as the population of the 3*d* orbitals increases going from the Mn to the Ni member of the family. The sign of the DMI, encoded in the phase of the magnetic scattering amplitude, is accessed by a novel approach based on a very peculiar interference between the NXMS amplitude and a subtle quadrupolar resonance present at the TM *K* absorption pre-edge. The measurements confirm the theoretical predictions remarkably well and represent a significant step towards the possibility of tuning the DMI in materials for spintronics application. The same calculations also result in a non-obvious trend of the orbital contribution to the magnetic moment across the series, with a particularly large value found in $CoCO_3$. These findings are again clearly supported by the NXMS and XMCD measurements: the latter also revealed that the coupling between the spin and the large orbital moment induced by SOC results in a significant single-ion anisotropy and, more spectacularly, in the emergence of a peculiar space-group forbidden scattering process induced by the magnetic order.

The chapter is organized as follows. The crystal and magnetic structure of the weak ferromagnets is described in Sec. 3.2, where the effect of the application of a small magnetic field on the magnetic ordering is also outlined. Sec. 3.3 summarises the results of bulk measurements of the net magnetisation and compares them to the

corresponding values found in the literature. Sec. 3.4 provides an overview of the main findings of the resonant scattering measurements addressing the sign of the DMI across the different compounds of the series, along with a full-field imaging investigation of the magnetic domains in $CoCO_3$. Most of the discussion will focus on the measurements presented in Sec. 3.5 and 3.6. In the former, I will discuss the results of a systematic NXMS investigation of the orbital contribution to the TM ion magnetic moment in the various members of the weak ferromagnets family, while the latter summarises specific results concerning $CoCO_3$. In particular, while Sec. 3.6.1 deals with a soft XMCD study of the relative size of the orbital and spin magnetic moment, Secs. 3.6.2, 3.6.3 and 3.6.4 discuss NXMS and diffraction measurements specifically addressing the single-ion anisotropy of the magnetic interactions, the presence of a weak forbidden term in the scattering amplitude and magneto-strictive effects, respectively. Sec. 3.5 and 3.6 represent a summary of the results of several experiments performed at the DLS over the course of more than three years which produced a large volume of data. Additional measurements not essential for the discussion are reported in Appendix A. Finally, the conclusions of the study are drawn in Sec. 3.7.

3.2 Crystal and magnetic structure: the Dzyaloshinskii-Moriya interaction

The weak ferromagnets ACO_3 (A = Mn,Co,Ni) and $FeBO_3$ represent the model systems for the investigation of the phenomenon of weak ferromagnetism and their crystallographic, magnetic and electronic properties have been extensively studied by several authors [91, 93–117, 126]. All the members of the series are isostructural compounds, with the trigonal $R\bar{3}c$ crystal structure (space group No. 167) [93, 107–110]. The latter consists of alternating TM and O-C/B layers, such that each TM ion is at the centre of a distorted TMO_6 octahedra. The lattice can be described by means of either rhombohedral ($a = b = c$, $\alpha = \beta = \gamma \neq 90°$) or hexagonal ($a = b \neq c$, $\alpha = \beta = 90°$, $\gamma = 120°$) axes: the second description is the one adopted throughout the present work. The hexagonal cell, which is shown in Fig. 3.1, is three times as large as the primitive rhombohedral one and contains six C/B atoms at the 6a sites, eighteen O^{2-} ions at the 18e sites and six TM ions at the 6b sites. All compounds display a Néel transition to a magnetically-ordered state where the magnetic moment of each TM ion couples antiferromagnetically with its six nearest neighbours. The single-ion anisotropy of the trigonal lattice forces the moments to

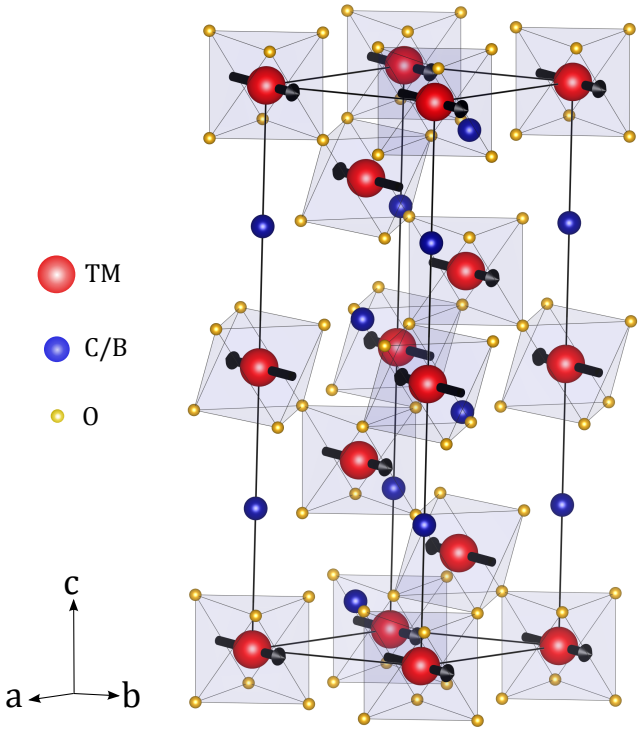

Figure 3.1: Trigonal crystal structure (space group $R\bar{3}c$, No. 167) of the weak ferromagnets ACO_3 (A = Mn,Co,Ni) and $FeBO_3$ in the hexagonal axes description. Large red spheres: TM atoms (Mn, Fe, Co, Ni); medium-size blue spheres: C/B; small yellow spheres: O. The TM, C/B and O atoms occupy the sites $(0,0,0)$ ($6b$), $(0,0,1/4)$ ($6a$) and $(x,0,1/4)$ ($18e$), respectively, with $x = 0.2695, 0.2981, 0.27660, 0.2799$ for $MnCO_3$, $FeBO_3$, $CoCO_3$ and $NiCO_3$ [107, 108, 110], respectively. The arrows represent the magnetic moments of the TM atoms in the AFM phase neglecting the canting induced by the DMI discussed in the text.

lie in the **ab** plane of the crystal. The resultant magnetic structure thus consists of a stack of FM layers along the trigonal **c** axis, each coupled antiferromagnetically to the neighboring ones (see Fig. 3.1). The TM layers occupy the position $z = n/6$ in hexagonal coordinates [see Fig. 3.2(a)], where z is the fractional coordinate along **c**. The structure is described by a propagation vector $\mathbf{k} = (0,0,0)$, so that the magnetic unit cell associated to the periodicity of the ordered moment coincides with the crystallographic one. Similar to the behaviour normally encountered in oxides, the exchange between TM ions is dictated by the oxygen-mediated superexchange and thus depends on the TM-O-TM bond geometry (see Sec. 1.1.2). The key aspect of the physics of weak ferromagnets lies in the structural twist which exists between the oxygen and the TM layers, as shown in Fig. 3.2(a). The latter causes a shift of the oxygen atoms away from the middle point between TM ions: as a result, the inversion symmetry at the oxygen sites is broken and, as I will discuss

hereafter, a finite DMI between magnetic moments becomes allowed. The twist alternates in sign from one oxygen layer to another, so that the crystal is globally centrosymmetric.

The DMI is one of the contributions to the coupling term between two spins $\mathbf{s}_i$ and $\mathbf{s}_j$, which is given by the following general bilinear form:

$$\mathscr{H}_{\text{two-spin}} = \mathbf{s}_i \cdot \underline{\underline{\mathbf{M}}} \cdot \mathbf{s}_j = \sum_{\alpha\beta} M_{\alpha\beta} s^i_\alpha s^j_\beta \tag{3.1}$$

where s^i_α indicates the α-th component of the i-th spin. As any 3×3 second-rank tensor, $M_{\alpha\beta}$ can be decomposed into (i) a multiple of the identity matrix $J\delta_{\alpha\beta}$ (one independent component), (ii) an antisymmetric part $M^A_{\alpha\beta}$ (three independent components) and (iii) a traceless symmetric part $M^S_{\alpha\beta}$ (five independent components). Eq. (3.1) thus becomes:

$$\mathscr{H}_{\text{two-spin}} = \sum_{\alpha\beta} J s^i_\alpha s^j_\beta \delta_{\alpha\beta} + s^i_\alpha s^j_\beta M^A_{\alpha\beta} + s^i_\alpha s^j_\beta M^S_{\alpha\beta} \tag{3.2}$$

where $\delta_{\alpha\beta} = 1(0)$ when $\alpha = \beta$ ($\alpha \neq \beta$). The term $J_{ij} s^i_\alpha s^j_\beta \delta_{\alpha\beta}$ corresponds to the well-known isotropic Heisenberg exchange interaction $\mathscr{H}_{\text{ex}} = J\mathbf{s}_i \cdot \mathbf{s}_j$, which is normally the dominant part of the Hamiltonian. The symmetric part [third term in Eq. (3.2)] expresses the anisotropic exchange interaction: this can always be diagonalized and, in the representative case of a tetragonal crystal, leads to the interaction $\mathscr{H}_{\text{anis. ex}} = J_\parallel s^z_i s^z_j + J_\perp (s^x_i s^x_j + s^y_i s^y_j)$ [1]. Considering $\delta J = J_\perp - J_\parallel$, one can show that $\delta J \approx (\delta g/g)^2 J$ [1]. The magnitude of the symmetric anisotropic exchange thus depends on the deviation $\delta g = |g - 2|$ of the Landé g-factor from the pure spin value and is generally much weaker than the isotropic exchange. The DMI arises from the antisymmetric part of the expansion, which can be written as[1]:

$$\mathscr{H}_{\text{DMI}} = \mathbf{D}_{ij} \cdot (\mathbf{s}_i \times \mathbf{s}_j) \tag{3.3}$$

where $\mathbf{D}_{ij}$ is referred to as the Dzyaloshinskii-Moriya (DM) vector. Following the perturbation theory treatment of Moriya [91, 126], the magnitude of the DM vector is given by $D_{ij} \approx (\delta g/g)J$. Thefore, when the DMI is allowed by symmetry, it is expected to be stronger than the symmetric anisotropic exchange mentioned above.

The presence of this term was first postulated by Igor Dzyaloshinskii on the

[1] By expressing the cross product of the two spins in terms of its Cartesian components, one can easily show that Eq. (3.3) leads to the antisymmetric term $s^i_\alpha s^j_\beta M^A_{\alpha\beta}$ of Eq. (3.2) with the antisymmetric tensor $M^A_{\alpha\beta}$ given by $M^A_{\alpha\beta} = \begin{pmatrix} 0 & D_z & -D_y \\ -D_z & 0 & D_x \\ D_y & -D_x & 0 \end{pmatrix}$, where $\mathbf{D} = (D_x, D_y, D_z)$.

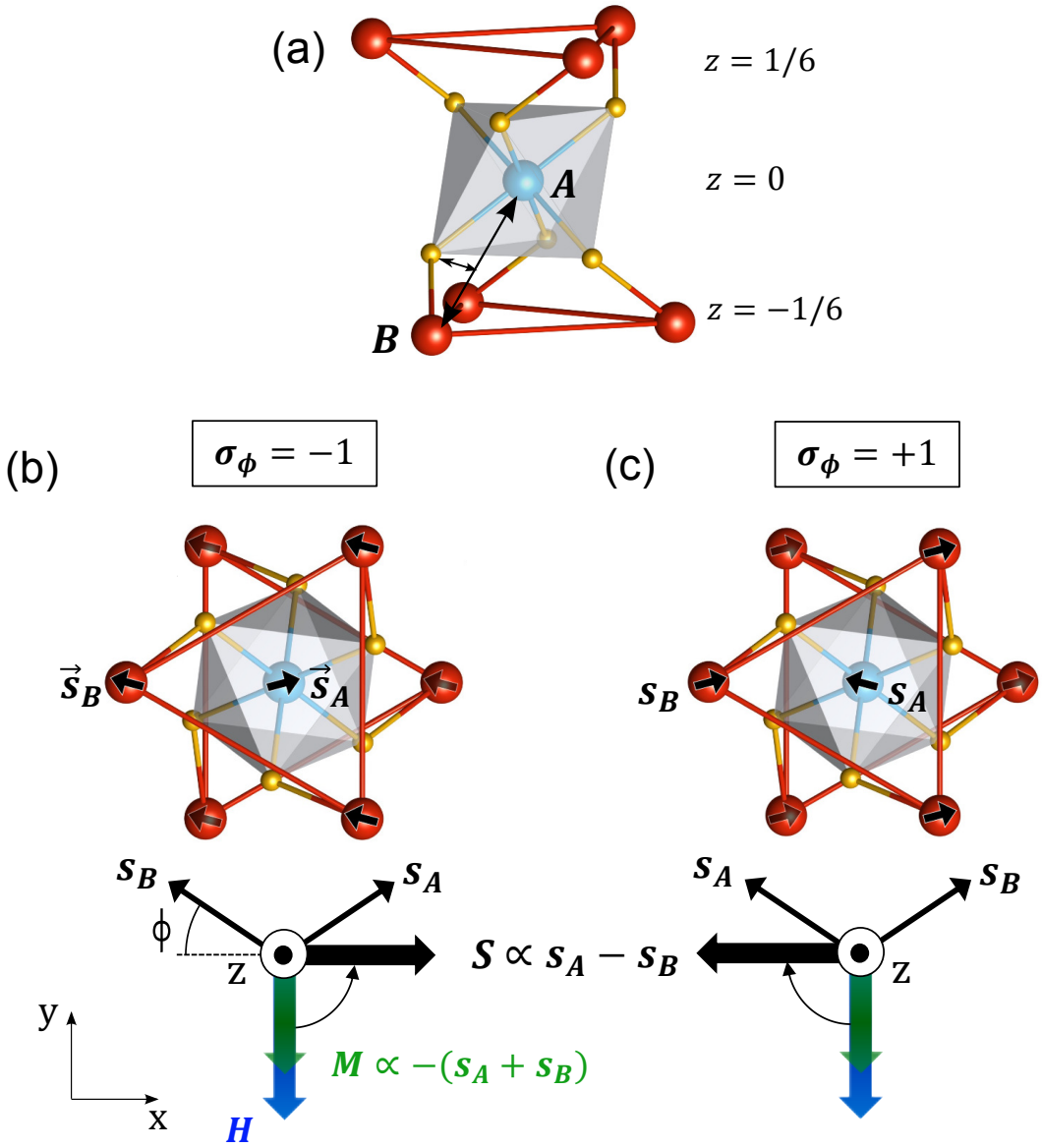

Figure 3.2: (a) Local environment of the TM ion at $(0,0,0)$ (magnetic sublattice A) and its six nearest neighbours (magnetic sublattice B) in the $R\bar{3}c$ crystal structure, with z fractional coordinate along the crystallographic **c** axis. The TM ions of the two sublattices are represented through the light blue (A) and red (B) spheres for clarity; the C/B atoms are omitted for the same reason while the O atoms are depicted through the small yellow spheres. The TMO_6 octahedra centred at $(0,0,0)$ is also displayed, highlighting the shift of the O atoms away from the TM-TM direction at the origin of the finite DMI. (b),(c) Possible spin arrangements for a fixed direction of an external magnetic field **H**. The two configurations differ in the sign σ_ϕ of the DMI-induced canting angle ϕ, defined as the sign of the DM vector **D** along the **c** axis, which is either (b) negative or (c) positive. $\mathbf{s}_A$ and $\mathbf{s}_B$ are the spin angular momenta of the two magnetic sublattices, **M** is the corresponding net magnetisation and **S** is the spin structure factor, opposite in (b) and (c). The **xyz** reference frame is defined such that **x** is perpendicular to a 2-fold axis and contained in a **c** glide plane of the $R\bar{3}c$ structure and **z** is parallel to the crystallographic **c** axis, analogous to Table 3.4.

grounds of phenomenological considerations based on Landau theory [92]. Tôru Moriya [91, 126] subsequently showed that its microscopic origin can be attributed to the SOC in the oxygen-mediated superexchange mechanism between TM ions: in particular, when the crystal symmetry is sufficiently low, the largest term of the anisotropic superexchange which is linear in the SOC has the antisymmetric form of Eq. (3.3). The energy term (3.3) is minimized when the spins lie at a right angle in a plane normal to $\mathbf{D}_{ij}$ such that their cross product is antiparallel to the DM vector. Its effect is thus to favour a spin canting of an otherwise collinear (FM or AFM) moment arrangement.

The existence of a finite antisymmetric term in the coupling energy between spins is dictated by the symmetry of the crystal structure. In crystals of high symmetry this coupling vanishes, while it plays an important role in structures with lower symmetry, such as the trigonal crystal of interest for the present work. The symmetry properties of antisymmetric exchange were first studied by Moriya, who introduced five rules governing the behavior of the vector $\mathbf{D}_{ij}$ [91]. These rules, which are summarised in Table 3.1, determine in which situations the interaction of Eq. (3.3) is non-zero for a particular TM-O-TM bond and in which directions $\mathbf{D}_{ij}$ is expected to point. They do not allow to make any prediction, however, on the magnitude of the DM vector or its sign. As mentioned before, in the specific case of the $R\bar{3}c$ space group of the weak ferromagnets under study, rule No.1 implies that a finite DMI is generally allowed given the shift of the oxygen atom away from the mid-point C between neighbouring TM ions [Fig. 3.2(a)]. A two-fold rotation axis passing through C and perpendicular to the AB direction connecting the TM ions is also present: according to rule No. 4, the DM vector is expected to be orthogonal to the two-fold axis. The $\mathbf{D}_{ij}$ vectors of the three nearest-neighbour pairs of two adjacent layers are related by the three-fold rotation symmetry about the **c** axis of the trigonal $R\bar{3}c$ structure. Their sum gives rise to a resultant **D** vector along the **c** axis. The effect of the DMI is thus to produce a small canting of the moments in the **ab** plane of the crystal, in the same direction for all the TM layers. Therefore, the magnetic ordering is not exactly collinear and a small net macroscopic magnetisation **M** is present in the crystal basal plane (hence the term *weak ferromagnets*).

The magnetic structure can be conveniently described by considering the interaction between the magnetic moment of one of the TM ions in the $z = 0$ layer (which I refer to as sublattice A) and one of its six nearest-neighbour in the layers $z = \pm 1/6$ (which I refer to as sublattice B). This is illustrated in Fig. 3.2. Considering the case of interest for the present discussion in which a small external magnetic field **H** is applied in the **ab** plane of the crystal and neglecting the single-ion anisotropy, the

magnetic Hamiltonian is thus given by:

$$\mathscr{H} = J\mathbf{s}_A \cdot \mathbf{s}_B + \mathbf{D} \cdot (\mathbf{s}_A \times \mathbf{s}_B) - \mu_B g_s \mathbf{H} \cdot (\mathbf{s}_A + \mathbf{s}_B) \tag{3.4}$$

where μ_B is the Bohr magneton, $g_s \approx 2$ is the spin g-factor and $\mathbf{s}_A$ ($\mathbf{s}_B$) is the spin angular momentum of sublattice A (B). The first, second and third term in Eq. (3.4) correspond to the isotropic Heisenberg exchange responsible for the main AFM order, the DMI just discussed and the Zeeman term describing the interaction of the net magnetic moment $\mathbf{m} = -\mu_B g_s(\mathbf{s}_A + \mathbf{s}_B)$ with the external field[2]. For simplicity, I explicitly refer to the TM spin in the present section: however, as I will show in Sec. 3.5, a significant orbital angular momentum $\mathbf{l}$ is present for $NiCO_3$ and $CoCO_3$. In this case, the corresponding contribution to the total magnetic moment, $\mathbf{m} = -\mu_B g_l(\mathbf{l}_A + \mathbf{l}_B)$ ($g_l = 1$), also enters the expression of the Zeeman term and responds to the application of the magnetic field. In the absence of the DMI, i.e. $\mathbf{D} = 0$, the two spins would be perfectly antiparallel ($\mathbf{s}_A = -\mathbf{s}_B$) thus resulting in $\mathbf{m} = 0$ and a corresponding vanishing net magnetisation $\mathbf{M}$. In the case of the finite DMI observed for the compounds of interest, and for small applied field values, the Hamiltonian is minimized introducing a small canting angle[3] $\phi \approx |\mathbf{D}|/(2J)$. The effect of a weak magnetic field ($\mu_B g_s|\mathbf{H}| \ll |\mathbf{D}|$), is to align the net moment $\mathbf{m}$ along the field direction, while maintaining the field-free value of the canting angle. This is strictly true neglecting the effect of the single-ion anisotropy in the **ab** plane of the crystal, which is expected to be small for the compounds of interest [97]. Most of the measurements presented in Sec. 3.4 and Sec. 3.5 are indeed compatible with a perfect alignment of the moment along the external field. However, a small in-plane anisotropy is still present: its role in the physics of the system will be discussed in Sec 3.6.2 in relation to the NXMS measurements. For larger field values, the canting angle increases as the spins rotate to maximize their component along the field direction (see Sec. 3.3). On the other hand, when no magnetic field is applied, multiple domains are expected to occur, with the net magnetisation $\mathbf{m}$ lying along one of the easy magnetisation axes (see Sec. 3.4.1).

For a fixed direction of the net magnetisation (determined by the direction of the external field), the two spin configurations shown in Figs. 3.2(b),(c) are possible. The difference between the latter lies in the direction of the vector $\mathbf{D}$. In the configuration of Fig. 3.2(b), $\mathbf{D}$ is antiparallel to the **c** axis, i.e. $\mathbf{D} < 0$: in this case,

[2] I use the symbol $\mathbf{m}$ instead of $\boldsymbol{\mu}$ for the net moment arising from the spin canting in order to avoid confusion with the total moment of each TM ion of the A and B sublattices, which I shall refer to as $\boldsymbol{\mu}_A$ and $\boldsymbol{\mu}_B$, respectively.

[3] In the present chapter, the canting angle ϕ must not be confused with the goniometer Φ (capital) stage of the diffractometer (see Sec. 2.1.1.3).

Moriya rules
1. When a centre of inversion is located at C, $\mathbf{D} = 0$
2. When a mirror plane perpendicular to AB passes through C, $\mathbf{D} \parallel$ mirror plane or $\mathbf{D} \perp AB$
3. When there is a mirror plane including A and B, $\mathbf{D} \perp$ mirror plane
4. When a two-fold rotation axis perpendicular to AB passes through C, $\mathbf{D} \perp$ two-fold axis
5. When there is an n-fold axis ($n \geq 2$) along AB, $\mathbf{D} \parallel AB$

Table 3.1: The Moriya rules [91] which govern the DM vector, $\mathbf{D}$, between two spins at points A and B with a mid-point at C.

the energy of the system is minimized for a counter-clockwise rotation of the $\mathbf{s}_A$ spin and a clockwise rotation for $\mathbf{s}_B$ around the $\mathbf{c}$ axis. The opposite spin rotation, clockwise for $\mathbf{s}_A$ and counter-clockwise for $\mathbf{s}_B$, occurs for $\mathbf{D}$ parallel to the $\mathbf{c}$ axis, i.e. $\mathbf{D} > 0$, as shown in Fig. 3.2(c). I define the sign of the canting angle ϕ, which I refer to with the symbol σ_ϕ, as the sign of $\mathbf{D}$: the configurations of Figs. 3.2(b) and 3.2(c) thus correspond to $\phi < 0$ ($\sigma_\phi = -1$) and $\phi > 0$ ($\sigma_\phi = +1$), respectively. The structure with $\phi > 0$ is obtained from the structure with $\phi < 0$ (and vice versa) by swapping $\mathbf{s}_A$ and $\mathbf{s}_B$. It should be noticed that the sign of the vector $\mathbf{D}$ cannot be predicted based on the symmetry arguments behind the rules of Table 3.1.

3.2.1 Magnetic structure factors and rotating field measurements

The very subtle difference between the magnetic structures of Figs. 3.2(b),(c) is encoded in the sign of the magnetic structure factors describing the moment arrangement in the magnetically-ordered phase (see Sec. 2.1.1.1). The magnetic structure factors, which are defined by Eq. (2.8), can be calculated for a given magnetic diffraction peak arising from the periodic arrangement of the ordered moments by extending the sums of Eq. (2.8) to the spin and orbital angular momenta of the magnetic species contained in the magnetic unit cell (equivalent to the crystallographic one in this system). As I will show later on in the present chapter, the canted AFM (C-AFM) structures of Figs. 3.2(b),(c) give rise to space-group forbidden magnetic diffraction peaks of the type $(00l)$, $l = 6n+3$ and $(h\bar{h}l), l = 2n+1$[4]. In this case,

[4]Given the three-fold symmetry about the $\mathbf{c}$ axis of the $R\bar{3}c$ space group, a reflection of the type $(h\bar{h}l)$ is equivalent by symmetry to $(0hl)$ and $(\bar{h}0l)$. The h and k values of this trio of equivalent reflections are simply obtained by permuting the three indices h, k and $\overline{h+k}$.

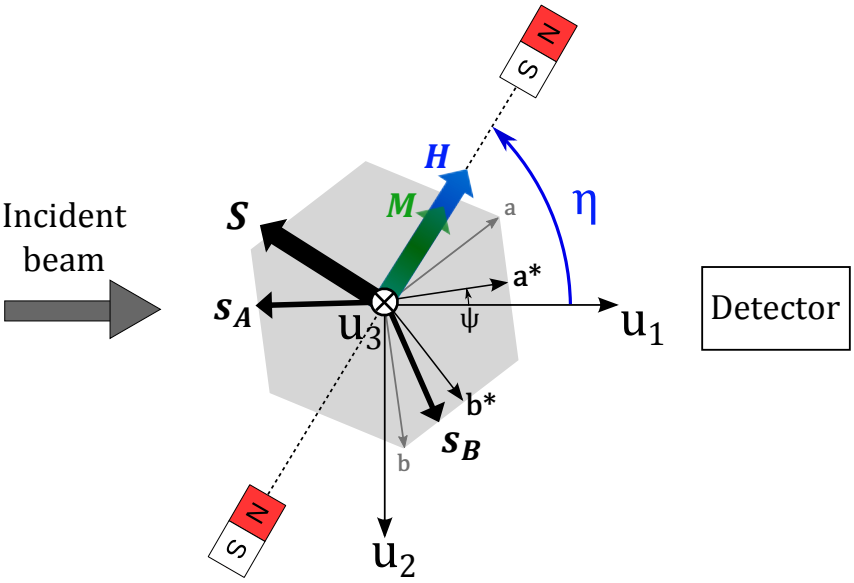

Figure 3.3: Schematic representation of the effect of the rotating magnetic field used to perform the scattering measurements discussed in Secs. 3.4 and 3.5 on the magnetic structure of the weak ferromagnets for the representative case of a specular geometry (crystallographic **c** axis parallel to $\mathbf{u}_3$ and orthogonal to the plane of the page). The spin arrangement corresponds to the case $\sigma_\phi = -1$ [Fig. 3.2(b)]. The $\mathbf{u}_1\mathbf{u}_2\mathbf{u}_3$ reference frame is attached to the vertical scattering plane ($\mathbf{u}_1\mathbf{u}_3$) as defined in Sec. 2.1.1.1. η defines the external field direction while the sample azimuth ψ the orientation of the crystal with respect to the scattering plane. **a** and **b** (**a*** and **b***) are the in-plane basis vectors of the direct (reciprocal) lattice hexagonal unit cell.

the spin structure factor is given by:

$$\mathbf{S} = 3 f_s(\mathbf{Q})(\mathbf{s}_A - \mathbf{s}_B) \tag{3.5}$$

where **Q** is the scattering transfer vector and $f_s(\mathbf{Q})$ is the spin form factor, both already defined in Sec. 2.1.1.1. The factor of 3 simply arises from the fact that the volume of the hexagonal unit cell here considered is three times larger the primitive rombohedral one and thus contains three *A*-*B* pairs of TM ions. An analogous expression holds for the orbital structure factor replacing the spin form factor with the orbital one and $\mathbf{s}_{A,B}$ with $\mathbf{l}_{A,B}$. Eq. (3.5) shows that the structure factors are proportional to the difference of the TM spin angular momenta and are thus orthogonal to the net magnetisation direction. Changing the sign of the canting angle results in changing the sign of **S**, which points in opposite directions for the moment arrangements of Figs. 3.2(b) and 3.2(c).

The magnitude of the canting angle ϕ directly affects the size of the net moment, which is given by $m = -\mu_B g_s |\mathbf{s}_A + \mathbf{s}_B| = \mu_B g_s 2|\mathbf{s}| \sin|\phi|$. The latter can be easily probed by means of bulk magnetisation measurements of the resulting net

magnetisation (see Sec. 3.3). On the other hand, its sign requires the extraction of the phase of the structure factor, which is not accessible in a conventional scattering experiment. Measurements to address the sign of the DMI are outlined in Sec. 3.4. Here, I will show that, although the main AFM order is the same for all the compounds of the series, the sign of the canting angle depends on the number of electrons in the $3d$ orbitals of the TM ion.

The scattering measurements presented in Secs. 3.4 and 3.5 were performed by applying a small magnetic field ($\mu_0 H \approx 35$ mT) in the **ab** plane of the trigonal crystal by means of the rotating magnet setup described in Sec. 2.1.1.3. As discussed in relation to Eq. (3.4), the magnetic moments respond to the presence of the field by aligning the corresponding net magnetisation along the field direction. Assuming a negligible effect of the single-ion anisotropy in the **ab** plane, the entire magnetic structure is then set to rigidly follow the magnet rotation as the field direction is varied with respect to the crystal axes. As a result, the magnetic structure factors, which are orthogonal to the net magnetisation (i.e. the field direction), rotate accordingly. The rotating magnet approach just described is analogous to a more conventional azimuthal scan, where the sample azimuth ψ is varied by physically rotating the sample with respect to the scattering plane. However, the latter is slower and produces significant artefacts in the corresponding intensity dependence due to grain hopping and ψ-dependent self-absorption effects. Therefore the resulting data quality is significantly poorer than for the rotating magnet approach.

In the present measurements, the magnetic scattering arising from the periodic spin arrangement was measured as a function of the field direction for a fixed crystal orientation. The corresponding intensity depends [see Eq. (2.9)] on the relative orientation of the magnetic structure factor of Eq. (3.5) with respect to the $\mathbf{u}_1\mathbf{u}_2\mathbf{u}_3$ frame defined in Sec. 2.1.1.1. Therefore, it is convenient to describe the direction of the external field through the angle η relative to the $\mathbf{u}_1\mathbf{u}_3$ scattering plane. I anticipate here that the crystals were mounted with their **c** axis along the diffractometer Φ axis (see Sec. 2.1.1.3) so that the rotation axis of the magnet is parallel to **c**. The definition of η is independent of the specific crystal orientation chosen for the experiment: in particular, the field lies in the vertical scattering plane (pointing towards the detector) for $\eta = 0^\circ$ and is perpendicular to the latter for $\eta = 90, 270^\circ$ regardless of the sample azimuth ψ, defined as the angle formed by the reciprocal lattice $(1\,0\,0)$ direction with respect to the $\mathbf{u}_1\mathbf{u}_3$ plane. This is schematically represented in the drawing of Fig. 3.3 for $\phi < 0$, where the basal plane of the $R\bar{3}c$ crystal is shown together with the $\mathbf{u}_1\mathbf{u}_2\mathbf{u}_3$ frame defining the scattering geometry. The experimental geometry depicted in Fig. 3.3 corresponds to the simple case where the crystallographic **c** axis is parallel to the $\mathbf{u}_3$ vector: this is true for a specular reflec-

tion of the type $(00l)$, relevant for the resonant measurements discussed in Sec. 3.4. In this case, the magnet rotates in the $\mathbf{u}_1\mathbf{u}_2$ plane and η is the angle between $\mathbf{H}$ and $\mathbf{u}_1$. For the case of a generic (hkl) reflection, like the ones presented in Sec. 3.5, the $\mathbf{c}$ axis is tilted away from $\mathbf{u}_3$ and the plane described by the field rotation has an arbitrary orientation with respect to the $\mathbf{u}_1\mathbf{u}_2$ plane. For a non specular geometry, η (and similarly ψ) are derived by first projecting the field direction and the reciprocal $\mathbf{a}^*$ axis onto the $\mathbf{u}_1\mathbf{u}_2$ plane, respectively, and by then calculating the angle formed by the projection with respect to the $\mathbf{u}_1$ axis.

In the case of specular geometry, the magnetic structure factor of Eq. (3.5) in the $\mathbf{u}_1\mathbf{u}_2\mathbf{u}_3$ reference frame is simply given by:

$$\mathbf{S} = 6 f_s(\mathbf{Q}) |\mathbf{s}| \sigma_\phi \cos\phi \begin{bmatrix} \sin\eta \\ \cos\eta \\ 0 \end{bmatrix} \tag{3.6}$$

where σ_ϕ is the sign of the canting angle defined in Fig. 3.2. Following from the third Hund's rule, the orbital angular momentum is expected to be parallel to the spin one: this is confirmed by the *ab-initio* calculations discussed in Sec. 3.5. Eq. (3.6) is then also valid for the orbital angular momentum by replacing $f_s(\mathbf{Q})$ with $f_l(\mathbf{Q})$ and $\mathbf{s}$ with $\mathbf{l}$. It should be noticed that for the general case of a non-specular geometry, the expression of the structure factor is more complicated, with a component along $\mathbf{u}_3$ generally different from zero.

3.3 Bulk magnetisation measurements

The measurements discussed in the present chapter were performed on large $MnCO_3$, $CoCO_3$ and $FeBO_3$ single crystals (a few millimetres wide) which were available to us prior to the start of the measurements. The investigation of $NiCO_3$ required a dedicated growth, which led to much smaller crystalline grains ($\approx 100 - 300\,\mu$m wide). The synthesis, described in more detail in Ref. [117], was performed at the Lomonosov Moscow State University, Faculty of Geology, by the hydrothermal method. The growth process resulted in a mixture of $NiCO_3$ crystals and other phases, with grains of the "right" phase appearing in the form of prismatic green crystals. These were initially selected by means of optical microscopy and the element content was subsequently confirmed by the refinement of their crystal structure. The latter was carried out through the Agilent SuperNova X-ray diffractometer at the Research Complex at Harwell (Didcot, UK) using labo-

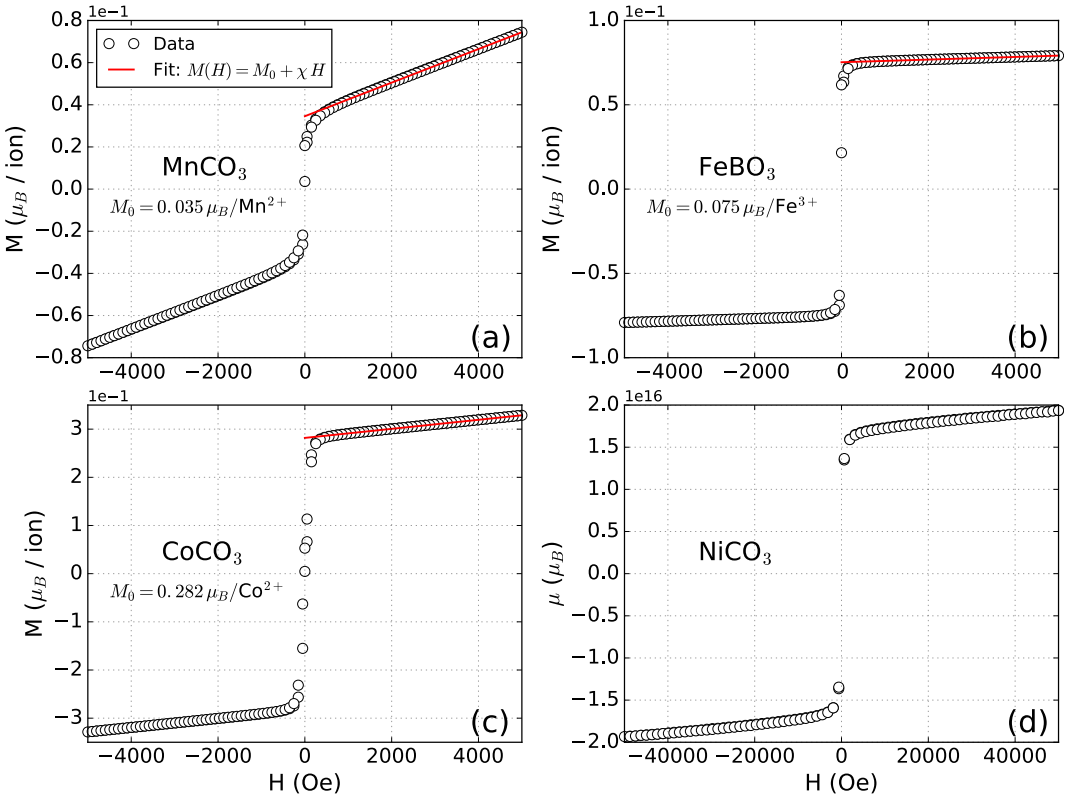

Figure 3.4: Magnetisation *vs* field measurements for the compounds of the series A(C,B)O_3 (A = Mn,Fe,Co,Ni). The open symbols refer to SQUID measurements performed by applying an external field in the **ab** basal plane of the crystal. The solid lines represent the best fits of the data in the region 1.5 Oe $< H <$ 5 kOe to the Eq. (3.7) used to extrapolate the zero-field value M_0 of the net magnetisation.

ratory Mo-Kα_1 ($\lambda = 0.709$ Å) and Cu-Kα_1 ($\lambda = 1.541$ Å) X-ray sources.

Magnetisation measurements were performed on single crystals from the same batches as those measured by X-ray diffraction (see Secs. 3.4 and 3.5) by means of a Quantum Design MPMS 3 SQUID vibrating-sample magnetometer (VSM) at beamline I10 of the DLS. The samples were glued on a quartz rod using GE Varnish. Magnetisation vs field ($M\,vs\,H$) curves were measured at T = 5 K with the external magnetic field applied perpendicular to the **c** axis of the trigonal structure, where the net magnetic moment of the C-AFM structure resides, by sweeping the magnetic field in the sequence $0 \to 5 \to -5 \to 5$ kOe for $MnCO_3$, $FeBO_3$ and $CoCO_3$ and $0 \to 50 \to -50 \to 50$ kOe for $NiCO_3$ (Fig. 3.4). The $CoCO_3$ and $FeBO_3$ samples were in the form of relatively thin plates and the direction of the **c** axis was easily identifiable as the orthogonal to the sample surface. In order to properly take into account the in-plane single-ion anisotropy, sets of measurements were repeated for: (i) two different orientations of the same crystal relative to the external magnetic field in the case of $CoCO_3$; (ii) two different crystals (with a generally different in-

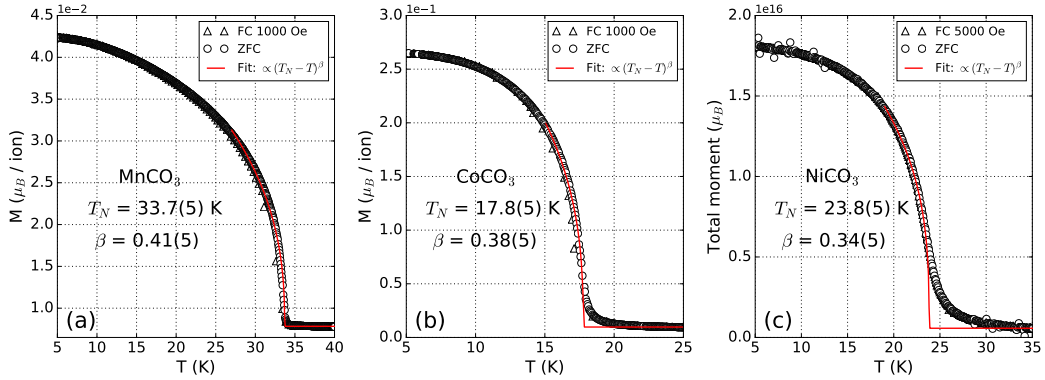

Figure 3.5: Field cooled (FC) and zero-field cooled (ZFC) magnetisation *vs* temperature for different members of the carbonates series. The open symbols refer to SQUID measurements performed by applying a magnetic field in the **ab** basal plane of the crystal. The solid lines represent the best fits to a power law, where β is the corresponding critical exponent and T_N the Néel transition temperature.

plane orientation) in the case of $FeBO_3$. The **c** axis direction was not as obvious for the $MnCO_3$ sample. The magnetisation in the latter was thus measured mounting the sample in three different orientations: the data set where $\mathbf{H} \perp \mathbf{c}$ could be assigned to the one displaying the strongest signal. The measurements corresponding to the other orientations were then discarded.

The magnetisation curves of Fig. 3.4 show that, for values of the field large enough to completely orient the magnetic domains, the magnetisation $M(H,T)$ perpendicular to the **c** axis exhibits the following linear dependence on the applied field H [96]:

$$M(H,T) = M_0(T) + \chi_\perp(T)H \tag{3.7}$$

where $\chi_\perp(T)$ is the magnetic susceptibility in the **ab** plane of the crystal and $M_0(T)$ is the spontaneous net magnetisation (at zero field) arising from the canted moment. $M_0(T)$ can then be extracted extrapolating to zero field the $M\,vs\,H$ curves: this is shown by the red solid lines in Fig. 3.4, which correspond to the fit of the experimental data in the region 1.5 kOe $< H <$ 5 kOe using Eq. (3.7). Table 3.2 summarises the results of the measurements and compares them with data from the literature. $M\,vs\,H$ measurements were also collected for a single crystal of $NiCO_3$: the latter shows an analogous linear dependence of the magnetisation as a function of the external field. However, due to the small size of the crystal, its mass could not be reliably determined and the magnetic moment per magnetic ion could not be calculated. For the other three samples, the spontaneous magnetisation is similar to the values found in the literature. Table 3.2 clearly shows that the value of the net moment in $CoCO_3$ and $NiCO_3$ is significantly larger than for $MnCO_3$ and $FeBO_3$.

	Spontaneous magnetisation (μ_B/ion)		Critical temperature (K)	
	Literature data	This work	Literature data	This work
$MnCO_3$	0.034 [95], 0.033 [103]	0.035	31.5 [94], 32.4 [95], 32.4 [106], 32.6 [101]	33.7(5)
$FeBO_3$	0.08 [102], 0.078 [112]	0.071, 0.075	348.5 [102], 346.5 [112]	345.0(5) [116]
$CoCO_3$	0.258 [96], 0.229 [97], 0.269 [98]	0.255, 0.282	18.1 [96], 17.5 [94]	17.8(5)
$NiCO_3$	0.372 [100], 0.412 [105], 0.391 [112]	-	25.2 [100], 25.2 [105]	23.8(5)

Table 3.2: Spontaneous magnetisation at low temperature and Néel transition temperature resulting from the VSM-SQUID measurements and reported in the literature. Only the literature data obtained from measurements performed on pure single crystals at low temperature ($T < 10$ K) are reported for $MnCO_3$, since the magnetisation of powder samples was found to be reduced [103] and magnetic impurities also suppress the magnetisation [99, 103]. For $FeBO_3$ and $CoCO_3$ I provide two experimental values of the spontaneous magnetisation collected from two independent measurements (see text for details). The critical temperature data selected from the literature concern the net magnetisation of both powder samples and single crystals; literature data measured on the AFM part were discarded, although it is generally accepted that the onset of the weak FM moment coincides with the onset of the AFM order (see also Sec. 3.5).

This trend mirrors the one present for the DMI-induced canting angle, which also increases in going from the Mn to the Ni member of the series (see Table 3.3), and can thus be attributed to a stronger DMI term for the Co and Ni compounds.

Magnetisation vs temperature (M *vs* T) measurements were also performed on $CoCO_3$, $MnCO_3$ and $NiCO_3$, in order to measure the critical temperature corresponding to the onset of the weak FM moment. The data were collected following the zero-field cooled (ZFC) - field-cooled (FC) protocol. The samples were first cooled below the Néel transition in zero field and the ZFC magnetisation was then measured on warming by the application of a small field of 1 kOe for $CoCO_3$ and $MnCO_3$ and 5 kOe for $NiCO_3$ applied in the **ab** plane of the crystal. Once in the high-temperature paramagnetic region, the FC magnetisation was measured on cooling the samples down to 5 K keeping the field to the same value used for the ZFC data.

The ZFC and FC data sets almost completely overlap, thus showing no significant irreversibility. The magnitude of the magnetisation M displays the expected critical dependence on the temperature: $\propto (T_N - T)^\beta$, where T_N is the Néel temperature and β is the critical exponent. T_N shows a good agreement with the literature data and is consistent with the corresponding value measured for the intensity of the magnetic reflections arising from the AFM order (Sec. 3.5). The temperature dependence of the magnetisation was not measured for $FeBO_3$ because the SQUID

Compound	Magnetic ion	Z	N_{3d}	Canting angle ϕ (deg.) experimental	Canting angle ϕ (deg.) *ab-initio*
$MnCO_3$	Mn^{2+}	25	5.0	-0.04 [113] , -0.4 [95, 100]	-0.05
$FeBO_3$	Fe^{3+}	26	5.8	-0.9 [102]	-0.8
$CoCO_3$	Co^{2+}	27	7.1	4.9 [96, 100]	4.7
$NiCO_3$	Ni^{2+}	28	8.2	10.8 [100]	7.4

Table 3.3: Experimental and theoretical values of the canting angle. The experimental magnitudes are taken from the literature, while the experimental signs and the *ab-initio* values are the ones derived from the present work. The sign of the canting angle corresponds to the sign of the DMI as described in Sec. 3.2. N_{3d} is the number of the $3d$ electrons per TM site obtained from the first-principle calculations.

apparatus did not allow to reach its Néel transition, which is above room temperature. Nevertheless, in Table 3.2 I report the transition temperature taken from Ref. [116], which was measured on a pure AFM reflection for a sample of the same batch as the one used for the M *vs* H measurements. The latter also agrees well with the data from the literature. The value of the critical exponent is compatible with the 3D Heisenberg ($\beta = 0.366$) [or 3D XY ($\beta = 0.349$)] universality class, consistent with the dimensionality of the order parameter in this system. A better estimate can however be obtained from the temperature dependence of the magnetic reflections (see Fig. 3.12): the value extracted from the SQUID measurements is generally less reliable due to the rounding of the transition caused by the application of the external field.

3.4 Band filling control of the Dzyaloshinskii-Moriya interaction

The work presented in this section has been published as "*Band Filling Control of the Dzyaloshinskii-Moriya Interaction in Weakly Ferromagnetic Insulators*" by G. Beutier, S.P. Collins, O.V. Dimitrova, V.E. Dmitrienko, M.I Katsnelson, Y.O. Kvashnin, A.I. Lichtenstein, V.V. Mazurenko, A.G.A. Nisbet, E.N. Ovchinnikova and D. Pincini, Physical Review Letters **119**, 167201 (2017) [117].

The electronic and magnetic properties of the selected weak ferromagnets were simulated by our collaborators using the Vienna *ab-initio* simulation package (VASP) [127, 128] within the local density approximation (LDA) taking into

account the on-site Coulomb repulsion U and the SOC (LDA + U + SOC) [129]. For each system, the value of U ($U = 3$ eV for $MnCO_3$ and $CoCO_3$ and $U = 4$ eV for $FeBO_3$ and $NiCO_3$) was chosen to obtain the best agreement between the absolute values of the canting angles and the experimental data taken from the literature, while the Hund's exchange constant (see Sec. 1.1.4) was assumed to be system-independent and set to 0.9 eV for all compounds. The results are summarised in Table 3.3, where the number of electrons in the TM $3d$ orbitals and the canting angle derived from the calculations are listed along with the corresponding $|\phi|$ values reported in the literature[5]. The calculations reveal that the chemical bonding between the TM and the surrounding ligands exhibits a rather covalent character, which is particularly pronounced in $FeBO_3$: here, the nominal oxidation state Fe^{3+} would result in five electrons in the $3d$ orbitals while the calculations predict a number closer to 6. As discussed in Sec. 3.2, the magnitude of the canting angle directly reflects the ratio between the DMI and the isotropic exchange term in the magnetic Hamiltonian. For small ϕ values, the canting angle is well approximated by the ratio $m/(2\mu)$ between the magnitude of the net moment m and the TM ion total moment μ. As a result, the absolute value of ϕ follows a similar trend to the one observed for the net magnetisation summarised in Table 3.2: the larger ϕ values in the Co and Ni compounds can then be attributed to an increased canted moment with respect to the Mn and Fe ones.

Interestingly, the density functional theory (DFT) calculations also show that the sign of the DMI, which is reflected in the sign of the canting angle, changes as the number of electrons in the $3d$ orbitals is increased going from Mn to Ni: in particular, the magnetic structure of $MnCO_3$ and $FeBO_3$ is predicted to have $\phi < 0$, as in Fig. 3.2(b), while $CoCO_3$ and $NiCO_3$ are expected to have $\phi > 0$, as shown in Fig. 3.2(c). As discussed in Sec. 3.2.1, for a given field direction the sign of the canting angle affects the sign of the magnetic structure factors. The latter determines the phase of the magnetic modulation, which is in turn encoded in the phase of the magnetic scattering amplitude. While the intensity, i.e. the modulus square of the amplitude, is easily accessible by measuring magnetic reflections arising from the ordered magnetic structure via neutrons or X-rays, the all-important sign is lost in a conventional scattering experiment. In order to access the phase of the magnetic scattering amplitude one must exploit the interference between the latter and a reference amplitude independent of the magnetic structure. Depending on the sign of the magnetic amplitude the interference will be either constructive or destructive, thus producing a detectable variation in the measured intensity. For the interference

[5]The sign of the measured ϕ values is the one found by the present investigation, as described hereafter.

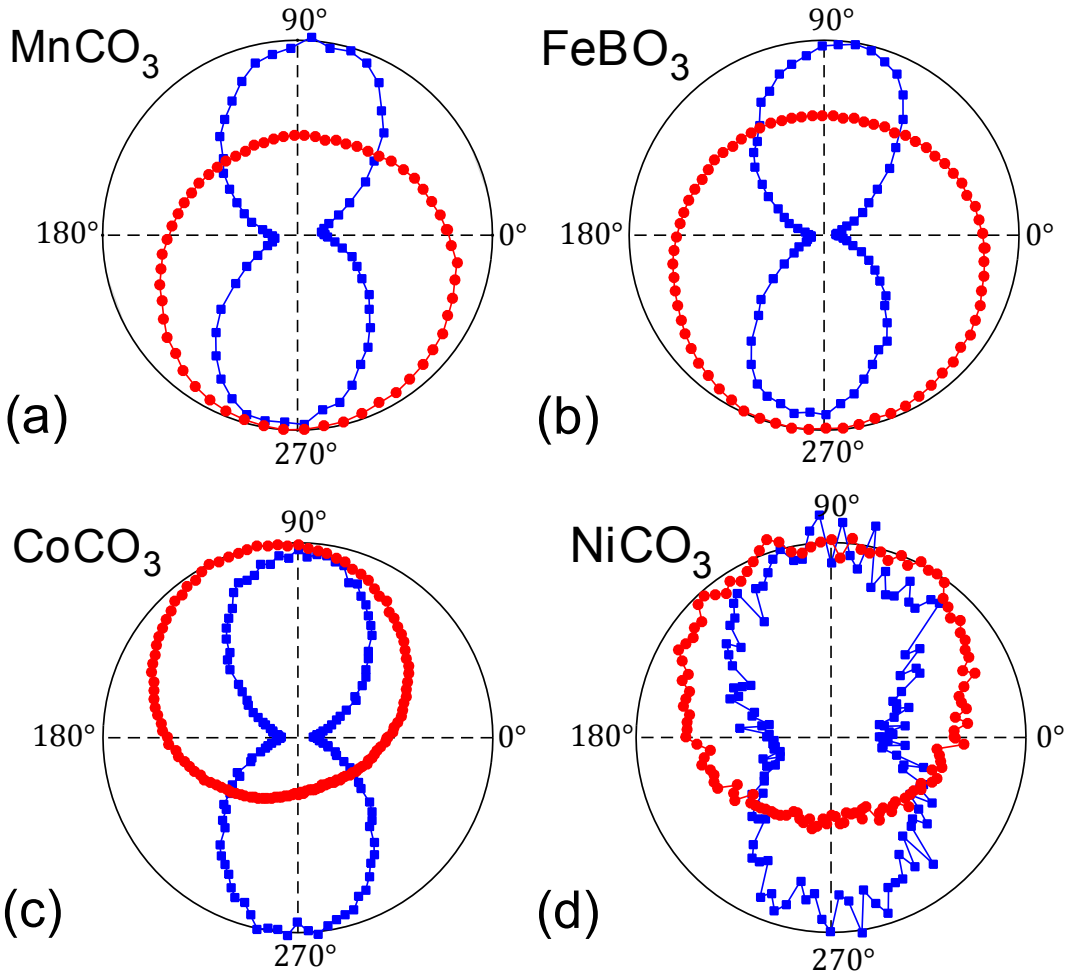

Figure 3.6: Normalized (009) intensity in the σ-π' polarisation channel as a function of the magnetic field direction η measured off-resonance (blue squares) and at the quadrupole resonance energy (red circles) for $0° \leq \psi \leq 30°$ in the different compounds of the series below their respective Néel transition temperature. The resonant energy was chosen such that the imaginary part $Q''(E)$ of the resonant amplitude is positive for all the compounds (see red dashed line in Fig. 3.7). The off-resonant data display the $\sin^2\eta$ behaviour expected for non-resonant magnetic scattering [Eq. (3.8)], while the resonant data include an interference term which shifts the corresponding polar plot downwards or upwards depending on the sign σ_ϕ of the DMI-induced canting angle ($\sigma_\phi = -1$ and $+1$, respectively), as explained in the text. The lower quality of the $NiCO_3$ data set is due to the much smaller crystal size and magnetic moment of the Ni^{2+} ion.

to occur, the reference amplitude must (i) have the same polarisation as the magnetic one, (ii) not be out of phase and (iii) have a similar magnitude. With neutrons, the nuclear amplitude arising from the periodicity of the lattice would constitute a suitable reference amplitude. However, the analogous process would not work with X-rays as the Thomson scattering at allowed Bragg reflections is several orders of magnitude larger than magnetic scattering, thus not allowing a reliable determination of the interference.

The investigation described in this section exploited a peculiar interference between non-resonant magnetic scattering (Sec. 2.1.1.1) and a rather exotic non-magnetic resonant amplitude present in the pre-edge region of the TM K absorption edge at the $(006n+3)$ space-group forbidden reflections. The X-ray diffraction measurements were performed on analogous crystals to the ones used for the bulk measurements of Sec. 3.3 at beamline I16 of the DLS, with preliminary data collected at beamline XMaS of the ESRF. The crystals were mounted on the goniometer rotational stages of the I16 6-axis kappa diffractometer with the **c** axis of the $R\bar{3}c$ trigonal structure aligned along the Φ axis. The (009) space-group forbidden reflection of the four crystals was measured in vertical scattering geometry using linearly polarised incident X-rays ($30\times200\,\mu m^2$ spot size) in the horizontal plane (σ polarisation) as a function of the direction of a small ($\mu_0 H \approx 35$ mT) magnetic field applied in the **ab** plane of the crystal by means of the permanent magnet setup described in Sec. 2.1.1.3. The impact of the field on the C-AFM structure is outlined in Sec. 3.2.1. The diffracted signal was measured in the π' polarisation channel by means of the (220) and (222) reflections of a copper single crystal for $MnCO_3$, $FeBO_3$ and $NiCO_3$, respectively, and the (006) reflection of a pyrolytic graphite (PG) single crystal for $CoCO_3$. The incident X-ray energy was tuned to the K absorption pre-edge of the TM, found at $E \approx 6.538, 7.112, 7.708, 8.332$ keV for $MnCO_3$, $FeBO_3$, $CoCO_3$ and $NiCO_3$, respectively. The experiments were performed in the magnetically-ordered phase of each sample at $T \approx 7, 300, 13, 5.5$ K for $MnCO_3$, $FeBO_3$, $CoCO_3$ and $NiCO_3$, respectively. The carbonates crystals were cooled to low temperature by means of a standard closed-cycle cryostat. In the case of $CoCO_3$, the temperature was chosen in order to obtain a sufficiently small in-plane magnetocrystalline anisotropy, whose effect will be discussed in Sec. 3.6.2. All the sample azimuth ψ values reported in this chapter are defined with respect to the (100) azimuthal reference as shown in Fig. 3.3 [$\psi = 0°$ when the (100) reciprocal direction lies in the scattering plane pointing towards the detector].

As already discussed in Sec. 3.2.1, the (009) reflection violates the $l = 2n$ selection rule for reflections of the type $(00l)$ and thus hosts a vanishing Thomson scattering amplitude. A NXMS contribution to the scattered intensity is present below the Néel transition temperature as a result of the periodic arrangement of the magnetic moments. The magnetic field dependence of the NXMS amplitude in σ-π' can be obtained by inserting Eq. (3.6) into Eq. (2.6), which leads to:

$$f_{\mathrm{mag}}^{\sigma\pi'} = -i\sigma_\phi f_m \sin\eta \tag{3.8}$$

where f_m is a real positive quantity:

$$f_m = 6\frac{\hbar\omega}{mc^2}\left[|\mathbf{l}|f_l(\mathbf{Q}) + |\mathbf{s}|f_s(\mathbf{Q})\right]\cos\phi\sin 2\theta\sin\theta \tag{3.9}$$

Here, θ is the Bragg angle of the selected reflection. I stress the fact that the magnetic contribution of Eq. (3.8) is non-resonant in nature and therefore does not depend on the incident X-ray energy. In general, close to the TM K edge a resonant contribution to the scattered intensity can be expected. As already mentioned in Sec. 2.1.1.2, the resonant scattering amplitude is normally written as a series of electric multipolar resonances. The electric dipole-dipole term (E1E1) is normally the dominant contribution: in the case of the $(0\,0\,9)$ reflection, however, it vanishes due to the high symmetry of the TM resonant atoms [130, 131]. The two next most common terms are the electric dipole-quadrupole (E1E2), which cancels out similarly to the E1E1 term, and the electric quadrupole-quadrupole (E2E2). Higher-order electric multipoles are more exotic and are thus expected to be much weaker. The E2E2 amplitude can be written as [131]:

$$f_{\mathrm{res}}^{\sigma\pi'} = Q(E)\cos 3\psi \tag{3.10}$$

where $Q(E) = Q'(E) + iQ''(E)$ is a complex spectrum and ψ is the sample azimuth defined in Fig. 3.3. $Q(E)$ is a unique spectrum for all forbidden reflections of the type $(0\,0\,6n+3)$ of a given compound of the series, except that it scales with $\cos^3\theta$ [131]. In contrast to the non-resonant magnetic scattering amplitude, this term resonates in a narrow energy range at the TM K pre-edge [116] and is not affected by the magnetic field direction: as I will argue in more detail hereafter, it represents a suitable reference wave for the investigation of the sign of the NXMS amplitude.

In general, XRMS can also be expected to be present in proximity to an absorption edge. The strongest contribution is normally the one arising from the electric dipole resonance involving a transition to the magnetic d shell: the latter, however, is not directly probed at the K absorption edge[6]. The XRMS amplitude is given by (see Sec. 2.1.1.2):

$$f_{\mathrm{XRMS}}^{\sigma\pi'} = 2iF^{(1)}(E)\sigma_\phi\cos\phi\cos\theta\sin\eta \tag{3.11}$$

and thus exhibits the same dependence on the magnetic field direction as non-resonant magnetic scattering. In contrast to the latter, the term of Eq. (3.11) is

[6]XRMS at the K edge can arise from either the hybridization of the p orbitals with the d states responsible for magnetism or the polarization of the p orbitals induced by SOC, as was found at the Ni K edge in NiO [132].

energy dependent due to the quantity $F^{(1)}(E)$ and, given its electric dipole origin, it is expected to resonate at a different energy with respect to the E2E2 term[7]. As a result, tuning the incident X-ray energy in the pre-edge region, its contribution can be neglected. Moreover, although the scattering amplitude of Eq. (3.11) could in principle be exploited as a reference wave for the extraction of the sign of the DMI, this would require a reliable model for the quantity $F^{(1)}(E)$, which is generally complex. Resonant magnetic quadrupole scattering is also expected to be negligible. The latter exhibits a more complicated dependence on the magnetic field direction, involving terms of the type $\sin n\eta$ ($n = 1,2,3$) [33]: the absence of these terms in the measured magnetic field dependence of the scattered intensity confirms the validity of this assumption.

The total diffracted intensity at the (009) space-group forbidden reflection in σ-π' thus results from the coherent sum of the NXMS scattering amplitude of Eq. (3.8) and the non-magnetic resonant quadrupole term of Eq. (3.10):

$$I^{\sigma\pi'}(E,\psi,\eta) = |f_{\text{mag}}^{\sigma\pi'} + f_{\text{res}}^{\sigma\pi'}|^2 = I_{\text{mag}} + I_{\text{res}} + I_{\text{interf}} \tag{3.12}$$

where

$$\begin{aligned} I_{\text{mag}} &= f_m^2 \sin^2\eta \\ I_{\text{res}} &= |Q(E)|^2 \cos^2 3\psi \\ I_{\text{interf}} &= 2\sigma_\phi f_m Q''(E) \cos 3\psi \sin\eta \end{aligned} \tag{3.13}$$

The modulus square of the two amplitude terms gives rise to a pure magnetic term I_{mag}, a pure resonant term I_{res} and, most importantly, the interference term I_{interf}. The validity of this model was already proved by Dmitrienko *et al.* [116] on $FeBO_3$ prior to the measurements here discussed, where the magnetic scattering and resonant scattering measured independently (off-resonance and above the Néel temperature, respectively) were found to behave as expected. In particular, the pure quadrupole resonance term, measured for $T > T_N$, was shown to display the expected $\cos^2 3\psi$ dependence on the sample azimuth.

As already mentioned, I_{res} exhibits a very sharp resonance in the pre-edge region of the TM K edge [116]. Far from the quadrupole resonance, $Q(E) \to 0$ and only the pure magnetic term is left: a symmetric oscillation of the type $\sin^2\eta$ is then expected as a function of the magnetic field direction below T_N. This is clearly visible from the magnetic field dependence of the scattered intensity measured at an

[7] A weak XRMS contribution was indeed found in $MnCO_3$ and $CoCO_3$ at energies higher than the quadrupole resonance.

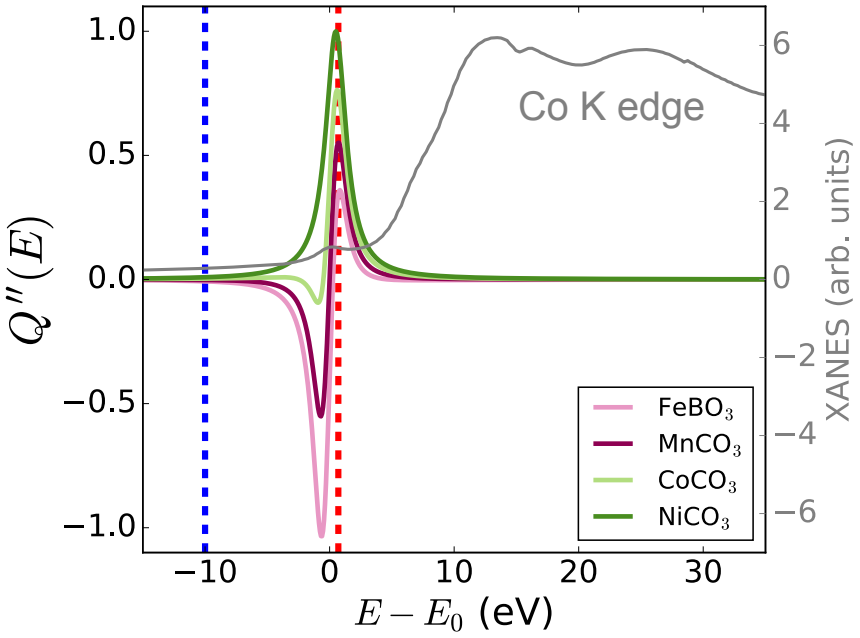

Figure 3.7: Imaginary part of the quadrupole resonance term $Q(E)$ discussed in the text for the different compounds of the series as a function of the incident X-ray energy. The plots have been obtained considering the double-Lorentzian model of Eq. (3.14) with $\Gamma = \Delta = 1$ eV and $\alpha = 1.5, 1, 0.5, 0$ for $FeBO_3$, $MnCO_3$, $CoCO_3$ and $NiCO_3$, respectively. The energy values on the x axis are expressed in terms of the relative shift to the resonance mean energy E_0. The vertical blue and red dashed lines (far from the resonance and just above E_0) correspond to the energy values where the measurements represented by the blue squares and red circles in Fig. 3.6 were collected, respectively. The Co K absorption energy is also reported as a reference.

energy below the quadrupole resonance represented by the blue squares in the polar plots of Fig. 3.6. For all the compounds of the series, the expected $\sin^2\eta$ behaviour, with zeros at $\eta = 0°, 180°$ and maxima at $\eta = 90°, 270°$, is present regardless of the sign of the canting angle. Tuning the incident X-rays to the quadrupole resonance energy causes the interference I_{interf} term to appear. The latter oscillates as $\sin\eta$, with an amplitude factor $2\sigma_\phi f_m Q''(E)\cos 3\psi$. The sign of the amplitude directly depends on the sign σ_ϕ of the canting angle and can be reversed from positive to negative by changing the magnetic field direction (η), the sample azimuth (ψ) or the energy of the incident beam through the imaginary part $Q''(E)$ of the complex spectrum $Q(E)$. The measurements presented in Fig. 3.6 were performed for $0° < \psi < 30°$ so that $\cos 3\psi > 0$: σ_ϕ can then be extracted from the magnetic field dependence of the scattered intensity at resonance provided that the sign of the term $Q''(E)$ can be reliably determined.

The resonant spectrum $Q''(E)$ can be computed by means of electronic structure codes: for the present investigation, the FDMNES software [133] based on the

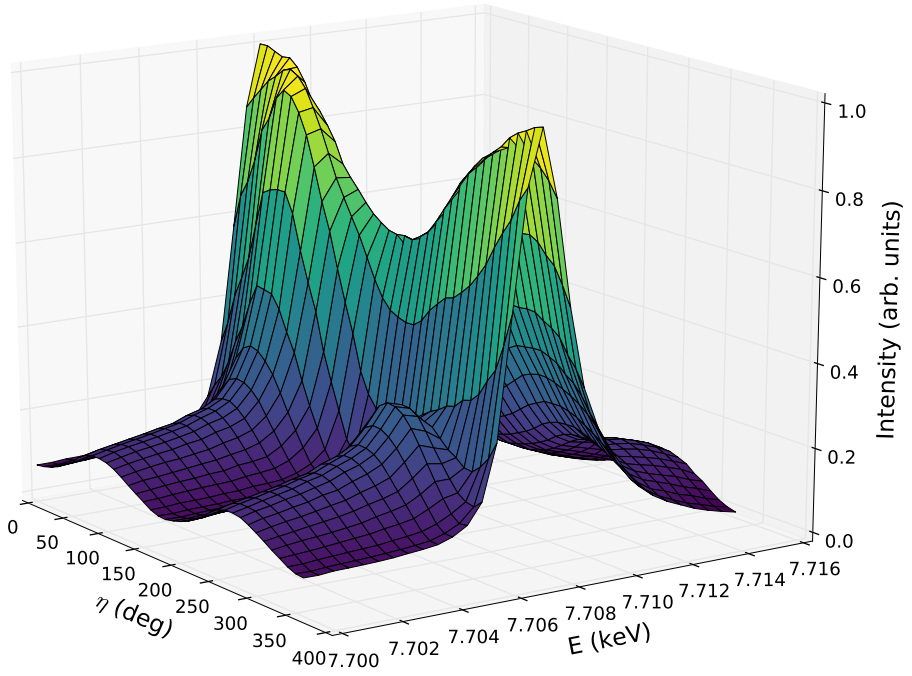

Figure 3.8: Dependence of the (009) space-group forbidden reflection in the σ-π' polarisation channel on the magnetic field direction η for different energy values across the K pre-edge quadrupolar resonance in $CoCO_3$ ($E \approx 7.708$ keV). The measurements were performed at $\psi = 50°$.

finite-difference method [134] was used. The calculations, which are described in more detail in Refs. [116, 117], were performed by considering the structural parameters reported in the literature [107, 108, 110] and ignoring the magnetic structure[8]. Particular care was taken in defining the crystal structure consistent with the definition used for the magnetic structure factor (see Sec. 3.2). In particular, when describing the $R\bar{3}c$ crystal using an hexagonal unit cell, the oxygens occupy the Wyckoff site e with multiplicity 18 at $(x, 0, 1/4)$: x can be chosen such that $0 \leq x \leq 1/2$ or $1/2 \leq x \leq 1$. The former definition was chosen for both the magnetic structure factor and the resonant amplitude in order to have a consistent description of the corresponding signs. The energy dependence of the resonant scattering term

[8] In the absence of magnetism, the resonant scattering tensor components can be calculated using a symmetry-based approach that considers the terms compatible with the local crystal field at the resonant atom sites.

$Q(E)$ resembles [116] the following double-Lorentzian model:

$$Q(E) = \frac{A_1}{E - E_0 + \Delta/2 - i\Gamma} + \frac{A_2}{E - E_0 - \Delta/2 - i\Gamma} \tag{3.14}$$

where $A_1 \leq 0$ and $A_2 > 0$ are the amplitudes of the Lorentzian resonances, E_0 is the mean resonant energy, Δ is their separation in energy and Γ is their common width. Considering the simple case of cubic symmetry, the two Lorentzian peaks correspond to transition to the t_{2g} and e_g levels of the TM ion, so that Δ corresponds to the octahedral crystal field. The overall shape of the resonance depends on the ratio $\alpha = |A_1/A_2|$: the latter depends, in turn, on the Fermi level of each of the compounds studied, which was adjusted to best reproduce the measured spectra.

The imaginary part $Q''(E)$ is reported for the different members of the series of compounds in Fig. 3.7, where the TM K absorption edge in the representative case of $CoCO_3$ is also plotted for reference. $FeBO_3$ and $MnCO_3$ are well described by a value of α around 1.5 and 1, respectively: in this case, both Lorentzian peaks contribute to the spectrum, which goes from negative to positive going from below to above E_0. On the other hand, the first Lorentzian is fully truncated in $NiCO_3$ ($\alpha = 0$) and a single positive peak at high energy is present. $CoCO_3$ corresponds to the intermediate case where the first Lorentzian is only partially truncated: although variations are observed depending on the specific azimuth value chosen for the measurements[9], a value $\alpha = 0.5$ provides a good description of the experimental data. It should be noted that the trend seen in the α values is consistent with an overall increase of the Fermi energy with the electron filling of the TM $3d$ levels. In particular, the t_{2g} orbitals are fully occupied for Ni^{2+} ($3d^8$), consistent with a fully-truncated low-energy Lorentzian. The crucial point emerging from Fig. 3.7 is that within a narrow energy range above the resonance mean energy E_0 the term $Q''(E)$ assumes a positive value for all the compounds of the series. This is true regardless of the particular choice of the Fermi energy (i.e. the parameters α), since the latter only affects the first part of the spectrum by truncating the corresponding negative Lorentzian. Therefore, by tuning the X-ray energy to the upper part of the resonance, the sign of the interference term I_{interf} directly reflects the sign σ_ϕ of the DMI.

Neglecting the field-independent I_{res} contribution, the measured magnetic field dependence of the scattered intensity of Eq. (3.13) will be proportional to $\sin^2\eta \pm C\sin\eta$ with $C > 0$, where the sign $+$ $(-)$ corresponds to $\sigma_\phi = +1$ $(\sigma_\phi = -1)$, i.e

[9] This does not affect the robustness of the present analysis since the interference measurements were performed using the high-energy part of the quadrupole resonance, which was found to be robust against sample azimuth variations.

$\phi > 0$ ($\phi < 0$). The magnetic field dependence of the scattered intensity in the resonant regime is represented by the red circles in Fig. 3.6. Contrary to the off-resonant case (blue curves), the intensity polar plots are not symmetric around the centre and show a clear dependence on the selected compounds: in particular, while the polar plot is shifted downwards for $MnCO_3$ and $FeBO_3$ (corresponding to a maximum in the intensity at $\eta = 270°$), the plot is shifted upwards in $CoCO_3$ and $NiCO_3$ (corresponding to a maximum in the intensity at $\eta = 90°$). This constitutes clear evidence that σ_ϕ goes from negative in $MnCO_3$ and $FeBO_3$ to positive in $CoCO_3$ and $NiCO_3$, in remarkable agreement with the predictions from DFT calculations (Table 3.3): for the former, the magnetic structure is thus the one of Fig. 3.2(b), while for the latter the magnetic moments are arranged as in Fig. 3.2(c). The filling of the TM $3d$ band thus affects the exchange interaction between magnetic moments and causes a sign reversal of the DMI. The results for $MnCO_3$ and $NiCO_3$ are consistent with the sign predicted theoretically by Moskvin [135] for pairs of $d^5 - d^5$ and $d^8 - d^8$ ions, respectively, following an approach based on the superexchange theory. The latter establishes a connection between the DMI sign and the occupation of the TM $3d$ shell, in agreement with our findings. The present investigation represents the first experimental determination of the sign of the DMI in insulating compounds. A similar manipulation of the antisymmetric exchange has been reported in the metallic alloys $Fe_{1-x}Co_xSi$ [136], $Mn_{1-x}Fe_xGe$ [137] and $Fe_{1-x}Co_xGe$ [138], where a very rich magnetic phase diagram depending on the doping and the applied magnetic field was found.

The scattering model of Eq. (3.12) is confirmed by the energy dependence of the magnetic field dependence collected scanning the incident X-ray energy across the quadrupole resonance. The data are plotted in the form of a surface plot in Fig. 3.8 for the representative case of $CoCO_3$, which can be used alternatively to the polar plots of Fig. 3.6. It should be noticed that the data of Fig. 3.8 were collected for $\psi = 50°$: the sign of the interference term is thus reversed compared to the case of Fig. 3.6(c). Far below and above the resonance ($E_0 \approx 7.708$ keV), only non-resonant magnetic scattering is present and a $\sin^2\eta$ oscillation, with maxima at $\eta = 90°, 270°$ is observed. This regime is the one used for the non-resonant measurements which will presented in Sec. 3.5, where the magnetic field dependence in the σ-σ' polarisation channel was also probed. As I will show in Sec. 3.5, the corresponding oscillations are out of phase compared to the σ-π' ones. As the incident energy is tuned to the resonance, the interference term appears and the symmetry between $\eta = 90°$ and $\eta = 270°$ is lost. The interference term changes sign going from the low to the high energy side (see also Fig. 3.7), so that a maximum or minimum in the intensity is present at $\eta = 90°$ on the left or right of the resonance,

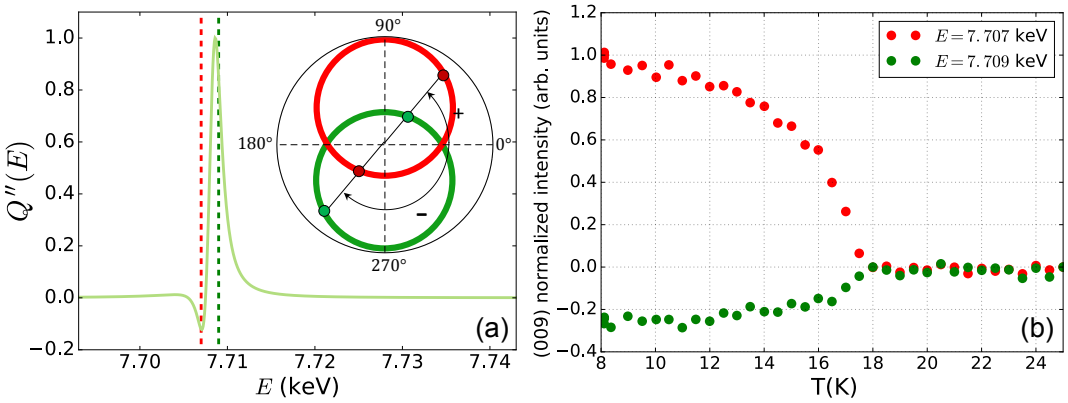

Figure 3.9: (a) Imaginary part of the quadrupole resonance term $Q(E)$ discussed in the text for $CoCO_3$ as a function of the incident X-ray energy. The plot has been obtained considering the double-Lorentzian model of Eq. (3.14) with $\Gamma = \Delta = 1$ eV, $\alpha = 0.5$ and $E_0 = 7.708$ keV. The red ($E_1 = 7.707$ keV) and green ($E_2 = 7.709$ keV) vertical dashed lines mark the two energy values at which the magnetic domain imaging measurements described in the text were performed. The inset schematically represents the expected magnetic field dependence of the (009) reflection in the σ-π' channel for $\psi > 30°$ at E_1 (red curve) and E_2 (green curve): the difference in intensity for opposite magnetisation orientations along an arbitrary direction is highlighted. (b) Temperature dependence of the (009) total scattered intensity measured at the two energies marked by the vertical dashed lines in (a). At each energy, the high-temperature value was subtracted from all the data points. Both data sets were further normalized to the low temperature value for $E = 7.707$ keV.

respectively. The intensity is overall larger close to the resonance due to the extra I_{res} term. Magnetic field scans as a function of energy analogous to the ones of Fig. 3.8 were used to extract the quantity $\sigma_\phi Q''(E)$ [117] and thus check the shape of the resonant term $Q''(E)$ calculated with FDMNES (see Fig. 3.7).

3.4.1 Magnetic domain imaging

The magnetic domain imaging measurements outlined in this section have been included in the publication "*Role of the orbital moment in a series of isostructural weak ferromagnets*" by D. Pincini, F. Fabrizi, G. Beutier, G. Nisbet, H. Elnaggar, V.E. Dmitrienko, M.I Katsnelson, Y.O. Kvashnin, A.I. Lichtenstein, V.V. Mazurenko, E.N. Ovchinnikova, O.V. Dimitrova and S.P. Collins, Physical Review B **98**, 104424 (2018) [139].

As I have already pointed out, the weak magnetic field applied in the **ab** plane of the crystal for the scattering measurements is sufficient to drive the system into

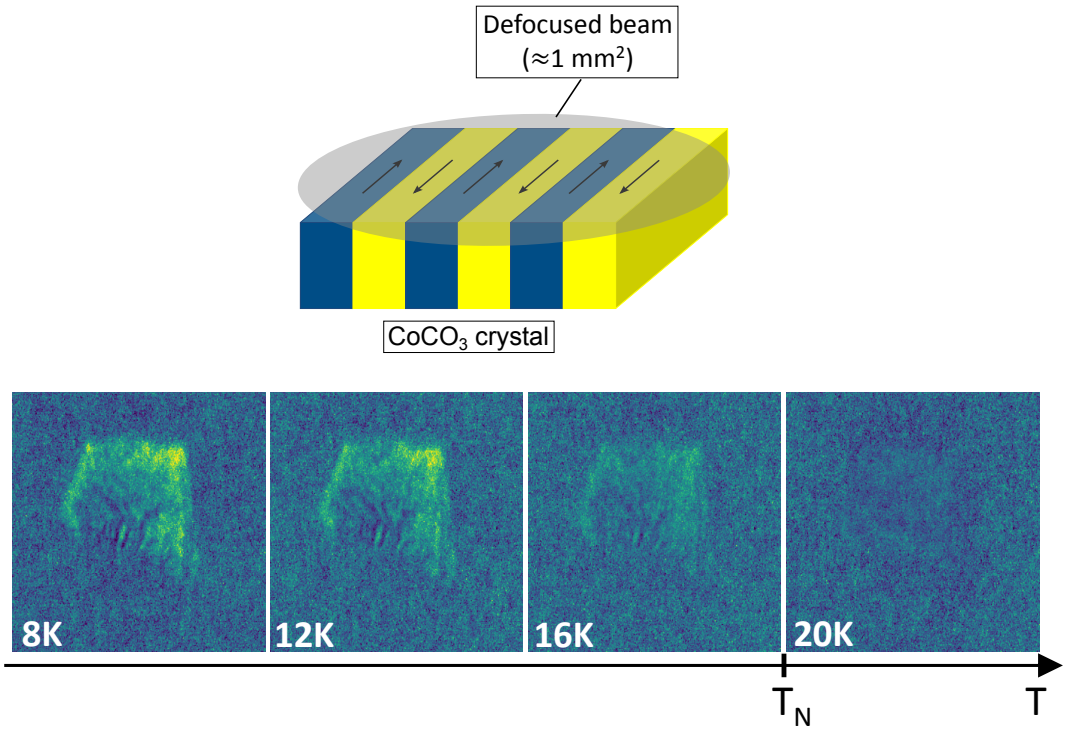

Figure 3.10: $CoCO_3$ magnetic domain pattern as a function of temperature. The colour scale represents the direction of the net magnetization arising from the canting of the magnetic moments. Each image corresponds to an illuminated area of size $\approx 1\,\mathrm{mm}^2$ and was obtained by subtracting the normalized background-subtracted detector acquisitions collected at the two energy values shown in Fig. 3.9(a) as described in the text. The drawing in the top panel schematically shows the magnetic domains with different net magnetisation directions (chosen to be opposite for the sake of clarity) and the large defocused beam used for the full-field imaging measurements.

a single-domain phase. However, magnetic domains with a different orientation of the DMI-induced net magnetisation are expected to be present in the absence of an applied field. The phase sensitivity provided by our novel interference technique allows the measurements of the net magnetisation direction and, in particular, its sign along one particular axis. The magnetic domains can be conveniently mapped following a full-field imaging approach. This consists in defocusing the incident X-ray beam to achieve an illuminated area ≈ 1 mm^2, comparable to the sample size (see top panel in Fig. 3.10), so that the domains can be imaged in a single detector acquisition by using a high-resolution CCD detector with a small pixel size.

The measurements were performed in a $CoCO_3$ single crystal recording the (009) total scattered signal at $\psi = 50°$ originating from the large illuminated area at different temperatures across the Néel transition. Spatial resolution was achieved by using a fibre-optic coupled CCD area detector with a $6.5\,\mu$m pixel size mounted on the I16 diffractometer detector arm close (170 mm) to the sample. The detector

distance was chosen to be close enough so that the scattered beam divergence did not significantly blur the image but not so close as to produce excessive fluorescence background. The raw detector acquisitions were collected measuring one-second CCD exposures for different values of the rocking angle, in order to integrate over the crystal mosaic spread. The domain patterns shown in Figs. 3.10 and 3.11 were subsequently obtained by combining the raw images summed over a rocking scan according to the following relation:

$$\begin{aligned}&\text{Domain image} = \\ &= \frac{\text{Image}(E_1,T) - \text{Image}(E_1,\text{T} = 22\,\text{K})}{\text{Image}(E_1,\text{T} = 22\,\text{K}) - \text{Image dark}} - \frac{\text{Image}(E_2,T) - \text{Image}(E_2,\text{T} = 22\,\text{K})}{\text{Image}(E_2,\text{T} = 22\,\text{K}) - \text{Image dark}}\end{aligned} \tag{3.15}$$

where E_1 (E_2) corresponds to an energy value slightly smaller (larger) than the quadrupole resonance mean energy and the dark images were measured in the absence of the incident beam. In Eq. (3.15), the high-temperature detector acquisitions are subtracted from the low temperature ones at each energy and use to normalize the data.

The working principle behind Eq. (3.15) is illustrated in Fig. 3.9(a). Tuning the incident energy to the left (E_1) or the right (E_2) of the quadruple resonance below the Néel transition reverses the sign of the imaginary part $Q''(E)$ of the quadrupole resonant spectrum: this, in turn, reverses the interference with the NXMS amplitude, which goes from constructive to destructive for $E = E_1$ and $E = E_2$, respectively, and changes the sign of the term I_{interf} in Eq. (3.12). The dependence of the (009) intensity in σ-π' at the two energy values as a function of the net magnetisation direction η[10] is schematically represented in the inset of Fig. 3.9(a)[11]. For a given net magnetisation direction, the subtraction of the detector acquisitions at the two energies produces a contrast, whose magnitude depends on the precise η value. In the ideal case where the imaginary part of the resonant spectrum assumes values precisely equal in magnitude and opposite in sign at the two energy values, domains polarised along opposite directions would result in values equal in magnitude and opposite in sign. Although the energy values were chosen to optimise the contrast between opposite magnetisation directions, deviations form this ideal case

[10] It should be noticed that the angle η defined in Fig. 3.3 can be equivalently used to define either the net magnetisation direction along an externally applied magnetic field or the one naturally occurring due to the presence of domains in zero field.

[11] Since imaging measurements were performed at $\psi > 30°$ ($\cos 3\psi < 0$), the interference is overall destructive for $Q''(E_2) > 0$, so that magnetic field dependence shifts downwards in the corresponding polar plot, and constructive for $Q''(E_1) < 0$, so that the polar plot is shifted upwards. This is opposite to the measurements of Fig. 3.6(c), where $\psi < 30°$ ($\cos 3\psi > 0$).

might be present. In general, the difference between detector acquisitions at the two energies taken at a specific temperature value also contains a field-independent term $I_{\mathrm{res}}(E_1) - I_{\mathrm{res}}(E_2)$. The latter is different from zero apart from the very specific case where the resonant term assumes exactly the same value at the two energies. This additional contribution, which would be detrimental for the contrast, does not depend on the temperature and is therefore eliminated by subtracting the high temperature data from each acquisition. It should also be noted that, since the measurement were performed without polarisation analysis, the σ'-polarised NXMS amplitude also contributes to the total scattered intensity. This additional energy-independent contribution (which has a different dependence on the net magnetisation direction, as I will show in Sec. 3.5), does not interfere with the quadrupole resonant scattering (which is π' polarised)[12] and cancels out by taking the difference at the two energy values (analogous to the pure magnetic term I_{magn} in σ-π').

Above $T_N = 16.7(5)$ (see Fig. 3.12), scattering originates only from the temperature independent quadrupole resonance: in this case, the interference term disappears and no contrast should be seen. This is shown in Fig. 3.9(b), where the total scattered intensity from the whole sample is reported as a function of temperature for two different X-ray energies. In contrast to the other data shown in the present section, for this specific set of measurements a magnetic field was applied at $\eta = 80°$ in order to polarise the magnetic structure. The intensity at the two energy values is different at low temperature due to the interference term. The difference decreases upon warming and eventually vanishes at the Néel temperature, above which only pure resonant scattering is present.

Domain patterns were recorded over multiple temperature cycles and corrected for the beam-illumination aspect ratio so that the final images correctly reflect the shape of the ≈ 1 mm-wide sample. One of the temperature cycles is reported in Fig. 3.10. A stripe domain pattern is clearly present at low temperature, with the stripes forming an angle of $\approx 60°$ (consistent with the crystal symmetry) one with respect to another. The contrast decreases upon warming and eventually vanishes in the paramagnetic phase. The domain pattern at low temperature for different cycles was compared in order to ascertain whether it is reproducible with temperature cycling. This is shown in Fig. 3.11, where the magnetic domains at T = 8 K for four different temperature cycles are reported: in order to facilitate the comparison, the difference between successive cycles is also shown. One might expect the domain walls to be partially pinned to the crystal structure as a result of the presence of, for instance, crystal defects. However, defects are not expected to break time reversal symmetry and the net magnetisation direction along a given axis should

[12] In fact, the measurements of Sec. 3.4 could have also been taken without polarisation analysis.

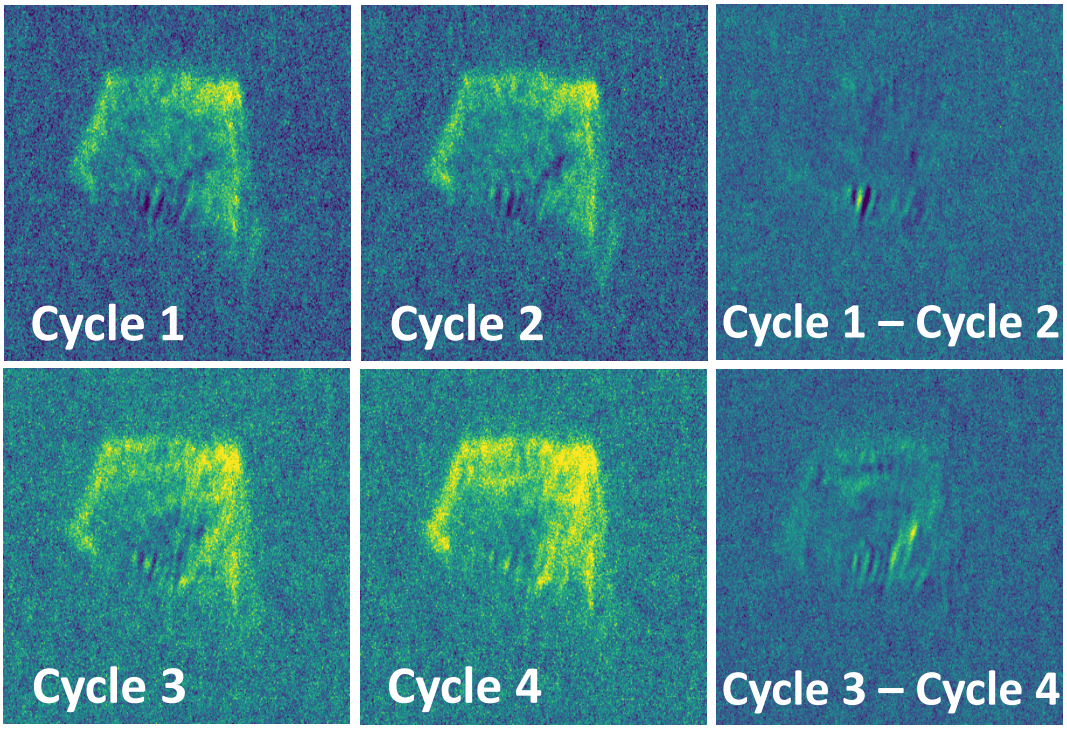

Figure 3.11: $CoCO_3$ magnetic domain patterns at T = 8 K for different temperature cycles across the Néel transition and corresponding difference. Each image corresponds to an illuminated area of size $\approx 1\,mm^2$ as for Fig. 3.10.

point randomly towards the positive or negative direction. While a definitive confirmation will require further work, the measurements do suggest such behaviour. In particular, although the top and sides of the sample appear to exhibit the same magnetisation direction (which might be attributed to the presence of small stray fields), the difference images between consecutive cycles (Fig. 3.11) show a very strong signal in the bottom part, which is indicative of magnetisation reversal. On the other hand, the domain walls seem to persist on temperature cycling, consistent with crystal-defects pinning[13]. It should be noticed that the stripe shape of the domains could be due to defects introduced by the crystal polishing.

[13]Cycles 1,2 and cycles 3,4 were collected at different times, which could explain the minor differences in the domain wall pattern between the two data sets.

3.5 Orbital contribution to the magnetic moment across the series

The work presented in this section has been included in the publication "*Role of the orbital moment in a series of isostructural weak ferromagnets*" by D. Pincini, F. Fabrizi, G. Beutier, G. Nisbet, H. Elnaggar, V.E. Dmitrienko, M.I Katsnelson, Y.O. Kvashnin, A.I. Lichtenstein, V.V. Mazurenko, E.N. Ovchinnikova, O.V. Dimitrova and S.P. Collins, Physical Review B **98**, 104424 (2018) [139].

Compound	AFM sublattice	Calculated spin and orbital angular momenta							Measured
		s_x	s_y	s_z	l_x	l_y	l_z	$\|l\|/\|s\|$	$\|l\|/\|s\|$
$MnCO_3$	A	2.068	0.014	0	0	0	0	0	0.05(2)
	B	-2.068	0.014	0	0	0	0		
$FeBO_3$	A	2.066	0.028	0	0.022	0	0	0.011	0.03(2)
	B	-2.066	0.028	0	-0.022	0	0		
$CoCO_3$	A	1.309	-0.071	-0.015	0.721	-0.036	-0.009	0.55	0.7(2)
	B	-1.309	-0.071	0.015	-0.721	-0.036	0.009		
$NiCO_3$	A	0.836	-0.083	0	0.236	-0.022	0	0.28	0.3(2)
	B	-0.836	-0.083	0	-0.236	-0.022	0		

Table 3.4: Spin and orbital angular momenta in units of $\hbar$ for the different compounds of the series A(C,B)O_3 (A = Mn,Fe,Co,Ni) as derived from DFT calculations and measured by means of NXMS. The **xyz** reference frame is defined such that **x** is perpendicular to a 2-fold axis and contained in a **c** glide plane of the $R\bar{3}c$ structure and **z** is parallel to the crystallographic **c** axis analogous to Fig. 3.2.

The same DFT calculations already used in Sec. 3.4 to predict the sign of the DMI were also exploited to calculate the orbital and spin angular momenta of the TM ion of the different compounds of the series. The initial magnetisation was set to lie along the **x** direction, with **x** perpendicular to a 2-fold axis and contained in a **c** glide plane of the $R\bar{3}c$ structure. This results in having a C-AFM state, which is the lowest-energy state for all compounds. The results of the DFT calculations are summarised in Table 3.4. The calculations predict a negligible orbital contribution to the total angular momentum of the Mn and Fe compounds. On the other hand, a significant orbital angular momentum is found in $CoCO_3$ and $NiCO_3$. The latter is particularly large for the Co^{2+} ion, where it reaches almost 60% of the spin value. This peculiar trend does not find a trivial explanation in a simple

isolated-ion picture. Although Hund's coupling applied to Mn^{2+} and Fe^{3+} ($3d^5$, $l = 0, s = 5/2$) predicts a zero orbital moment, the orbital contribution should be larger in Ni^{2+} ($3d^8$, $l = 3, s = 1$) than in Co^{2+} ($3d^7$, $l = 3, s = 3/2$). Moreover, despite the nominal 3+ oxidation state of the magnetic ion in $FeBO_3$, the calculations predict a covalent, rather than ionic, character for the Fe-O bond: this results in an electronic configuration close to $3d^6$ ($l = 2, s = 2$), which is then expected to host a finite orbital moment. The calculated orbital moment cannot be accounted for even considering the high-spin state (typically found for $3d$ TMOs [1]) of the corresponding TM ion in a cubic crystal field: in this scenario, the orbital moment should be quenched for both $MnCO_3$ ($l_{\text{eff}} = 0, s = 5/2$) and $NiCO_3$ ($l_{\text{eff}} = 0, s = 1$), while a comparable orbital contribution should be present in $FeBO_3$ ($l_{\text{eff}} = 1, s = 2$ for a $3d^6$ configuration) and $CoCO_3$ ($l_{\text{eff}} = 1, s = 3/2$). It should be noticed that the values of spin and orbital angular momenta reported in the present work are projections of the magnetisation density onto a sphere around the corresponding TM ion. Due to covalent bonding of the TM $3d$ orbitals with the oxygens $2p$ states, part of the magnetisation density appears on the ligand sites. The latter also contributes to the net magnetic moment.

In order to verify the theoretical predictions, the well-established polarisation dependence of NXMS (see Sec. 2.1.1.1) was combined with the novel rotating magnet technique described in Sec. 3.2.1 and already successfully used for the resonant measurements outlined in the previous section. The experiments were performed on crystals of the same batches as the ones used for the measurements presented in Secs. 3.3 and 3.4 at beamline I16 of the DLS (unless otherwise stated) by means of an analogous setup to the one of Sec. 3.4. The diffracted signal arising from the long-range (LR) AFM order was measured off resonance at several space-group forbidden reflections of the type $(00l)$, $l = 6n+3$ and $(h\bar{h}l)$, $l = 2n+1$ in both the rotated (σ-π') and unrotated (σ-σ') polarisation channels as a function of the magnetic field direction η (see Sec. 3.2.1). Polarisation analysis of the scattered beam was achieved by means of the (004) reflection of a PG single crystal [with the exception of the data presented in Sec. 3.6.2, for which the (006) was used instead]. The total scattered intensity without polarisation analysis was also measured for $MnCO_3$, $FeBO_3$ and $CoCO_3$ in order to correct for the different reflection efficiencies of the PG crystal in the σ-π' and σ-σ' polarisation channels. The energy of the incident beam was kept fixed to $E = 5.223$ keV ($E = 7.684$ keV for the data of Sec. 3.6.2), chosen for being away from any sample absorption edges and for minimizing the leakage between the two orthogonal light polarisations. For most of the measured reflections, equivalent data sets were collected at several different sample azimuths [(100) azimuthal reference], whose values were selected to minimize the

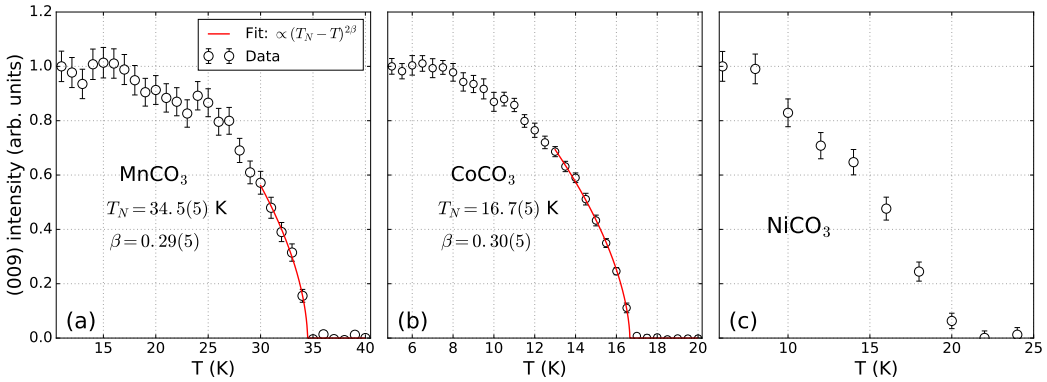

Figure 3.12: Temperature dependence of the (009) magnetic reflection for different members of the carbonates series. A fit to a power law, where β is the corresponding critical exponent and T_N the Néel transition temperature, is also shown for $MnCO_3$ and $CoCO_3$. The data were measured in the σ-π' channel of the polarisation analyser for $MnCO_3$ and $NiCO_3$ and collecting the total intensity without polarisation analysis for $CoCO_3$. The $MnCO_3$ data set was collected at the XMaS beamline [140] of the ESRF at $E = 6.531$ keV using a similar setup to one described in Sec. 2.1.1.3. The other measurements were performed on I16 of the DLS at $E = 5.223$ keV.

contribution of multiple scattering to the diffracted intensity. The corresponding results were then averaged together.

The scattered signal at the measured space-group forbidden reflections is purely magnetic in origin, as proved by the fact that the intensity vanishes upon warming above T_N following the expected critical behaviour as a function of the temperature (Fig. 3.12). The only exception is represented by the $(\bar{1}05)$ and $(\bar{2}07)$ reflections in $CoCO_3$, which will be discussed in Sec. 3.6.3. In particular, the onset of AFM order roughly coincides with the appearance of the net magnetisation at low temperature, reported in Fig. 3.5. For each reflection, the signal in the σ-σ' and σ-π' channels was measured as a function of a 360° rotation of the external field in the basal plane of the crystal. The C-AFM structure rotates in response to the application of the field as described in Sec. 3.2.1 in order to keep the net magnetisation arising from the moment canting parallel to the latter[14]: the corresponding magnetic field dependence of the scattered intensity can then be exploited to extract the relative orbital and spin contribution to the magnetic moment, as outlined here below.

The NXMS intensity in the σ-σ' and σ-π' channels is described by the cross sections of Eq. (2.9), which depend on the magnetic structure factors (2.8). The latter are defined through a summation over the spin and orbital angular momenta

[14]This is strictly speaking true if one neglects the small single-ion anisotropy in the **ab** plane, whose effect will be discussed in Sec. 3.6.2.

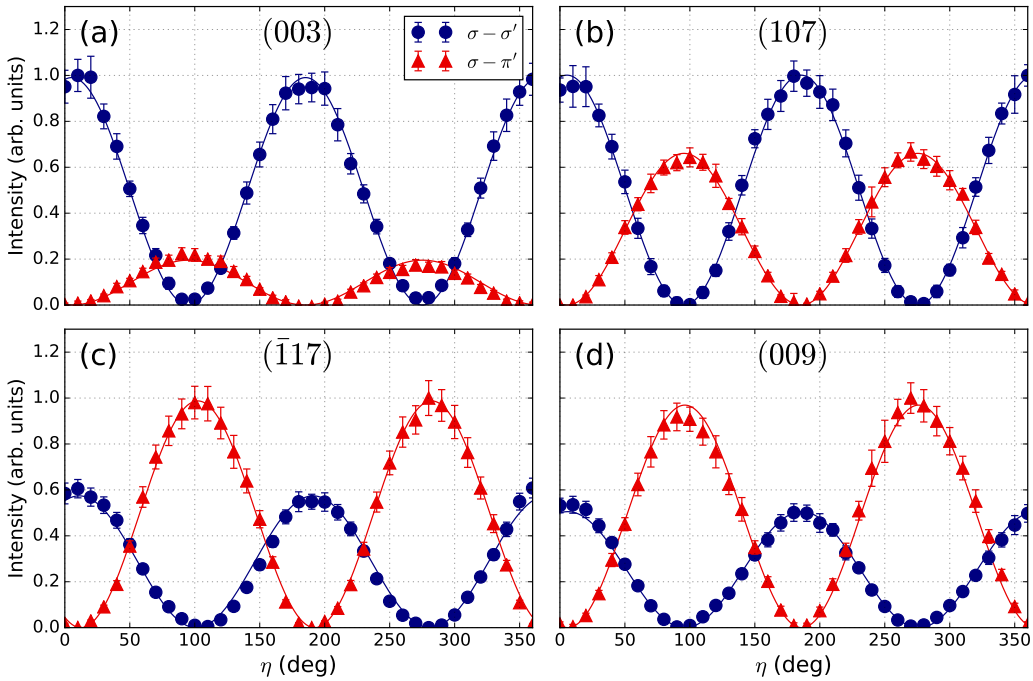

Figure 3.13: Dependence of representative magnetic reflections on the magnetic field direction for two different polarisation states of the diffracted X-ray beam in $CoCO_3$. The data points represent the diffracted intensity integrated over a rocking scan while the solid curves correspond to the best fit to Eq. (3.20). The data were collected at $T = 5-6$ K and $\psi = 83°, 0°, 108°, 30°$ for the (003), (107), $(\bar{1}17)$ and (009) reflection, respectively. A small constant background originating from residual multiple scattering has been removed from all the data sets. For each reflection, the intensity is normalized to the maximum value across both polarisation channels.

of the magnetic ions in the magnetic unit cell, which, in the case of the compounds of interest for the present work, coincides with the crystallographic one. In the case where $\mathbf{j} = \mathbf{s} + \mathbf{l}$ is a good quantum number, the following relations hold between the spin and orbital angular momenta and the total magnetic moment $\boldsymbol{\mu}$ of the magnetic ion [141]:

$$\begin{aligned} \mathbf{s} &= (g-1)\mathbf{j} = \frac{1-g}{g}\frac{1}{\mu_B}\boldsymbol{\mu} \\ \mathbf{l} &= (2-g)\mathbf{j} = \frac{g-2}{g}\frac{1}{\mu_B}\boldsymbol{\mu} \end{aligned} \tag{3.16}$$

where g is the Landé factor. Inserting Eq. (3.16) into Eq. (2.8) and extending the summation of Eq. (2.8) to the TM ions inside the $R\bar{3}c$ hexagonal unit cell, the struc-

ture factors can be expressed as follows:

$$\begin{aligned}\mathbf{S} &= \frac{1-g}{g} f_s(Q) \frac{\mu}{\mu_B} \sum_i \hat{\boldsymbol{\mu}}_i e^{i\mathbf{Q}\cdot\mathbf{r}_i} = C_s(\hat{\boldsymbol{\mu}}_A - \hat{\boldsymbol{\mu}}_B) \\ \mathbf{L} &= \frac{g-2}{g} f_l(Q) \frac{\mu}{\mu_B} \sum_i \hat{\boldsymbol{\mu}}_i e^{i\mathbf{Q}\cdot\mathbf{r}_i} = C_l(\hat{\boldsymbol{\mu}}_A - \hat{\boldsymbol{\mu}}_B)\end{aligned} \tag{3.17}$$

Here, $\hat{\boldsymbol{\mu}} = \boldsymbol{\mu}/|\mu|$ is the magnetic moment unit vector, $C_s = 3\dfrac{1-g}{g} f_s(Q) \dfrac{\mu}{\mu_B}$ and $C_l = 3\dfrac{g-2}{g} f_l(Q) \dfrac{\mu}{\mu_B}$. The isotropic approximation of Eq. (2.10) for the magnetic form factors has also been considered. The expression (3.17) for the magnetic structure factors is equivalent to the one of Eq. (3.5). The only difference is that, in this case, I decided to explicitly write the structure factors as a function of the magnetic moment direction rather than the spin and orbital angular momenta for reasons of convenience.

Expressing the difference of the magnetic moments of the two sublattices with respect to the $\mathbf{u}_1\mathbf{u}_2\mathbf{u}_3$ reference frame defined in Sec. 2.1.1.1, Eq. (3.17) can be written as:

$$\begin{aligned}L_i &= C_l(\hat{\mu}_A^{(i)} - \hat{\mu}_B^{(i)}) \\ S_i &= C_s(\hat{\mu}_A^{(i)} - \hat{\mu}_B^{(i)})\end{aligned} \tag{3.18}$$

where $\hat{\mu}_A^{(i)}$ $[\hat{\mu}_B^{(i)}]$ is the i-th component of the magnetic moment unit vector of the A (B) sublattice along the $\mathbf{u}_i$ direction of the $\mathbf{u}_1\mathbf{u}_2\mathbf{u}_3$ frame. In the case of a specular $(00l)$ reflection, the structure factors assume the simple form of Eq. (3.6): for a general (hkl) geometry, however, the component along $\mathbf{u}_3$ is different from zero and Eq. (3.6) is no longer valid. The ratio of the C_l and C_s constants depends on the relative magnitude of the orbital (l) and spin (s) angular momenta and the orbital $[f_l(Q)]$ and spin $[f_s(Q)]$ form factors:

$$\frac{C_l}{C_s} = \frac{l(Q)}{s(Q)} = \frac{|l|}{|s|} \frac{f_l(Q)}{f_s(Q)} \tag{3.19}$$

where Q is the modulus of the scattering vector associated to the selected (hkl) reflection and the form factors are defined such that $f_s(0) = f_l(0) = 1$ (Sec. 2.1.1.1). The reader is invited to notice that the quantity of Eq. (3.19) could have been alternatively defined in terms of the magnetic moments $\mu_l = -\mu_B l$ and $\mu_s = -2\mu_B s$, leading to a factor of 2 difference.

In the case of negligible magnetocrystalline anisotropy (see Sec. 3.6.2 for the

case when this assumption no longer holds), the sum $\hat{\boldsymbol{\mu}}_A + \hat{\boldsymbol{\mu}}_B$ of the moments of the two sublattices aligns along the direction of the rotating external field $\mathbf{H}(\eta)$: the difference $\hat{\boldsymbol{\mu}}_A - \hat{\boldsymbol{\mu}}_B$ of Eq. (3.18), perpendicular to the field, is forced to follow and causes the scattering amplitudes to vary accordingly. After inserting Eqs. (3.19) and (3.18) into Eq. (2.9), the corresponding diffracted intensities are described by the following relations:

$$\begin{aligned} I_{\sigma\sigma'}(\eta) \propto |M_{\sigma\sigma'}(\eta)|^2 &= \left|\sin 2\theta\,(\hat{\mu}_A^{(2)} - \hat{\mu}_B^{(2)})(\eta)\right|^2 \\ I_{\sigma\pi'}(\eta) \propto |M_{\sigma\pi'}(\eta)|^2 &= \Bigg|2\sin^2\theta\,\Bigg[\cos\theta\left(\frac{l(Q)}{s(Q)}+1\right)\cdot \\ &\quad \cdot\,(\hat{\mu}_A^{(1)} - \hat{\mu}_B^{(1)})(\eta) + \sin\theta\,(\hat{\mu}_A^{(3)} - \hat{\mu}_B^{(3)})(\eta)\Bigg]\Bigg|^2 \end{aligned} \tag{3.20}$$

where the dependence of the magnetic moment differences $(\hat{\mu}_A^{(i)} - \hat{\mu}_B^{(i)})$ on the field angle η has been emphasised. The momentum-dependent orbital-to-spin ratio $l(Q)/s(Q)$ can be extracted through a fit to Eq. (3.20) of the measured dependence of the diffracted intensities on the magnetic field direction in the σ-π' and σ-σ' polarisation channels. Data for two different light polarisations are needed due to the arbitrary scale factor relating the modulus squared of the scattering amplitudes to the measured intensity values.

The scattered intensity in the two polarisation channels would be sufficient in the ideal case where the reflection efficiencies of the analyser crystal in the two channels are equivalent. In practice, this is not exactly true due to the different beam divergence in the vertical and horizontal planes: as a result, the intensity detected in σ-σ' and σ-π' will generally be different even in the case of an equal distribution of σ' and π' polarisation. This effect can be corrected for by additionally measuring the total NXMS intensity I_{tot} without polarisation analysis and introducing a compensation factor f defined as follows:

$$I_{\text{tot}} = C_{\sigma\sigma'} I_{\sigma\sigma'}^{\text{Measured}} + C_{\sigma\pi'} I_{\sigma\pi'}^{\text{Measured}} = C_{\sigma\sigma'}(I_{\sigma\sigma'}^{\text{Measured}} + f I_{\sigma\pi'}^{\text{Measured}}) \tag{3.21}$$

Here, $f = \dfrac{C_{\sigma\pi'}}{C_{\sigma\sigma'}}$ is the ratio of the two arbitrary scale factors which link the intensity measured in the two polarisation channels to the total one recorded through the area detector. In the ideal case in which the reflection efficiencies for the two polarisation channels are equivalent, only one scale factor would be necessary, which corresponds to having $f = 1$. In practice, the compensation factor f can be extracted using Eq. (3.21) to fit the total intensity as a function of a 360° rotation of the magnetic field measured with the 2D detector from the σ-σ' and σ-π' magnetic

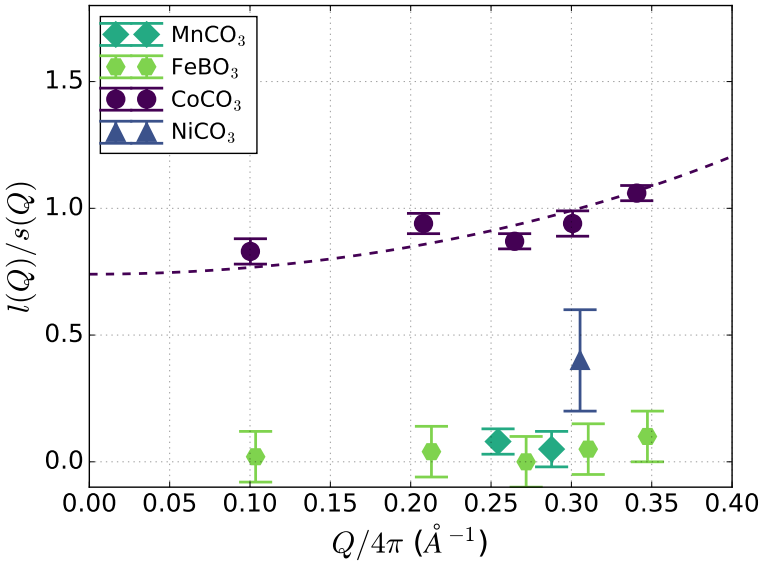

Figure 3.14: Orbital-to-spin angular momenta ratio for the different compounds of the series as a function of the momentum transfer. For each compound, the $l(Q)/s(Q)$ value of each magnetic reflection (and the corresponding error bar) was calculated combining measurements at different temperatures and azimuth values (see Appendix A). The dashed line represents a fit to Eq. (3.19) of the $CoCO_3$ data considering the isotropic approximation (2.10) for the magnetic form factors.

field dependences. The measured data can then be corrected by multiplying the intensity in σ-π' by f: finally, Eq. (3.20) can be used to fit the corrected values. The measurements presented in this work have been corrected for the analyser crystal reflection efficiencies following the procedure outlined above, except for the $NiCO_3$ ones. Given the much longer counting time needed for the latter, the total scattered intensity could not be measured: the error on the corresponding $l(Q)/s(Q)$ value is therefore larger than for the other compounds.

Representative data measured in σ-σ' and σ-π' in $CoCO_3$ for four different magnetic reflections are displayed in Fig. 3.13 along with the best fits to Eq. (3.20). A complete summary of the reflections measured for each compound can be found in Appendix A along with the relevant experimental parameters and representative data on the other members of the series. The data were collected by measuring the integrated intensity of the diffraction peak over a rocking scan of the sample at each value of the magnetic field angle η. The magnetic intensity displays very well-defined[15] 180°-periodic sinusoidal oscillations. The latter can be easily understood in the case of specular $(00l)$ reflections, for which the magnetic structure factors display a zero component along $\mathbf{u}_3$ and are simply given by Eq. (3.6). The inten-

[15] As already pointed out in Sec. 3.2.1, the data are of extremely high quality since the magnetic field measurements of Fig. 3.13 were performed without moving the sample.

sity in σ-σ' and σ-π' depends on the components of the structure factors along $\mathbf{u}_2$ and $\mathbf{u}_1$ which, following from Eq. (3.6), oscillate as $\cos\eta$ and $\sin\eta$, respectively. This results in intensity oscillations of the type $\cos^2\eta$ and $\sin^2\eta$, perfectly out of phase one with respect to the other. In the case of non-specular reflections, the structure factors have a non-zero component along $\mathbf{u}_3$ and the phase of the corresponding σ-π' oscillations will depend on the precise azimuth value chosen for the measurements. For any given reflection, the $l(Q)/s(Q)$ ratio is encoded in the relative amplitude of the σ-σ' and σ-π' intensity modulations. It should be noticed that the measured σ-σ'/σ-π' amplitude ratio is also subject to a trivial azimuth-dependent geometrical factor related to the components of the magnetic moments in the $\mathbf{u}_1\mathbf{u}_2\mathbf{u}_3$ reference frame [i.e. the quantities $(\hat{\mu}_A^{(i)} - \hat{\mu}_B^{(i)})$ of Eq. (3.20)]: this explains why the two symmetrically-equivalent $(1\,0\,7)$ and $(\bar{1}\,1\,7)$ reflections show significantly different amplitudes in Fig. 3.13 despite being characterised by the same value for the orbital-to-spin ratio.

The $l(Q)/s(Q)$ values (averaged over all the measured temperatures and sample azimuths reported in Appendix A) corresponding to different space-group forbidden reflections are shown as a function of the momentum transfer in Fig. 3.14 for the different compounds of the family. Following from Eq. (3.19), the relative orbital and spin contributions to the total angular momentum of each compound, i.e. $|l|/|s| = l(0)/s(0)$, can be ultimately extracted by extrapolating the ratio $l(Q)/s(Q)$ to $Q = 0$. This can be achieved through a fit to Eq. (3.19) of the measured $l(Q)/s(Q)$ values assuming the isotropic approximation of the orbital and spin magnetic form factors of Eq. (2.10). The fit for the case of $CoCO_3$ is reported as a dashed line in Fig. 3.14. The resulting $|l|/|s|$ values are summarised in Table 3.4 along with the corresponding values from the DFT calculations.

There is generally a very good agreement between the measurements and the calculations. In particular, the trend across the series of compounds is confirmed: while $MnCO_3$ and $FeBO_3$ behave as almost pure spin systems, a significant unquenched orbital moment is found for both $CoCO_3$ and $NiCO_3$. Most importantly, the predicted large value of the orbital moment in $CoCO_3$ is confirmed. A substantial unquenched orbital contribution to the magnetic moment has been also reported for several Ni and Co oxides [49, 142–147]; in particular, a large orbital contribution was found in crystals [144, 145, 147] and thin films [148] of CoO. In this case, the coupling between spin and orbital moment caused by the SOC can generally produce a strong magnetoelastic coupling and lead to the appearance of a large single-ion anisotropy and magneto-strictive effects [1]. The magnetic properties will then considerably differ from the case of a spin-only system with quenched orbital degrees of freedom. As I will show in Sec. 3.6, the presence of a large or-

bital moment is confirmed by XMCD measurements and results in the emergence of several interesting phenomena in the physics of $CoCO_3$.

When comparing the measurements with the calculations, it is important to bear in mind that due to the covalent bonding of the TM 3*d* orbitals with the oxygen 2*p* states, part of the magnetisation density appears on the ligand sites. While the NXMS measurements are sensitive to both, the projected values of Table 3.4 from the DFT calculations neglect the oxygen contribution. This could explain, for instance, the partial discrepancy (still within the experimental uncertainty) between the measured and calculated values for $CoCO_3$. This seems to be confirmed by the XMCD measurements outlined in Sec. 3.6.1, which selectively probe the magnetisation of the TM ion.

3.6 Role of the orbital moment in $CoCO_3$

The work presented in this section has been included in the publication "*Role of the orbital moment in a series of isostructural weak ferromagnets*" by D. Pincini, F. Fabrizi, G. Beutier, G. Nisbet, H. Elnaggar, V.E. Dmitrienko, M.I Katsnelson, Y.O. Kvashnin, A.I. Lichtenstein, V.V. Mazurenko, E.N. Ovchinnikova, O.V. Dimitrova and S.P. Collins, Physical Review B **98**, 104424 (2018) [139].

3.6.1 Orbital moment contribution investigated by XMCD

In-plane moments: low-field measurements

One of the main results of the previous section is the presence of an unusually large unquenched orbital moment in $CoCO_3$. In order to confirm this finding, XMCD was measured on a single crystal of $CoCO_3$ at the high-field magnet end station of beamline I10 of the DLS. A thin film of Pt ($\approx$ 2 nm) was deposited via sputter coating on the crystal's facet orthogonal to the **c** axis at the Research Complex at Harwell prior to the XMCD measurements. The purpose of the Pt coating was to create an electrical contact with the illuminated area of the sample. The latter allowed the drain current of photo-generated electrons to be extracted thus making TEY detection (see Sec. 2.2.1) possible despite the strong insulating character of $CoCO_3$. The crystal was clamped on an electrically-grounded copper holder and

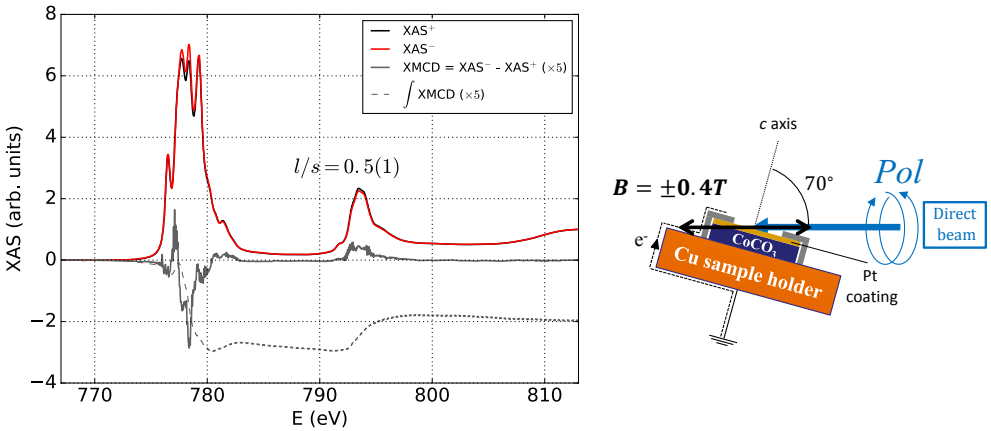

Figure 3.15: Absorption spectra measured with the external magnetic field parallel (XAS^-) and antiparallel (XAS^+) to the helicity of the incident circularly polarised light and corresponding circular dichroism (XMCD). The data were collected at T = 3 K using a magnetic field $\mu_0 H = 0.4$ T applied in the **ab** plane of the crystal. The dashed grey line represents the integrated XMCD signal used for the application of the sum rules: the l/s value refers to the corresponding orbital-to-spin angular momenta ratio. The XAS data are normalized such that the post-edge spectral weight is equal to unity. The drawing on the right schematically represents the experimental geometry.

inserted in the UHV sample environment of the I10 superconducting magnet with the coated surface facing the incident beam. The measurements were performed at a shallow (20°) incident X-ray angle, so that the external magnetic field, directed along the incident beam wave vector, was almost perpendicular to the **c** axis (see drawing in Fig. 3.15). A relatively small field value ($\mu_0 H = 0.4$ T) was used: this was chosen to be sufficiently large to suppress the magnetic domain structure and generate a significant net magnetisation along the field while being, at the same time, small enough not to strongly distort the in-plane C-AFM order of the Co^{2+} moments. XAS measurements were collected across the Co L_3 (778.2 eV) and L_2 (793.1 eV) edges for opposite helicities of the incident circularly-polarised soft X-ray beam ($20 \times 100\,\mu m^2$ spot size) and opposite directions of the external field. Several XAS spectra were collected and averaged for each permutation of light polarisation and field direction and the resulting spectra combined to obtain the XMCD signal.

The results are summarised in Fig. 3.15, where the absorption spectra obtained by combining the field and polarisation reversal measurements are plotted along with the corresponding dichroism. The presence of a significant unquenched orbital moment is immediately evident from the much larger XMCD signal at the Co L_3 edge compared to the L_2 one. The application of the sum rules (see Sec. 2.2.2) for the spin (μ_s) [86] and orbital (μ_l) [85] magnetic moment to the integrated XMCD signal shown in Fig. 3.15 leads to a value of the orbital-to-spin ratio

$l/s = 2\mu_l/\mu_s = 0.5(1)$. The latter is additionally confirmed by the multiplet calculations outlined in Sec. 3.6.3.2, which give $l/s \approx 0.6$. This value agrees with the one derived from the NXMS measurements within the experimental uncertainty and thus further consolidates the experimental findings. One could argue that the nominal value of the l/s ratio found by means of XMCD is closer to the calculated one (Table 3.4), which neglects the oxygen contribution to the total magnetisation density. This is perfectly consistent with the resonant nature of the absorption process which, contrary to NXMS, selectively probes the magnetisation density localised on the Co^{2+} ions.

Out-of-plane moments: high-field measurements

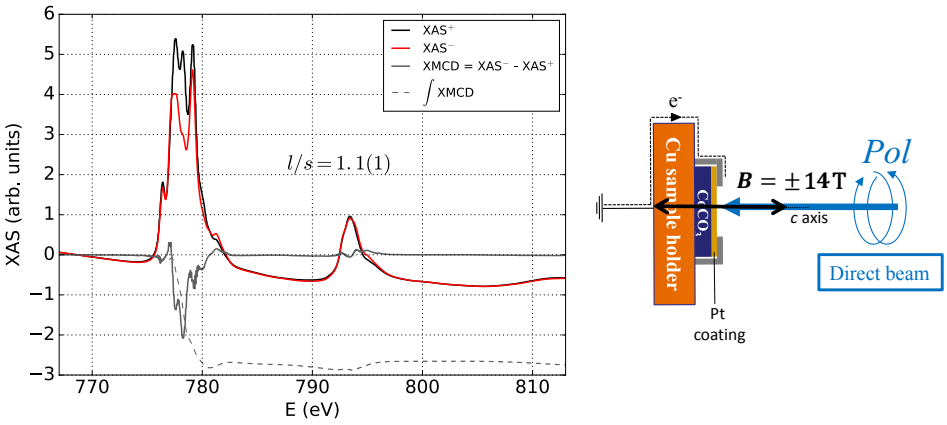

Figure 3.16: Absorption spectra measured with the external magnetic field parallel (XAS^-) and antiparallel (XAS^+) to the helicity of the incident circularly polarised light and corresponding circular dichroism (XMCD). The data were collected at T = 3 K by applying a magnetic field $\mu_0 H = 14$ T along the crystallographic **c** axis (normal incidence). The dashed grey line represents the integrated XMCD signal used for the application of the sum rules: the l/s values refers to the corresponding orbital-to-spin angular momenta ratio.

The LDA + U + SOC calculations already discussed in Secs. 3.4 and 3.5 have also revealed a very strong anisotropy of the orbital magnetic moment of the Co^{2+} ion in $CoCO_3$. It was found that the value of the orbital moment decreases from about 0.72 μ_B for in-plane (along the **x** axis) moments to 0.2 μ_B for out-of-plane (along the **z** axis) orientation. An analogous effect was explicitly reported in Co thin films [149–152], where XMCD measurements revealed a different orbital and spin contribution to the magnetic moment depending on the external field direction relative to the easy magnetisation axis. Such sensitivity of the orbital magnetic moment to the magnetisation direction is intimately related [153] to the strong magnetocrystalline anisotropy of $CoCO_3$, which will be discussed in more detail in the next section.

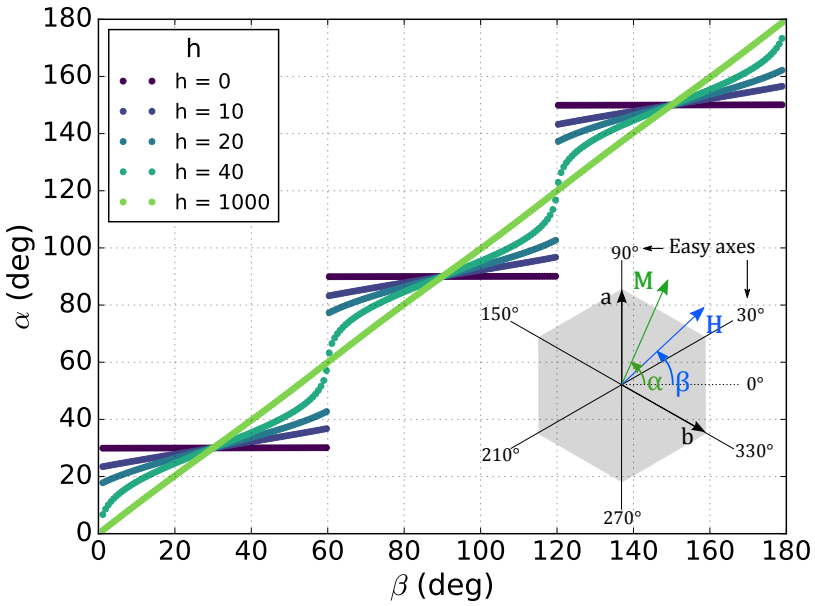

Figure 3.17: Direction of the weak net magnetisation **M** as a function of the external magnetic field **H** direction in the basal plane of the crystal for different values of the anisotropy parameter $h = \frac{\mu_0 HM}{K}$ discussed in the text. Each curve $\alpha(\beta)$ corresponds to a solution of Eq. (3.24) for a different value of h. The inset shows the definitions of the magnetisation (α) and external magnetic field (β) angles in the **ab** basal plane of the $R\bar{3}c$ crystal structure.

In order to test this prediction, a second set of XMCD measurements was performed where the moments were dragged out of the **ab** plane through the application of a strong ($\mu_0 H = 14$ T) magnetic field along the trigonal **c** axis (normal incidence geometry). The corresponding spectra are shown in Fig. 3.16 along with the l/s value extracted through the application of the sum rules. At odds with the theoretical predictions, the latter is about a factor of 2 larger than the one found through the in-plane field measurements regardless of the temperature or the field strength used for the experiment. It should be noted, however, that the pronounced negative slope in the background of the data of Fig. 3.16 makes the extraction of the orbital and spin contribution through the application of the sum rules significantly less reliable and could have an impact in the validity of these results. Further investigation will be needed to address this issue.

3.6.2 Magnetocrystalline anisotropy

The strong dependence of the orbital moment on the field direction predicted by the first-principle calculations is usually accompanied by a large magnetocrystalline

anisotropy [153]. The latter was estimated by means of the so-called constrained LDA + U + SOC calculations in which the direction of the magnetic moments was fixed along either the out-of-plane or in-plane crystallographic directions. The resulting anisotropy energy of ≈ 9 meV/Co^{2+} is remarkably large. For instance, the corresponding value in $SmCo_5$ and Co/Pt multilayers [154, 155] does not exceed 2 meV/Co atom. At the same time, the magnetocrystalline anisotropy energy in $CoCO_3$ is almost the same as estimated for individual cobalt atoms deposited on the Pt(111) surface [156]. In general, a strong uniaxial anisotropy is somewhat expected for systems which, in a symmetric situation, have partially filled t_{2g} orbitals with strong enough SOC [1], as is the case for the Co^{2+} ion.

The magnetic anisotropy within the **ab** plane is expected to be significantly smaller [97]. However, as I will show hereafter, its effect on the magnetic field dependence of the scattered intensity is clearly visible. For a crystal of space group $R\bar{3}c$, the single-ion anisotropy in the **ab** plane is described by the following energy cost per unit volume [157]:

$$\left(\frac{E_{\text{anis.}}}{V}\right) = K_0(T) + K(T)\cos 6\alpha \tag{3.22}$$

where $K_0(T)$ and $K(T)$ are temperature-dependent constants (in energy per unit volume) which express the strength of the anisotropy and α is the angle describing the magnetisation direction with respect to the crystal axes. This is defined such that the net magnetisation resulting from the canting of the magnetic moments (which I shall refer to simply with the term "magnetisation" from now on) is orthogonal to the $[1\,0\,0]$ crystallographic direction for $\alpha = 0^\circ$ (see inset in Fig. 3.17). This six-fold energy term is minimized for $\alpha = 30^\circ + n60^\circ$ (n integer index) and thus defines three main easy magnetisation axes along the $[1\,0\,0]$, $[1\,1\,0]$ and $[0\,\bar{1}\,0]$ crystallographic directions.

In the presence of an external magnetic field $\mathbf{H}(\beta)$, the total energy per unit volume can be written as [dropping the constant K_0 in Eq. (3.22)]:

$$\begin{aligned}\frac{E}{V} &= \frac{E_{\text{anis.}}}{V} + \frac{E_{\text{field}}}{V} = \\ &= K(T)\cos 6\alpha - \mu_0 HM(T)\cos(\alpha - \beta)\end{aligned} \tag{3.23}$$

where $M(T)$ is the temperature-dependent magnitude of the magnetisation. Analogous to the magnetisation angle α, β defines the direction of the external magnetic field with respect to the orthogonal to the $[1\,0\,0]$ direction. This is related to the angle η used to express the magnetic field dependence of the scattered intensity

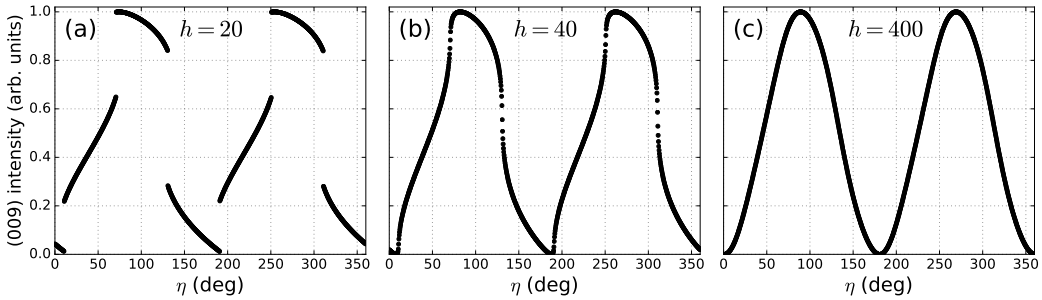

Figure 3.18: Calculated dependence of the (009) magnetic reflection in the σ-π' polarisation channel on the external magnetic field direction for different values of the anisotropy parameter $h = \frac{\mu_0 HM}{K}$ discussed in the text. The diffracted intensity was calculated using analogous solutions of Eq. (3.24) to the ones shown in Fig. 3.17.

through the relation $\beta = \psi - \eta + 60^\circ$, where ψ is the sample azimuth and the 60° offset is simply due to the initial magnet position with respect to the crystal axes. In Eq. (3.22), E_{field} represents the Zeeman interaction of the net magnetic moment with the external field. For the case of negligible anisotropy considered in Sec. 3.5 ($E_{\text{anis.}} \approx 0$), the Zeeman term forces the magnetisation to align parallel to the applied field ($\alpha = \beta$). In the general case of non-negligible anisotropy, however, **M** and **H** will lie along different directions. For any given direction β of the external field, the equilibrium direction α of the magnetisation is obtained by minimizing the energy term of Eq. (3.23):

$$\frac{d}{d\alpha}\left(\frac{E}{KV}\right) = 0 \tag{3.24}$$

The solutions $\alpha(\beta)$ of Eq. (3.24) can be calculated numerically for different values of the dimensionless quantity $h(T) = \dfrac{\mu_0 HM(T)}{K(T)}$, which parametrises the relative strength of the Zeeman and anisotropy energy terms. These are plotted over a 180° range of β values in Fig. 3.17. The limiting case of negligible anisotropy considered in Sec. 3.5 corresponds to large h values and leads to the trivial solution $\alpha = \beta$. At the other extreme, for very large anisotropy values (small values of h) the magnetisation is locked on the easy magnetisation axes ($\alpha = 30^\circ, 90^\circ \ldots$) regardless of the direction of the field and jumps discontinuously from one easy axes to another as the field rotates. A non-trivial six-fold periodic function is obtained in the intermediate regime.

The solutions $\alpha(\beta)$ can be used to calculate the magnetic structure factors (3.18) and simulate the magnetic scattering intensities of Eq. (3.20) for different h values. The simulations are reported in Fig. 3.18 for the (009) σ-π' intensity and three representative h values. For negligible anisotropy (large h) a smooth

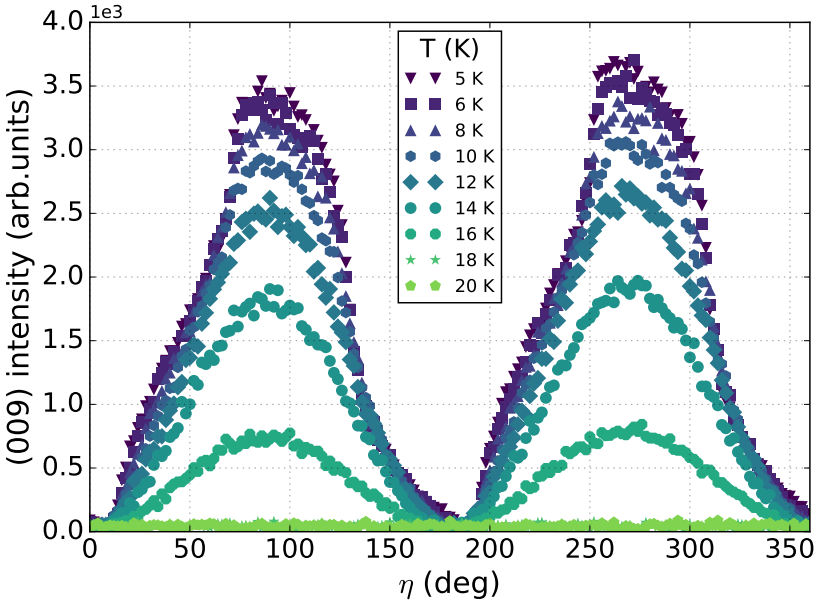

Figure 3.19: Dependence of the $CoCO_3$ (009) reflection on the magnetic field direction in σ-π' at different temperatures across the Néel transition at $T_N = 16.7(5)$ K.

sinusoidal oscillation is obtained, analogous to the data shown in Fig. 3.13. As the anisotropy increases (h decreases) the intensity modulation takes on a peculiar "shark-fin" shape and eventually becomes discontinuous. Remarkably, an identical trend is clearly seen in the measured data as a function of temperature shown in Fig. 3.19. Increasing the temperature towards the Néel transition has, in this case, the effect of weakening the magnetocrystalline anisotropy: upon warming, the shark-fin shape progressively disappears and symmetric sinusoidal oscillations are recovered close to T_N.

The scattered intensity calculated from the solutions of Eq. (3.24) can be used to fit the experimental data of Fig. 3.19 leaving the anisotropy constant $K(T)$ as a free fitting parameter and using the magnetisation values of Ref. [114] in the parameter h. The calculations reproduce extremely well the measurements, as shown in the two representative fits of Fig. 3.20 for data collected well below and close to the magnetic transition. The values of $K(T)$ obtained from the fits are displayed in Fig. 3.21. As expected, the basal plane anisotropy constant decreases with increasing temperature: a quadratic dependence of the type $\propto (T_N - T)^2$ is observed over most of the temperature range explored, similar to what was reported by Kaczer [97]. A value $K = 11(2)$ neV/Co^{2+} is found at T = 4 K, in agreement with a previous estimate [97]. Although almost 6 orders of magnitude smaller than the out-of-plane value, the effect of a finite basal plane anisotropy is clearly visible in the data and proves the extremely high sensitivity of our novel rotating magnetic

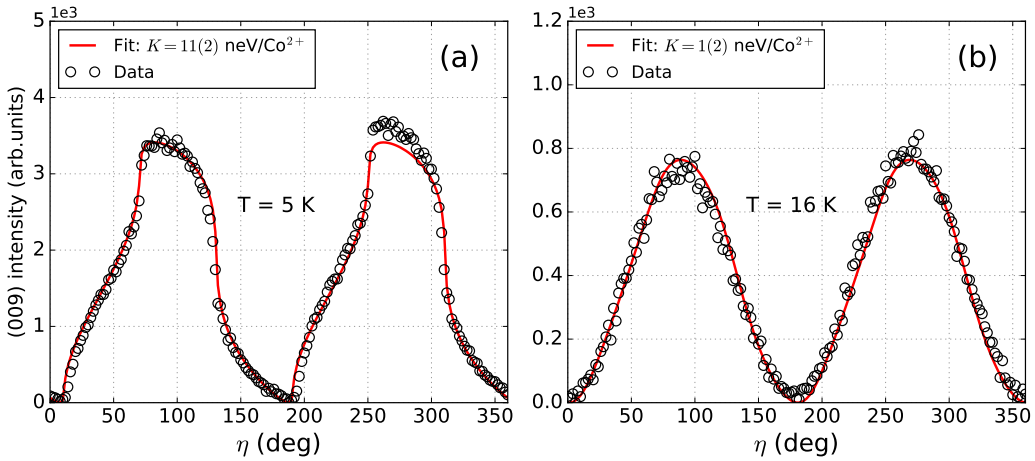

Figure 3.20: Fit detail of two representative data sets of Fig. 3.19 measured well below and close to the Néel transition. The solid lines represent the best fit to the calculated intensity (see Fig. 3.18) leaving the anisotropy constant K as a free parameter. The results of the fit of the data sets at all temperatures are shown in Fig. 3.21.

technique to small interaction terms of the magnetic Hamiltonian.

The anisotropy-induced distortion at low temperature is not as evident in the data of Fig. 3.13 collected around T = 5 K. The two sets of data were measured during different experiments on two different crystals and several factors might explain the observed discrepancy. As well as differences in the crystal quality (crystal defects could, for instance, impact the field dependence of the scattered intensity), a significant beam heating has been observed in several occasions and might have also played a role despite the precautions taken to minimize it. The latter is very sensitive to the exact experimental conditions (which were different for the two data sets), such as sample mounting and incident flux: a sample temperature just a few degrees higher than the nominal value could explain the apparent lack of anisotropy in Fig. 3.13. Moreover, unlike the data presented in Fig. 3.13, the measurements of Fig. 3.19 were not collected integrating the intensity over a rocking scan at each value of the field angle. This allowed a much larger number of data points to be collected in a significantly shorter time (minutes compared to hours). Both the coarser sampling and the averaging of any long term drifts could be at the origin of the apparent lack of any significant shark-fin distortion. It should also be noticed that the magnetic field value depends on the exact position of the permanent magnet used for the measurements. This was fixed on the diffractometer rotational stages manually: a slightly different position between the measurements of Fig. 3.13 and Fig. 3.19 is likely to play a role in the observed discrepancy. The anisotropy is also not clearly seen in the measurements presented in Sec. 3.6.3 and its effect has therefore been

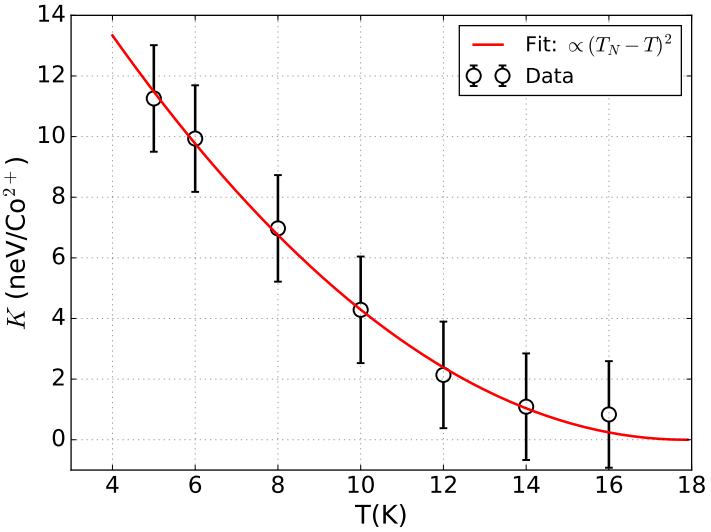

Figure 3.21: Temperature dependence of the in-plane magnetocrystalline anisotropy constant K in $CoCO_3$. The data points were obtained through analogous fits to the ones shown in Fig. 3.20: the error bars include the fit statistical error and the additional systematic error on the magnetic field value of the permanent magnet which appears in the anisotropy parameter h discussed in the text. The solid line represents the best fit to the quadratic law $\propto (T_N - T)^2$ proposed by Kaczer [97].

neglected in the corresponding analysis.

3.6.3 Forbidden charge scattering

3.6.3.1 Experimental data and empirical model

All the measured space-group forbidden reflections are purely magnetic in origin. As already mentioned earlier on in the present chapter, the only exception is represented by the $(\bar{2}07)$ and $(\bar{1}05)$ in $CoCO_3$. Here, the dependence of the scattered intensity in the σ-σ' channel generally differs from the two-fold oscillation observed at the other (hkl) values (see Fig. 3.13) and strongly depends on the precise sample azimuth at which the magnetic field dependence is measured. This is evident from the colour map of Fig. 3.22(a), where the magnetic field dependences of the $(\bar{2}07)$ reflection measured at different ψ values are reported: a peculiar interference pattern with abrupt variations is present as a function of ψ. A similar behaviour is also observed by changing the energy of the incident X-rays while staying away from any absorption edges, as shown by the colour map as a function of energy of Fig. 3.24(a). This behaviour contrasts the scattered intensity in the σ-π' channel,

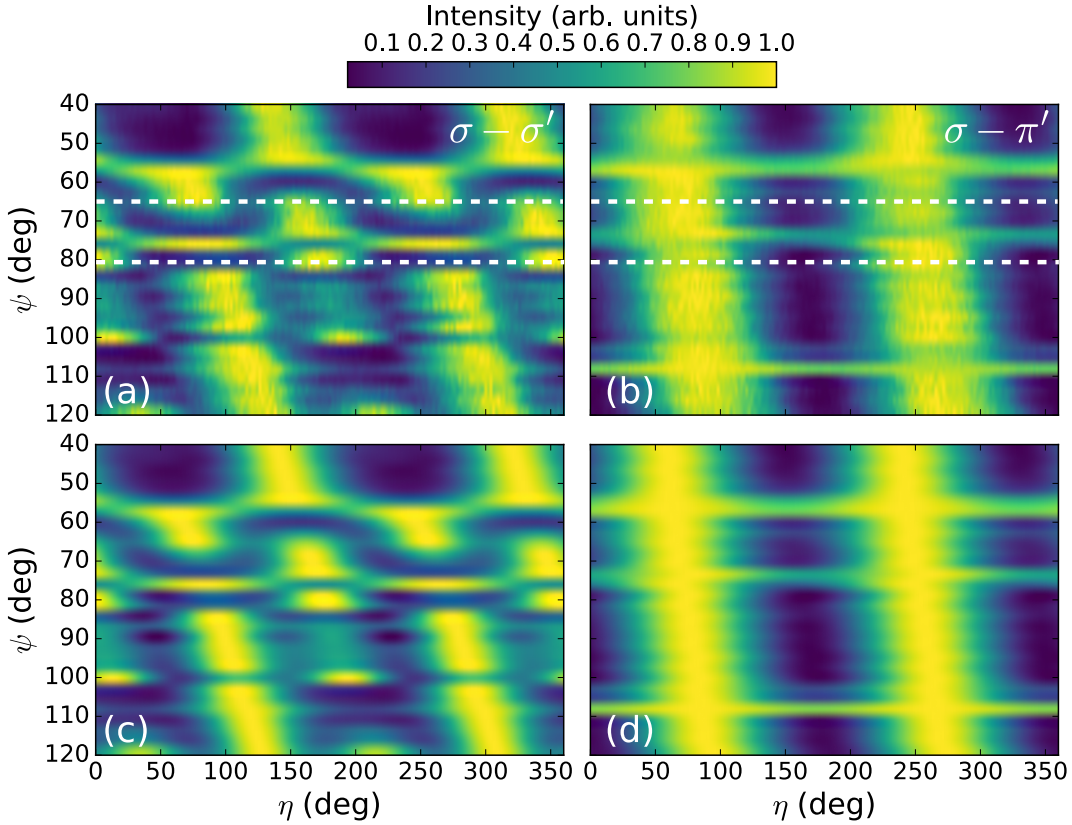

Figure 3.22: (a),(b) Magnetic field direction dependence of the $(\bar{2}07)$ intensity as a function of the sample azimuth ψ for two different polarisation states of the diffracted X-ray beam. For each azimuth value and polarisation channel, the measured intensity (represented through the colour scale) as a function of the field direction is normalized to its maximum value. A detail of the $\psi = 65°$ and $\psi = 80°$ data sets (dashed horizontal lines) is shown in Fig. 3.23. (c),(d) Global fit of the $(\bar{2}07)$ magnetic field direction dependence shown in (a),(b). The σ-σ' and σ-π' data at each azimuth value have been fitted to Eq. (3.25) and the second line of Eq. (3.20), respectively, as shown in Fig. 3.23. The ratio between the magnetic and forbidden charge amplitudes in σ-σ' was kept constant across all ψ values, while the multiple scattering amplitude was left free to vary: the resulting values are plotted in Fig. 3.28.

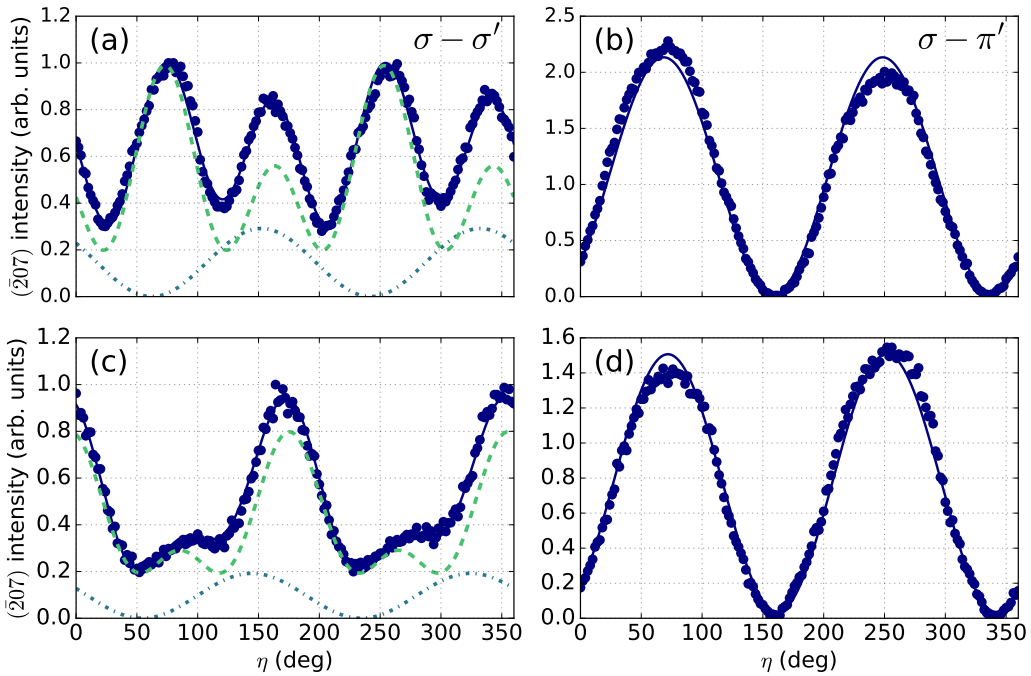

Figure 3.23: $(\bar{2}07)$ intensity magnetic field dependence in (left) σ-σ' and (right) σ-π' at (a),(b) $\psi = 65°$ and (c),(d) $\psi = 80°$ [see dashed horizontal lines of Figs. 3.22(a),(b)]. The symbols represent the measured diffracted intensity, while the solid line refers to the global fit as explained in the text. In (a) and (c) the dashed green line and the dash-dot light blue line correspond to the charge and magnetic contribution to the global fit, respectively. The data were collected at T = 4 K and are normalized to the peak intensity of the σ-σ' channel. A constant background originating from multiple scattering has been removed from the σ-π' data set.

which, regardless of the ψ [Fig. 3.22(b)] and energy [Fig. 3.24(b)] value exhibits the normal two-fold oscillation seen for the other reflections (Fig 3.13)[16].

The presence of an azimuthal dependence is somewhat unexpected, given the off-resonant nature of the scattering process at the energy used for the experiment. A detail of the $(\bar{2}07)$ magnetic field dependence at $\psi = 65°$ and $\psi = 80°$ [dashed lines in Figs. 3.22(a),(b)] is shown in Figs. 3.23(a),(b) and Figs. 3.23(c),(d), respectively. Magnetic scattering alone cannot account for the pattern observed in the measured intensity in σ-σ': an extra contribution, displayed as a green dashed line in Figs. 3.23(a) and 3.23(c), must be introduced[17]. The latter, in turn, can be suc-

[16]The bright streaks observed at certain ψ values are simply due to the higher background caused by the presence of nearby multiple diffraction peaks. Moreover, the shift in the oscillation pattern with the sample azimuth stems from a trivial ψ-dependent offset (also present in σ-σ') affecting the definition of the magnetic field angle η for off-specular reflections [i.e. other than $(00l)$].

[17]It should be stressed that the σ-σ' and σ-π' data sets were fitted simultaneously so that the phase of the magnetic oscillations in the former is constrained by the latter, where only the magnetic contribution is present.

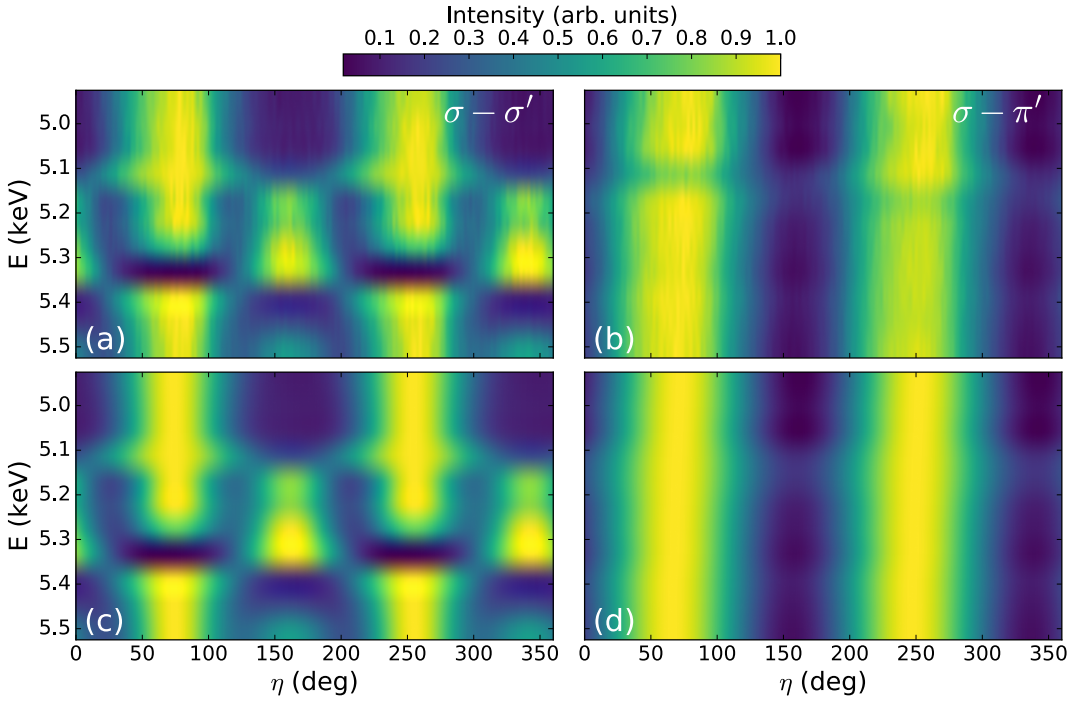

Figure 3.24: (a),(b) Magnetic field direction dependence of the $(\bar{2}07)$ intensity as a function of the incident X-ray energy for two different polarisation states of the diffracted X-ray beam at $\psi = 65°$. For each energy value and polarisation channel, the measured intensity (represented through the colour scale) as a function of the field direction is normalized to its maximum value. (c),(d) Global fit of the $(\bar{2}07)$ magnetic field direction dependence shown in (a),(b). The σ-σ' and σ-π' data at each azimuth value have been fitted to Eq. (3.25) and the second line of Eq. (3.20), respectively. The ratio between the magnetic and forbidden charge amplitudes in σ-σ' was kept constant across all energy values, while the multiple scattering amplitude was left free to vary.

cessfully accounted for by two interfering scattering amplitudes of charge origin: (i) a sinusoidally-oscillating forbidden scattering term, $C^{FS}_{\sigma\sigma'}(\eta)$, plotted in Fig. 3.26 as a function of the field direction and (ii) a field-independent multiple-scattering amplitude, $C^{MS}_{\sigma\sigma'}$. The total scattered intensity in the σ-σ' channel is therefore correctly described by:

$$I^{(\bar{2}07),(\bar{1}05)}_{\sigma\sigma'}(\eta) = I^{\text{Magnetic}}_{\sigma\sigma'} + I^{\text{Charge}}_{\sigma\sigma'} \propto |M_{\sigma\sigma'}(\eta)|^2 + \left|C^{FS}_{\sigma\sigma'}(\eta) + C^{MS}_{\sigma\sigma'}\right|^2 \qquad (3.25)$$

where $I^{\text{Magnetic}}_{\sigma\sigma'} \propto |M_{\sigma\sigma'}(\eta)|^2$ is given by the first line of Eq. (3.20). The charge origin of $C^{FS}_{\sigma\sigma'}(\eta)$ is suggested by the absence of the interference effect in the rotated polarisation channel: charge scattering does not rotate the polarisation of the incident X-rays and therefore cannot contribute to the scattered intensity in σ-π'. Further confirmation comes from the temperature dependence of the $(\bar{2}07)$ intensity at $\psi = 65°$ shown in Fig. 3.27. The signal vanishes at the Néel transition temperature

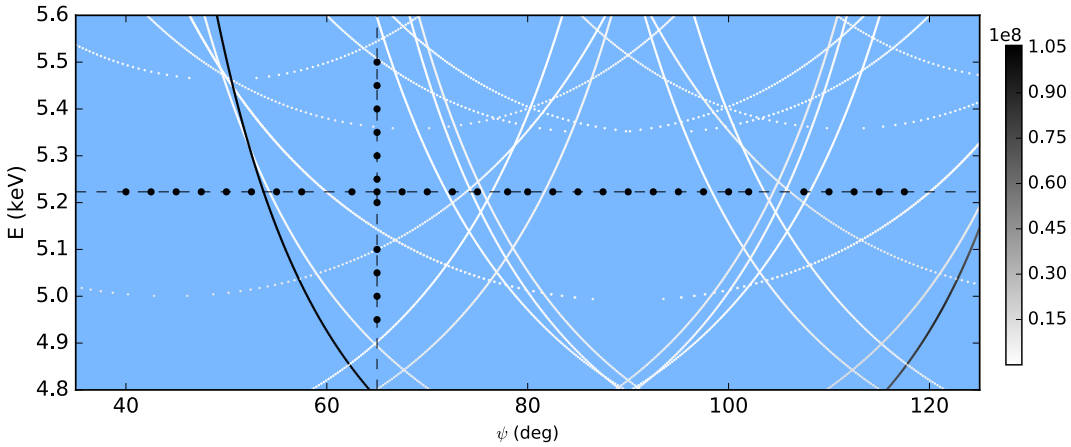

Figure 3.25: $(\bar{2}07)$ multiple scattering energy and azimuth (ψ) dependence in the σ-σ' polarisation channel. The small symbols in the grey colour scale correspond to multiple scattering peaks, with the colour representing the scattered intensity. The large black circles represent the energy and azimuth values at which the measurements displayed in Fig. 3.24 (along the dashed vertical line) and Fig. 3.22 (along the dashed horizontal line) were performed.

analogous to the reflections exhibiting a "normal" magnetic behaviour, indicating that the extra component is linked to the LR magnetic order. More importantly, the critical exponent of the $C^{FS}_{\sigma\sigma'}(\eta)$ amplitude is twice as large as the magnetic one, as expected for magnetic-induced charge scattering [141].

The forbidden amplitude stems from a peculiar distortion of the Co^{2+} electron cloud induced by the magnetic moment in the magnetically-ordered phase. While a microscopic description requires detailed calculations of the Co^{2+} ground-state wave function (see Sec. 3.6.3.2), most aspects of the resulting scattering process are captured by the simple "toy model" sketched in the drawing of Fig. 3.26. This assumes a small elongation of the Co^{2+} electron cloud along the magnetic moment direction, which is modelled by artificially adding a pair of negative charges to either side of each Co^{2+} ion along $\boldsymbol{\mu}$. The electron cloud distortion reduces the symmetry of the crystal in the magnetically-ordered phase such that, for an arbitrary field direction, only the inversion centre is left [space group $P\bar{1}$ (No.2)]. The two extra charges are set to rigidly follow the rotation of $\boldsymbol{\mu}$ as this is dragged around by the external field. The corresponding structure factor can be calculated for the space-group forbidden reflections of interest by summing the contribution from each Co^{2+} ion in the unit cell. The Co^{2+} ions of the two FM sublattices give rise to two contributions of opposite sign, which oscillate as a function of the field direction with a slightly different phase: their sum results in the field-dependent term $C^{FS}_{\sigma\sigma'}(\eta)$ shown in Fig. 3.26.

The amplitude term $C^{FS}_{\sigma\sigma'}(\eta)$ alone cannot account for the interference pattern

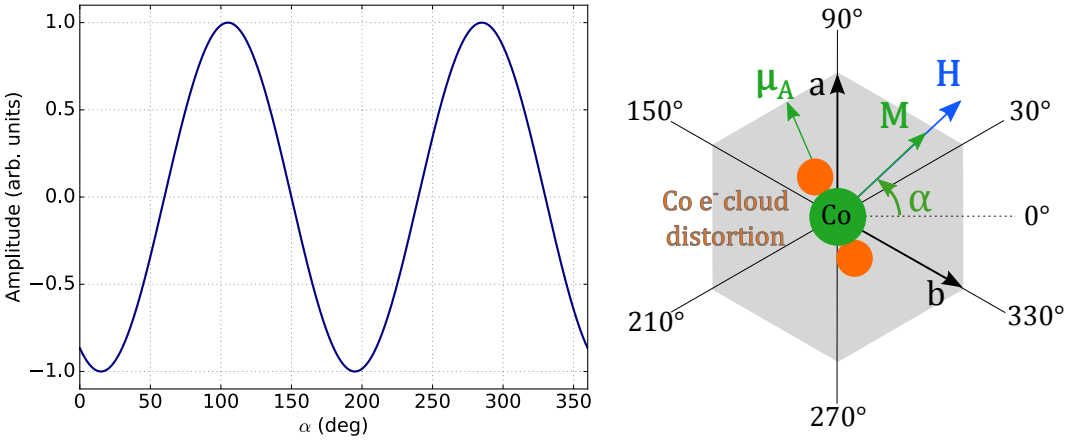

Figure 3.26: Magnetic field direction dependence of the forbidden charge scattering amplitude $C^{FS}_{\sigma\sigma'}$ normalized to its peak value. The drawing illustrates the empirical model for the Co electron cloud distortion discussed in the text. The Co^{2+} ion of one of the two magnetic sublattices (A) is shown together with the two negative charges used to model the elongation along the magnetic moment $\boldsymbol{\mu}_A$ direction. The definition of the field angle α is analogous to the one given in the inset of Fig. 3.17 in the case of negligible single-ion anisotropy ($\mathbf{H} \parallel \mathbf{M}$).

of Figs. 3.22(a) and 3.24(a) as it does not depend on either the sample azimuth or the incident energy. The azimuth and energy dependence is accounted for by the multiple scattering amplitude $C^{MS}_{\sigma\sigma'}$, which plays a key role in our observations. Contrary to standard Bragg diffraction (also referred to as two-wave diffraction), where the diffracted radiation originates from a single scattering event of the primary beam, in multiple-wave diffraction the secondary beam originated from the scattering of the incident X-rays can act as a primary beam for a second scattering process, thus giving rise to a tertiary reflection [158]. This results in additional diffraction peaks, which can appear at nominally forbidden (hkl) values. Although much weaker than Bragg reflections, multiple scattering peaks can have a comparable intensity to the magnetic ones. The condition for generating multiple-wave diffraction is much more stringent than in the two-wave case: as a result, the multiple scattering amplitude displays a strong dependence on the sample azimuth (see Fig. 3.28) as opposed to Bragg scattering, which does not depend on ψ. Moreover, while the latter does not change the polarisation of the primary beam, multiple scattering can in general give rise to both σ' and π'-polarised radiation.

Although multi-wave scattering is fully described within the dynamical theory of diffraction [158], the nominal azimuth and energy values at which multiple diffraction peaks occur can be calculated in the kinematical approximation as described in Ref. [159]. The multiple scattering peaks are conveniently displayed by means of energy-azimuth maps analogous to the one reported in Fig. 3.25 for the

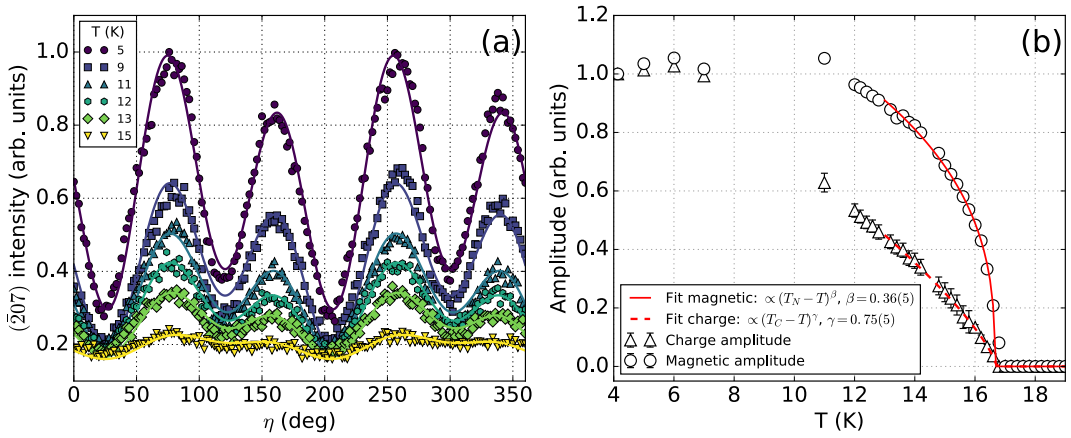

Figure 3.27: (a) $(\bar{2}07)$ σ-σ' intensity dependence on the magnetic field direction for different temperatures below the Néel transition. The symbols represent the measured diffracted intensity, while the solid lines refer to the corresponding global fit as explained in the text. The data were collected at $\psi = 65°$ analogous to the ones of Fig. 3.23(a) and are normalized to the peak intensity at T = 5 K. (b) Magnetic and forbidden charge amplitudes as a function of temperature resulting from the fit shown in (a).

case of the $(\bar{2}07)$ in the σ-σ' polarisation channel. Here, the azimuth and energy values at which the measurements of Figs. 3.22(a) and 3.24(a) were performed are represented through the black solid circles along the lines at constant energy and azimuth, respectively. Multiple scattering peaks (represented through small solid symbols) line up along curved trajectories in the energy-azimuth space[18]: these can then be avoided during a diffraction experiment in order to prevent a significant contamination to the single-wave diffraction intensity. However, the kinematical calculations fail to reproduce the complete azimuthal and energy dependence of the multiple scattering amplitude, which exhibits tails of non-zero intensity away from the nominal diffraction peak condition. This is shown in the pseudo-dynamical calculations of the $(\bar{2}07)$ multiple scattering amplitude represented through the solid line of Fig. 3.28. The calculations were performed using a mixed kinematical/dynamical approach where the standard kinematical structure factors of the secondary and tertiary reflection are weighted by terms calculated in a dynamical framework [160, 161]. The broad tails of the multiple scattering signal generally result in a residual contribution in both polarisation channels.

Because of the inversion centre of the $R\bar{3}c$ space group, all structure factors, including the multiple scattering one, are real if one considers only Thomson scattering far from any absorption edge. Therefore, multiple scattering interferes with the "forbidden" amplitude arising from the electron cloud distortion (which turns out to be of Thomson nature and is thus real), but not with non-resonant magnetic

[18] An analogous trend (not shown here) is also present in the σ-π' channel.

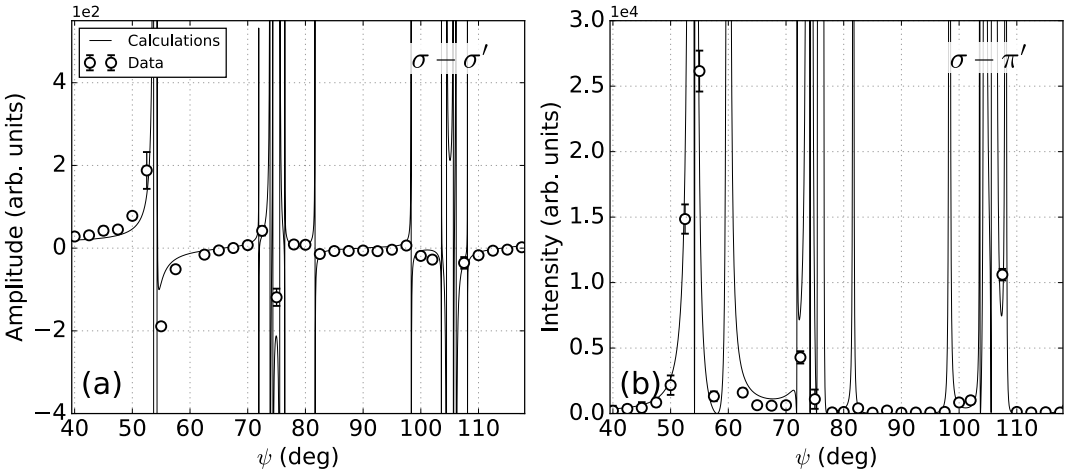

Figure 3.28: Multiple scattering (a) σ-σ' amplitude and (b) σ-π' intensity azimuthal dependence. The data points are the results of the fit of the data shown in Figs. 3.22(a),(b), while the solid lines represent the corresponding pseudo-dynamical calculations.

scattering, which is out of phase by 90°, and gives rise to the dramatic variations with the sample azimuth [Fig. 3.22(a)] and incident energy [Fig. 3.24(a)]. In particular, the nearly four-fold pattern of the contribution superimposed to the magnetic signal observed at $E = 5.223$ keV around $\psi = 65°$ [see Fig. 3.23(a)] results from the modulus square[19] of the sum of the two-fold amplitude $C^{FS}_{\sigma\sigma'}(\eta)$ of Fig. 3.26 with a small positive multiple scattering amplitude $C^{MS}_{\sigma\sigma'}$ (smaller than the $C^{FS}_{\sigma\sigma'}(\eta)$ peak value): the latter does not depend on the field direction and add as a constant in Fig. 3.26. Following a similar reasoning, a fairly large negative $C^{MS}_{\sigma\sigma'}$ value is responsible for the nearly two-fold pattern seen around $\psi = 80°$ [see Fig. 3.23(c)]; a similar intensity pattern, but with the minima and maxima exchanged, is observed in the opposite case of large positive $C^{MS}_{\sigma\sigma'}$ values (e.g. for $\psi = 40 - 50°$). In the absence of the forbidden amplitude, as is the case of the σ-π' intensity of all the reflections and the σ-σ' one when the additional term $C^{FS}_{\sigma\sigma'}(\eta)$ is absent (Fig. 3.13), multiple scattering simply results in a constant background superimposed to the intensity of magnetic origin. A significant multiple scattering background is, for instance, responsible for the high-intensity streaks visible in the σ-π' colour map of Fig. 3.22(b).

The interference between the amplitude induced by the electron cloud distortion and multiple scattering reproduces extremely well the data: this is clearly shown by the colour maps of Figs. 3.22(c) and 3.24(c), which display the fit of the measured intensity of Figs. 3.22(a) and 3.24(a) to Eq. (3.25), respectively. The fit of the σ-π' intensity [Figs. 3.22(d) and 3.24(d)] was performed using the second

[19] The measured intensity is proportional to the modulus square of the scattering amplitude.

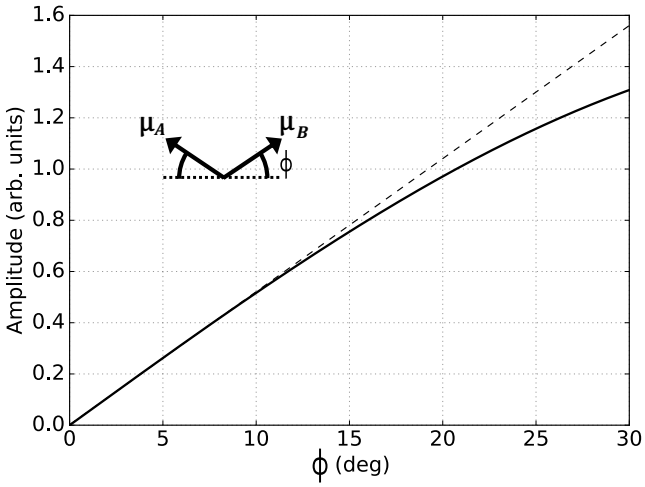

Figure 3.29: Dependence of the forbidden charge scattering amplitude in $CoCO_3$ on the canting angle of the Co^{2+} magnetic moments. The dashed line corresponds to a linear fit at small angles.

line of Eq. (3.20), analogous to Sec. 3.5. An arbitrary positive scale factor, whose ratio to the magnetic amplitude was kept constant throughout all ψ and energy values[20], was used for the forbidden charge amplitude of Fig. 3.26 in the fit of the σ-σ' intensity. This is because the empirical model is not capable of reproducing a physically-meaningful value of the scattering amplitude. On the other hand, the phase of the oscillations (including its sign) is correctly predicted. This is elegantly proved by the values of the multiple scattering amplitude $C^{MS}_{\sigma\sigma'}$ extracted from the fits of Figs. 3.22(c),(d), which are reported in Fig. 3.28 along with the amplitude calculated using the pseudo-dynamical approach. The ψ dependence of the measured amplitude, in particular its sign, is remarkably consistent with the calculations, thus confirming the correctness of the forbidden amplitude phase.

The empirical model also grasps other significant features of the forbidden amplitude that are confirmed by the form factor calculations of Sec. 3.6.3.2. In particular, it predicts a vanishing amplitude when the canting of the Co^{2+} magnetic moments is set to zero (perfect AFM alignment). This is shown in Fig. 3.29, where the structure factor associated to the electron cloud elongation is calculated as a function of the canting angle. For small values of the latter the amplitude increases linearly with the canting and vanishes for canting equal to zero. This is due to the fact that for perfect AFM alignment, the electron cloud elongation lies along the

[20]The experimental geometry significantly changes with the azimuth value (and, to a smaller extent, with the energy value as well). This means that the overall scattered intensity shows significant variations from one ψ value to another, due to, for instance, a different impact of self-absorption effects. However, the geometry should equally affect the charge and magnetic contribution, whose ratio is thus expected to be constant.

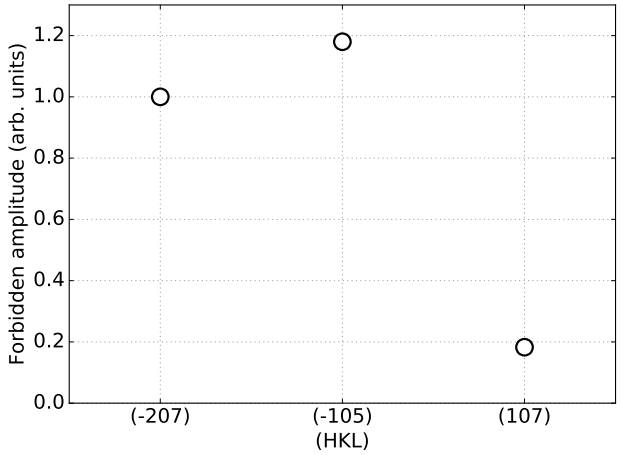

Figure 3.30: Peak amplitude of the forbidden charge scattering contribution of Fig. 3.26 for different space-group forbidden reflections in $CoCO_3$. The amplitude values were extracted through fits of the $(\bar{2}07)$, $(\bar{1}05)$ and (107) σ-σ' magnetic field dependences (at $\psi = 65°$, 90° and 0°, respectively) analogous to the ones shown in Fig. 3.23 and are normalized to the $(\bar{2}07)$ value.

same direction for the two magnet sublattices regardless of the field direction. The contributions to the structure factor from sublattice A and B are, in this case, opposite in sign and perfectly cancel out. For analogous reasons, the toy model also predicts a vanishing amplitude for specular $(00l)$ reflections. This is confirmed by the data on the (003) and (009) reflections, which display a normal magnetic behaviour [see Figs. 3.13(a) and 3.13(d)]. Within this simple model, a non-vanishing forbidden amplitude is expected to be present also for the two equivalent reflections (107), $(\bar{1}17)$. However, this term appears to be much smaller than the magnetic contribution and is not clearly visible in the measured data [see Figs. 3.13(b) and 3.13(c)]: a satisfactory description of the scattered intensity can be obtained by the magnetic contribution alone. Nonetheless, a small forbidden amplitude is still compatible with the experimental observations: in fact, the fit of the (107) magnetic field dependence to Eq. 3.25 results in a small non-zero value for $C^{FS}_{\sigma\sigma'}(\eta)$. The latter is reported in Fig. 3.30 together with values extracted for the $(\bar{2}07)$ and $(\bar{1}05)$ reflections for comparison.

The peculiar forbidden charge scattering just described was not detected for the other compounds of the series. In particular, the magnetic field dependence of the $(\bar{2}07)$ and $(\bar{1}05)$ reflections was also measured in $FeBO_3$ (see Fig. A.3), for which a normal magnetic behaviour was found. Given the negligible value of the orbital moment in $FeBO_3$, it seems natural to attribute the forbidden scattering amplitude to the large l value in $CoCO_3$. This is somewhat confirmed by the microscopic model presented in the following section.

3.6.3.2 Microscopic model and role of the SOC

Hamiltonian parameters (eV)						Expectation values					
$F^{(2)}_{3d-3d}$	$F^{(4)}_{3d-3d}$	$10Dq$	D_σ	H_{ex}	SOC	$\hat{s}_x$	$\hat{s}_y$	$\hat{s}_z$	$\hat{l}_x$	$\hat{l}_y$	$\hat{l}_z$
7.9072	5.0463	1	0.06	0.0018	0.052	-0.791	0.051	0.000	-0.501	0.032	0.000

Table 3.5: Hamiltonian parameters used to perform the multiplet calculations of the Co^{2+} ground-state wavefunction in $CoCO_3$ and corresponding spin and orbital angular momenta expectation values. The spin and orbital angular momenta components of one of the two magnetic sublattices, in units of $\hbar$, are expressed in the local **xyz** cubic frame of the CoO_6 octahedra, such that **x** is parallel to the **a** crystallographic axis and **z** is parallel to the crystallographic **c** axis.

In order to achieve a microscopic understanding of the electron cloud distortion induced by the ordered moment, the $3d$ electron ground-state wave function was derived for different directions of the external field by means of multiplet calculations performed by our collaborators. The latter were carried out using a Hartree-Fock method in the mean-field approximation, using the code RCN [162] for the radial part of the Co^{2+} wave function and Quanty [163] for the angular one. The ground state was computed separately for two non-interacting clusters of Co^{2+} ions. The latter correspond to the two unique orientations of CoO_6 octahedra of the $R\bar{3}c$ crystal structure, one rotated by 164° about the **c** axis with respect to the other. The $[\bar{1}\,1\,1]$ direction of the local octahedral frame is parallel to the unit cell **c** axis for both clusters; the $[1\,1\,0]$ direction of cluster one (two) is rotated by 22° (−142°) about **c** relative to the unit cell **a** axis. The Hamiltonian used for the calculations consists of the following terms: (i) Coulomb interaction [$F^{(2)}_{3d-3d}$, $F^{(4)}_{3d-3d}$], (ii) crystal field ($10Dq$, D_σ), (iii) SOC, (iv) magnetic exchange (H_{ex}) and (v) Zeeman term of interaction with the external field. The values of the main parameters used for the calculations are summarised in Table 3.5. These were obtained refining the initial atomic values to reproduce the XMCD spectra of Fig. 3.15. In particular, the CoO_6 octahedra are known to have [111] a small trigonal distortion, which was simulated through the parameter D_σ. Fig. 3.31 shows the effect of D_σ on the Co L_3-edge XANES and XMCD signal: a small positive value $D_\sigma = 0.06$ eV correctly grasps all the main features of the white line and the corresponding circular dichroism.

The corresponding ground-state Hamiltonian expectation values are also summarised in Table 3.5: despite the absolute values of the spin and orbital angular momenta are somewhat different from the ones obtained through DFT (Table 3.4), a large value of the orbital contribution ($l/s \approx 0.6$) is confirmed. Moreover, as well as reproducing the absorption spectra, the electronic structure of the Co^{2+} ion thus

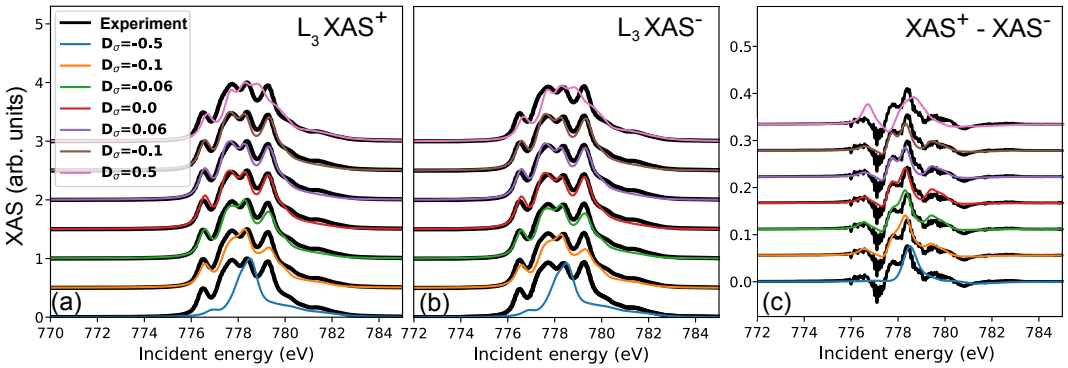

Figure 3.31: Multiplet calculations of the Co L_3 absorption spectrum measured with the external magnetic field (a) antiparallel and (b) parallel to the helicity of the incident circularly polarised light and (c) corresponding XMCD for different values of the trigonal distortion parameter D_σ in eV. The experimental data are the same already reported in Fig. 3.15.

calculated is consistent with the one reported by Meshcheryakov [111]. The large single-ion anisotropy already predicted by the DFT calculations is also confirmed and attributed to the interplay between SOC and the small trigonal distortion. The discrepancy between the ground-state expectation values of the DFT and multiplet calculations could be explained either by uncertainties in the background extraction of the XMCD measurements or, alternatively, by the inherently different calculation methods. In particular, projecting the DFT wave functions onto atomic ones could give rise to differences. Additionally, multiplet calculations do not account for charge transfer effects: the latter are simply modelled by reducing the values of the Slater integrals used to express the Coulomb repulsion to 87% of the atomic value.

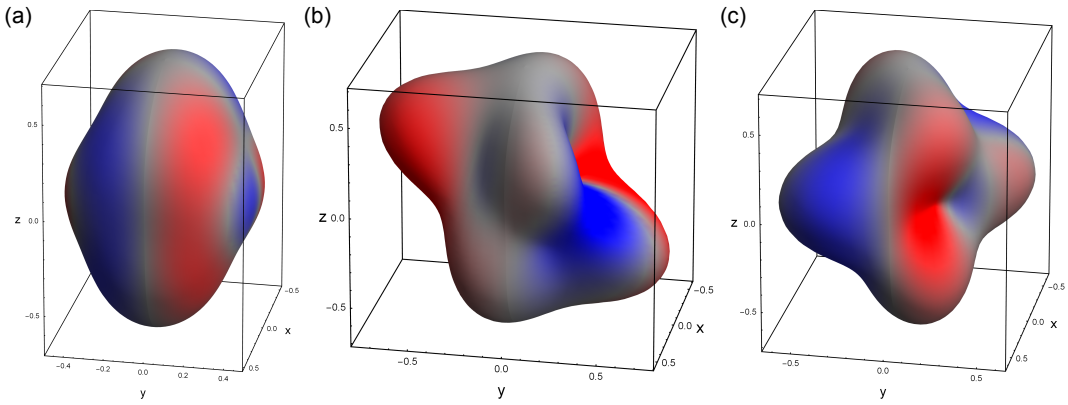

Figure 3.32: Charge density of the Co^{2+} $3d$ valence electrons for an external field direction (a) 0°, (b) 60° and (c) 90° away from the crystallographic **a** axis as derived from the multiplet calculations discussed in the text. The plots refer to one of the two Co^{2+} clusters used for the calculations (cluster two). The colours correspond to different spin directions with red and blue for down and up character, respectively.

The results of the calculations confirm that, as predicted by the empirical model, the charge density of the valence $3d$ electrons depends on the magnetic moment orientation. This is shown in Fig. 3.32, where a real-space representation of the charge density is reported for different directions of the external magnetic field. The Co^{2+} ground-state wave functions for different field directions can then be used to calculate the corresponding atomic form factor. The resulting $(\bar{2}07)$ and $(\bar{1}05)$ scattering amplitudes show a sinusoidal magnetic field dependence analogous to the one of Fig. 3.26. Although the exact phase of the oscillations is not correctly reproduced in the current version[21], the multiplet calculations confirm all the predictions of the toy model: in particular, they result in a vanishing scattering amplitude for specular $(00l)$ reflections and when the magnetic moment canting angle is set to zero. Most importantly, the calculations show that the amplitude also vanishes when the SOC is artificially switched off, as displayed in Fig. 3.33 for the case of the $(\bar{2}07)$ reflection. This attributes the magnetic-moment-induced distortion of the Co^{2+} electron cloud to the coupling between orbital and magnetic degrees of freedom driven by SOC and further highlights the fundamental role played by the large unquenched orbital moment in the physics of $CoCO_3$.

3.6.4 Magneto-striction

Another distinctive evidence of the elongation of the Co^{2+} electron cloud along the magnetic moment direction is the resulting expansion of the unit cell in-plane lattice parameters, which is revealed by the angular shift of the Bragg peak of symmetry-allowed reflections as a function of the field direction in the magnetically-ordered phase. This is shown for the (119) reflection in Fig. 3.34(a). The angular shift was measured by tracking the resulting intensity oscillations at fixed Bragg angle θ_B as the external field is rotated in the **ab** plane of the crystal. The oscillations observed for $\theta_B > \theta_B^{max}$, being θ_B^{max} the value corresponding to the maximum of the rocking curve, are shown in Fig. 3.35(a) for different temperatures. An intensity oscillation with the opposite phase is present for $\theta_B < \theta_B^{max}$: this is simply explained by considering that a shift of the rocking curve towards, for instance, higher angle values results in an increase (decrease) of the intensity measured at a fixed angle for $\theta_B > \theta_B^{max}$ ($\theta_B < \theta_B^{max}$). The angular shifts reported in Fig. 3.34(a) correspond

[21] An angular shift is present between the oscillations of Fig. 3.26 obtained through the empirical model (which correctly reproduce the measured data) and the multiplet calculations of Fig. 3.33. The presence of such offset remains an open issue. However, given the ability of the multiplet calculations to reproduce most of the experimental observations, its origin appears merely to be a subtle inconsistency in one of the angles defining the geometry.

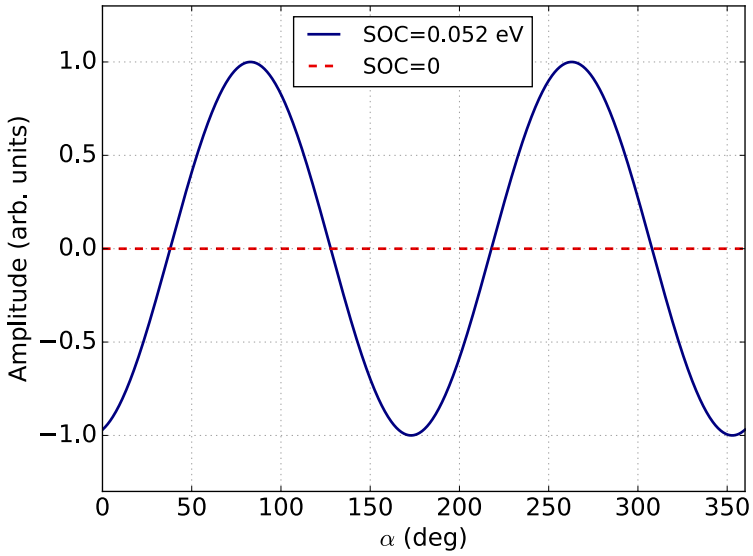

Figure 3.33: Magnetic field dependence of the $(\bar{2}07)$ forbidden charge scattering amplitude (normalized to its peak value) calculated using the Co^{2+} atomic form factor derived from the multiplet calculations discussed in the text. The blue solid and the red dashed lines refer to calculations performed with a SOC constant equal to 0.052 eV and with SOC artificially quenched, respectively. The definition of the magnetic field angle α, given in Fig. 3.17, is the same used for Fig. 3.26.

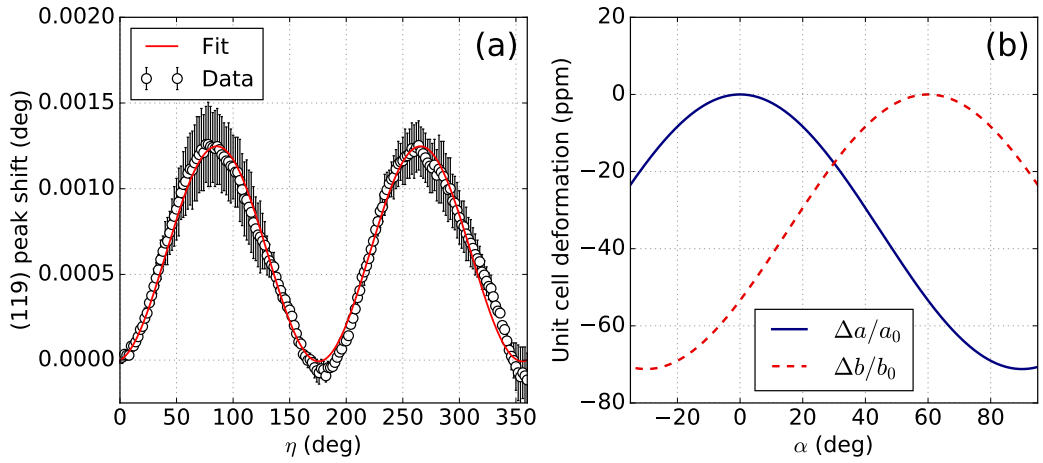

Figure 3.34: (a) Angular shift of the $(1\,1\,9)$ Bragg peak as a function of the magnetic field direction at T = 5 K. The solid line represents a fit to the shift calculated using the unit cell deformation of Eq. (3.26). (b) Relative deformation of the in-plane lattice parameters of the $R\bar{3}c$ hexagonal unit cell at T = 5 K as obtained from the fit of the $(1\,1\,9)$ angular shift shown in (a).

to the average of the values extracted for the two cases (the error bars represent the corresponding sample standard deviation).

Calling a_0 and b_0 the values of the in-plane lattice parameters when the magnetic moment of the Co^{2+} ion (which is orthogonal to the magnetic field if one neglects the small canting) lies along the **a** and **b** axis, respectively, the angular shift is correctly described by the following field-dependent distortion:

$$\begin{aligned} a(\alpha) &= a_0 - \Delta l \sin^2 \alpha \\ b(\alpha) &= b_0 - \Delta l \sin^2(60^\circ - \alpha) \end{aligned} \tag{3.26}$$

where $\Delta l > 0$ is the maximum deformation amplitude and α is defined in the drawing of Fig. 3.17[22]. The distortion is defined such that a and b assume their minimum value when the magnetic field is orthogonal to the $[1\,0\,0]$ and $[0\,1\,0]$ direction (i.e. $\alpha = 0^\circ$ and $\alpha = 60^\circ$), in which case, $a = a_0 - \Delta l$ and $b = b_0 - \Delta l$, respectively. On the other hand, they are maximum and equal to a_0 and b_0 for magnetic moment along the **a** and **b** axis, respectively. The lattice parameter c is assumed to be independent of the field direction. The field-dependent lattice parameters of Eq. (3.26) can be used to calculate the Bragg angle corresponding to a given $(h\,k\,l)$ reflection using the following relation valid for an hexagonal unit cell:

$$\theta_B(\alpha) = \arcsin\left[\frac{\lambda}{2}\sqrt{\frac{1}{\sin^2\beta}\left(\frac{h^2}{a(\alpha)^2} + \frac{l^2\sin^2\beta}{c^2} + \frac{k^2}{b(\alpha)^2} - \frac{2hk\cos\beta}{a(\alpha)b(\alpha)}\right)}\right] \tag{3.27}$$

where $\beta = 120^\circ$ is the angle between the **a** and **b** crystallographic axes and λ is the wavelength of the incident X-rays.

The magnitude of the unit cell distortion Δl can be obtained by fitting the measured shift of the Bragg peak to the one calculated through Eq. (3.27). This is shown by the red solid line of Fig. 3.34(a). The resulting unit cell deformation along the **a** and **b** axes is plotted as function of the field direction in Fig. 3.34(b). The deformation amounts to ≈ 70 ppm at T = 5 K (which corresponds to a change in the lattice parameters of ≈ 35 fm). Although this value is extremely small, its effect is clearly seen in the data. The distortion decreases with temperature, as shown by the temperature dependence of the $(1\,1\,9)$ intensity oscillations plotted in Fig. 3.35. In particular, the amplitude of the intensity oscillations vanishes around T_N following a similar critical behaviour to the one of the magnetic scattering intensity [Fig. 3.35(b)]. This further confirms the magneto-strictive origin of the Bragg

[22] As for Sec. 3.6.3, the effect of the in-plane magnetic anisotropy can be neglected for the present discussion.

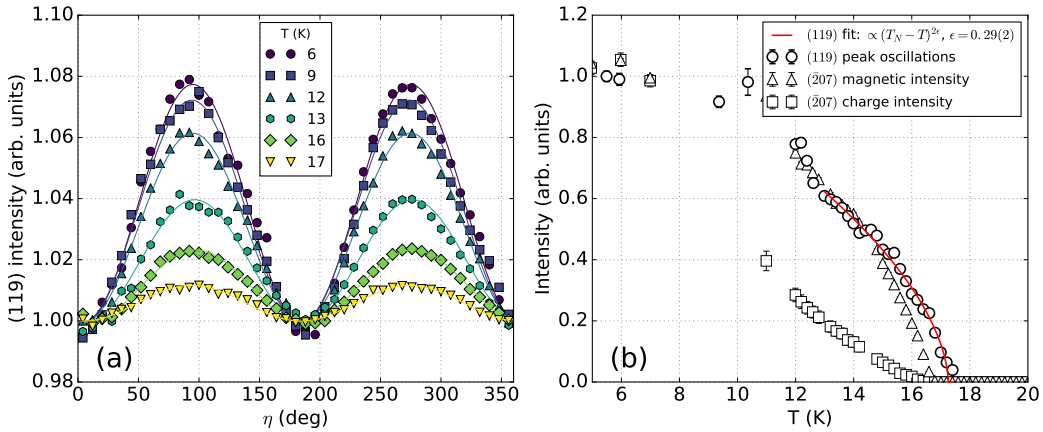

Figure 3.35: (a) $(1\,1\,9)$ magnetic field direction dependence as a function of temperature. The intensity was measured at a fixed Bragg angle θ_B while rotating the external field. The oscillations arise from the angular shift of the peak as illustrated in Fig. 3.34(a). The solid line at each temperature represents a fit to a sinusoidal function. (b) Temperature dependence of the $(1\,1\,9)$ intensity oscillations as extracted from the fits shown in (a). The red solid line corresponds to a fit to a power law with critical exponent ε. The magnetic and charge contributions to the intensity of the $(\bar{2}\,0\,7)$ forbidden reflection are also shown for comparison [the corresponding amplitudes and their fit are reported in Fig. 3.27(b)].

peak oscillations and constitutes further evidence of the coupling between crystallographic and magnetic properties resulting from the large unquenched orbital moment.

3.7 Conclusions

In this chapter, I presented a systematic investigation of the magnetic properties of the series of isostructural weak ferromagnets ACO_3 (A = Mn,Co,Ni) and $FeBO_3$ by means of *ab-initio* calculations and a combination of experimental techniques, including bulk magnetisation measurements, REXS, NXMS and XMCD. The measurements show that the filling of the TM ion 3*d* band tunes the magnetic properties of the system. In particular, it causes a sign change in the DM vector, which is found to be negative in $MnCO_3$ and $FeBO_3$ and positive in $CoCO_3$ and $NiCO_3$. The sign of the DMI represents a very subtle change in the magnetic moment arrangement, which is encoded in the phase of the magnetic scattering amplitude. Although the latter is normally lost in the measured scattered intensity, a reliable extraction was made possible by our novel X-ray scattering technique based on the interference between the magnetic amplitude and weak quadrupole resonant scattering.

The results discussed in this chapter also reveal a non-obvious trend of the or-

bital contribution to the magnetic moment, which was found to be particularly large in $CoCO_3$. The latter stands out with respect to the other members of the family in that the coupling of the large orbital moment and the spin of the Co^{2+} ion induced by SOC gives rise to a sizeable single-ion anisotropy and a peculiar distortion of the Co^{2+} electron cloud in the magnetically-ordered phase. The latter is evidenced by a bizarre interference pattern of the scattered intensity at space-group forbidden reflections and a significant magnetoelastic coupling in the ordered phase. All the results combined together show how, even in the case of 3*d* TMOs, SOC can have a significant impact on the magnetic properties of the system whenever the orbital degrees of freedom are not quenched. Finally, the present investigation also proves the ability of modern first-principle calculations to predict the properties of non-collinear magnetic structures of great contemporary interest for the fundamental understanding of the underlying interactions and the potential for spintronics applications.

Chapter 4

The 4d case: persistence of antiferromagnetic order and Ru^{4+} orbital population tuning upon La substitution in $Ca_{2-x}La_xRuO_4$

Contents

4.1 Introduction 144

4.2 Overview of the magnetic and electronic properties of $Ca_{2-x}La_xRuO_4$ 146

4.2.1 Pure Ca_2RuO_4 146

4.2.2 Impact of chemical substitution on Ca_2RuO_4 153

4.3 Ru^{4+} single-ion Hamiltonian 156

4.4 Sample growth and characterisation 163

4.4.1 Bulk magnetisation measurements 164

4.4.2 Structural characterisation by neutron diffraction 166

4.5 Impact of La doping on the low-temperature magnetic structure studied by REXS 169

4.6 Evolution of the Ru^{4+} 4d orbital population upon La substitution: an O K-edge XANES study 183

4.7 Impact of La doping on the local electronic properties of the Ru^{4+} ion: a Ru L-edge XANES and XMCD study 193

4.8 Conclusions 200

4.1 Introduction

4*d* TMOs cover an interesting intermediate regime between the 3*d* case, where the investigation of strongly correlated electron systems has traditionally taken place, and the exotic phases of matter stabilized by the strong SOC in 5*d* oxides of more recent interest (Chapter 5). For TM elements in the 4*d* row of the periodic table, SOC is stronger than in the 3*d* case and can compete with the other relevant energy scales, such as non-cubic crystal-field terms, on an equal footing (see Chapter 1). Considerable experimental and theoretical effort has been directed towards Ru oxides of the Ruddlesden-Popper series $(Sr,Ca)_{n+1}Ru_nO_{3n+1}$ [17, 18, 164]. The single-layer members ($n = 1$) of the family have received particular attention due to the strikingly different properties: while Sr_2RuO_4 is a metal hosting unconventional spin-triplet superconductivity [165], Ca_2RuO_4 is a Mott insulator at room temperature which undergoes a Néel transition upon cooling [164]. Further impetus was added by the prediction of a non-magnetic singlet ground state stabilized by the moderate SOC of 4*d* electrons in the Ru^{4+} ion ($4d^4$) [1, 26, 166]. The singlet ground state was recently explicitly proposed for Ca_2RuO_4, where magnetic ordering can result from the condensation of magnetic excited states driven by intersite interactions [166]. This unusual singlet magnetism is expected to result in peculiar magnetic properties which have been the subject of several studies in recent years [166–171]. The low-energy physics of the Ru^{4+} ion in Ca_2RuO_4 is further enriched by significant tetragonal distortions away from the perfect cubic symmetry of the crystalline environment [172], which were found to play a key role in the stabilization of the Mott insulating state [18, 173–177]. The subtle interplay between the tetragonal crystal field and the comparably strong SOC gives rise to an entangled ground-state wave function with significant many-body effects [169, 178].

One way of tuning the electronic and magnetic properties of Ca_2RuO_4 is by means of substitution of divalent Ca with trivalent La. Interesting physics is often associated with doping a Mott insulator, including the appearance of novel electronic phases such as unconventional superconductivity, pseudo-gap states, charge density wave order, etc. [17, 147]. La doping destroys the parent compound insulating state and drives the system into a paramagnetic metal [179]. A net magnetisation appears for increasing La contents starting from the parent compound AFM order [179–181], which has led to the prediction of a FM phase induced by the extra electron injected by the dopant atom for small enough values of the SOC constant [168]. Moreover, the internal chemical pressure associated with the larger La^{3+} ion with respect to Ca^{2+} is expected to tune the crystal field at the Ru site and

to have a significant impact on the Ru^{4+} ground-state electronic properties. However, despite its relevance in light of the unusual parent compound electronic and magnetic properties, experimental studies on La-doped Ca_2RuO_4 reported to date have been limited to bulk measurements [179–181]: a detailed investigation of the ground-state magnetic and electronic properties is thus still missing.

The measurements presented in this chapter aim at filling this gap by addressing the impact of La doping on both the Ca_2RuO_4 magnetic ordering and the Ru^{4+} electronic structure. The experimental investigation has been conducted by a variety of X-ray scattering (REXS) and absorption (O *K*-edge XANES and Ru *L*-edge XANES and XMCD) techniques, supported by bulk magnetisation measurements and neutron diffraction. The present results show that La doping induces significant changes in the local crystalline environment at the Ru sites. The parent compound AFM structure persists upon La substitution, thus excluding the presence of a FM phase; the impact of La substitution is limited to a suppression of one of the two magnetic modes allowed by symmetry and the stabilization of a weakly FM structure. These changes are interpreted as resulting from the corresponding structural effects, which appear to play a more important role than the extra electron introduced by La in the physics of the doped compounds. The tuning of the crystal field caused by the structural distortions is also evidenced by significant changes in the low-energy electronic structure as observed in the absorption measurements, which is consistent with the evolution of the local Ru crystalline environment. All the results combined together clarify several aspects of the physics of the doped samples and provide valuable insight on the subtle nature of the Ca_2RuO_4 ground-state properties.

The chapter is organized as follows. After a brief overview of the properties of the parent and doped samples reported in the literature (Sec. 4.2) and the main aspects of the Ru^{4+} single-ion physics (Sec. 4.3), Sec. 4.4 presents the results of bulk magnetisation and neutron diffraction measurements on single crystals of $Ca_{2-x}La_xRuO_4$, along with some details on the sample preparation. Sec. 4.5 describes REXS measurements performed at the Ru *L* edges addressing the magnetic structure of the doped samples; the results are compared to the case of Sr doping and discussed in relation to the doping-induced structural changes. Sec. 4.6 includes a XANES investigation performed at the O *K* absorption edge which revealed a significant impact of La doping on the low-energy electronic structure of the Ru^{4+} ion; once again, the results are related to the corresponding changes in the parent compound crystal structure and interpreted in terms of a minimal O $2p$ - Ru $4d$ hybridization model. In Sec. 4.7, I will briefly outline the main findings of a combined XANES and XMCD study at the Ru *L* edges on the electronic properties

of the parent and doped system. These results, the first of their kind on this compound, offer the possibility to gain unprecedented insight on the impact of SOC on the low-energy physics. Finally, the conclusions of the study are drawn in Sec. 4.8.

4.2 Overview of the magnetic and electronic properties of $Ca_{2-x}La_xRuO_4$

4.2.1 Pure Ca_2RuO_4

Ca_2RuO_4 has attracted considerable attention in recent years as the Mott-insulating analogue of the unconventional superconductor Sr_2RuO_4 [166, 169–175, 178, 182–187]. Ca_2RuO_4 is the $n = 1$ member of the layered Ruddlesden-Popper series $Ca_{n+1}Ru_nO_{3n+1}$, with a single RuO_2 layer in the unit cell [Fig. 4.1(a)]. A well documented MIT occurs at $T_{MIT} = 357$ K upon cooling. The MIT is concomitant with a first-order structural transition from a high-temperature quasi-tetragonal phase ($a \approx b$) with a long c axis (L-*Pbca*) to a low-temperature orthorhombic phase with a short c axis (S-*Pbca*) [179, 182–184] [see Fig. 4.2(a)]. The structural transition does not change the space group of the crystal, which is the orthorhombic *Pbca* (No. 61) [Fig. 4.1(a)]. The Ru^{4+} ions occupy the Wyckoff site a with multiplicity 4 of the orthorhombic cell [which corresponds to the positions with fractional coordinates $(0,0,0)$, $(1/2,0,1/2)$, $(0,1/2,1/2)$ and $(1/2,1/2,0)$] and are surrounded by 6 O^{2-} ions in octahedral coordination. Significant distortions are present with respect to the perfect perovskite structure. In particular the RuO_6 octahedra are rotated in the **ab** plane of the crystal by about 11.8°, independent of temperature, and tilted away from the **c** axis by 11.2° at room temperature and 12.7° at T = 11 K [172]. This results in a Ru-O-Ru bond angle around 151°. The tilt occurs around an axis which is rotated away from the **b** axis by an angle equal to the octahedra in-plane rotation so that the apical oxygens are shifted away from the **c** axis along a direction almost parallel to **a**. The unit cell lattice parameters show a pronounced temperature dependence (Fig. 4.2): c decreases upon cooling, while b increases and is significantly elongated compared to the a axis at low temperature. Moreover, while the octahedra are almost regular at room temperature, a significant compression sets is when cooling the crystal [172] [Fig. 4.2(b)].

Ca_2RuO_4 exhibits AFM order with propagation vector $\mathbf{k} = (0,0,0)$ below $T \approx 110$ K, with the Ru^{4+} magnetic moments ($\approx 1.3\mu_B$) aligned predominantly

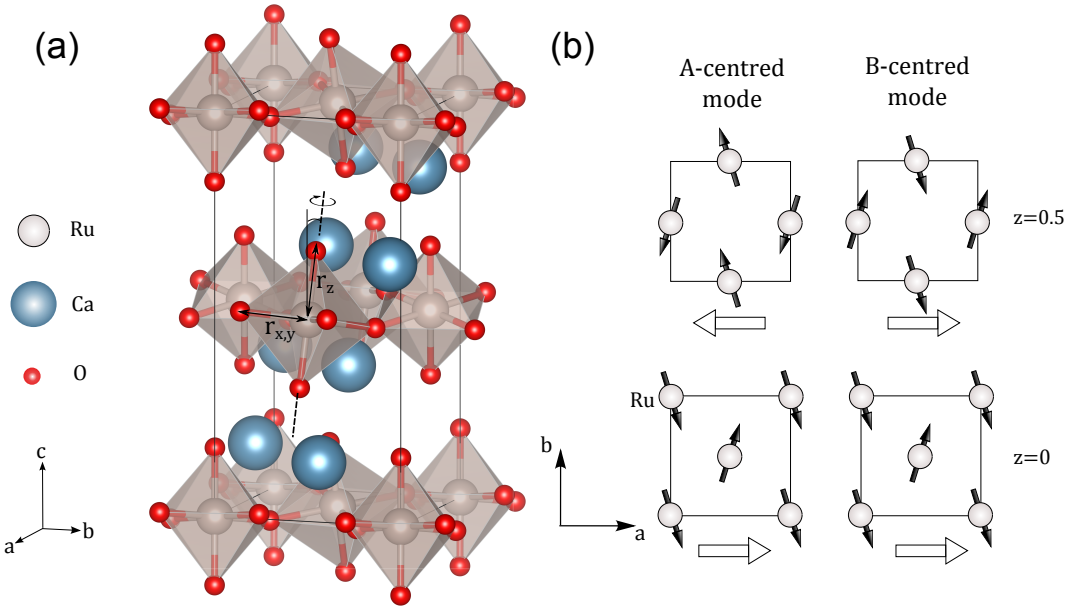

Figure 4.1: (a) Ca_2RuO_4 crystal structure (*Pbca* space group, No. 61) highlighting the RuO_6 octahedra tilt and rotation discussed in the text. r_z and $r_{x,y}$ correspond to the apical and in-plane Ru-O bond lengths, respectively. (b) Magnetic ordering of neighbouring RuO_2 layers for the A- and B-centred magnetic modes [172]. The black arrows represent the Ru^{4+} ordered moments, while the white horizontal arrows correspond to the direction of the net magnetisation induced by the moment canting.

along the elongated **b** axis [172] [Fig. 4.1(b)]. The lattice distortions allow a finite DMI to be present (see Sec. 3.2) and give rise to a small canting of the magnetic moments of the two AFM sublattices. As a result, a small net moment appears in each RuO_2 layer along the **a** axis [172]. Considering magnetic moments lying in the **ab** plane of the crystal, the two magnetic structures (or magnetic *modes*) of Fig. 4.1(b) are allowed for the *Pbca* space group with $\mathbf{k} = (0,0,0)$ (see Sec. 4.5 and Appendix B.2 for more details). Following the nomenclature first introduce by Braden *et al.* [172], these are normally referred to as A-centred and B-centred modes. The component of the magnetic moment along **b** of the Ru^{4+} ion at $(0,0,0)$ is equal to the one of the moment at $(0,1/2,1/2)$ and $(1/2,0,1/2)$ for the A- and B-centred mode, respectively. The main difference between the two structures lies in the relative orientation of the canting-induced net moments within each layer [white arrows in Fig. 4.1(b)]: the net moments couple antiferromagnetically in the A-centred structure and ferromagnetically in the B-centred one. The A-centred mode is thus globally AFM while a small net magnetisation appears in the B-centred one. The initial neutron diffraction investigation by Braden *et al.* [172] reported a coexistence of the two modes, with the A-centred structure being dominant. However, pure stoichiometric crystals of Ca_2RuO_4 were later found to host only the A-centred

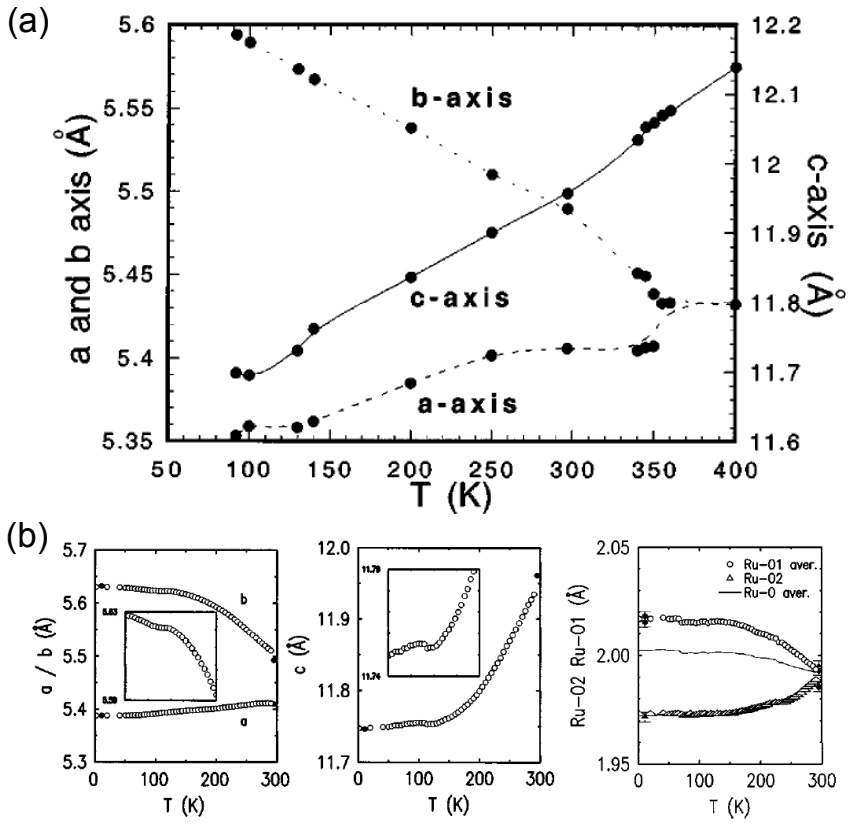

Figure 4.2: Ca_2RuO_4 structural changes as a function of temperature reported in the literature. (a) Lattice parameters of the *Pbca* unit cell as a function of temperature resulting from the X-ray single-crystal diffraction measurements by Alexander *et al.* [184]. (b) Lattice parameters, Ru-O2 (apical) and Ru-O1 (in-plane) bond length extracted from the neutron single-crystal diffraction measurements by Braden *et al.* [172].

.

structure and the presence of the B-centred one was attributed to contaminations of the non stoichiometric compound $Ca_2RuO_{4+\delta}$ with oxygen excess [188]. The latter was indeed reported to host the B-centred structure [172].

The magnetic excitation spectrum was measured by several authors using single-crystal inelastic neutron scattering [169–171]. Ruthenate crystals are normally grown at high temperature using the floating zone method. The samples tend to shatter when they undergo the structural transition upon cooling, so that crystals large enough for inelastic neutron measurements cannot in general be obtained. This issue was overcome by either co-aligning a large number of crystals [169] or by doping the parent compound with Ti [170, 171]. The latter was found [170] to broaden the structural transition thus preventing the crystals from breaking upon cooling without significantly altering the properties of the pure compound [171]. The magnetic modes dispersion is reported in Fig. 4.3(a). The excitation spectrum significantly differs from the one expected for a pure-spin Heisenberg antiferromag-

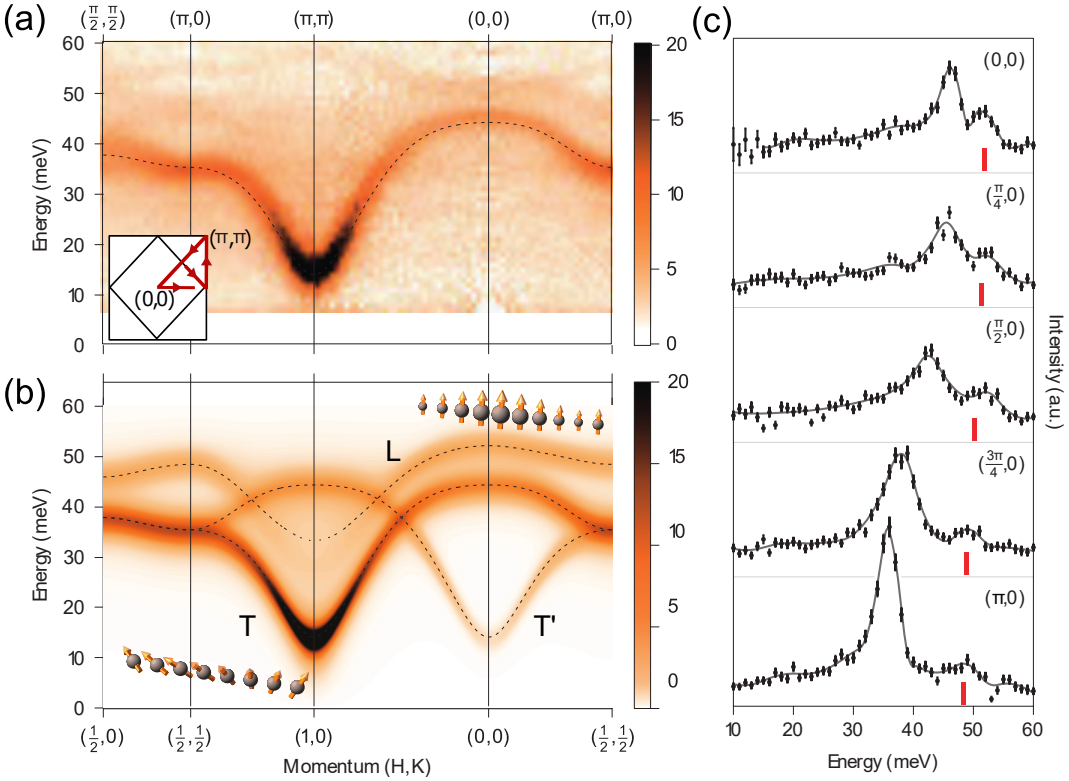

Figure 4.3: Summary of the inelastic neutron scattering investigation on the magnetic excitations in Ca_2RuO_4 by Jain *et al.* [169]. (a) Magnetic excitation spectrum at T = 5 K. The in-plane momentum transfer values reported on the top axis refer to the undistorted square lattice unit cell (see large square in the inset), while the values on the bottom one correspond to the Miller indices expressed in terms of the unit cell of Fig. 4.1(a) (the corresponding BZ is represented by the small rotated square in the inset). (b) Linear spin-wave solutions of the magnetic Hamiltonian of Eq. (4.1) convolved with the instrumental resolution calculated for $E = 25$ meV, $J = 5.8$ meV, $\alpha = 0.15$, $\varepsilon = 4.0$ meV and $A = 2.3$ meV. The transverse (T) and longitudinal (L) modes are shown along with a schematic representation of the corresponding magnetic moment fluctuations. The T' transverse mode arises from back-folding of the T mode by the magnetic (π,π) scattering and its intensity vanishes when approaching the QCP discussed in the text. The T and T' modes are polarised in the **ab** plane of the crystal (x) and out-of-plane (z), respectively. (c) Inelastic spectra collected along the $(0,0) \rightarrow (\pi,0)$ direction. The vertical red lines mark the position of the calculated longitudinal magnon peak. Figure adapted from Ref. [169].

net. In particular the main transverse mode (T in Fig. 4.3) exhibits a maximum at the crystallographic zone centre $(0,0)$, while a minimum would be present in the Heisenberg case. Moreover, a Higgs-like amplitude mode (L in Fig. 4.3) is also present at higher energies. This is clearly visible in the inelastic spectra collected along the $(0,0) \rightarrow (\pi,0)$ direction of the undistorted[1] Brillouin zone of Fig. 4.3(c), where the corresponding inelastic peak is highlighted by the vertical red lines. The Higgs mode corresponds to amplitude fluctuations of the magnetic moments[2] and is expected to appear as a well-defined collective excitation near a quantum critical point (QCP) [169]. As I will discuss in more detail in Sec. 4.3, the distinctive excitation spectrum arises as a result of the non-negligible SOC of 4*d* electrons. The latter mixes together the Ru t_{2g} orbitals and produces a ground state of mixed spin and orbital character with an unquenched orbital moment. A similar situation is present for the case of 5*d* oxides discussed in Chapter 5.

The excitation spectrum of Fig. 4.3 was accounted for by Jain *et al.* [169] based on the following Hamiltonian:

$$\mathscr{H} = J \sum_{\langle ij \rangle} (\tilde{\mathbf{S}}_i \cdot \tilde{\mathbf{S}}_j - \alpha \tilde{S}_i^z \tilde{S}_j^z) + E \sum_i (\tilde{S}_i^z)^2 + \varepsilon \sum_i (\tilde{S}_i^x)^2 \mp A \sum_{\langle ij \rangle} (\tilde{S}_i^x \tilde{S}_j^y + \tilde{S}_i^y \tilde{S}_j^x) \quad (4.1)$$

where $\tilde{\mathbf{S}}$ denotes a pseudospin-1 operator describing the entangled orbital and spin degrees of freedom[3], the indices i and j correspond to pairs of nearest-neighbour Ru sites within one RuO_2 plane and x, y, z are taken along the crystallographic $\mathbf{a}, \mathbf{b}, \mathbf{c}$ axes, respectively. The Hamiltonian of Eq. (4.1) includes single-ion terms of tetragonal (E) and orthorhombic symmetry (ε), XY-type exchange anisotropy ($\alpha > 0$) and a bond directional pseudo-dipolar term (A). The measured excitation spectrum is well reproduced by a value of the tetragonal single-ion anisotropy $E \approx 25$ meV much larger than the nearest-neighbour isotropic exchange $J \approx 5.8$ meV. The large E value is responsible for the unusual spin-wave dispersion with a maximum at $(0,0)$. Its origin is the SOC of 4*d* electrons; in fact, in the case of perfect cubic

[1] Spin-wave dispersions in layered compounds are normally described in terms of a two-dimensional (2D) unit cell with **a** and **b** axes of equal length rotated by 45° with respect to the crystallographic axis. This would be the correct crystallographic unit cell in the case of a tetragonal crystal with 180° TM-O-TM bonds (i.e. for the undistorted perovskite structure). The formalism used to express the in-plane momentum transfer in this description will be described in more detail in Chapter 5 for the case of iridium oxides (see Fig. 5.3).

[2] Conventional spin-wave excitations correspond to fluctuations of the magnetic moment components in the direction orthogonal to the direction of the order moment (transverse modes). The Higgs mode corresponds to a longitudinal mode, i.e. a fluctuation of the magnitude of the magnetic moments.

[3] The concept of describing SOC-entangled spin and orbital moments by means of a pseudospin operator will be extensively used in Chapter 5 for the ground state produced by the strong SOC in 5*d* oxides.

symmetry (i.e. negligible tetragonal distortion) one can show that $E = \lambda$, where λ is the SOC constant. This term also tends to suppress magnetic ordering by favouring a non-magnetic singlet ground state (see Sec. 4.3) and is responsible for the reduction of the Ru^{4+} magnetic moment from the nominal $2\mu_B$ value expected for a $S = 1$ system [169]. An equally satisfactory description of the measured dispersion was provided by Kunkemöller *et al.* [171] using an analogous model to the one of Eq. (4.1), simplified to the case $\alpha = A = 0$; similar values for the remaining exchange parameters were obtained. The authors of Ref. [171], however, suggested that the longitudinal mode of Fig. 4.3 simply arises from two-magnon excitations and is thus not indicative of the proximity of Ca_2RuO_4 to a QCP. It should be noted that the decisive impact of SOC on the magnon dispersion is not clear in the first report on the magnetic excitations of Ref. [170]. This is due to the fact that the measurements did not cover the momentum transfer range $(\pi/2, \pi/2) \rightarrow (0,0)$, which is the one where the deviations from a standard Heisenberg model are most pronounced.

One of the main features that triggered the interest in Ca_2RuO_4 is the unusual nature of the insulating state, which has prompted considerable experimental and theoretical attention in recent years [18, 173–177]. Compared to $3d$ TMOs, the larger $4d$ orbitals result in weaker electronic correlations ($U \sim 2$ eV) and relatively broad bands ($W \sim 3$ eV) [18]. Considering a standard Mott scenario, where the Mott insulating gap emerges due to a high Coulomb interaction to bandwidth ratio (see Sec. 1.1.1), the ruthenates are thus expected to be metallic. In fact, Ca_2RuO_4 is the only insulating compound of the series of perovskite ruthenates $A_{n+1}Ru_nO_{3n+1}$ (A = Ca or Sr) [18]. For instance, the Sr analogue Sr_2RuO_4 is a paramagnetic metal with Fermi-liquid behaviour at low temperature and a transition to an unconventional superconducting state at $T_c = 1.5$ K [165, 189]. Moreover, the electronic structure is quite different from the one encountered in many Mott insulators, such as the parent compounds of the high-T_c cuprates superconductors, where a single active electronic band half-filled with electrons crosses the Fermi level. In the case of Ca_2RuO_4, the large cubic crystal field acting on the Ru sites ($10Dq \approx 3$ eV [190]) forces the four electrons of the Ru^{4+} ion to reside in the t_{2g} states [190, 191] and results in a $2/3$-filled t_{2g} manifold. All three degenerate t_{2g} xy, yz, zx orbitals are active in the absence of non-cubic crystal field terms: this requires a multi-band description of the Mott insulating state, where the precise nature of the electronic ground state depends on the relative magnitude of the Hund's coupling, Coulomb repulsion and bandwidth [18]. In this scenario, a so-called orbital-selective Mott phase can occur when the carriers on a subset of orbitals undergo a Mott transition while the others remain itinerant [18].

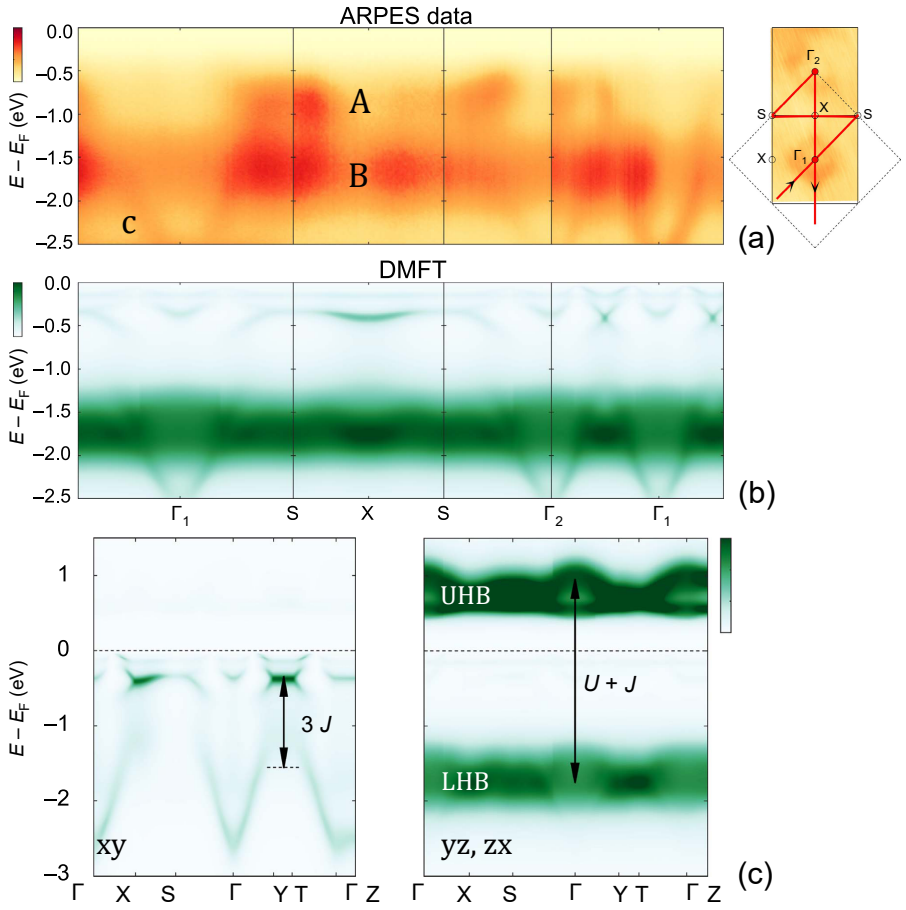

Figure 4.4: Summary of the combined angle-resolved photoemission spectroscopy (ARPES) and first-principle investigation on the band structure in the paramagnetic insulating phase of Ca_2RuO_4 by Sutter *et al.* [175]. (a) ARPES data recorded along high-symmetry directions (see panel on the right) at T = 150 K using 65 eV circularly-polarised light. The panel on the right correspond to a constant energy map at binding energy $E - E_F = -2.7$ eV, with E_F Fermi energy. The labels A, B and C highlight the three main bands observed in the data (see text for more details). (b) DMFT calculations of the band structure, with Coulomb interaction $U = 2.3$ eV and Hund's coupling $J = 0.4$ eV. (c) Contributions of the Ru 4*d* *xy*, *yz*, *zx* states to the total calculated spectral function shown in (b) highlighting the UHB and the LHB of predominant yz, zx character. The indicated energy splittings correspond to the multiplet structure in the atomic limit calculated in Ref. [175]. In (a), (b) and (c) the colour scale corresponds to the spectral weight (higher for darker colours). Figure adapted from Ref. [175].

The tetragonal compression of the RuO_6 octahedra removes the degeneracy of the t_{2g} states in the case of Ca_2RuO_4. The resulting stabilization of the xy states was suggested to play an important role in the formation of the insulating state: in the current commonly accepted picture, a Mott gap is opened by Coulomb interactions in the narrower half-filled bands spanned by the yz, zx orbitals (for which $W < U$), with a lower localised band of predominant xy character [18, 173–177]. The band structure of Ca_2RuO_4 in the paramagnetic insulating phase is shown in Fig. 4.4(a). Two relatively flat bands centred around -0.8 eV (A) and -1.7 eV (B) and a fast dispersing one emanating from the zone centre Γ (C) are observed. The measured band structure is reproduced reasonably well by dynamical mean-field theory (DMFT) calculations with Coulomb interaction $U = 2.3$ eV and Hund's coupling $J = 0.4$ eV [175] [Fig. 4.4(b)]. In particular, the DMFT calculations suggest that the LHB [B in Fig. 4.4(a)] and the UHB are predominantly of yz, zx character, while the fast dispersing band C below the Fermi level arises mainly from the xy orbitals [175] [see Fig. 4.4(c)]. As I will show in more detail in Sec. 4.3, the picture is made somewhat more involved by the SOC, which mixes the Ru t_{2g} orbitals and results in a ground state of mixed xy, yz, zx orbital character. Recent O K-edge absorption measurements [178, 185, 187] and first-principle calculations [192] reported a finite hole population of the xy orbital indicating that the latter also contribute to the empty density of states above the Fermi level. A more detailed discussion will be provided in relation to the O K-edge absorption measurements presented in Sec. 4.6.

4.2.2 Impact of chemical substitution on Ca_2RuO_4

Given the subtle balance between different energy scales at the origin of the insulating ground state, the low-energy electronic structure is expected to be extremely sensitive to structural distortions acting on the local Ru^{4+} crystalline environment. Dramatic changes in the electronic and magnetic ground-state properties, including the appearance of superconductivity, have been indeed achieved by means of epitaxial strain [193], application of hydrostatic pressure to bulk crystals [188, 194] or internal chemical pressure [173, 179–181, 190, 192, 195–207]. The latter has been mainly realized by substitution of Ca with Sr [173, 190, 192, 195–207] and La [179–181]. Given the unconventional superconductivity found in Sr_2RuO_4 [165], most of the literature has focused on $Ca_{2-x}Sr_xRuO_4$. The different ionic radii of the Sr^{2+} ($r = 1.21$ Å) and Ca^{2+} ($r = 1.18$ Å) [208] induce significant changes in the parent compound crystal structure. The latter were found to suppress both the

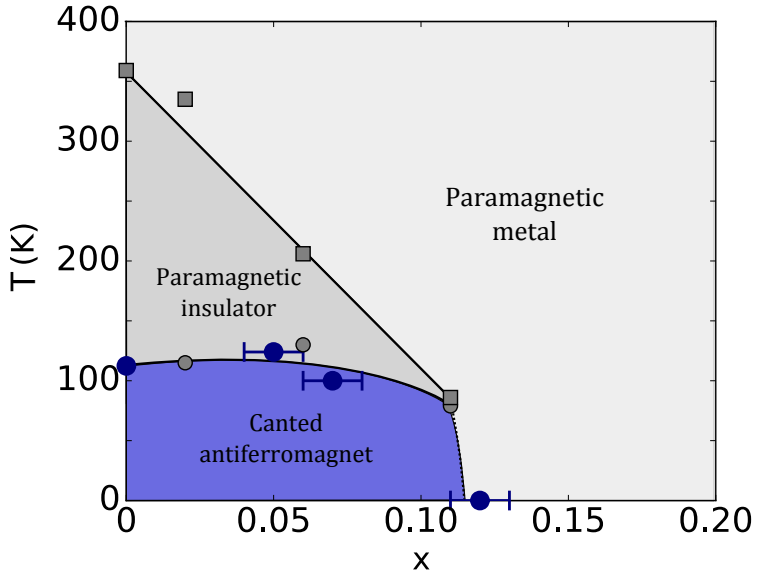

Figure 4.5: $Ca_{2-x}La_xRuO_4$ temperature-doping phase diagram. The filled squares represent the temperatures (from Ref. [179]) at which the transition between the high-temperature quasi-tetragonal metallic phase (L-*Pbca*) and the low-temperature orthorhombic one (S-*Pbca*) occurs. The small and large filled circles are the Néel temperatures taken from Ref. [179] and derived from the bulk magnetisation measurements, respectively. The error bars reflect the uncertainty in the doping level measured by means of energy-dispersive X-ray (EDX) spectroscopy.

MIT and the Néel transition and drive the parent crystal into a paramagnetic metallic state [198]. In the present chapter, I will focus on the impact of La doping on the parent compound insulating phase. Similar to Sr^{2+}, La^{3+} ($r = 1.22$ Å) is considerably larger than Ca^{2+} [208] and should thus have a significant impact on the structural properties. Moreover, while Sr and Ca are both divalent, La is trivalent so that La substitution also injects electrons into the system. Therefore La doping is expected to tune two of the fundamental parameters of the parent Mott insulator, i.e. the one-electron bandwidth (via the corresponding structural changes) and the band filling of the Ru 4*d* band as a result of the extra electron made available by La^{3+}. These effects are normally referred to as *bandwidth control* and *filling control*, respectively, and allow a rich phase diagram of electronic and magnetic states to be accessed [17].

The study of $Ca_{2-x}La_xRuO_4$ has so far received much less attention and has been limited to bulk measurements (resistivity, magnetisation and specific heat) and powder X-ray diffraction using a laboratory source [179–181]. The $Ca_{2-x}La_xRuO_4$ temperature-doping phase diagram is summarised in Fig. 4.5. Here, the results from the bulk measurements by Fukazawa and Maeno [179] are combined with the magnetisation data collected on the single crystals grown for the present investigation

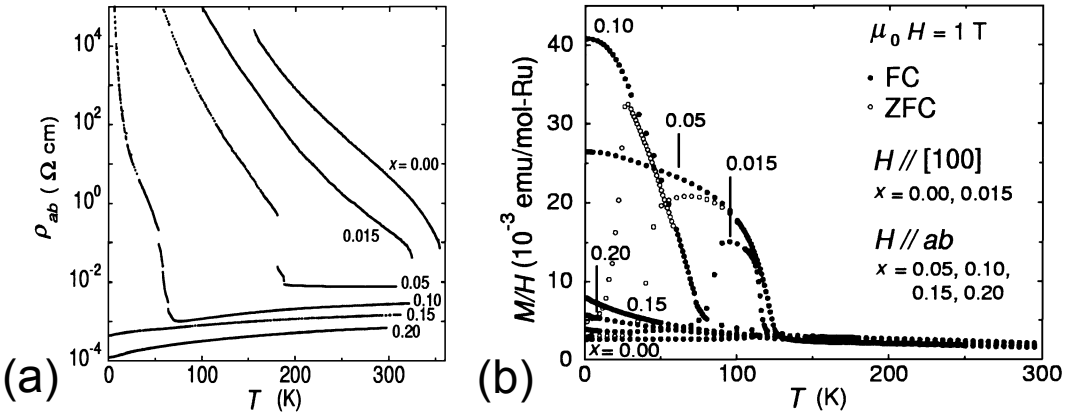

Figure 4.6: Summary of the bulk measurements performed on single crystals of $Ca_{2-x}La_xRuO_4$ with varying La content x by Fukazawa and Maeno [179]. The x values reported in the figure correspond to the nominal La contents. The actual doping levels as measured by EDX analysis by the authors of Ref. [179] are $x = 0, 0.02(1), 0.06(2), 0.11(2), 0.18(2)$ and $0.18(2)$. (a) Temperature dependence of the in-plane resistivity. The transition from insulating to metallic behaviour occurs between $x = 0.11(2)$ and $x = 0.18(2)$. (b) Magnetic susceptibility in the **ab** plane of the crystal as a function of temperature. Magnetic order is absent for the nominal doping levels $x = 0.15, 0.20$.

(see Sec. 4.4.1). Similar to the case of Sr doping, La substitution suppresses the MIT and AFM magnetic order, turning the system into a paramagnetic metal at a critical concentration slightly larger than $x = 0.11(2)$ [179]. A summary of the bulk measurements by Fukazawa and Maeno [179] is provided in Fig. 4.6. Similar bulk magnetisation measurements have also been reported by Cao *et al.* [180, 181]. In all studies a net magnetisation appears in the insulating phase at low temperature upon La substitution[4]. However, its origin has been subject to two conflicting interpretations: Fukazawa and Maeno [179] interpreted the observed net magnetisation as resulting from the canting of antiferromagnetically-coupled moments analogous to the parent case [see Fig. 4.1(b)], while Cao *et al.* [180, 181] proposed the presence of FM ordering.

$Ca_{2-x}La_xRuO_4$ has also been recently suggested as a candidate material for the investigation of the impact of electron doping on a d^4 Mott insulator [168]. Here, the magnetic ground state of the parent compound was predicted to strongly depend on the relative strength of the hopping integral, the SOC constant λ, and the correlation energy U. In particular, through electron doping of the parent AFM phase, the system is expected to evolve towards either a FM or a paramagnetic phase depending on the size of λ. The presence of a FM phase was explicitly suggested by the authors of Ref. [168] considering a value $\lambda \approx 75$ meV [26, 185].

[4]This is confirmed by the magnetisation measurements presented in Sec. 4.4.1

Despite its relevance in light of the peculiar Mott insulating state of Ca_2RuO_4, the magnetic structure of the La doped samples is thus still unresolved. This point will be addressed by the REXS measurements presented in Sec. 4.5, while Sec. 4.6 and 4.7 will deal with the impact of La substitution on the parent compound ground-state electronic properties. Before discussing the experimental results, I will present in Sec. 4.3 a quick overview of the main aspect of the Ru^{4+} single-ion physics which will be useful for the discussion of the measurements.

I briefly mention that an investigation on the impact of Pr doping on the electronic properties of Ca_2RuO_4 was conducted in parallel to the one on the La-doped samples discussed in this chapter by our collaborators [177]. Pr is trivalent like La and, although the ionic radius of Pr^{3+} ($r = 1.18$ Å) is smaller than the one of La^{3+}, the physics of $Ca_{2-x}Pr_xRuO_4$ was found to be analogous to the one of $Ca_{2-x}La_xRuO_4$. In particular, the ARPES measurements performed by Riccò *et al.* [177] suggest that the extra electrons injected by Pr substitution remain localised and therefore do not realize a significant filling control of the parent compound Ru $4d$ bands. This points towards a similar behaviour in the La-doped samples. Anticipating the results that I will be presenting later on in the chapter, the measurements are indeed consistent with a limited role of the electron filling effect in the physics of La-doped Ca_2RuO_4.

4.3 Ru^{4+} single-ion Hamiltonian

TM ions with a d^4 electronic configuration (as is the case of Ru^{4+} in Ca_2RuO_4) are particularly interesting from the point of view of the single-ion physics. As mentioned in Sec. 4.2, the large cubic crystal field ($10Dq \approx 3$ eV [190]) sensed by the $4d$ orbitals results in a low-spin state with all four electrons in the lower t_{2g} orbitals (Fig. 4.7): the upper e_g levels can then be ignored in the description of the electronic ground state. In the absence of non-cubic crystal field terms, the t_{2g} energy levels are degenerate. Following from the first Hund's rule, the four electrons will tend to maximize their total spin, resulting in a state with nominal $L_{\text{eff}} = 1$ and $S = 1$. The effect of the moderate SOC coupling of $4d$ electrons is to split the degenerate t_{2g} levels into states described by the quantum number $J_{\text{eff}} = L_{\text{eff}} - S, \ldots, L_{\text{eff}} + S$ (see Sec. 1.1.4). As first shown by Abragam and Bleaney [26], in the case of four t_{2g} electrons, (more than half-filled t_{2g} subshell) the two lowest-lying electronic levels are a $J_{\text{eff}} = 0$ singlet ground state and an excited $J_{\text{eff}} = 1$ triplet. This is schematically shown in Fig. 4.7(a). Despite the non-magnetic singlet

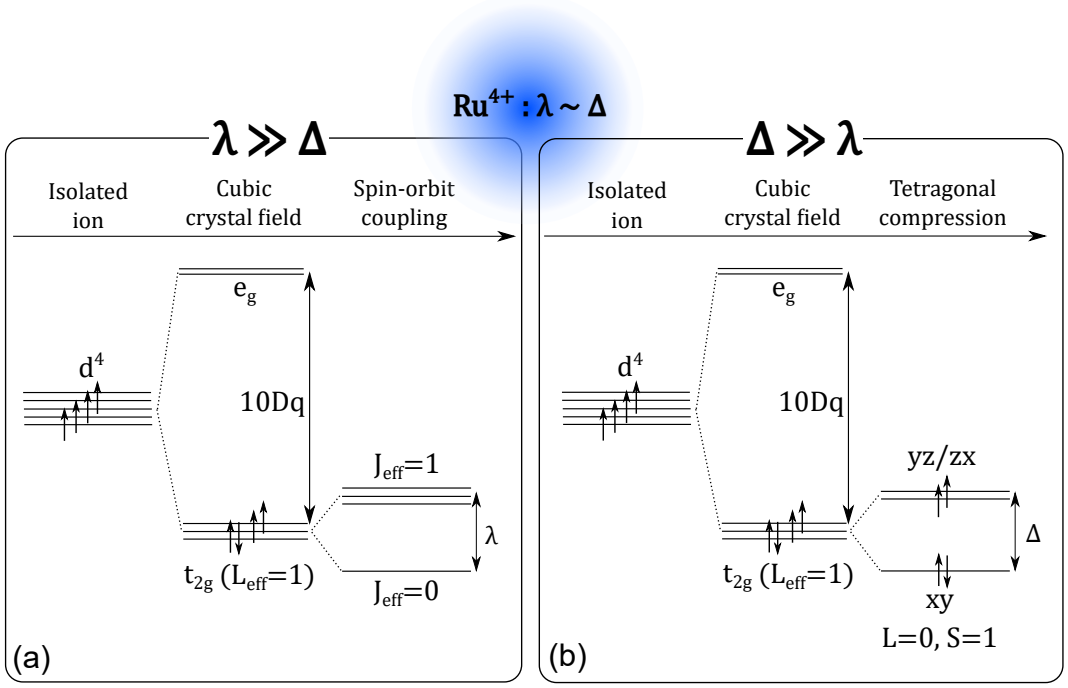

Figure 4.7: Schematic representation of the energy levels of a TM ion with four electrons in the d orbitals (d^4) in a cubic crystal field ($10Dq$) under the influence of strong (a) spin-orbit interaction λ or (b) tetragonal compressive field Δ. A non-magnetic $J_{\rm eff} = 0$ state is stabilized in the former case [26], while a fully occupied xy orbital and half-filled yz, zx orbitals are present in the latter, leading to a quenched orbital moment and $S = 1$. The Ru^{4+} ion sits in an intermediate range where SOC and tetragonal distortion compete on an equal footing.

ground state, magnetic order can result from the condensation of the excited triplet driven by intersite interactions [1, 166], provided that the exchange coupling is strong enough to overcome the energy of promotion of the ion to the excited state (separated from ground state by λ). This scenario, which can be viewed as a Bose condensation of the $J_{\rm eff} = 1$ state [166], is normally referred to as *singlet* or *Van-Vleck* type magnetism [1], in analogy with the Van-Vleck paramagnetic response of systems with a non-magnetic ground state.

The $J_{\rm eff} = 0$ description is strictly valid in the case of a crystalline environment with cubic symmetry. However, as I discussed in Sec. 4.2, a significant compression of the RuO_6 octahedra is present in the AFM phase. If one neglects the SOC of the $4d$ electrons the corresponding tetragonal field (Δ) is expected to stabilize the xy orbitals [Fig. 4.7(b)]. This results in a state with quenched orbital angular momentum[5] and $S = 1$, with standard magnetic interactions of Heisenberg nature. The case of Ru^{4+} in Ca_2RuO_4 corresponds to the more subtle situation where both SOC

[5]This simply derives from having two electrons in a singlet state in the xy orbital and one electron in each one of the yz and zx orbitals.

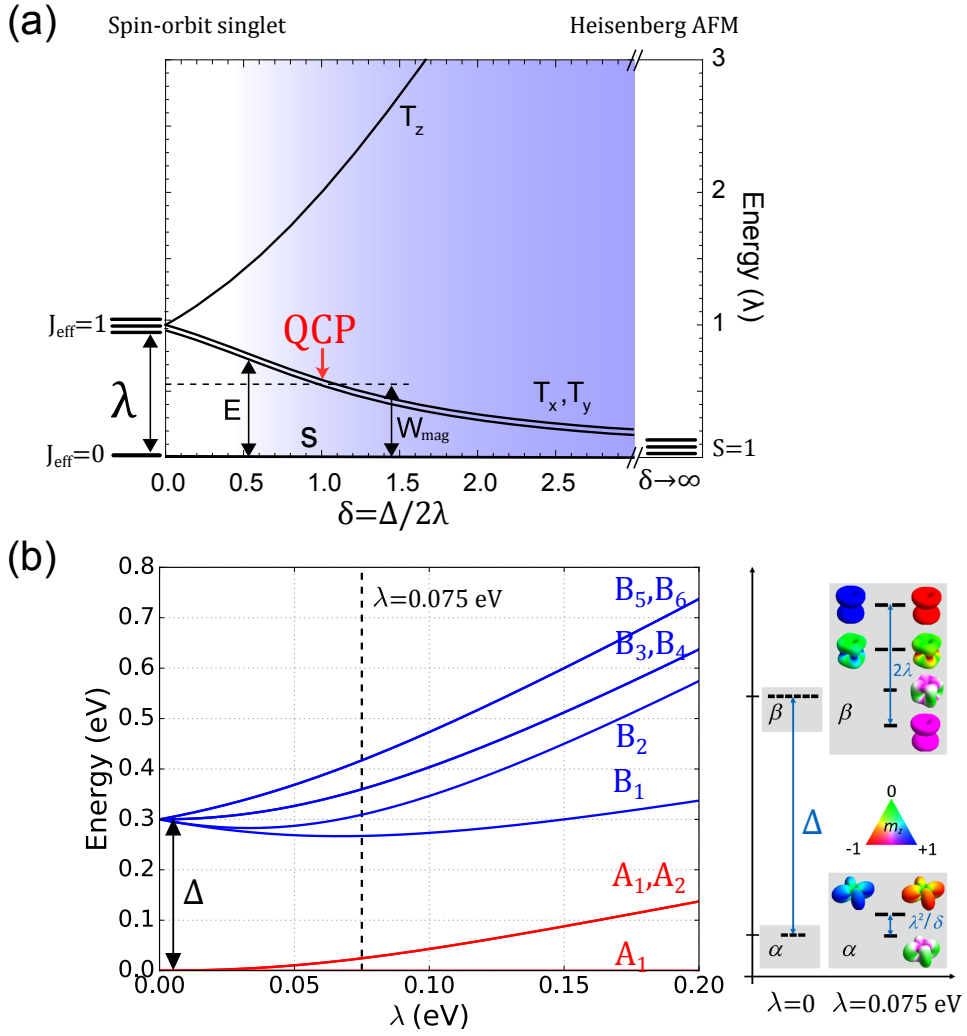

Figure 4.8: Summary of the electronic structure calculations of the Ru^{4+} ion in Ca_2RuO_4 performed by different authors. (a) Ru^{4+} electronic structure as a function of the relative strength δ of the tetragonal compressive field (Δ) and SOC (λ) as calculated by Jain *et al.* [169]. The tetragonal field splits the $J_{\text{eff}} = 1$ triplet present for perfect cubic symmetry ($\delta = 0$) into an upper singlet T_z and a lower doublet (T_x,T_y). The QCP discussed in the text occurs when the energy E of the excited levels becomes equal to the single-magnon bandwidth W_{mag}. The shaded area indicates the region where the effective pseudospin $\tilde{\mathbf{S}} = 1$ model consisting of the three levels $\{s, T_x, T_y\}$ and used to describe the magnetic excitation spectrum [Eq. (4.1)] is valid. Here, s denotes the singlet originating from the $J_{\text{eff}} = 0$ level. A conventional $S = 1$ system with standard Heisenberg interactions is recovered in the limiting case $\delta \to \infty$. Figure adapted from Ref. [169]. (b) Ru^{4+} multiplet structure as a function of the SOC constant for $\Delta = 0.3$ eV calculated by Das *et al.* [178]. The SOC splits the states produced by the tetragonal field and results in the α ($A_1 - A_3$) and β ($B_1 - B_6$) sectors of energy levels. The panel on the right schematically represents the energy levels for $\lambda = 0.075$ eV along with a real-space representation of the doubly occupied orbital wave function (the colour scale corresponds to the z projection of the spin angular momentum). The levels $\{A_1, A_2, A_3\}$ correspond to the triple of states $\{s, T_x, T_y\}$ in (a). Figure adapted from Ref. [178].

and tetragonal field compete on an equal footing to determine the electronic ground state. This intermediate regime poses serious challenges in terms of the theoretical description of the ground-state wave function since its precise expression depends on the exact relative ratio Δ/λ of the two energy scales. The task is rendered even more complicated by the multi-body nature of the problem (four electrons or two holes in the t_{2g} orbitals), which makes a simple single-particle picture generally not valid[6]. As I will briefly discuss below, there is indeed still some debate as to the precise value of the tetragonal distortion and SOC relative strength and the corresponding nature of the Ru^{4+} ground state.

A microscopic description of the Ru^{4+} electronic structure in Ca_2RuO_4 was proposed by Jain *et al.* [169] to derive the exchange model of Eq. (4.1) used to reproduce the magnetic excitation spectrum of Fig. 4.3. This is illustrated in Fig. 4.8(a), where a schematic energy level diagram is reported as a function of the parameter $\delta = \Delta/2\lambda$. Starting from the perfect cubic case ($\delta = 0$) with a $J_{\text{eff}} = 0$ singlet ground state and excited $J_{\text{eff}} = 1$ triplet, the tetragonal distortion splits the excited triplet into a high-energy singlet (T_z) and a low-energy doublet (T_x,T_y). The high-energy singlet can be neglected so that the low-energy physics of Ca_2RuO_4 is accounted for by the three levels $\{s, T_x, T_y\}$ (with s indicating the singlet state deriving from the $J_{\text{eff}} = 0$ level). These three levels can be described in terms of a $\tilde{\mathbf{S}} = 1$ pseudospin, whose magnetic exchange interactions are properly reproduced by the Hamiltonian of Eq. (4.1). The effect of the tetragonal field is thus to lower the energy barrier from the ground to the excited states from λ (for $\delta = 0$) to the generic value E[7]. A QCP is expected to occur when $E \approx W_{\text{mag}}$, where W_{mag} is the single-magnon bandwidth. Considering the free-ion value $\lambda \approx 75$ meV [26] and the value W_{mag} extracted from the magnon dispersion [169], the model predicts a QCP for $\delta \approx 1$. For larger δ values the system finds energetically favourable to occupy the excited T_x, T_y levels as a result of the intersite exchange interactions between the excited states. A good description of the magnetic excitation spectrum of Fig. 4.3 is obtained for $\delta = 1.5$, which results in exchange parameters in agreement with the ones reported in the caption of Fig. 4.3; for $\lambda = 75$ meV, one gets $\Delta = 3\lambda = 225$ meV. A standard $S = 1$ system with conventional Heisenberg exchange interactions is recovered for $\delta \to \infty$ [Fig. 4.8(a)].

[6] This is a significant difference with respect to the case of the Ir^{4+} ion in the perovskite iridium oxides presented in Chapter 5, where a single hole is present in the t_{2g} orbitals.

[7] This is the same parameter that dictates the single-ion anisotropy with tetragonal symmetry in Eq. (4.1).

The multiplet structure of the Ru^{4+} ion was also recently calculated by Das *et al.* [178] considering a local ruthenium Hamiltonian $\mathscr{H} = \mathscr{H}_{\text{el-el}} + \mathscr{H}_{\text{SOC}} + \mathscr{H}_{\text{CF}}$ consisting of electron-electron interaction ($\mathscr{H}_{\text{el-el}}$), SOC ($\mathscr{H}_{\text{SOC}}$) and crystal field ($\mathscr{H}_{\text{CF}}$) terms. In particular, the term $\mathscr{H}_{\text{el-el}}$ models the complete Coulomb interactions of the t_{2g} electrons, including the intra-orbital Coulomb repulsion U, Hund's coupling J_H, the inter-orbital electron-electron interaction and the hopping term. The corresponding low-energy eigenvalues are reported in Fig. 4.8(b) as a function of the SOC constant λ for a representative value $\Delta = 0.3$ eV of the tetragonal crystal field. As one can see, the multiplet structure consists of two distinct blocks which are referred to as α and β [see panel on the right of Fig. 4.8(b)]: the former includes three different energy levels (A_1, A_2 and A_3), while the latter consists of six different states (labelled B_i, $i = 1,\dots,6$). For vanishing SOC ($\lambda = 0$) the levels in each sector are degenerate. A satisfactory agreement with the excitation spectrum measured by RIXS at the O K-edge was found considering the single-ion value $\lambda = 75$ meV [178]. In this case, in agreement with the model of Fig. 4.8(a), the low-energy physics can be described in terms of a ground state singlet (A_1) and an excited doublet (A_2, A_3), which correspond to s and T_x, T_y of Fig. 4.8(a), respectively. Following from Ref. [178], their wave functions can be expressed in terms of basis functions $|S, m_S, d\rangle$ characterised by the quantum numbers S of the total spin, m_S of the spin z projection and the orbital $d \in \{xy, yz, xz\}$ which is doubly occupied[8]. The α sector eigenfunctions are then given by [178]:

$$
\begin{aligned}
A_1 &= \frac{1}{\sqrt{c_1}}\left[a_1(|1,-1,yz\rangle - i|1,-1,xz\rangle) - a_1(|1,1,yz\rangle + i|1,1,xz\rangle) + |1,0,xy\rangle\right] \\
A_2 &= \frac{1}{\sqrt{c_2}}\left[a_2(|1,0,yz\rangle - i|1,0,xz\rangle) + |1,1,xy\rangle\right] \\
A_3 &= \frac{1}{\sqrt{c_3}}\left[a_3(|1,0,yz\rangle + i|1,0,xz\rangle) + |1,-1,xy\rangle\right]
\end{aligned}
\tag{4.2}
$$

with

$$
\begin{aligned}
a_1 &= \frac{\sqrt{2}\lambda}{\Delta - \lambda + \sqrt{\Delta^2 - 2\Delta\lambda} + 9\lambda^2} \\
c_1 &= 1 + 4a_1^2 \\
a_2 &= -a_3 = \frac{-\Delta + \sqrt{\Delta^2 + 4\lambda^2}}{2\sqrt{2}\lambda} \\
c_2 &= c_3 = \frac{2}{1 + \dfrac{\Delta}{\sqrt{\Delta^2 + 4\lambda^2}}}
\end{aligned}
\tag{4.3}
$$

Eq. (4.2) shows that the SOC of $4d$ electrons mixes the t_{2g} orbitals and produces

[8] Considering four electrons in the d states one can have either a doubly occupied orbital (*doublon*) and the other two electrons in the remaining states with parallel spins or two doubly occupied orbital with zero total spin. The possible occupation numbers n_i of the t_{2g} orbitals for the 1-doublon configuration are $\{n_{xy}, n_{yz}, n_{zx}\} \in \{(1,1,2),(1,2,1),(2,1,1)\}$, while in the 2-doublon case one has $\{n_{xy}, n_{yz}, n_{zx}\} \in \{(0,2,2),(2,0,2),(2,2,0)\}$.

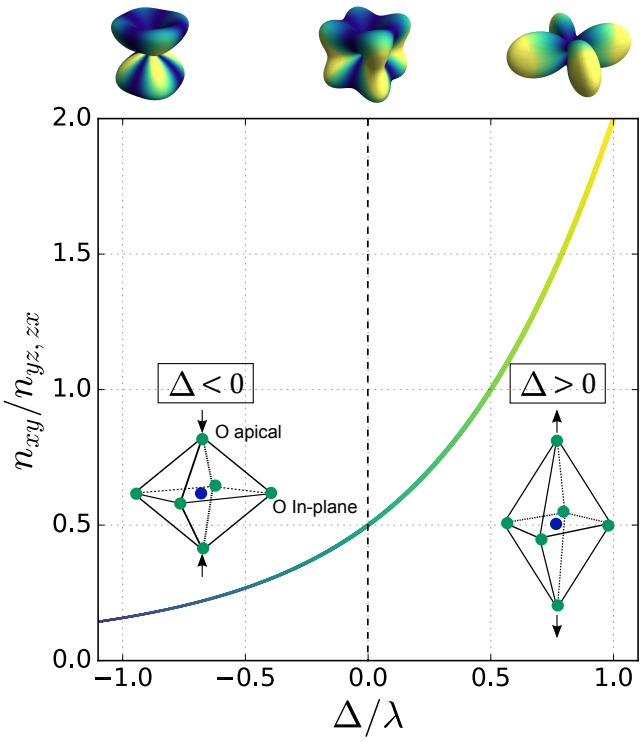

Figure 4.9: Calculated orbital hole population dependence of the Ru^{4+} ground state on the tetragonal field ($\Delta < 0$ for tetragonal compression and $\Delta > 0$ for tetragonal elongation) and SOC (λ) relative strength [187]. The top panel shows the corresponding evolution of the ground-state wave function charge density: the colour scale indicates the $|zx\rangle \pm i|yz\rangle$ (blue) and $|xy\rangle$ (yellow) orbital contribution.

an entangled ground-state wave function of mixed spin and orbital character. The precise expression depends on the relative strength of the SOC and crystal field parameter: for $\lambda = 0$ the wave functions Eq. (4.2) simply describe a state with two electrons in the xy orbitals and half-filled yz, zx orbitals in a triplet state as expected for the case of tetragonal compression.

The low-energy electronic structure of the Ru^{4+} ion was also modelled using a minimal Hamiltonian consisting of SOC and tetragonal field which neglects the Hund's coupling of $4d$ electrons [187]:

$$\mathscr{H} = \lambda \mathbf{L}_{\text{eff}} \cdot \mathbf{S} + \Delta/3\langle L_z \rangle^2 \tag{4.4}$$

This model was successfully used to describe the ground state of the Ir^{4+} ion in iridium oxides of the Ruddlesden-Popper series $Sr_{n+1}Ir_nO_{3n+1}$ and will be discussed in more detail in Chapter 5 in relation to the single layer compound Sr_2IrO_4. As I will show later on, in this case a single hole occupies the t_{2g} levels: the ground state properties can then be described in terms of a single-particle picture and are correctly reproduced by the model of Eq. (4.4). The latter, on the other hand, rep-

resents a strong approximation of the single-ion physics in the case of the 2/3-filled t_{2g} orbitals of Ru^{4+} as it neglects the electron-electron interactions. However, it can be conveniently adopted to gain a qualitative understanding of the evolution of the ground state as a function of the relative strength of the SOC and tetragonal field. As I will show in Sec. 4.6, the model captures the global trend extracted from the XANES measurements at the O K edge.

Following from Ref. [187], the ground state of the system in the hole representation derived from Eq. (4.4) can be written as $\psi^{\pm} = |zx,\pm\rangle \pm i|yz,\pm\rangle + \sqrt{n_{xy}}|xy,\pm\rangle$, where the $\pm$ sign refers to states with opposite spin z component and n_{xy} is the hole occupancy of the xy orbital [187]. The latter is given by

$$n_{xy} = (2\delta - 1 + C)^2/4 \tag{4.5}$$

with $\delta = \Delta/\lambda$ and $C = \sqrt{9+4\delta(\delta-1)}$. The resulting hole occupancy ratio $n_{xy}/n_{yz,zx}$ (with $n_{yz,zx} = n_{yz} + n_{zx}$) predicted by the model is reported in Fig. 4.9 along with a real-space representation of the ground-state wave function (see top panel). It should be noted that the sign of the crystal field parameter in Fig. 4.9 is opposite to the one of Fig. 4.8, i.e. $\Delta < 0$ for the case of octahedral compression. Fig. 4.9 shows that changing the crystal field tunes the t_{2g} orbital contributions to the ground-state wave function and causes an increase in the xy orbital hole population going from tetragonal compression to tetragonal elongation. A $n_{xy}/n_{yz,zx}$ ratio in the range $0.15-0.3$ was reported for Ca_2RuO_4 [185, 187, 192], which in the model of Fig. 4.9 would correspond to δ values between about -1 and -0.4. Comparing the electronic structure calculated from Eq. (4.4) with RIXS spectra measured at the O K edge, Fatuzzo *et al.* [187] inferred a value $\lambda \approx 200$ meV for the SOC constant, significantly larger than the single-ion value $\lambda \approx 75$ meV considered by other authors [169, 185, 209].

Overall, the picture emerging from this overview of the single-ion physics just presented is one where the low-energy electronic structure of the Ru^{4+} ion stems from a subtle interplay between crystal field and SOC and is thus expected to be extremely sensitive to structural distortions acting on the local Ru^{4+} crystalline environment. As I mentioned earlier on, the internal chemical pressure achieved by elemental substitution provides a viable way of tuning the crystal field acting on the Ru site. In this chapter, I will focus on the case of La doping, whose impact on the Ru^{4+} t_{2g} orbital population in Ca_2RuO_4 was investigated through the absorption measurements presented in Sec. 4.6.

4.4 Sample growth and characterisation

The work presented in this section has been included in the publication "*Persistence of antiferromagnetic order upon La substitution in the* $4d^4$ *Mott insulator* Ca_2RuO_4" by D. Pincini, S. Boseggia, R. Perry, M.J. Gutmann, S. Riccò, L.S.I. Veiga, C.D. Dashwood, S.P. Collins, G. Nisbet, A. Bombardi, D.G. Porter, F. Baumberger, A.T. Boothroyd and D.F. McMorrow, Physical Review B **98**, 014429 (2018) [210].

The measurements discussed in this chapter (with the only exception of the results presented in Sec. 4.7) were performed on single crystals of $Ca_{2-x}La_xRuO_4$, with $x = 0$, $0.05(1)$, $0.07(1)$ and $0.12(1)$ [corresponding to the nominal dopings $x = 0$, 0.05, 0.10 and 0.15, respectively]. The crystals were grown through the floating zone technique using a Crystal System Corporation FZ-T10000-H-VI-VPO-IHR-PC four-mirror optical furnace. Samples were prepared in 0.8 bar partial oxygen pressure, and the initial Ru concentration in the polycrystalline rods was about 20% higher than the nominal value to compensate for evaporation during the growth. This resulted in plate-like crystals a few millimetres wide. In particular, the crystals used for the bulk magnetisation (Sec. 4.4.1) and REXS (Sec. 4.5) measurements were approximately 1×1 mm^2 in size, with a crystal mosaic of about 0.05° as extracted from the width of the Bragg peak rocking curve. It should be noted that the crystal size of the parent compound is limited by the first-order structural transition which causes the crystals to break upon cooling to room temperature after the growth. As for the doped samples, I tried to avoid the largest crystals as the structural transition seems to have a more limited effect on the smaller ones: the latter tend to stay intact as they undergo the transition upon cooling. The doping level was determined by means of energy-dispersive X-ray (EDX) spectroscopy, while the bulk magnetic properties and crystal structure were characterised by means of SQUID magnetisation measurements and neutron diffraction as described in Sec. 4.4.1 and Sec. 4.4.2, respectively.

Powder samples of the same compounds were also synthesised between 1400°C and 1500°C (the temperature was increased with the La content) and 1% O_2 atmosphere. The conditions were adapted from Ref. [183]. The composition was checked by means of X-ray powder diffraction using a standard laboratory setup. The powders were used to collect the XANES and XMCD data at the Ru L edges presented in Sec. 4.7; the same XANES spectra were also used to correct the REXS data of Sec. 4.5 for the self-absorption effect.

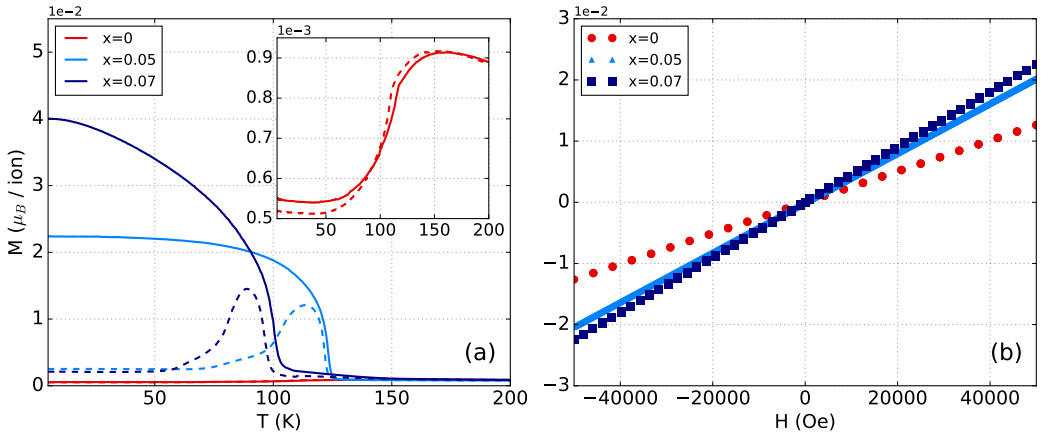

Figure 4.10: Bulk magnetisation SQUID measurements for the undoped ($x = 0$) and doped ($x = 0.05, 0.07$) samples. (a) ZFC (dashed lines) and FC (solid lines) magnetisation *vs* temperature. The ZFC measurements were performed upon warming after cooling the sample in zero field, while the FC data were collected while cooling in an applied field $H = 2$ kOe. The inset shows a detail of the $x = 0$ data set. (b) Magnetisation *vs* field at T = 5 K. Each data set was collected by sweeping the external magnetic field in the sequence $0 \rightarrow 5 \rightarrow -5 \rightarrow 5$ kOe after having cooled the sample from room temperature in zero field. For both (a) and (b) the external field was applied perpendicular to the **c** axis.

4.4.1 Bulk magnetisation measurements

Bulk magnetisation measurements were performed on single crystals by means of a Quantum Design MPMS 3 SQUID VSM at beamline I10 of the DLS. The magnetisation as a function of temperature ($M\,vs\,$T) and external field ($M\,vs\,H$) for the different doping levels is reported in Fig. 4.10. The $M\,vs\,$T ZFC measurements were performed upon warming after cooling the sample in zero field, while the FC data were collected while cooling in an applied field $H = 2$ kOe. All $M\,vs\,H$ data here reported were collected by sweeping the external magnetic field in the sequence $0 \rightarrow 5 \rightarrow -5 \rightarrow 5$ kOe after having cooled the samples down to T = 5 K from room temperature in zero field.

The $M\,vs\,$T data are consistent with those reported by other authors [172, 179–181]. In particular, while the parent compound shows a typical AFM behaviour, the doped samples display a finite net magnetisation at low temperature. The latter has been subject to two conflicting interpretations: Fukazawa and Maeno [179] interpreted the observed net magnetisation as resulting from the canting of antiferromagnetically-coupled moments analogous to the parent case [172] (Fig. 4.5), while Cao *et al.* [180, 181] proposed the presence of FM ordering. The nature of the magnetic ground state, which cannot be unequivocally distinguished

on the basis of bulk measurements alone, will be addressed in detail in Sec. 4.5. The Néel transition temperature follows a similar trend with doping to the one reported by Fukazawa and Maeno [179], with the $x = 0.07$ crystal ordering at a lower temperature than the $x = 0, 0.05$ samples. The net magnetisation also seems to increase with the La content, consistent to previous studies [179–181]. However, it should be noted that the value of the low-temperature magnetisation in the M *vs* T data significantly depends on the particular orientation of the magnetic field. Although the latter was always applied in the basal plane of the crystal, its orientation with respect to the crystallographic **a** and **b** axes was not obvious from the crystal morphology and could not be controlled. Analogous measurements repeated on different crystals with the same composition and a generally different in-plane alignment indeed show visible variations.

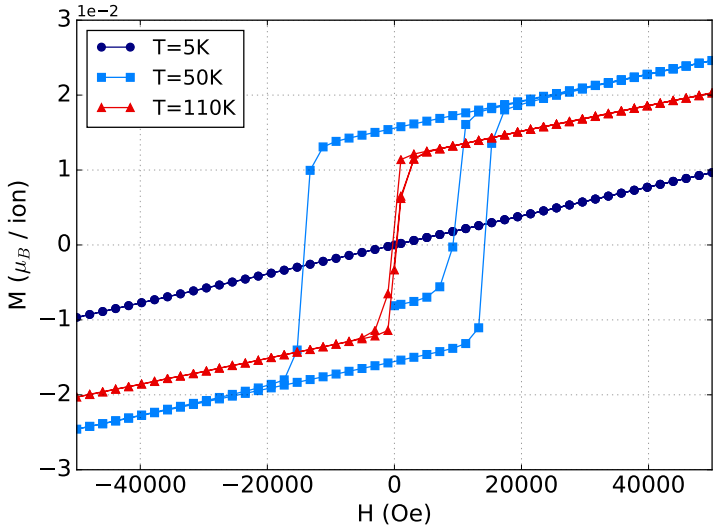

Figure 4.11: Magnetisation *vs* field at different temperatures below the Néel transition in the $x = 0.05$ compound. Each data set was collected by sweeping the external magnetic field (perpendicular to the **c** axis) in the sequence $0 \rightarrow 5 \rightarrow -5 \rightarrow 5$ kOe after having cooled the sample from room temperature in zero field [same thermal history as for Fig. 4.10(b)].

The M *vs* H data [Fig. 4.10(b)] at T = 5 K show a linear behaviour over the range of field values explored, as expected for the AFM order of pure Ca_2RuO_4 [180–183]. The only visible impact of doping is an increase in the slope of the M *vs* H curve, which suggests that the AFM order of the parent compound is not substantially altered by La substitution. Increasing the temperature towards the Néel transition results in the opening of a hysteresis loop, where the value of the coercive field decreases with temperature. This is shown in Fig. 4.11, where M *vs* H curves measured in the $x = 0.05$ sample at different temperatures are reported. This behaviour is consistent with a C-AFM structure, where the hysteresis appears as a

result of the presence of multiple domains with a different net magnetisation direction. At very low temperature the magnetic moments are locked along the easy **b** axis of the AFM structure and no domains are thus present. Furthermore, the reduction of the coercive field upon warming is consistent with a reduced magnetic anisotropy close to the paramagnetic phase. In this regime, the measurements show similar results to the one reported by Cao *et al.* [180, 181] at a similar temperature.

4.4.2 Structural characterisation by neutron diffraction

The structural properties of $Ca_{2-x}La_xRuO_4$ as a function of doping were investigated by means of single-crystal neutron diffraction at the Laue single-crystal diffractometer at the SXD instrument of the ISIS Neutron and Muon Source [211]. Neutron data were collected for all available doping levels at T = 10 K, while additional room-temperature measurements were performed for $x = 0$, 0.05 and 0.07. The results of the structural refinement are summarised in Table 4.1. The corresponding R factors and goodness of fit (χ^2) are reported in Appendix B.3 along with the refined components of the thermal ellipsoid tensor **U**. No significant twinning ($< 1\%$) was detected for the parent and $x = 0.07$ crystals, while the $x = 0.05$ sample was found to be moderately twinned with a twin volume fraction smaller than 5%. Significant twinning was detected in the $x = 0.12$ crystal, with a volume fraction of about 18%. It should also be noted that the magnetic structure was not considered in the low-temperature refinement since the magnetic intensity is negligible for the counting time used for the measurements.

The parent compound exhibits the S-*Pbca* structure both at room and low temperature [183, 184], with similar structural properties to the ones already reported by Braden *et al.* [172]. The doped samples retain the same space group and undergo the first-order structural transition from the high-temperature L-*Pbca* to the low-temperature S-*Pbca* structure below the critical concentration $x \approx 0.11$, consistent with a previous study [179]. The structural transition is absent in the $x = 0.12$ sample, which exhibits the L-*Pbca* structure down to T = 10 K. As I will discuss hereafter, the different radii of the La^{3+} ($r = 1.22$ Å) and Ca^{2+} ($r = 1.18$ Å) ions[9] result in significant structural changes in the S-*Pbca* structure observed for $x < 0.11$. These changes are reported for the first time in the present work: previous measurements [179] were performed on powdered single crystals using a laboratory X-ray source and did not report detailed structural information.

[9] These values refer to the Shannon radii [208] for ions with coordination number IX (9).

		T = 10 K			
		$x = 0$	$x = 0.05$	$x = 0.07$	$x = 0.12$
a		5.379(2)	5.387(2)	5.3857(19)	5.3709(19)
b		5.630(2)	5.573(2)	5.512(2)	5.3808
c		11.732(4)	11.833(4)	11.957(5)	12.211(4)
$1-a/b$ (%)		4.458	3.338	2.291	0.184
Volume		355.0(3)	355.2(2)	354.9(2)	352.9(2)
Ru	x	0.5	0.5	0.5	0.5
	y	0	0	0	0
	z	0	0	0	0
Ca (La)	x	0.4971(3)	0.49454(11)	0.49229(19)	0.48898(13)
	y	0.0587(4)	0.05422(15)	0.04755(18)	0.03483(11)
	z	0.35281(14)	0.35197(5)	0.35124(7)	0.34955(5)
O(1)	x	0.3055(2)	0.30500(8)	0.30422(15)	0.30381(11)
	y	0.3003(4)	0.30074(13)	0.30095(16)	0.30342(11)
	z	0.02799(13)	0.02614(5)	0.02429(7)	0.01920(5)
O(2)	x	0.5689(2)	0.56535(8)	0.56000(15)	0.54884(10)
	y	-0.0224(4)	-0.02096(13)	-0.01992(17)	-0.01364(11)
	z	0.16471	0.16502	0.16534	0.16608
Ru-O(1)	r_x	2.015(3)	2.0021(9)	1.9869(11)	1.9572(8)
Ru-O(1)	r_y	2.0180(17)	2.0071(8)	1.9931(10)	1.9587(8)
Ru-O(2)	r_z	1.9702(16)	1.9876(9)	2.0062(11)	2.0462(9)
$1-(r_x+r_y)/(2r_z)$ (%)		-2.350	-0.855	0.808	4.313
Ru-O-Ru bond (°)		149.74(12)	150.33(8)	150.99(9)	152.21(8)
RuO_6 tilt		11.46(5)	10.76(4)	9.79(5)	7.65(4)

		T = 300 K		
		$x = 0$	$x = 0.05$	$x = 0.07$
a		5.409(2)	5.361(2)	5.378(2)
b		5.500(2)	5.3716(9)	5.369(2)
c		11.910(4)	12.236(4)	12.239(5)
$1-a/b$ (%)		1.655	0.197	-0.168
Volume		354.3(2)	352.4(2)	353.4(2)
Ru	x	0.5	0.5	0.5
	y	0	0	0
	z	0	0	0
Ca (La)	x	0.4921(5)	0.48970(18)	0.4898(4)
	y	0.0470(6)	0.0298(3)	0.0298(4)
	z	0.3516(2)	0.34886(8)	0.34994(15)
O(1)	x	0.3031(3)	0.30562(14)	0.3044(3)
	y	0.3011(6)	0.3055(2)	0.3031(3)
	z	0.02386(18)	0.01691(7)	0.01682(14)
O(2)	x	0.5600(3)	0.54365(14)	0.5432(2)
	y	-0.0183(6)	-0.0112(2)	-0.0111(4)
	z	0.16460(16)	0.16558(6)	0.16572(13)
Ru-O(1)	r_x	1.989(3)	1.9549(12)	1.9486(18)
Ru-O(1)	r_y	1.991(3)	1.9542(11)	1.9596(18)
Ru-O(2)	r_z	1.990(3)	2.0404(10)	2.0424(18)
$1-(r_x+r_y)/(2r_z)$ (%)		0.000	4.208	4.323
Ru-O-Ru bond (°)		151.37(15)	152.19(10)	152.93(13)
RuO_6 tilt		9.83(6)	6.80(4)	6.74(5)

Table 4.1: Summary of the results of the neutron structural refinement for the parent and La-doped samples at T = 10 K and room temperature. The lattice parameters are given in Å, while the atomic positions are expressed in terms of fractional coordinates of the *Pbca* unit cell. The Ru atoms occupy the inversion centre 4*b*, while the O and Ca atoms sit on the generic site 8*c*. The La dopant atoms replace the Ca ones and thus occupy the same site.

The structural changes can be described in terms of the following four parameters [schematically represented in Fig. 4.1(a)]:

- unit cell distortion $A = 1 - \frac{a}{b}$, where a and b are the in-plane lattice constants of the *Pbca* unit cell [see Fig. 4.1(a)]. $A = 0$ in the case of a perfect tetragonal cell with $a = b$, while it increases as b increases with respect to a.

- octahedral distortion $B = 1 - \frac{r_x + r_y}{2r_z}$, where $r_{x,y}$ and r_z are the in-plane and apical Ru-O bond lengths of the RuO_6 octahedra, respectively. $B > 0$ when the average $\frac{r_x + r_y}{2}$ of the in-plane Ru-O bond lengths is smaller than the apical one, i.e. in the case of elongation of the octahedral cage, while $B < 0$ in the opposite case of octahedral compression. It should be noted that, while r_x and r_y shall be referred to as *in-plane* lengths, the corresponding Ru-O bonds do not lie in the **ab** plane in the general case of finite octahedral tilt.

- Ru-O-Ru bond angle $\alpha_{\text{Ru-O-Ru}}$. $\alpha_{\text{Ru-O-Ru}}$ decreases with respect to the perfect perovskite structure ($\alpha_{\text{Ru-O-Ru}} = 180°$) as the RuO_6 octaedra are rotated along an axis parallel to the apical Ru-O bond direction.

- octahedral tilt angle α_{tilt} away from the crystallographic **c** axis. $\alpha_{\text{tilt}} = 0°$ in the perfect perovskite structure.

At T = 10 K, the unit cell of the parent compound at low temperature is orthorhombic, with a b lattice parameter elongated by about 4.4% with respect to a. Large distortions away from the perfect perovskite structure are also present: the RuO_6 octahedra are significantly compressed along the local z axis ($B < 0$) and display both a sizeable rotation around the apical Ru-O bond direction and tilt away from the **c** axis [Fig. 4.1(a)]. La substitution is found to cause a reduction of the orthorhombicity of the unit cell ($A \to 0$), in agreement with a previous study [179], and an elongation of the octahedral cage ($B > 0$). This results in the phase diagram of Fig. 4.12(a), where, for increasing doping levels, the system evolves from an orthorhombic cell with compressed octahedra ($x = 0, 0.05$) to a quasi-tetragonal cell with elongated ones ($x = 0.07, 0.12$). Doping also reduces the rotations of the octahedral cage and causes the structure to relax towards the undistorted perovskite lattice. This is clearly evidenced by the increase in the Ru-O-Ru bond angle and the reduction of the octahedral tilt reported in Fig. 4.12(b). The parent compound refinement at T = 300 K also reveals that the crystal structure is extremely sensitive to the temperature in the S-*Pbca* phase. In particular, analogous to the effect seen with doping, both the octahedral compression and rotations are strongly reduced upon warming to room temperature.

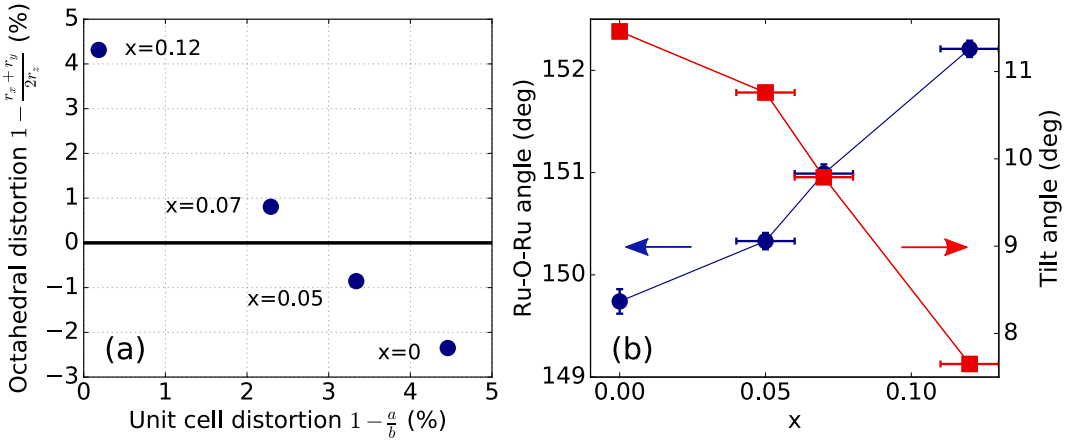

Figure 4.12: Structural changes of $Ca_{2-x}La_xRuO_4$ as a function of doping at T = 10 K. (a) Phase diagram as a function of the RuO_6 octahedra distortion $1-\frac{r_x+r_y}{2r_z}$ (with $r_{x,y}$ and r_z in-plane and apical Ru-O bond length, respectively) and unit cell distortion $1-\frac{a}{b}$ (a,b in-plane lattice parameters of the *Pbca* unit cell). The horizontal line separates the regions corresponding to octahedral compression ($1-\frac{r_x+r_y}{2r_z}<0$) and elongation ($1-\frac{r_x+r_y}{2r_z}>0$). (b) Ru-O-Ru bond angle (circles) and RuO_6 octahedra tilt angle away from the **c** axis (squares) as a function of the La content. The horizontal error bars reflect the uncertainty in the doping level measured by means of EDX.

In marked contrast to the behaviour observed in the insulating region of the phase diagram, Table 4.1 reveals that the crystal structure is almost completely insensitive to the La content and the temperature in the metallic L-*Pbca* phase. The trends just discussed are consistent with the results from the O K-edge absorption measurements outlined in Sec. 4.6.

4.5 Impact of La doping on the low-temperature magnetic structure studied by REXS

The work presented in this section has been published as "*Persistence of antiferromagnetic order upon La substitution in the* $4d^4$ *Mott insulator* Ca_2RuO_4" by D. Pincini, S. Boseggia, R. Perry, M.J. Gutmann, S. Riccò, L.S.I. Veiga, C.D. Dashwood, S.P. Collins, G. Nisbet, A. Bombardi, D.G. Porter, F. Baumberger, A.T. Boothroyd and D.F. McMorrow, Physical Review B **98**, 014429 (2018) [210].

The impact of La substitution on the magnetic ground state of the parent compound was investigated by means of REXS at the Ru L_3 and L_2 absorption edges. The REXS measurements were performed using the 6-axis kappa diffractometer

at the I16 beamline of the DLS (see Sec. 2.1.1.3). The scattered signal of several space-group forbidden reflections was measured tuning the incident X-rays energy to the Ru L_3 ($E = 2.838$ keV) and L_2 ($E = 2.967$ keV) absorption edges by means of a channel-cut Si (111) crystal. Experiments at the Ru L edges are particularly problematic from a technical point of view as they fall into the "tender" region of the X-ray spectrum. This corresponds to energy values significantly lower than the ones at which most hard-X-ray diffraction beamlines operate. At I16, this energy window can be covered by using the monochromator in a non-standard four-bounce mode and by taking extra-care to minimize air absorption. The data were collected in vertical scattering geometry, using σ incident polarisation (see Sec. 2.1.1). The samples were mounted with the **c** axis of the *Pbca* structure in the scattering plane for $\chi = 90°$; different values of the sample azimuth ψ were used, where $\psi = 0°$ corresponds to having **b** in the scattering plane. Polarisation analysis of the diffracted beam was achieved by means of a PG (002) crystal in 90°-scattering geometry placed upstream with respect to an APD detector. This provided a scattering angle of $\theta = 40.66°$ and $\theta = 38.51°$ at the L_3 and L_2 edge, respectively. The total scattered intensity was measured using the beamline Pilatus 100K area detector. The latter was operated in ultra-high gain mode, since the energy values used for the experiment are right at the limit of the detector detection window. The samples were cooled down below the Néel transition temperature by means of the closed-cycle cryostat, while focusing of the incident beam was achieved to $\approx 250(V) \times 250(H)\,\mu m^2$ at the Ru L edges by use of the horizontally deflecting cylindrical and bending mirrors.

AFM reflections		Weak FM reflections ($\phi \neq 0°$)
A-centred mode	B-centred mode	A-centred mode
(100)	(010)	(001)
(011)	(101)	(003)
(013)	(012)	(110)
(120)	(103)	(201)
	(014)	(005)

Table 4.2: Space-group forbidden magnetic reflections arising from the main AFM order of the two magnetic modes in Ca_2RuO_4 [172] [see Fig. 4.1(b)] and from the canting ϕ of the magnetic moments in the A-centred magnetic structure.

As already mentioned in Sec. 4.2, the magnetic structure of Ca_2RuO_4 can be described in terms of the A-centred and B-centred magnetic modes shown in Fig. 4.1(b). The two modes correspond to two of the four irreducible representations

allowed by symmetry for space group *Pbca* with propagation vector $\mathbf{k} = (0,0,0)$ (see Appendix B.2). In particular, mode A and B correspond to the irreducible representations Γ_1 and Γ_3, respectively. Although the latter allow a finite magnetic moment component along the crystallographic **c** axis[10], the measurements here discussed are consistent with moments confined in the **ab** plane as reported by Braden *et al.* [172] and Zegkinoglou *et al.* [186] and shown in Fig. 4.1(b). In this case, the two magnetic modes give rise to the two separate sets of AFM space-group forbidden reflections listed in Table 4.2: the two modes can then be selectively accessed in a scattering experiment by measuring the magnetic signal at one of the corresponding (hkl) values. The AFM reflections of Table 4.2 arise from the **b**-axis AFM order and are thus expected to host a finite intensity even in the case of a collinear structure with vanishing canting angle. However, the AFM coupling of the canting-induced net magnetisation between consecutive RuO_2 layers in the globally AFM A-centred structure [Fig. 4.1(b)] results in additional FM reflections. The latter scale with the magnitude of the canting angle ϕ and are thus expected to be weak for small values of ϕ; in particular, they vanish for perfectly antiparallel moments ($\phi = 0°$). The canting of the moments does not give rise to additional magnetic reflections in the weakly FM B-centred structure since the resulting net magnetisation is coupled ferromagnetically between consecutive layers.

In contrast to the previous REXS study on the parent compound [186], where the $(1\,0\,0)$ magnetic reflection was probed, the present scattering geometry limited the investigation to the magnetic diffraction peaks with a non-zero l component [i.e. of the type $(h0l)$ or $(0kl)$]. The energy dependence of the $(0\,1\,3)$ magnetic peak (A-centred mode) in the parent compound is shown in Fig. 4.13. As already reported by Zegkinoglou *et al.* [186], a strong resonant enhancement of the diffracted intensity is present at both the Ru L_3 and L_2 absorption edges. The resonance originates from electric dipole $2p \rightarrow 4d$ transitions which directly probe the partially filled Ru $4d$ states responsible for magnetism. Each resonance displays two distinct features residing at $E = 2.8383(2), 2.8417(2)$ keV (L_3) and $E = 2.9674(2), 2.9721(2)$ keV (L_2), which arise from transitions to the crystal-field-split t_{2g} and e_g Ru $4d$ orbitals, respectively [186].

All magnetic resonances displayed in this section have been corrected for self-absorption. The corrected resonance is obtained by multiplying the raw intensity by $\mu(E)\left(1+\frac{\sin\alpha}{\sin\beta}\right)$, where $\mu(E)$ is the energy-dependent absorption coefficient at the absorption edge of interest and α (β) is the angle between the incident (diffracted) X-ray beam and the sample surface. $\mu(E)$ was measured at the

[10] A small **c**-axis component has been indeed recently reported in pure Ca_2RuO_4 [212].

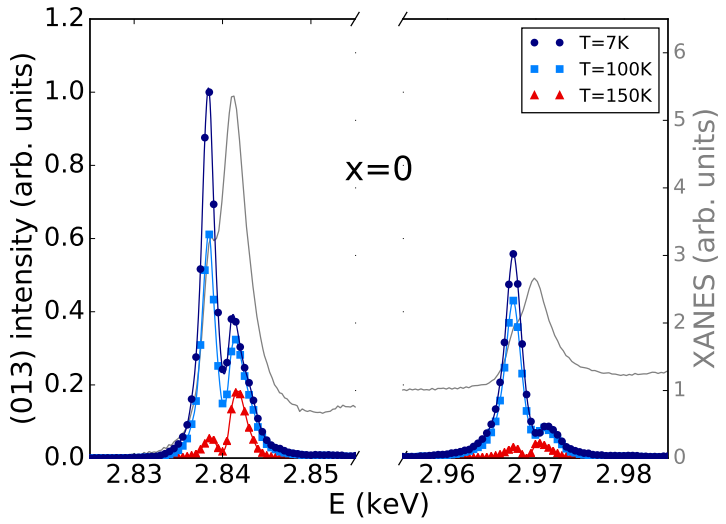

Figure 4.13: Ru L_3 and L_2 energy resonances of the $(0\,1\,3)$ magnetic diffraction peak at different temperatures across the Néel transition in the undoped sample. The filled symbols refer to the total scattered intensity measured at $\psi = 0^\circ$ corrected for self-absorption and normalized to the L_3 peak intensity. The solid lines represent a quadratic interpolation to the data points and are meant just as a guide to the eye. The normalized XANES used for the self-absorption correction is also shown.

ID12 beamline of the ESRF. XANES data were collected on powder pellets of $Ca_{2-x}La_xRuO_4$ by measuring the sample drain current (TEY detection mode) as the energy of the incident beam was scanned across the Ru L_3 and L_2 absorption edges. The absorption spectra are shown in Fig. 4.13, while further details on the absorption measurements can be found in Sec. 4.7. Given the low energy of the X-ray beam, the measured scattered intensity was further corrected by the energy-dependent absorption of the different mediums along the beam path between the last beam intensity monitor and the detector. These include several Kapton, SiN_3 and Beryllium windows, the Beryllium dome of the closed-cycle cryostat and ≈ 6 cm of ambient pressure air path. The quantum efficiency of the Pilatus detector had also to be taken into account, as it strongly depends on the photon energy in the tender X-ray region. While the above-mentioned beam-path correction can be normally neglected at higher energy, in this case it significantly impacts the relative resonant enhancement at the Ru L_3 and L_2 absorption edges.

The $(0\,1\,3)$ signal is largely magnetic in origin as demonstrated by its temperature (Fig. 4.14), polarisation [Fig. 4.15(a)] and azimuthal (Fig. 4.16) dependences. In particular, the signal vanishes around $T_N \approx 110$ K in agreement with previous reports [172, 186] and the bulk magnetisation measurements of Fig. 4.10(a), and is predominantly π' polarised, as expected for XRMS (see Sec. 2.1.1.2). Moreover,

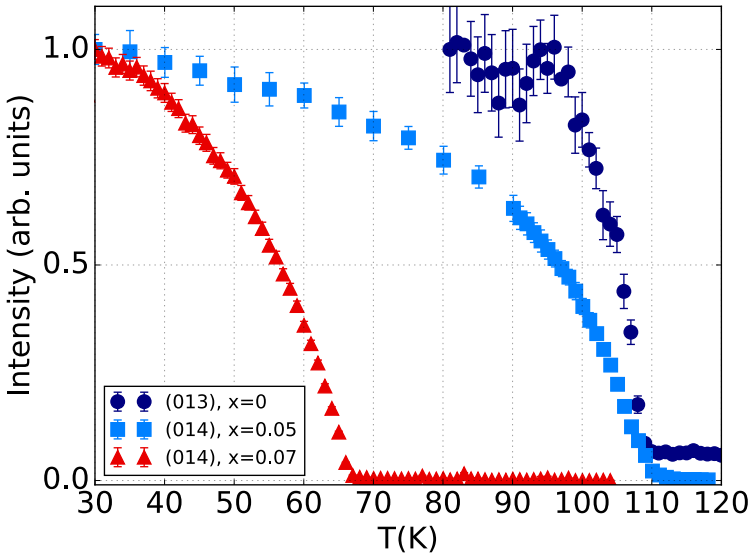

Figure 4.14: Temperature dependence of the $(0\,1\,3)$ (dark blue circles) and $(0\,1\,4)$ magnetic diffraction peaks in the undoped and $x = 0.05$ (light blue squares), $x = 0.07$ (red triangles) samples, respectively. The data points correspond to the total diffracted intensity integrated over a rocking curve at $E = 2.838$ keV and $\psi = 0°$ and normalized to the low temperature value.

the measured azimuthal dependence is consistent with the calculations (solid grey line in Fig. 4.16) performed assuming the **b**-axis AFM order[11] of Fig. 4.1(b) [172]. The weak diffracted signal observed above the Néel temperature (see blue circles in Fig. 4.14) can be attributed to a small contribution from anisotropic tensor of susceptibility (ATS) scattering, a weak scattering process arising from the anisotropy of the X-ray susceptibility tensor [213] (see Appendix B.1). A significant intensity for $T > T_N$ was indeed reported for the $(1\,0\,0)$ and $(1\,1\,0)$ space-group forbidden reflections by Zegkinoglou *et al.* [186], who attributed it to orbital ordering of the Ru t_{2g} electrons[12] characterised by the same propagation vector as the magnetic order. ATS scattering might also be responsible for the residual intensity in the σ-σ' polarisation channel [Fig. 4.15(a)]. The latter is also partially accounted for by the leakage from the σ-π' channel, caused by the fact that the scattering angle of the analyser crystal was not exactly 90°.

As well as the $(0\,1\,3)$, a large energy resonance was also found for the $(0\,1\,1)$ A-centred reflection with a similar L_3/L_2 intensity ratio. Several B-centred peaks

[11] It should be noted that the azimuthal dependence does not depend on the particular value of the canting angle chosen for the calculations (apart from a small scale factor) and is not modified by the inclusion of a finite **c** axis component.

[12] The origin of the orbital ordering was identified in the cooperative tilt of the RuO_6 octahedra, similar to what was reported by Nakao *et al.* [214] in $YTiO_3$. A detailed investigation of the orbital ordering has been recently provided by Porter *et al.* [212], which partially challenged the previously accepted interpretation.

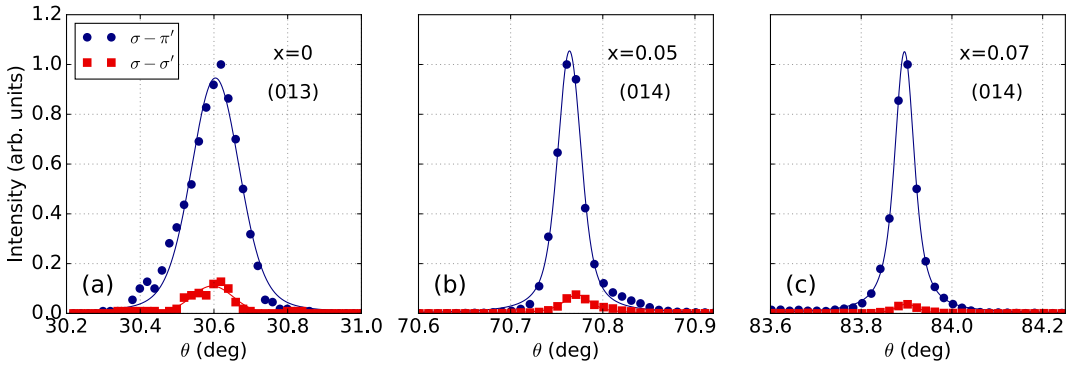

Figure 4.15: Polarisation dependence of magnetic diffraction peaks in the (a) undoped, (b) $x = 0.05$ and (c) $x = 0.07$ samples at $T = 7 - 8$ K. The filled symbols refer to the scattered intensity measured over a rocking scan in the σ-π' (blue circles) and σ-σ' (red squares) channels of the polarisation analyser crystal normalized to the σ-π' peak intensity, while the solid lines represent a fit to Voigt profile. The data were collected at $E = 2.838$ keV and $\psi = 110°, 50° 30°$ for $x = 0, 0.05, 0.07$, respectively.

(Table 4.2) were also investigated at various sample azimuth values, but no significant diffracted intensity was detected in the parent compound. This is clearly shown in Fig. 4.17(a), where the $(0\,1\,3)$ and $(0\,1\,4)$ self-absorption corrected Ru L_3 resonances at low temperature are reported on the same scale. The $(0\,1\,4)$ intensity is negligible and mostly resonates at the e_g levels energy, thus suggesting that the signal is dominated by weak ATS scattering. This is consistent with previous neutron scattering measurements [172, 188], which found a prevalence of the A-centred mode.

In order to verify whether the magnetic structure of the parent compound is retained upon La substitution, several A-centred and B-centred magnetic reflections were probed in the doped samples. A significant diffracted intensity was found at the same $\mathbf{k} = (0,0,0)$ reflections. However, in stark contrast to the undoped crystal, a large resonance at the t_{2g} energy is present for the B-centred peaks only [Figs. 4.17(b),(c)]. The B-centred resonances display similar features to the A-centred ones in the parent compound, as illustrated in Fig. 4.18 for the $(0\,1\,4)$ reflection. In particular, a double peak arising from transitions to the t_{2g} and e_g states is present at both the Ru L_3 and L_2 edge.

The magnitude of the resonant enhancement carries important information on the resonating atom electronic structure. A prominent example is provided by iridium oxides with the perovskite structure, where the lack of an L_2 resonance constitutes evidence of strong SOC in the Ir $5d$ band [215–217]. The resonances of Figs. 4.13 and 4.18 seem to suggest that, while the resonant enhancement at the two edges for $x = 0.05$ is comparable to the one observed in the parent case, a weaker L_2 resonance is present in the $x = 0.07$ sample. However, similar measurements

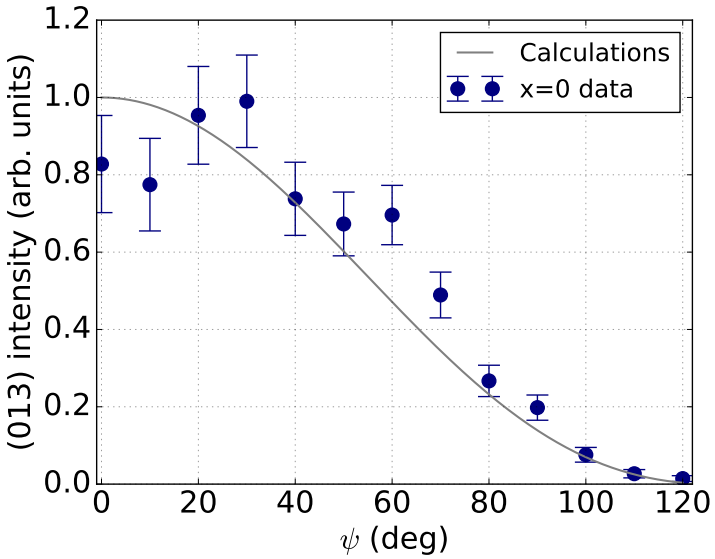

Figure 4.16: Azimuthal dependence [azimuthal reference $(0\,1\,0)$] of the $(0\,1\,3)$ magnetic diffraction peak in the undoped sample at T = 8 K. The filled symbols refer to the scattered intensity integrated over a rocking curve at $E = 2.838$ keV corrected for the geometry-dependent self-absorption factor. The solid lines represent the calculated azimuthal dependence (except for an arbitrary scale factor) assuming the C-AFM structure with **b**-axis moments reported by Braden *et al.* [172]. The intensity is normalized to the calculated value at $\psi = 0°$.

performed at the $(1\,0\,3)$ magnetic peak resulted in an L_2 resonance of comparable magnitude to the one reported for the $(0\,1\,4)$ at lower doping. In general, sizeable variations were observed in all samples for measurements collected at different reflections or different sample azimuths at fixed (hkl). The L_3/L_2 resonant ratio is not expected to depend on the particular azimuth or magnetic reflection used for the measurements once the geometry-dependent self-absorption correction already mentioned is applied to the energy resonances. Nonetheless, the simple geometrical factor $1+\frac{\sin\alpha}{\sin\beta}$ considered in the present work is strictly valid only for a perfectly flat sample surface: any deviation from this ideal case will result in a residual impact of self-absorption in the measured data, thus giving rise to slightly different resonant enhancements depending on the specific geometry used. Residual ATS scattering intensity might also contribute to the overall variability.

The L_3/L_2 intensity ratio extracted from measurements performed at different magnetic reflections and azimuth values in each sample is shown in Fig. 4.19 as a function of doping. The resonant enhancement at each edge has been extracted by fitting the corresponding energy dependence of the diffracted intensity to a double

Lorentzian peak modelling the t_{2g} and e_g features[13]. The error bars reflect the variability (quantified as the sample standard deviation) resulting from measurements collected for different ψ and/or (hkl) values. Contrary to the case of iridium oxides, a strong resonance is present at both edges. The L_3 resonance is roughly twice as large as the L_2 one in the $x = 0$ and $x = 0.05$ sample, while a larger ratio seems to be present for $x = 0.07$. The interpretation of the measured ratio is more complicated than in the case of Ir^{4+} compounds ($5d^5$), since two holes are present in the Ru $4d$ band: a simple picture based on single-particle electronic levels cannot be used. A quantitative modelling of the resonant enhancement, which goes beyond the purpose of the present work, will require *ab-initio* calculation accounting for multiple-particle effects. Despite the large variability seen between the resonant enhancement of the $(0\,1\,4)$ and $(1\,0\,3)$ magnetic reflections, the measurements suggest that La substitution might lead to an increased L_3/L_2 ratio in the $x = 0.07$ compound. The magnitude of the energy resonance depends on the Ru^{4+} electronic levels in proximity of the Fermi energy: a smaller enhancement at the L_2 edge might then be due to variations in the electronic structure caused by the doping-induced structural changes discussed in Sec. 4.4.2. This is somewhat consistent with the XANES measurements reported in Sec. 4.6, where doping was indeed found to alter the t_{2g} orbital contribution to the Ru^{4+} ground-state wave function.

In addition to the resonant enhancement, the magnetic origin of the $\mathbf{k} = (0,0,0)$ space-group forbidden reflections in the doped samples is strongly supported by the fact that (i) the scattered intensity vanishes upon warming beyond $T_N \approx 110$ K ($T_N \approx 70$ K) in the $x = 0.05$ ($x = 0.07$) sample (Fig. 4.14) and (ii) the scattered signal is predominantly π' polarised [Figs. 4.15(b),(c)] regardless of the X-ray energy and ψ value chosen for the measurements. As for the parent compound, the weak intensity in the σ-σ' polarisation channel is due to leakage from the σ-π' channel and a residual contribution of σ'-polarised ATS scattering. The transition temperature measured at AFM reflections is lower than the one observed in the FC magnetisation measurements of Fig. 4.10(a) and seems to be closer to the maximum of the ZFC curves. Moreover, the azimuthal dependence of the $(0\,1\,4)$ [Fig. 4.20(a)] and $(1\,0\,3)$ [Fig. 4.20(b)] reflections is consistent with the calculations performed assuming the B-centred AFM structure reported in Fig. 4.1(b).

The B-centred mode in the doped samples was found to be predominant across the whole crystal without any significant spatial dependence. This is shown in the

[13] It should be noted that the L_3/L_2 ratio absolute values here reported might be affected by a non-negligible systematic error. This is because the beam-path absorption correction mentioned earlier in this section strongly depends on the length of the air path and the thickness of the various windows. Although these were measured during the experiment, their accuracy might not be sufficient to obtain a precise quantitative estimation.

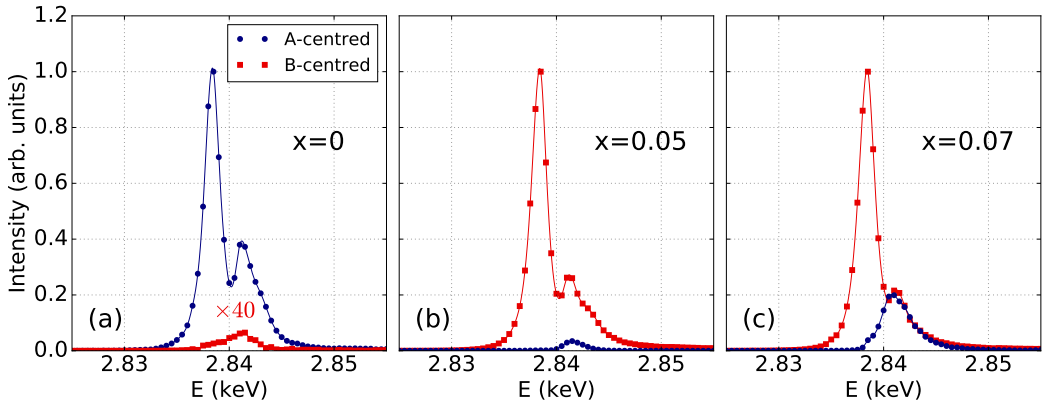

Figure 4.17: Comparison between the $(0\,1\,3)$ (blue circles) and $(0\,1\,4)$ (red squares) Ru L_3 resonances in the (a) undoped, (b) $x = 0.05$ and (c) $x = 0.07$ sample. The filled symbols refer to the total scattered intensity at $T = 7 - 8$ K corrected for self-absorption and normalized to the peak intensity of the dominant mode. The solid lines represent a quadratic interpolation to the data points and are meant just as a guide to the eye. The data were measured at $\psi = 0°$, apart from the $(0\,1\,4)$ in the undoped sample, for which $\psi = 80°$.

colour maps of Fig. 4.21, where the spatial dependence of the $(0\,1\,4)$ magnetic peak in the $x = 0.05$ crystal is reported along with the one of the $(0\,0\,4)$ Bragg peak. The measurements were performed translating the sample under the beam focal spot and collecting a rocking scan in each position. The size of the incident beam was reduced to 0.1×0.1 mm^2 through a set of slits. The $(0\,1\,4)$ intensity shows limited variations throughout the measured sample area, with minor changes resulting from trivial inhomogeneities in the crystal quality across the sample [as can be seen from the comparison to the $(0\,0\,4)$ map]. This excludes the presence of phase-separated domains of prevalent A or B character.

Discussion

The results just outlined clearly show that the doped samples retain the same $\mathbf{k} = (0,0,0)$ C-AFM structure of the parent compound. In particular, as shown by the azimuthal dependence of Fig. 4.20, the Ru^{4+} moments preserve their **b** alignment. The impact of La substitution is limited to a suppression of the globally AFM A-centred mode, predominant in the parent compound, and a concomitant stabilisation of the B-centred structure, where a weak net magnetisation is present as a result of the FM alignment of the canting-induced net moments. A similar effect has been reported both in $Ca_{2-x}Sr_xRuO_4$ [198] and Ca_2RuO_4 under pressure [188]. Contrary to the La case, Sr and Ca are both divalent. Sr doping thus only realises a bandwidth control of the parent insulator, due to the different radii of the Sr^{2+} ($r = 1.31$ Å) and Ca^{2+} ($r = 1.18$ Å) ions [208]. Moreover, the internal chemical pressure

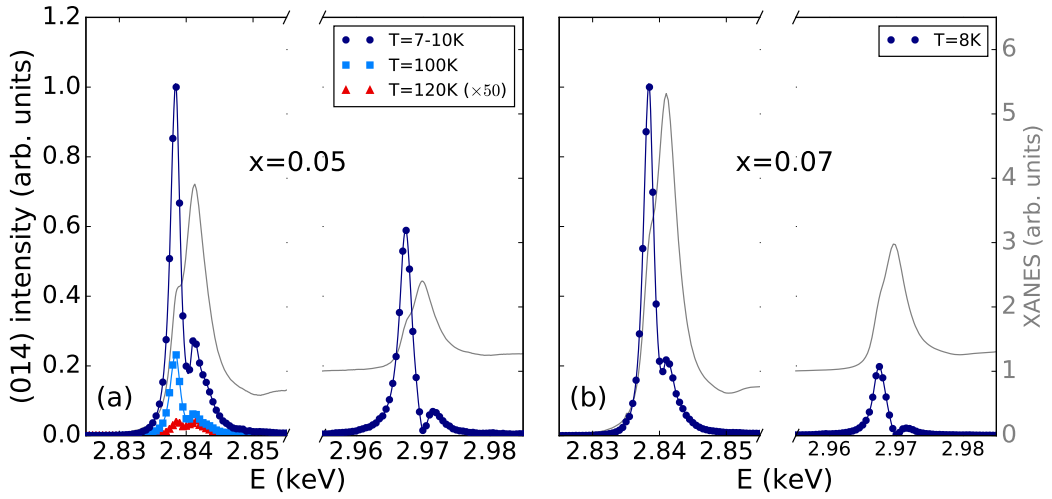

Figure 4.18: Ru L_3 and L_2 energy resonances of the $(0\,1\,4)$ magnetic diffraction peak at different temperatures across the Néel transition in the (a) $x = 0.05$ and (b) $x = 0.07$ sample. The filled symbols refer to the total scattered intensity corrected for self-absorption and normalized to the L_3 peak intensity for each sample. The solid lines represent a quadratic interpolation to the data points and are meant just as a guide to the eye. The data were measured at $\psi = 0°$ for $x = 0.05$ at T = 100, 120 K, while the low temperature $x = 0.05$ and $x = 0.07$ data sets correspond to an average of the spectra collected in the range $\psi = 0 - 60°$ and at $\psi = 0°, 30°$, respectively. The normalized XANES used for the self-absorption correction is also shown.

originating from Sr doping and the application of external pressure have similar structural effects [188]. The latter also resemble the neutron scattering results of Sec. 4.4.2 and therefore strongly suggest that the changes in the crystal structure may be responsible for the observed transition from A- to B-type order. In this respect, the evolution of the Ru-O-Ru bond angle upon doping could be of particular importance since it directly controls the oxygen-mediated superexchange between Ru atoms [218]. This could favour the FM alignment of the net moments and might be one of the mechanisms involved in the stabilisation of the B-centred structure. As I will show in Sec. 4.6, the doping-induced structural changes were also found to impact the ground-state wave function of the Ru^{4+} ion. The latter consists of an admixture of *xy*, *yz* and *zx* orbitals, whose respective contribution depends on the relative strength of the tetragonal crystal field Δ and SOC λ [178, 185, 187, 196, 205, 219, 220]. The tuning of the crystal field caused by the elongation of the RuO_6 octahedra [Fig. 4.12(a)] results in an enhanced *xy* hole occupancy in the doped compounds with respect to the parent case. An analogous scenario is also realized in $Ca_{2-x}Sr_xRuO_4$. Here, the orbital degeneracy control achieved by Sr doping shifts the Ru 4*d* *xy* bands towards the Fermi level and turns the AFM exchange of the parent compound into a FM one at $x_c = 0.5$ [196]. A similar effect might be present

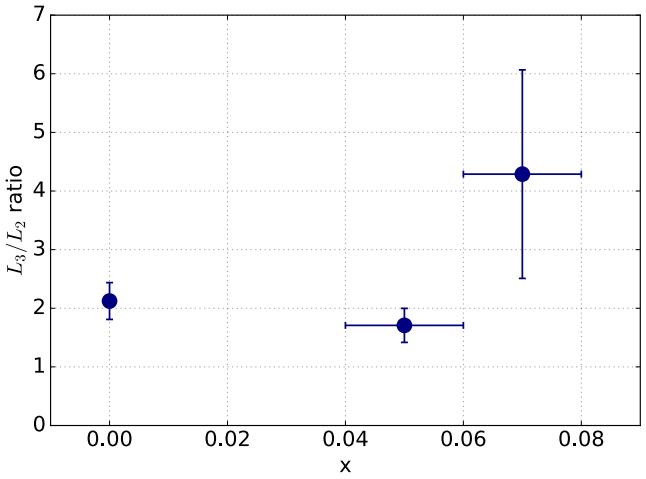

Figure 4.19: Intensity ratio of the Ru L_3 and L_2 energy resonance of magnetic diffraction peaks as a function of the La content. The values were extracted through a fit of the L_3 and L_2 resonances to a double Lorentzian peak modelling the t_{2g} and e_g features. The data points represent the average between (i) the values extracted from the $(0\,1\,3)$ (Fig. 4.13) and $(0\,1\,1)$ resonances in the parent compound; (ii) the $(0\,1\,4)$ resonances measured at different azimuth values ($\psi = 0 - 60°$) in the $x = 0.05$ sample and (iii) the $(0\,1\,4)$ resonances measured at $\psi = 0°, 30°$ and the $(1\,0\,3)$ resonance in the $x = 0.07$ sample. The vertical error bars reflect the variability ($\pm 1\,\sigma$ intervals) in the ratio measured for the different magnetic reflections and/or azimuth values.

also in the case of La doping and contribute to the stabilisation of the B-centred structure.

Hartree-Fock calculations [185, 220] predicted that the increase in the *xy* hole population driven by tetragonal elongation should result into a **c** alignment of the Ru magnetic moments. The presence of a small finite **c** component, which is allowed by symmetry (see Appendix B.2), cannot be completely excluded by the measurements presented in this section. As mentioned earlier, this is due to the fact that the scattered intensity would show an analogous azimuthal dependence to the one of Fig. 4.20 even in the case of a non-zero component along the **c** axis. However, a spin-flop transition to a **c**-axis AFM structure in the tetragonally elongated $x = 0.07$ sample is not compatible with the experimental observations. A **c**-axis AFM ordering for the irreducible representation Γ_3 responsible for mode B would imply a moment arrangement of the type $\boldsymbol{\mu}_1 = (0,0,-z)$, $\boldsymbol{\mu}_2 = (0,0,z)$, $\boldsymbol{\mu}_3 = (0,0,-z)$ and $\boldsymbol{\mu}_4 = (0,0,z)$ for the Ru atoms at positions $\mathrm{Ru}_1 : (0,0,0)$, $\mathrm{Ru}_2 : (1/2,0,1/2)$, $\mathrm{Ru}_3 : (0,1/2,1/2)$ and $\mathrm{Ru}_4 : (1/2,1/2,0)$, respectively. In this case, the intensity of the B-centred reflections of Table 4.2 would vanish, in clear contrast to what was observed in the measurements. The latter cannot be accounted for even assuming the persistence of the A-centred mode in the doped compounds with moments pointing along the **c** axis. The irreducible representation Γ_1 would, in this

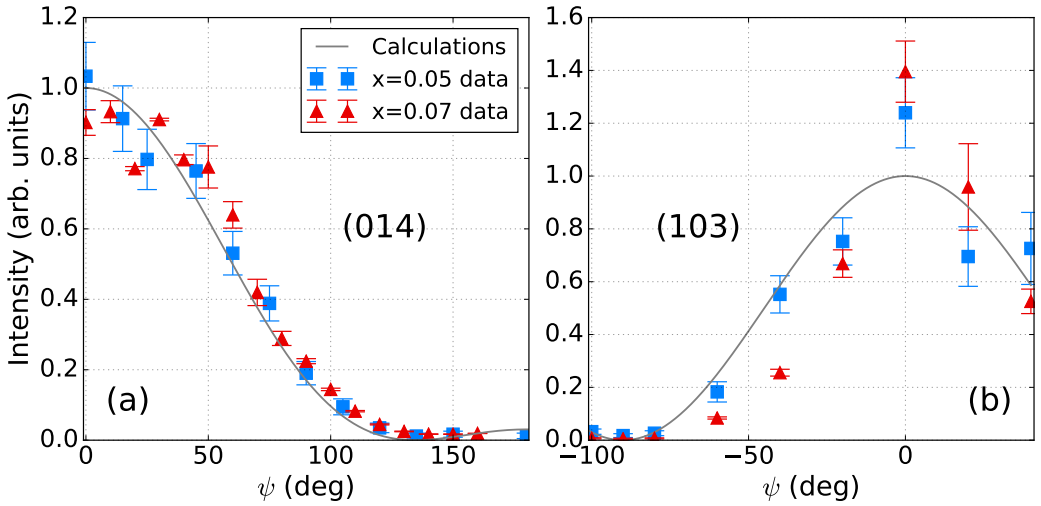

Figure 4.20: Azimuthal dependence [azimuthal reference $(0\,1\,0)$] of the (a) $(0\,1\,4)$ and (b) $(1\,0\,3)$ magnetic diffraction peaks in the doped samples at $T = 7-10$ K. The filled symbols refer to the scattered intensity integrated over a rocking curve at $E = 2.838$ keV corrected for the geometry-dependent self-absorption factor. The solid lines represent the calculated azimuthal dependence (except for an arbitrary scale factor) assuming the C-AFM structure with **b**-axis moments reported by Braden *et al.* [172]. The intensity is normalized to the calculated value at $\psi = 0°$.

case, corresponds to a magnetic order of the type $\boldsymbol{\mu}_1 = (0,0,-z)$, $\boldsymbol{\mu}_2 = (0,0,-z)$, $\boldsymbol{\mu}_3 = (0,0,z)$ and $\boldsymbol{\mu}_4 = (0,0,z)$. This gives rise to a finite scattered intensity for the $(0\,1\,4)$ and $(1\,0\,3)$ reflections, but with azimuthal dependences completely different[14] to the ones shown in Fig. 4.20. In general, when a finite component of the magnetic moments along **c** is included, each one of the two magnetic modes will contribute to the scattered intensity of both the A-centred and B-centred reflections listed in Table 4.2. This, however, does not affect the validity of the present conclusion on the doping-induced suppression of mode A. As just discussed, the azimuthal dependence of B-centred reflections arising from the A-centred aligned moments with a finite **c** component would significantly differ from the one of Fig. 4.20.

The evolution from A- to B-type magnetic order naturally explains the FM behaviour seen in the bulk magnetisation measurements [179–181] (see Sec. 4.4.1) as resulting from the weak FM component of the B-centred C-AFM mode, rather than a doping-induced local FM alignment (FM polarons) of Ru moments [180, 181]. This is consistent with the interpretation given by Fukazawa and Maeno [179] based on their SQUID data. Given their sensitivity to the macroscopic magnetisation of the sample, bulk measurements alone are not capable of unequivocally distinguish-

[14] Considering the $(0\,1\,0)$ direction as azimuthal reference, the corresponding azimuthal dependence has a maximum at $\psi = 180°$ and a minimum at $\psi = 0°$.

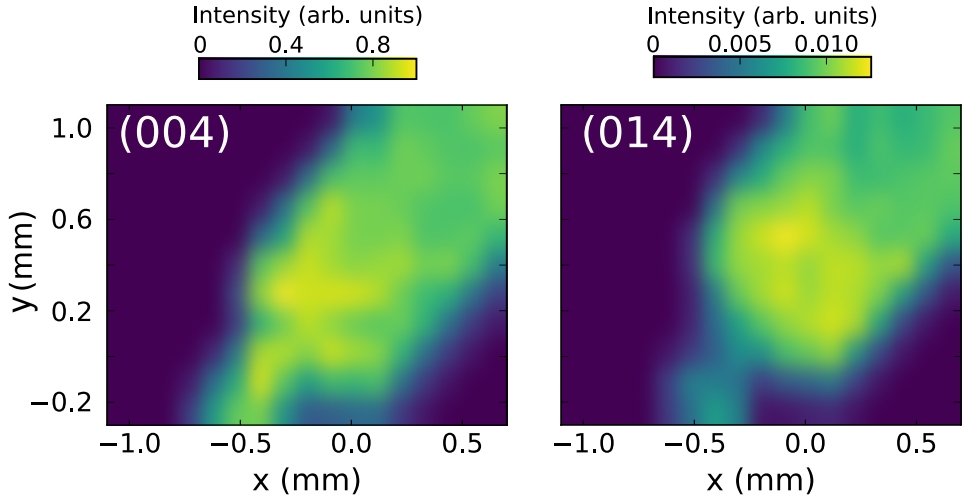

Figure 4.21: Intensity maps of the (004) Bragg peak and (014) magnetic reflection (T = 8 K, $\psi = 0°$) in the $x = 0.05$ sample as a function of the incident X-ray beam position on the crystal (beam size 0.1×0.1 mm^2). The colour scale represents the integrated intensity over a rocking scan measured in each position normalized to the (004) peak value (the dark regions are off the sample).

ing between the two scenarios: similar results are indeed expected regardless of whether the magnetisation arises from a FM ordering with a small ordered moment or an AFM structure with a weak net magnetisation due to moments canting. A further confirmation comes from the measurements performed on non-stoichiometric $Ca_2RuO_{4+\delta}$ [172]. Here, a B-type C-AFM structure was also found and the bulk magnetisation shows similar features to the ones of the La-doped compounds. The increase in the net moment seen for increasing levels of La content [180] is also compatible with the C-AFM scenario, where it could arise from an increase of either the B-centred mode volume fraction or the DMI-induced canting angle. However, minor changes in the magnitude of the latter could not be investigated since the resulting weak FM component, contrary to the case of the A-centred mode, does not give rise to any space-group forbidden reflections[15].

Although most of the literature on $Ca_{2-x}La_xRuO_4$ focuses on the filling control of the Ru 4*d* bands associated with the extra electron introduced by the La^{3+} ion [168, 179–181], the findings presented in this section show that the concomitant structural effects are likely to play a crucial role in the physics of the system. This scenario is somewhat confirmed by recent resistivity and ARPES measurements on Pr-doped Ca_2RuO_4 [177], which suggest that, in contrast to lightly doped cuprates [221] and iridates [222, 223], the doped electrons remain fully localised in the S-*Pbca* phase irrespective of the Pr content. A pronounced sensitivity to the doping-

[15] If this was the case, the magnitude of the canting angle could be estimated by the intensity ratio between the weak FM reflections and the ones arising from the main AFM order.

induced structural changes is also expected in light of the importance of lattice energies in the stabilization of the low-temperature insulating state highlighted by recent *ab-initio* calculations in the parent compound [176].

Nonetheless, $Ca_{2-x}La_xRuO_4$ was explicitly identified as an example of an electron-doped system in recent theoretical calculations [168]. The latter found that the impact of the injection of free carriers on the ground state of d^4 Mott insulators dramatically depends on the interplay between the exchange interaction K, the hopping integral t_0 and the SOC constant λ. In particular, starting from the parent compound AFM ground state, a FM phase is predicted to rapidly appear upon electron doping for sufficiently weak SOC. This scenario has been explicitly supported by Chaloupka and Khaliullin [168] who, backed by the interpretation of the bulk magnetisation data given by Cao *et al.* [180], based their conclusion on previous estimates for λ [26, 185]. The measurements presented in this section, however, show that the FM phase is not realized in $Ca_{2-x}La_xRuO_4$. AFM order survives up to $x = 0.07(1)$, while the system is found to be paramagnetic at $x = 0.12(1)$. Assuming the filling of the Ru $4d$ bands is the dominant effect in the physics of La-doped Ca_2RuO_4, this sets a lower boundary to the SOC constant: considering $t_0 \approx 300$ meV [168], the FM phase is predicted to be absent for $\lambda > 77$ meV. The latter estimate is compatible with the value $\lambda \approx 200$ meV from a recent O K-edge RIXS investigation [187]. Approximating to $x = 0.10$ the value of the doping level at which the transition between the C-AFM and paramagnetic states occurs [179], the phase diagram of Ref. [168] gives $\lambda \approx 400$ meV. This is comparable to the value found for $5d$ TMOs [224] and thus seems overestimated. The theoretical phase diagram of Ref. [168], however, neglects the structural changes discussed in the present investigation (as well as distortions away from the perfect cubic symmetry of the RuO_6 octahedra and deviations from two-dimensionality) and, as a result, it does not provide an accurate description of the physics of $Ca_{2-x}La_xRuO_4$.

Summary

The REXS investigation outlined in this section establishes, for the first time, the persistence of the C-AFM structure of the parent compound in $Ca_{2-x}La_xRuO_4$. The AFM order was found to be present up to $x = 0.07(1)$, while LR order is absent in the $x = 0.12(1)$ sample. La substitution suppresses the globally AFM A-centred mode, dominant in pure Ca_2RuO_4, and favours the B-centred structure, which displays a net magnetisation as a result of the canting of the magnetic moments of the two sublattices. The experimental findings suggest that the structural changes which accompany La doping are likely to play a pivotal role in the observed mag-

netic properties and should be considered alongside the electron doping effect in any meaningful description of the physics of the system.

4.6 Evolution of the Ru^{4+} 4d orbital population upon La substitution: an O K-edge XANES study

The work presented in this section has been included in "*Tuning of the Ru^{4+} ground-state orbital population in the $4d^4$ Mott insulator Ca_2RuO_4 achieved by La doping*" by D. Pincini, L.S.I Veiga, C.D. Dashwood, F. Forte, M. Cuoco, R.S. Perry, P. Bencok, A.T. Boothroyd, D.F. McMorrow, arXiv:1810.11044 (2018) [225]. Submitted to Physical Review B.

In Sec. 4.3, I showed how the ground state of the Ru^{4+} ion in Ca_2RuO_4 is the result of the competition between the moderate SOC coupling of $4d$ electrons and the tetragonal distortion of the RuO_6 octahedra. The low-energy electronic structure is thus expected to be extremely sensitive to structural distortions acting on the local Ru^{4+} crystalline environment. The neutron diffraction measurements discussed in Sec. 4.4.2 revealed that the different radii of the La^{3+} ($r = 1.22$ Å) and Ca^{2+} ($r = 1.18$ Å) ions cause the compressed RuO_6 octahedra of pure Ca_2RuO_4 to be progressively stretched along the **c** axis for increasing doping levels. This is expected to significantly change the local physics of the Ru^{4+} ion and thus have a sizeable impact on the parent compound electronic properties. However, experimental studies on La-doped Ca_2RuO_4 reported to date have been limited to bulk measurements [179–181] and did not address in detail the impact of the structural changes on the low-energy electronic structure.

In order to investigate this point, XANES measurements were performed at the absorption branch of beamline I10 of the DLS. Absorption spectra were collected on the same single crystals used for the measurements of Sec. 4.5 by scanning the incident, circularly-polarised, X-rays ($20 \times 100\,\mu m^2$ spot size) across the O K-edge energy (543.1 eV) for different values of the angle θ_S between the incident beam and the sample surface normal in the range $0 - 70^{\circ}$. The degree of circular polarisation provided by the APPLE II helical undulator was always larger than 99% [89]. For each doping level, an equivalent data set was measured at both low (T = 10 K) and room temperature, as schematically shown by the symbols in the phase diagram of Fig. 4.22(a). The crystals were mounted on an electrically-grounded cop-

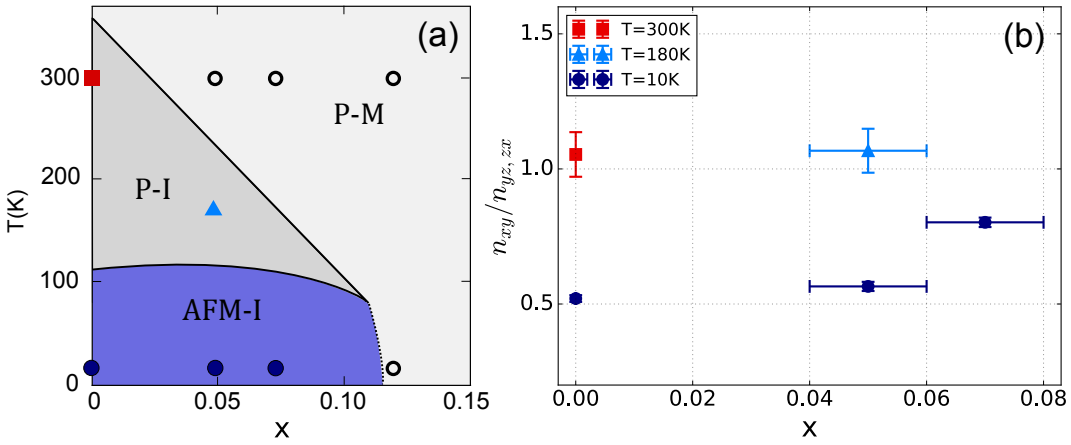

Figure 4.22: (a) $Ca_{2-x}La_xRuO_4$ temperature-doping phase diagram showing the paramagnetic metallic (P-M), paramagnetic insulating (P-I) and AFM insulating (AFM-I) phases. The filled and open symbols refer to the temperature and La content values in the insulating and metallic region, respectively, at which the XANES data were collected. The corresponding hole occupancies in the insulating phase are reported in (b) as a function of the doping level. (b) Hole occupancy ratio $n_{xy}/n_{yz,zx}$ at different temperatures as a function of the La content extracted from the angular dependence of the apical and in-plane O $2p$ - Ru t_{2g} features of the XANES spectra (see Fig. 4.24). The horizontal error bars correspond to the uncertainty in the doping level values measured through EDX. The vertical error bars at T = 180 K have been increased by 50% to include the error introduced by the bond length dependence of the hybridization strength (see discussion in the text).

per holder and inserted in the UHV sample environment with their crystallographic **c** axis aligned parallel to the incident beam for $\theta_S = 0°$. The absorption was simultaneously measured in both TEY and TFY detection mode, averaging several spectra for each θ_S value. The analysis of both sets of data led to similar conclusions and only the TEY measurements are shown in the present work[16]. Cleaving the crystals *in situ* did not result in any appreciable difference in the absorption spectra with respect to the non-cleaved ones, thus excluding any impact of surface contamination[17].

Low-temperature O K-edge spectra at normal incidence for parent Ca_2RuO_4 and the $x = 0.07$ sample are shown in Fig. 4.23. As first reported by Mizokawa *et al.* [185], the XANES signal shows several features arising from the hybridization of the O $2p$ orbitals with the Ru $4d$ t_{2g} ($E < 530$ eV), Ru $4d$ e_g (530 eV $< E <$ 535 eV) and Ca $3d$ / Ru $5s$, $5p$ ($E > 535$ eV) orbitals. La doping has a significant impact on

[16]The other reason behind the choice of presenting only the TEY data is that the TFY measurements are affected by self-absorption effects. These are generally not easy to correct for and, given the large changes in the experimental geometry that the measurements involved, are likely to have an impact on the final result.

[17]This is further confirmed by the fact that the analysis of the TFY measurements, which are more bulk sensitive than the TEY ones, led to similar results.

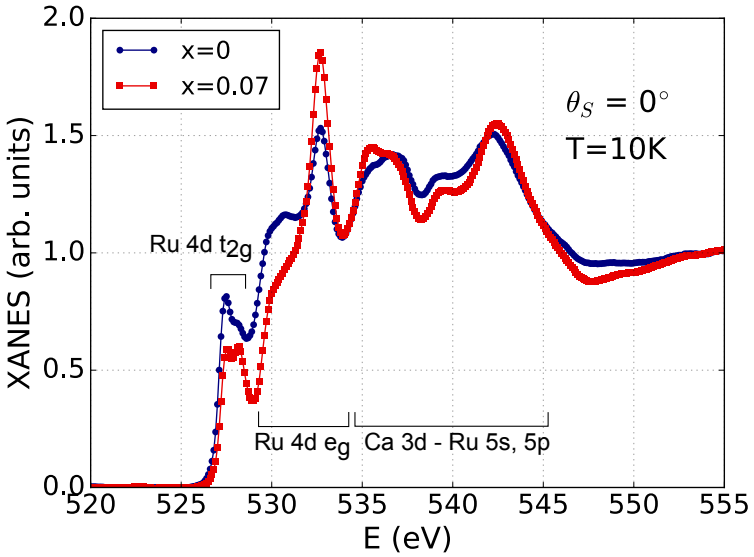

Figure 4.23: O K-edge XANES spectra for the parent (blue circles) and $x = 0.07$ (red squares) compound collected at normal incidence and low temperature. The spectra were normalized using the spectral weight at $E > 553$ eV.

the relative ratio of the different features, thus revealing the occurrence of sizeable changes in the empty density of states of the Ru^{4+} ion. In the present work, I focus the attention on the t_{2g} region of the spectrum. The latter consists of two separate features centred around $E \approx 527.5$ eV and $E \approx 528.2$ eV. Following the peak assignments in pure Ca_2RuO_4 [178, 185, 187] and Sr_2RuO_4 [226, 227] and the band structure calculations in Ca_2RuO_4 [192] and Sr_2RuO_4 [228], I attribute the two features to the hybridization of the Ru t_{2g} orbitals with the apical and in-plane O $2p$ orbitals of the RuO_6 octahedra, respectively. Their relative intensity depends on the angle of incidence of the X-ray beam: this is clearly shown in Fig. 4.24, which reports spectra collected for different θ_S values in the range $0 - 70°$ at different temperatures in the parent and doped samples insulating phase [see Fig. 4.22(a)]. The in-plane/apical intensity ratio tends to increase as θ_S is increased away from normal incidence. Most importantly, doping also affects the relative ratio of the apical and in-plane features, as can be seen by simply comparing spectra collected at the same θ_S in different crystals.

A quantitative analysis of the angular dependence was achieved by fitting the low-energy region of the spectra ($E < 530$ eV) to the sum of three Gaussian peaks modelling the apical and in-plane O $2p$ - Ru t_{2g} features and the e_g region of the spectrum at higher energy (see insets in Fig. 4.24). The results of the fits for the different insulating samples at low temperature are reported in Fig. 4.25. Here, the peak integrated areas of the apical and in-plane features are shown along with their ratio. A clear evolution of the angular dependence is seen as a function of doping,

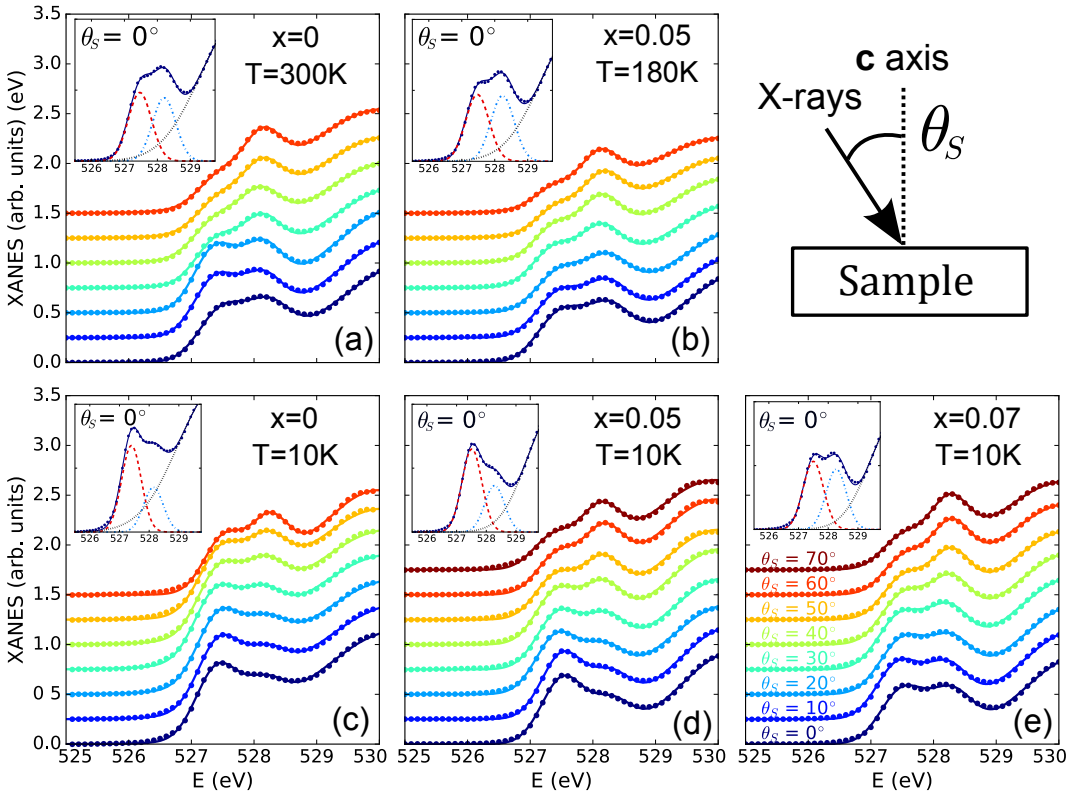

Figure 4.24: XANES spectra collected at different values of the angle θ_S between the incident X-ray beam and the sample surface normal (**c** axis) for samples with different La contents and at different temperature values within the insulating region of the phase diagram [see Fig. 4.22(a)]. Spectra at different angles were normalized using the spectral weight at $E > 553$ eV. The insets show the fit detail of the spectra measured at normal incidence ($\theta_S = 0°$). The measured absorption (filled circles) was fitted to the sum (solid line) of three Gaussian profiles modelling the apical (red dashed line) and in-plane (blue dot-dash line) O $2p$ - Ru t_{2g} features and the e_g region of the spectrum (black dotted line). The corresponding angular dependence of the apical and in-plane features integrated area at low temperature is reported in Fig. 4.25. The drawing schematically represents the experimental geometry.

with the in-plane/apical ratio increasing with the La content.

The dependence on the incident angle is determined by the dipole matrix elements of the O $1s \rightarrow 2p$ transition. Following the minimal hybridization model already exploited for Ca_2RuO_4 [185, 187], the θ_S dependence of transitions to the O $2p_x$, $2p_y$ and $2p_z$ orbitals for circularly polarised light is given by $\frac{1}{2}\cos^2\theta_S$, $\frac{1}{2}$ and $\frac{1}{2}\sin^2\theta_S$, respectively[18] [185, 229]. The $2p_{x,y}$ and $2p_z$ orbitals of the in-plane O atoms hybridize with the Ru xy and yz, zx orbitals, respectively. On the other hand,

[18]These expressions of the angular dependence of the transitions to the $2p$ orbitals are valid in the case where the crystallographic $[0\,1\,0]$ direction lies along the θ_S rotation axis [185]. However, the resulting angular dependence of the intensity of the XANES features does not depend on this assumption.

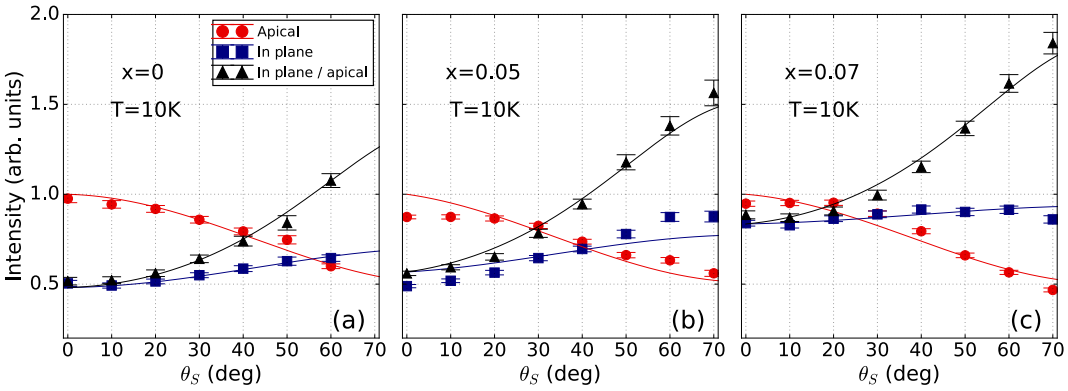

Figure 4.25: Angular dependence of the apical and in-plane O $2p$ - Ru t_{2g} features of the XANES spectra in the (a) parent, (b) $x = 0.05$ and (c) $x = 0.07$ compound at low temperature. The filled symbols were extracted through fits of the measured XANES spectra analogous to the ones shown in Figs. 4.24(c)-(e), while the solid lines correspond to the best fit to the cross sections of Eq. (4.6). The resulting $n_{xy}/n_{yz,zx}$ ratio is reported in Fig. 4.22(b).

the $2p_x$ ($2p_y$) orbital of the apical O atoms hybridizes with the Ru zx (yz) orbital. The XANES intensities of the apical (I_A) and in-plane (I_P) oxygens features for circularly polarised light are thus given by the following relations [185]:

$$\begin{aligned} I_A(\theta_S) &\propto r_A^{-3.5}\frac{1}{2}(\cos^2\theta_S + 1)n_{yz,zx} \\ I_P(\theta_S) &\propto r_P^{-3.5}\left[\frac{1}{2}(\cos^2\theta_S + 1)n_{xy} + \frac{1}{2}\sin^2\theta_S\, n_{yz,zx}\right] \end{aligned} \tag{4.6}$$

where r_A (r_P) is the apical (in-plane) Ru-O bond length and n_{xy} ($n_{yz,zx}$) is the number of holes in the Ru xy (yz, zx) orbitals. In Eq. (4.6), I assumed that the hybridization strength decays with the Ru-O bond length as $r^{-3.5}$, similar to a previous XANES investigation on the parent compound [187]. It should also be noted that the cross sections of Eq. (4.6) do not depend on the particular in-plane orientation of the crystallographic **a** and **b** axes, which was not defined in the measurements here discussed.

Considering two holes in the t_{2g} orbitals of the Ru^{4+} ion ($n_{xy} + n_{yz,zx} = 2$) and neglecting the small effect of the octahedral tilt away from the **c** axis[19], the ratio $I_P(\theta_S)/I_A(\theta_S)$ from Eq. (4.6) can be used to fit the measured angular dependences and extract the hole occupancy ratio $n_{xy}/n_{yz,zx}$. As a result of the arbitrary scale factor which relates the cross sections to the intensity derived from the XANES

[19] Eq. (4.6) does not consider the tilt of the RuO_6 octahedra [see Fig. 4.12(b)]. However, the tilt angle changes only by about 4° from the parent to the heavily doped $x = 0.12$ sample and, alone, cannot account for the significant changes in the spectra as a function of doping. Moreover, assuming the tilt θ_{tilt} enters the cross section in the form of a multiplicative factor $\cos^2\theta_{\text{tilt}}$, considering $\theta_{\text{tilt}} = 0°$ introduces an error smaller than 4% ($\cos^2\theta_{\text{tilt}} \approx 0.96$ for $\theta_{\text{tilt}} \approx 11°$).

spectra, only the ratio is accessible through a fit of the data rather than the separate quantities n_{xy} and $n_{yz,zx}$. The best-fit curves for the insulating samples at low temperature are plotted as solid lines in Fig. 4.25. These were obtained considering $r_A = 1.9702, 1.9876, 2.0062$ Å and $r_P = 2.017, 2.005, 1.990$ Å for $x = 0, 0.05, 0.07$, respectively (see Table 4.1). A small angular offset was also included as a free fitting parameter to account for small misalignments of the sample surface normal with respect to the incident X-rays direction. Eq. (4.6) provides a good description of the experimental data. The resulting $n_{xy}/n_{yz,zx}$ values are reported in Fig. 4.22(b) as a function of the doping level. Given the lack of detailed structural information at T = 180 K, $r_A = r_P$ was considered for the $x = 0.05$ sample at this temperature and the corresponding vertical error bars in Fig. 4.22(b) were increased by an arbitrary factor of 50% to account for the additional uncertainty introduced by the bond length dependence of the hybridization strength[20].

Analogous measurements to the ones here discussed have already been performed in pure Ca_2RuO_4 using both circular [185] and linear [187] incident polarisation. A similar study was also performed by Moretti Sala *et al.* [229] to investigate the orbital occupancies of the Ir^{4+} ion in Ba_2IrO_4. The present measurements show that, at low temperature, the $n_{xy}/n_{yz,zx}$ value increases from 0.52(1) in the parent compound up to 0.80(2) in the $x = 0.07$ sample. Consistent with the early report on pure Ca_2RuO_4 by Mizokawa *et al.* [185], the hole occupancy of the xy orbitals is also found to increase up to $n_{xy}/n_{yz,zx} \approx 1$ upon warming to the paramagnetic insulating phase in the $x = 0$ (T = 300 K) and $x = 0.05$ (T = 180 K) samples. Previous XANES studies on the parent compound reported somewhat smaller $n_{xy}/n_{yz,zx}$ values in the AFM phase [185, 187]. In particular, Mizokawa *et al.* [185] found $n_{xy}/n_{yz,zx} \approx 0.3$ using circularly polarised light at T = 90 K, while XANES measurements performed with linearly polarised X-rays in normal and grazing incidence geometry at T = 20 K reported a value $0.15 < n_{xy}/n_{yz,zx} < 0.2$[21] [187]. A significant change in the orbital population between 90 and 20 K seems unlikely given the substantial insensitivity of the Ca_2RuO_4 crystal structure on the temperature below the Néel transition [172]. The variability between different studies might stem from small variations in the oxygen content; these are likely to affect the orbital population at the Ru site due to the covalent character of the Ru-O bond [172]. Although the origin of the discrepancy remains an open issue, this does not affect

[20] A factor of 50% is largely overestimated as the impact of the ratio $r_P^{-3.5}/r_A^{-3.5}$ for the other samples amounts to only a few percent.

[21] However, the XANES matrix elements in the case of linear polarisation depend on the exact orientation of the in-plane crystal axes relative to the incident wave electric field vector [229]: a small misalignment with respect to the orientation considered by the authors might partially account for the variability in the $n_{xy}/n_{yz,zx}$ values.

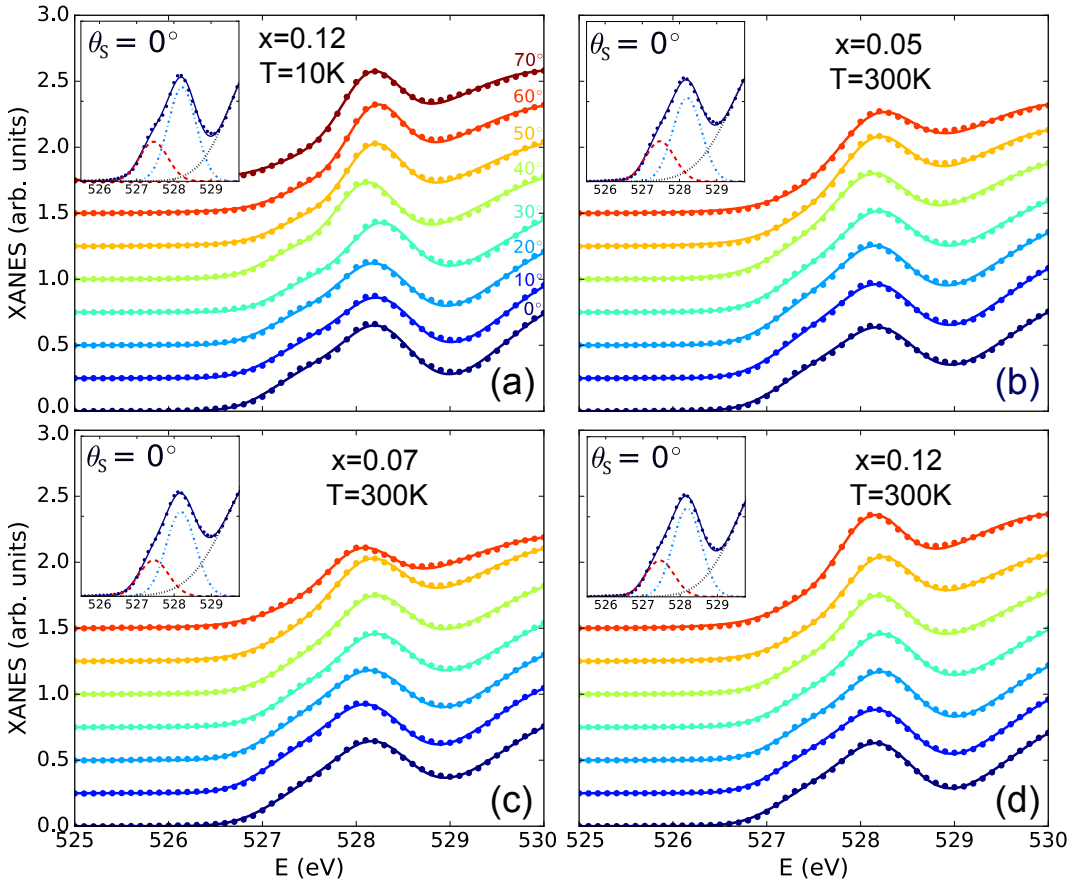

Figure 4.26: XANES spectra collected at different values of the angle θ_S between the incident X-ray beam and the sample surface normal in (a) the $x = 0.12$ sample at T = 10 K and the (b) $x = 0.05$, (c) $x = 0.07$ and (d) $x = 0.12$ sample at room temperature. Spectra at different angles were normalized using the spectral weight at $E > 553$ eV. The insets show the fit detail of the spectra measured at normal incidence ($\theta_S = 0°$). The measured absorption (filled circles) was fitted to the sum (solid line) of three Gaussian profiles modelling the apical (red dashed line) and in-plane (blue dot-dash line) O $2p$ - Ru t_{2g} features and the e_g region of the spectrum (black dotted line). The corresponding angular dependence of the apical and in-plane features integrated area is reported in Fig. 4.27(a) for the plots in (a).

the validity of our conclusions.

The in-plane and apical features of the XANES spectra exhibit a markedly different behaviour in the metallic phase. In particular, the apical feature is found to be less pronounced than the in-plane one at all θ_S values. Most importantly, contrary to the insulating phase, almost identical XANES spectra are found at all measured temperatures and La content values. This is clearly shown in Fig. 4.26, which reports the spectra measured at various points of the metallic region of the phase diagram [see open symbols in Fig. 4.22(a)]. The insensitivity to either temperature or doping level of the empty density of states mirrors the behaviour observed in the neutron diffraction results (Table 4.1) and, as I will argue later on, points to-

wards a structural origin of the evolution seen in the insulating phase. The angular dependence of the apical and in-plane features extracted from the fit of the spectra is reported in Fig. 4.27(a) for the representative case of the $x = 0.12$ crystal at T = 10 K. Eq. (4.6) does not provide a satisfactory fit of the data in this case. This is not surprising, since the simple hybridization model is based on an atomic orbital picture and cannot properly account for the itinerant character of the Ru 4*d* electrons in the metallic state. Nonetheless, the measured data are in qualitative agreement with the theoretical cross sections calculated for $n_{xy}/n_{yz,zx} >> 1$ [Fig. 4.27(b)].

Discussion

As outlined in Sec. 4.3, the Ru^{4+} single-ion physics has been described in terms of the minimal Hamiltonian of Eq. (4.4) consisting of the SOC (λ) and tetragonal crystal field (Δ) term [187]. As I will show here below, the latter allows a simple qualitative description of the trend extracted from the absorption spectra despite neglecting the Hund's coupling and the Coulomb interaction between the t_{2g} electrons. Within this model, the ground-state orbital population, given by Eq. (4.5), is determined by the relative strength of tetragonal distortion and SOC. This is shown in Fig. 4.9 where the hole occupancy ratio $n_{xy}/n_{yz,zx}$ predicted by the model is plotted as a function of Δ/λ along with a real-space representation of the corresponding orbital. Going from tetragonal compression ($\Delta < 0$) to tetragonal elongation ($\Delta > 0$) the *xy* contribution to the ground-state wave function increases and, as a result, the corresponding hole occupancy ratio $n_{xy}/n_{yz,zx}$ is enhanced. An equal population of *xy*, *yz* and *zx* orbitals ($n_{xy}/n_{yz,zx} = 0.5$) is expected in the limiting case of regular octahedra. Therefore, considering a single-ion picture, the changes in the hole occupancy of the Ru^{4+} t_{2g} orbitals upon La substitution in the insulating phase can be qualitatively interpreted in light of the doping-induced structural effects revealed by the neutron diffraction measurements (Sec. 4.4.2). In particular, the latter show that the internal chemical pressure induced by La substitution causes a progressive elongation of the RuO_6 octahedra along the apical Ru-O direction [see Fig. 4.12(a)]. The octahedra are compressed by about -2.4% in the parent compound; the compression reduces to -0.9% in the $x = 0.05$ sample, while the octahedra are elongated by about 0.8% for $x = 0.07$. Temperature was found to have a similar effect in the parent compound insulating phase: the tetragonal distortion is released upon warming, leading to almost regular octahedra at T = 300 K.

Consistent with the calculations displayed in Fig. 4.9, the ratio $n_{xy}/n_{yz,zx}$ increases in going from the parent to the doped compounds and is larger in the paramagnetic insulating phase than in the AFM one. In particular, the *xy* orbital population

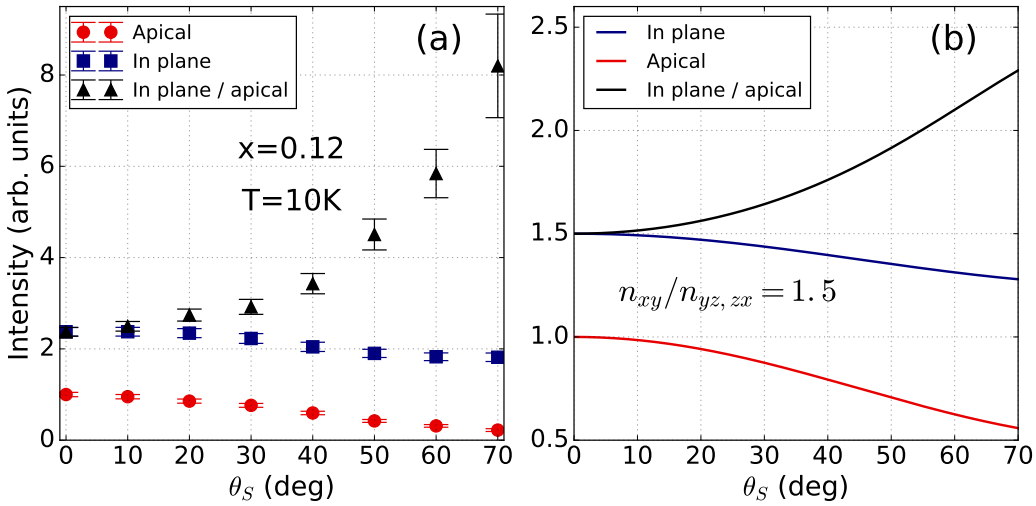

Figure 4.27: (a) Angular dependence of the apical and in-plane O $2p$ - Ru t_{2g} features of the XANES spectra in the metallic $x = 0.12$ sample at low temperature as extracted through the fit shown in Fig. 4.26(a). (b) Apical and in-plane angular dependence calculated using Eq. (4.6) with $n_{xy}/n_{yz,zx} = 1.5$.

at low temperature is significantly enhanced in the case of the $x = 0.07$ elongated octahedra with respect to the $x = 0, 0.05$ compressed ones. The attribution of the observed evolution to structural effects is further cofirmed by the insensitivity of the XANES spectra of the metallic samples to both temperature and La content. The neutron diffraction measurements of Sec. 4.4.2 indeed found that the RuO_6 octahedra are elongated by about $4.3 - 4.5\%$ in the metallic region of the phase diagram regardless of the temperature or doping level. A substantial octahedral elongation is expected to result in a large $n_{xy}/n_{yz,zx}$ value, consistent with the qualitative agreement between the calculations of Fig. 4.27(b) and the measurements of Fig. 4.27(a).

Although the trends seen in the data qualitatively follow the model predictions, the measured $n_{xy}/n_{yz,zx}$ absolute values do not generally show a satisfactory agreement with the calculated ones. In particular, values close to or slightly larger than 0.5 are found for the parent and $x = 0.05$ sample at T = 10 K, respectively, where the small tetragonal compression is expected to result in $n_{xy}/n_{yz,zx} < 0.5$. Moreover, the value $n_{xy}/n_{yz,zx} \approx 1$ emerging from the analysis of the parent compound spectra at room temperature is twice as large as the value expected for regular octahedra. It should be noted, however, that an accurate quantitative assessment of the hole occupancy values cannot be obtained within the assumptions of the present analysis. In particular, the single-ion model here considered neglects many-body effects of the system of four t_{2g} electrons. A more exhaustive description of the low-energy Hamiltonian, including the Hund's coupling and Coulomb interactions of the Ru

4*d* electrons, is provided by the model proposed by Das and co-authors [178] and outlined in Sec. 4.3 [see Fig. 4.8(b) and Eq. (4.2)]. In this case, many-body effects are relevant and a simple picture based on single-particle states no longer holds. A single-ion approach also neglects the charge transfer between the Ru 4*d* orbitals and the ligand O 2*p* ones: given the pronounced covalent character of the Ru-O bond [172], the latter is expected to cause significant deviations from the nominal 4+ oxidation state of the Ru ion, thus affecting the hole occupancy. Furthermore, the $n_{xy}/n_{yz,zx}$ values derived through the minimal hybridization model of Eq. (4.6) are only approximate and do not allow a precise quantitative estimation. In the specific case of the doping evolution, one must also bear in mind that, although the structural effects are probably dominant (see discussion in Sec. 4.5), the injection of free carriers achieved by substitution of divalent Ca with trivalent La might play a role in the observed properties. Despite the quantitative discrepancies, the trend seen in the data is significant and highlights the sensitivity of the spin-orbit entangled ground state of the Ru^{4+} ion to structural distortions.

Summary

In summary, the present XANES investigation has revealed that the elongation of the RuO_6 octahedra induced by either La substitution or temperature increase results in an enhancement of the *xy* hole population of the Ru^{4+} ground-state wave function in the insulating region of the temperature-doping phase diagram. The *xy* hole population further increases in the metallic phase with substantially elongated octahedra. Here, the hole occupancy shows little variation with temperature and doping, consistent with the lack of significant structural changes. The sensitivity of the orbital population of the Ru^{4+} ground-state to the local crystalline environment has been shown to directly result from the peculiar entanglement of *xy*, *yz* and *zx* orbitals caused by the sizeable SOC of 4*d* electrons. The experimental findings confirm the subtle nature of the low-energy Hamiltonian of perovskite ruthenates, where, despite the presence of a rather weaker spin-orbit interaction compared to the case of iridium oxides (see Chapter 5), a peculiar coupling between orbital and lattice degrees of freedom still arises from the competition between tetragonal field and SOC.

4.7 Impact of La doping on the local electronic properties of the Ru^{4+} ion: a Ru L-edge XANES and XMCD study

In the previous section, I showed how the electronic properties of the Ru^{4+} ion in $Ca_{2-x}La_xRuO_4$ can be indirectly accessed at the O K edge thanks to the hybridization of the Ru $4d$ orbitals with the O $2p$ ones. The Ru $4d$ valence states can be probed directly by means of absorption measurements at the Ru L edges. In particular, the branching ratio BR reflects the strength of the SOC of the $4d$ electrons (see Sec. 2.2.1), while L-edge XMCD allows the determination of the orbital and spin magnetic moment of the Ru^{4+} ion (see Sec. 2.2.2). These two pieces of information combined can provide valuable insights on the relative strength of the crystal field and SOC and help to answer the question as to how close Ca_2RuO_4 is to the realization of the $J_{\text{eff}} = 0$ ground state (see Sec. 4.1). Significant deviations from the $J_{\text{eff}} = 0$ scenario ($L_{\text{eff}} = 1$) are expected to result in a reduction of the orbital moment, which is fully quenched for the case of octahedral compression and negligible SOC ($\Delta \gg \lambda$). In this case, a statistical absorption white line ratio $BR \approx 2$ should be present.

In this section, I briefly outline XANES and XMCD measurements at the Ru L_3 and L_2 edges which were performed on powder pellets of $Ca_{2-x}La_xRuO_4$ with nominal La contents $x = 0, 0.05, 0.10$ and a single crystal of $Ca_{1.88}La_{0.12}RuO_4$ analogous to the one used for the neutron and X-ray measurements discussed earlier in the chapter. None of the compounds (except RuO_2) used during the growth process are volatile and, as a result, the doping level is not expected to show significant variations with respect to the nominal La concentration. Although the interpretation of the data is yet to be completed at the time of the draft of the present work, valuable insights can still be gained based on the current results of the analysis.

The data were collected at the ID12 hard X-ray beamline of the ESRF [230]. The X-ray source is a helical undulator of the APPLE-II type, which can provide both linear and circular polarisation, while further monochromatisation was achieved by means of a Si(111) double-crystal monochromator. The tender X-ray energy window between 2 and 4 keV where the Ru L edges reside is particularly challenging for XMCD experiments. This is due to the fact that the degree of circular polarisation transmitted by the monochromator strongly depends on the X-ray energy below about 4 keV and approaches zero around 2.8 keV. At this energy, the monochromator Bragg angle is equal to the Brewster's angle and thus results in a

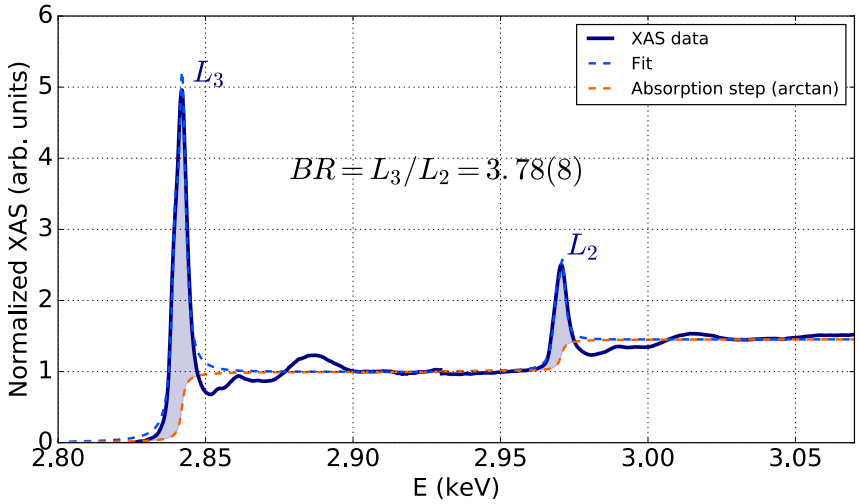

Figure 4.28: Parent compound XAS spectra measured in TEY at T = 10 K. The data (blue solid line) have been normalized so that the edge jump is equal to 1 and $1/2.2$ for the L_3 and L_2 edge, respectively. The measured spectra have been fitted to the sum (dashed blue line) of an arctangent function (orange dashed line), which models the absorption jump, and two Lorentzian peaks at each absorption edge, which model the e_g and t_{2g} features of the white line. The *BR* value results from the average of (i) the fitted white line area and (ii) a numerical integration (shaded area) from the pre-edge to the intersection between the white line and the arctangent function.

linearly polarised reflected beam[22] [230]. In order to circumvent this issue, a 5 μm-thick Si quarter-wave phase plate[23] was used, which resulted in a degree of circular polarisation around 62%. The residual linear contribution to the dichroic signal is averaged out in the powder samples, thus maximizing the sensitivity of the measurements to the circular part. The samples were mounted on the electrically-grounded cold finger of a helium continuous-flow cryostat (so that the sample surface was perpendicular to the incident X-ray beam) and inserted in the vacuum chamber of the high-field magnet.

Absorption spectra were collected by scanning the incident X-rays across the Ru L_3 and L_2 absorption edges. The absorption was simultaneously measured in both TEY and TFY detection mode, the latter by means of a diode placed along the direct beam direction. For each doping level, two separate measurements were

[22] At the Brewster's angle, the reflected intensity of the X-ray radiation with polarisation parallel to the plane of incidence (i.e. the plane defined by the incident and reflected beams) vanishes, such that the reflected light is polarised perpendicular to the plane of incidence.

[23] X-ray phase plates exploit the birefringence of a perfect crystal close to a Bragg diffraction peak [230, 231]. In particular, in Bragg diffraction geometry, the transmitted beam electric field components parallel and perpendicular to the scattering plane experience a phase shift which depends on the angular offset away from the perfect Bragg diffraction condition. By tuning the angular offset so that the phase shift is equal to $\pi/2$, the incident linear polarisation can be converted into an elliptical (circular) one.

performed. The first one consisted in the collection of absorption spectra over an extended energy range from below the L_3 pre-edge up to the L_2 post-edge at both room and low (T = 10 K) temperature in zero field. These spectra were collected without the Si phase-plate in order to maximize the intensity on the sample and used to extract the *BR*. For the second set of data, a magnetic field $B = 12$ T was applied along the direct beam direction and absorption spectra were measured at T = 10 K over a reduced energy range around the L_3 and L_2 white line peaks for opposite helicities of the incident circularly-polarised X-ray beam and opposite directions of the external field. Several spectra were collected and averaged for each permutation of light polarisation and field direction and the resulting spectra combined to obtain the XMCD signal. The TFY spectra were corrected for self-absorption (see Sec. 2.2.1) by means of the *XANES dactyloscope* software utility [232] based on the approach first discussed by Iida and Noma [77]. The correction parameters were adjusted to maximize the agreement between the corrected TFY spectra and the TEY ones: the latter are directly proportional to the absorption coefficient and can then be conveniently used as a reference. The absorption spectra presented in this section are the same ones shown in Fig. 4.13 and Fig. 4.18, which were used to correct the REXS data for self-absorption.

Fig. 4.28 shows XAS spectra collected in TEY mode over an extend energy range in the representative case of pure Ca_2RuO_4 at T = 10 K. Self-absorption corrected TFY spectra measured on a narrower energy range around the Ru L_3 and L_2 white lines are shown in Fig. 4.29 for the different doping levels. At each edge, the white line consists of two features centred at around $E = 2.8397$ keV and $E = 2.8421$ keV at the L_3 edge and $E = 2.9688$ keV and $E = 2.9709$ keV at the L_2 edge. The weaker feature at lower energy is due to transitions between the core Ru $2p$ levels to the partially occupied t_{2g} orbitals, while the absorption peak at higher energy arises from transition to the unoccupied e_g orbitals [233, 234]. A similar splitting is also observed in the diffraction data presented in Sec. 4.5. While the t_{2g} and e_g features appear to be relatively sharp in the insulating samples ($x = 0 - 0.10$), a significant broadening is seen in the heavily doped $x = 0.12$ metallic crystal, where the two peaks are less clearly distinguished.

A quantitative analysis of the XAS measurements was achieved by treating the L_3 and L_2 data sets separately. A linear pre-edge background was subtracted from both the L_3 and L_2 spectra. The latter were further normalized using the corresponding spectral weight in the post-edge region so that the absorption step was set equal to 1 and $1/2.2$ at the L_3 and L_2 edge, respectively. The ratio of 2.2 between the L_3 and L_2 edge jump reflects the statistical ratio of the transitions from the $2p_{3/2}$ and

$2p_{1/2}$ core levels in the case of significant SOC acting on the $2p$ electrons[24]. In order to extract the area of the white line, two different approaches were followed which are illustrated in Fig. 4.28. The first one consisted in fitting the XANES signal at each edge to the sum of an arctangent function simulating the absorption step and two Lorentzian peaks corresponding to the t_{2g} and e_g features of the white line; the white line area was then calculated as the sum of the areas of the two fitted Lorentzian profiles. In the second method, the XANES signal was numerically integrated from the pre-edge to the intersection between the measured XANES and the arctangent function (see shaded areas in Fig. 4.28). In both cases, the width of the arctangent profile at each edge was fixed to the tabulated lifetime broadening of the $2p_{3/2} \rightarrow 4d$ (L_3) and $2p_{1/2} \rightarrow 4d$ (L_2) transition (equal to 2 and 2.23 eV, respectively [235]), while its centre was constrained to the white line peak energy. The values of the white line area obtained following the two approaches are very similar and were averaged together. The standard deviation of the two values was used to express the corresponding uncertainty.

The resulting L_3/L_2 *BR* is reported in Fig. 4.30(a) as a function of the La content x for two different temperatures. The *BR* is significantly larger than the statistical one at all doping levels, thus revealing the presence of a non-negligible SOC acting on the Ru $4d$ valence electrons. At low temperature the *BR* appears to decrease with the La content in the insulating phase, while the heavily doped metallic sample exhibits a value comparable to the one observed in the parent compound. The data at higher temperature follows a similar trend. At each doping level, temperature does not significantly change the *BR*. The only exception seems to represented by the $x = 0.05$ sample, where the present analysis leads to a significant smaller value at high temperature. The non-statistical value of the *BR* is related to the mean value of the angular part of the SOC operator (Sec. 2.2.1). The latter could, in turn, be related to the relative strength of the SOC and the tetragonal distortion using the single-ion model of Sec. 4.3, analogous to what was already done for the Ir^{4+} ion using the model discussed in Chapter 5 [217].

The calculations are still ongoing. Further work will also be needed to ascertain whether the observed evolution as a function of doping (as well as temperature in the $x = 0.05$ sample) is related to corresponding variations in the Ru^{4+} electronic structure or simply reflects the intrinsic variability of the data or the analysis method. Should the observed trend stem from the physics of the system, the structural changes discussed in Sec. 4.4.2 alone seem incapable to account for the data

[24] For $2p$ core states with a large SOC splitting the L_3/L_2 edge jump ratio is expected to deviate from the statistical value of 2 based on the degeneracy of the $2p_{3/2}$ and $2p_{1/2}$ levels [88]. It should be noted that choosing a values of 2 for Ru does not impact the results presented in this section.

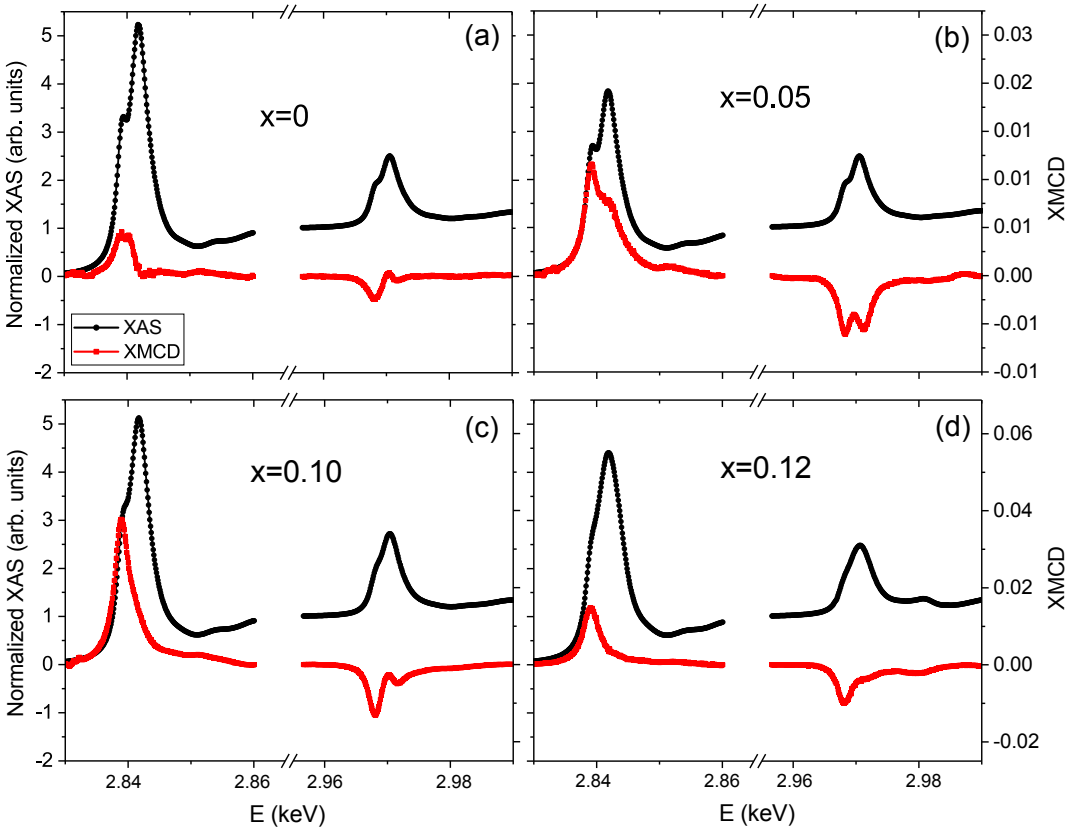

Figure 4.29: Normalized XAS (black circles) and corresponding XMCD (red squares) measured in TFY at T = 10 K for different levels x of La content. The data have been obtained combining the polarisation and field reversal ($B = \pm 12T$) spectra and have been corrected for self-absorption as outlined in the text.

of Fig. 4.30(a). In particular, the $x = 0.12$ sample (at both 10 and 300 K) exhibits very similar structural properties to the $x = 0.05$ and $x = 0.10$ samples at room temperature: one would then expect the BR to be of similar magnitude. Moreover, at T = 10 K the system displays a smooth evolution from an orthorhombic cell with compressed octahedra to a quasi-tetragonal cell with elongated octahedra [see Fig. 4.12(a)] for increasing La contents: therefore, one would expect the BR of the $x = 0.12$ sample to follow the same decreasing trend at lower doping based on the sole structural effects. Additional theoretical effort will be needed in order to assess the robustness of these findings and to explain the observed evolution.

Let us now move to the discussion of the XMCD spectra. The dichroic signal extracted from the self-absorption corrected TFY absorption spectra at the Ru L_3 and L_2 edges is reported in Fig. 4.29, where the polarisation and field reversal measurements were combined together. Although a similar dichroic signal is also present for the TEY spectra, the XMCD appears to be generally noisier and larger variations are observed between consecutive equivalent data sets for

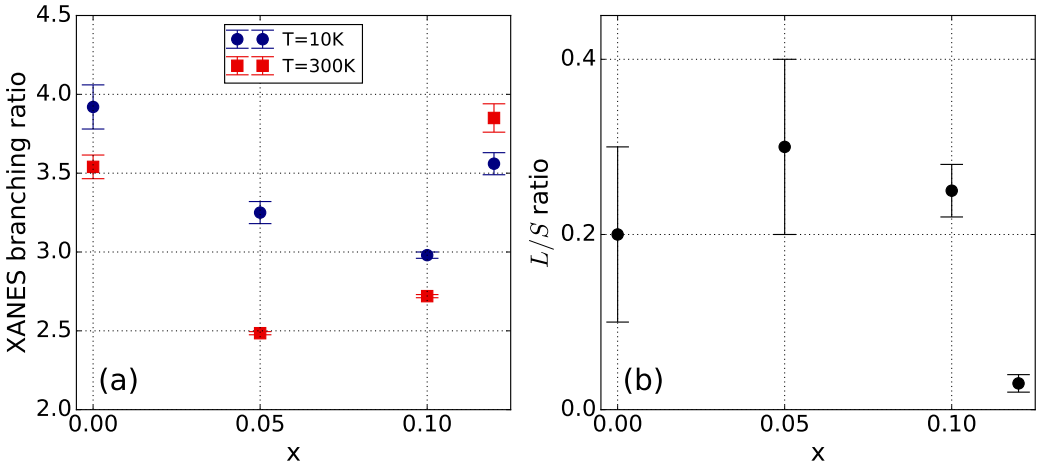

Figure 4.30: (a) XANES L_3/L_2 *BR* as a function of the doping level for two different temperatures. The values have been derived extracting the L_3 and L_2 white line areas as shown in Fig. 4.28 and averaging the values obtained by varying the centre of the arctangent function used to model the absorption step. (b) Ratio of the orbital (L) and spin (S) magnetic moments as extracted from the application of the sum rules to the XMCD data at T = 10 K. The orbital and spin magnetic moment values are the result of the average of the TEY and TFY measurements for $x = 0.10, 0.12$, while the average of the TFY measurements across two different experiments was considered for $x = 0, 0.05$. The error bars reflect the variability in the corresponding values.

$x = 0 - 0.10$. This can be attributed to the insulating character of the samples in the range $x = 0 - 0.10$, which makes TEY detection overall less reliable. In particular, charging effects can easily explain the observed instabilities. Given the AFM ordering of $Ca_{2-x}La_xRuO_4$ for $x = 0 - 0.10$, the net magnetisation along the field direction is only a small fraction of the sublattice magnetisation despite the high magnitude of the external field. As a result, the XMCD signal is extremely weak. This is particularly true in the globally AFM parent compound, while a larger signal is present in the $x = 0.05, 0.10$ samples due to the weak net magnetisation induced by La substitution (see Sec. 4.5). It should be noted that the $x = 0.12$ is paramagnetic and the measured XMCD thus arises from the polarisation of the disordered moments induced by the external field. A dichroic signal of similar magnitude to the one at lower doping is, in this case, present. The measurements are further complicated by the significant linear contribution to the polarisation of the incident X-rays. This results in a sizeable linear contribution to the measured dichroic signal, which is superimposed to the circular one. This contribution, however, is averaged out in the powder samples[25] due to the random orientation of the crystalline powder grains; moreover, since the charge linear dichroism is field independent, any resid-

[25] Preliminary measurements performed on a single crystal of pure Ca_2RuO_4 resulted in a linear contribution much larger than the circular one: the latter could not then be reliably measured.

ual contribution can be easily subtracted from the total dichroic signal extracted from polarisation reversal measurements performed for opposite field directions. This is also the case for the $x = 0.12$ sample, for which powder samples were not available.

The XMCD signal shows an opposite sign at the L_3 and L_2 edges in all samples, with the modulus of the amplitude peaked around the t_{2g} feature energy. The sum rules for the orbital and spin contribution to the magnetic moment introduced in Sec. 2.2.2 were applied to the XMCD spectra. The resulting orbital to spin magnetic moment ratio L/S is reported in Fig. 4.30(b) as a function of the doping level. For $x = 0, 0.05$ the L/S values refer to the average of the values obtained from the TFY data collected in two separate experiments on the same samples. The data from the first experiment (not reported in the present work) have been collected with a preliminary setup and show a generally lower signal-to-noise ratio. The TEY signal at these two doping levels proved to be particularly unstable and the corresponding data sets were thus discarded. For the $x = 0.10, 0.12$ samples (which were not measured during the first experiment) the L/S values correspond to the average of the values obtained through the application of the sum rules to the TFY and TEY data (with the latter not reported in the present work). The error bars in the range $x = 0 - 0.10$ reflect the variability seen between equivalent measurements, while for $x = 0.12$ they correspond to the variability resulting from choosing slightly different integration ranges for the sum rules (for this sample only one data set was collected).

Although the error on the extracted values is significant, the present analysis suggests that a sizeable unquenched orbital moment, around 25% of the spin value, is present in the insulating phase of the phase diagram (see Fig. 4.5). On the other hand, L appears to be much smaller for the metallic sample, where an almost pure spin moment seems to be present. As already mentioned at the beginning of this section, the presence of an unquenched orbital moment constitutes a valuable piece of information in addressing the nature of the Ru^{4+} ion ground-state wave function. In particular it shows that the spin-orbit interaction is strong enough to cause a significant departure from the scenario with fully occupied xy orbitals, where a pure $S = 1$ ground state with quenched orbital moment is expected to be present (see Sec. 4.3). This is consistent with both the O K-edge measurements of Sec. 4.6 and previous reports on the parent compound [178, 185, 187], which suggest that SOC coupling mixes together the Ru t_{2g} orbitals and results in a ground state of mixed orbital character. Similar to what has been done for the Ir^{4+} ion in the perovskite iridates [217], additional work is currently under way with the goal of using the single-ion model introduced in Sec. 4.3 to calculate the evolution of the orbital and spin moment as a function of the relative strength of the tetragonal field and the

SOC. The latter could then be inferred from the measured L/S value. Further work will also be needed to explain the drop in the orbital contribution to the magnetic moment observed in going from the insulating to the metallic phase.

Summary

In summary, the combined XAS and XMCD Ru *L*-edge investigation confirms the presence of a non-negligible SOC in the Ru 4*d* valence electronic levels, which is evidenced by the non-statistical value of the white line *BR*. A sizeable unquenched orbital moment was also found in the insulating region of the $Ca_{2-x}La_xRuO_4$ phase diagram, while *L* is considerably reduced in the metallic phase. Although the interpretation of the results will require further theoretical work, the findings presented in this section suggest that the ground-state of the Ru^{4+} ion significantly deviates from the pure $S = 1$ spin scenario with fully occupied *xy* orbitals expected for negligible SOC. This is consistent with the results from the present and previous measurements performed at the O *K* edge. The measurements here discussed, the first performed at the Ru *L* edge in $Ca_{2-x}La_xRuO_4$, were made possible by a technical upgrade of beamline ID12 of the ESRF, which was necessary to overcome the hurdles of performing experiments with circularly polarised X-rays in the tender region of the X-ray spectrum.

4.8 Conclusions

In this chapter, I presented an extensive investigation of several aspects of the physics of $Ca_{2-x}La_xRuO_4$ by means of a combination of experimental techniques. The main findings are:

- The internal chemical pressure produced by La substitution causes an evolution from the parent compound orthorhombic crystal with compressed octahedra towards a quasi-tetragonal phase with elongated octahedra in the insulating phase at low temperature. On the other hand, the structure was found to be insensitive to the doping level in the metallic region of the phase diagram.

- The doped samples retain the parent compound $\mathbf{k} = (0,0,0)$ magnetic structure. Doping suppresses the globally AFM A-centred mode present in Ca_2RuO_4 and favours the weakly FM B-centred one, thus naturally explaining the low-temperature net magnetisation observed in the doped crystals.

- The crystal field tuning caused by the structural distortion has a visible impact on the empty density of states as probed by O *K*-edge XANES in the insulating phase. Using a minimal model of the O 2*p* - Ru 4*d* hybridization, the observed evolution of the spectra can be interpreted in terms of a redistribution of the Ru t_{2g} orbital contributions to the ground-state wave function, which corresponds to an increase in the *xy* orbital hole population. Mirroring the behaviour observed in the crystal structure, the spectra are insensitive to the La content in the metallic region.

- Both the non-statistical absorption *BR* and the sizeable Ru orbital moment revealed by XANES and XMCD measurements at the Ru *L* edges confirm a significant impact of SOC in the low-energy physics of the insulating phase.

The measurements outlined in the present work represent the first detailed experimental investigation of the microscopic magnetic and electronic properties of La-doped Ca_2RuO_4. Although the existing literature on $Ca_{2-x}La_xRuO_4$ focuses on the filling control of the Ru 4*d* bands associated with the extra electron introduced by the La^{3+} ion [168, 179–181], the experimental findings presented in this chapter strongly suggest that the concomitant structural effects are likely to play a more important role in the physics of the system. This is somewhat confirmed by recent resistivity and ARPES measurements on Pr-doped Ca_2RuO_4 [177], which suggest that, in contrast to lightly doped cuprates [221] and iridates (see Chapter 5), the doped electrons remain fully localised in the S-*Pbca* phase irrespective of the Pr content.

In terms of the more general context of the peculiar ground-state properties of Ca_2RuO_4, the present measurements highlight the subtle competition of tetragonal field and SOC in the low-energy physics of this system. Further theoretical work will be needed to provide (i) a detailed microscopic explanation for the observed magnetic structure change, (ii) a more quantitatively accurate description of the doping-induced orbital population evolution beyond the simple hybridization model discussed in the present work and (iii) a quantitative interpretation of the Ru *L*-edge XANES and XMCD results.

Chapter 5

The 5d case: anisotropic exchange and spin-wave damping in $(Sr_{1-x}La_x)_2IrO_4$

Contents

5.1 Introduction 204

5.2 Overview of the magnetic and electronic properties of $(Sr_{1-x}La_x)_2IrO_4$ 205

5.2.1 Pure Sr_2IrO_4 205

5.2.2 $(Sr_{1-x}La_x)_2IrO_4$: impact of La doping 211

5.3 Sr_2IrO_4 magnetic Hamiltonian 214

5.3.1 Ir^{4+} single-ion Hamiltonian 215

5.3.2 Exchange interaction between $J_{\text{eff}} = 1/2$ magnetic moments 219

5.3.3 Single-magnon excitation spectrum 223

5.3.3.1 Magnetic excitations in pure and electron-doped Sr_2IrO_4: previous reports 228

5.4 Magnetic excitations in $(Sr_{1-x}La_x)_2IrO_4$ studied by means of RIXS at the Ir L_3 edge 232

5.4.1 Doping evolution of long-range magnetic order 233

5.4.2 Single-magnon excitation spectrum 235

5.4.2.1 Energy gap and impact of the momentum resolution 240

5.4.2.2 Anisotropic magnon damping 243

5.4.2.3 Energy dispersion: anisotropic exchange interactions 245

5.5 Conclusions 251

5.1 Introduction

As I have discussed in Chapter 1, the strength of the SOC increases moving from the $3d$ series of the periodic table to the heavier $4d$ and $5d$ TMs. In $5d$ TMOs the spin-orbit interaction is much larger than the other relevant energy scales and thus represents the main ingredient of the low-energy physics. This is expected to give rise to a plethora of exotic electronic phases of matter [7]. Among all $5d$ compounds, iridium oxides of the Ruddlesden-Popper series $Sr_{n+1}Ir_nO_{3n+1}$ have attracted most of the attention of the scientific community since the discovery, in the single layer ($n = 1$) compound Sr_2IrO_4, of a novel $J_{\text{eff}} = 1/2$ Mott insulating ground state resulting from the subtle interplay of SOC and electron-electron correlations [8]. The peculiar electronic and magnetic properties associated with the $J_{\text{eff}} = 1/2$ state have been extensively addressed by both theoretical and experimental studies [8, 215–217, 222, 223, 236–243]. In the specific case of Sr_2IrO_4, the interest has been further boosted by its structural and electronic similarities with La_2CuO_4, the parent compound to a series of high-T_c superconductors. Both compounds display a perovskite-like crystal structure comprising single layers of corner-sharing TMO_6 octahedra separated by Sr or La cations. The metal sites form a square lattice and each have a single hole residing in the d orbitals. This gives rise to $S = 1/2$ (Cu^{2+}) or $J_{\text{eff}} = 1/2$ (Ir^{4+}) magnetic moments coupled antiferromagnetically within the TMO_2 planes and led to the prediction of a superconducting state upon electron doping [244–246], with similar features to the one generated by hole doping in La_2CuO_4.

This chapter focuses on the peculiar magnetic interactions of the $J_{\text{eff}} = 1/2$ moments in Sr_2IrO_4 and their response to the injection of free carriers achieved by La doping. In particular, I will present an investigation on the collective magnetic excitation spectrum in $(Sr_{1-x}La_x)_2IrO_4$ performed by means of RIXS at the Ir L_3 absorption edge. In contrast to earlier studies [236, 247, 248], a full line-shape analysis of the RIXS spectra was performed, including, most importantly, the effect of the finite momentum and energy resolution. The excitation spectrum is shown to be fully gapped at all wave vectors in the BZ up to $x = 0.10(1)$, indicating the existence of anisotropic exchange interactions, and a previously unreported anisotropic damping away from the zone centres is revealed.

The chapter is organized as follows. After a brief literature overview of the relevant magnetic and electronic properties (Sec. 5.2), I will discuss the magnetic exchange interactions between the Ir^{4+} moments (Sec. 5.3), describing both the magnetic Hamiltonian (Sec. 5.3.1 and 5.3.2) and the resulting single-magnon ex-

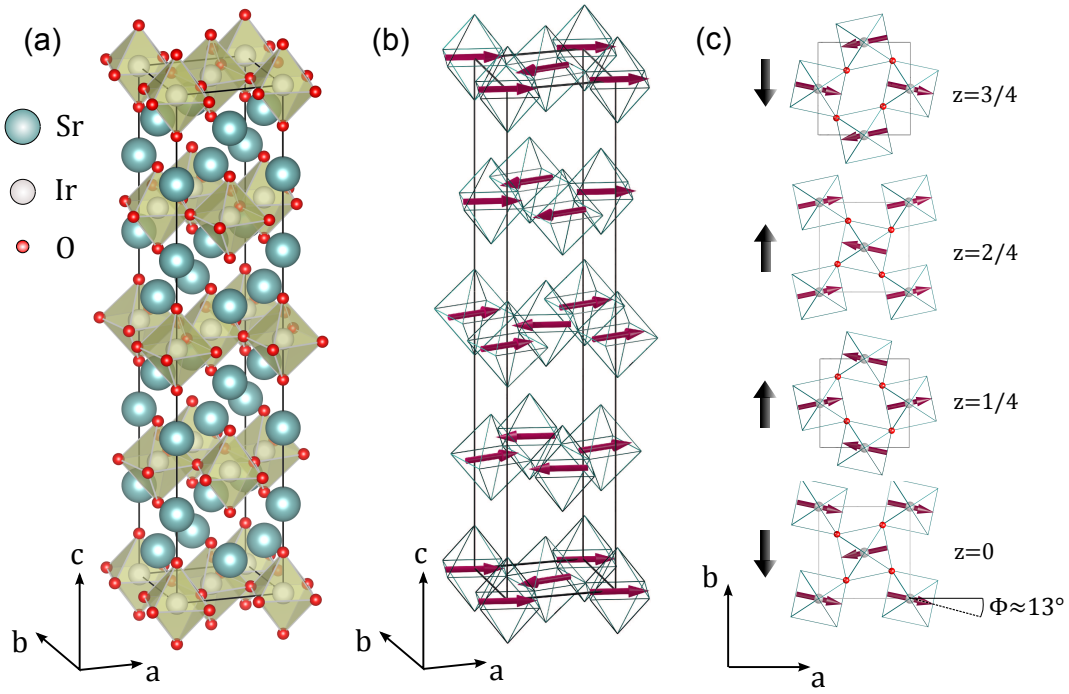

Figure 5.1: (a) Sr_2IrO_4 tetragonal crystal structure (space group $I4_1/acd$, $a = b = 5.48$ Å, $c = 25.8$ Å). (b) Magnetic ordering of the Ir^{4+} moments. (c) Detail of the moment arrangement of different IrO_2 planes inside the unit cell. The vertical black arrows indicate the direction of the net moment arising from the canting angle ϕ within each plane.

citation spectrum (Sec. 5.3.3). The RIXS measurements are presented in Sec. 5.4, along with the details of the data analysis and the main results. Finally, the conclusions of the study are summarised in Sec. 5.5.

5.2 Overview of the magnetic and electronic properties of $(Sr_{1-x}La_x)_2IrO_4$

5.2.1 Pure Sr_2IrO_4

Sr_2IrO_4 crystallizes in the tetragonal space group $I4_1/acd$ (No. 142) with $a = b = 5.48$ Å, $c = 25.8$ Å [249]. The symmetry is reduced from the K_2NiF_4-type structure ($I4/mmm$, No. 139) by a correlated staggered rotation of the IrO_6 octahedra by about 11.8° [238, 249] around the **c** axis. This generates a larger $(\sqrt{2}a \times \sqrt{2}b \times 2c)$ unit cell which is rotated by 45° with respect to the $I4/mmm$ one. The crystal structure is shown schematically in Fig. 5.1. IrO_2 layers alternate with SrO ones along

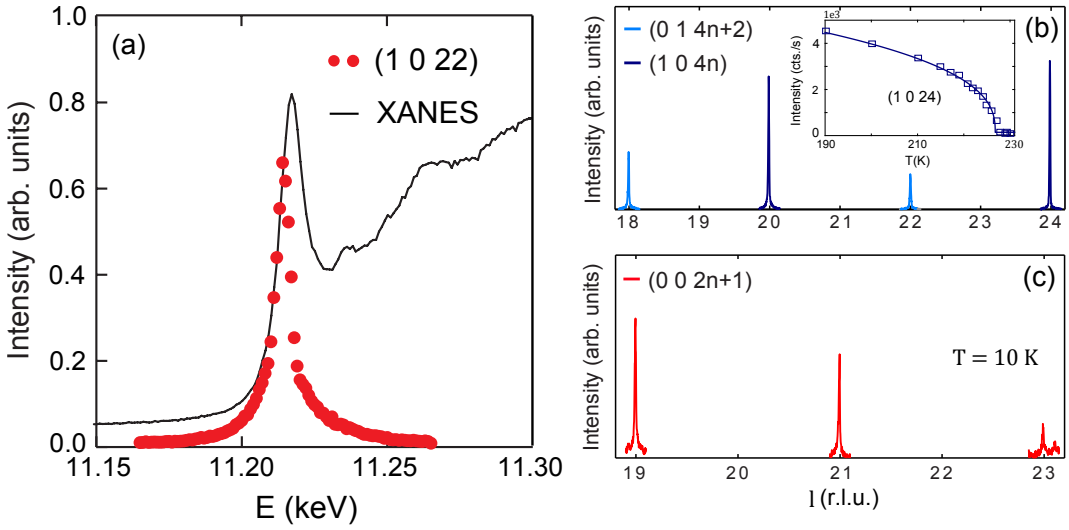

Figure 5.2: Overview of the static magnetic order in Sr_2IrO_4 investigated by REXS at the Ir L_3 absorption edge. (a) Resonant enhancement of the $(1\,0\,22)$ magnetic reflection and Ir L_3 XANES spectrum. Adapted from Ref. [215]. (b),(c) l dependence (with l out-of-plane Miller index) of magnetic Bragg peaks arising from (b) the main AFM order of the Ir^{4+} moments and (c) the moment canting measured at T = 10 K. Adapted from Ref. [51]. The inset in (b) shows the temperature dependence of the $(1\,0\,24)$ scattered intensity. Adapted from Ref. [242].

the **c** axis so that each Ir atom is at the centre of a slightly (4% [249]) elongated IrO_6 octahedron. Recent neutron diffraction studies [250, 251] revealed the presence of temperature-dependent $I4_1/acd$-forbidden peaks of the type $(2n+1\ 0\ 2n+1)$ (with n integer number). The latter were accounted for by the presence of two non-equivalent Ir sites displaying staggered tetragonal distortions of the octahedral cage along the **c** axis [251]. This was predicted to further lower the symmetry to $I4_1/a$ (No. 88), where the c and d glide planes of the $I4_1/acd$ structure are absent. However, if one neglects the weak $(2n+1\ 0\ 2n+1)$ structural reflections, the $I4_1/acd$ space group provides a good description of the crystal structure and is the one used in most of the studies dealing with the magnetic properties.

Sr_2IrO_4 orders into a C-AFM structure below $T_N \approx 230$ K [215, 242] (Fig. 5.2). The ordered magnetic moments of the Ir^{4+} ions ($\approx 0.2\,\mu_B/Ir^{4+}$ ion[1] [251, 252]) lie in the **ab** plane of the crystal and deviate by $\approx 13°$ [216, 238, 251] away from the tetragonal $[1\,0\,0]$ direction. As shown in Fig. 5.1, the canting rigidly follows the staggered rotation of the IrO_6 octahedra. As a result, the moments on different Ir sites do not exactly cancel out and give rise to a net component orthogonal to the main AFM axis. The net moments of neighbouring IrO_2 layers follow the stacking sequence $\downarrow\uparrow\uparrow\downarrow$ so that the magnetic structure is globally AFM. The locking of

[1] A larger value ($\approx 0.4\,\mu_B/\ Ir^{4+}$ ion) was found by Dhital *et al.* [250].

the moment canting to the in-plane rotation of the oxygen octahedra stems from the peculiar magneto-elastic coupling produced by the spin-orbit entangled nature of the Ir^{4+} $J_{\text{eff}} = 1/2$ ground state [238, 239]. This aspect will be discussed in more detail in Sec. 5.3.2.

The magnetic structure has been extensively studied by both neutron diffraction [250, 251] and REXS [215, 216, 238]. Resonant X-ray scattering proved to be particularly well suited for the investigation of the magnetic properties of iridium oxides due to the large resonant enhancement of the magnetic scattering signal at the Ir L_3 absorption edge[2] [Fig. 5.2(a)]. The magnetic ordering can be described as consisting of a basal plane AFM sublattice (A), where the moments lie along the $[1\,0\,0]$ direction, and a $\downarrow\uparrow\uparrow\downarrow$ stacking of $[0\,1\,0]$ net moments originating from the canting (sublattice B). It should be noted that, given the tetragonal symmetry of the crystal, one could have equivalently chosen the $[0\,1\,0]$ direction for sublattice A and the $[1\,0\,0]$ for sublattice B. Sublattice A gives rise to magnetic reflections of the type $(0\,1\,4n+2)$ and $(1\,0\,4n)$ [or, equivalently, $(1\,0\,4n+2)$ and $(0\,1\,4n)$], while sublattice B is responsible for the weaker $(0\,0\,2n+1)$ magnetic peaks [238] [see Figs. 5.2(b),(c)]. Kim *et al.* [215] showed that the application of an external field $H > H_c = 0.2$ T applied in the **ab** plane induces a transition to a new magnetic order in which the magnetic peaks of the type $(0\,1\,4n+2)$ disappear and are replaced by $(0\,1\,2n+1)$ reflections. In the new structure, the net moments arising from the canting stack ferromagnetically along the **c** axis and, as a consequence, the magnetic peaks of the type $(0\,0\,2n+1)$ are also absent. The resulting global weak net magnetisation is evident in bulk magnetisation measurements [253]. In the $I4_1/acd$ description, the magnetic order is described by a propagation vector $\mathbf{k} = (0,0,0)$: the magnetic unit cell thus coincides with the crystallographic one and the magnetic peak Miller indices are all integers.

The large separation between the IrO_2 layers (> 6 Å) implies that the orbitals of the Ir^{4+} ions on different layers do not significantly overlap with each other. As a result, the out-of-plane interactions between Ir^{4+} magnetic moments can also be neglected to first order, as I will show in more detail in Sec. 5.3. Consequently, the magnetic excitation spectrum depends almost exclusively on the projection $\mathbf{Q}_\perp = (Q_x, Q_y)$ of the momentum transfer $\mathbf{Q}$ on the **ab** plane of the tetragonal

[2] Moretti Sala *et al.* [217] showed that the resonant enhancement of the magnetic signal in the case of an Ir^{4+} ion with magnetic moments lying in the **ab** plane of the tetragonal crystal structure is identically zero at the Ir L_2 edge irrespective of the relative strength of the SOC and tetragonal crystal field. Contrary to the case of **c** axis moments realized in the bilayer $Sr_3Ir_2O_7$, the L_3/L_2 resonant enhancement ratio in Sr_2IrO_4 does not provide any relevant information on the local physics of the Ir^{4+} ion.

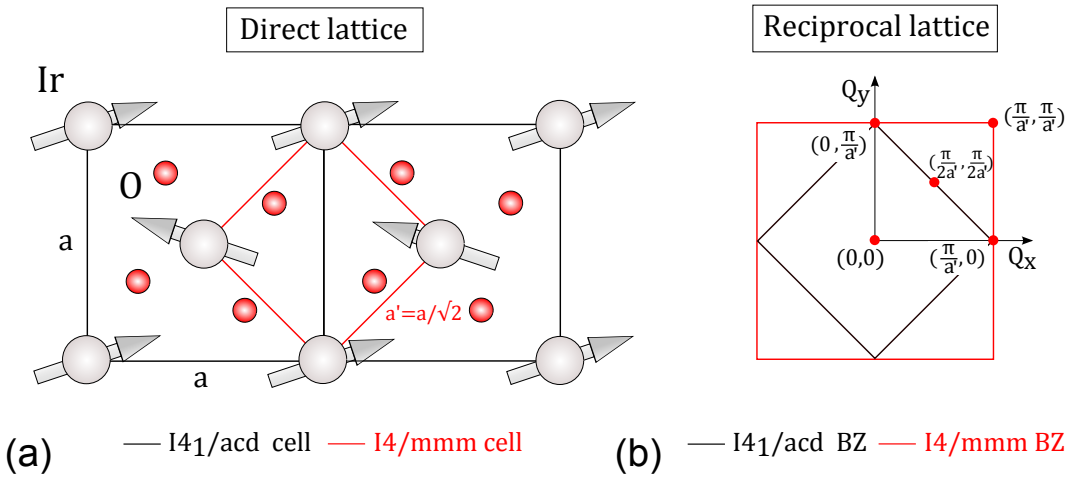

Figure 5.3: (a) Crystal and magnetic structure of a representative IrO_2 plane. The black and red (rotated) squares represent the in-plane projections of the $I4_1/acd$ and the higher symmetry $I4/mmm$ unit cells, respectively. (b) First BZ for the two choices of unit cell shown in (a). The Q_x and Q_y values refer to high-symmetry points in the $I4/mmm$ BZ (red square). The first BZ of the $I4_1/acd$ cell (black rotated square) coincides with the magnetic BZ in the $I4/mmm$ description.

structure (i.e. perpendicular to the **c** axis, hence the notation $\mathbf{Q}_\perp$)[3]. The same is true for the energy of the electron in the bands originating from the Ir 5*d* orbitals, whose dispersion will be briefly discussed below. Therefore, from the point of view of its electronic and magnetic properties, Sr_2IrO_4 behaves as an almost perfect 2D system. The (hkl) values of the magnetic peaks arising from the static magnetic order are normally indexed in terms of the reciprocal lattice defined with respect to the $I4_1/acd$ unit cell (this is the convention used in Fig. 5.2 and the related discussion). However, the literature dealing with the 2D band structure and the spin-wave dispersion (see Sec 5.3.3) expresses the x and y components of the in-plane momentum transfer in terms of the reciprocal space basis vectors in the high-symmetry $I4/mmm$ setting. This is the convention used in most of the literature on high-T_c superconductors, where the $\langle 1\,0\rangle$ direction in the $I4/mmm$ cell (normally referred to as *antinodal* direction) runs along a Cu-Cu nearest-neighbour pair (Ir-Ir pair in the case of Sr_2IrO_4)[4]. In the $I4/mmm$ description, the magnetic unit cell (which coincides with the $I4_1/acd$ crystallographic cell) is doubled and the propagation vector is $\mathbf{k} = (\frac{1}{2}, \frac{1}{2})$: a magnetic peak of the type $(1\,0\,l)$ in the $I4_1/acd$ description is indexed as $(\frac{1}{2}\,\frac{1}{2}\,l)$ in the $I4/mmm$ one.

The **ab** plane projections of the $I4_1/acd$ and $I4/mmm$ crystallographic unit

[3] Although technically the momentum transfer is given by $\hbar\mathbf{Q}$, I will use the expression momentum transfer to refer to the $\mathbf{Q}$ and $\mathbf{Q}_\perp$ vectors from now on.

[4] Here, the angular brackets notation refer to the $[1\,0]$ direction of the direct lattice and all the symmetrically equivalent ones (i.e. $[0\,1]$).

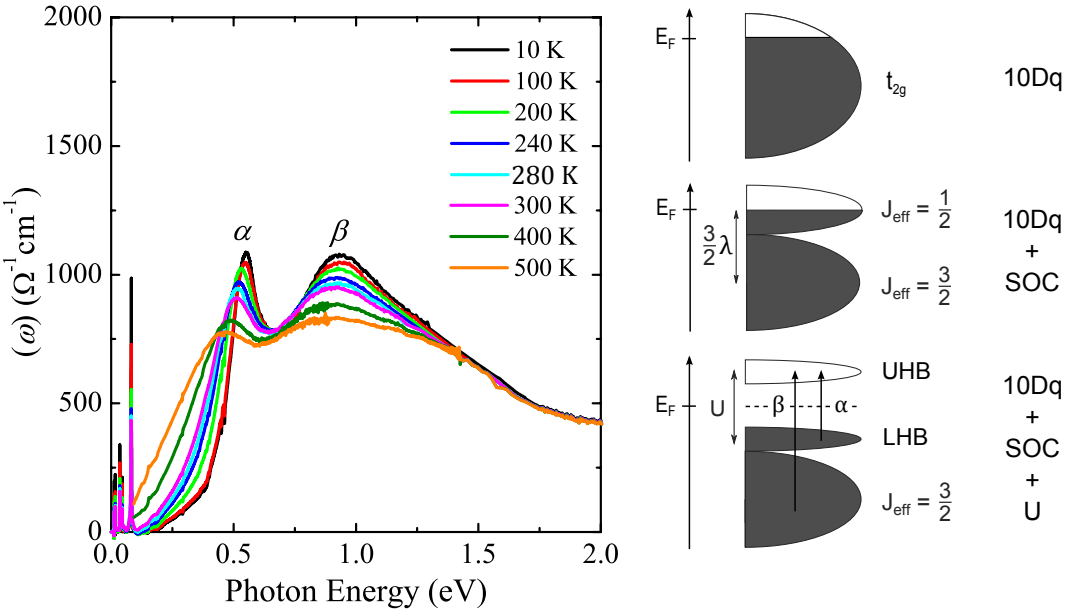

Figure 5.4: Sr_2IrO_4 optical conductivity measurements from Ref. [254]. The diagram on the right shows the effect of the cubic crystal field ($10Dq$), spin-orbit coupling (SOC) and electronic correlations (U) on the Ir $5d$ bands and highlights the origin of the α and β features seen in the optical conductivity.

cells are schematically shown in Fig. 5.3(a), while the corresponding 2D BZs are displayed in Fig. 5.3(b). The smaller $I4/mmm$ crystallographic cell [red square in Fig. 5.3(a)] is rotated by 45° with respect to the large $I4_1/acd$ one [black square in Fig. 5.3(a)] and its lattice constant is given by $a' = a/\sqrt{2} = 3.87\,\text{Å}$ (a being the lattice constant of the $I4_1/acd$ cell). The corresponding crystallographic BZ [red square in Fig. 5.3(b)] is therefore larger (lattice constant $2\pi/a'$) and, again, rotated by 45° with respect to the $I4_1/acd$ one [black square in Fig. 5.3(b)]. The $\{1\,0\}$ direction[5] in the $I4/mmm$ space group corresponds to the $\{1\,1\}$ in the $I4_1/acd$ description, while the $\{1\,1\}$ direction, normally referred to as the *nodal* direction in the cuprates literature, corresponds to the $\{1\,0\}$ one. The magnetic BZ in the $I4/mmm$ description coincides with the $I4_1/acd$ crystallographic one. Rather than using the Miller indices (hk), the $\mathbf{Q}_\perp = (Q_x, Q_y)$ vector is normally written expressing Q_x and Q_y in units of $1/a'$, so that the zone boundary in the antinodal direction $(hk) = (\frac{1}{2}\,0)$ is written as $(\pi, 0)$, while the magnetic propagation vector $(hk) = (\frac{1}{2}\,\frac{1}{2})$ corresponds to (π, π). This nomenclature is the one adopted in the remainder of this chapter.

Given the large value of the cubic crystal field ($10Dq = 3.8$ eV [255]), the five electrons of the Ir^{4+} ion occupy a low-spin state and results in a partially filled t_{2g} band. The Coulomb repulsion U is generally considered to have a limited impact

[5] Analogous to the angular brackets notation for the direct lattice, the curly brackets refer to the $(1\,0)$ direction of the reciprocal space and all the symmetrically equivalent ones.

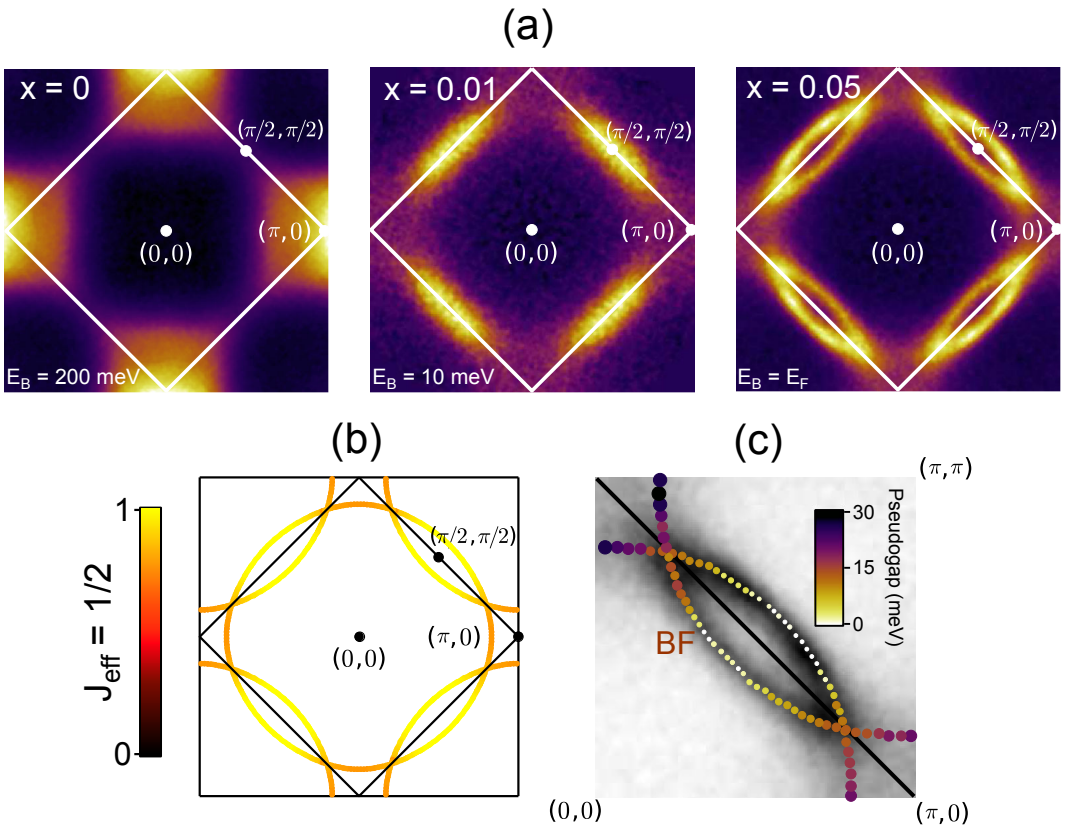

Figure 5.5: Summary of the ARPES investigation in $(Sr_{1-x}La_x)_2IrO_4$ from Ref. [222]. (a) Constant energy cuts for $x = 0$ ($E = E_F - 200$ meV), 0.01 ($E = E_F - 10$ meV) and 0.05 ($E = E_F$). (b) Tight binding calculation of the Fermi surface performed considering $U = 0$ and $1 + 2x$ free carriers per Ir site. The color scale represent the $J_{\text{eff}} = 1/2$ character. (c) Detail of the pseudogap values along the Fermi arcs in the $x = 0.05$ sample.

on the wide bands generated by the large $5d$ orbitals and, as a result, Sr_2IrO_4 was initially expected to be a metal. However, as it was shown by the seminal paper by Kim *et al.* [8], the strong SOC acting on the $5d$ electrons splits the t_{2g} band into a lower $J_{\text{eff}} = 3/2$ band and an upper, half-filled, $J_{\text{eff}} = 1/2$ one (see Sec. 5.3.1 for a detailed discussion on the Ir^{4+} single-ion Hamiltonian and the effect of SOC). The modest U can then effectively open a Mott gap in the much narrower $J_{\text{eff}} = 1/2$ band and gives rise to a full LHB and an empty UHB. The Mott insulating state was confirmed by resistivity [215, 256] and optical conductivity measurements [254]. The latter are reported in Fig. 5.4 along with a schematic band structure diagram. An optical gap of about 0.25 eV is present at room temperature. Furthermore, two distinct peaks at about 0.5 eV (α) and 1 eV (β) are seen which correspond to transitions from the LHB and the $J_{\text{eff}} = 3/2$ band, respectively.

5.2.2 $(Sr_{1-x}La_x)_2IrO_4$: impact of La doping

As mentioned previously, Sr_2IrO_4 exhibits a number of similarities with La_2CuO_4. In particular, electron-doped Sr_2IrO_4 is expected to host analogous properties to hole-doped La_2CuO_4 due to the opposite sign of the next-nearest-neighbour hopping amplitude between the two systems [244]. The impact of electron doping on the electronic structure of the parent Mott insulator has been investigated in detail by means of ARPES in $(Sr_{1-x}La_x)_2IrO_4$ [222]. Here, substitution of divalent Sr with trivalent La injects $2x$ electrons per Ir atom into the Ir $5d$ bands while preserving the strong SOC responsible for the insulating ground state found in the parent compound. The data are summarised in Fig. 5.5.

In undoped Sr_2IrO_4 ($x = 0$) the low-energy electronic structure is dominated by the LHB, whose gapped hole-like states display maxima at the antinodal points $\{\pi, 0\}$ [Fig. 5.5(a)]. Tight binding calculations performed including a realistic value for the SOC ($\lambda = 0.57$ eV) and the Coulomb repulsion ($U = 2$ eV) [222] confirmed that the LHB is of $J_{\text{eff}} = 1/2$ character. La substitution causes dramatic changes in the band structure: upon increasing the carrier concentration, the gap is progressively closed and the low-energy spectral weight shifts from the antinodal points to the nodes $\{\pi/2, \pi/2\}$. For $x = 0.05$, coherent excitations appear at the Fermi level in the form of arcs and result in four lens-like electron pockets centred around $\{\pi/2, \pi/2\}$[6]. The Fermi arcs arise from states with a quasilinear dispersion along the nodal direction which emanate from a Dirac point located around -0.1 eV below the Fermi level [222]. Around the antinodal points, the hole-like $J_{\text{eff}} = 1/2$ band of the parent compound shifts towards the Fermi level to give a band apex above the latter. This results in the appearance of a weak spectral weight devoid of any sharp features. As expected, the $J_{\text{eff}} = 3/2$ states are not strongly affected by doping.

Similar to the case of hole-doped cuprates [257], the band structure of the $x = 0.05$ sample is well approximated by calculations performed assuming a weakly interacting metallic state with $U = 0$ and $1 + 2x$ itinerant carriers per Ir site [222] [see Fig. 5.5(b)]. The Fermi surface appears to be constituted by the lens-like electron pockets of $J_{\text{eff}} = 1/2$ character already visible in the measured data and nearly square hole pockets centered at the antinodes. This distinctive configuration can be ascribed to the reduction of the crystal symmetry due to the in-plane rotation of

[6] Similar to the case of the cuprates, a previous ARPES study [223] on surface-doped Sr_2IrO_4 found a significant spectral weight only on the outer Fermi arc. The ARPES intensity of the inner part was found to be strongly dependent on the photon energy by de la Torre *et al.* [222], which could explain its absence in other investigations.

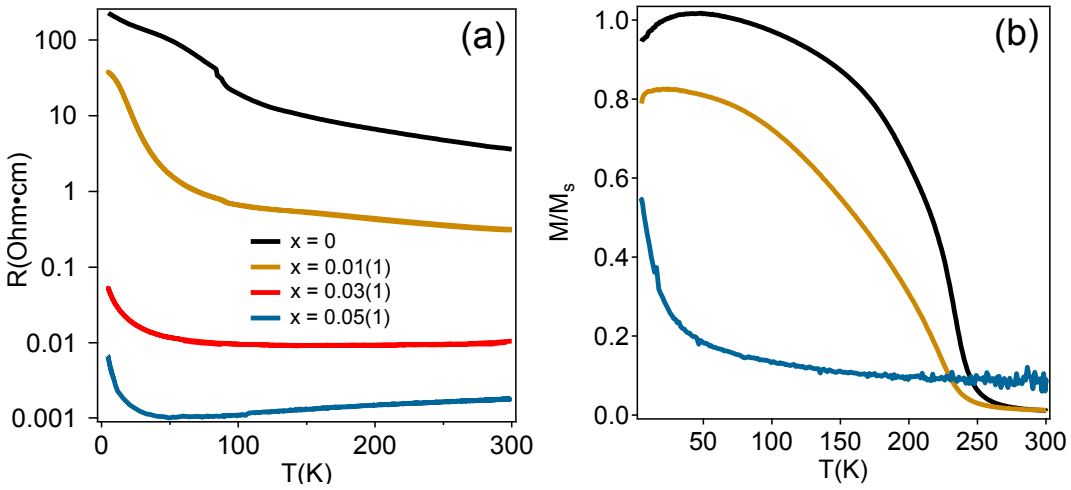

Figure 5.6: Bulk resistivity (a) and magnetisation (b) as a function of temperature for pure Sr_2IrO_4 and different levels x of La substitution. The magnetisation data were measured with an applied field of $B = 1$ T after zero-field cooling. Adapted from Ref. [222].

the IrO_6 octahedra. The smaller BZ of the resulting $I4_1/acd$ structure is associated to a backfolding by the (π,π) vector of the large circular Fermi surface centred at the $(0,0)$ that would be present in the case of an undistorted $I4/mmm$ crystal structure. A detailed analysis of the measured ARPES intensity along the Fermi arcs [222] [Fig. 5.5(c)] shows that electrons populate states localised at the Fermi level in proximity of the nodal direction, whereas a depletion of spectral weight occurs moving towards the antinodes. This phenomenon is also observed in hole-doped cuprates where it was associated to a momentum dependent energy gap, often referred to as *pseudogap* [221]. In general, the behaviour of the Sr_2IrO_4 electronic structure upon electron doping (in particular the appearance of Fermi arcs and the presence of the pseudogap) bears striking similarities to the hole-doped cuprates [221, 257–259]. The similarities extend beyond the evolution of the band structure and also concern the magnetic properties, as I will show in multiple occasions in the remainder of this chapter. The collapse of the Mott gap is far more rapid in Sr_2IrO_4 than in the cuprates, since already at $x = 0.05$ no trace of the LHB remains. On the other hand, in the cuprates the transition from the insulating to the metallic state proceeds through a more gradual transfer of spectral weight from the LHB to the Fermi arcs [258].

The destruction of the Mott insulating state upon doping is further confirmed by the evolution of the resistivity shown in Fig. 5.6(a). As free carriers are injected into the Ir 5*d* bands, the resistivity drops by several orders of magnitude and displays a positive derivative as a function of temperature for high enough doping levels, consistent with the presence of a conductive state. The upturn at low temperature

persists in the doped compounds and mirrors the behaviour reported for underdoped cuprates [260]. The evolution of the bulk magnetisation [Fig. 5.6(b)] also shows that, as the system turns metallic, the LR C-AFM order of the parent compound is suppressed and the samples become paramagnetic.

Fig. 5.7 shows the temperature-doping phase diagram proposed by Chen *et al.* [87] based on a combination of bulk measurements and neutron diffraction. In particular, the authors suggest that while LR magnetic order quickly disappears, short-range (SR) interactions persist up to the highest measured doping level [$x = 0.06(1)$]. The presence of SR order was subsequently confirmed by resonant X-ray scattering [248] and will be discussed in more detail in Chapter 5.4. An exact estimation of the boundary between the LR and SR regions of the phase diagram is prevented by the usually large error bars in the doping level values[7] and the intrinsic variability between different crystals and within different portions of the same crystal. The authors of Ref. [87] suggest that SR correlations are present for $x > 0.02$. In particular, their neutron data show that magnetic scattering is barely discerned already for $x = 0.02$ and is completely absent for $x = 0.04$. In the resonant X-ray data by Gretarsson *et al.* [248], however, no sign of LR order was found already for $x = 0.02$. A reasonable estimate for the critical concentration at which the AFM order is destroyed thus seems to be $x_c = 0.02(1)$.

In order to facilitate the comparison between different references, it is worth pointing out at this point that two different notations are found in the literature to express the doping concentration. The one used throughout the present work, i.e. $(Sr_{1-x}La_x)_2IrO_4$, is the same adopted by Chen *et al.* [87] (and the RIXS investigation by Liu *et al.* [247] discussed in Sec. 5.3.3). The La doping concentration is given by $x/(1-x)$ which, for any value of x achievable in practice, is well approximated by $x/(1-x) \approx x$. The value of x thus directly reflects the level of La substitution (e.g. $x = 0.1$ corresponds to 10% La substitution). The second notation is the one adopted by Gretarsson *et al.* [248], where the doping level is given in terms of the stoichiometry y, i.e. $Sr_{2-y}La_yIrO_4$ (here y instead of x is used to avoid confusion). In this case, the La doping concentration is given by $y/(2-y) \approx y/2$. The value of y is thus equal to twice the level of La substitution (e.g. $y = 0.1$ corresponds to 5% La substitution). The corresponding number of injected electrons in the two notations is $2x$ / Ir atom and y / Ir atom, respectively.

The phase diagram of Fig. 5.7 is analogous to the one of the hole-doped cuprates [261], confirming the similarities between these two classes of compounds. In particular, the parent compound AFM order is quickly suppressed, while SR cor-

[7] Doping levels measured by the commonly used EDX spectroscopy, as is the case for the study of Ref. [87], have an uncertainty of around 1%.

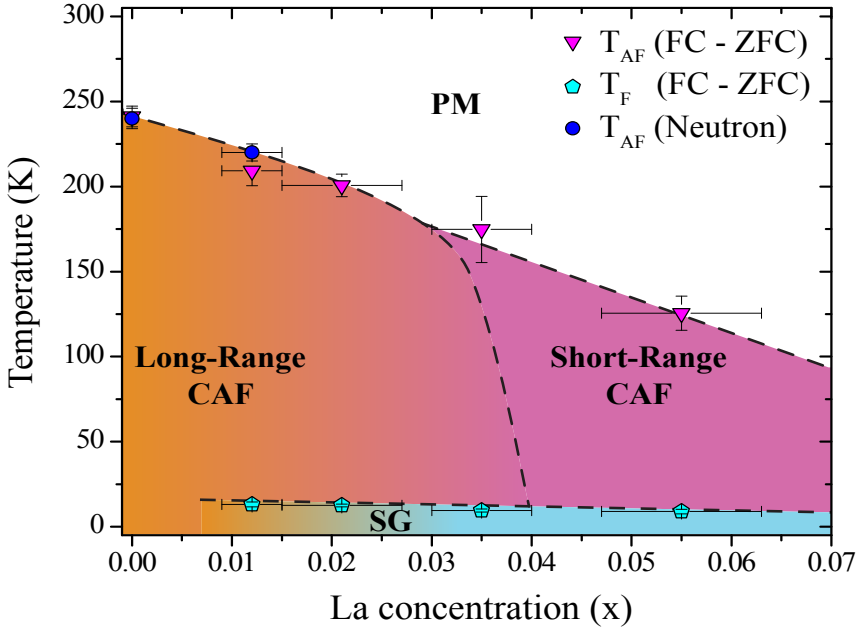

Figure 5.7: Temperature-doping phase diagram proposed by Chen *et al.* [87]. The data points correspond to the transition temperature from the paramagnetic (PM) state to the LR or SR C-AFM ordered state (T_{AF}) and to the low-temperature spin-glass (SG) state as determined by FC and ZFC bulk magnetisation measurements and neutron scattering. The dashed lines are just meant as a guide to the eye.

relations persist at high doping levels. The analogies are further strengthened by the evidence of spin-glass behaviour found in bulk magnetisation and magneto-transport data for Sr_2IrO_4 at low temperature [87], similar to the one reported for $(La_{1-x}Sr_x)_2CuO_4$ [261]. Scanning tunneling microscopy measurements performed in electron-doped Sr_2IrO_4 also show that the injection of free carriers results in an electronically phase-separated ground state where nanometer-size metallic patches appear in proximity of the dopant atoms and coexist with insulating regions persisting beyond the suppression of LR magnetic order [87]. The area probed by the measurements discussed in Sec. 5.4, and, more generally by standard scattering experiments, is several orders of magnitude larger than the metallic and insulating regions and is thus representative of their average: for $x > x_c$ the latter corresponds to a state where LR order is no longer present.

5.3 Sr_2IrO_4 magnetic Hamiltonian

The peculiar electronic and magnetic properties induced by the interplay of spin-orbit coupling and electronic correlations in iridium oxides have been a major focus

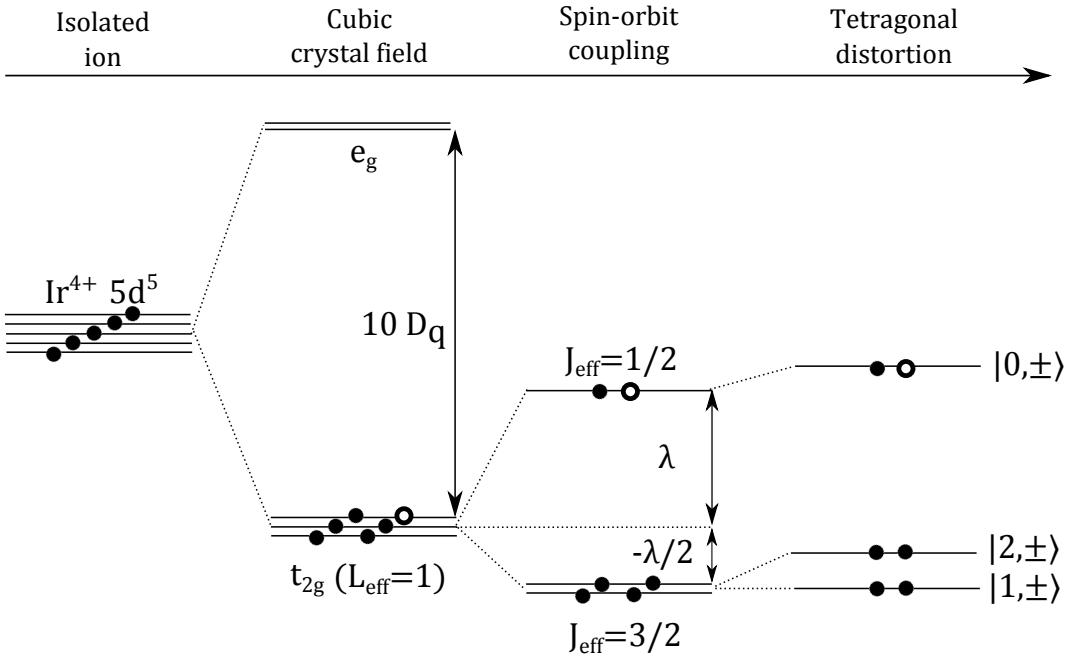

Figure 5.8: Electron energy level diagram of the Ir^{4+} ion showing the effect of the relevant terms in the Hamiltonian in order of decreasing strength (going from left to right) for the representative case of tetragonal elongation. The filled symbols correspond to electrons, while the open ones represent the hole in the t_{2g} manifold. $|0,\pm\rangle$, $|1,\pm\rangle$, $|2,\pm\rangle$ are the Kramers doublets discussed in the text, while λ is the SOC constant.

of the scientific community in recent years and extensive literature can be found on the subject. The current section provides a selection of the results which will be used to support the experimental discussion of Sec 5.4. A thorough literature review is beyond the purpose of the present work: the reader is referred to the relevant references for more details.

5.3.1 Ir^{4+} single-ion Hamiltonian

The main aspects of the local physics of Sr_2IrO_4 can be described by considering an Ir^{4+} ion ($5d^5$) at the centre of an IrO_6 octahedron. The cubic crystal field splits the $5d$ orbitals into a lower t_{2g} triplet and an upper e_g doublet. Given the large ($10Dq = 3.8$ eV [255]) crystal field splitting, all five $5d$ electrons reside in the t_{2g} manifold: the system can be treated considering a single hole in the t_{2g} subspace, while the e_g orbitals can be neglected to a good degree of approximation. As discussed in Sec. 1.1.4, the t_{2g} orbitals can be mapped onto a triplet of states with an effective orbital angular momentum $L_{\text{eff}} = 1$ [1, 26]. The strong SOC of $5d$ electrons can then act on the t_{2g} orbitals and cause a splitting of the single-ion energy levels. SOC

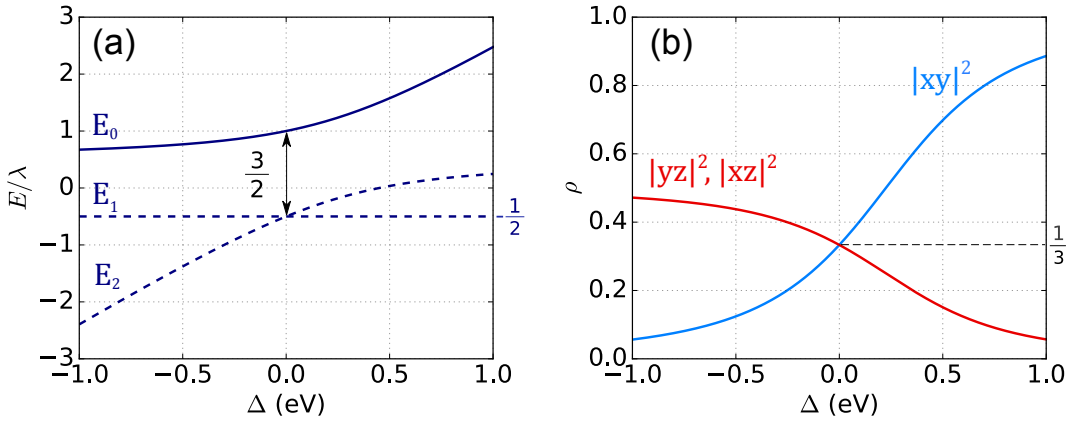

Figure 5.9: (a) Ir^{4+} eigenvalues of Eq. (5.2) as a function of the tetragonal distortion Δ. The solid line corresponds to the energy of the ground state $|0,\pm\rangle$ in the hole representation. The energies are expressed in units of the SOC constant λ. (b) Relative contributions of the different t_{2g} orbitals to the ground-state wave function $|0,\pm\rangle$ calculated as the modulus square of the corresponding prefactors in Eq. (5.3). Figure adapted from Ref. [217].

is a key ingredient of the local physics of the Ir^{4+} ion, whose main aspects have been captured by the following Hamiltonian [217, 239, 262–265]:

$$\mathscr{H} = \lambda \mathbf{L}_{\text{eff}} \cdot \mathbf{S} + \Delta \langle L_z \rangle^2 \tag{5.1}$$

where $\lambda \approx 0.4$ eV [236] is the SOC constant and $\mathbf{L}_{\text{eff}}$ and $\mathbf{S}$ are the effective orbital and spin angular momenta, respectively. This model is analogous to the one introduced to describe the Ru^{4+} ion local physics in Sec. 4.3. In the case of the Ir^{4+} ion, however, it represents a more accurate description of the single-ion physics given the single-particle nature of the electronic ground state. The second term in Eq. (5.1) models the tetragonal distortion acting on the t_{2g} manifold ($\Delta > 0$ for elongation along the c axis) which has been estimated to be in the energy range -60 meV $\leq \Delta \leq 35$ meV for Sr_2IrO_4 [238]. Five electrons, or equivalently one hole, reside in the t_{2g} levels and the electronic state is described by the orbital and spin quantum number $L_{\text{eff}} = 1$ and $S = 1/2$ [26]. Neglecting for the moment the tetragonal distortion, the spin-orbit interaction of Eq. (5.1) removes the orbital degeneracy and splits the more than half-filled t_{2g} states into an upper $J_{\text{eff}} = L_{\text{eff}} + S = 3/2$ quartet and the celebrated $J_{\text{eff}} = L_{\text{eff}} - S = 1/2$ doublet ground state [217, 236, 239] (see Sec. 1.1.4). Following a simple single-particle level approach, with the energy levels progressively filled with electrons in order of increasing energy, the order of the quartet and the doublet is normally represented inverted (as in Fig. 5.8), so that a single hole populates the $J_{\text{eff}} = 1/2$ state.

The weak tetragonal distortion further splits the $J_{\text{eff}} = 3/2$ quartet and results in three separate Kramers doublets $|0,\pm\rangle$ $|1,\pm\rangle$, $|2,\pm\rangle$, with eigenvalues respectively

given by [217]:

$$\begin{aligned} E_0 &= \frac{\lambda}{4}(1+\delta+\sqrt{9+\delta(\delta-2)}) \\ E_1 &= -\frac{\lambda}{2} \\ E_2 &= \frac{\lambda}{4}(1+\delta-\sqrt{9+\delta(\delta-2)}) \end{aligned} \tag{5.2}$$

where $\delta = 2\Delta/\lambda$ parametrizes the relative strength of the SOC and tetragonal distortion. A schematic diagram of the electronic energy levels for the Ir^{4+} ion highlighting all the relevant energy scales is reported in Fig. 5.8. In the hole representation, the state at energy E_0 is the ground state of the system. The expression of the corresponding Kramers doublet $|0,\pm\rangle$ depends on whether the Ir^{4+} magnetic moments lie along the crystallographic **c** axis or in the **ab** plane [217]:

$$\begin{aligned} |0,\pm\rangle_c &= \frac{C_0}{\sqrt{2+C_0^2}}|xy,\pm\rangle + \frac{1}{\sqrt{2+C_0^2}}(|yz,\mp\rangle \pm i|xz,\mp\rangle) \\ |0,\pm\rangle_{ab} &= \frac{1}{\sqrt{2}}\frac{C_0}{\sqrt{2+C_0^2}}(\pm|xy,\pm\rangle \mp i|xy,\mp\rangle) + \frac{1}{\sqrt{2+C_0^2}}(|yz,\mp\rangle + i|xz,\pm\rangle) \end{aligned} \tag{5.3}$$

with $C_0 = \dfrac{\delta-1+\sqrt{9+\delta(\delta-2)}}{2}$. In Eq. (5.3), $|+\rangle$ and $|-\rangle$ represent states with spin $S_z = 1/2$ (spin up) or $S_z = -1/2$ (spin down), respectively.

The eigenvalues of Eq. (5.2) (in units of λ) are represented in Fig. 5.9(a) as a function of the tetragonal distortion Δ, while Fig. 5.9(b) shows the corresponding contributions of the $|xy\rangle$, $|yz\rangle$ and $|xz\rangle$ orbitals to the ground-state wave function. As can be seen from the figure, three states at different energies are generally present and the relative contributions of the $|xy\rangle$, $|yz\rangle$ and $|xz\rangle$ orbitals depend on the strength of the tetragonal distortion. In particular, for $\Delta \gg \lambda$ only the $|xy\rangle$ state enters the expression of the ground-state wave function. This can be qualitatively understood considering that in the case of tetragonal elongation the $|yz\rangle$ and $|xz\rangle$ states become energetically unfavourable and the hole tends to reside on the $|xy\rangle$ orbital. The opposite is true for $\Delta \ll \lambda$, in which case the ground state is made of an equal admixture of $|yz\rangle$ and $|xz\rangle$ orbitals. The pure $J_{\text{eff}} = 1/2$ ground state, first reported in Sr_2IrO_4 by Kim *et al.* [8], is strictly speaking realized only for perfect cubic symmetry, i.e. when $\Delta = 0$. The tetragonal field in Sr_2IrO_4 is much smaller than the SOC [238] and the electronic structure of the Ir^{4+} ion thus represents a close realization of the $J_{\text{eff}} = 1/2$ state [216, 217, 238]. In this case, the E_1 and E_2 levels become degenerate and give rise to the $J_{\text{eff}} = 3/2$ quartet, which is separated with respect to the $J_{\text{eff}} = 1/2$ doublet by an amount equal to $3\lambda/2$ [Fig. 5.9(a)].

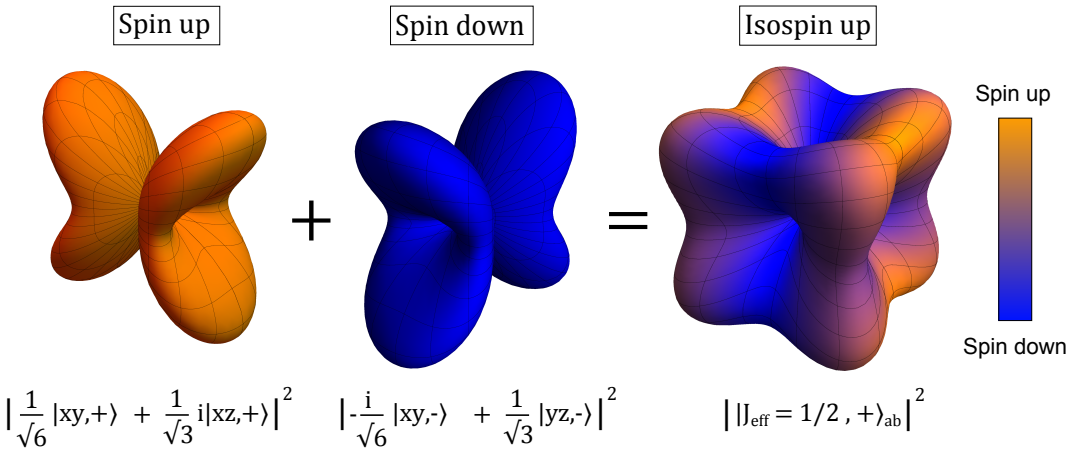

Figure 5.10: Real-space representation of the $|J_{\text{eff}}=1/2,+\rangle_{ab}$ charge density of Eq. (5.4). The colour scale represents the spin up (orange) or spin down (blue) character of the electron.

The $J_{\text{eff}}=1/2$ ground-state wave function is easily obtained from Eq. (5.3) for $\Delta=0$ ($C_0=1$):

$$|J_{\text{eff}}=1/2,\pm\rangle_c=\frac{1}{\sqrt{3}}|xy,\pm\rangle+\frac{1}{\sqrt{3}}(|yz,\mp\rangle\pm i|xz,\mp\rangle)$$
$$|J_{\text{eff}}=1/2,\pm\rangle_{ab}=\frac{1}{\sqrt{6}}(\pm|xy,\pm\rangle\mp i|xy,\mp\rangle)+\frac{1}{\sqrt{3}}(|yz,\mp\rangle+i|xz,\pm\rangle) \tag{5.4}$$

Considering the linear combinations of Eq. (1.9)[8], the $|J_{\text{eff}}=1/2,\pm\rangle_c$ state can be explicitly expressed in terms of the $L_{\text{eff}}=0$ and $L_{\text{eff}}=\pm1$ orbitals:

$$-\frac{1}{\sqrt{3}}|t_{2g}^{0},\pm\rangle+\frac{\sqrt{2}i}{\sqrt{3}}|t_{2g}^{\mp1},\mp\rangle \tag{5.5}$$

In the case of perfect cubic symmetry, $|xy\rangle$, $|yz\rangle$ and $|xz\rangle$ equally contribute to the ground-state wave function [Fig. 5.9(b)]. One of the main features of the Ir^{4+} $J_{\text{eff}}=1/2$ state, which can be appreciated from Eqs. (5.4) and (5.5), is the peculiar admixture of orbital and spin degrees of freedom induced by the strong spin-orbit interaction. The latter results in an entangled ground state with markedly different properties to the ones of lighter TM elements, where the role of SOC is relegated to a weak perturbation. The unique nature of the $J_{\text{eff}}=1/2$ state is made even clearer by the real-space representation of its electron cloud, shown in Fig. 5.10

[8]The $|t_{2g}\rangle^{\pm1}$ states of Eq. (1.9) can be rewritten as follows: $|t_{2g}^{1}\rangle=-\frac{i}{\sqrt{2}}(-i|xz\rangle+|yz\rangle)$ and $|t_{2g}^{-1}\rangle=-\frac{i}{\sqrt{2}}(i|xz\rangle+|yz\rangle)$.

for the case of **ab**-plane moments relevant for Sr_2IrO_4. This displays a distinctive cubic shape with concomitant spin up and down character arising from the coherent superposition of the original t_{2g} orbitals and the hole spin. The reader is invited to notice that the particular expression of the $J_{\text{eff}} = 1/2$ wave function does not have significant consequences on the physics of the system and will not impact the considerations on the magnetic Hamiltonian presented in the remainder of this section. However, it does have an impact on the resonant elastic scattering cross-section and the interpretation of the corresponding experimental data [217].

5.3.2 Exchange interaction between $J_{\text{eff}} = 1/2$ magnetic moments

The $|J_{\text{eff}} = 1/2, \pm\rangle$ states of Eq. (5.4) are normally referred to as *isospins* (or, equivalently, *pseudospins*), in analogy with the $|S = \pm 1/2\rangle$ states of a pure spin system. Given the peculiar entanglement of orbital and spin degrees of freedom of the $|J_{\text{eff}} = 1/2, \pm\rangle$ wave function, however, the exchange interactions between Ir^{4+} isospins are markedly different from the ones of standard $S = 1/2$ spins. In particular, the isospin exchange Hamiltonian shows a unique dependence on the geometry of the oxygen-mediated superexchange path which controls the interaction between the Ir^{4+} moments in an oxide. In the seminal paper by Jackeli and Khaliullin [239] a superexchange model is developed for two Ir-O-Ir bond geometries commonly found in Ir oxides: (i) a 180°-bond geometry formed by corner-sharing octahedra (Fig. 5.11) and (ii) a 90°-bond one formed by edge-sharing octahedra. My discussion will focus on the former case since, as can be seen from the crystal structure of Fig. 5.1, Sr_2IrO_4 is closer to the 180° limit. The 90° geometry results in a completely different magnetic Hamiltonian, which represents the quantum analogue of the so-called *compass model* [266]. The latter has attracted a great attention in recent years as it represents a realization of the well-known Kitaev model [267] on layered honeycomb iridates A_2IrO_3 (where A is an alkali atom).

In the case of 180° bonds, one can show [239] that the nearest-neighbour t_{2g} hopping matrix is diagonal in the orbital space and, on a given bond, only two orbitals are active: considering, for instance, a bond along the **x** direction, only the $|xy\rangle$ and $|xz\rangle$ orbitals contribute to the superexchange process (Fig. 5.11). The corresponding exchange Hamiltonian for Ir^{4+} isospins can be calculated by projecting the superexchange model onto the isospins states of Eq. (5.4). In the limit of strong SOC (i.e. larger than the exchange interactions between isospins) and considering

for the moment perfect cubic symmetry ($\Delta = 0$), this leads to the following expression [239]:

$$\mathscr{H}_{ij} = J_1 \tilde{\mathbf{S}}_i \cdot \tilde{\mathbf{S}}_j + J_2 (\tilde{\mathbf{S}}_i \cdot \hat{\mathbf{r}}_{ij})(\hat{\mathbf{r}}_{ij} \cdot \tilde{\mathbf{S}}_j) \tag{5.6}$$

where $\hat{\mathbf{r}}_{ij}$ is the unit vector along the ij bond, $J_{1(2)} = 16t^2/(9U)\nu_{1(2)}$ is the isotropic (anisotropic) exchange integral (with t hopping amplitude and U on-site Coulomb repulsion) and $\tilde{\mathbf{S}}_i$ is the operator acting on the i-th $J_{\text{eff}} = 1/2$ isospin. The i and j sites correspond to two nearest-neighbour[9] Ir^{4+} ions within an IrO_2 plane. As mentioned in Sec 5.2, given the 2D character of Sr_2IrO_4, interactions between neighbouring planes are expected to be much weaker and can thus be neglected. Here, $\tilde{\mathbf{S}}$ is used instead of $\mathbf{J}_{\text{eff}}$ to avoid confusion with the exchange constants $J_{1(2)}$. The latter are expressed in terms of the quantities $\nu_1 = (3r_1 + r_2 + 2r_3)$ and $\nu_2 = (r_1 - r_2)/4$, where r_n are parameters controlling the multiplet structure of the excited states. These are given by $r_1 = 1/(1-3\eta)$, $r_2 = 1/(1-\eta)$ and $r_3 = 1/(1+2\eta)$ and thus depend exclusively on the ratio $\eta = J_H/U$ of the Hund's coupling J_H and the Coulomb repulsion U. Eq. (5.6) consists of an isotropic Heisenberg interaction and an anisotropic pseudodipolar term. The size of the anisotropy is entirely controlled by the relative strength of J_H and U through the parameter η. In particular, for small values of η, $\nu_1 \approx 1$ and $\nu_2 \approx \eta/2$: the Hamiltonian is, in this case, predominantly isotropic with only a weak dipolar-like term. Therefore in the strong SOC regime, despite the peculiar physics of the Ir^{4+} ion ground state, the anisotropy of the magnetic Hamiltonian is not controlled by λ, but rather by the Hund's coupling J_H, analogous to the case of negligible SOC.

The Hamiltonian of Eq. (5.6) can be specialized for the case of Sr_2IrO_4, where, taking into account the rotations of the IrO_6 octahedra (see Sec. 5.2) and extending it to include a finite tetragonal distortion Δ, it can be written as follows [216, 239]:

$$\mathscr{H}_{ij} = J \tilde{\mathbf{S}}_i \cdot \tilde{\mathbf{S}}_j + J'_z \tilde{S}^z_i \tilde{S}^z_j + \mathbf{D} \cdot (\tilde{\mathbf{S}}_i \times \tilde{\mathbf{S}}_j) + \mathscr{H}' \tag{5.7}$$

The first term on the right-hand side is the isotropic Heisenberg exchange. The corresponding exchange integral is given by $J = 4t^2\nu_1(t_s^2 - t_a^2)/U$, where $t_s = \sin^2\theta + \frac{1}{2}\cos^2\theta\cos 2\alpha$ and $t_a = \frac{1}{2}\cos^2\theta\sin 2\alpha$. Here $\alpha \approx 11.8°$ [238, 249] is the in-plane rotation of the IrO_6 octahedra described in Sec. 5.2, while θ is a parameter defined such that $\tan 2\theta = \dfrac{2\sqrt{2}}{\lambda/(\lambda - 2\Delta)}$, which thus depends on the relative strength of the tetragonal field and SOC. The second and third terms in Eq. (5.7) correspond to the symmetric[10] and antisymmetric anisotropic exchange (i.e. the DMI

[9] As I will show later on, an accurate description of the magnetic excitation spectrum requires the addition of next-nearest-neighbour interactions.

[10] Starting from the general form of a two-spin interaction Hamiltonian one can see that the gen-

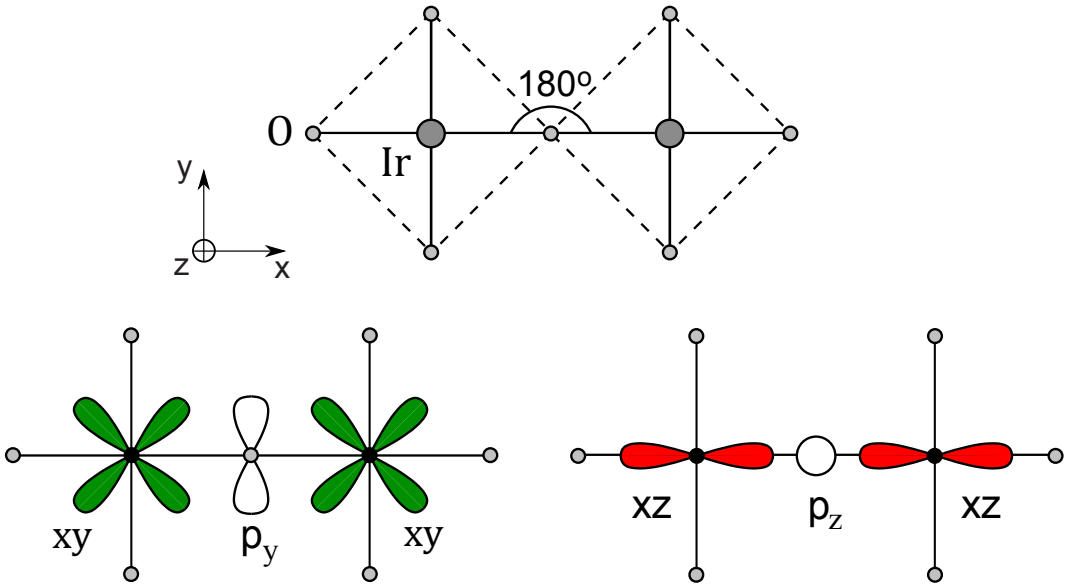

Figure 5.11: Ir-O-Ir 180°-bond geometry relevant for the case of Sr_2IrO_4 and Ir t_{2g} and O p orbitals which contribute to the superexchange interaction between the Ir^{4+} magnetic moment in the model discussed in the text.

described in Sec. 3.2), respectively. Here, $J'_z = 8t^2\nu_1 t_a^2/U$ while $\mathbf{D}$ is the DM vector. This is directed along the crystallographic $[00\bar{1}]$ direction and can be written as $\mathbf{D} = (0,0,-D)$, with $D = 2\nu_1 t_s t_a$. Finally, the additional term $\mathscr{H}'$ includes the anisotropic contributions arising as a result of the finite Hund's coupling J_H. The symmetric and antisymmetric anisotropic terms of Eq. (5.7) vanish when $\alpha = 0$, in which case anisotropic interactions between the iridium moments only arise as a result of the finite Hund's coupling. However, this is true even in the case of non-zero octahedral rotations. Indeed, Shekhtman *et al.* [268] showed that, neglecting the $\mathscr{H}'$ term, Eq. (5.7) can be effectively rewritten in terms of an isotropic Heisenberg term between two spin operators rotated with respect to the original ones by the spin canting angle $\pm\phi$, with $\tan 2\phi = D/J$. Therefore, there is no true magnetic anisotropy in the absence of Hund's coupling.

Following the derivation by Jackeli and Khaliullin [239], in the general case of finite Hund's coupling the magnetic Hamiltonian includes anisotropic terms and can be written as follows:

$$\mathscr{H}_{ij} = J_{\rm ex}\tilde{\mathbf{S}}_i \cdot \tilde{\mathbf{S}}_j + J_z \tilde{S}_i^z \tilde{S}_j^z \pm J_{xy}(\tilde{S}_i^x \tilde{S}_j^x - \tilde{S}_i^y \tilde{S}_j^y) \tag{5.8}$$

where $J_{\rm ex} = 4t^2\nu_1(t_s^2 + t_a^2)/U - J_z$, $J_z = -(4t^2/U)\nu_2 \cos^2\theta\cos 2\theta$, $J_{xy} = (4t^2/U)\nu_2 \sin^2\theta\cos^2\theta$ and a $+(-)$ sign is taken for a bond along the x(y)-axis.

eral form of the symmetric anisotropic exchange is $J_{ij}^{xy}(S_i^x S_j^x + S_i^y S_j^y) + J_{ij}^z S_i^z S_j^z$ (see Sec. 3.2).

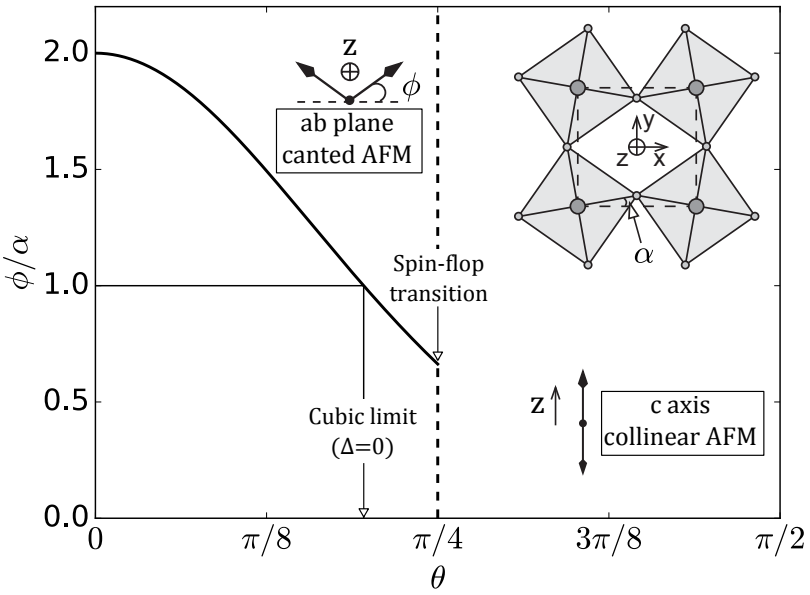

Figure 5.12: Ir^{4+} magnetic moment canting angle ϕ (in units of the IrO_6 octahedra rotation α) as a function of the tetragonal distortion parameter $\theta = 1/2 \arctan[2\sqrt{2}\lambda/(\lambda - 2\Delta)]$. In the cubic limit, $\theta = \arcsin 1/\sqrt{3} \approx \pi/5$ and $\phi/\alpha = 1$. The vertical dashed line at $\theta = \pi/4$ marks the spin-flop transition from the **ab**-plane C-AFM structure to the **c**-axis collinear one discussed in the text. The inset shows a projection of the IrO_6 octahedra onto the Sr_2IrO_4 **ab** plane, which are rotated by an angle $\pm\alpha$ about the **c** axis. Figure adapted from Ref. [239].

An analogous Hamiltonian was also derived by Igarashi and Nagao [240] starting from a multi-orbital Hubbard model by means of a second-order perturbation theory approach. The latter explicitly shows that the anisotropic exchange coupling constants J_z and J_{xy} vanish when $J_H = 0$.

Eq. (5.8) supports two different magnetic ground states, depending on the relative strength of the spin-orbit interaction λ and the tetragonal distortion Δ. For $\theta \leq \pi/4$ ($\Delta \leq \lambda/2$), $J_z < 0$ and Eq. (5.8) gives rise to the C-AFM ground state with magnetic moments lying in the **ab** of the crystal found in Sr_2IrO_4 (see Sec. 5.2). In this phase, the magnetic canting angle ϕ is given by the relation

$$\phi = \frac{1}{2}\arctan\frac{D}{J} = \frac{2t_s(\theta,\alpha)t_a(\theta,\alpha)}{t_s^2(\theta,\alpha) - t_a^2(\theta,\alpha)} \tag{5.9}$$

where the dependence of t_s and t_a on the parameter θ and the IrO_6 octahedra rotation α reported earlier in this section has been highlighted. The canting angle ϕ as a function of θ is reported in Fig. 5.12 for a fixed value $\alpha = 11^\circ$ of the octahedral rotation. In the cubic limit $\Delta = 0$ ($\theta = \arcsin 1/\sqrt{3}$), $\phi = \alpha$. This implies that, for a pure $J_{\text{eff}} = 1/2$ state, the magnetic canting angle rigidly follows the octahedral rotation. Eq. (5.8) thus naturally accounts for one of the distinctive aspects of

the physics of Sr_2IrO_4, i.e. the locking of the Ir^{4+} magnetic moments to the staggered rotations of the IrO_6 octahedra and the consequent anomalously large value of the net magnetisation [253] compared to the one in La_2CuO_4 [269]. Tetragonal compression ($\Delta < 0$, $\theta < \arcsin 1/\sqrt{3}$) causes an increase in the ϕ/α ratio and, as a result, of the net magnetic moment. On the other hand, tetragonal elongation ($\Delta > 0$, $\theta > \arcsin 1/\sqrt{3}$) forces the canting angle to decrease. In general, this represents a clear manifestation of the magneto-elastic coupling induced by the entangled nature of the Ir^{4+} ground state [Eq. (5.3)]. For large enough elongations, i.e. $\theta > \pi/4$ ($\Delta > \lambda/2$), the coupling constant J_z becomes positive and a spin-flop transition to a collinear **c**-axis antiferromagnet occurs. This ground state is realized in the bilayer compound $Sr_3Ir_2O_7$, which exhibits markedly different static and dynamic magnetic properties with respect to its single layer counterpart [270–273]. The presence of a spin-flop transition sets an upper limit of $\Delta = \lambda/2 \approx 0.2$ meV to the value of the tetragonal distortion in Sr_2IrO_4, consistent with the experimental estimate -60 meV $\leq \Delta \leq 35$ meV [238].

5.3.3 Single-magnon excitation spectrum

The presence of anisotropic interaction terms breaks the full rotational symmetry of the magnetic Hamiltonian and is expected to give rise to a finite spin-wave gap in the magnetic excitation spectrum. The latter was calculated by Igarashi and Nagao [240, 241] in a localised spin picture considering an analogous Hamiltonian to the one of Eq. (5.8) in the case of zero tetragonal distortion ($\Delta = 0$) and extended to include next-nearest-neighbour (J'_{ex}) and third-nearest-neighbour (J''_{ex}) interactions:

$$\mathscr{H}_{ij} = J_{ex}\tilde{\mathbf{S}}_i \cdot \tilde{\mathbf{S}}_j + J'_{ex}\tilde{\mathbf{S}}_i \cdot \tilde{\mathbf{S}}_j + J''_{ex}\tilde{\mathbf{S}}_i \cdot \tilde{\mathbf{S}}_j + J_z \tilde{S}^z_i \tilde{S}^z_j \pm J_{xy}(\tilde{S}^x_i \tilde{S}^x_j - \tilde{S}^y_i \tilde{S}^y_j) \tag{5.10}$$

The Hamiltonian of Eq. (5.10) can be solved in the linear spin-wave theory approximation, which leads to the following two magnetic modes [240]:

$$E_{\pm}(\mathbf{Q}_\perp) = 2J_{ex}\sqrt{[1 - \xi(\mathbf{Q}_\perp) \pm |B(\mathbf{Q}_\perp)|]^2 - [A(\mathbf{Q}_\perp)]^2} \tag{5.11}$$

where $\mathbf{Q}_\perp$ is the in-plane momentum transfer defined inside the first magnetic BZ (see Fig 5.3). The parameters in Eq. (5.11) are given by

$$\begin{aligned} A(\mathbf{Q}_\perp) &= (1+g_z)\gamma(\mathbf{Q}_\perp) - g_{xy}\eta(\mathbf{Q}_\perp) \\ B(\mathbf{Q}_\perp) &= g_z\gamma(\mathbf{Q}_\perp) + g_{xy}\eta(\mathbf{Q}_\perp) \\ \xi(\mathbf{Q}_\perp) &= \frac{J'_{\rm ex}}{J_{\rm ex}}[1-\gamma'(\mathbf{Q}_\perp)] + \frac{J''_{\rm ex}}{J_{\rm ex}}[1-\gamma''(\mathbf{Q}_\perp)] \end{aligned} \tag{5.12}$$

where $\gamma(\mathbf{Q}_\perp) = \frac{1}{2}(\cos Q_x + \cos Q_y)$, $\gamma'(\mathbf{Q}_\perp) = \cos Q_x \cos Q_y$, $\gamma''(\mathbf{Q}_\perp) = \frac{1}{2}[\cos(2Q_x) + \cos(2Q_y)]$, $\eta(\mathbf{Q}_\perp) = \frac{1}{2}(\cos Q_x - \cos Q_y)$, $g_z = J_z/(2J_{\rm ex})$, and $g_{xy} = J_{xy}/(2J_{\rm ex})$.

Following the derivation by Igarashi and Nagao [241], one can introduce the so-called bonding (+) and antibonding (−) combinations of the Fourier transforms $\mathbf{S}_{a,b}(\mathbf{Q}_\perp)$ of the isospin operators in the first magnetic BZ, defined as $\mathbf{S}_\pm(\mathbf{Q}_\perp) = \frac{1}{\sqrt{2}}[\mathbf{S}_a(\mathbf{Q}_\perp) \pm \mathbf{S}_b(\mathbf{Q}_\perp)]$. Here, a and b labels the two sublattices of the Sr_2IrO_4 AFM structure. The magnetic excitation spectra probed by inelastic neutron or X-ray scattering are given by the correlation functions of these operators:

$$R^{\mu\mu}_\pm(\mathbf{Q}_\perp,\omega) = \int S^\mu_\pm(\mathbf{Q}_\perp,t) S^\mu_\pm(-\mathbf{Q}_\perp,0) e^{i\omega t} dt \tag{5.13}$$

where $\mu = x, y, z$ and the bonding and antibonding combinations are valid for in-plane momentum transfers inside and outside the first magnetic BZ, respectively. Calling $\mathbf{x}$ the direction along the isospin vector, the single-magnon modes are associated to the in-plane $R^{yy}_\pm(\mathbf{Q}_\perp,\omega)$ and out-of-plane $R^{zz}_\pm(\mathbf{Q}_\perp,\omega)$ transverse correlation functions. The longitudinal component $R^{xx}_\pm(\mathbf{Q}_\perp,\omega)$ is linked to two-magnon excitations and can be neglected for the purpose of the present discussion. For $\mathbf{Q}_\perp$ values inside the first magnetic BZ, one can show [241] that $R^{yy}(\mathbf{Q}_\perp,\omega)$ and $R^{zz}(\mathbf{Q}_\perp,\omega)$ are given by δ functions centred at E_+ and E_- [see Eq. (5.11)], respectively. On the other hand, for $\mathbf{Q}_\perp$ values outside the first magnetic BZ, $R^{yy}(\mathbf{Q}_\perp,\omega)$ and $R^{zz}(\mathbf{Q}_\perp,\omega)$ are centred at E_- and E_+, respectively. The corresponding spectral weights are given by:

$$I_\pm(\mathbf{Q}_\perp) \propto \left[\cosh\theta^\pm(\mathbf{Q}_\perp) - \sinh\theta^\pm(\mathbf{Q}_\perp)\right]^2 \tag{5.14}$$

with $\tanh 2\theta^\pm(\mathbf{Q}_\perp) = \dfrac{A(\mathbf{Q}_\perp)}{1-\xi(\mathbf{Q}_\perp) \pm |B(\mathbf{Q}_\perp)|}$.

Within the multi-orbital Hubbard model by Igarashi and Nagao [240], J_z is found to be negative for all values of U and J_H explored [consistent with the basal plane AFM structure of Sr_2IrO_4 (see Fig. 5.12)], while $J_{xy} = -J_z$. The value of the

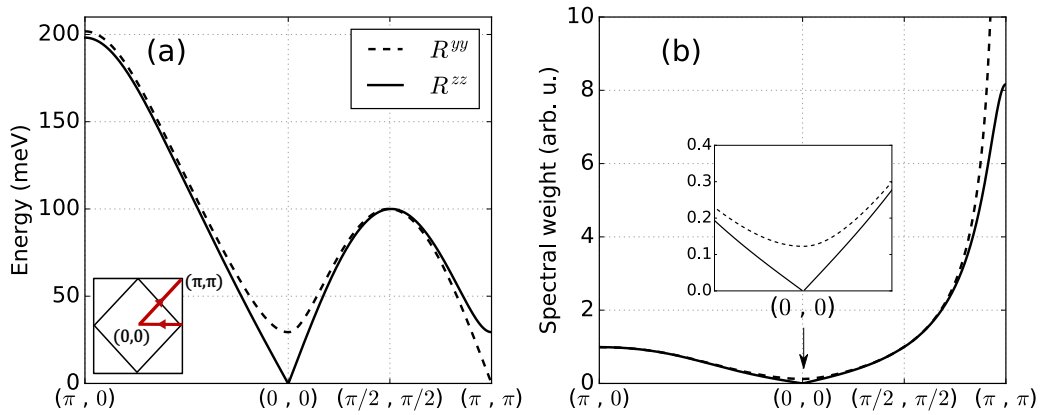

Figure 5.13: Energy (a) and spectral weight (b) of the in-plane (dashed line) and out-of-plane (solid line) single-magnon modes in the model of Eq. (5.10) calculated for $J_{\rm ex} = 60$ meV, $J'_{\rm ex} = -20$ meV, $J''_{\rm ex} = 15$ meV, $J_z = -1.8$ meV and $J_{xy} = 1.8$ meV [240, 241]. The inset in (a) displays the path in the first BZ along which the spin-spin correlation functions $R^{\mu\mu}(\mathbf{Q}_\perp, \omega)$ of Eq. (5.13) associated to the single-magnon modes have been evaluated, while the inset in (b) shows a detail of the spectral weight around $(0,0)$. Figure adapted from Ref. [241].

isotropic exchange integral $J_{\rm ex} = 60$ meV [236] is well reproduced by considering $U = 3.5$ eV, $U' = U - 2J_H = 2.6$ meV, $J_H = 0.45$ eV, $t = 0.3$ eV and $\lambda = 0.4$ eV, which give $J_z = -J_{xy} = -1.8$ meV. The corresponding single-magnon energy dispersion and spectral weight in the first BZ are shown in Fig. 5.13, where the values $J'_{\rm ex} = -20$ meV and $J''_{\rm ex} = 15$ meV have been considered [236]. Although significantly smaller than the isotropic exchange integrals, J_z and J_{xy} have a sizeable impact on the calculated magnetic excitation spectrum. The latter consists of two distinct magnetic modes, which are non-degenerate throughout the entire BZ with the exception of $(\pi/2, \pi/2)$, where they intersect. The one corresponding to fluctuations in the **ab** of the crystal (R^{yy}) displays a finite gap at the Γ point $(0,0)$ and is gapless at the AFM propagation vector (π,π), while the opposite is true for the out-of-plane one (R^{zz}). The size of the gap is given by $E^{\rm gap}_{(0,0)} = 4\sqrt{-J_z J_{\rm ex}}/\sqrt{2} \approx 29$ meV. The spectral weight of the out-of-plane mode vanishes at $(0,0)$ and reaches its (finite) maximum value at (π,π), while the in-plane one is non-zero at $(0,0)$ and diverges at (π,π). As mentioned earlier, J_z and J_{xy} vanish for $J_H = 0$: in this case, the two magnetic modes become degenerate and display a zero energy gap at both $(0,0)$ and (π,π) (Goldstone modes). The corresponding spectral weight is zero at the Γ point and diverges at the AFM propagation vector.

An alternative Hamiltonian to the one of Eq. (5.10) was proposed by Vale *et al.* [242] to account for the temperature dependence of the magnetic critical fluctuations above the Néel transition in Sr_2IrO_4. The latter was found to be consistent with

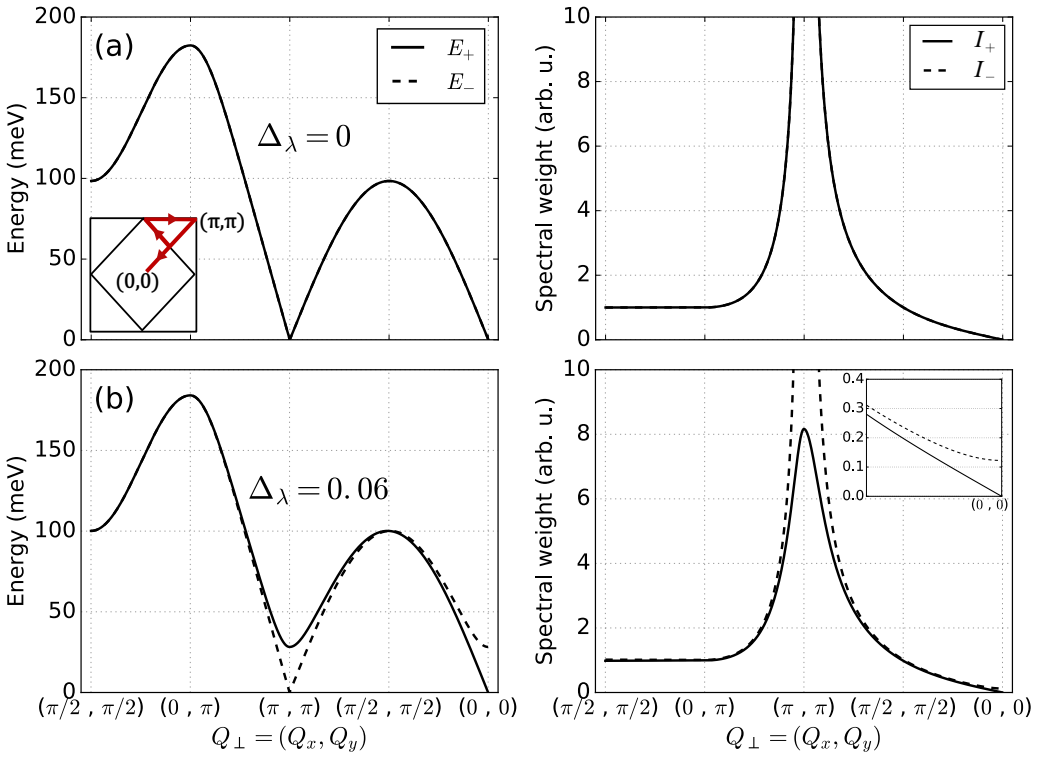

Figure 5.14: Energy (left) and spectral weight (right) of the 2DAH model linear spin-wave solutions for vanishing (a) and finite (b) values of the anisotropy parameter Δ_λ. The inset in (a) displays the path in the first BZ along which the linear spin-wave solutions of Eq. (5.16) have been evaluated, while the inset in (b) shows a detail of the spectral weight around $(0,0)$.

the presence of a significant XY anisotropy in the interaction between magnetic moments. In particular, both the critical scattering measurements and previously collected RIXS data [237] were successfully interpreted in terms of the following 2D anisotropic Heisenberg (2DAH) Hamiltonian [274, 275]:

$$\mathscr{H}^{ij}_{\text{2DAH}} = \tilde{J}\left[\tilde{S}^x_i \tilde{S}^x_j + \tilde{S}^y_i \tilde{S}^y_j + (1-\Delta_\lambda)\tilde{S}^z_i \tilde{S}^z_j\right] + J'_{\text{ex}}\tilde{\mathbf{S}}_i \cdot \tilde{\mathbf{S}}_j + J''_{\text{ex}}\tilde{\mathbf{S}}_i \cdot \tilde{\mathbf{S}}_j, \qquad (5.15)$$

where $\tilde{J} = J_{\text{ex}}/(1-\Delta_\lambda)$ is an effective nearest-neighbour exchange integral depending on the dimensionless in-plane anisotropy parameter $0 \leq \Delta_\lambda \leq 1$ [276] and J'_{ex} and J''_{ex} model the next-nearest-neighbour and third-nearest-neighbour interactions, respectively. The description of the magnetic exchange interactions provided by the 2DAH model is equivalent to the one of Eq. (5.10) in that they both consider a different coupling for the in-plane (x, y) and out-of-plane (z) components of the $\tilde{\mathbf{S}}_i$ isospins. This reflects an XY anisotropy of the exchange interactions. In the case of Eq. (5.15), the anisotropy is parametrized by the quantity Δ_λ, which can be related

to the anisotropic exchange integrals J_z and J_{xy} of Eq. (5.10) by $\Delta_\lambda = \dfrac{J_{xy}-J_z}{J_{\rm ex}+J_{xy}}$.

Following an analogous derivation to the one leading to Eq. (5.11), the linear spin-wave solutions of the 2DAH Hamiltonian are given by the following two transverse magnetic modes:

$$E_\pm(\mathbf{Q}_\perp) = 2\tilde{S}\sqrt{[A(\mathbf{Q}_\perp)]^2 - [B^\pm(\mathbf{Q}_\perp)]^2} \tag{5.16}$$

Here, $\tilde{S} = 1/2$ is the Ir^{4+} isospin and the parameters A and $B^\pm$ are defined as follows

$$\begin{aligned} A(\mathbf{Q}_\perp) &= 2\left(\tilde{J} - J'_{\rm ex} - J''_{\rm ex} + J_2\cos Q_x \cos Q_y\right) + J''_{\rm ex}\left(\cos 2Q_x + \cos 2Q_y\right) + \Gamma \\ B^\pm(\mathbf{Q}_\perp) &= \tilde{J}(\cos Q_x + \cos Q_y) \pm \Gamma \end{aligned} \tag{5.17}$$

where $\Gamma = \tilde{J}\Delta_\lambda/2$. The corresponding spectral weights are given by Eq. (5.14) with, in this case, $\tanh 2\theta^\pm(\mathbf{Q}_\perp) = \dfrac{B^\pm(\mathbf{Q}_\perp)}{A(\mathbf{Q}_\perp)}$. Consistent to the solutions of the model by Igarashi and Nagao [241] (see Fig. 5.13), E_- is polarised in the **ab** plane of the crystal while E_+ is perpendicular to it.

The two modes are displayed in Fig. 5.14 for two different values of the anisotropy parameter Δ_λ. For $\Delta_\lambda = 0$ [Fig. 5.14(a)], the 2DAH Hamiltonian reduces to a standard isotropic Heisenberg model. Two degenerate gapless modes are in this case present, with a spectral weight which diverges at (π,π) and vanishes at $(0,0)$. Introducing a finite value of Δ_λ removes the degeneracy between the two magnetic modes. In particular, considering $J_{\rm ex}$ and $J_z = -J_{xy} = -1.8$ meV [240] one obtains $\Delta_\lambda = 0.06$. In this case, E_+ [solid line in Fig. 5.14(b)] is gapless at $(0,0)$ and gapped at (π,π), while the exact opposite is true for E_- [dashed line in Fig. 5.14(b)]. The value of the gap is the same for the two modes. The latter are also degenerate at $(\pi/2,\pi/2)$ and $(0,\pi)$. With regard to the spectral weight, S_+ vanishes at $(0,0)$ and reaches its (finite) maximum value at (π,π), while S_- (larger than I_+ throughout the entire first BZ) is non-zero at $(0,0)$ and divergent at (π,π). For $\Delta_\lambda \neq 0$ the 2DAH model thus results in a magnetic excitation spectrum analogous to the one of Fig. 5.13. Similar models to the ones of Eqs. (5.10) and (5.15) were also derived by other authors [243, 277, 278] following several different approaches. Although the details of the resulting Hamiltonian show slight variations from one study to another, they all agree on the presence of a significant in-plane anisotropy in the exchange interactions between Ir^{4+} isospins. In particular Solovyev *et al.* [243] predicted a value of 0.087 for the anisotropy parameter Δ_λ, close to the estimate of 0.06 by Igarashi and Nagao [240].

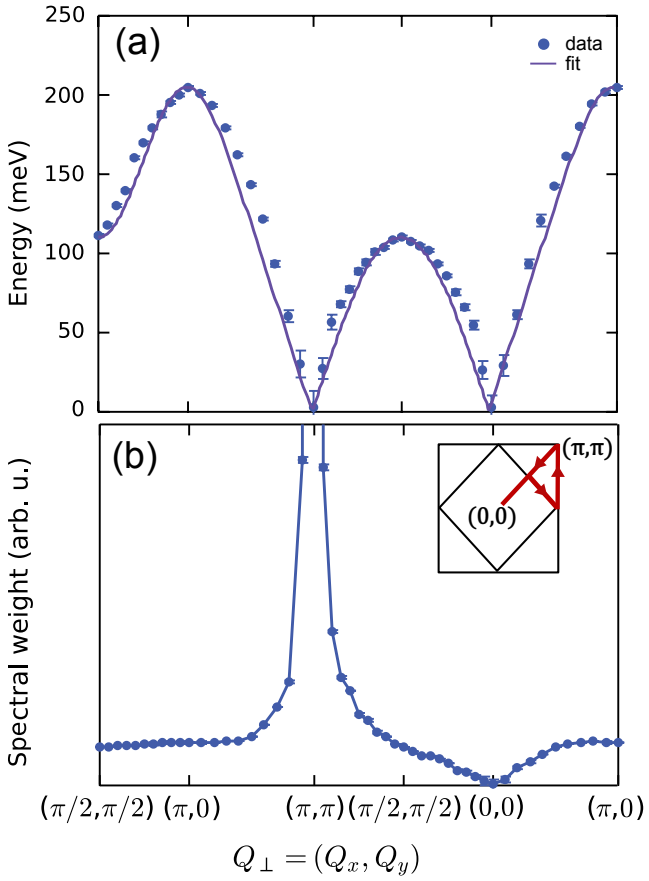

Figure 5.15: Sr_2IrO_4 single-magnon (a) energy and (b) spectral weight as a function of the in-plane momentum transfer reported by Kim *et al.* [236]. The solid lines represent the best fit to an isotropic Heisenberg model, with the best fit parameters reported in Table 5.1. Figure adapted from Ref. [236].

5.3.3.1 Magnetic excitations in pure and electron-doped Sr_2IrO_4: previous reports

The investigation of the magnetic excitations in $(Sr_{1-x}La_x)_2IrO_4$ has been mainly carried out on single crystal samples by means of RIXS at the Ir L_3 edge (see Sec. 2.1.2). The small crystal size and large neutron absorption cross section of the Ir atom have hindered the exploitation of inelastic neutron scattering. The single-magnon excitation spectrum of the parent compound was first reported by Kim *et al.* [236]. Their study made use of an early RIXS spectrometer with an energy resolution of ≈ 130 meV, well below the standard of current state-of-the-art RIXS setups. A gapless magnon mode dispersing from the AFM zone centre (π,π) and extending up to about 0.2 eV was found, which was interpreted in terms of an isotropic Heisenberg model including nearest-neighbour (J_{ex}), next-nearest-neighbour (J'_{ex})

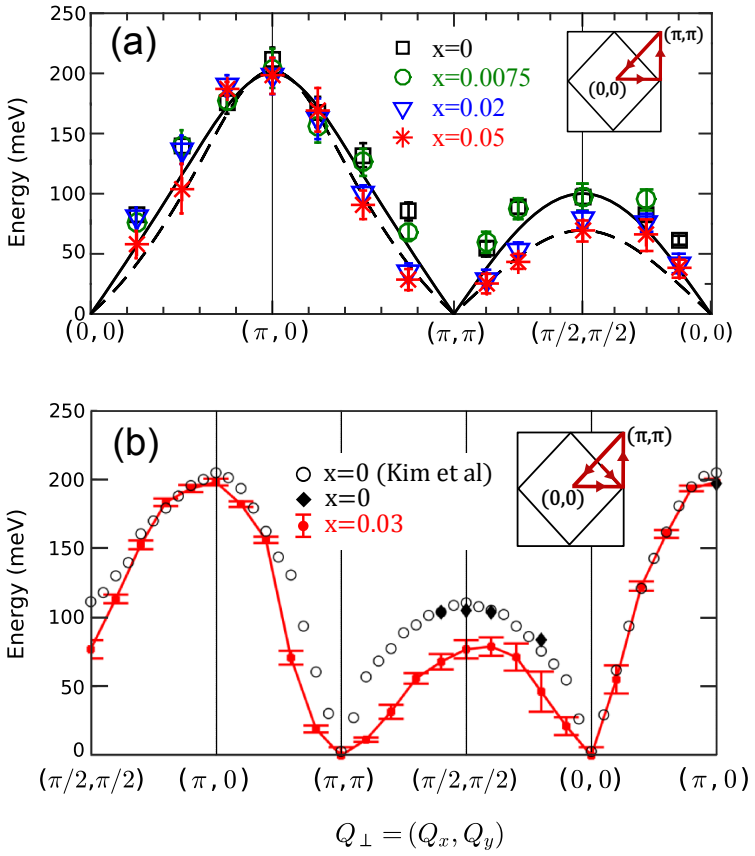

Figure 5.16: $(Sr_{1-x}La_x)_2IrO_4$ single-magnon energy dispersion reported by (a) Gretarsson *et al.* [248] and (b) Liu *et al.* [247]. The solid and dashed lines in (a) represent the best fit to an isotropic Heisenberg model of the $x = 0$, 0.0075 and $x = 0.02$, 0.05 data, respectively. The corresponding values of the exchange integrals are summarised in Table 5.1. The doping levels of the original reference have been adapted to the notation used in the present work. The open symbols in (b) correspond to the parent compound dispersion reported by Kim *et al.* [236] (see Fig. 5.15). Figure adapted from Refs. [247, 248].

and third-nearest-neighbour (J''_{ex}). This is shown in Fig. 5.15 along with the corresponding spectral weight. Both the energy dispersion and the spectral weight momentum dependence show striking similarities to those observed in La_2CuO_4 by inelastic neutron scattering [90]. This reinforces the analogies between Sr_2IrO_4 and La_2CuO_4 and, despite the markedly different local physics of the Ir^{4+} (Sec. 5.3.1) and Cu^{2+} ions, was presented as evidence that the magnetic excitation spectrum can be accounted for by rotationally-invariant magnetic interactions in both compounds.

The effect of electron doping on the collective magnon mode was addressed by more recent investigations by Liu *et al.* [247] and Gretarsson *et al.* [248], based on data collected using higher resolution RIXS spectrometers ($\approx$ 37 meV and 25 meV, respectively). The resulting energy dispersion is displayed in Fig. 5.16. Despite the destruction of LR magnetic order for $x > 0.02(1)$ (see Sec 5.2), both studies found

x	Reference	J_{ex} (meV)	J'_{ex} (meV)	J''_{ex} (meV)	Δ_λ
0	Kim *et al.* [236]	60	-20	15	0
0	Vale *et al.* [242]	57(7)	-18(3)	14(2)	0.08(1)
0	Gretarsson *et al.* [248]	60	-20	15	0
0.0075	”	60	-20	15	0
0.02	”	48	-27	20	0
0.05	”	48	-27	20	0

Table 5.1: Nearest-neighbour (J_{ex}), next-nearest-neighbour (J'_{ex}) and third-nearest-neighbour (J''_{ex}) isotropic exchange integrals and anisotropy parameter Δ_λ for different values of the La content x as reported by different authors. The values were extracted through a fit of the measured dispersion to an isotropic Heisenberg model ($\Delta_\lambda = 0$) for Kim *et al.* [236] (Fig. 5.15) and Gretarsson *et al.* [248] [Fig. 5.16(a)], while the 2DAH model of Eq. (5.15) was used by Vale *et al.* [242] [Figs. 5.17(b),(c)]. $|J'_{ex}|/J_{ex}$ was kept fixed to 1.33 in the investigation by Kim *et al.* [236] and Gretarsson *et al.* [248].

that heavily damped magnetic excitations, also known as *paramagnons*, with a similar in-plane dispersion to the one of the parent compound survive up to $x = 0.05$. This behaviour mirrors the one found in the hole-doped cuprates [279], where paramagnons arising from persisting SR correlations are also found at doping concentrations where LR order is suppressed. The injection of free carriers into the Ir $5d$ orbitals achieved by La substitution causes a softening of the magnon energy. This effect is particularly pronounced along the nodal direction of the first BZ and was compared to the nodal-antinodal asymmetry of the hole doping response in Bi-based cuprates [280, 281].

The energy dispersion in the $x = 0.03$ sample reported by Liu *et al.* [247] [Fig. 5.16(b)] displays a vanishing energy at both $(0,0)$ and (π,π). On the other hand, the energy of the magnon extracted from the RIXS spectra at the latter two $\mathbf{Q}_\perp$ values is not shown in the study by Gretarsson *et al.* [248] since, as the authors argue, the magnon peak could not be accurately determined due to the low intensity of the magnetic signal and the strong elastic line, respectively. As a result, the excitation spectrum was fitted to the same isotropic Heinsenberg model originally used by Kim *et al.* [236]. The corresponding exchange integrals are reported in Table 5.1 as a function of the doping level along with the values for the parent compound found by other authors. The observed softening of the magnon dispersion is mainly accounted for by a reduction of the nearest-neighbour exchange integral for increasing doping levels, accompanied by an enhancement of the longer-range interactions. This finding is in qualitative agreement with the more itinerant nature of the electrons in the doped system. The reader is invited to notice, however, that the authors

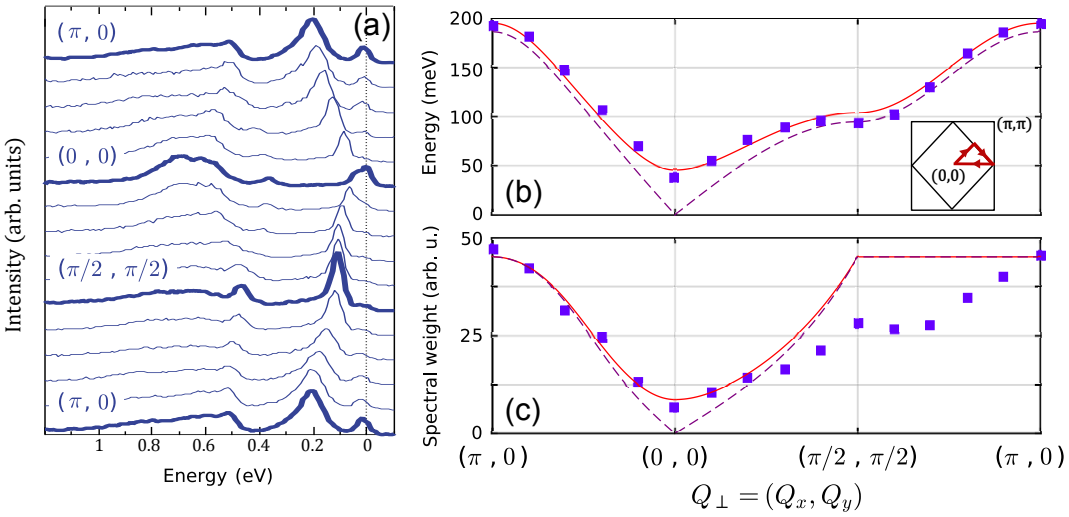

Figure 5.17: (a) RIXS spectra collected along high-symmetry directions of the first BZ [see inset in (b)] in Sr_2IrO_4 by Kim *et al.* [237]. Adapted from Ref. [237]. (b),(c) Single-magnon energy dispersion and spectral weight in-plane momentum dependence extracted by Vale *et al.* [242] fitting the RIXS spectra shown in (a). The solid and dashed lines represent the best fit to the 2DAH model of Eq. (5.15) with the best-fit parameters reported in Table 5.1. Adapted from Ref. [242].

extracted the energy dispersion simply by taking the maximum of the magnon peak rather than by a proper fit of the whole RIXS spectrum. This approach prevents a detailed evaluation of the impact of electron doping on the spectral weight and lifetime broadening of the magnetic excitations. These aspects were addressed in detail in the experimental study presented in Sec. 5.4.

The experimental reports of a purely isotropic exchange model for Sr_2IrO_4 are, in fact, at variance with the predictions of anisotropic magnetic interactions arising from the finite Hund's coupling J_H discussed earlier in this section. Experimental evidence supporting the presence of anisotropic magnetic interactions has come from a number of resources, including the detailed study of the magnetic critical scattering which led to the anisotropic Hamiltonian of Eq. (5.15) and the observation of a small magnon energy gap in electron spin resonance (0.83 meV) [282] and Raman spectroscopy (1.38 meV) [283]. On the other hand, as this brief overview of the literature data should have made clear, all previous RIXS investigations on the excitation spectrum of the parent and electron-doped compounds have not explicitly reported the presence of a gap, nor have they discussed the role of the anisotropic terms in the magnetic Hamiltonian. The only exception is represented by recent data collected on the parent compound [237], where a magnon peak of finite energy (≈ 30 meV) is visible at the Γ point [Fig. 5.17(a)]. However, the authors focus their discussion on the charge excitations and do not mention the presence of a gap nor

do they analyse it in detail. Vale *et al.* [242] fitted their data [Figs. 5.17(b),(c)] to the linear spin-wave solutions of the 2DAH Hamiltonian of Eq. (5.15) and found an anisotropic parameter $\Delta_\lambda = 0.08(1)$, consistent with the theoretical predictions by Igarashi and Nagao [240, 241] and Solovyev *et al.* [243].

5.4 Magnetic excitations in $(Sr_{1-x}La_x)_2IrO_4$ studied by means of RIXS at the Ir L_3 edge

The work presented in this section has been published as "*Anisotropic exchange and spin-wave damping in pure and electron-doped Sr_2IrO_4*" by D. Pincini, J.G. Vale, C. Donnerer, A. de la Torre, E.C. Hunter, R. Perry, M. Moretti Sala, F. Baumberger and D.F. McMorrow, Physical Review B **96**, 075162 (2017) [284].

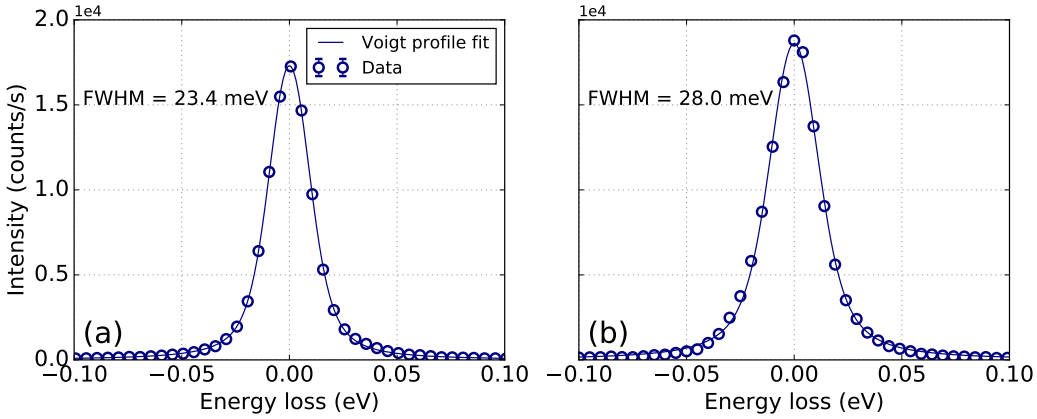

Figure 5.18: ID20 setup energy resolution function for the (a) $x = 0, 0.01, 0.04$ and (b) $x = 0.1$ data sets.

In order to investigate in more detail the magnetic excitation spectrum of Sr_2IrO_4 and its evolution upon electron doping, RIXS experiments were performed at the Ir L_3 edge. Single crystals of $(Sr_{1-x}La_x)_2IrO_4$ with varying La concentration [$x = 0$, $0.01(1)$, $0.04(1)$, $0.10(1)$] were flux grown using standard methods and characterised by resistivity and susceptibility measurements as described in Ref. [222] for samples of the same batch (see Fig. 5.6). The doping level of each of the crystals was checked by means of EDX spectroscopy. All bulk properties were found to be consistent with the ones reported in the literature and discussed in more detail in Sec. 5.2.

The RIXS measurements were performed over the course of two experiments at the ID20 beamline of the ESRF. The experiments were carried out in horizontal scattering geometry using a spherical ($R = 2$ m) Si(844) diced analyser with a 60 mm mask and a Si(844) secondary monochromator. The resulting energy resolution, which was measured using the scattering from an amorphous target, is best described by a Voigt profile with FWHM = 23.4 meV for the experiment on the $x = 0, 0.01, 0.04$ samples and FWHM = 28.0 meV for the one on the $x = 0.1$ crystal (Fig. 5.18). This was assumed to be fixed throughout the experiment and used to fit the elastic line of the RIXS spectra. The in-plane momentum resolution was calculated for the particular scattering geometry and analyser mask used and found to be $\Delta Q_\perp \approx 0.18\,\text{Å}^{-1}$. The samples were mounted with their crystallographic $[0\,0\,1]$ axis and either the $[1\,1\,0]$ ($x = 0, 0.01$) or $[1\,0\,0]$ ($x = 0.04, 0.1$) axis in the scattering plane and were cooled down to T = 20 K (below the Néel transition at $T_N \approx 230$ K found in undoped Sr_2IrO_4 [242]) by means of a He-flow cryostat.

5.4.1 Doping evolution of long-range magnetic order

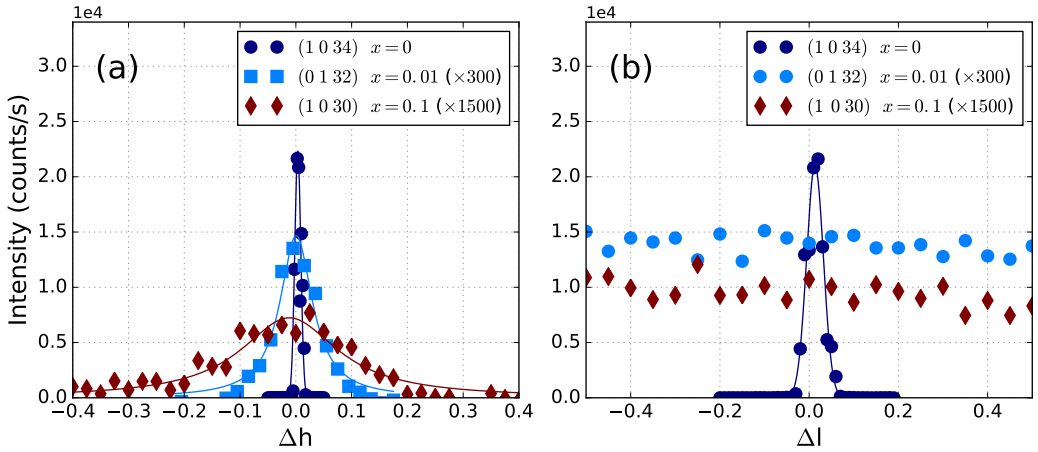

Figure 5.19: Doping level dependence of magnetic diffraction peaks (a) in-plane and (b) out-of-plane reciprocal space scans at T = 20 K.

The evolution of LR magnetic order as a function of the La content was investigated by means of REXS performed using the elastic channel of the RIXS spectrometer. Keeping the incident energy fixed at the Ir L_3 absorption edge, reciprocal space scans were performed measuring the dependence of the elastic scattering signal on the momentum transfer through Bragg positions associated with

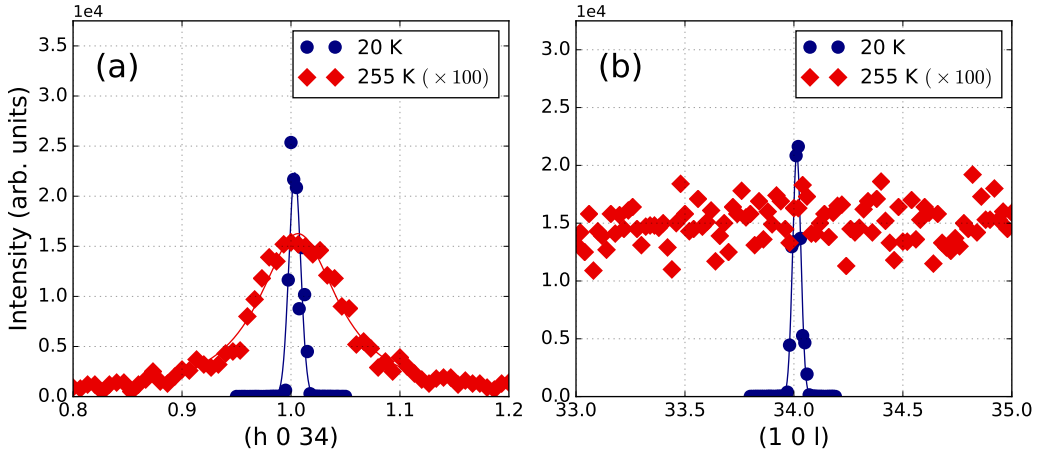

Figure 5.20: Temperature dependence of the $(1\,0\,34)$ magnetic diffraction peak (a) in-plane and (b) out-of-plane reciprocal space scans in the parent compound ($x = 0$).

magnetic diffraction peaks in the undoped ($x = 0$) compound. The data for the different samples are shown in Fig. 5.19 for magnetic peaks of the type $(0\,1\,4n)$ and $(1\,0\,4n+2)$ [where (hkl) are the Miller indices with respect to the large $I4_1/acd$ cell (see Sec. 5.2)]. LR 3D order is suppressed already for $x = 0.01(1)$, as can be seen from the complete lack of correlations along l. However, SR 2D correlations in the basal plane of the crystal persist up to $x = 0.10(1)$, where a broad peak in the h scan is still present. These findings confirm results from analogous measurements [248] (within the uncertainty of the doping level determined with EDX) and extend them up to 10% La substitution, which represents the highest reported doping level at the time of the draft of the present work. This supports the notion that, similar to the superconducting cuprates, SR magnetic correlations are extremely robust to the injection of free carriers.

Extending significantly the range of x over which the evolution of the magnetic order is followed also facilitates a comparison with hole-doped La_2CuO_4. In the latter, the low-energy magnetic response becomes incommensurate for $x > 0.05$, heralding the formation of stripe order [285–287]. A recent REXS study on $(Sr_{0.96}La_{0.04})_2IrO_4$ [288], published shortly after the investigation here presented, suggests the presence of an incommensurate magnetic state reminiscent of the spin density waves observed in $(La_{1-x}Sr_x)_2CuO_4$. Nonetheless, all the doped Sr_2IrO_4 samples considered in the present work reflect the persistence of commensurate SR order, with no clear evidence of incommensurate magnetic order found up to $x = 0.10(1)$.

Temperature was found to affect the magnetic correlations in a similar fashion to the doping level. Fig. 5.20 displays the $(1\,0\,34)$ reciprocal space scans collected

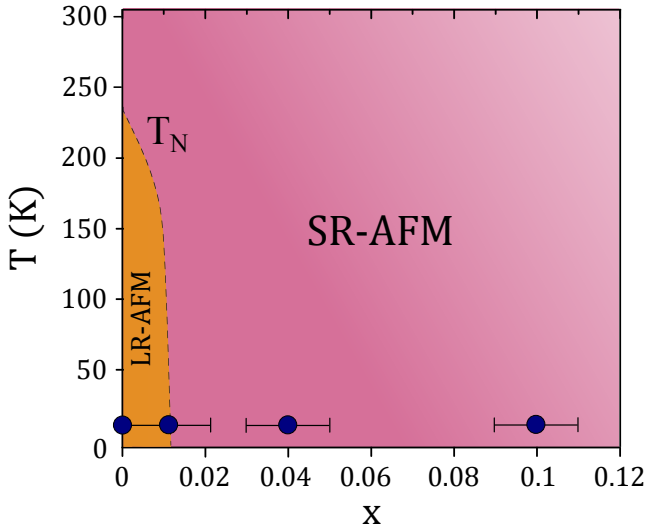

Figure 5.21: Proposed $(Sr_{1-x}La_x)_2IrO_4$ temperature-doping phase diagram based on the REXS measurements presented in this section. The filled symbols correspond to the temperature and doping values probed during the experiments. The dashed line separating the LR AFM phase from the SR one is just meant as a guide to the eye.

on the undoped sample ($x = 0$) at two different temperatures, both below and above the Néel transition at $T_N \approx 230$ K [242]. At high temperature the LR order is lost, but SR correlations still persist within the IrO_2 planes. In Fig. 5.21, I report an updated version of the temperature-doping phase diagram of Fig. 5.7 based on the present resonant elastic measurements, which highlights the persistence of SR order deep into the metallic phase. The evolution of the Nèel temperature as a function of doping was not investigated in detail and is just meant as a qualitative guide to the eye. The absence of LR order in the $x = 0.01(1)$ crystal seems to disagree with the bulk measurements of Fig. 5.6 and with the critical concentration $x_c \approx 0.02$ found by Chen *et al.* [87]. This, however, should come as no surprise. Considering the experimental uncertainty in the doping level determination, this crystal sits close to the boundary between the LR and SR regions of the phase diagram: minor variations in the actual La content (between, for instance, different crystals of the same batch) are expected to have a large impact on the magnetic order.

5.4.2 Single-magnon excitation spectrum

RIXS spectra were collected keeping the incident energy fixed to the Ir L_3 absorption edge and measuring the energy of the scattered photons in the energy loss range $E_{\text{loss}} = -0.2 - 0.6$ eV. For each value x of La content, several spectra were collected

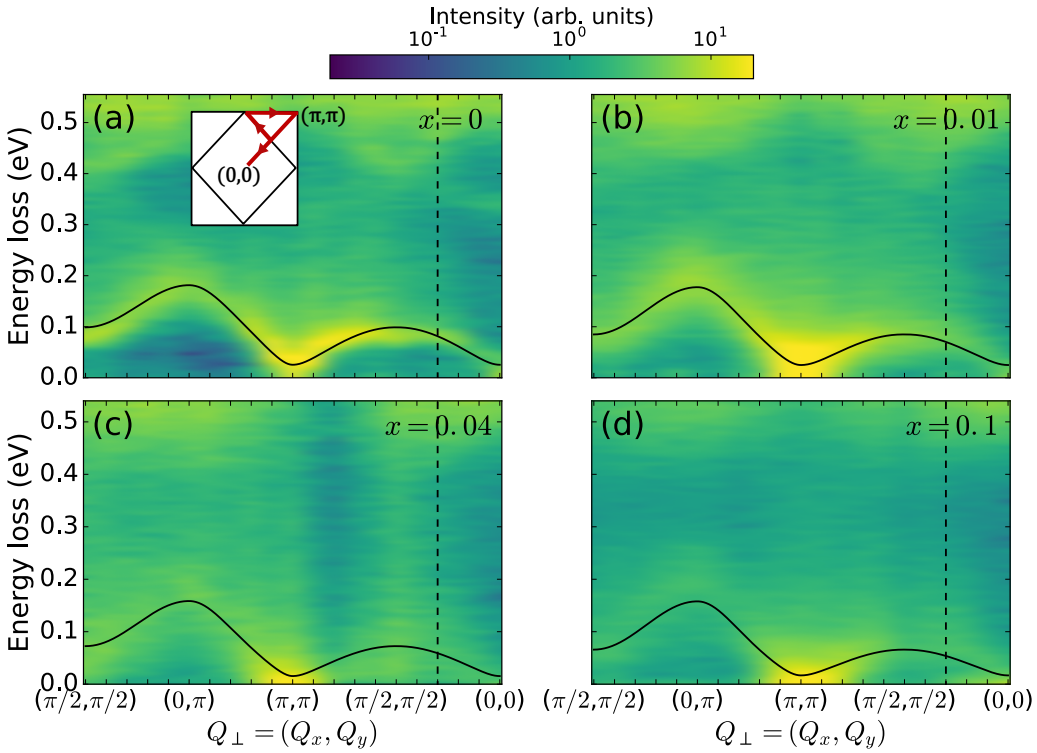

Figure 5.22: RIXS spectra as a function of the in-plane momentum transfer $\mathbf{Q}_\perp$ along high-symmetry directions of the $(0\,0\,33)$ first BZ [see inset in (a)] for (a) $x = 0$, (b) $x = 0.01$, (c) $x = 0.04$ and (d) $x = 0.1$. The solid lines represent the fit of the single magnon energy to the 2DAH model discussed in the text (see Fig. 5.30). The energy loss spectra along the vertical dashed lines are plotted in Fig. 5.24. The data from different samples were normalised to the spectral weight around $E_{\text{loss}} = 1$ eV of the $(0,0)$ spectrum.

for different values of $\mathbf{Q}_\perp$ along high-symmetry directions of the $(0\,0\,33)$ first BZ. The latter was chosen to provide a scattering angle $2\theta \approx 90^\circ$ and thus suppress elastic scattering[11]. The spectra for the different samples are plotted in the colour maps of Fig. 5.22 as a function of $\mathbf{Q}_\perp$. All in-plane momentum transfer values $\mathbf{Q}_\perp = (Q_x, Q_y)$ are quoted in units of $1/a$, where $a = 3.89$ Å is the in-plane lattice constant of the undistorted $I4/mmm$ unit cell (see Fig. 5.3), unless otherwise specified. The out-of-plane component was kept fixed to $l = 33$ for all the spectra, where l is the out-of-plane Miller index. The only exception is represented by the $(0,0)$ spectrum in the $x = 0$ sample: this was measured for $l = 32.85$ to minimize the strong elastic signal arising from the ordered magnetic structure.

As first reported by Kim *et al.* [236], the parent compound data show a collective magnetic excitation dispersing from the AFM zone centre (π,π) and ex-

[11] In the horizontal scattering geometry used for the measurements, the Thomson scattering cross section for the horizontal linear polarisation of the incident X-rays vanishes for $2\theta = 90^\circ$.

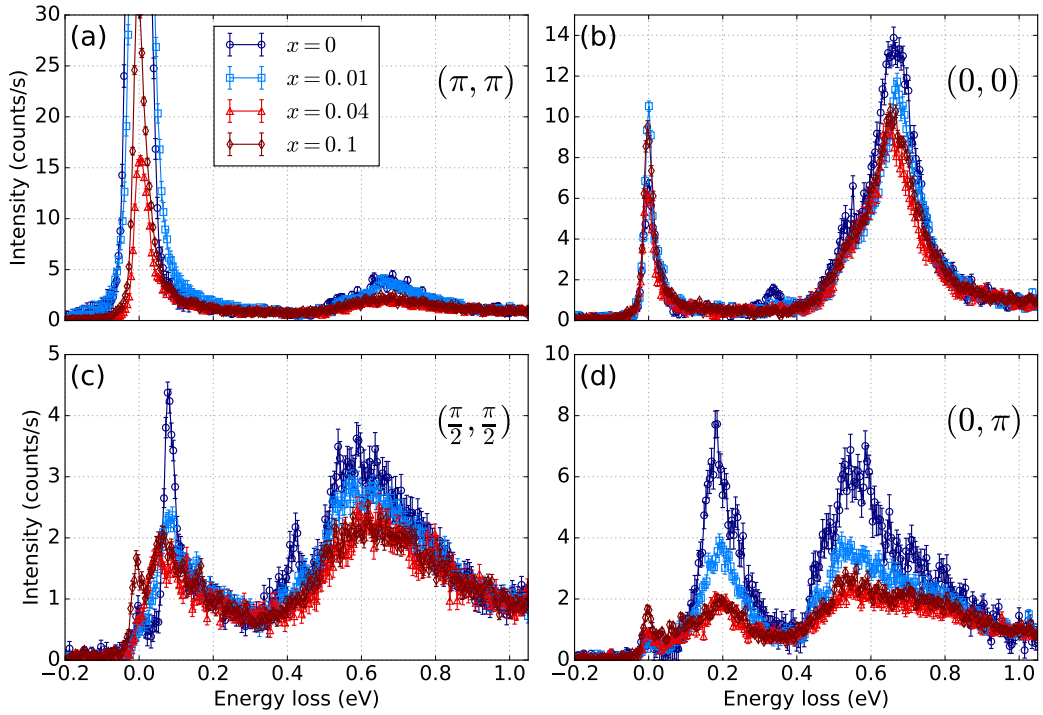

Figure 5.23: Extended RIXS spectra collected at high-symmetry $\mathbf{Q}_\perp$ values of the (0033) first BZ as a function of the doping level. The spectra of different samples for each $\mathbf{Q}_\perp$ point have been normalised to the spectral weight around $E_{\text{loss}} = 1$ eV.

tending up to about 0.2 eV. In agreement with earlier studies [247, 248], damped magnetic excitations with a similar in-plane dispersion survive in the doped compounds deep into the metallic phase, where the LR magnetic order is suppressed. As already mentioned in Sec. 5.4.1 in relation to the REXS scans, the magnons in the heavily doped ($x = 0.1$) sample still reflect the persistence of commensurate SR order, in contrast to hole-doped La_2CuO_4 [285–287]. Although the main focus of the present measurements was the investigation of the spin-wave excitations, RIXS spectra over an extended range of energy loss up to $E_{\text{loss}} = 1.2$ eV were measured at high-symmetry points of the first BZ (Fig. 5.23). These mainly served as a reference and were conveniently used to normalise the data of different samples using the spectral weight around $E_{\text{loss}} = 1$ eV. Both the parent and electron-doped samples long spectra display a broad, weakly-dispersive feature in the energy loss range $0.4 - 1$ eV. The latter consists of two overlapping peaks which were assigned to charge transitions within the spin-orbit split t_{2g} orbitals [236, 237].

A quantitative analysis of the spin-wave spectrum was achieved by fitting the RIXS data of Fig. 5.22 by a sum of an elastic line and the following inelastic features: (A) single-magnon excitation, (B) a multimagnon continuum and (C),(D) intra-t_{2g} excitations (which are visible in their full extent in the long spectra of

Fig. 5.23). This is shown for representative spectra in Fig. 5.24. The elastic line was fitted to the Voigt profile describing the instrument resolution function shown in Fig. 5.18. The width, determined by the experimental energy resolution, was kept fixed while allowing both its amplitude and peak energy value to vary. The peak energy value, in particular, was kept as a free parameter in order to account for small time drifts in the elastic energy over time. The extracted value was then used to define the $E_{\text{loss}} = 0$ point in each spectrum[12]. The line shape of the inelastic features

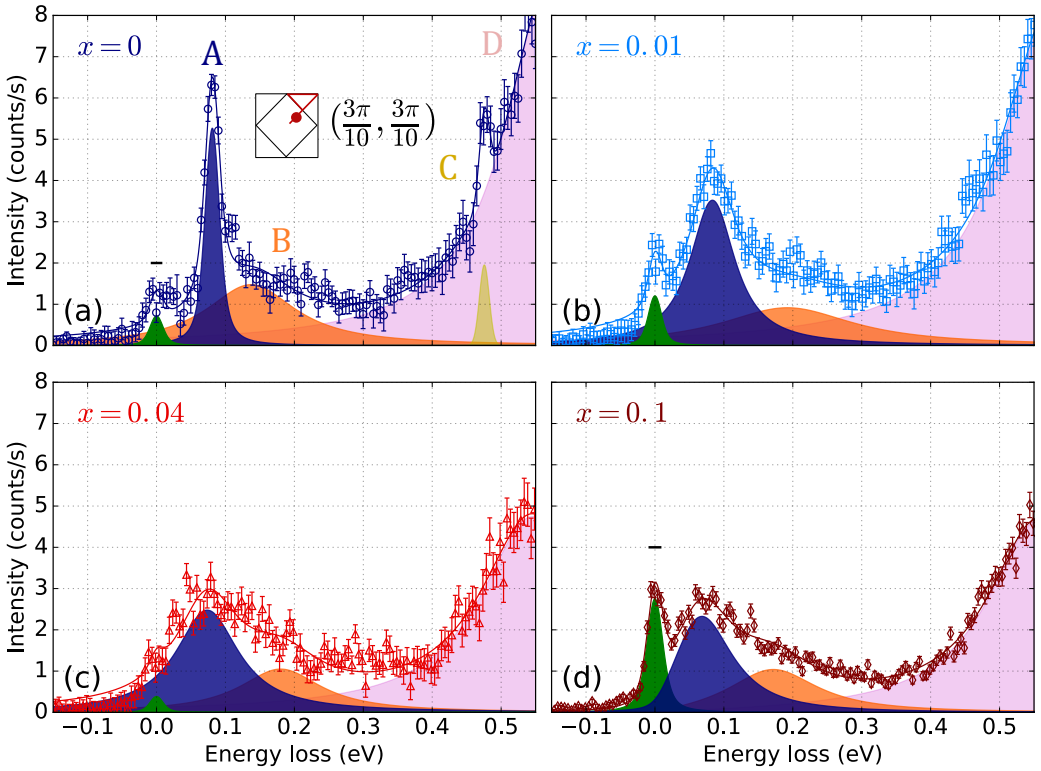

Figure 5.24: Fit detail of representative RIXS spectra for (a) $x = 0$, (b) $x = 0.01$, (c) $x = 0.04$ and (d) $x = 0.1$. Open symbols and solid lines represent the measured intensity and the fit of the spectra, respectively. The Voigt functions used to fit the elastic line and the various inelastic contributions (A: single-magnon, B: multimagnon continuum, C-D: intra-t_{2g} excitations) are displayed through the shaded regions. The horizontal lines in the $x = 0$ (same as $x = 0.01, 0.04$) and $x = 0.1$ panels represent the Gaussian width of the resolution function (fixed during the fit). The spectra from different samples were normalised to the spectral weight around $E_{\text{loss}} = 1$ eV of the $(0,0)$ spectrum.

is the result of the convolution between the resolution function Voigt profile and a Lorentzian function modelling the lifetime broadening of the core hole generated by the absorption of the incident resonant X-rays. Therefore, the inelastic peaks were

[12]The position of the elastic line was constantly checked during the data fitting and was found to be always within $\pm$FWHM$/2$ from the nominal $E_{\text{loss}} = 0$. This excludes anomalies in the fitting procedures.

x	Measured gap (meV)		Corrected values (meV)	
	$(0,0)$	(π,π)	$(0,0)$	(π,π)
0	24(5)	27(4)	19(7)	22(4)
0.01	33(5)	19(4)	29(7)	13(4)
0.04	22(6)	20(4)	12(11)	14(4)
0.1	23(6)	20(4)	16(8)	14(4)

Table 5.2: Measured and Q-resolution-corrected magnon energy gap values for the different doping concentrations. The values in parentheses represent the maximum between the statistical 2σ confidence interval and the estimated additional sources of error as explained in the text.

fitted using a Voigt profile, with the FWHM of the Gaussian component fixed to the correspoding value of the instrument resolution function (black horizontal lines in Fig. 5.24) and the width of the Lorentzian component left as a free fitting parameter. This properly accounts for the contribution of the experimental energy resolution: the resulting Lorentzian component thus reflects the intrinsic width of the inelastic transition.

For the $x = 0.1$ data, the principle of detailed balance[13] was used to suppress the energy gain tails of the inelastic features, which resulted in significantly lower χ^2 values. Given the smaller FWHM of the excitations, the applications of detailed balance did not lead to a substantial improvement in the fit quality at lower doping levels. In general, no particular constraints were applied to the fitting parameters. The only exception is represented by the multi-magnon peak profile in the $x = 0.04$ and $x = 0.1$ samples. For these doping levels, the large broadening of the single-magnon peak produces a significant overlap of the single- and multi-magnon excitations. The latter are thus strongly intermingled with the nearby features and much harder to resolve. Nonetheless, a reliable fit could be obtained by fixing the value of the single- to multi-magnon peak amplitude ratio and the Lorentzian width of the multi-magnon Voigt profile. These values were found from a global optimization of all the RIXS spectra and kept unaltered during the fit of the other parameters.

[13] The principle of detailed balance is mostly found in the literature of phonon excitations, where it relates the spectral weight I_{creation} of a phonon creation peak ($E_{\text{loss}} = E_{\text{creation}} > 0$) to the spectral weight $I_{\text{annihilation}}$ of the corresponding phonon annihilation one ($E_{\text{loss}} = -E_{\text{creation}} < 0$): $I_{\text{annihilation}} = I_{\text{creation}} e^{\frac{-E_{\text{loss}}}{k_B T}}$.

5.4.2.1 Energy gap and impact of the momentum resolution

One of the main features emerging from the RIXS data is the presence of a finite gap in the single-magnon energy at all doping levels. This is evident from the low-energy detail of the spectra collected at the crystallographic and AFM zone centres shown in Fig. 5.25, where simple inspection reveals a separate energy-loss peak partially overlapping with the elastic line. The gap appears relatively robust against the injection of free carriers and does not show any systematic doping dependence.

Extra care must be taken, however, when assessing the presence of a small gap in the excitation spectrum. This is because, as it will be shown hereafter, the finite Q resolution of the spectrometer can have a significant impact on the measured energy at the minima of the magnon dispersion. The in-plane momentum resolution function (i.e. within the **ab** basal plane of the Sr_2IrO_4 tetragonal crystal) of the ID20 spectrometer in proximity of $\mathbf{Q} = (0, 0, 33)$ was calculated to be about $\Delta Q_\perp \approx 0.18\,\text{Å}^{-1}$. This corresponds to $\Delta Q_\perp \approx 0.2\pi$ in units of $1/a$, where $a = 3.89\,\text{Å}$ is the in-plane lattice constant of the undistorted $I4/mmm$ unit cell. In general, the in-plane momentum resolution along a given crystal direction depends on the specific orientation of the **a** and **b** crystal axes with respect to the scattering plane. The resolution is worse when varying the momentum transfer perpendicular to the scattering plane (horizontal in the measurements here discussed). The reported $\Delta Q_\perp$ value refers to this worst case scenario.

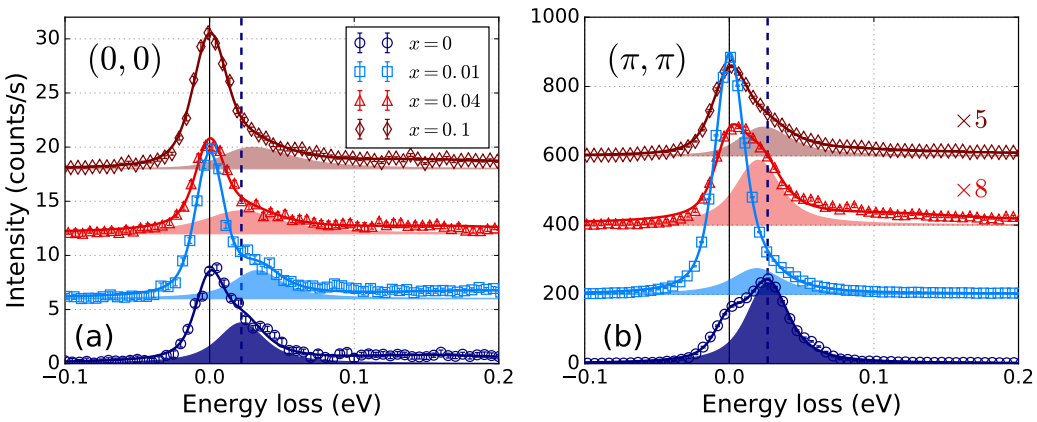

Figure 5.25: Doping level dependence of the low-energy region of the RIXS spectra at (a) $(0,0)$ and (b) (π,π). Open symbols and solid lines represent the measured intensity and the fit of the spectra, respectively. The shaded regions show the fitted single-magnon peak, highlighting the presence of a finite spin-wave gap. The vertical dashed lines mark the value of the magnon energy in the parent compound $(x = 0)$. The data are offset for clarity. The fitted magnon energies and the corresponding Q-resolution-corrected values are reported in Table 5.2.

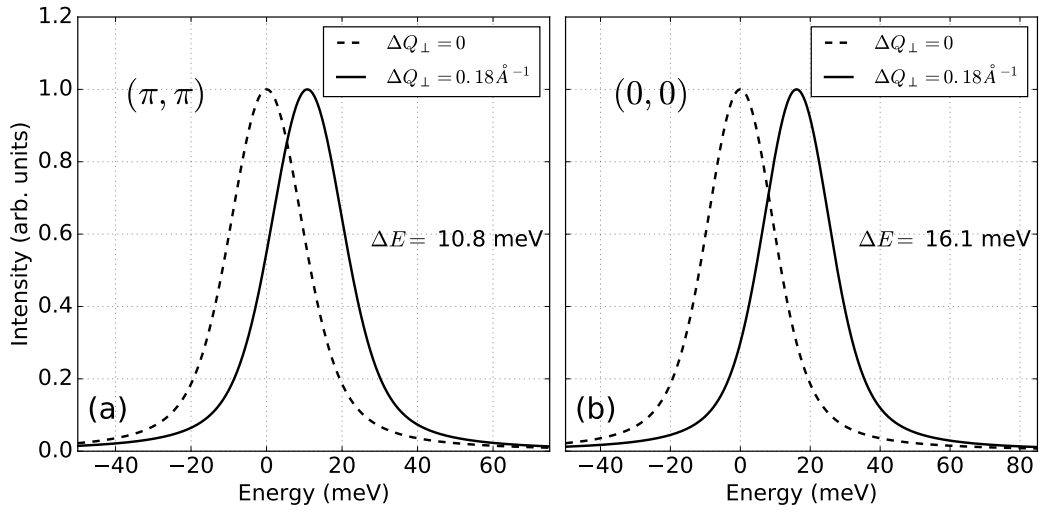

Figure 5.26: Impact of the RIXS spectrometer momentum resolution at (a) (π,π) and (b) $(0,0)$ in the case of gapless magnetic excitations ($\Delta_\lambda = 0$). The dashed and solid lines are Voigt profiles representing the magnon peak for the ideal case of vanishing momentum resolution and for $\Delta Q_\perp = 0.18\,\text{Å}^{-1}$, respectively. ΔE is the energy shift seen between the two cases. The width of the Voigt profiles has been set equal to the experimental energy resolution of 23.4 meV.

The effect of the momentum resolution on the measured dispersion at a given $\mathbf{Q}_\perp$ value is to average the energy values corresponding to nearby momentum transfers. Its impact is thus expected to be particularly large at (π,π) and $(0,0)$, where the energy rapidly increases from its minimum value. This is clearly shown in Fig. 5.26, where the impact of the finite momentum resolution was calculated convolving an originally gapless excitation spectrum with a rectangular approximation of width $\Delta Q_\perp = 0.18\,\text{Å}^{-1}$ of the actual Q resolution profile. With respect to the ideal case $\Delta Q_\perp = 0$, the convolution causes an upwards shift in the magnon energy and thus results in the appearance of a fictitious gap of 10.8 and 16.1 meV at (π,π) and $(0,0)$, respectively. These values were intentionally calculated in the worst-case scenario of initially gapless excitations and a rectangular approximation of the resolution function and are thus to be considered as upper limits. As shown in Table 5.2 (see measured gap values), the gap values extracted from the data are larger at all doping levels and indicate that resolution effects alone cannot account for the observed magnon gap.

This result is robust against the fit statistical error within a 2σ confidence interval, with the latter always smaller than 6 meV. In general, additional sources of error might be present which increase the uncertainty beyond the statistical one. This might contribute to the variability in the gap values seen for different doping levels and might account, for instance, for the large value of the $(0,0)$ gap in the $x = 0.01$

sample[14]. The extra variability was estimated by evaluating the standard deviation $1/\sqrt{(N-1)}\sum_x(E_x-\bar{E})^2$ of the gap values for different doping levels, which was found to be about 5 and 4 meV at $(0,0)$ and (π,π), respectively. These values are comparable to the 2σ statistical error for each x value and do not undermine the validity of our results. The uncertainty in the measured gap values in Table 5.2 corresponds, for each doping level, to the maximum between the statistical 2σ error and the estimated variability across the various samples. Different choices of the initial fitting parameters for the RIXS spectra were also tried in order to verify the robustness of the fit, leading to a spread in the fitted energy values always smaller than 2σ. Moreover, given the huge difference in the magnon spectral weight between the crystallographic and AFM zone centre (see Sec. 5.4.2.3 for more details), an artificial resolution-induced gap would display substantially different values at (π,π) and $(0,0)$, in contrast to what is observed in the measurements. The presence of gapped magnons is thus to be considered an intrinsic property of the excitation spectrum in $(Sr_{1-x}La_x)_2IrO_4$.

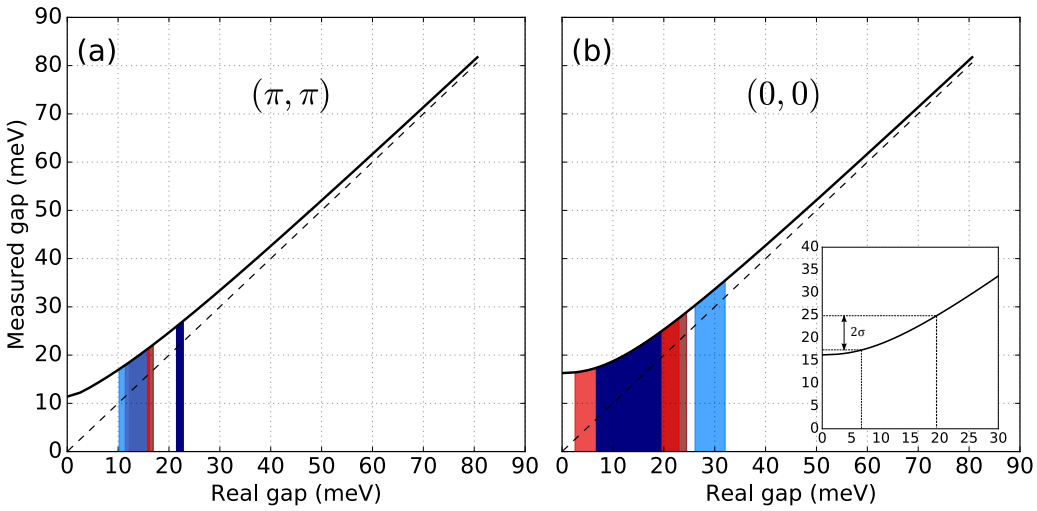

Figure 5.27: Calculated values of the measured vs *real* spin-wave energy gap in the case of $\Delta Q_\perp = 0.18\,\text{Å}^{-1}$ (solid lines) and an ideal spectrometer with $\Delta Q_\perp = 0$ (dashed lines). The shaded regions represent 2σ confidence intervals for the Q-resolution-corrected (real) gap values calculated from the measured ones (as shown in the inset). The color code is the same used for the others figures of this chapter and refers to samples with different doping levels: $x = 0$ (dark blue), $x = 0.01$ (light blue), $x = 0.04$ (light red), $x = 0.1$ (dark red).

Although the finite Q resolution of the RIXS spectrometer alone is not capable of accounting for the measured values of the energy gap, the latter are overestimated with respect to the case of an ideal spectrometer. Nonetheless, the impact of

[14] One possible cause can be identified in the presence a few outliers in the corresponding RIXS spectrum in the energy loss range where the magnon resides.

the Q resolution can be factored out from the measured energy values by extending the calculations performed for gapless magnetic excitations (Fig. 5.26) to the case of an arbitrary initial gap. The results are shown in Fig. 5.27, where the solid lines represent the energies that one would measure in the RIXS spectra for a given starting value of the *real* gap (i.e. the one arising from the physics of the system) with a finite Q resolution of $\Delta Q_\perp = 0.18\,\text{Å}^{-1}$. The impact of the latter decreases for increasing gap values, since the spin-wave dispersion becomes more rounded in proximity of $(0,0)$ and (π,π) (see Sec. 5.4.2.3). For values large enough, the measured gap approaches the real one, as would be the case for an ideal spectrometer with $\Delta Q_\perp = 0$ (dashed lines in Fig. 5.27). On the other hand, the measured gap departs significantly from the ideal case as the real gap is decreased, with the largest difference occurring for the case of gapless excitations already discussed. Given a certain interval of measured gap values, which can be taken as the value extracted from the fit $\pm 2\sigma$, one can use the solid line of Fig. 5.27 to trace back the corresponding Q-resolution-corrected gap interval (which will be generally larger then the measured one). The latter is represented through the shaded regions of Fig. 5.27, where different colors correspond to different doping levels (the color code is the same used for Figs. 5.23 and 5.24).

The corrected gap values are reported in Table 5.2. An average gap of 19(9) and 16(4) meV is present at $(0,0)$ and (π,π), respectively[15]. Here, the values in round brackets give an estimate of both the statistical uncertainty and the variability seen across the different doping levels. These values appear to be roughly consistent with a previous estimate in the undoped compound (≈ 30 meV [242]) and the calculations by Igarashi and Nagao [240, 241], which predicted a value of about 29 meV. A comparable value was also recently reported by an analogous RIXS investigation to the one here discussed in pure Sr_2IrO_4 [289]. On the other hand, smaller energy gaps have been reported by recent electron spin resonance [282] and Raman spectroscopy [283] studies. The origin of the discrepancy with the above analysis remains an open issue.

5.4.2.2 Anisotropic magnon damping

Besides displaying a finite energy gap largely insensitive to the La content, the fit detail of Fig. 5.25 reveals that the magnon peak at $(0,0)$ and (π,π) does not

[15] As I will argue in more detail in Sec. 5.4.2.3, the value of the gap at (π,π) is expected to be underestimated given the presence of a gapless mode with non-vanishing spectral weight (see Sec. 5.3.3).

considerably broaden as the dopant concentration is increased. In particular, the FWHM increases by only 60% going from the parent to the heavily doped $x = 0.1$ sample. For other values of the momentum transfer however, the response of the magnon upon injection of free carriers is markedly different. This is evident from the low-energy detail of representative spectra collected along the anti-nodal and nodal direction shown in Fig. 5.28, which the reader is invite to compare with the zone centre ones of Fig. 5.25. Away from $(0,0)$ and (π,π), the magnon displays both a significant softening (which will be discussed in more detail in Sec. 5.4.2.3) and broadening for increasing values x of La content. This is further emphasized in Fig. 5.29, where the Lorentzian width of the single magnon peak extracted from the fit of the RIXS spectra across the entire first BZ is reported as a function of the doping level. In general, a remarkably pronounced anisotropic broadening occurs moving away from the zone centres. The largest effect is seen at the zone boundaries $(0,\pi)$ and $(\pi/2,\pi/2)$, where the FWHM increases by a factor of about 3 and 4, respectively, going from $x = 0$ to $x = 0.1$. Here, heavily damped paramagnons are thus present. As a result, while the magnon lifetime broadening of the parent compound displays only moderate variations as a function of the in-plane momentum transfer, a peculiar dependence is seen in the doped samples, which resembles the single-magnon energy dispersion (see Fig. 5.30).

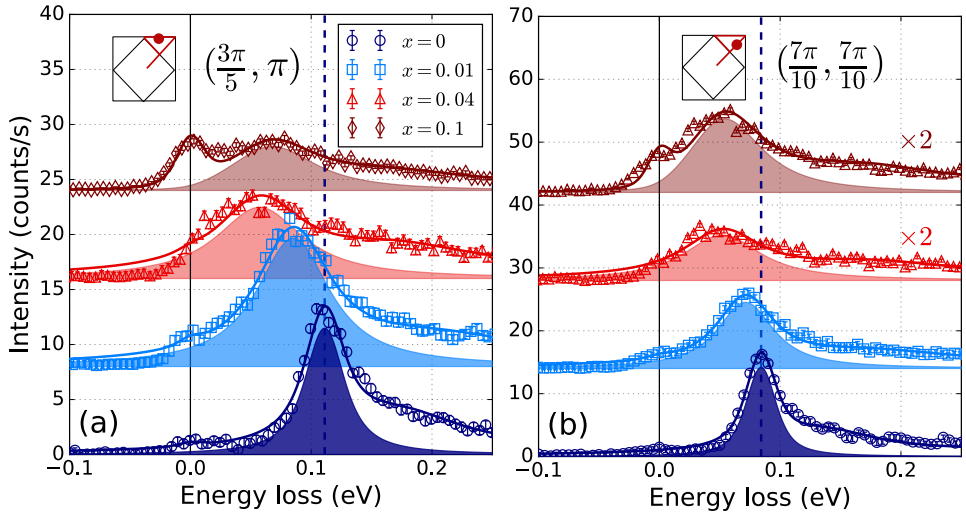

Figure 5.28: Doping level dependence of the low-energy region of the RIXS spectra at two different $\mathbf{Q}_\perp$ values along the (a) antinodal and (b) nodal direction. Open symbols and solid lines represent the measured intensity and the fit of the spectra, respectively. The shaded regions show the fitted single-magnon peak while the vertical dashed lines mark the value of the magnon energy in the parent compound $(x = 0)$. The data are offset for clarity.

The pronounced anisotropic broadening of the magnetic excitations was not addressed by previous studies on parent [236] and electron-doped [247, 248]

Sr_2IrO_4 and suggests that the injection of free carriers causes a strong enhancement of the scattering processes along the magnetic BZ boundary $(\pi/2, \pi/2) \rightarrow (0, \pi)$, which shortens the excitation lifetime with respect to the crystallographic and AFM zone centres. A significant damping of the single-magnon excitations was also documented for the hole-doped cuprates, where it was attributed to the magnons coupling with (and consequent decay into) the Stoner continuum of incoherent electron-hole excitations [279, 290]. Although in both LSCO and YBCO the magnon broadening was found to be weakly dependent on the in-plane momentum transfer along the antinodal direction [279, 290, 291], the same coupling mechanism could play a role also in Sr_2IrO_4. An asymmetric doping response reminiscent of the one here reported was found in Bi-based cuprates [280, 281]. In this case, the single-magnon peaks in the hole-doped samples display a significant softening and damping along the nodal direction compared to the parent compound, while it appears to be more robust along the antinodal one. This peculiar behaviour was associated to the decaying of spin-wave excitations into the electron-hole continuum due to the emergence of itinerant, or partially itinerant, states in the form of Fermi arcs around $(\pi/2, \pi/2)$ upon hole doping. Similar changes were recently found to take place in electron-doped Sr_2IrO_4 [222] (see Sec. 5.2). Given the even more pronounced itinerant character of the Ir 5*d* electrons compared to the Cu 3*d* ones, this is likely to impact the magnetic excitation spectrum analogous to the cuprates case. Additional theoretical effort will be needed to clarify this point.

It should be noted that a high-energy continuum was found by means of inelastic neutron scattering around $(0, \pi)$ in La_2CuO_4 [292], which was presented as evidence of the presence of fractional excitations referred to as *spinons*. The presence of such continuum in the case of Sr_2IrO_4 could contribute to the width of the magnon peak extracted from the fit of the spectra and partially explain the corresponding large lifetime broadening. However, as it will be shown in the next section, the depression in the magnon energy and spectral weight around $(0, \pi)$ normally accompanying the existence of spinon excitations is not visible in the data. No clear evidence of fractional excitations can thus be inferred from the results presented in this section.

5.4.2.3 Energy dispersion: anisotropic exchange interactions

The presence of a finite gap in the single-magnon energy is at odds with previous reports of fully isotropic Heisenberg interactions [236, 247, 248] (see Sec. 5.3.3) and constitutes clear evidence of a non-negligible anisotropy in the coupling be-

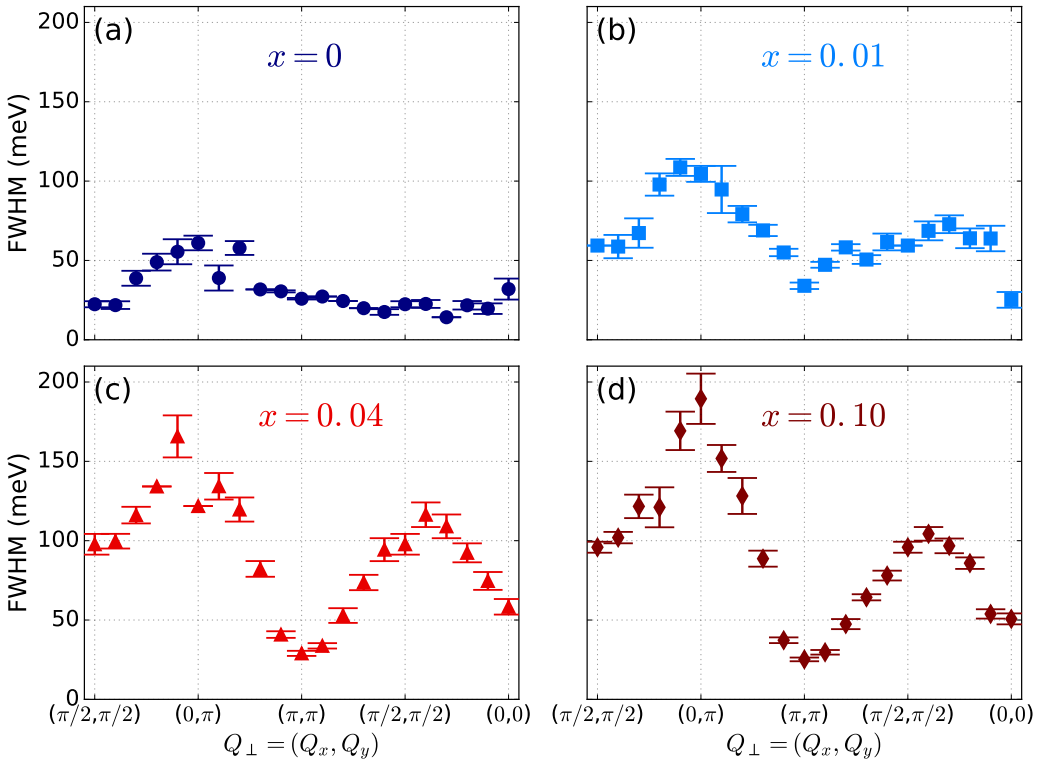

Figure 5.29: Single-magnon Lorentzian lifetime broadening for (a) $x = 0$, (b) $x = 0.01$, (c) $x = 0.04$ and (d) $x = 0.1$. The data points were extracted fits analogous to the ones of Fig. 5.24, with the error bars representing 1σ confidence intervals.

tween $J_{\text{eff}} = 1/2$ moments in $(Sr_{1-x}La_x)_2IrO_4$. As already discussed in Sec. 5.3.2, this is consistent with the prediction of significant deviations from the rotationally-invariant Heisenberg model when Hund's coupling and distortions away from cubic symmetry are taken into account [239–241, 243, 277, 278]. In this case, the magnetic exchange Hamiltonian is expected to assume the form of Eq. (5.10), or, equivalently, the one of the 2DAH model reported in Eq. (5.15). For the sake of clarity, the following discussion and the fits shown in the figures explicitly refer to the latter, which was already used to provide with a satisfactory description of the parent compound single-magnon spectrum [242]. However, as mentioned in Sec. 5.3.3, the two models correspond to an equivalent physical description of the exchange interactions and result in a single-magnon energy dispersion and spectral weight momentum dependence which are indistinguishable for any practical purposes. For this reason, the model of Eq. (5.10) was also used to fit the experimental data and led to an equally satisfactory description of the observed dispersion. The parameters derived from the fit are reported and commented along with the ones of the 2DAH model.

The two magnetic modes $E_\pm$ expected to arise from the presence of a signif-

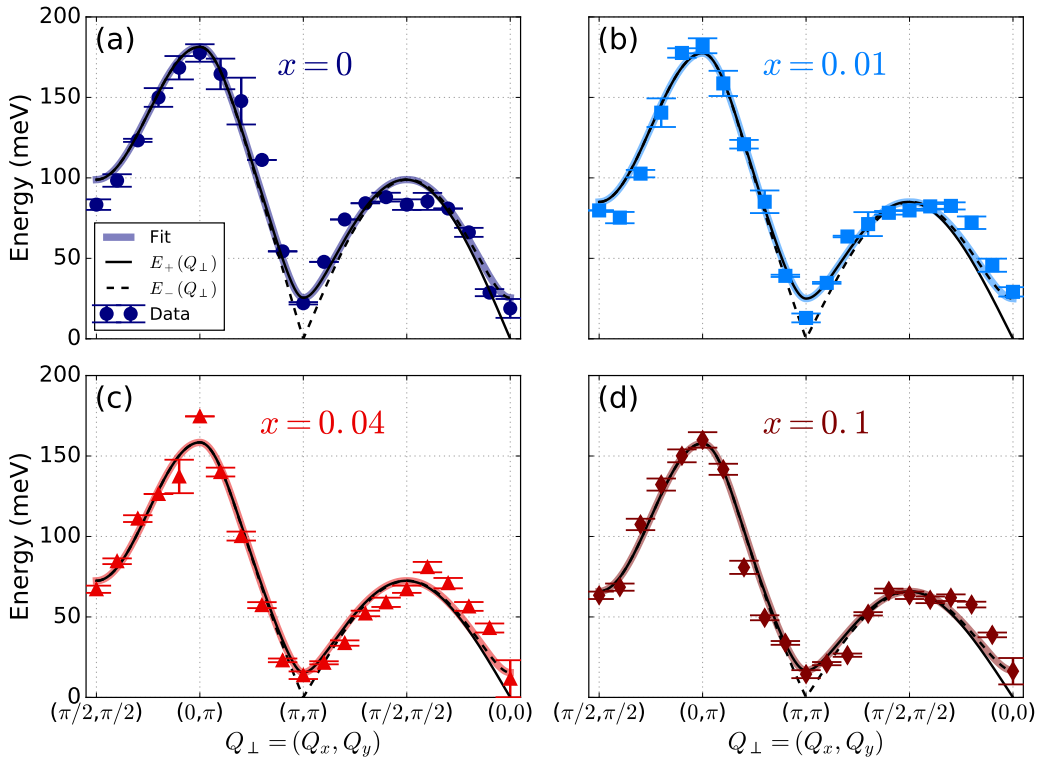

Figure 5.30: Q-resolution-corrected single-magnon energy dispersion for (a) $x = 0$, (b) $x = 0.01$, (c) $x = 0.04$ and (d) $x = 0.1$. The data points were extracted through fits analogous to the ones of Fig. 5.24. The error bars represent 1σ confidence intervals [apart from $(0,0)$ and (π,π), where the 2σ interval is reported instead]. The thick solid lines in colour show the fit to the 2DAH model described in the text (best-fit values reported in Table 5.3), while the thin solid and dashed black lines represent the two magnetic modes calculated for the best-fit parameters.

icant anisotropy in the magnetic interactions [see Fig. 5.14(b)] are not resolved in the measurements. The reason is that their energy is almost degenerate for most of the $\mathbf{Q}_\perp$ values explored, with a non-negligible splitting is present only at the zone centres. Moreover, as can be seen from Fig. 5.14(b), the gapless mode carries a vanishingly small spectral weight at $(0,0)$, while it is hidden by the elastic signal arising from the weak structural reflections of the type $(1\,0\,l)$ (with $l = 2n+1$) [250, 251] at (π,π) [which corresponds to $(1\,0\,33)$ in $(h\,k\,l)$ notation]. Only the gapped mode is thus expected to be visible in the RIXS spectra and to account for the observed magnon gap. Following this reasoning, the measured dispersion was then fitted to (i) E_+ along the path $(\pi/2,\pi/2) \to (0,\pi) \to (\pi,\pi)$ and (ii) E_- along the path $(\pi/2,\pi/2) \to (0,0)$. The measured single-magnon energy in-plane dispersion for the various doping levels is shown in Fig. 5.30 along with the fit to the 2DAH model. Here, the measured energy values at the zone centres were corrected

to take into account the finite Q resolution of the RIXS spectrometer as explained in Sec. 5.4.2.1. The corresponding best-fit parameters are summarised in Table 5.3. It should be noted that, due to the non-vanishing spectral weight of the gapless magnon at (π,π) and the finite energy and momentum resolution of the RIXS spectrometer, the magnon peak measured in proximity of the AFM propagation vector is expected to result from the weighted average of the two modes: neglecting the gapless one thus leads to an overestimation of the corresponding energy values (and, consequently, the magnon gap).

Despite the presence of a significant anisotropy in the magnetic interaction, the isotropic exchange integrals are the leading terms in the magnetic Hamiltonian and still account for most of the magnon dispersion away from the zone centre and the AFM propagation vector. The fit to the 2DAH model was thus performed following an incremental approach consisting of three steps: (i) the isotropic exchange integrals J_{ex}, J'_{ex} and J''_{ex} were first determined by fixing $\Delta_\lambda = 0$; (ii) keeping the exchange integrals fixed to the values found in step (i), the anisotropy parameter Δ_λ was then allowed to vary to best describe the observed gap; (iii) fixing Δ_λ to the value found in step (ii), the isotropic integrals were refined fitting them again to the measured data. The values obtained in step (iii) are generally different from the initial ones; their spread is expressed by the values in round brackets shown in Table 5.3 (the round brackets values for Δ_λ correspond to the 1σ statistical uncertainty). The difference is however reasonably small indicating a good convergence of the model. In order to reduce the correlations between the fitting parameters and improve the stability of the fit, the ratio $|J'_{ex}|/J''_{ex}$ was fixed to 1.33, which seems to correctly describe the relative strength of the two interactions [236, 248]. The anisotropic parameters J_z and J_{xy} derived from the fit to the model of Eq. (5.10) (keeping $J_z = -J_{xy}$ [240]) are also reported in Table 5.3. The corresponding isotropic exchange integrals have been omitted since their values are equivalent to the ones of the 2DAH model within the error bars.

Fig. 5.30 shows that the 2DAH Hamiltonian of Eq. (5.15) provides a good description of the magnetic excitation spectrum of pure and electron-doped Sr_2IrO_4. An equally satisfactory fit was achieved using the model of Eq. (5.10) by Igarashi and Nagao [240, 241]. In particular, the Q-resolution-corrected gap at all doping levels is correctly reproduced by a value of the easy-plane anisotropy Δ_λ in the range $0.03 - 0.06$. As it can be seen from Table 5.4, these values show a good agreement with the experimental estimate by Vale *et al.* [242] based on the parent compound RIXS spectra reported by Kim *et al.* [237] and previous theoretical predictions, which have been already discussed in more detail in Sec. 5.3.2. The anisotropic exchange integrals J_z and J_{xy} of Eq. (5.10) are also roughly consistent

x	$\tilde{J}$ (meV)	J'_{ex} (meV)	J''_{ex} (meV)	Δ_λ	J_z (meV)	J_{xy} (meV)
0	57(1)	-16.5(4)	12.4(3)	0.05(2)	-1.4(6)	1.4(6)
0.01	51(1)	-18.5(4)	13.9(3)	0.06(2)	-1.7(6)	1.7(6)
0.04	44.5(5)	-17.2(2)	12.9(1)	0.03(2)	-0.5(5)	0.5(5)
0.1	41.7(5)	-18.4(2)	13.8(2)	0.04(2)	-0.9(5)	0.9(5)

Table 5.3: Best-fit parameters of the 2DAH model [Eq. (5.15)] as extracted from the Q-resolution-corrected single-magnon dispersion (Fig. 5.30) for the different doping concentrations. The values of the anisotropic exchange integrals of the model of Eq. (5.10) derived from a similar fit are also reported. $|J'_{ex}|/J''_{ex}$ was kept fixed to 1.33 for all samples and the constraint $J_z = -J_{xy}$ was also used. The values in parentheses for $\tilde{J}$, J'_{ex} and J''_{ex} represent an estimate of the experimental uncertainty as outlined in the text, while they correspond to the statistical 1σ confidence interval for Δ_λ, J_z and J_{xy}.

	Experiments		Theory	
	Present work	Vale [242]	Igarashi [240, 241]	Solovyev [243]
Δ_λ	$0.03(2) - 0.06(2)$	0.08(1)	0.06	0.087

Table 5.4: Comparison of the anisotropy parameter Δ_λ derived from the present investigation with experimental and theoretical values reported by other authors.

with the theoretical prediction $J_z = -J_{xy} = -1.8$ meV [240, 241]. It is worth noticing, as the authors of Ref. [242] point out, that their result overestimates the true anisotropy since the effect of the finite Q resolution of the RIXS spectrometer is not properly taken into account. The smaller values presented in this work are thus to be considered more accurate.

As already noted by Vale *et al.* [242], a much smaller value $\Delta_\lambda = 2.0(5) \times 10^{-4}$ [293] was reported for La_2CuO_4. The present RIXS results thus confirm the critical scattering data [242] and firmly establish the importance of easy-plane anisotropy in the low-energy Hamiltonian of Sr_2IrO_4. The anisotropy does not show any significant dependence on the La content within the experimental uncertainty, thus suggesting that it is robust with carrier doping. The impact of electron doping on the spin-wave energy dispersion is limited to a renormalisation of the nearest-neighbour exchange interaction: this decreases as x is increased in agreement with what was reported by Gretarsson *et al.* [248]. In general the isotropic exchange parameters display similar values to the ones found by previous investigations [236, 247, 248].

As well as displaying a good agreement with the measured energy, the 2DAH model also provides a satisfactory description (up to an arbitrary scale factor) of the spectral weight momentum dependence. This is shown in Fig. 5.31, where the spec-

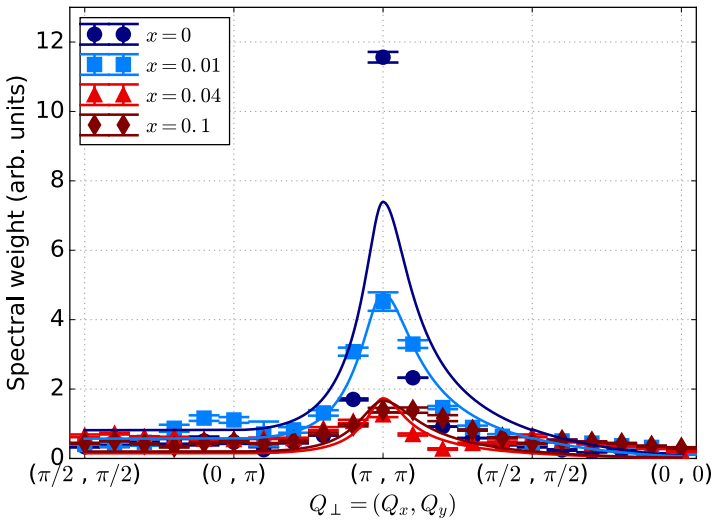

Figure 5.31: Single-magnon spectral weight for different values x of La content. The data points were extracted through fits analogous to the ones of Fig. 5.24, while the error bars represent 1σ confidence intervals. The solid lines show the fit to the 2DAH model described in the text.

tral weight calculated from Eq. (5.14) using the parameters of Table 5.3 is plotted along with the integrated area of the single-magnon peak extracted from the fit of the RIXS spectra. The latter shows a pronounced enhancement at the AFM propagation vector (π,π) both in the parent compound and in the $x = 0.01$ sample as expected for magnetic excitations on a square lattice of antiferromagnetically-aligned moments. The enhancement is less pronounced for the $x = 0.04$ and $x = 0.1$ samples, where the spectral weight displays a weaker dependence on $\mathbf{Q}_\perp$. Fig. 5.31, however, is just meant as a qualitative visual comparison since the RIXS cross-section is related, but not identical, to the spectral weight calculated through linear spin-wave theory. In general, the intensity of the two modes in the RIXS spectra depends on the experimental geometry and the polarisation of the incident and scattered beam. A detailed treatment of the RIXS cross section goes beyond the scope of the present investigation and can be found elsewhere [39, 294]. Moreover, following the same approach used for the fit of the energy dispersion, I_+ and I_- were considered along the paths $(\pi/2,\pi/2) \to (0,\pi) \to (\pi,\pi)$ and $(\pi/2,\pi/2) \to (0,0)$, respectively. This neglects the intensity contribution of the other mode for those $\mathbf{Q}_\perp$ where the two modes almost completely overlap.

5.5 Conclusions

In this chapter, I presented a detailed RIXS investigation of the magnetic excitation spectrum in pure Sr_2IrO_4 and electron-doped $(Sr_{1-x}La_x)_2IrO_4$. This study has revealed the presence of gapped magnons up to $x = 0.10(1)$. The magnon appears to be robust upon carrier doping at the crystallographic and AFM zone centre, while paramagnons exhibiting a pronounced anisotropic damping are found elsewhere in the BZ. Consistent with the theoretical prediction by Jackeli and Khaliullin [239] and Igarashi and Nagao [240, 241] formulated for the case of a non-negligible Hund's coupling of the Ir $5d$ electrons, the gap can be ascribed to a significant in-plane anisotropy in the interaction between Ir^{4+} $J_{\text{eff}} = 1/2$ isospins which breaks the full rotational symmetry of the magnetic Hamiltonian. Despite the similarities with the superconducting cuprates, the present results show that the entangled nature of the $J_{\text{eff}} = 1/2$ ground state produced by the strong SOC gives rise to magnetic interactions which differ significantly from the pure spin ones encountered in the cuprates. This will hopefully pave the way to a deeper understanding of the differences between the two classes of compounds in light of the long sought after superconductivity in iridate oxides.

Chapter 6

Conclusions and future perspectives

In this thesis, I have presented three different case studies of TMOs across the periodic table, from the traditional 3*d* case to novel 4*d* and 5*d* compounds of more recent interest. In each case, I have discussed electronic and magnetic properties arising from a non-obvious competition between several energy scales, namely electronic correlations, Hund's coupling, crystal field and SOC. The key results are based on a wide range of modern X-ray experimental techniques. In most cases, these were either extended beyond their conventional field of applicability or pushed to their limit, and proved to be an extremely versatile and powerful tool for the investigation of different aspects of the physics of the system. In the following sections, I will summarise the conclusions of each of the three main experimental chapters along with corresponding future perspectives.

6.1 The 3d case: the weak ferromagnets (Mn,Co,Ni)CO_3 and $FeBO_3$

A variety of theoretical methods and X-ray techniques was used to investigate the weakly FM 3*d* oxides (Mn,Co,Ni)CO_3 and $FeBO_3$. Although weak ferromagnets have been extensively studied in the past few decades since the discovery of the DMI, our detailed investigation revealed an incredibly rich physics, including previously unexplored effects. In particular, first-principle calculations performed by our collaborators revealed both a change in the sign of the DMI, found to be negative in $MnCO_3$ and $FeBO_3$ and positive in $CoCO_3$ and $NiCO_3$, and a non-trivial trend of the orbital contribution to the TM magnetic moment as a function of the filling of the 3*d* orbitals, with a particularly large value in $CoCO_3$. The sign of the DMI was accessed by a novel interference technique based on the coherent super-

position of a quadrupole resonant amplitude at the TM *K* pre-edge and the NXMS amplitude originating from the low-temperature C-AFM order. This allowed the predicted sign change to be unequivocally confirmed. Moreover, the orbital and spin moments were measured by means of NXMS and XMCD at the Co *L* edge at low temperature and the large unquenched orbital contribution in the Co member of the family [orbital to spin angular momenta ratio $l/s = 0.7(2)$] was confirmed. Here, the combination of SOC and large orbital moment was found to give rise to (i) a significant magnetocrystalline anisotropy, (ii) magnetostrictive effects and, more interestingly, (iii) an elongation of the Co electron cloud along the ordered moment in the magnetically-ordered phase. The latter was evidenced by the interference of the forbidden amplitude stemming from the distortion (which was successfully accounted for by both an empirical model and more sophisticated multiplet calculations) and the multiple scattering amplitude at space-group forbidden reflections.

The findings presented in this work highlight the prominent role played by SOC in the physics of the system, with particular emphasis for $CoCO_3$, apparently at odds with the common wisdom of a limited impact of SOC in 3*d* TMOs. In particular, the multiplet calculations showed that the forbidden amplitude produced by the Co electron cloud distortion vanishes for zero SOC. As a result, the exact value of the SOC constant could be estimated provided that one could express the forbidden and multiple scattering amplitudes from the scattering experiment on an absolute scale (rather than arbitrary units).

Given the similarities between weak ferromagnets and many non-collinear magnetic phases of modern interest (such as spin spirals and skyrmions) in terms of the underlying physics, the impact of the present investigation extends beyond the specific compounds measured. All results combined prove the ability of modern first-principle calculations to reproduce the properties of strongly correlated oxides. They also show how the phase of subtle scattering amplitudes can be reliably modelled and measured by using interference effects. Of particular significance is the possibility of reliably predict and measure the sign of the DMI, which represents an important step towards finding suitable magnetic materials for spintronics applications.

Despite the intrinsically weak nature of all scattering processes involved in the measurements, an exceptionally high data quality was obtained thanks to a novel rotating magnet approach (as well as the high crystal quality), which involved recording the scattered intensity as a function of the direction of a small applied magnetic field. In contrast to the more conventional azimuthal scans normally used in the field of X-ray scattering, the rotating magnet approach permits to collect an equivalent set of data without moving the sample and, therefore, does not introduce artefacts in

the measured intensity. This method could be adopted for any magnetically-ordered system with a net magnetisation (such as canted antiferromagnets) and with sufficiently small magnetic anisotropy in the plane of application of the field to allow the magnetic moments to freely rotate with the field.

6.2 The 4d case: $Ca_{2-x}La_xRuO_4$

A combination of REXS at the Ru *L* edge, XANES at the O *K* edge, XANES and XMCD at the Ru *L* edge and neutron diffraction was used to address the magnetic ordering and ground-state electronic structure of the 4*d* oxide $Ca_{2-x}La_xRuO_4$. All ingredients of TMOs physics compete on an equal footing in Ca_2RuO_4 and the corresponding ground state is extremely sensitive to external perturbations.

Substitution of divalent Ca with trivalent La is expected to dope the system with electrons. The neutron diffraction data revealed that significant structural changes also occur as a result of the different ionic radii of La^{3+} and Ca^{2+}. In particular the RuO_6 octahedra rotations are reduced and the system evolves from the orthorhombic cell with compressed octahedra of the parent compound to a quasi-tetragonal cell with elongated octahedra in the $x = 0.07$ and $x = 0.12$ doped samples.

The REXS measurements addressed the magnetic structure of the doped samples for the first time and showed that the $\mathbf{k} = (0,0,0)$ propagation vector of the parent compound is preserved upon La doping. The latter, however, suppresses the globally AFM A-centred magnetic mode of the parent compound in favour of the weakly FM B-centred one, also allowed by symmetry. A similar transition is observed as a function of external pressure and Sr substitution (Sr^{2+}), thus suggesting a structural origin.

The changes in the local crystalline environment also affect the orbital population of the Ru^{4+} ion t_{2g} orbitals as probed by O *K*-edge XANES. In particular, using a minimal Ru 4*d* - O 2*p* hybridization model it is possible to interpret the evolution of the measured spectra as resulting from an increase in the *xy* orbital hole occupancy. This is consistent with the doping-induced octahedral elongation in a simple single-ion model comprising crystal field and SOC.

SOC produces a ground-state wave function of mixed orbital character and seems to have a central role in the low-energy physics. This is confirmed by the Ru *L*-edge XANES and XMCD measurements, which revealed a white line branching ratio significantly larger than the statistical one and a sizeable unquenched orbital moment (around 25% of the spin value) in the insulating phase, respectively. On

the other hand, L appears to be much smaller in the metallic phase at high doping, where an almost pure spin moment seems to be present.

The experimental results confirm the sensitivity of the Ca_2RuO_4 ground state to external perturbations and further support an intermediate scenario between the pure $J_{\text{eff}} = 0$ state stabilized by SOC and the $S = 1$ state with fully occupied xy orbitals expected for the case of strong octahedral compression. The microscopic mechanism behind the change in the magnetic structure established by the REXS measurements will have to be addressed by detailed fist-principle calculations. The current experimental evidence points towards the doping(pressure)-induced changes of the Ru-O-Ru bond geometry as a possible responsible of the observed transition. I am also currently working together with our collaborators on a more sophisticated model, which includes electron-electron correlations and Hund's coupling, to provide a more quantitative description of the O K-edge and Ru L-edge absorption data. Preliminary results at the O K edge seem to confirm the interpretation given on the basis of the minimal model used in the present work.

Resonant X-ray measurements on ruthenium oxides pose serious technical challenges as the Ru L edge sits between the energy range normally available in soft and hard X-ray beamlines. I16 at the DLS can cover the required region of the spectrum by using a non-standard setup, which the REXS measurements helped to further develop and optimize. This is now becoming routinely available to external users. On the other hand, the L-edge absorption measurements could be performed thanks to a major upgrade of beamline ID12 at the ESRF (which was previously limited to higher energies) and are also now part of the beamline capabilities. Valuable information on the still debated Ru^{4+} ion electronic structure might also be gained by probing the low-energy excitations using RIXS at the Ru L edges. Unfortunately, high-resolution RIXS spectrometers covering the tender X-ray spectrum are still not available at the time of the draft of the present work. As a result, the study of the electronic structure by means of X-ray have been so far performed indirectly at the O K edge [178]. However, new instruments are currently being developed at beamline I21 of the DLS and P-01 at PETRA III (Hamburg, Germany), which will open entire new possibilities in the investigation of the physics of ruthenium oxides in the next few years.

6.3 The 5d case: $(Sr_{1-x}La_x)_2IrO_4$

RIXS at the Ir L_3 edge was used to investigate the magnetic excitation spectrum in the pure and La-doped $5d$ oxide Sr_2IrO_4. Although the LR AFM order of the parent compound is destroyed by La doping, spin-wave excitations with a similar in-plane dispersion were found up to $x = 0.10(1)$. This is similar to the behaviour reported in the high-T_c superconductors parent compound La_2CuO_4 and can be attributed to persisting SR correlations confined in the IrO_2 planes. In contrast with previous reports, our measurements revealed the presence of a finite energy gap in the excitation spectrum; once the effect of the finite momentum resolution of the RIXS spectrometer is factored out, a value of the gap equal to 19(9) and 16(4) meV is obtained at $(0,0)$ and (π,π), respectively.

The gap was successfully modelled using a 2DAH Hamiltonian with anisotropic exchange interactions between the Ir^{4+} $J_{\text{eff}} = 1/2$ isospins. In general, a finite exchange anisotropy is expected whenever a realistic value of Hund's coupling for $5d$ electrons is considered. This constitutes an important difference with respect to the case of La_2CuO_4, where substantially isotropic Heisenberg interactions were found.

Although great experimental and theoretical effort has been directed towards the investigation of iridium oxides, a complete understanding of the physics of Sr_2IrO_4 has yet to be achieved. Future theoretical work will be needed to address the question as to whether (and how) the exchange anisotropy could have an impact on the long sought after superconductivity in the iridates. The recent report of stripe order in lightly-doped crystals will also have to be confirmed and reconciled with the absence of the hour-glass dispersion observed in the cuprates at the AFM propagation vector. The latter might have been overlooked as a result of the limited energy and momentum resolution of the current RIXS spectrometers at the Ir L_3 edge. This limitation could be overcome by either the new spectrometer being developed at beamline 27-ID of the Advanced Photon Source (USA), which promises an energy resolution of ≈ 10 meV[1], or, alternatively, O K-edge RIXS at the new high-resolution setup available at beamline I21 of the DLS.

Another pathway to the investigation of incommensurate order is also provided by measurements of the phonon excitation spectrum, which is still largely unexplored both in the parent and doped compounds. Electron-phonon coupling

[1] Recent RIXS measurements collected at the crystallographic zone centre using the new high-resolution setup [289] found a magnon gap value consistent with the one reported in the present work.

could also be relevant in light of the recent prediction [295] of a significant impact of the Jahn-Teller effect on the low-energy magnetic Hamiltonian of $J_{\text{eff}} = 1/2$ and $J_{\text{eff}} = 0$ systems. While Jahn-Teller and magnetic transitions are traditionally considered independent, the assumption of spin-orbital separation no longer holds for the spin-orbit-entangled isospin wave function. In Sr_2IrO_4, this is expected [295] to induce a tetragonal-to-orthorhombic transition at the onset of the AFM order upon cooling, with potential consequences on the magnetic anisotropy and the observed magnon gap. A prominent role of the isospin-lattice coupling seems to be supported by recent experimental findings on pure Sr_2IrO_4 [289].

Appendix A

Weak ferromagnets: supporting data

In the present appendix, I report additional measurements and experimental details which support the discussion of Sec. 3.5. In particular, a complete list of the space-group forbidden reflections used for the extraction of the $l(Q)/s(Q)$ values reported in Fig. 3.14 is provided in Table A.1, along with the different temperatures and azimuth values at which the data (σ-σ', σ-π' and total scattered intensity for each reflection) were collected and the corresponding mean $l(Q)/s(Q)$ value. The relative orbital to spin contribution to the magnetic moment is not expected to depend on the particular ψ value chosen to perform the measurements. However, a residual contribution of multiple scattering (which, on the other hand, strongly depends on ψ) in one of the two polarisation channels can produce a significant error in the $l(Q)/s(Q)$ ratio extracted from the field direction dependence of the scattered intensity. Data collected at different azimuths thus serve as a check of the robustness of the resulting values. Although the azimuth values were chosen in order to minimize the multiple scattering amplitude, the error introduced by any residual contribution outweighs the statistical error resulting from the fit to Eq (3.20). This is true for all the reflections except for the $CoCO_3$ $(\bar{1}05)$ and $(\bar{2}07)$, where the statistical uncertainty is larger due to the presence of the additional charge scattering amplitude discussed in Sec. 3.6.3, and the $NiCO_3$ (009), where large error bars are caused by the weak signal resulting from the small crystal size and moment magnitude.

The additional error was estimated by collecting, for the $CoCO_3$ (107) and $(\bar{1}17)$ reflections, an equivalent data set to the one shown in Fig. 3.13 over a wide range of azimuths. (107) and $(\bar{1}17)$ are symmetrically-equivalent reflections of the type $(h\bar{h}07)$ and should thus display the same $l(Q)/s(Q)$ value. A certain variability is however observed due to residual multiple scattering: the corresponding standard deviation ($\pm\sigma \approx \pm 0.1$) has been used as an estimate of the experimental uncertainty in the $l(Q)/s(Q)$ values for all the reflections in all compounds under consideration. For the $CoCO_3$ $(\bar{1}05)$ and $(\bar{2}07)$ and $NiCO_3$ (009) a value twice as

$MnCO_3$				
(hkl)	$Q(Å^{-1})$	T (K)	$\psi(^\circ)$	$l(Q)/s(Q)$
$(1\,0\,7)$	0.25	5	$-65,-45,-31,0$	0.08(5)
$(\bar{1}\,1\,7)$	0.25	5	63	
$(0\,0\,9)$	0.29	5	30,71	0.05(7)

$FeBO_3$				
(hkl)	$Q(Å^{-1})$	T (K)	$\psi(^\circ)$	$l(Q)/s(Q)$
$(0\,0\,3)$	0.10	300	81.5	0.0(1)
$(\bar{1}\,0\,5)$	0.21	300	75	0.0(1)
$(1\,0\,7)$	0.27	300	-45	0.0(1)
$(0\,0\,9)$	0.31	300	13	0.1(1)
$(\bar{2}\,0\,7)$	0.35	300	90	0.1(1)

$CoCO_3$				
(hkl)	$Q(Å^{-1})$	T (K)	$\psi(^\circ)$	$l(Q)/s(Q)$
$(0\,0\,3)$	0.10	5,6,10	83,95	0.83(5)
$(\bar{1}\,0\,5)$	0.21	5	90,105	0.94(4)
$(1\,0\,7)$	0.27	5,6,810,12	$-115,100,-90,-81,-65,-45,0$	0.87(3)
$(\bar{1}\,1\,7)$	0.27	5,6,10	63,108,128,144	
$(0\,0\,9)$	0.30	6,8,10.12	30	0.94(5)
$(\bar{2}\,0\,7)$	0.34	4,5,6,10	$40-120$	1.06(3)

$NiCO_3$				
(hkl)	$Q(Å^{-1})$	T (K)	$\psi(^\circ)$	$l(Q)/s(Q)$
$(0\,0\,9)$	0.31	6	21	0.4(2)

Table A.1: Space-group forbidden reflections measured for each compound of the series A(C,B)O_3 (A = Mn, Fe, Co, Ni) along with the relevant experimental parameters and the average $l(Q)/s(Q)$ ratio over all temperatures and sample azimuth values. The momentum transfer values are normalised to 4π ($Q = \sin\theta/\lambda$).

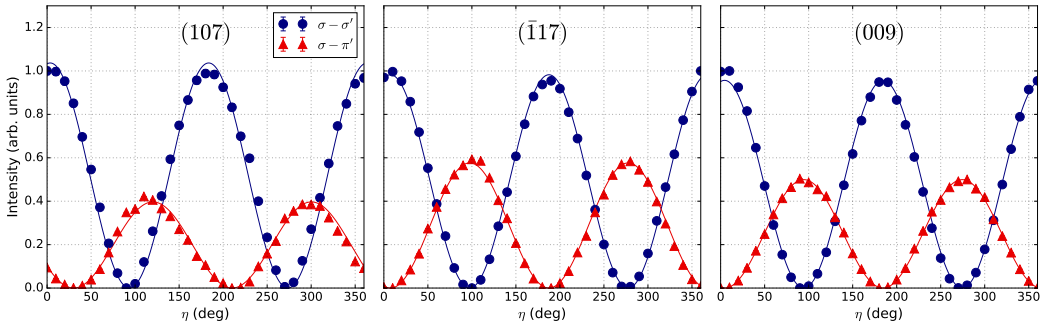

Figure A.1: Dependence of representative $MnCO_3$ magnetic reflections on the magnetic field direction for two different polarisation states of the diffracted X-ray beam. The data points represent the diffracted intensity integrated over a rocking scan while the solid curves correspond to the best fit to Eq. (3.20). The data were collected at T = 5 K and $\psi = -65°, 63°, 30°$ for the (107), $(\bar{1}17)$ and (009) reflections, respectively. A small constant background originating from residual multiple scattering has been removed from all the data sets. For each reflection, the intensity is normalised to the maximum value in σ-σ'.

large has been considered.

For all but the $(\bar{1}05)$ reflection in $CoCO_3$, σ-σ' and σ-π' *vs* field data were also collected at different temperatures below T_N in order to check whether the relative orbital and spin contributions to the magnetic moment exhibit any temperature-dependent behaviour. No temperature dependence was detected within the experimental uncertainty in the temperature range $6-12$ K. Therefore, the $l(Q)/s(Q)$ values (and the corresponding error bars) reported in Fig. 3.14 correspond to the average over all the azimuth and temperature values used for each reflection.

Representative NXMS data analogous to the ones shown in Fig. 3.13 for $CoCO_3$ are reported for the other members of the weak ferromagnet family in Fig. A.1 ($MnCO_3$), Figs. A.2,A.3 ($FeBO_3$) and Fig. A.4 ($NiCO_3$). Out-of-phase oscillations are present in σ-σ' and σ-π' as a function of the magnetic field direction as already discussed in the case of $CoCO_3$. It should be noticed that, in contrast to $CoCO_3$ (see Fig. 3.23), the $(\bar{2}07)$ and $(\bar{1}05)$ reflections in $FeBO_3$ (Fig. A.3) exhibit the normal behaviour expected from the NXMS cross sections. This confirms that the forbidden amplitude discussed in Sec. 3.6.3 is a peculiar aspect of the physics of the Co compound arising from the large value of the orbital moment of the Co^{2+} ion.

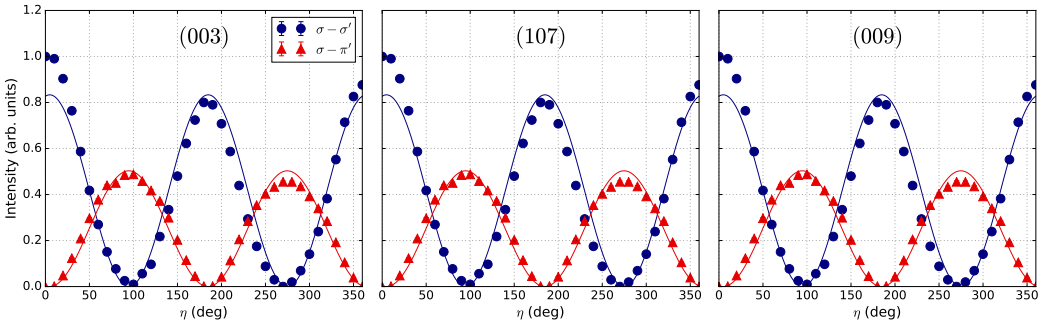

Figure A.2: Dependence of $FeBO_3$ magnetic reflections on the magnetic field direction for two different polarisation states of the diffracted X-ray beam. The data points represent the diffracted intensity integrated over a rocking scan while the solid curves correspond to the best fit to Eq. (3.20). The data were collected at T = 300 K and $\psi = 81.5°, -45°, 13°$ for the (003), (107) and (009) reflections, respectively. A small constant background originating from residual multiple scattering has been removed from all the data sets. For each reflection, the intensity is normalised to the maximum value in σ-σ'.

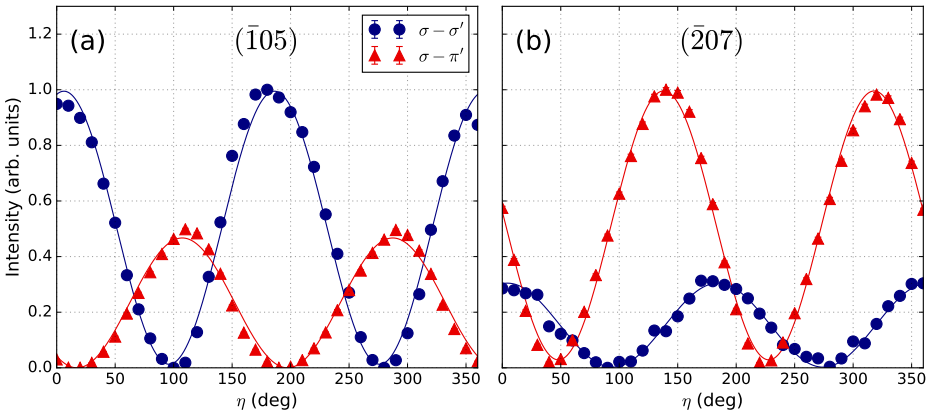

Figure A.3: Dependence of $FeBO_3$ magnetic reflections on the magnetic field direction for two different polarisation states of the diffracted X-ray beam. The data points represent the diffracted intensity integrated over a rocking scan while the solid curves correspond to the best fit to Eq. (3.20). The data were collected at T = 300 K and $\psi = 75°, 90°$ for the $(\bar{1}05)$ and $(\bar{2}07)$ reflections, respectively. A small constant background originating from residual multiple scattering has been removed from all the data sets. For each reflection, the intensity is normalised to the maximum value across both polarisation channels.

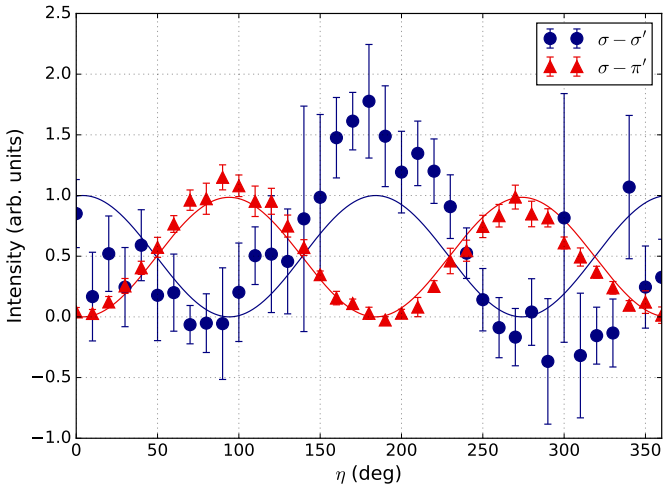

Figure A.4: Dependence of the $NiCO_3$ (009) magnetic reflection on the magnetic field direction for two different polarisation states of the diffracted X-ray beam. The data points represent the diffracted intensity integrated over a rocking scan while the solid curves correspond to the best fit to Eq. (3.20). The data were collected at T = 6 K and $\psi = 21^\circ$. A constant background originating from residual multiple scattering has been removed from all the data sets. The intensity is normalised to the maximum value of the fit in σ-σ'. The large error bars originate from the weak signal resulting from the small size of the $NiCO_3$ crystal and moment magnitude.

Appendix B

$Ca_{2-x}La_xRuO_4$: additional measurements and data analysis details

B.1 Anisotropic tensor of susceptibility (ATS) scattering

The measurements discussed in Sec. 4.5 show that a significant magnetic contribution to the diffracted intensity is present only for A-centred and B-centred forbidden reflections in the parent and doped compounds, respectively. A much weaker signal is generally observed for the (hkl) values associated to the other mode (see Fig. 4.17). However, this contribution displays markedly different properties with respect to the magnetic intensity. Fig. B.1 shows the energy resonance of the $(0\,0\,3)$ and $(0\,1\,3)$ reflections in the $x = 0.05$ sample expected to arise from the AFM arrangement of the canting-induced net moments and the main AFM order of the A-centred mode, respectively (see Table 4.2). The shape of the resonance and the L_3/L_2 intensity ratio are generally different from the ones of the magnetic peaks of Figs. 4.13 and 4.18. In the $(0\,1\,3)$, in particular, the main resonance occurs at the e_g energy, contrary to what expected for magnetic scattering. Moreover, the diffracted signal displays a much weaker temperature dependence than the magnetic one, as clearly illustrated by the energy scans collected above the Néel transition.

These features suggest that the scattered intensity originates from ATS scattering. The latter arises from the anisotropy of the X-ray susceptibility tensor, which breaks the symmetry between otherwise equivalent sites in a crystal [213]. In resonant diffraction, this can result in a weak scattered intensity at space-group "forbidden" reflections. ATS scattering can be generally present in both the σ-σ' and

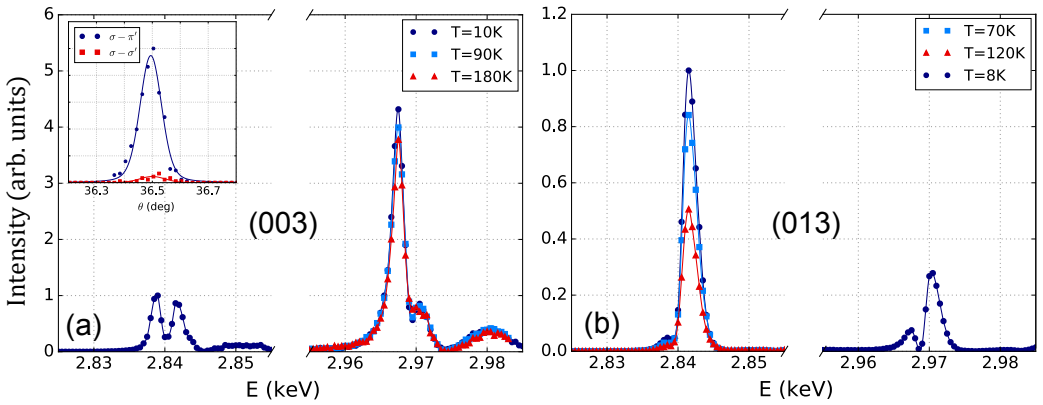

Figure B.1: Ru L_3 and L_2 energy resonances of the (a) (003) ($\psi = 90°$) and (b) (013) ($\psi = 0°$) ATS scattering peaks at different temperatures across the Néel transition in the $x = 0.05$ sample. The filled symbols refer to the total scattered intensity corrected for self-absorption and normalised to the L_3 peak intensity. The solid lines represent a quadratic interpolation to the data points and are meant just as a guide to the eye. The inset in (a) shows the polarisation dependence of the (003) reflection measured at $E = 2.838$ keV: the filled symbols refer to the scattered intensity measured over a rocking scan in the σ-π' (blue circles) and σ-σ' (red squares) channels of the polarisation analyser normalised to the σ-π' peak intensity, while the solid lines represent a fit to a Voigt profile.

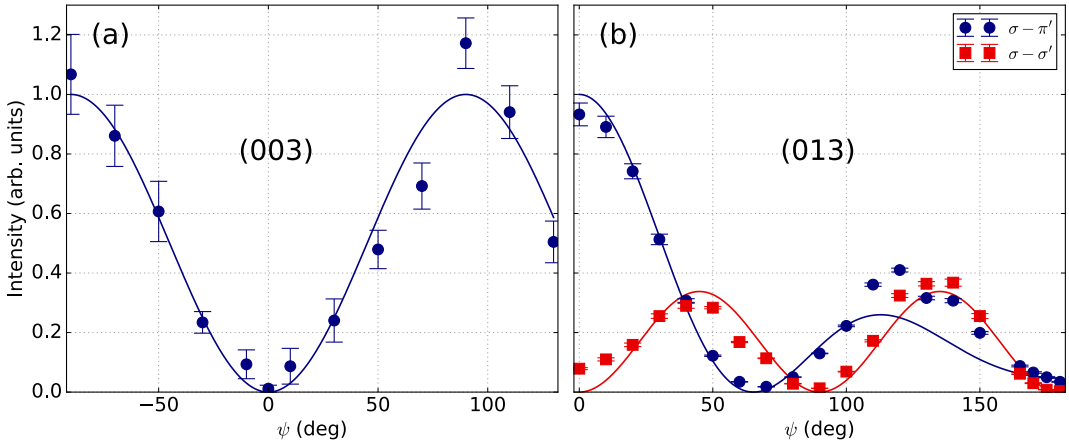

Figure B.2: Azimuthal dependence [azimuthal reference (010)] of the (a) (003) and (b) (013) ATS scattering peaks at (a) $E = 2.967$ keV and (b) $E = 2.9704$ keV in the $x = 0.05$ sample. The filled symbols refer to the (a) total and (b) σ-π' (blue circles) and σ-σ' (red squares) scattered intensity integrated over a rocking curve. The solid lines represent the calculated ATS azimuthal dependences in both polarisation channels (except for an arbitrary scale factor). The (003) signal is entirely π' polarised, as shown in the inset of Fig. B.1(a). The intensity is normalised to the σ-π' calculated value at $\psi = 0°$.

σ-π' channels of the polarisation analyser; it also generally displays a different dependence on the sample azimuth with respect to the one of dipole XRMS. The azimuthal dependence is related to the local site symmetries of the resonant atom and can be calculated for both polarisation states of the diffracted beam [213].

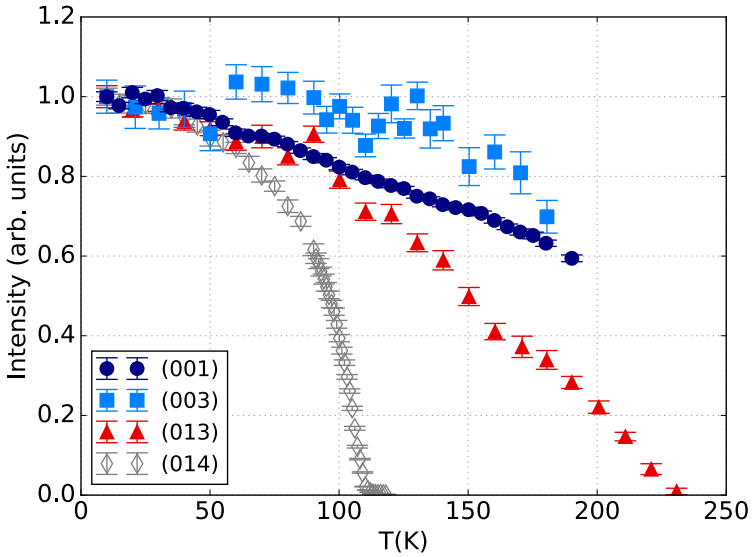

Figure B.3: Temperature dependence of the $(0\,0\,1)$, $(0\,0\,3)$ and $(0\,1\,3)$ ATS scattering peaks in the $x = 0.05$ sample. The data points correspond to the total diffracted intensity integrated over a rocking curve. The temperature dependence of the $(0\,1\,4)$ magnetic peak (same as Fig. 4.14) is also reported for comparison.

The measured $(0\,1\,3)$ intensity in σ-σ' and σ-π' as a function of the sample azimuth in the $x = 0.05$ sample is shown in Fig. B.2(b) along with the corresponding calculations. The latter match remarkably well the measurements and further confirm the ATS origin of the scattered intensity. The $(00l)$ peaks constitute a special case where the azimuthal dependence of ATS scattering [Fig. B.2(a)] exactly coincides with the one expected for the A-centred magnetic mode. Furthermore, analogous to XRMS, the signal is entirely π'-polarised, as shown in the inset of Fig. B.1(a). Nonetheless, its resonance and temperature dependence confirm that they are not magnetic in origin.

A detailed temperature dependence of the $(0\,0\,1)$, $(0\,0\,3)$ and $(0\,1\,3)$ A-centred peaks in the $x = 0.05$ sample is shown in Fig. B.3; here, the temperature dependence of the magnetic $(0\,1\,4)$ B-centred peak is also reported for comparison. The ATS peaks display a much weaker temperature dependence compared to magnetic scattering: the scattered intensity survives well beyond T_N and exhibits an almost linear drop upon warming. A similar behaviour was reported by Zegkinoglou *et al.* [186] in pure Ca_2RuO_4, who attributed the scattered intensity above the Néel transition to orbital ordering of the Ru t_{2g} electrons associated to the cooperative rotation of the RuO_6 octahedra. Although this point was not addressed in detail in the measurements here discussed, an analogous mechanism might be behind the observed ATS scattering in the doped compounds. In particular, the temperature dependence might be accounted for by the structural changes discussed in Sec. 4.4.2. The ATS

intensity seems to vanish around $T \approx 230$ K, as illustrated by the $(0\,1\,3)$ temperature dependence of Fig. B.3. This is lower than in the parent compound, where orbital ordering sets in below $T \approx 260$ K, and roughly coincides with the concomitant structural transition and MIT (see phase diagram of Fig. 4.5).

B.2 Representational analysis of the space group Pbca with the propagation vector $\mathbf{k} = (\mathbf{0},\mathbf{0},\mathbf{0})$

The symmetry-allowed magnetic structures that can result from a second-order magnetic phase transition can be determined by means of representational analysis [296–303] given the crystal structure before the transition and the propagation vector of the magnetic ordering. Calculations for the case of Ca_2RuO_4 [space group *Pbca* (No. 61) with propagation vector $\mathbf{k} = (0,0,0)$] were carried out using version 2*K* of the program SARA*h*-Representational Analysis [304]. They involve first the determination of the space group symmetry elements that leave the propagation vector $\mathbf{k}$ invariant: these form the little group $G_\mathbf{k}$. In the case under study, $G_\mathbf{k}$ includes all 8 symmetry operations of the *Pbca* space group. The magnetic representation of a crystallographic site can then be decomposed in terms of the irreducible representations (IRs) of $G_\mathbf{k}$:

$$\Gamma_{\text{Mag}} = \sum_\nu n_\nu \Gamma_\nu^\mu \tag{B.1}$$

where n_ν is the number of times that the IR Γ_ν^μ of order μ appears in the magnetic representation Γ_{Mag} for the chosen crystallographic site. The decomposition of the magnetic representation Γ_{Mag} in terms of the non-zero IRs of $G_\mathbf{k}$ for the Ru site, and their associated basis vectors, ψ_n, are given in Table B.1. The labelling of the propagation vector and the IRs follows the scheme used by Kovalev [305].

As discussed in Chapter 4, the measured magnetic structure of pure Ca_2RuO_4 is compatible with the Γ_1 IR, which is referred to as A-centred mode. On the other hand, the ordering of the La-doped samples is compatible with the Γ_3 IR (referred to as B-centred mode), where a net moment along the **a** axis is present. Although both IRs allow a finite component of the moment along the **c** axis, this could not be distinguished either in the measurements presented in this work or in the neutron data by Braden *et al.* [172].

IR	BV	Atom	BV components					
			$m_{\parallel a}$	$m_{\parallel b}$	$m_{\parallel c}$	$im_{\parallel a}$	$im_{\parallel b}$	$im_{\parallel c}$
Γ_1	ψ_1	1	2	0	0	0	0	0
		2	2	0	0	0	0	0
		3	-2	0	0	0	0	0
		4	-2	0	0	0	0	0
	ψ_2	1	0	2	0	0	0	0
		2	0	-2	0	0	0	0
		3	0	2	0	0	0	0
		4	0	-2	0	0	0	0
	ψ_3	1	0	0	2	0	0	0
		2	0	0	-2	0	0	0
		3	0	0	-2	0	0	0
		4	0	0	2	0	0	0
Γ_3	ψ_4	1	2	0	0	0	0	0
		2	2	0	0	0	0	0
		3	2	0	0	0	0	0
		4	2	0	0	0	0	0
	ψ_5	1	0	2	0	0	0	0
		2	0	-2	0	0	0	0
		3	0	-2	0	0	0	0
		4	0	2	0	0	0	0
	ψ_6	1	0	0	2	0	0	0
		2	0	0	-2	0	0	0
		3	0	0	2	0	0	0
		4	0	0	-2	0	0	0
Γ_5	ψ_7	1	2	0	0	0	0	0
		2	-2	0	0	0	0	0
		3	-2	0	0	0	0	0
		4	2	0	0	0	0	0
	ψ_8	1	0	2	0	0	0	0
		2	0	2	0	0	0	0
		3	0	2	0	0	0	0
		4	0	2	0	0	0	0
	ψ_9	1	0	0	2	0	0	0
		2	0	0	2	0	0	0
		3	0	0	-2	0	0	0
		4	0	0	-2	0	0	0
Γ_7	ψ_{10}	1	2	0	0	0	0	0
		2	-2	0	0	0	0	0
		3	2	0	0	0	0	0
		4	-2	0	0	0	0	0

IR	BV	Atom	BV components					
			m_a	m_b	m_c	im_a	im_b	im_c
	ψ_{11}	1	0	2	0	0	0	0
		2	0	2	0	0	0	0
		3	0	-2	0	0	0	0
		4	0	-2	0	0	0	0
	ψ_{12}	1	0	0	2	0	0	0
		2	0	0	2	0	0	0
		3	0	0	2	0	0	0
		4	0	0	2	0	0	0

Table B.1: Basis vectors for the space group *Pbca* with $\mathbf{k} = (0,0,0)$. The decomposition of the magnetic representation for the *Ru* site $(0,0,0)$ is $\Gamma_{\text{Mag}} = 3\Gamma_1^1 + 0\Gamma_2^1 + 3\Gamma_3^1 + 0\Gamma_4^1 + 3\Gamma_5^1 + 0\Gamma_6^1 + 3\Gamma_7^1 + 0\Gamma_8^1$. The atomic positions are defined according to 1: $(0,0,0)$, 2: $(1/2,1/2,0)$, 3: $(0,1/2,1/2)$, 4: $(1/2,0,1/2)$.

B.3 Neutron structural refinement details

Tables B.2 and B.3 summarise the *R* factors and goodness of fit (χ^2) of the structural refinement of the neutron diffraction data discussed in Sec. 4.4.2, along with the refined components of the thermal ellipsoid tensor **U**. The latter is a symmetric tensor which describes the thermal motion of the atoms about their nominal position in the unit cell. The diagonal elements (U_{ii}) are always positive and express the atomic displacements along the crystallographic axes. On the other hand, the off-diagonal elements ($U_{ij}, i \neq j$) describe the rotations of the ellipsoid with respect to the crystallographic axes and can be either positive or negative depending on the orientation of the ellipsoid in space. Isotropic atomic displacements correspond to the case $U_{11} = U_{22} = U_{33}$ and $U_{ij} = 0$ for $i \neq j$.

Table B.2: *R* factors, goodness of fit and components of the thermal ellipsoid tensor (in units of $Å^2$) resulting from the neutron structural refinement at T = 10 K. The *R* factors and χ^2 values refer to the refinement performed with the intensity threshold $I > 3\sigma$. Anisotropic thermal parameters were refined for all samples with the only exception of the Ru sites in the parent compound, where an isotropic thermal parameter $U_{iso} = U_{11} = U_{22} = U_{33}$ was considered: given the small value of the Ru thermal parameters in pure Ca_2RuO_4 at low temperature, a reliable refinement of the anisotropic components was not possible.

		T = 10 K			
		$x = 0$	$x = 0.05$	$x = 0.07$	$x = 0.12$
R factor		0.0992	0.0748	0.0769	0.0752
χ^2		2.84	2.45	2.38	1.93
Ru	U_{11}	0.0003(2)	0.00301(14)	0.0020(3)	0.0034(3)
	U_{22}	0.0003(2)	0.0049(3)	0.0019(3)	0.0029(2)
	U_{33}	0.0003(2)	0.00313(18)	0.0021(3)	0.0032(2)
	U_{12}	-	-0.0002(2)	-0.0001(4)	-0.0003(2)
	U_{13}	-	0.00011(13)	0.0006(3)	0.00000(17)
	U_{23}	-	0.00050(20)	-0.0004(2)	-0.00007(17)
Ca (La)	U_{11}	0.0019(4)	0.00493(16)	0.0039(4)	0.0055(3)
	U_{22}	0.0037(10)	0.0074(4)	0.0057(4)	0.0066(2)
	U_{33}	0.0006(5)	0.0042(2)	0.0025(3)	0.0044(2)
	U_{12}	0.0016(7)	-0.0001(2)	-0.0003(3)	0.0004(2)
	U_{13}	0.0006(6)	-0.00037(15)	-0.0004(3)	0.00009(20)
	U_{23}	0.0011(6)	-0.0001(2)	-0.0001(3)	-0.00020(19)
O(1)	U_{11}	0.0012(4)	0.00510(13)	0.0038(3)	0.0052(2)
	U_{22}	0.0071(10)	0.0061(3)	0.0044(3)	0.00477(18)
	U_{33}	0.0017(5)	0.00664(19)	0.0060(3)	0.0085(2)
	U_{12}	0.0000(6)	0.00060(17)	0.0009(3)	0.00081(16)
	U_{13}	0.0002(4)	-0.00010(14)	0.0000(3)	0.0002(2)
	U_{23}	-0.0009(7)	-0.0007(2)	-0.0006(3)	-0.0001(2)
O(2)	U_{11}	0.0038(4)	0.00670(14)	0.0058(3)	0.0078(2)
	U_{22}	0.0072(11)	0.0096(4)	0.0073(4)	0.0092(2)
	U_{33}	0.0003(5)	0.00518(19)	0.0033(3)	0.0044(2)
	U_{12}	-0.0006(6)	0.00010(17)	-0.0003(3)	-0.00034(17)
	U_{13}	0.0004(4)	-0.00074(13)	-0.0002(2)	-0.00041(16)
	U_{23}	-0.0001(7)	-0.0004(2)	0.0003(3)	0.0002(2)

Table B.3: *R* factors, goodness of fit and components of the thermal ellipsoid tensor (in units of Å^2) resulting from the neutron structural refinement at T = 300 K. The *R* factors and χ^2 values refer to the refinement performed with the intensity threshold $I > 3\sigma$.

		T = 300 K		
		$x = 0$	$x = 0.05$	$x = 0.07$
R factor		0.1057	0.0750	0.0844
χ^2		3.43	1.94	2.21
Ru	U_{11}	0.0026(7)	0.0068(3)	0.0027(6)
	U_{22}	0.0033(16)	0.0074(6)	0.0044(9)
	U_{33}	0.0006(7)	0.0068(3)	0.0058(8)
	U_{12}	0.0018(12)	0.0006(4)	-0.0001(8)
	U_{13}	-0.0004(7)	0.0006(2)	0.0003(6)
	U_{23}	-0.0007(9)	-0.0003(3)	0.0004(7)
Ca (La)	U_{11}	0.0075(9)	0.0139(4)	0.0109(8)
	U_{22}	0.015(2)	0.0167(7)	0.0125(11)
	U_{33}	0.0024(9)	0.0080(4)	0.0068(9)
	U_{12}	0.0037(12)	0.0018(4)	0.0011(9)
	U_{13}	0.0003(8)	0.0000(3)	-0.0004(7)
	U_{23}	0.0010(10)	0.0004(4)	0.0012(7)
O(1)	U_{11}	0.0045(6)	0.0084(3)	0.0065(5)
	U_{22}	0.0126(17)	0.0107(5)	0.0068(8)
	U_{33}	0.0068(9)	0.0160(4)	0.0165(9)
	U_{12}	0.0024(9)	0.0019(3)	0.0025(6)
	U_{13}	-0.0006(7)	-0.0010(3)	-0.0016(6)
	U_{23}	-0.0009(10)	-0.0012(4)	-0.0023(7)
O(2)	U_{11}	0.0087(7)	0.0150(3)	0.0117(6)
	U_{22}	0.0156(18)	0.0175(6)	0.0134(9)
	U_{33}	0.0018(8)	0.0074(3)	0.0039(7)
	U_{12}	-0.0007(10)	-0.0007(4)	-0.0004(8)
	U_{13}	-0.0006(6)	-0.0008(2)	-0.0013(5)
	U_{23}	0.0002(12)	0.0001(4)	0.0000(8)

Appendix C

$(Sr_{1-x}La_x)_2IrO_4$: alternative Hamiltonian and details of the spectra

C.1 Alternative magnetic Hamiltonian: XYh_4 model

As discussed in Sec. 5.4.2.3, the 2DAH Hamiltonian successfully describes both the single-magnon excitation spectrum presented in the present work and the magnetic critical fluctuations above the Néel transition reported by Vale *et al.* [242]. In the latter, the magnetic order parameter below T_N was also found to be consistent with the XYh_4 universality class [306]. A model Hamiltonian for systems falling into this category has the following form [306–308]:

$$\mathscr{H}^{ij}_{XYh_4} = J_{ex}\tilde{\mathbf{S}}_i\cdot\tilde{\mathbf{S}}_j + J'_{ex}\tilde{\mathbf{S}}_i\cdot\tilde{\mathbf{S}}_j + J''_{ex}\tilde{\mathbf{S}}_i\cdot\tilde{\mathbf{S}}_j + D\sum_i(\tilde{S}^z_i)^2 + \frac{1}{2}e\sum_i(S_i^{+4}+S_i^{-4}) \quad \text{(C.1)}$$

The first three terms correspond to a traditional Heisenberg model with nearest-neighbour (J_{ex}), next-nearest-neighbour (J'_{ex}) and third-nearest neighbour (J''_{ex}) interactions. While in the models discussed in Sec. 5.3 the anisotropy stems from a different coupling of the x, y and z components of the magnetic moments, in this case it is ascribed to a four-fold crystal field [306, 307]: the latter consists of the easy-plane term D, responsible for confining the moments in the IrO_2 planes, and the four-fold term e, which breaks the symmetry within the plane. It should be noted that the quartic term in the spin operators can be decoupled [307] in the random-phase approximation into the quadratic term $E\sum_i(S_i^{x\,2}-S_i^{y\,2})$, where $E = 6e\langle S_i^{x\,2}-S_i^{y\,2}\rangle$. The anisotropic terms in Eq. (C.1) thus effectively represent a single-ion anisotropy. Although the latter is expected to vanish [209] for $S = 1/2$

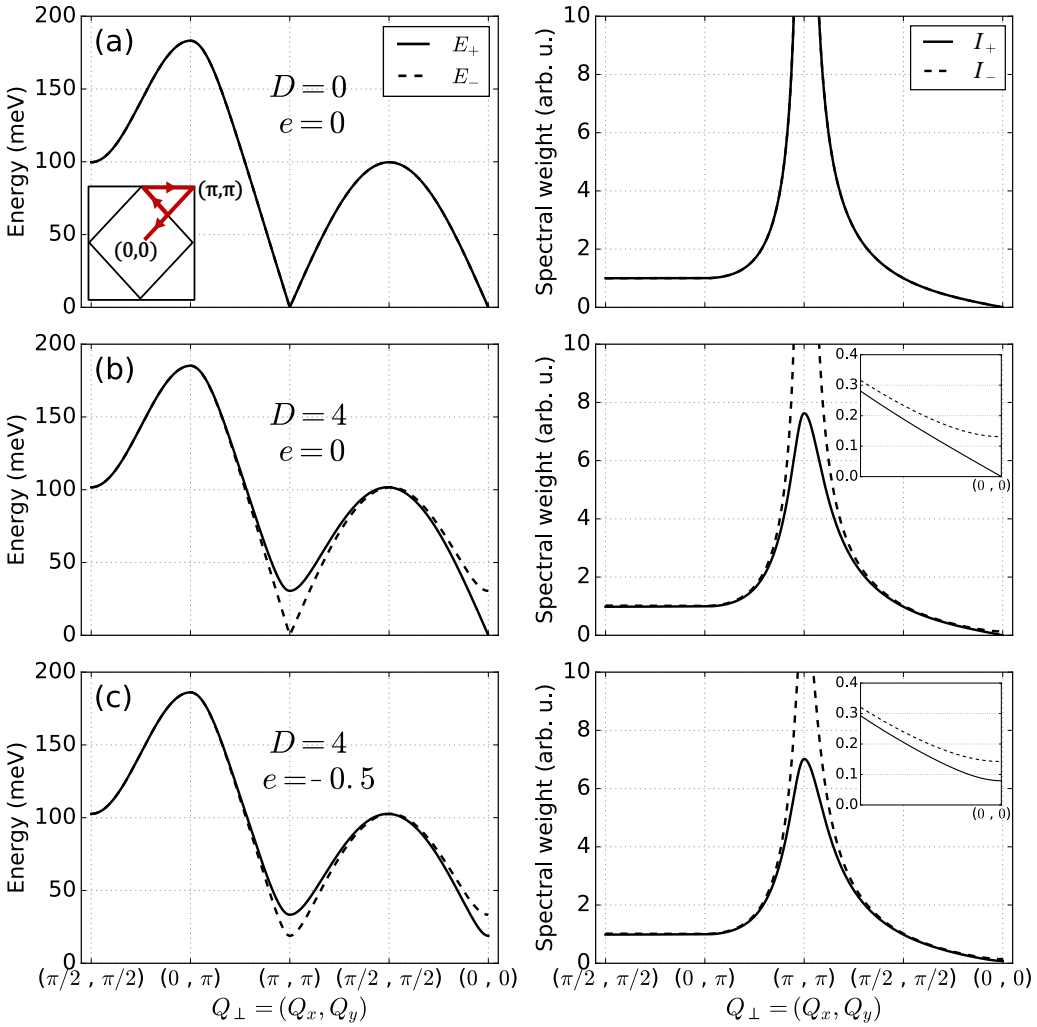

Figure C.1: Energy (left) and spectral weight (right) of the XYh_4 model linear spin-wave solutions for (a) vanishing anisotropy and (b),(c) different values of the anisotropy parameters D and e. The inset in (a) displays the path in the first BZ along which the linear spin-wave solutions of Eq. (C.1) have been evaluated, while the insets in (b) and (c) show a detail of the spectral weight around $(0,0)$.

(and, equivalently, $J_{\text{eff}} = 1/2$) systems, tetragonal distortions cause the admixing of $J_{\text{eff}} = 1/2$ and $J_{\text{eff}} = 3/2$ states, thus giving rise to a non-vanishing single-ion anisotropy.

In the linear spin-wave approximation, Eq. (C.1) results in the following two magnetic modes [307]:

$$\begin{aligned} E_{\pm}(\mathbf{Q}_{\perp}) &= 2\tilde{S}\sqrt{(A_{\mathbf{Q}_{\perp}})^2 - (B^{\pm}_{\mathbf{Q}_{\perp}})^2} \\ A(\mathbf{Q}_{\perp}) &= 2|J_{\text{ex}}|\left[1 + \frac{J'_{\text{ex}}}{J_{\text{ex}}}\big(\gamma_2(\mathbf{Q}_{\perp}) - 1\big) + \frac{J''_{\text{ex}}}{J_{\text{ex}}}\big(\gamma_3(\mathbf{Q}_{\perp}) - 1\big) + X\right] \\ B^{\pm}(\mathbf{Q}_{\perp}) &= 2|J_{\text{ex}}|\,(\gamma_1(\mathbf{Q}_{\perp}) \pm Y) \end{aligned} \tag{C.2}$$

where $X = (D-3E)/(4|J_{\text{ex}}|)$, $Y = (D+E)/(4|J_{\text{ex}}|)$, $\gamma_1(\mathbf{Q}_{\perp}) = \frac{1}{2}(\cos Q_x + \cos Q_y)$, $\gamma_2(\mathbf{Q}_{\perp}) = \cos Q_x \cos Q_y$, $\gamma_3(\mathbf{Q}_{\perp}) = \frac{1}{2}(\cos 2Q_x + \cos 2Q_y)$, $E = 6e\tilde{S}^2$ and $\tilde{S} = 1/2$ is the Ir^{4+} isospin. The spectral weight is given by Eq. (5.14), where $A(\mathbf{Q}_{\perp})$ and $B^{\pm}(\mathbf{Q}_{\perp})$ are, in this case, those of Eq. (C.2). For $e = 0$, the anisotropy within the plane vanishes and the linear spin-wave solutions are analogous to the ones of the 2DAH model: the in-plane anisotropy parameter D has in this case a similar impact on the magnon dispersion to the one of the anisotropy parameter Δ_{λ} in Eq. (5.15). This can be seen by comparing Figs. C.1(a),(b) with Fig. 5.14. Eq. (C.2) can then be equivalently used to fit the magnon energy, following the same approach outlined in Sec. 5.4.2.3. The fit describes the single-magnon excitation spectrum, in particular the presence of a finite gap, equally well: the best fit values of the isotropic exchange integrals are the same as the ones reported in Table 5.3, while the in-plane anisotropy D converges to 3.6 ± 1.3, 3.9 ± 1.2, 1.4 ± 1.0, 1.9 ± 1.0 meV for $x = 0, 0.01, 0.04, 0.1$, respectively. These values are larger than a previous theoretical prediction [309] ($D = 0.10$ meV) but smaller than the value estimated from the crystal field parameters ($D \approx 60$ meV[1]).

For $e \neq 0$ both magnetic modes of Eq. (C.2) are gapped throughout the entire BZ and display a finite non-vanishing spectral weight at all values of the in-plane momentum transfer [see Fig. C.1(c)]. One might argue that considering a non-zero value for the anisotropy parameter e naturally accounts for both the presence of a magnon gap both at $(0,0)$ and (π,π) and the absence of gapless magnetic modes. Following this approach, and bearing in mind that only one magnon mode

[1] This value was calculated using a known relation for D_{4h} symmetry between the single-ion anisotropy parameter D and the crystal field parameters $10Dq$, D_s and D_t [310]. The latter were derived from the tetragonal splitting of the t_{2g} ($\Delta_1 = 3D_s - 5D_t = 10$ meV [238]) and e_g ($\Delta_3 = 4D_s + 5D_t = 1.6$ eV [255]) orbitals. The following values were also considered $10Dq = 3.8$ eV [255], $\lambda_{\text{SOC}} = 0.4$ eV [8], $B = 420$ cm^{-1}, $C = 2100$ cm^{-1}. B and C are the Racah parameters for Ir^{4+} taken from Ref. [311].

is visible in the RIXS spectra, the single-magnon energy dispersion can be fitted to a weighted sum (with weights given by the corresponding spectral weights) of the two unresolved modes predicted by the XYh_4 model. Given the addition of one free parameter, the fit is in general less stable. In particular D and e are strongly couple together and the model shows a tendency to converge to the non-physical scenario where $D = 0$ and the gap is accounted for by the sole e parameter. Yet, a satisfactory description of the data can be achieved by including a value of e equal to $-0.7(4)$, $-0.2(2)$, $-0.4(2)$ for $x = 0, 0.01, 0.04$, respectively. The four-fold anisotropy within the **ab** plane is expected to be negligible compared to the easy-plane term D [312]. Although smaller, the values of e extracted from the RIXS spectra are comparable in magnitude to the ones for D: this suggests that the fitting procedure just outlined is likely to result in a substantially overestimated anisotropy within the **ab** plane of the crystal.

C.2 Charge excitations

As discussed at length in Chapter 5, the RIXS investigation of Sec. 5.4 mainly addressed the magnetic excitation spectrum. The higher energy region of the RIXS spectra (Fig. 5.23) displays a reach structure arising from electronic transitions within the Ir t_{2g} orbitals. A detailed discussion is given by Kim *et al.* [236, 237]. In particular, a sharp feature dispersing between 0.4 and 0.5 eV is present in the spectra of the parent compound. This feature, named C in the fit detail of Fig. 5.24, is clearly visible both in the intensity map of Fig. 5.22 and in the $(\pi/2, \pi/2)$ spectrum of Fig. 5.23. Its dispersion along the $(\pi/2, \pi/2) \rightarrow (0,0)$ direction is highlighted by blue dots in the spectra of Fig. C.2(a). Feature C has been assigned to a spin-orbit exciton [237] and is not clearly seen in the doped compounds.

Furthermore, the parent compound spectra collected in proximity of $(0,0)$ show a weakly dispersive inelastic feature around $E_{\text{loss}} = 0.35$ eV [yellow dots in Fig. C.2(a)]. The latter, which is already visible both in the intensity map of Fig. 5.22 and in the $(0,0)$ spectrum of Fig. 5.23, is further highlighted in Fig. C.2(b), where the corresponding Voigt profile used for the fit is displayed through the yellow shaded region. This feature is also clearly present in the data collected by Kim *et al.* [237] [see spectra close to $(0,0)$ in Fig. 4(b) of Ref. [237]] who did not provide any comments as to its origin. Its energy scale (and the fact that the feature is absent in the doped compounds spectra) suggests to ascribe it to the Mott gap of undoped Sr_2IrO_4 [313]. However, a clear understanding of its nature goes beyond

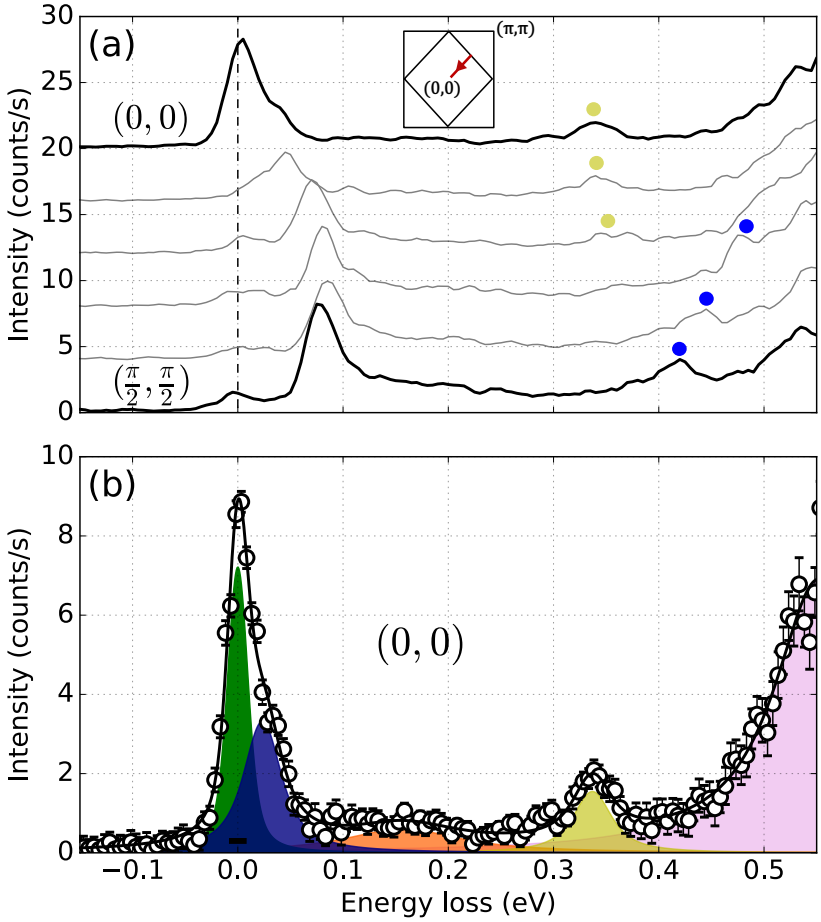

Figure C.2: (a) Parent compound RIXS spectra as a function of the in-plane momentum transfer $\mathbf{Q}_\perp$ along the nodal direction of the (0033) first BZ (see inset). The spectra were offset for clarity. The yellow filled symbols highlight the unassigned inelastic feature discuss in the text, while the blue symbols mark the spin-orbit exciton reported by Kim *et al.* [237]. (b) Fit detail of the $(0,0)$ spectrum. The yellow shaded region around 0.35 eV corresponds to the unassigned feature highlighted by the yellow filled symbols in (a). The other inelastic features are the same reported in Fig. 5.24.

the scope of the present investigation and will require further work.

Bibliography

[1] D. I. Khomskii, *Transition Metal Compounds* (Cambridge University Press, Cambridge, 2014).

[2] P. A. Lee, N. Nagaosa, and X.-G. Wen, Reviews of Modern Physics **78**, 17 (2006).

[3] A. P. Ramirez, Journal of Physics: Condensed Matter **9**, 8171 (1997).

[4] S.-W. Cheong and M. Mostovoy, Nature materials **6**, 13 (2007).

[5] Z. Yang, C. Ko, and S. Ramanathan, Annual Review of Materials Research **41**, 337 (2011).

[6] J. Ngai, F. Walker, and C. Ahn, Annual Review of Materials Research **44**, 1 (2014).

[7] W. Witczak-Krempa, G. Chen, Y. B. Kim, and L. Balents, Annual Review of Condensed Matter Physics **5**, 57 (2014).

[8] B. J. Kim, H. Jin, S. J. Moon, J. Y. Kim, B. G. Park, C. S. Leem, J. Yu, T. W. Noh, C. Kim, S. J. Oh, J. H. Park, V. Durairaj, G. Cao, and E. Rotenberg, Physical Review Letters **101**, 1 (2008).

[9] D. Pesin and L. Balents, Nature Physics **6**, 376 (2010).

[10] X. Wan, A. M. Turner, A. Vishwanath, and S. Y. Savrasov, Physical Review B **83**, 205101 (2011).

[11] A. Go, W. Witczak-Krempa, G. S. Jeon, K. Park, and Y. B. Kim, Physical Review Letters **109**, 066401 (2012).

[12] W. Witczak-Krempa and Y. B. Kim, Physical Review B **85**, 045124 (2012).

[13] A. A. Burkov and L. Balents, Physical Review Letters **107**, 127205 (2011).

[14] J. Hubbard, Proceedings of the Royal Society A: Mathematical, Physical and Engineering Sciences **276**, 238 (1963).

[15] J. Hubbard, Proceedings of the Royal Society A: Mathematical, Physical and Engineering Sciences **281**, 401 (1964).

[16] N. F. Mott, *Metal-insulator transitions* (Taylor & Francis, London, 1974).

[17] M. Imada, A. Fujimori, and Y. Tokura, Reviews of Modern Physics **70**, 1039 (1998).

[18] A. Georges, L. de' Medici, and J. Mravlje, Annual Review of Condensed Matter Physics **4**, 137 (2012).

[19] P. W. Anderson, Physical Review **115**, 2 (1959).

[20] D. Khomskii, *Basic aspects of the quantum theory of solids : order and elementary excitations* (Cambridge University Press, Cambridge, 2010).

[21] J. B. Goodenough, Physical Review **100**, 564 (1955).

[22] J. B. Goodenough, Journal of Physics and Chemistry of Solids **6**, 287 (1958).

[23] J. Kanamori, Journal of Physics and Chemistry of Solids **10**, 87 (1959).

[24] C. J. Ballhausen, *Introduction to Ligand Field Theory* (McGraw-Hill Book Co., New York, 1962).

[25] R. Schlapp and W. G. Penney, Physical Review **42**, 666 (1932).

[26] A. Abragam and B. Bleaney, *Electron Paramagnetic Resonance of Transition Ions* (Oxford University Press, Oxford, 1970).

[27] J. Als-Nielsen and D. McMorrow, *Elements of modern X-ray physics* (Wiley, Chichester, UK, 2011).

[28] P. Willmott, *An Introduction to Synchrotron Radiation: Techniques and Applications* (John Wiley & Sons, Ltd, Chichester, UK, 2011).

[29] F. de Bergevin and M. Brunel, Acta Crystallographica Section A **37**, 314 (1981).

[30] M. Blume and D. Gibbs, Physical Review B **37**, 1779 (1988).

[31] M. Blume, Journal of Applied Physics **57**, 3615 (1985).

[32] J. P. Hannon, G. T. Trammell, M. Blume, and D. Gibbs, Physical Review Letters **61**, 1245 (1988).

[33] J. P. Hill and D. F. McMorrow, Acta Crystallographica Section A: Foundations of Crystallography Foundations of Crystallography **52**, 236 (1996).

[34] M. Altarelli, in *Magnetism: A Synchrotron Radiation Approach* (Springer, Berlin, Heidelberg, 2006) pp. 201–242.

[35] S. P. Collins and A. Bombardi, in *Magnetism and Synchrotron Radiation*, Vol. 133 (Springer, Berlin, Heidelberg, 2010) pp. 223–262.

[36] Y. Joly, S. D. Matteo, and O. Bunău, The European Physical Journal Special Topics **208**, 21 (2012).

[37] S. Grenier and Y. Joly, Journal of Physics: Conference Series **519**, 012001 (2014).

[38] W. Sch{\"u}lke, *Electron dynamics by inelastic X-ray scattering* (Oxford University Press, Oxford, 2007).

[39] L. J. P. Ament, M. van Veenendaal, T. P. Devereaux, J. P. Hill, and J. van den Brink, Reviews of Modern Physics **83**, 705 (2011).

[40] L. L. Foldy, Physical Review **87**, 688 (1952).

[41] F. De Bergevin and M. Brunel, Physics Letters A **39**, 141 (1972).

[42] D. Gibbs, D. E. Moncton, K. L. D'Amico, J. Bohr, and B. H. Grier, Physical Review Letters **55**, 234 (1985).

[43] K. Namikawa, M. Ando, T. Nakajima, and H. Kawata, Journal of the Physical Society of Japan **54**, 4099 (1985).

[44] D. Gibbs, D. R. Harshman, E. D. Isaacs, D. B. McWhan, D. Mills, and C. Vettier, Physical Review Letters **61**, 1241 (1988).

[45] F. Fabrizi, H. C. Walker, L. Paolasini, F. de Bergevin, A. T. Boothroyd, D. Prabhakaran, and D. F. McMorrow, Physical Review Letters **106**, 239902 (2011).

[46] E. Prince, *International tables for crystallography. Volume C, Mathematical, physical and chemical tables* (Published for the International Union of Crystallography by Kluwer Academic Publishers, 2004).

[47] M. Blume, Physical Review **124**, 96 (1961).

[48] S. Langridge, G. H. Lander, N. Bernhoeft, A. Stunault, C. Vettier, G. Grübel, C. Sutter, F. de Bergevin, W. J. Nuttall, W. G. Stirling, K. Mattenberger, and O. Vogt, Physical Review B **55**, 6392 (1997).

[49] V. Fernandez, C. Vettier, F. de Bergevin, C. Giles, and W. Neubeck, Physical Review B **57**, 7870 (1998).

[50] C. Vettier, The European Physical Journal Special Topics **208**, 3 (2012).

[51] S. Boseggia, *Magnetic order and excitations in perovskite iridates studied with resonant X-ray scattering techniques*, Ph.D. thesis, University College London (2014).

[52] S. P. Collins, A. Bombardi, A. R. Marshall, J. H. Williams, G. Barlow, A. G. Day, M. R. Pearson, R. J. Woolliscroft, R. D. Walton, G. Beutier, G. Nisbet, R. Garrett, I. Gentle, K. Nugent, and S. Wilkins, in *AIP Conference Proceedings*, Vol. 1234 (2010) pp. 303–306.

[53] J. H. Beaumont and M. Hart, Journal of Physics E: Scientific Instruments **7**, 823 (1974).

[54] M. Lohmeier and E. Vlieg, Journal of Applied Crystallography **26**, 706 (1993).

[55] C. Detlefs, M. S. del Rio, and C. Mazzoli, The European Physical Journal Special Topics **208**, 359 (2012).

[56] L. J. P. Ament, G. Ghiringhelli, M. M. Sala, L. Braicovich, and J. van den Brink, Physical Review Letters **103**, 117003 (2009).

[57] L. Braicovich, J. van den Brink, V. Bisogni, M. M. Sala, L. J. P. Ament, N. B. Brookes, G. M. De Luca, M. Salluzzo, T. Schmitt, V. N. Strocov, and G. Ghiringhelli, Physical Review Letters **104**, 077002 (2010).

[58] J. van den Brink, Europhysics Letters (EPL) **80**, 47003 (2007).

[59] M. Moretti Sala, K. Martel, C. Henriquet, A. Al Zein, L. Simonelli, C. J. Sahle, H. Gonzalez, M.-C. Lagier, C. Ponchut, S. Huotari, R. Verbeni, M. Krisch, and G. Monaco, Journal of Synchrotron Radiation **25**, 580 (2018).

[60] S. Huotari, C. J. Sahle, C. Henriquet, A. Al-Zein, K. Martel, L. Simonelli, R. Verbeni, H. Gonzalez, M.-C. Lagier, C. Ponchut, M. Moretti Sala, M. Krisch, and G. Monaco, Journal of Synchrotron Radiation **24**, 521 (2017).

[61] P. Kirkpatrick and A. V. Baez, Journal of the Optical Society of America **38**, 766 (1948).

[62] M. Rossi, *Resonant inelastic X-ray scattering on spin-orbit-induced correlated-electron systems: scientific applications and instrumental developments*, Ph.D. thesis, Uninversité Grenoble Alpes (2017).

[63] B. W. Batterman and H. Cole, Reviews of Modern Physics **36**, 681 (1964).

[64] A. Authier, *Dynamical Theory of X-Ray Diffraction* (Oxford University Press, Oxford, 2003).

[65] S. Huotari, G. Vankó, F. Albergamo, C. Ponchut, H. Graafsma, C. Henriquet, R. Verbeni, and G. Monaco, Journal of Synchrotron Radiation **12**, 467 (2005).

[66] S. Huotari, F. Albergamo, G. Vankó, R. Verbeni, and G. Monaco, Review of Scientific Instruments **77**, 053102 (2006).

[67] C. Ponchut, J. M. Rigal, J. Clément, E. Papillon, A. Homs, and S. Petitdemange, Journal of Instrumentation **6**, C01069 (2011).

[68] H. H. Johann, Zeitschrift für Physik **69**, 185 (1931).

[69] J. E. Penner-Hahn, in *Encyclopedia of Life Sciences* (John Wiley & Sons, Ltd, Chichester, UK, 2005).

[70] K. Z. Bencze, K. C. Kondapalli, and T. L. Stemmler, in *Encyclopedia of Inorganic and Bioinorganic Chemistry* (John Wiley & Sons, Ltd, Chichester, UK, 2011).

[71] P. Fornasini, in *Synchrotron Radiation: Basics, Methods and Applications* (Springer, Berlin, Heidelberg, 2015) pp. 181–211.

[72] L. Mino, E. Borfecchia, J. Segura-Ruiz, C. Giannini, G. Martinez-Criado, and C. Lamberti, Reviews of Modern Physics **90**, 025007 (2018).

[73] G. van der Laan and B. T. Thole, Physical Review letters **60**, 1977 (1988).

[74] B. T. Thole and G. van der Laan, Physical Review B **38**, 3158 (1988).

[75] B. T. Thole and G. van der Laan, Physical Review A **38**, 1943 (1988).

[76] S. Eisebitt, T. Böske, J.-E. Rubensson, and W. Eberhardt, Physical Review B **47**, 14103 (1993).

[77] A. Iida and T. Noma, Japanese Journal of Applied Physics **32**, 2899 (1993).

[78] M. Pompa, A. M. Flank, R. Delaunay, A. Bianconi, and P. Lagarde, Physica B: Condensed Matter Proceedings of the 8th International Conference on X-ray Absorption Fine Structure, **208**, 143 (1995).

[79] R. Carboni, S. Giovannini, G. Antonioli, and F. Boscherini, Physica Scripta **2005**, 986 (2005).

[80] C. T. Chen, Y. U. Idzerda, H.-J. Lin, N. V. Smith, G. Meigs, E. Chaban, G. H. Ho, E. Pellegrin, and F. Sette, Physical Review Letters **75**, 152 (1995).

[81] B. T. Thole, G. van der Laan, and G. A. Sawatzky, Physical Review Letters **55**, 2086 (1985).

[82] J. L. Erskine and E. A. Stern, Physical Review B **12**, 5016 (1975).

[83] G. van der Laan, B. T. Thole, G. A. Sawatzky, J. B. Goedkoop, J. C. Fuggle, J.-M. Esteva, R. Karnatak, J. P. Remeika, and H. A. Dabkowska, Physical Review B **34**, 6529 (1986).

[84] G. Schütz, W. Wagner, W. Wilhelm, P. Kienle, R. Zeller, R. Frahm, and G. Materlik, Physical Review Letters **58**, 737 (1987).

[85] B. T. Thole, P. Carra, F. Sette, and G. van der Laan, Physical Review Letters **68**, 1943 (1992).

[86] P. Carra, B. T. Thole, M. Altarelli, and X. Wang, Physical Review Letters **70**, 694 (1993).

[87] X. Chen, T. Hogan, D. Walkup, W. Zhou, M. Pokharel, M. Yao, W. Tian, T. Z. Ward, Y. Zhao, D. Parshall, C. Opeil, J. W. Lynn, V. Madhavan, and S. D. Wilson, Physical Review B **92**, 075125 (2015).

[88] A. Rogalev and F. Wilhelm, The Physics of Metals and Metallography **116**, 1285 (2015).

[89] H. Wang, P. Bencok, P. Steadman, E. Longhi, J. Zhu, and Z. Wang, Journal of Synchrotron Radiation **19**, 944 (2012).

[90] R. Coldea, S. M. Hayden, G. Aeppli, T. G. Perring, C. D. Frost, T. E. Mason, S. W. Cheong, and Z. Fisk, Physical Review Letters **86**, 5377 (2001).

[91] T. Moriya, Physical Review **120**, 91 (1960).

[92] I. Dzyaloshinsky, Journal of Physics and Chemistry of Solids **4**, 241 (1958).

[93] R. W. Wyckoff, American Journal of Science **4**, 317 (1920).

[94] A. S. Borovik-Romanov and M. P. Orlova, Soviet Physics, JETP **4**, 531 (1957).

[95] A. S. Borovik-Romanov, Soviet Physics, JETP **9**, 539 (1959).

[96] A. S. Borovik-Romanov and V. I. Ozhogin, Soviet Physics, JETP **12**, 18 (1961).

[97] J. Kaczer, Soviet Physics, JETP **16**, 1443 (1963).

[98] VI Ozhogin, Soviet Physics, JETP **18**, 1156 (1964).

[99] I. Maartense, Physical Review **188**, 924 (1969).

[100] N. M. Kreines and T. A. Shal'Nikova, Soviet Physics, JETP **31**, 280 (1970).

[101] H. Meijer, L. Pimmelaar, S. Brouwer, and J. Van den Handel, Physica **46**, 279 (1970).

[102] M. P. Petrov, G. A. Smolensky, A. P. Paugurt, S. A. Kizhaev, C. D. Graham Jr, and J. J. Rhyne, in *AIP Conference Proceedings*, Vol. 5 (AIP, 1972) pp. 379–391.

[103] I. Maartense, Physical Review B **6**, 4324 (1972).

[104] N. Kharchenko, V. Eremenko, and O. Tutakina, Soviet Physics, JETP **37**, 672 (1973).

[105] A. N. Bazhan, Soviet Physics, JETP **39**, 531 (1974).

[106] A. S. Borovik-Romanov, N. M. Kreĭnes, A. A. Pankov, and M. A. Talalaev, Soviet Physics, JETP **39**, 378 (1974).

[107] R. Diehl, Solid State Communications **17**, 743 (1975).

[108] F. Pertlik, Acta Crystallographica Section C: Structural Chemistry **C42**, 4 (1986).

[109] R. W. Wyckoff, *Crystal structures. Vol. 2, Inorganic compounds RXn, RnMX2, RnMX3* (John Wiley & Sons, Ltd, New York, 1986).

[110] E. N. Maslen, V. A. Streltsov, N. R. Streltsova, and N. Ishizawa, Acta Crystallographica Section B: Structural Science, Crystal Engineering and Materials **51**, 929 (1995).

[111] V. F. Meshcheryakov, JETP **98**, 144 (2004).

[112] U. Köbler, A. Hoser, J. Bos, W. Schäfer, and L. Pohlmann, Physica B: Condensed Matter **355**, 90 (2005).

[113] A. Kosterov, T. Frederichs, and T. von Dobeneck, Physics of the Earth and Planetary Interiors **154**, 234 (2006).

[114] V. F. Meshcheryakov, JETP **105**, 998 (2007).

[115] V. E. Dmitrienko, E. N. Ovchinnikova, J. Kokubun, and K. Ishida, JETP Letters **92**, 383 (2010).

[116] V. E. Dmitrienko, E. N. Ovchinnikova, S. P. Collins, G. Nisbet, G. Beutier, Y. O. Kvashnin, V. V. Mazurenko, A. I. Lichtenstein, and M. I. Katsnelson, Nature Physics **10**, 202 (2014).

[117] G. Beutier, S. P. Collins, O. V. Dimitrova, V. E. Dmitrienko, M. I. Katsnelson, Y. O. Kvashnin, A. I. Lichtenstein, V. V. Mazurenko, A. G. A. Nisbet, E. N. Ovchinnikova, and D. Pincini, Physical Review Letters **119**, 167201 (2017).

[118] M. Bode, M. Heide, K. Von Bergmann, P. Ferriani, S. Heinze, G. Bihlmayer, A. Kubetzka, O. Pietzsch, S. Blügel, and R. Wiesendanger, Nature **447**, 190 (2007).

[119] X. Z. Yu, Y. Onose, N. Kanazawa, J. H. Park, J. H. Han, Y. Matsui, N. Nagaosa, and Y. Tokura, Nature **465**, 901 (2010).

[120] S. Heinze, K. Von Bergmann, M. Menzel, J. Brede, A. Kubetzka, R. Wiesendanger, G. Bihlmayer, and S. Blügel, Nature Physics **7**, 713 (2011).

[121] S. X. Huang and C. L. Chien, Physical Review Letters **108**, 267201 (2012).

[122] H. Katsura, N. Nagaosa, and A. V. Balatsky, Physical Review Letters **95**, 057205 (2005).

[123] I. A. Sergienko and E. Dagotto, Physical Review B **73**, 094434 (2006).

[124] S. Emori, U. Bauer, S.-M. Ahn, E. Martinez, and G. S. D. Beach, Nature Materials **12**, 611 (2013).

[125] F. Buijnsters, Y. Ferreiros, A. Fasolino, and M. Katsnelson, Physical Review Letters **116**, 147204 (2016).

[126] T. Moriya, Physical Review Letters **4**, 228 (1960).

[127] G. Kresse and J. Hafner, Physical Review B **47**, 558 (1993).

[128] G. Kresse and J. Furthmüller, Physical Review B **54**, 11169 (1996).

[129] I. V. Solovyev, A. I. Liechtenstein, and K. Terakura, Physical Review Letters **80**, 5758 (1998).

[130] V. E. Dmitrienko, K. Ishida, A. Kirfel, and E. N. Ovchinnikova, Acta Crystallographica Section A: Foundations of Crystallography **61**, 481 (2005).

[131] S. Lovesey, E. Balcar, K. Knight, and J. Fernández Rodríguez, Physics Reports **411**, 233 (2005).

[132] M. Usuda, M. Takahashi, and J.-i. Igarashi, Physical Review B **69**, 014408 (2004).

[133] Y. Joly, O. Bunău, J. E. Lorenzo, R. M. Galéra, S. Grenier, and B. Thompson, Journal of Physics: Conference Series **190**, 012007 (2009).

[134] Y. Joly, Physical Review B **63**, 125120 (2001).

[135] A. Moskvin, Journal of Magnetism and Magnetic Materials **400**, 117 (2016).

[136] S.-A. Siegfried, E. V. Altynbaev, N. M. Chubova, V. Dyadkin, D. Chernyshov, E. V. Moskvin, D. Menzel, A. Heinemann, A. Schreyer, and S. V. Grigoriev, Physical Review B **91**, 184406 (2015).

[137] S. V. Grigoriev, N. M. Potapova, S.-A. Siegfried, V. A. Dyadkin, E. V. Moskvin, V. Dmitriev, D. Menzel, C. D. Dewhurst, D. Chernyshov, R. A. Sadykov, L. N. Fomicheva, and A. V. Tsvyashchenko, Physical Review Letters **110**, 207201 (2013).

[138] S. V. Grigoriev, S.-A. Siegfried, E. V. Altynbayev, N. M. Potapova, V. Dyadkin, E. V. Moskvin, D. Menzel, A. Heinemann, S. N. Axenov, L. N. Fomicheva, and A. V. Tsvyashchenko, Physical Review B **90**, 174414 (2014).

[139] D. Pincini, F. Fabrizi, G. Beutier, G. Nisbet, H. Elnaggar, V. E. Dmitrienko, M. I. Katsnelson, Y. O. Kvashnin, A. I. Lichtenstein, V. V. Mazurenko, E. N. Ovchinnikova, O. V. Dimitrova, and S. P. Collins, Physical Review B **98**, 104424 (2018).

[140] S. D. Brown, L. Bouchenoire, D. Bowyer, J. Kervin, D. Laundy, M. J. Longfield, D. Mannix, D. F. Paul, A. Stunault, P. Thompson, M. J. Cooper, C. A. Lucas, and W. G. Stirling, Journal of Synchrotron Radiation **8**, 1172 (2001).

[141] S. W. Lovesey and S. P. Collins, *X-ray Scattering and Absorption by Magnetic Materials* (Oxford University Press, Oxford, 1996).

[142] W. Neubeck, C. Vettier, V. Fernandez, F. de Bergevin, and C. Giles, Journal of Applied Physics **85**, 4847 (1999).

[143] S. K. Kwon and B. I. Min, Physical Review B **62**, 73 (2000).

[144] W. Neubeck, C. Vettier, F. De Bergevin, F. Yakhou, D. Mannix, L. Ranno, and T. Chatterji, in *Journal of Physics and Chemistry of Solids*, Vol. 62 (Pergamon, 2001) pp. 2173–2180.

[145] R. J. Radwanski and Z. Ropka, Physica B: Condensed Matter **345**, 107 (2003).

[146] J. Okamoto, H. Nakao, Y. Yamasaki, H. Wadati, A. Tanaka, M. Kubota, K. Horigane, Y. Murakami, and K. Yamada, Journal of the Physical Society of Japan **83**, 044705 (2014).

[147] S. Lee, Y. Ishikawa, P. Miao, S. Torii, T. Ishigaki, and T. Kamiyama, Physical Review B **93**, 064429 (2016).

[148] S. I. Csiszar, M. W. Haverkort, Z. Hu, A. Tanaka, H. H. Hsieh, H. J. Lin, C. T. Chen, T. Hibma, and L. H. Tjeng, Physical Review Letters **95**, 187205 (2005).

[149] D. Weller, J. Stöhr, R. Nakajima, A. Carl, M. G. Samant, C. Chappert, R. Mégy, P. Beauvillain, P. Veillet, and G. A. Held, Physical Review Letters **75**, 3752 (1995).

[150] H. A. Dürr, G. van der Laan, and B. T. Thole, Physical Review Letters **76**, 3464 (1996).

[151] H. A. Durr, G. Y. Guo, G. van der Laan, J. Lee, G. Lauhoff, and J. A. C. Bland, Science **277**, 213 (1997).

[152] H. A. Dürr and G. van der Laan, Journal of Applied Physics **81**, 5355 (1998).

[153] P. Bruno, Physical Review B **39**, 865 (1989).

[154] D. Weller and A. Moser, IEEE Transactions on Magnetics **35**, 4423 (1999).

[155] N. Nakajima, T. Koide, T. Shidara, H. Miyauchi, H. Fukutani, A. Fujimori, K. Iio, T. Katayama, M. Nývlt, and Y. Suzuki, Physical Review Letters **81**, 5229 (1998).

[156] P. Gambardella, S. Rusponi, M. Veronese, S. S. Dhesi, C. Grazioli, A. Dallmeyer, I. Cabria, R. Zeller, P. H. Dederichs, K. Kern, C. Carbone, and H. Brune, Science **300**, 1130 (2003).

[157] P. J. Besser, A. H. Morrish, and C. W. Searle, Physical Review **153**, 632 (1967).

[158] E. Weckert and K. Hümmer, Acta Crystallographica Section A: Foundations of Crystallography Foundations of Crystallography **53**, 108 (1997).

[159] A. G. Nisbet, G. Beutier, F. Fabrizi, B. Moser, and S. P. Collins, Acta Crystallographica Section A: Foundations of Crystallography **71**, 20 (2015).

[160] J. Kokubun, K. Ishida, and V. E. Dmitrienko, Journal of the Physical Society of Japan **67**, 1291 (1998).

[161] J. Kokubun, K. Ishida, D. Cabaret, F. Mauri, R. V. Vedrinskii, V. L. Kraizman, A. A. Novakovich, E. V. Krivitskii, and V. E. Dmitrienko, Physical Review B **69**, 245103 (2004).

[162] R. D. Cowan, Physical Review **163**, 54 (1967).

[163] M. W. Haverkort, M. Zwierzycki, and O. K. Andersen, Physical Review B **85**, 165113 (2012).

[164] G. Cao, C. Alexander, S. McCall, J. Crow, and R. Guertin, Materials Science and Engineering: B **63**, 76 (1999).

[165] A. P. Mackenzie and Y. Maeno, Reviews of Modern Physics **75**, 657 (2003).

[166] G. Khaliullin, Physical Review Letters **111**, 197201 (2013).

[167] A. Akbari and G. Khaliullin, Physical Review B **90**, 035137 (2014).

[168] J. Chaloupka and G. Khaliullin, Physical Review Letters **116**, 017203 (2016).

[169] A. Jain, M. Krautloher, J. Porras, G. H. Ryu, D. P. Chen, D. L. Abernathy, J. T. Park, A. Ivanov, J. Chaloupka, G. Khaliullin, B. Keimer, and B. J. Kim, Nature Physics **13**, 633 (2017).

[170] S. Kunkemöller, D. Khomskii, P. Steffens, A. Piovano, A. A. Nugroho, and M. Braden, Physical Review Letters **115**, 247201 (2015).

[171] S. Kunkemöller, E. Komleva, S. V. Streltsov, S. Hoffmann, D. I. Khomskii, P. Steffens, Y. Sidis, K. Schmalzl, and M. Braden, Physical Review B **95**, 214408 (2017).

[172] M. Braden, G. André, S. Nakatsuji, and Y. Maeno, Physical Review B **58**, 847 (1998).

[173] A. Liebsch and H. Ishida, Physical Review Letters **98**, 216403 (2007).

[174] E. Gorelov, M. Karolak, T. O. Wehling, F. Lechermann, A. I. Lichtenstein, and E. Pavarini, Physical Review Letters **104**, 226401 (2010).

[175] D. Sutter, C. G. Fatuzzo, S. Moser, M. Kim, R. Fittipaldi, A. Vecchione, V. Granata, Y. Sassa, F. Cossalter, G. Gatti, M. Grioni, H. M. Rønnow, N. C. Plumb, C. E. Matt, M. Shi, M. Hoesch, T. K. Kim, T. R. Chang, H. T. Jeng, C. Jozwiak, A. Bostwick, E. Rotenberg, A. Georges, T. Neupert, and J. Chang, Nature Communications **8**, 15176 (2017).

[176] Q. Han and A. Millis, Physical Review Letters **121**, 067601 (2018).

[177] S. Riccò, M. Kim, A. Tamai, S. McKeown Walker, F. Y. Bruno, I. Cucchi, E. Cappelli, C. Besnard, T. K. Kim, P. Dudin, M. Hoesch, M. J. Gutmann, A. Georges, R. S. Perry, and F. Baumberger, Nature Communications **9**, 4535 (2018).

[178] L. Das, F. Forte, R. Fittipaldi, C. G. Fatuzzo, V. Granata, O. Ivashko, M. Horio, F. Schindler, M. Dantz, Y. Tseng, D. E. McNally, H. M. Rønnow, W. Wan, N. B. Christensen, J. Pelliciari, P. Olalde-Velasco, N. Kikugawa, T. Neupert, A. Vecchione, T. Schmitt, M. Cuoco, and J. Chang, Physical Review X **8**, 011048 (2018).

[179] H. Fukazawa and Y. Maeno, Journal of the Physical Society of Japan **70**, 460 (2001).

[180] G. Cao, S. McCall, V. Dobrosavljevic, C. S. Alexander, J. E. Crow, and R. P. Guertin, Physical Review B **61**, R5053 (2000).

[181] G. Cao, C. S. Alexander, S. McCall, J. E. Crow, and R. P. Guertin, Journal of Magnetism and Magnetic Materials Proceedings of the International Conference on Magnetism (ICM 2000), **226–230**, 235 (2001).

[182] G. Cao, S. McCall, M. Shepard, J. E. Crow, and R. P. Guertin, Physical Review B **56**, R2916 (1997).

[183] S. Nakatsuji, S.-i. I. Ikeda, and Y. Maeno, Journal of the Physical Society of Japan **66**, 1868 (1997).

[184] C. S. Alexander, G. Cao, V. Dobrosavljevic, S. McCall, J. E. Crow, E. Lochner, and R. P. Guertin, Physical Review B **60**, R8422 (1999).

[185] T. Mizokawa, L. H. Tjeng, G. A. Sawatzky, G. Ghiringhelli, O. Tjernberg, N. B. Brookes, H. Fukazawa, S. Nakatsuji, and Y. Maeno, Physical Review letters **87**, 077202 (2001).

[186] I. Zegkinoglou, J. Strempfer, C. S. Nelson, J. P. Hill, J. Chakhalian, C. Bernhard, J. C. Lang, G. Srajer, H. Fukazawa, S. Nakatsuji, Y. Maeno, and B. Keimer, Physical Review letters **95**, 136401 (2005).

[187] C. G. Fatuzzo, M. Dantz, S. Fatale, P. Olalde-Velasco, N. E. Shaik, B. Dalla Piazza, S. Toth, J. Pelliciari, R. Fittipaldi, A. Vecchione, N. Kikugawa, J. S. Brooks, H. M. Rønnow, M. Grioni, C. Rüegg, T. Schmitt, and J. Chang, Physical Review B **91**, 155104 (2015).

[188] P. Steffens, O. Friedt, P. Alireza, W. G. Marshall, W. Schmidt, F. Nakamura, S. Nakatsuji, Y. Maeno, R. Lengsdorf, M. M. Abd-Elmeguid, and M. Braden, Physical Review B **72**, 094104 (2005).

[189] C. Bergemann, A. P. Mackenzie, S. R. Julian, D. Forsythe, and E. Ohmichi, Advances in Physics **52**, 639 (2003).

[190] H. J. Noh, S. J. Oh, B. G. Park, J. H. Park, J. Y. Kim, H. D. Kim, T. Mizokawa, L. H. Tjeng, H. J. Lin, C. T. Chen, S. Schuppler, S. Nakatsuji, H. Fukazawa, and Y. Maeno, Physical Review B **72**, 052411 (2005).

[191] M. Cuoco, F. Forte, and C. Noce, Physical Review B **73**, 094428 (2006).

[192] Z. Fang, N. Nagaosa, and K. Terakura, Physical Review B **69**, 045116 (2004).

[193] H. Nobukane, K. Yanagihara, Y. Kunisada, Y. Ogasawara, K. Nomura, Y. Asano, and S. Tanda, (2017), arXiv:1703.09459 .

[194] P. L. Alireza, F. Nakamura, S. K. Goh, Y. Maeno, S. Nakatsuji, Y. T. C. Ko, M. Sutherland, S. Julian, and G. G. Lonzarich, Journal of Physics Condensed Matter **22**, 052202 (2010).

[195] S. Nakatsuji and Y. Maeno, Journal of Low Temperature Physics **117**, 1593 (1999).

[196] S. Nakatsuji and Y. Maeno, Physical Review B **62**, 6458 (2000).

[197] S. Nakatsuji and Y. Maeno, Physical Review Letters **84**, 2666 (2000).

[198] O. Friedt, M. Braden, G. André, P. Adelmann, S. Nakatsuji, and Y. Maeno, Physical Review B **63**, 174432 (2001).

[199] V. Anisimov, I. Nekrasov, D. Kondakov, T. Rice, and M. Sigrist, The European Physical Journal B **25**, 191 (2002).

[200] A. Liebsch, Europhysics Letters (EPL) **63**, 97 (2003).

[201] M. Sigrist and M. Troyer, The European Physical Journal B **39**, 207 (2004).

[202] S. Wang and H. Ding, New Journal of Physics **7**, 112 (2005).

[203] J. Baier, P. Steffens, O. Schumann, M. Kriener, S. Stark, H. Hartmann, O. Friedt, A. Revcolevschi, P. G. Radaelli, S. Nakatsuji, Y. Maeno, J. A. Mydosh, T. Lorenz, and M. Braden, Journal of Low Temperature Physics **147**, 405 (2007).

[204] E. Ko, B. J. Kim, C. Kim, and H. J. Choi, Physical Review Letters **98**, 226401 (2007).

[205] G. Q. Liu, Physical Review B **84**, 235136 (2011).

[206] M. Karolak, T. O. Wehling, F. Lechermann, and A. I. Lichtenstein, Journal of Physics: Condensed Matter **23**, 085601 (2011).

[207] P. Steffens, O. Friedt, Y. Sidis, P. Link, J. Kulda, K. Schmalzl, S. Nakatsuji, and M. Braden, Physical Review B **83**, 054429 (2011).

[208] R. D. Shannon, Acta Crystallographica Section A: Foundations of Crystallography **32**, 751 (1976).

[209] D. Dai, H. Xiang, and M.-H. Whangbo, Journal of Computational Chemistry **29**, 2187 (2008).

[210] D. Pincini, S. Boseggia, R. Perry, M. J. Gutmann, S. Riccò, L. S. I. Veiga, C. D. Dashwood, S. P. Collins, G. Nisbet, A. Bombardi, D. G. Porter, F. Baumberger, A. T. Boothroyd, and D. F. McMorrow, Physical Review B **98**, 014429 (2018).

[211] D. A. Keen, M. J. Gutmann, and C. C. Wilson, Journal of Applied Crystallography **39**, 714 (2006).

[212] D. G. Porter, V. Granata, F. Forte, S. Di Matteo, M. Cuoco, R. Fittipaldi, A. Vecchione, and A. Bombardi, Physical Review B **98**, 125142 (2018).

[213] V. E. Dmitrienko, Acta Crystallographica Section A: Foundations of Crystallography Foundations of Crystallography **39**, 29 (1983).

[214] H. Nakao, Y. Wakabayashi, T. Kiyama, Y. Murakami, M. v. Zimmermann, J. P. Hill, D. Gibbs, S. Ishihara, Y. Taguchi, and Y. Tokura, Physical Review B **66**, 184419 (2002).

[215] B. J. Kim, H. Ohsumi, T. Komesu, S. Sakai, T. Morita, H. Takagi, and T. Arima, Science **323**, 1329 (2009).

[216] S. Boseggia, R. Springell, H. C. Walker, H. M. Rønnow, C. Rüegg, H. Okabe, M. Isobe, R. S. Perry, S. P. Collins, and D. F. McMorrow, Physical Review Letters **110**, 117207 (2013).

[217] M. Moretti Sala, S. Boseggia, D. F. McMorrow, and G. Monaco, Physical Review Letters **112**, 026403 (2014).

[218] J. B. Goodenough, *Magnetism and the chemical bond* (Interscience, New York, 1963).

[219] G. Q. Liu, Physical Review B **88**, 104428 (2013).

[220] M. Kurokawa and T. Mizokawa, Physical Review B **66**, 024434 (2002).

[221] A. Damascelli, Z. Hussain, and Z.-X. Shen, Reviews of Modern Physics **75**, 473 (2003).

[222] A. de la Torre, S. McKeown Walker, F. Y. Bruno, S. Riccó, Z. Wang, I. Gutierrez Lezama, G. Scheerer, G. Giriat, D. Jaccard, C. Berthod, T. K. Kim, M. Hoesch, E. C. Hunter, R. S. Perry, A. Tamai, and F. Baumberger, Physical Review Letters **115**, 176402 (2015).

[223] Y. K. Kim, O. Krupin, J. D. Denlinger, A. Bostwick, E. Rotenberg, Q. Zhao, J. F. Mitchell, J. W. Allen, and B. J. Kim, Science **345**, 187 (2014).

[224] B. J. Kim, H. Jin, S. J. Moon, J.-Y. Kim, B.-G. Park, C. S. Leem, J. Yu, T. W. Noh, C. Kim, S.-J. Oh, J. H. Park, V. Durairaj, G. Cao, and E. Rotenberg, Physical Review letters **101**, 076402 (2008).

[225] D. Pincini, L. S. I. Veiga, C. D. Dashwood, F. Forte, M. Cuoco, R. S. Perry, P. Bencok, A. T. Boothroyd, and D. F. McMorrow, (2018), arXiv:1810.11044 .

[226] M. Schmidt, T. R. Cummins, M. Bürk, D. H. Lu, N. Nücker, S. Schuppler, and F. Lichtenberg, Physical Review B **53**, R14761 (1996).

[227] S. J. Moon, M. W. Kim, K. W. Kim, Y. S. Lee, J.-Y. Kim, J.-H. Park, B. J. Kim, S.-J. Oh, S. Nakatsuji, Y. Maeno, I. Nagai, S. I. Ikeda, G. Cao, and T. W. Noh, Physical Review B **74**, 113104 (2006).

[228] D. J. Singh, Physical Review B **52**, 1358 (1995).

[229] M. Moretti Sala, M. Rossi, S. Boseggia, J. Akimitsu, N. B. Brookes, M. Isobe, M. Minola, H. Okabe, H. M. Rønnow, L. Simonelli, D. F. McMorrow, and G. Monaco, Physical Review B **89**, 121101 (2014).

[230] A. Rogalev, J. Goulon, C. Goulon-Ginet, and C. Malgrange, in *Magnetism and Synchrotron Radiation* (Springer, Berlin, Heidelberg, 2001) pp. 60–86.

[231] C. Giles, C. Malgrange, J. Goulon, F. de Bergevin, C. Vettier, E. Dartyge, A. Fontaine, C. Giorgetti, and S. Pizzini, Journal of Applied Crystallography **27**, 232 (1994).

[232] K. V. Klementiev, *XANES dactyloscope for Windows*.

[233] H. H. Wu, S. W. Chen, B. N. Lin, Y. Y. Hsu, J. F. Lee, L. Y. Jang, and H. C. Ku, Journal of Low Temperature Physics **131**, 1193 (2003).

[234] Z. Hu, H. von Lips, M. S. Golden, J. Fink, G. Kaindl, F. M. F. de Groot, S. Ebbinghaus, and A. Reller, Physical Review B **61**, 5262 (2000).

[235] M. O. Krause, Journal of Physical and Chemical Reference Data **8**, 307 (1979).

[236] J. Kim, D. Casa, M. H. Upton, T. Gog, Y.-J. J. Kim, J. F. Mitchell, M. van Veenendaal, M. Daghofer, J. Van Den Brink, G. Khaliullin, and B. J. Kim, Physical Review Letters **108**, 177003 (2012).

[237] J. Kim, M. Daghofer, A. H. Said, T. Gog, J. van den Brink, G. Khaliullin, B. J. Kim, J. Van Den Brink, G. Khaliullin, and B. J. Kim, Nature Communications **5**, 4453 (2014).

[238] S. Boseggia, H. C. Walker, J. Vale, R. Springell, Z. Feng, R. S. Perry, M. M. Sala, H. M. Rønnow, S. P. Collins, and D. F. McMorrow, Journal of Physics: Condensed Matter **25**, 422202 (2013).

[239] G. Jackeli and G. Khaliullin, Physical Review Letters **102**, 017205 (2009).

[240] J.-i. Igarashi and T. Nagao, Physical Review B **88**, 104406 (2013).

[241] J.-i. I. Igarashi and T. Nagao, Physical Review B **89**, 064410 (2014).

[242] J. G. Vale, S. Boseggia, H. C. Walker, R. Springell, Z. Feng, E. C. Hunter, R. S. Perry, D. Prabhakaran, A. T. Boothroyd, S. P. Collins, H. M. Rønnow, and D. F. McMorrow, Physical Review B **92**, 020406 (2015).

[243] I. V. Solovyev, V. V. Mazurenko, and A. A. Katanin, Physical Review B **92**, 235109 (2015).

[244] F. A. Wang and T. Senthil, Physical Review Letters **106**, 136402 (2011).

[245] H. Watanabe, T. Shirakawa, and S. Yunoki, Physical Review Letters **110**, 027002 (2013).

[246] Z. Y. Meng, Y. B. Kim, and H.-Y. Kee, Physical Review Letters **113**, 177003 (2014).

[247] X. Liu, M. P. M. Dean, Z. Y. Meng, M. H. Upton, T. Qi, T. Gog, Y. Cao, J. Q. Lin, D. Meyers, H. Ding, G. Cao, and J. P. Hill, Physical Review B **93**, 241102 (2016).

[248] H. Gretarsson, N. H. Sung, J. Porras, J. Bertinshaw, C. Dietl, J. A. Bruin, A. F. Bangura, Y. K. Kim, R. Dinnebier, J. Kim, A. Al-Zein, M. Moretti Sala, M. Krisch, M. Le Tacon, B. Keimer, and B. J. Kim, Physical Review Letters **117**, 107001 (2016).

[249] M. K. Crawford, M. A. Subramanian, R. L. Harlow, J. A. Fernandez-Baca, Z. R. Wang, and D. C. Johnston, Physical Review B **49**, 9198 (1994).

[250] C. Dhital, T. Hogan, Z. Yamani, C. de la Cruz, X. Chen, S. Khadka, Z. Ren, and S. D. Wilson, Physical Review B **87**, 144405 (2013).

[251] F. Ye, S. Chi, B. C. Chakoumakos, J. A. Fernandez-Baca, T. Qi, and G. Cao, Physical Review B **87**, 140406 (2013).

[252] S. W. Lovesey, D. D. Khalyavin, P. Manuel, L. C. Chapon, G. Cao, and T. F. Qi, Journal of Physics Condensed Matter **24**, 496003 (2012).

[253] G. Cao, J. Bolivar, S. McCall, J. E. Crow, and R. P. Guertin, Physical Review B **57**, R11039 (1998).

[254] S. J. Moon, H. Jin, W. S. Choi, J. S. Lee, S. S. A. Seo, J. Yu, G. Cao, T. W. Noh, and Y. S. Lee, Physical Review B **80**, 195110 (2009).

[255] M. M. Sala, M. Rossi, A. Al-Zein, S. Boseggia, E. C. Hunter, R. S. Perry, D. Prabhakaran, A. T. Boothroyd, N. B. Brookes, D. F. McMorrow, and Others, Physical Review B **90**, 85126 (2014).

[256] N. S. Kini, A. M. Strydom, H. S. Jeevan, C. Geibel, and S. Ramakrishnan, Journal of Physics Condensed Matter **18**, 8205 (2006).

[257] K. M. Shen, F. Ronning, D. H. Lu, F. Baumberger, N. J. Ingle, W. S. Lee, W. Meevasana, Y. Kohsaka, M. Azuma, M. Takano, H. Takagi, and Z. X. Shen, Science **307**, 901 (2005).

[258] K. M. Shen, F. Ronning, D. H. Lu, W. S. Lee, N. J. Ingle, W. Meevasana, F. Baumberger, A. Damascelli, N. P. Armitage, L. L. Miller, Y. Kohsaka, M. Azuma, M. Takano, H. Takagi, and Z. X. Shen, Physical Review Letters **93**, 267002 (2004).

[259] X. J. Zhou, T. Yoshida, D. H. Lee, W. L. Yang, V. Brouet, F. Zhou, W. X. Ti, J. W. Xiong, Z. X. Zhao, T. Sasagawa, T. Kakeshita, H. Eisaki, S. Uchida, A. Fujimori, Z. Hussain, and Z. X. Shen, Physical Review Letters **92**, 187001 (2004).

[260] H. Takagi, B. Batlogg, H. L. Kao, J. Kwo, R. J. Cava, J. J. Krajewski, and W. F. Peck, Physical Review Letters **69**, 2975 (1992).

[261] M. A. Kastner, R. J. Birgeneau, G. Shirane, and Y. Endoh, Reviews of Modern Physics **70**, 897 (1998).

[262] K. Ohgushi, J.-i. Yamaura, H. Ohsumi, K. Sugimoto, S. Takeshita, A. Tokuda, H. Takagi, M. Takata, and T.-h. Arima, Physical Review Letters **110**, 217212 (2013).

[263] L. J. P. Ament, G. Khaliullin, and J. van den Brink, Physical Review B **84**, 020403 (2011).

[264] L. Hozoi, H. Gretarsson, J. P. Clancy, B.-G. Jeon, B. Lee, K. H. Kim, V. Yushankhai, P. Fulde, D. Casa, T. Gog, J. Kim, A. H. Said, M. H. Upton, Y.-J. Kim, and J. van den Brink, Physical Review B **89**, 115111 (2014).

[265] X. Liu, V. M. Katukuri, L. Hozoi, W.-G. Yin, M. P. M. Dean, M. H. Upton, J. Kim, D. Casa, A. Said, T. Gog, T. F. Qi, G. Cao, A. M. Tsvelik, J. van den Brink, and J. P. Hill, Physical Review Letters **109**, 157401 (2012).

[266] J. Dorier, F. Becca, and F. Mila, Physical Review B **72**, 024448 (2005).

[267] A. Kitaev, Annals of Physics January Special Issue, **321**, 2 (2006).

[268] L. Shekhtman, O. Entin-Wohlman, and A. Aharony, Physical Review Letters **69**, 836 (1992).

[269] T. Thio, T. R. Thurston, N. W. Preyer, P. J. Picone, M. A. Kastner, H. P. Jenssen, D. R. Gabbe, C. Y. Chen, R. J. Birgeneau, and A. Aharony, Physical Review B **38**, 905 (1988).

[270] M. Moretti Sala, V. Schnells, S. Boseggia, L. Simonelli, A. Al-Zein, J. G. Vale, L. Paolasini, E. C. Hunter, R. S. Perry, D. Prabhakaran, A. T. Boothroyd, M. Krisch, G. Monaco, H. M. Ronnow, D. F. McMorrow, and F. Mila, Physical Review B **92**, 024405 (2015).

[271] J. Kim, A. H. Said, D. Casa, M. H. Upton, T. Gog, M. Daghofer, G. Jackeli, J. Van Den Brink, G. Khaliullin, B. J. Kim, J. V. D. Brink, G. Khaliullin, and B. J. Kim, Physical Review Letters **109**, 157402 (2012).

[272] S. Boseggia, R. Springell, H. C. Walker, A. T. Boothroyd, D. Prabhakaran, D. Wermeille, L. Bouchenoire, S. P. Collins, and D. F. McMorrow, Physical Review B **85**, 184432 (2012).

[273] S. Boseggia, R. Springell, H. C. Walker, A. T. Boothroyd, D. Prabhakaran, S. P. Collins, and D. F. McMorrow, Journal of Physics: Condensed Matter **24**, 312202 (2012).

[274] A. Cuccoli, T. Roscilde, R. Vaia, and P. Verrucchi, Physical Review Letters **90**, 167205 (2003).

[275] A. Cuccoli, T. Roscilde, V. Tognetti, R. Vaia, and P. Verrucchi, Physical Review B **67**, 104414 (2003).

[276] M. Greven, R. J. Birgeneau, Y. Endoh, M. A. Kastner, M. Matsuda, and G. Shirane, Zeitschrift für Physik B Condensed Matter **96**, 465 (1995).

[277] B. H. Kim, G. Khaliullin, and B. I. Min, Physical Review Letters **109**, 167205 (2012).

[278] N. B. Perkins, Y. Sizyuk, and P. Wölfle, Physical Review B **89**, 035143 (2014).

[279] M. P. M. Dean, G. Dellea, R. S. Springell, F. Yakhou-Harris, K. Kummer, N. B. Brookes, X. Liu, Y.-J. Sun, J. Strle, T. Schmitt, L. Braicovich, G. Ghiringhelli, I. Božović, and J. P. Hill, Nature Materials **12**, 1019 (2013).

[280] M. P. M. Dean, A. J. A. James, A. C. Walters, V. Bisogni, I. Jarrige, M. Hücker, E. Giannini, M. Fujita, J. Pelliciari, Y. B. Huang, R. M. Konik, T. Schmitt, and J. P. Hill, Physical Review B **90**, 220506 (2014).

[281] M. Guarise, B. D. Piazza, H. Berger, E. Giannini, T. Schmitt, H. M. Rønnow, G. A. Sawatzky, J. van den Brink, D. Altenfeld, I. Eremin, and M. Grioni, Nature Communications **5**, 5760 (2014).

[282] S. Bahr, A. Alfonsov, G. Jackeli, G. Khaliullin, A. Matsumoto, T. Takayama, H. Takagi, B. Büchner, and V. Kataev, Physical Review B **89**, 180401 (2014).

[283] Y. Gim, A. Sethi, Q. Zhao, J. F. Mitchell, G. Cao, and S. L. Cooper, Physical Review B **93**, 24405 (2016).

[284] D. Pincini, J. G. Vale, C. Donnerer, A. de La Torre, E. C. Hunter, R. Perry, M. Moretti Sala, F. Baumberger, and D. F. McMorrow, Physical Review B **96**, 075162 (2017).

[285] M. Fujita, H. Hiraka, M. Matsuda, M. Matsuura, J. M. Tranquada, S. Wakimoto, G. Xu, and K. Yamada, Journal of the Physical Society of Japan **81**, 011007 (2012).

[286] B. Vignolle, S. M. Hayden, D. F. McMorrow, H. M. Rønnow, B. Lake, C. D. Frost, and T. G. Perring, Nature Physics **3**, 163 (2007).

[287] S. W. Cheong, G. Aeppli, T. E. Mason, H. Mook, S. M. Hayden, P. C. Canfield, Z. Fisk, K. N. Clausen, and J. L. Martinez, Physical Review Letters **67**, 1791 (1991).

[288] X. Chen, J. L. Schmehr, Z. Islam, Z. Porter, E. Zoghlin, K. Finkelstein, J. P. C. Ruff, and S. D. Wilson, Nature Communications **9**, 103 (2018).

[289] J. Porras, J. Bertinshaw, H. Liu, G. Khaliullin, N. H. Sung, J. W. Kim, S. Francoual, P. Steffens, G. Deng, M. M. Sala, A. Effimenko, A. Said, D. Casa, X. Huang, T. Gog, J. Kim, B. Keimer, and B. J. Kim, (2018), arXiv:1808.06920 .

[290] M. Le Tacon, G. Ghiringhelli, J. Chaloupka, M. M. Sala, V. Hinkov, M. W. Haverkort, M. Minola, M. Bakr, K. J. Zhou, S. Blanco-Canosa, C. Monney, Y. T. Song, G. L. Sun, C. T. Lin, G. M. De Luca, M. Salluzzo, G. Khaliullin, T. Schmitt, L. Braicovich, and B. Keimer, Nature Physics **7**, 725 (2011).

[291] M. Le Tacon, M. Minola, D. C. Peets, M. Moretti Sala, S. Blanco-Canosa, V. Hinkov, R. Liang, D. A. Bonn, W. N. Hardy, C. T. Lin, T. Schmitt, L. Braicovich, G. Ghiringhelli, and B. Keimer, Physical Review B **88**, 020501 (2013).

[292] N. S. Headings, S. M. Hayden, R. Coldea, and T. G. Perring, Physical Review Letters **105** (2010), 10.1103/PhysRevLett.105.247001.

[293] B. Keimer, R. J. Birgeneau, A. Cassanho, Y. Endoh, M. Greven, M. A. Kastner, and G. Shirane, Zeitschrift für Physik B Condensed Matter **91**, 373 (1993).

[294] M. W. Haverkort, Physical Review Letters **105**, 167404 (2010).

[295] H. Liu and G. Khaliullin, (2018), arXiv:1808.06919 .

[296] E. F. Bertaut, Journal of Applied Physics **33**, 1138 (1962).

[297] E. F. Bertaut, Acta Crystallographica Section A: Crystal Physics, Diffraction, Theoretical and General Crystallography **24**, 217 (1968).

[298] E. F. Bertaut, Le Journal de Physique Colloques **32**, 462 (1971).

[299] E. Bertaut, Journal of Magnetism and Magnetic Materials **24**, 267 (1981).

[300] Y. A. Izyumov, V. E. Naish, and R. P. Ozerov, *Neutron Diffraction of Magnetic Materials* (Springer US, Consultants Bureau, New York, 1991).

[301] C. J. Bradley and A. P. Cracknell, *The mathematical theory of symmetry in solids : representation theory for point groups and space groups* (Clarendon Press, Oxford, 1972).

[302] A. P. Cracknell, *Magnetism in crystalline materials; applications of the theory of groups of cambiant symmetry* (Pergamon Press, Oxford, 1975).

[303] A. S. Wills, Physical Review B **63**, 064430 (2001).

[304] A. Wills, Physica B: Condensed Matter **276-278**, 680 (2000).

[305] O. Kovalev, *Representations of the crystallographic space groups: irreducible representations, induced representations, and corepresentations.* (Gordon and Breach Science Publishers, Switzerland, 1993).

[306] A. Taroni, S. T. Bramwell, and P. C. W. Holdsworth, Journal of Physics: Condensed Matter **20**, 275233 (2008).

[307] M. P. H. Thurlings, E. Frikkee, and H. W. de Wijn, Physical Review B **25**, 4750 (1982).

[308] J. M. Kosterlitz and D. J. Thouless, Journal of Physics C: Solid State Physics **6**, 1181 (1973).

[309] P. Liu, S. Khmelevskyi, B. Kim, M. Marsman, D. Li, X.-Q. Chen, D. D. Sarma, G. Kresse, and C. Franchini, Physical Review B **92**, 54428 (2015).

[310] L. Giovanelli, A. Savoyant, M. Abel, F. Maccherozzi, Y. Ksari, M. Koudia, R. Hayn, F. Choueikani, E. Otero, P. Ohresser, J.-M. Themlin, S. S. Dhesi, and S. Clair, The Journal of Physical Chemistry C **118**, 11738 (2014).

[311] E. M. Pärschke and R. Ray, (2018), arXiv:1802.04158 .

[312] L. Fruchter, D. Colson, and V. Brouet, Journal of Physics: Condensed Matter **28**, 126003 (2016).

[313] S. J. Moon, H. Jin, K. W. Kim, W. S. Choi, Y. S. Lee, J. Yu, G. Cao, A. Sumi, H. Funakubo, C. Bernhard, and T. W. Noh, Physical Review Letters **101**, 226402 (2008).